Georgia Tech Sponsored Research

6383003

Project	E-20-W29	Z87
Project director	Zureick	Abdul - Hamid
Research unit	Civil Engr	
Title	Curved Steel Bridge Research	
Project date	4/1/2000	

28

✓

E-20-W3

CURVED STEEL BRIDGE RESEARCH PROJECT

EVALUATION OF MOMENT-SHEAR TEST SPECIMENS

Narin Phoawanich, Donald W. White and Abdul Hamid Zureick
Georgia Institute of Technology
July 2, 1999

EXECUTIVE SUMMARY

The objective of this research is to determine the influence of shear on the strength of curved steel bridge I girders. This includes evaluation of: (1) shear capacity for high levels of shear in the presence of low bending moment, (2) interaction between flexural and shear strengths for high levels of combined bending and shear, in which case, the magnitude of the shear force may cause some reduction in the flexural capacity, and (3) influence of shear on the bending strength for low levels of shear combined with large moments, in which case, the moment gradient associated with the presence of shear can result in an increase in the capacity over that attained under pure bending.

In a companion report by the authors (Phoawanich, et al. 1999), a single-girder test configuration is developed, results from analyses of girders subjected to high shear forces are presented, and four experimental shear capacity tests are proposed. This report focuses on the development and analysis of eight additional experimental tests needed to verify and quantify the interrelationships between flexure and shear in curved bridge I girders – items (2) and (3) above. Two values of the web-panel aspect ratio d_0/D (3.0 and 1.5) and two values of L/R (0.057 and 0.10) are targeted. Furthermore, two tests are proposed for each combination of these variables: one test at a moment-shear ratio for which the interaction between the moment and shear strengths is expected to be a maximum, and a second test at a moment-shear ratio for which the moment capacity is maximized based on finite element predictions. A symmetric girder cross-section with a D/t_w of 153.6 is targeted in all of the suggested tests.

The significance of the above test variables is as follows. A d_0/D of 3.0 is defined as the limit between a stiffened and unstiffened girder in the current *AASHTO Guide Specifications for Horizontally Curved Highway Bridges*, and this ratio is considered to be unstiffened in the *Recommended Specifications for Steel Curved-Girder Bridges*. Also, L/R = 0.057 is just below the limit at which the *Recommended Specifications* suggest that a curved girder may be designed as a tangent girder, and 0.10 is the current maximum L/R allowed in both the *AASHTO Guide Specifications* and the *Recommended Specifications*. A D/t_w of 153.6 is selected largely because there have been no tests to date of curved unstiffened web panels subjected to high shear at web slenderness ratios larger than about 70. As a result, the *Recommended Specifications* limit the web slenderness to 100 for curved girders with unstiffened web panels and a radius of curvature less than 700 ft. Furthermore, they restrict the web-panel aspect ratio to

$d_o/D \leq 1.0$ for girders designed with stiffened web panels. Also, $D/t_w = 153.6$ is close to the maximum limits on D/t_w for unstiffened tangent girders in the *AASHTO LRFD Specifications* and for transversely stiffened curved girders in the *Recommended Specifications*. The finite element predictions summarized in this report indicate significant increases in the moment capacity due to moment-gradient effects at low levels of shear force, and only minor interaction between the bending and shear strengths as the bending to shear ratios (M/V) is decreased and the shear capacity of the girder is approached. The proposed studies will test the behavior of curved girders at the above limits, and they will provide necessary verification of the finite element models to allow researchers to proceed confidently with a broad range of parametric studies.

The complete set of proposed experimental tests, including the shear tests evaluated in (Phoawanich et al. 1999), is summarized in Table A. The finite element predictions for each of the shear studies are summarized in the companion report. The overall layout and arrangement of the loads and supports for the moment-shear tests are the same as that of the companion report; however, the ratios of the loads on the two actuators are varied in these tests such that the behavior for different moment-shear ratios can be investigated. The moment-shear studies have a flange slenderness b/t_f of 23.3, and a ratio of the web area to the compression flange area A_w/A_f of 1.36. In contrast, the shear capacity tests have a larger b/t_f of 24.5 and a smaller A_w / A_f of 0.8, to accommodate large shear forces while holding to certain limits on the flange warping stresses.

Table A. Complete set of proposed experimental tests ($D/t_w = 153.6$ for all the tests).

Test	**Coincident moment**	**d_o / D**	**L/R**	**A_w/A_f**	**b/t_f**
S1-0.06	Low	3.0	0.057	0.8	24.5
S1-0.10	Low	3.0	0.10	0.8	24.5
S1-S-0.06	Low	1.5	0.057	0.8	24.5
S1-S-0.10	Low	1.5	0.10	0.8	24.5
MS1-0.06	Intermediate	3.0	0.057	1.36	23.3
MS1-0.10	Intermediate	3.0	0.10	1.36	23.3
MS1-S-0.06	Intermediate	1.5	0.057	1.36	23.3
MS1-S-0.10	Intermediate	1.5	0.10	1.36	23.3
MS2-0.06	High	3.0	0.057	1.36	23.3
MS2-0.10	High	3.0	0.10	1.36	23.3
MS2-S-0.06	High	1.5	0.057	1.36	23.3
MS2-S-0.10	High	1.5	0.10	1.36	23.3

INTRODUCTION

The presence of shear force can cause either a positive or a negative effect on the load capacity of a curved steel I girder. If the shear force is large, but the concurrent bending moment is small, the strength can be governed by the shear capacity of the curved web panel. This situation can exist typically at end support locations, where the end moment within the girder is zero. Alternatively, if both the shear and the bending moment are large, it is possible that there may be an interaction between the shear and bending strengths, such that the magnitude of the shear force causes some reduction in the flexural capacity. This situation can occur at interior supports of continuous-span girders. Finally, for low levels of shear combined with large bending moments, the moment gradient associated with the presence of shear can result in an increase in the moment capacity over that attained under pure bending.

Although there have been various important contributions to the state-of-the-art, including (FHWA, 1996) and (Lee and Yoo, 1998), the shear capacity of curved steel I girders still is not well understood. For instance, at the present time, there have been no tests of curved unstiffened web panels subjected to high shear at web slenderness ratios greater than about 70. As a result, the *Recommended Specifications for Steel Curved-Girder Bridges* (Hall and Yoo, 1998) limit the web slenderness to 100 for girders with unstiffened web panels and a radius of curvature less than 700 ft. Also, they limit the aspect ratio of the web panels, d_o/D, to a maximum value of one for girders designed with stiffened web panels.

Furthermore, for curved girders, the interaction between the shear and moment strengths at high levels of combined shear and bending has not been studied in detail. The *AASHTO Guide Specifications* and the *Recommended Specifications* do not account for an interaction between the bending and shear strengths, whereas the current AASHTO tangent girder specifications (AASHTO 1997 & 1998) assume a simple linear interaction between the moment and shear strengths between 0.75 of the nominal bending strength and 0.60 of the nominal shear strength. The AASHTO interaction equations are based in large part on (Cooper et al. 1978) and (Basler 1961b). A succinct derivation of this interaction relationship is presented in (Salmon and Johnson 1996). This derivation shows that the AASHTO linear interaction equation is a close approximation of a nonlinear equation obtained by assuming that the shear stress is equal to zero within the portion of the web which participates with the flanges in flexure (see Fig. 1). The nonlinear relationship is essentially linear for $A_w/A_f \geq 2$. Although this interaction relationship is developed based on the assumption of compact section behavior and elastic-perfectly plastic material response, it has been applied to describe the interaction between the ultimate shear and moment capacities of plate girders with non-compact webs. Basler (1961b) has been shown some agreement between test data and the interaction equation applied in this way. Basler (1961b) also developed a more refined approximation of the interaction between the moment and shear strengths (strictly applicable only for compact sections and elastic-perfectly plastic material behavior) by assuming constant shear and bending stresses (τ and σ) within the web, as shown in Fig. 2, and basing the value of these stresses on the Mises yield condition $\sigma^2 + 3\tau^2 = F_y^2$.

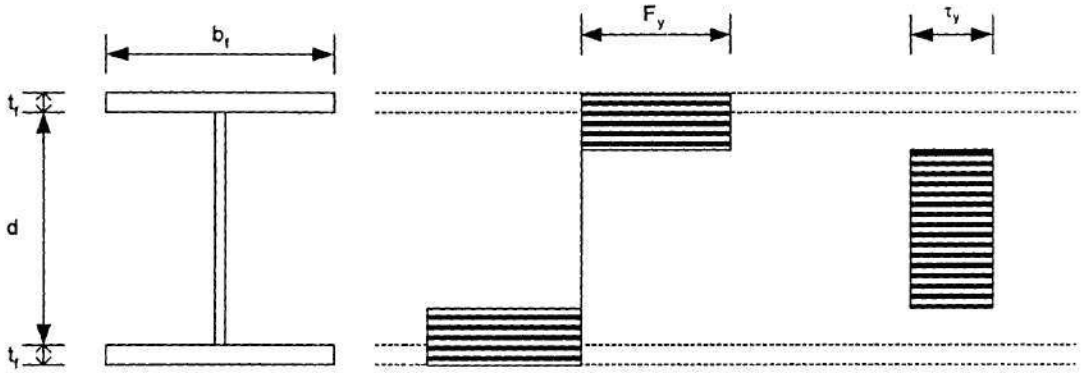

Figure 1. Basis of AASHTO moment-shear interaction equations.

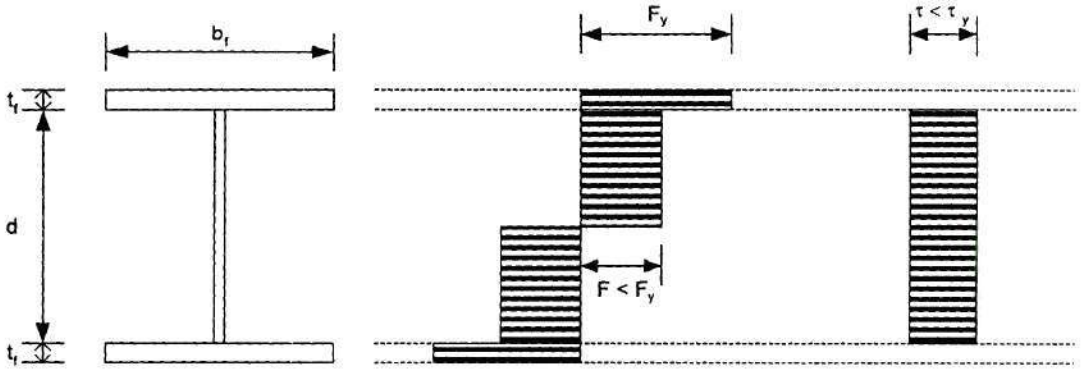

Figure 2. Basler's refined model for moment-shear interaction.

Finally, the positive effect that moment gradients can have on the moment capacity is well recognized in the design of tangent girders. This effect is accounted for through the parameter C_b in the current AASHTO Bridge Design Specifications (AASHTO 1997 & 1998). However, this positive effect is not accounted for in any of the current design specifications for curved bridge girders.

This report presents the development and analyses of eight experimental tests needed to verify and quantify the interrelationships between flexure and shear in curved bridge I girders. The proposed tests include the consideration of stiffened and unstiffened web panels, two different L/R ratios, and two different loading configurations involving intermediate shear and bending moment, and low shear with high bending moment. The next section of the report discusses the overall layout and arrangement of the loads and supports for these tests. This is followed in Section 3 by an overview of the proposed test

specimens. Section 4 then presents the results of a detailed parametric study that the authors have conducted to ascertain the interaction relationships between the bending and shear capacities for the proposed specimens. This parametric study is used to select the specific loading and moment/shear ratios to be applied in the proposed experimental tests. In addition to providing information on the moment-shear interaction behavior, the data from this section provides specific information regarding the effect of horizontal curvature, as represented by the parameter L/R. Finally, Section 5 summarizes details of the predicted behavior for each of the proposed moment-shear experiments. Appendix 1 discusses detailed finite element modeling decisions behind the analysis predictions, and Appendix 2 summarizes various studies that have been conducted to investigate the sensitivity of the finite element predictions to variations or uncertainties in certain parameters.

2. OVERALL LAYOUT AND ARRANGEMENT OF TESTS

The primary layout and arrangement suggested for all the tests to be considered in the present study is shown in Fig. 3. This is a three-span test configuration in which the center span (span 2-3) contains the "test girder." The outside spans (spans 1-2 and 3-4) are reinforced, by increasing the thickness of the flanges and adding transverse stiffeners, such that they do not fail prior to the failure of span 2-3. Vertical loads of P_2 and $P_4 = \alpha P_2$ are applied at locations 2 and 4, and vertical supports are positioned at locations 1 and 3. By varying the ratio of these loads, $\alpha = P_4/P_2$, a complete range of the maximum moment-shear force ratio (M/V) may be developed within the test span. Radial braces are provided at the top and the bottom of the web at the vertical supports and at the load locations. This effectively simulates the limit-states behavior of an individual unsupported segment of a curved girder, including the constraint provided by the other portions of the bridge at the ends of this segment. These constraints are idealized as follows: the web of the girder is effectively held in the vertical position at the location of the crossframes, and the critical unsupported segment is continuous with the adjacent segments. The effect of vertical loadings that might be applied directly to the critical unsupported segment is not considered by this arrangement.

Two values are considered for the radius of curvature in the proposed tests, R = 208.75 ft. and 120 ft., and the unsupported span lengths are all equal to 12 ft. in each of the tests. The value 208.75 is equal to the radius of curvature for the test specimens in the bridge test being conducted at the FHWA Turner-Fairbanks Laboratory. However, the span length of 12 ft. is slightly shorter than the unsupported length of 15.65 ft. employed for the bending test specimens. This shorter length is necessary such that the web shear strength can be developed in the shear capacity tests without generating excessive flange warping stresses. These selected L and R values give L/R ratios of 0.057 and 0.10 respectively. The value of L/R = 0.057 is just below the limit at which the *Recommended Specifications* suggest that a curved girder may be designed as a tangent girder, and 0.10 is the current maximum L/R allowed in both the *AASHTO Guide Specifications* and the *Recommended Specifications*. All of the proposed tests have a web slenderness ratio, D/t_w ,of 153.6. This value is selected largely because there have been no tests to date of curved unstiffened web panels subjected to high shear at web

slenderness ratios larger than about 70. As a result, the *Recommended Specifications* limit the web slenderness to 100 for curved girders with unstiffened web panels and a radius of curvature less than 700 ft. Furthermore, they restrict the aspect ratio of the web panels, d_o/D, to a maximum value of one for girders with stiffened web panels. Also, D/t_w = 153.6 is close to the maximum limits on D/t_w for unstiffened tangent girders in (AASHTO 1998) and for transversely stiffened curved girders in the *Recommended Specifications* (Hall and Yoo 1998).

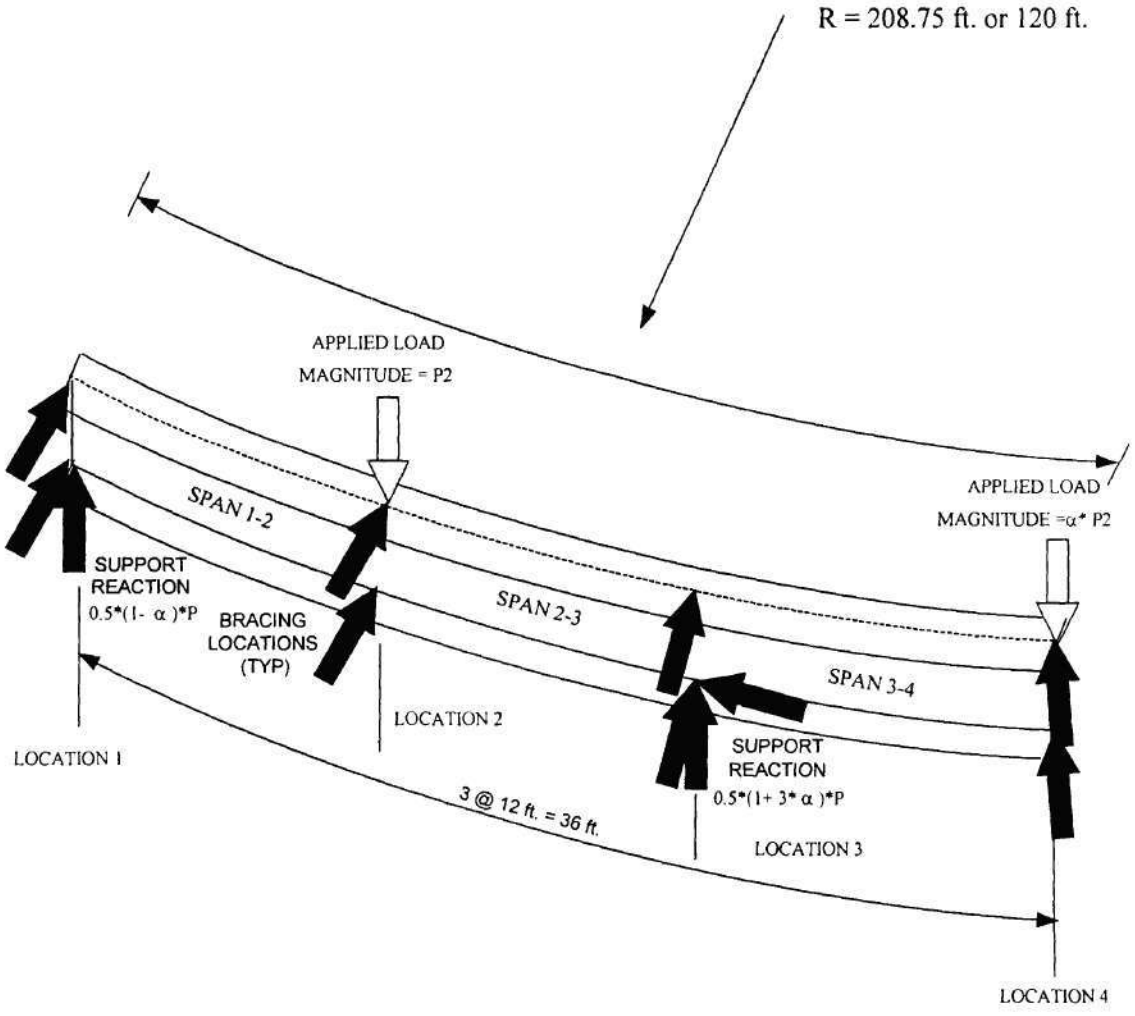

Figure 3. Primary test configuration.

Figure 4 illustrates the influence of the parameter α on the values of the shear and bending moment within the three unsupported lengths of the test specimen shown in Fig. 3.

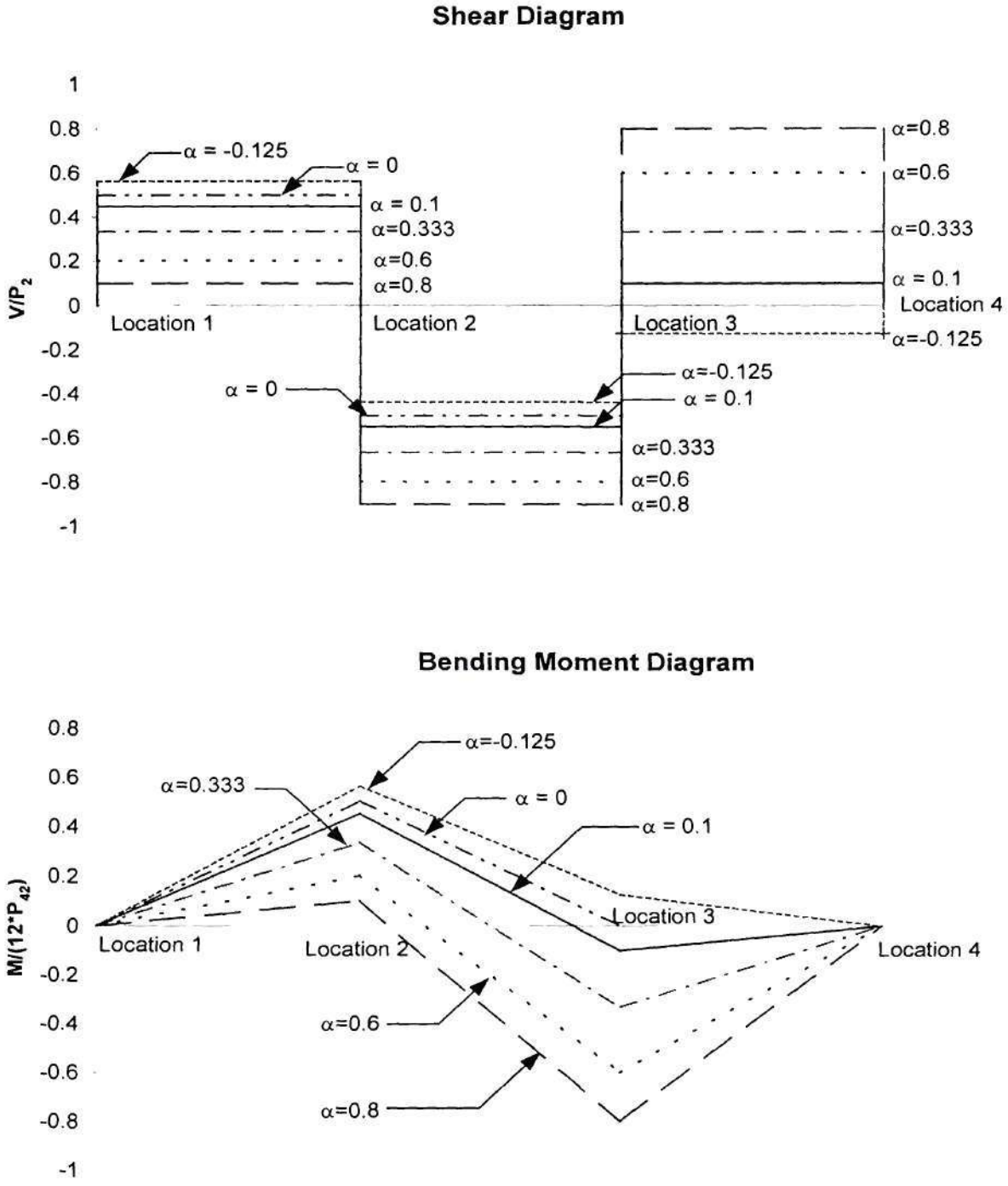

Figure 4. Shear and bending moment diagram for various α.

From Fig. 4, it can be seen that as the value of α increases, the shear force in span 1-2 decreases. However the shear forces within spans 2-3 and 3-4 increase with increasing α. Also, as shown by the bending moment diagrams in Fig. 4, when α is less than 0.333, the maximum moment occurs at location 2, which is one of the loading locations.

Furthermore, as long as α is greater than zero, there is a negative moment (compression in the bottom flange) over the support at location 3. For $\alpha = 0.333$, equal and opposite maximum moments occur at locations 2 and 3. Finally, for $\alpha > 0.333$, the maximum moment occurs at location 3. Most important to the issues of moment-shear interaction, the ratio of the moment to the shear (M/V) changes in the test span as a function of α. The lowest value of M/V occurs within span 2-3. When $\alpha = 0.333$ (see Fig. 5). Therefore, this value of α is selected for the shear capacity tests in the companion report (Phoawanich, et al. 1999). Furthermore, the ratio M/V increases with increases in the value of $|\alpha - 0.333|$. That is, for increasing values of α larger than 0.333, M/V increases; and, for decreasing values of α smaller than 0.333, M/V increases. Obviously, as M/V increases, the mode of failure of the specimen tends to change from one that is dominated by shear to one that is dominated by flexure.

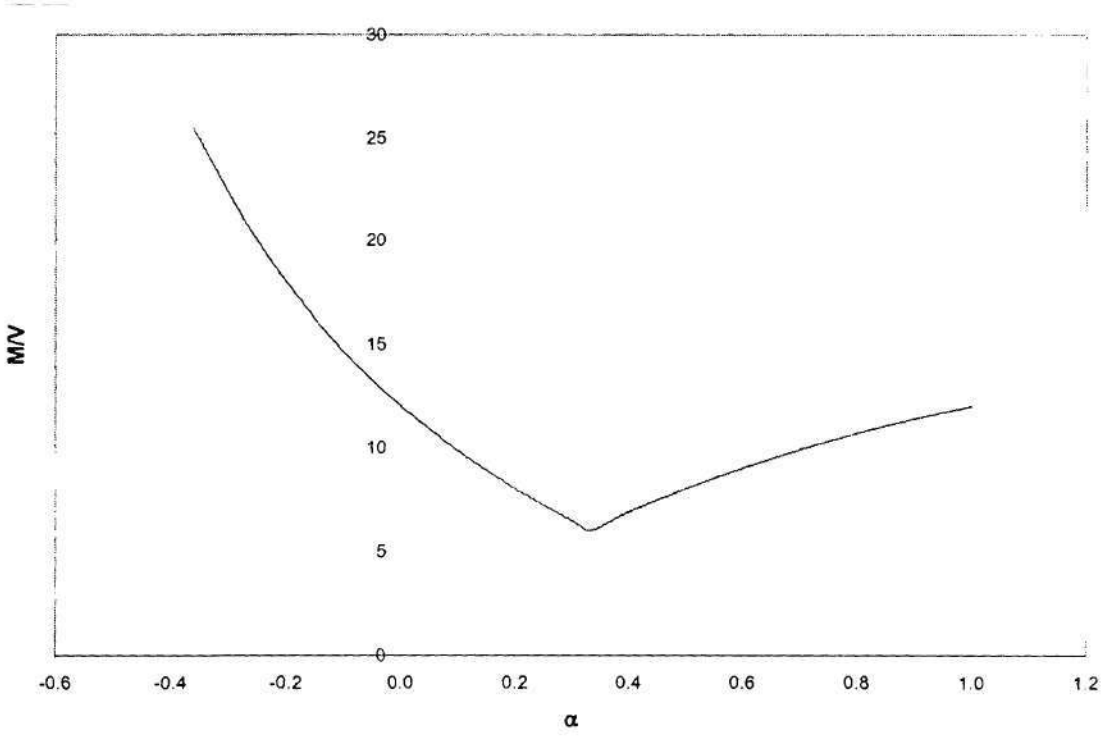

Figure 5. M/V in the test span as a function of α.

For the case of $\alpha = 0$, models of the equivalent three-point bending tests (see Fig. 6) have been analyzed and compared to models of a three-span test configuration (see Fig. 3). The results show that, as might be expected, the maximum applied load P_2 predicted by the two models is indistinguishable. Therefore, for $\alpha = 0$, a three-point bending specimen would be the most appropriate for experimental testing.

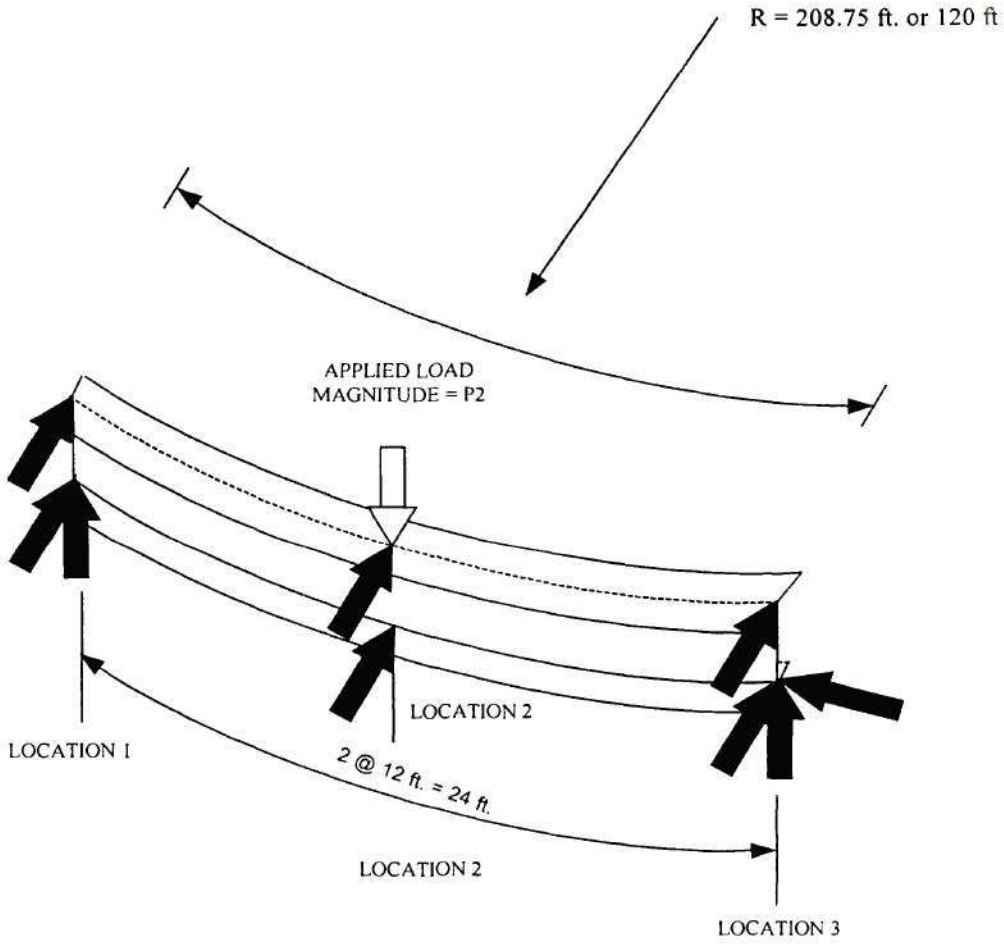

Figure 6. Three-point bending test configuration.

3. OVERVIEW OF MOMENT-SHEAR TEST SPECIMENS

3.1 UNSTIFFENED TEST SPECIMENS

An elevation of the unstiffened three-point bending test specimens (equivalent to the primary test specimens with $\alpha = 0$) is shown in Fig. 7 whereas an elevation of the more general unstiffened test specimens is shown in Fig. 8. The more general or primary specimen geometry of Fig.8 is very similar to the geometry of the unstiffened shear test specimens of the companion report (Phoawanich, et al. 1999). However, spans 1-2 and 2-4 are reinforced for the moment-shear test to prevent the outer spans from failing before the test span reaches its capacity for some values of α. Also, the cross-section of the moment-shear tests has a b/t_f of 23.3 and an A_w/A_f of 1.36 versus corresponding values of 2.45 and 0.8 for the shear test specimens. The flanges were increased in size for the shear test to increase their moment capacities and reduce the flange warping stresses.

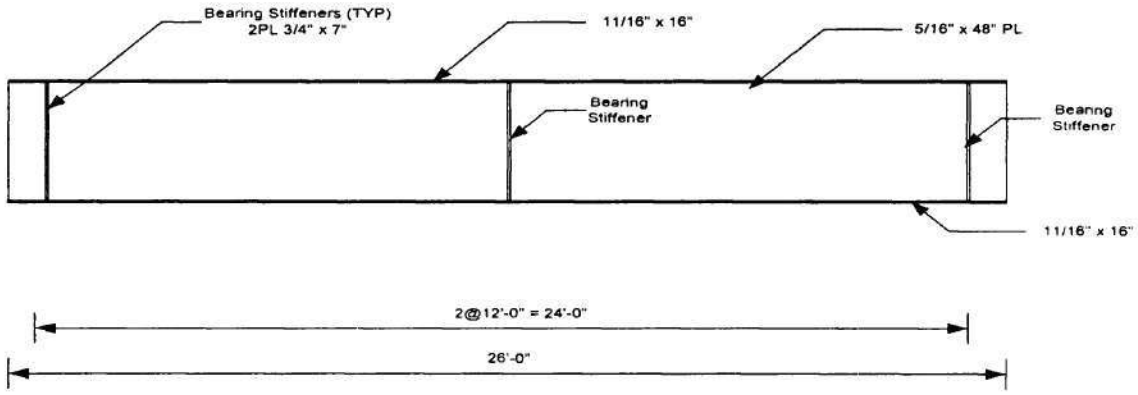

Figure 7. Unstiffened test specimen for three-point bending test.

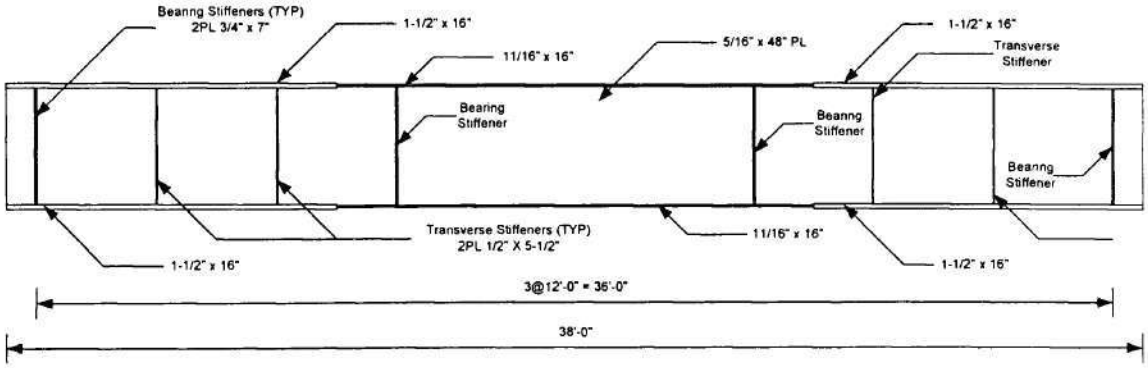

Figure 8. Unstiffened test specimen for $\alpha \neq 0$.

The primary purpose of this test is to determine the coincident shear and moment capacities of curved unstiffened web panels with a web slenderness ratio of approximately 150.

3.2 STIFFENED TEST SPECIMENS

The stiffened moment-shear test specimens are configured by placing a single transverse stiffener at the center of the test panel of the unstiffened test specimens (see Figs. 9 and 10). This produces a web panel aspect ratio of $d_0/D = 1.5$. Otherwise, the stiffened test specimens have the same cross-section geometry and overall layout as the unstiffened test specimens.

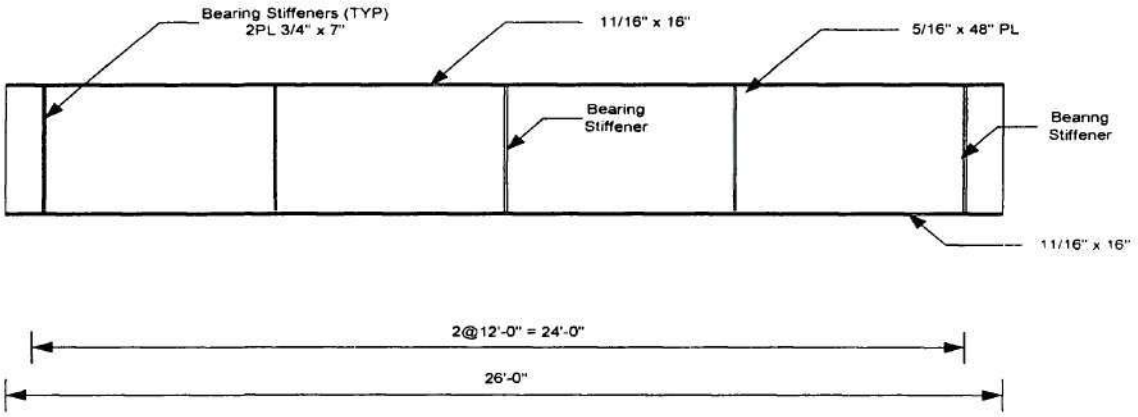

Figure 9. Stiffened test specimen for three-point bending test.

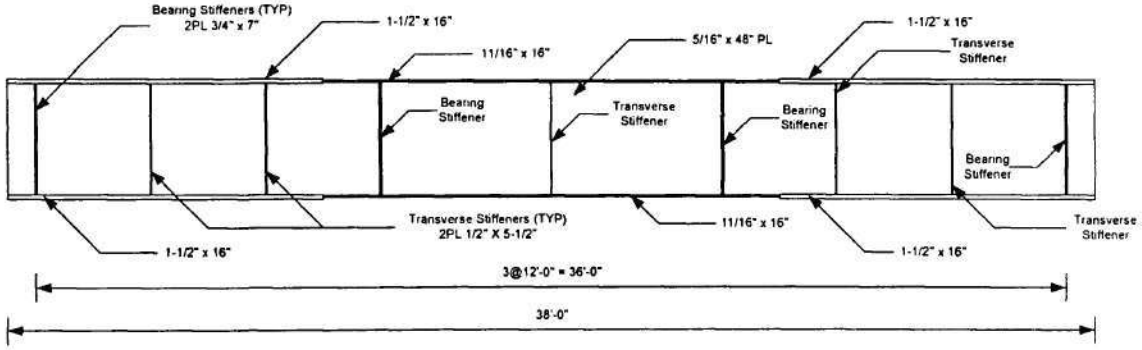

Figure 10. Stiffened test specimen for $\alpha \neq 0$.

4. PARAMETRIC STUDY

A large number of tests with different values of the load parameter $\alpha = P_2 / P_4$ and corresponding values of M/V (see Fig. 3) are necessary to construct the "true" interaction diagram, and thus to understand the detailed interaction behavior between moment and shear strength. In the opinion of the authors, this interaction curve can best be constructed by conducting a limited number of experimental tests, which can then be used to verify refined finite element models, and then to generate the large number of points needed to construct the strength interaction curve by finite element analysis. However, the initial problem is to define the parameters for the limited experimental tests. The shear tests described in the companion report (Phoawanich et al. 1999) produce one point on the moment-shear interaction curve for each of the shear specimens. In the introduction, we have suggested that two different loading configurations should be executed in the experimental moment-shear tests, producing two points on the moment-shear interaction curve for each of these specimens. Based on the shear test results, it is expected that we will be able to confidently compute the shear capacity of the moment-shear specimens using FEA. Therefore, two points that may be of greatest interest for the moment-shear experimental tests might be: (1) the point associated with the largest moment-shear interaction, which would be located approximately along a 45 degree line in a plot of normalized V/V_u versus M/M_u, and (2) the point at which the largest moment capacity is reached (due to moment-gradient effects). It is important to predict these two points, as well as other possible target points for the experimental tests, so that the load ratio $\alpha = P_2 / P_4$ can be finalized. This is one of the goals of this section. This section presents the results of analyses of each of the four test specimens described in Section 3 for a range of α values. Also, the analysis results for the specimens with different L/R ratios are compared to quantify the effect of the different horizontal curvatures for the stiffened and unstiffened girders.

Figures 11 through 22 show the results of these parametric studies. Three different normalized plots (V/V_u versus M/M_u) are shown for each of the test specimens, where V is the maximum shear attained within the test segment, M is the maximum moment attained within the test segment, and V_u and M_u are ultimate shear and moment capacities calculated as discussed below. Figures 11-13 are for the unstiffened specimen with L/R = 0.057, Figs. 14-16 are for the unstiffened specimen with L/R = 0.10, Figs. 17-19 are for the stiffened specimen with L/R = 0.057, and Figs. 20-22 are for the stiffened specimen with L/R = 0.10. In all of these figures, values of M/V and α are shown for each of the FEA data points (V/V_u, M/M_u) within the key for the plot. In each of these sets of plots, the ultimate shear capacity V_u is obtained in two different ways. In the first two figures of each set, V_u is calculated for the corresponding moment-shear specimen using $\alpha = 1/3$. This loading ratio is the same as that proposed for the shear tests in the companion report. In the third plot, V_u is calculated using the shear capacity equations from the *Recommended Specifications* (Hall and Yoo 1998). These equations are equivalent to the shear capacity equations in the *AASHTO Guide Specifications* (AASHTO 1993), but the *Recommended Specifications* consider web panels with $d_o / D > 1$ as unstiffened. In the first figure of each of the sets of plots, M_u is calculated based on equations proposed by Barth and White (1997) for tangent girders. These equations do not account directly for

moment-gradient effects, but their applicability it restricted to a certain maximum lateral brace spacing (which depends on the moment gradient), and within this limit, they have good accuracy. In the second figure of each set, M_u is obtained using the *AASHTO LRFD* provisions for tangent girders (AASHTO 1998). These moment capacity equations account for a moment-gradient effect, based on the C_b parameter. However, for short spacing of lateral braces and/or large moment gradient, the C_b parameter does not affect the computed bending strength. Finally, in the third figure of each set, M_u is obtained from the moment capacity equations of the *Recommended Specifications* (Hall and Yoo 1998). These equations are equivalent to the corresponding moment capacity equations in the *AASHTO Guide Specifications* (AASHTO 1993).

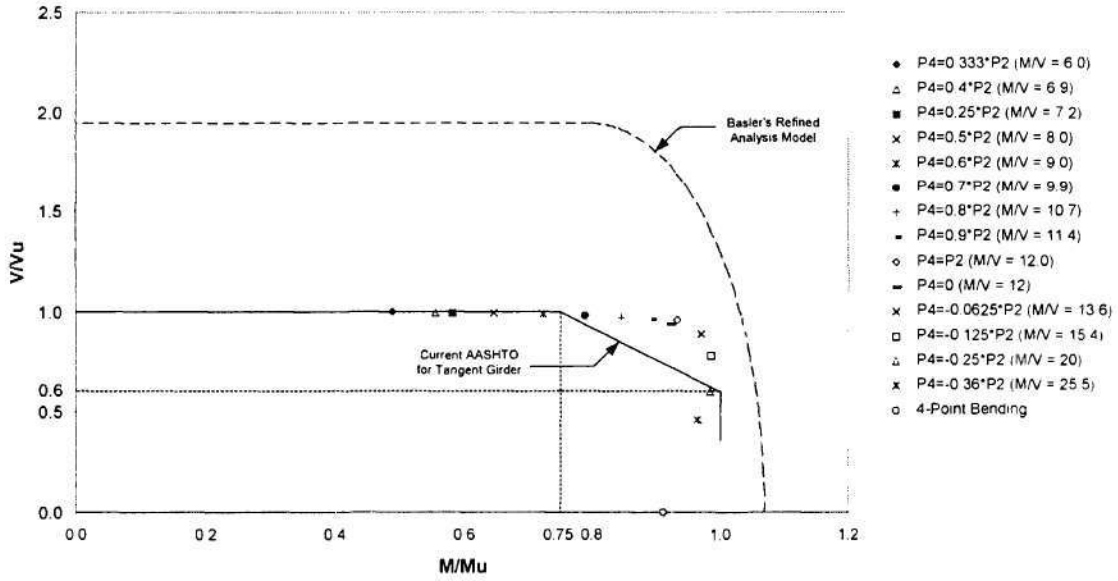

Figure 11. V/V_u versus M/M_u for the unstiffened specimens with $L/R = 0.057$ (V_u obtained by FEA and M_u calculated from (Barth and White 1997)).

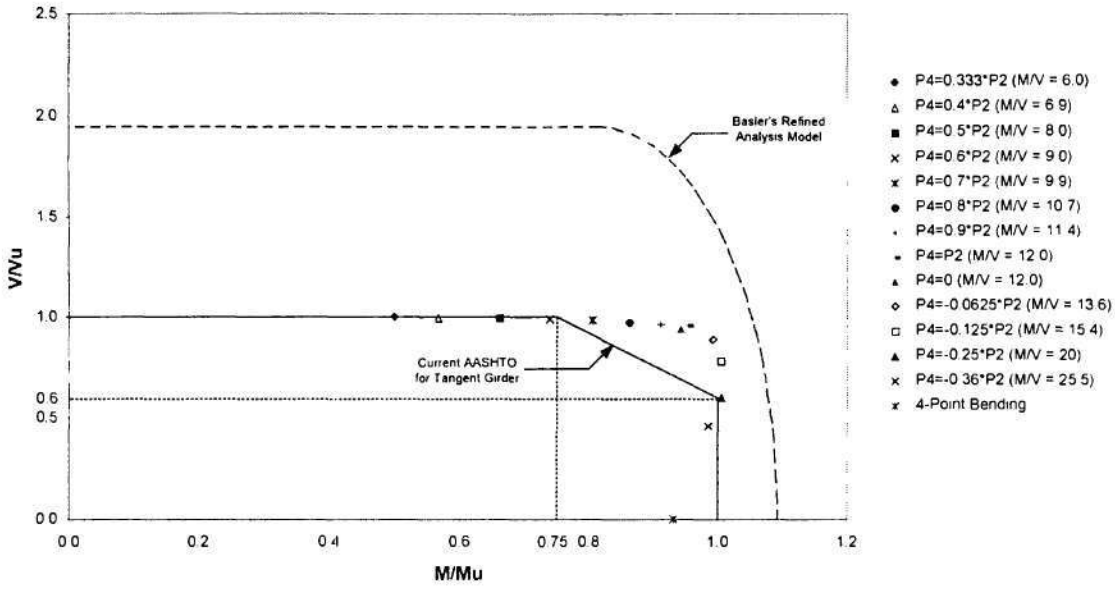

Figure 12. V/V_u versus M/M_u for the unstiffened specimens with L/R = 0.057 (V_u obtained by FEA and M_u calculated from AASHTO (1998)).

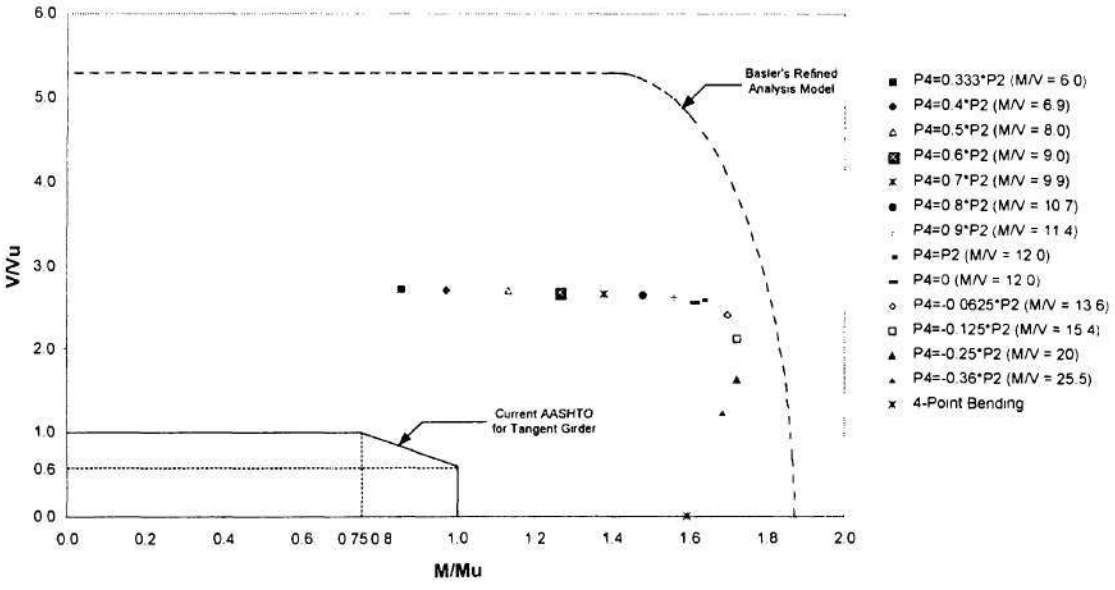

Figure 13. V/V_u versus M/M_u for the unstiffened specimens with L/R = 0.057 (V_u and M_u calculated from the *Recommended Specifications for Steel Curved-Girder Bridge* (Hall and Yoo1998)).

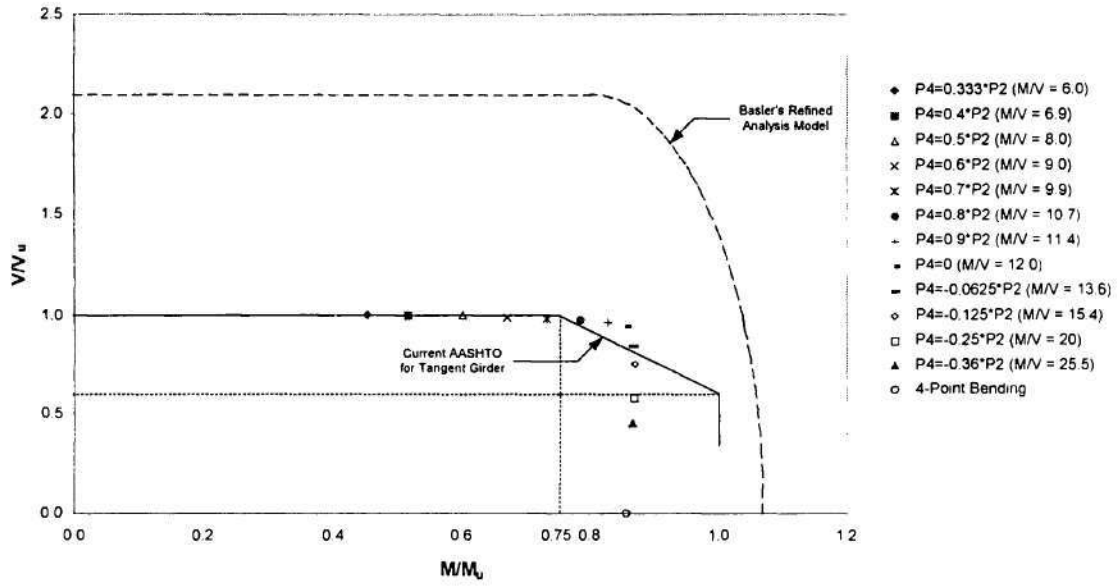

Figure 14. V/V_u versus M/M_u for the unstiffened specimens with L/R = 0.10 (V_u obtained by FEA and M_u calculated from (Barth and White1997)).

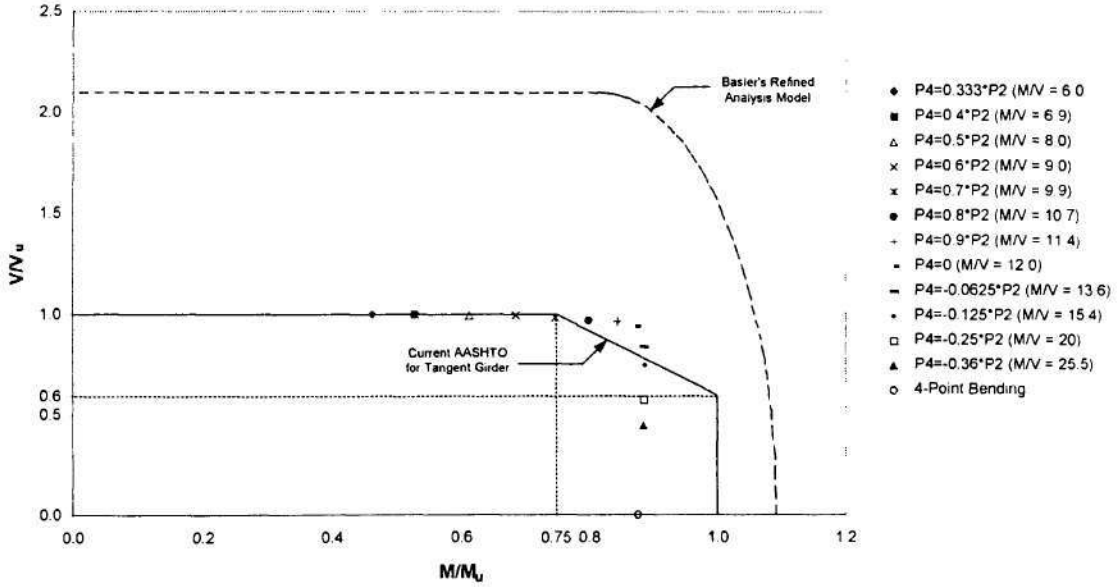

Figure 15. V/V_u versus M/M_u for the unstiffened specimens with L/R = 0.10 (V_u obtained by FEA and M_u calculated from AASHTO (1998)).

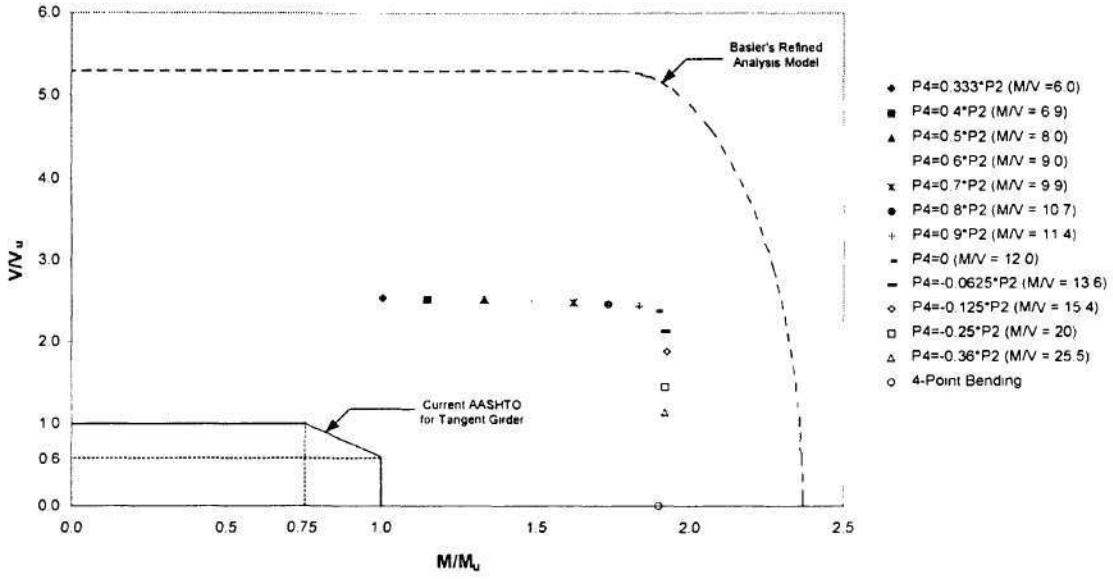

Figure 16. V/V_u versus M/M_u for the unstiffened specimens with L/R = 0.10 (V_u and M_u calculated from the *Recommended Specifications for Steel Curved-Girder Bridge* (Hall and Yoo 1998).

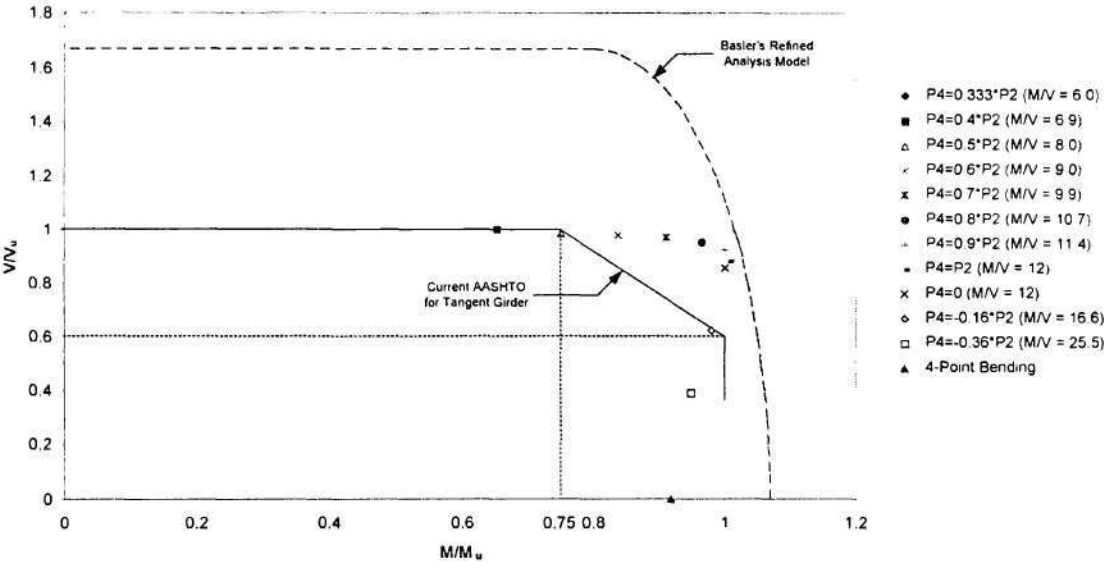

Figure 17. V/V_u versus M/M_u for the stiffened specimens with L/R = 0.057 (V_u obtained by FEA and M_u calculated from (Barth and White1997)).

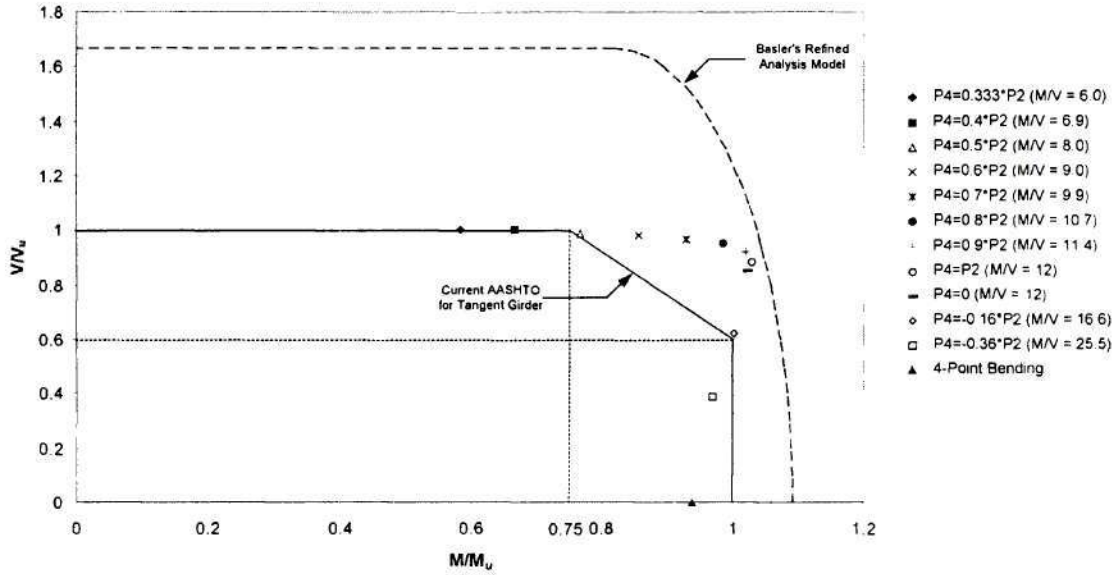

Figure 18. V/V_u versus M/M_u for the stiffened specimens with L/R = 0.057 (V_u obtained by FEA and M_u calculated from AASHTO (1998)).

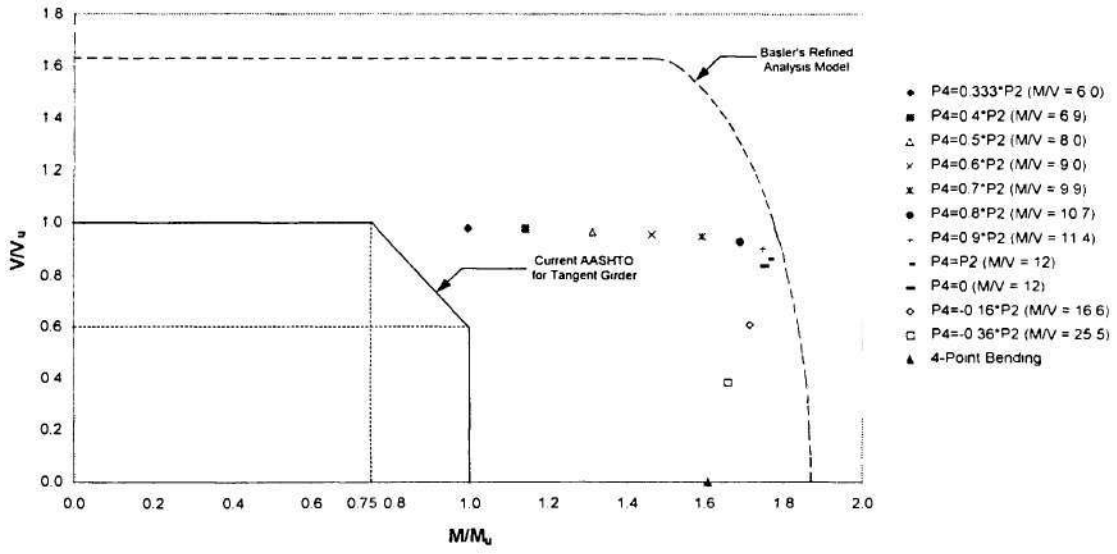

Figure 19. V/V_u versus M/M_u for the stiffened specimens with L/R = 0.057 (V_u and M_u calculated from the *Recommended Specifications for Steel Curved-Girder Bridge* (Hall and Yoo 1998)).

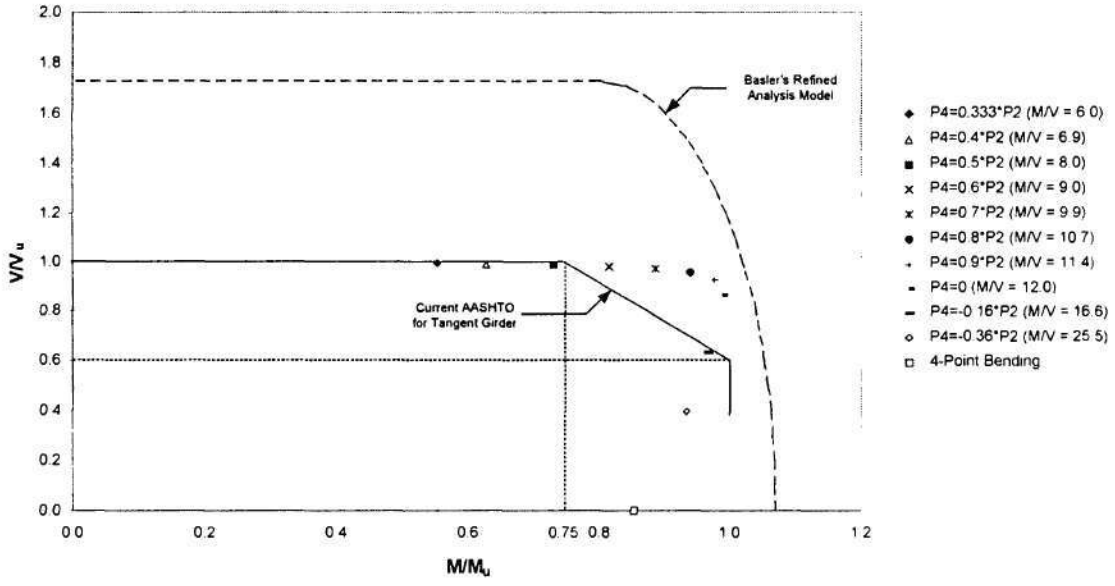

Figure 20. V/V_u versus M/M_u for the stiffened specimens with $L/R = 0.10$ (V_u obtained by FEA and M_u calculated from (Barth and White (1997)).

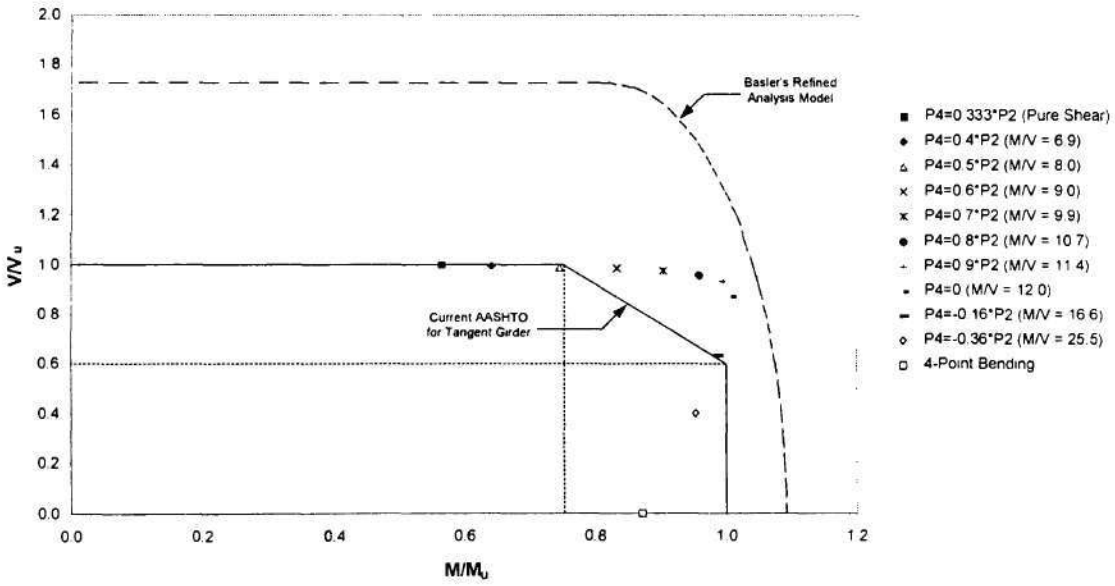

Figure 21. V/V_u versus M/M_u for the stiffened specimens with $L/R = 0.10$ (V_u obtained by FEA and M_u calculated from AASHTO (1998)).

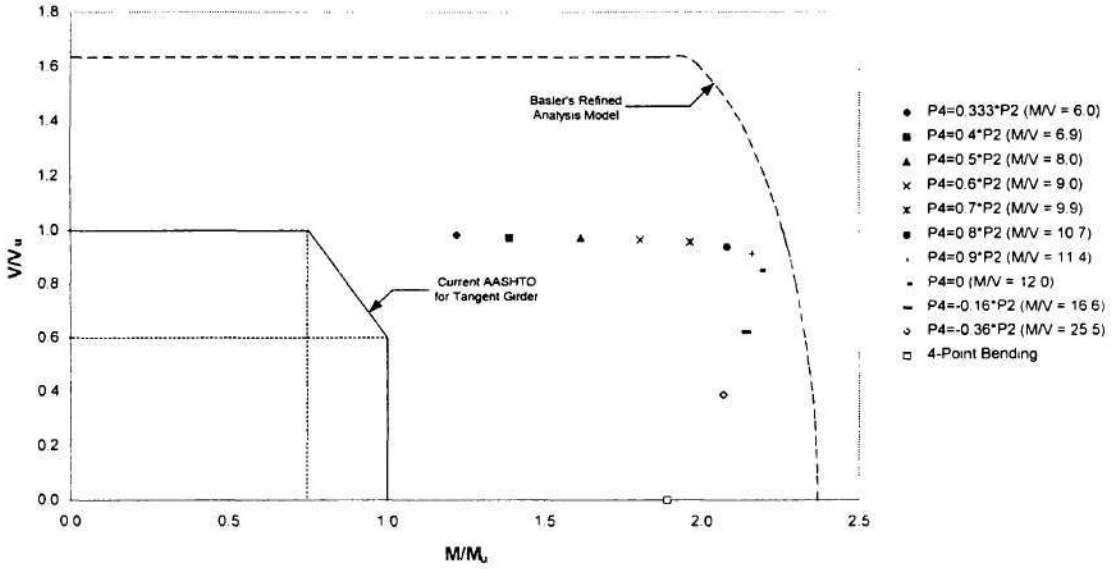

Figure 22. V/V_u versus M/M_u for the stiffened specimens with L/R = 0.10 (V_u and M_u calculated from the *Recommended Specifications for Steel Curved-Girder Bridge* (Hall and Yoo 1998)).

In addition to the FEA results shown in Figs. 11-22, two strength interaction curves are shown. The strength interaction curve based on the AASHTO tangent girder Specifications (AASHTO 1998 & 1997) is shown by a solid line. This curve assumes that the moment capacity is equal to M_u for $V/V_u < 0.6$, the shear capacity is equal to V_u for $M/M_u < 0.75$, and a linear interaction between V_u and M_u between these limits. This curve closely approximates the interaction effects based on Fig. 1 when $A_w/A_f \geq 2$. In the figures for which M_u is calculated based on (Barth and White 1997), this solid line is stopped at the V/V_u below which the M_u equation is not valid. It should be noted that neither the current *AASHTO Guide Specifications* nor the *Recommended Specifications* account for any moment-shear interaction effects. Also, it is expected that the moment-shear interaction assumed by the AASHTO tangent girder specifications is conservative for certain proportions of tangent girders. The second strength interaction curve, which is shown as a dashed line in the plots, is the one first developed by Basler based on the assumptions illustrated in Fig. 2. This interaction curve is an idealized plastic strength of the cross-section for an elastic perfectly plastic material. Therefore, it represents an expected upper bound for all the analysis results.

Based on Figs. 11-22, one can make the following observations:

1. The moment-shear interaction effect is quite small for all the specimens. Therefore, it appears that the AASHTO tangent girder interaction equations would be overly conservative for the test girders. The predicted moment capacity approaches that

associated with Basler's plastic interaction equation for the stiffened girders at the location on the FEA based interaction curves associated with maximum M/M_u (see Figs. 17-22), but otherwise Basler's plastic interaction equation is quite unconservative as would be expected.

2. For the girders with L/R = 0.057, there is a significant moment gradient effect for V/V_u approximately less than 0.8 in the first two of the three plots of each set. However, for the girders with L/R = 0.10, the unstiffened girder shows little moment gradient effect, while the stiffened girders shows a significant moment gradient effect for V/V_u approximately less than 0.9 in the first two of the three plots. For V/V_u values larger than the above limits, the curves have a sharp knee as the shear capacity of the girder webs is approached.
3. The shear capacity (V/V_u) of all the girders is nearly constant for M/M_u less than about 0.9.
4. The Barth and White equations for M_u are reasonably accurate for the range of V/V_u for which they are applicable, for the girders with L/R = 0.057. However, the bracing limit required for the use of these formulas, which is a limit intended to allow tangent girders to develop inelastic bending strengths larger than M_y at pier locations, is too restrictive for the Barth and White equations to be of practical use in locations where the moment-gradient is small. For the unstiffened girder with L/R = 0.10, the Barth and White equations is somewhat unconservative.
5. The *AASHTO LRFD* provisions for tangent girders (AASHTO 1998) overestimate the bending strength of the specimens with L/R = 0.10. However, the (AASHTO 1998) predict quite accurate for the maximum moment in the presence of moment-gradient for the specimens with L/R = 0.057 with the maximum difference of 8% in the case of four-point bending test of stiffened specimen.
6. The *Recommended Specifications* base the shear capacity on the elastic buckling strength of the web for $d_0/D > 1.0$. However, the analysis results show that for the unstiffened specimens ($d_0/D = 3.0$), there is significant post-buckling strength developed in all these specimens. The actual capacities are much higher than V_{cr}

According to the *Recommended Specifications*, the curvature effect can be neglected when the ratio of L/R is less than 0.06 and the maximum allowable limit ratio of L/R is equal to 0.10. That is, if the ratio of L/R is less than 0.06, the design specifications for tangent girder can be applied and the strength of the curved girder is equal to that of tangent girder with the same cross-section geometry and overall layout. In contrast, if the ratio of the curvature exceeds 0.10, the ultimate strength of the curved steel I girder will be significantly affected by the effect of the curvature. Furthermore, in general, the L/R ratio of the practical curved girder is less than 0.10.

To evaluate the effect of both limitations corresponding to the *Recommended Specifications* to the effect of the strength of both the unstiffened and stiffened test specimens, the finite element analyses have been conducted for the L/R ratio = 0.057 and 0.10. The results are summarized in Table 1 for the unstiffened test specimens and Table 2 for the stiffened test specimens.

Table 1. The maximum shear forces and the corresponding maximum bending moments from various loading proportions for L/R = 0.057 and L/R = 0.10 of the unstiffened test specimens.

M/V	Loading Configurations	V_{max} (kips)		M_{max} (kips-ft)		% Difference
		L/R = 0.057	L/R = 0.10	L/R = 0.057	L/R = 0.10	
6	$\alpha = 0.333$	246	228	1475	1368	-7.25
6.9	$\alpha = 0.4$	245	227	1679	1559	-7.13
8.0	$\alpha = 0.5$	244	227	1954	1816	-7.06
9.0	$\alpha = 0.6$	243	225	2185	2026	-7.28
9.9	$\alpha = 0.7$	241	224	2381	2212	-7.11
10.7	$\alpha = 0.8$	239	222	2552	2365	-7.33
11.4	$\alpha = 0.9$	237	220	2694	2498	-7.28
12	Three-Point Bending	232	215	2784	2580	-7.33
13.6	$\alpha = -0.0625$	218	201	2965	2734	-7.80
15.4	$\alpha = -0.125$	193	179	2975	2761	-7.18
20	$\alpha = -0.25$	148	137	2960	2740	-7.43
25.5	$\alpha = -0.36$	113	104	2874	2652	-7.74
-	4-Point Bending	0	0	2752	2590	-5.90

Table 2. The maximum shear forces and the corresponding maximum bending moments from various loading proportions for L/R = 0.057 and L/R = 0.10 for the stiffened test specimens.

M/V	Loading Configurations	V_{max} (kips)		M_{max} (kips-ft)		% Difference
		L/R = 0.057	L/R = 0.10	L/R = 0.057	L/R = 0.10	
6.0	$\alpha = 0.333$	287	277	1722	1664	-3.34
6.9	$\alpha = 0.4$	287	276	1970	1892	-3.97
8.0	$\alpha = 0.5$	283	275	2266	2201	-2.87
9.0	$\alpha = 0.6$	281	273	2529	2457	-2.85
9.9	$\alpha = 0.7$	278	271	2747	2673	-2.69
10.7	$\alpha = 0.8$	273	266	2916	2832	-2.88
11.4	$\alpha = 0.9$	265	259	3018	2941	-2.55
12.0	Three-Point Bending	245	241	2944	2897	-1.60
16.6	$\alpha = -0.16$	179	176	2958	2918	-1.37
25.5	$\alpha = -0.36$	112	111	2854	2819	-1.25
-	4-Point Bending	0	0	2831	2675	-5.51

From Tables 1 and 2, the change in L/R ratio from L/R = 0.057 to L/R ratio = 0.10 introduces reductions in both maximum shear forces and maximum bending moments. These reductions are more pronounced in the unstiffened specimens. For the unstiffened specimens, the reductions range from 5.90%-7.80% while in the stiffened specimens, the reductions are 1.25%-5.51%. Therefore, the stiffeners provide a significant contribution to the strength of the specimens when the curvature ratio, L/R, increases by restrain the web distortion.

From the above results, the loading configuration at which the largest moment-shear interaction can be obtained are the three-point bending test for the unstiffened specimens and three-span test with $\alpha = 0.80$ for the stiffened specimens. In addition, the point at which the largest moment capacity is reached (due to moment-gradient effects) can be attained by the three-span test with $\alpha = -0.125$ and the three-point bending test for the unstiffened and stiffened specimens, respectively. Therefore the proposed test configurations for both L/R = 0.057 and 0.10 are:

1. Unstiffened test specimens
   - Three-point bending test (MS1-0.06 and MS1-0.10)
   - Three-span test with $\alpha = -0.125$ (MS2-0.06 and MS2-0.10).

2. Stiffened test specimens with
   - Three-span test with $\alpha = 0.80$ (MS1-S-0.06 and MS1-S-0.10)
   - Three-point bending test (MS2-S-0.06 and MS2-S-0.10)

5. PREDICTED BEHAVIOR FOR THE PROPOSED TEST SPECIMENS

The maximum shear forces, maximum applied forces, and maximum support reactions of the proposed test specimens are summarized in Table 3. The warping to bending stress ratios at the maximum load level are shown in Table 4. It should be noted that since the flanges have already yield prior to the maximum applied load level, therefore the linear elastic analyses are used to obtain the f_w/f_b ratios. Furthermore, the radial reactions of the proposed specimens at the maximum applied load are shown in Tables 5. Finally vertical and tangential displacements at the maximum load level of the proposed test specimens are summarized in Table 6.

Table 3. Maximum shear forces, maximum applied forces, and maximum support reactions.

d_0/D	L/R	Specimens	M_{max}/V_{max}	Loading Configuration	V_{max} (kips)	P_{max} (kips)	Maximum Support Reaction (kips)
3.0	0.057	MS1-0.06 MS2-0.06	12 15.4	Three-Point Bending α = -0.125	232 193	464 441	232 248
	0.10	MS1-0.10 MS2-0.10	12 15.4	Three-Point Bending α = -0.125	215 179	430 409	215 230
1.5	0.057	MS1-S-0.06 MS2-S-0.06	10.7 12.0	α = 0.8 Three-Point Bending	273 245	304 491	516 245
	0.10	MS1-S-0.10 MS2-S-0.10	10.7 12.0	α = 0.8 Three-Point Bending	266 241	295 482	502 241

Table 4. Warping to bending stress ratio obtained by linear elastic analyses.

d_0/D	L/R	Specimens	M_{max}/V_{max}	Loading Configuration	Location 2		Location 3	
					Top	Bottom	Top	Bottom
3.0	0.057	MS1-0.06 MS2-0.06	12.0 15.4	Three-Point Bending α = -0.125	0.258 0.134	0.254 0.221	- 0.575	- 0.423
	0.10	MS1-0.10 MS2-0.10	12.0 15.4	Three-Point Bending α = -0.125	0.442 0.385	0.439 0.383	- 0.985	- 0.735
1.5	0.057	MS1-S-0.06 MS2-S-0.06	10.7 12.0	α = 0.8 Three-Point Bending	0.213 0.236	0.337 0.247	0.202 -	0.183 -
	0.10	MS1-S-0.10 MS2-S-0.10	10.7 12.0	α = 0.8 Three-Point Bending	0.370 0.406	0.573 0.427	0.350 -	0.318 -

Table 5. Radial reactions at the maximum load level.

d_0/D	L/R	Specimens	M_{max}/V_{max}	Loading Configuration	Radial Reactions (k)							
					Location 1		Location 2		Location 3		Location 4	
					Top	Bottom	Top	Bottom	Top	Bottom	Top	Bottom
3.0	0.057	MS1-0.06 MS2-0.06	12.0 15.4	Three-Point Bending α = -0.125	-2.235 -5.342	2.098 4.883	-35.445 -30.78	34.308 31.635	-1.339 -16.613	2.269 13.841	- 1.121	- 0.974
	0.10	MS1-0.10 MS2-0.10	12.0 15.4	Three-Point Bending α = -0.125	-3.868 -2.349	4.229 2.786	-56.750 1.064	53.960 -0.595	-2.649 53.535	4.497 -52.680	- 8.895	- -9.285
1.5	0.057	MS1-S-0.06 MS2-S-0.06	10.7 12.0	α = 0.8 Three-Point Bending	-1.319 -4.623	1.577 4.290	-0.383 -32.385	0.6375 31.261	33.210 -4.398	-32.775 5.522	5.019 -	-5.277 -
	0.10	MS1-S-0.10 MS2-S-0.10	10.7 12.0	α = 0.8 Three-Point Bending	-2.349 -7.911	2.786 7.969	1.064 -55.149	-0.595 52.171	53.535 -7.746	-52.680 10.130	8.895 -	-9.285 -

Table 6. Vertical displacements and tangential displacements at the maximum load level.

d_y/D	L/R	Specimens	M_{max}/V_{max}	Loading Configuration	Vertical Displacement (in)		Tangential Displacement (in)	
					Location 2	Location 4	Location 2	Location 4
3.0	0.057	MS1-0.06	12.0	Three-Point Bending	1.097	-	0.093	-
		MS2-0.06	15.4	α = -0.125	0.948	-1.101	0.113	0.349
	0.10	MS1-0.10	12.0	Three-Point Bending	1.036	-	0.089	-
		MS2-0.10	15.4	α = -0.125	0.946	-1.098	0.109	0.345
1.5	0.057	MS1-S-0.06	10.7	α = 0.8	0.2158	1.643	-0.1957	-0.3827
		MS2-S-0.06	12.0	Three-Point Bending	1.116	-	0.1167	-
	0.10	MS1-S-0.10	10.7	α = 0.8	0.267	1.744	-0.2294	-0.4145
		MS2-S-0.10	12.0	Three-Point Bending	1.151	-	0.128	-

From Table 4, the ratios of f_w/f_b from the three-point bending tests with both stiffened and unstiffened specimens are below the limit of 0.5 according to both the *Recommended Specifications for Steel Curved-Girder (1998)* and the *AASHTO Guide Specifications for Horizontally Curved Highway Bridges (1993).* In contrast, for the unstiffened specimens with α = -0.125, the f_w/f_b ratios exceed the limit of 0.5 at location 3. The exceeding of f_w/f_b is more pronounced when the curvature ratio, L/R = 0.10. However, the high values of f_w/f_b ratio appear to be insignificant to the strength of the girders (the maximum shear force and maximum bending moment decrease by approximately 7%).

For the stiffened specimens with α = 0.8 and L/R = 0.057, the f_w/f_b ratios are under the limit of 0.5. However, as the curvature ratio increases from 0.057 to 0.10, the f_w/f_b ratios increase to be higher than the limit of 0.5 at bottom flange at location 2. Once again, the increase in f_w/f_b ratio produces no effect to the strengths of the girder (the maximum shear force and maximum bending moment of the girder decrease by only 3% when L/R ratio increases from 0.057 to 0.10). It should be noted that, at the maximum load level, the flange stresses are beyond the elastic range.

The total applied load P_2 versus the radial reactions at the locations that have the largest values are shown in Figs 23-30. In addition, the total applied load P2 versus the vertical displacements at the load points and the deformed shapes at the maximum load level of the proposed test specimens are shown in Figs 31-46.

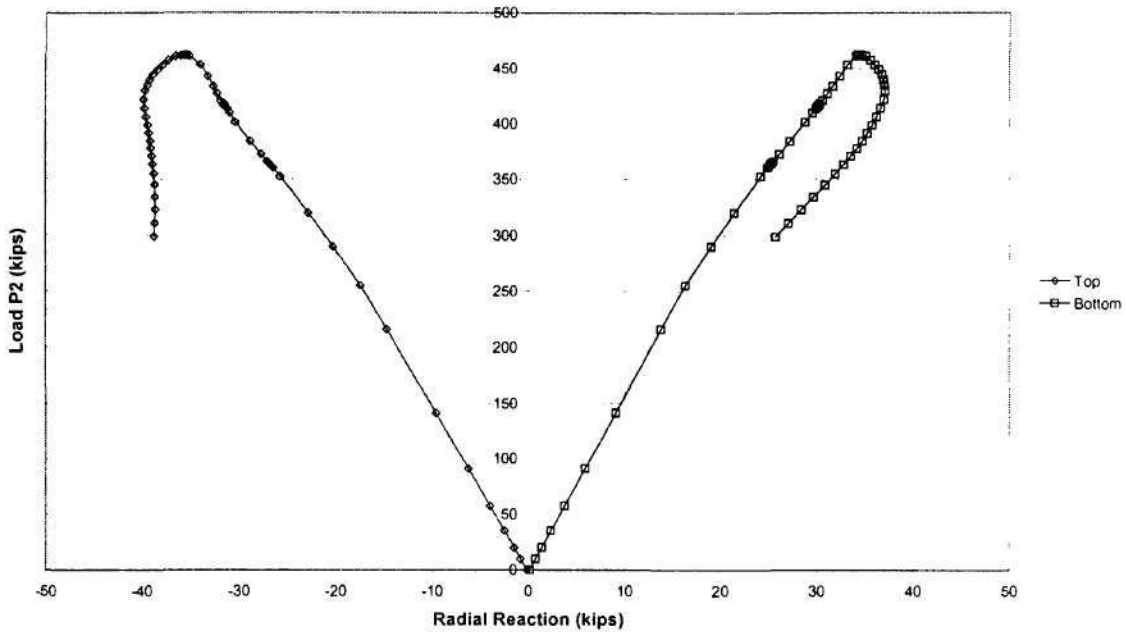

Figure 23. Load P_2 versus radial reactions at location 2 for Specimen MS1-0.06.

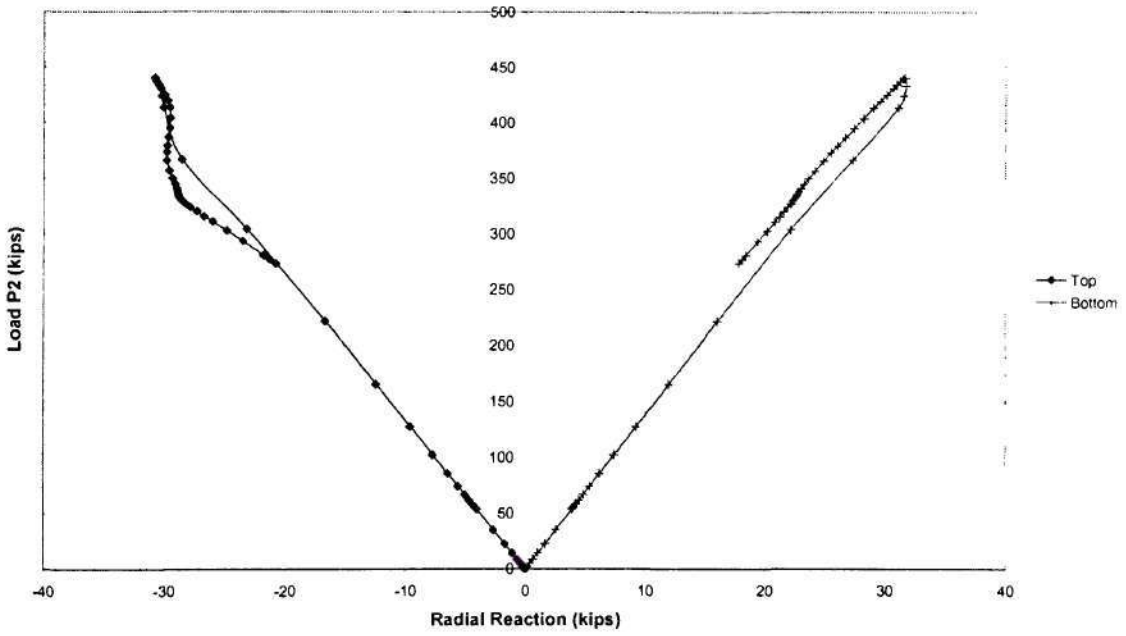

Figure 24. Load P_2 versus radial reactions at location 2 for Specimen MS2-0.06.

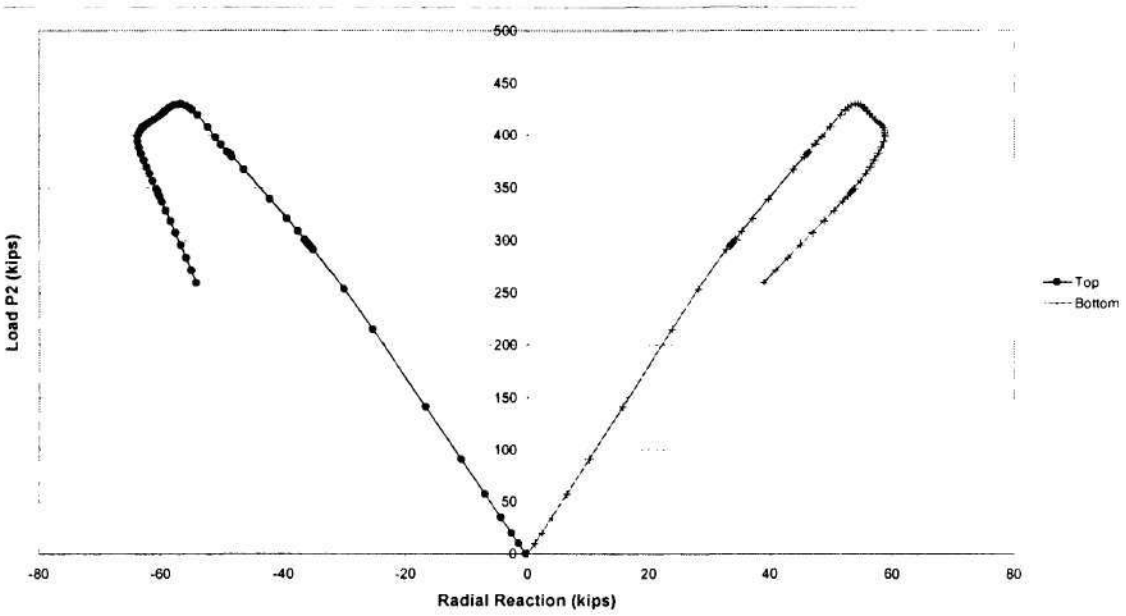

Figure 25. Load P_2 versus radial reactions at location 2 for Specimen MS1-0.10.

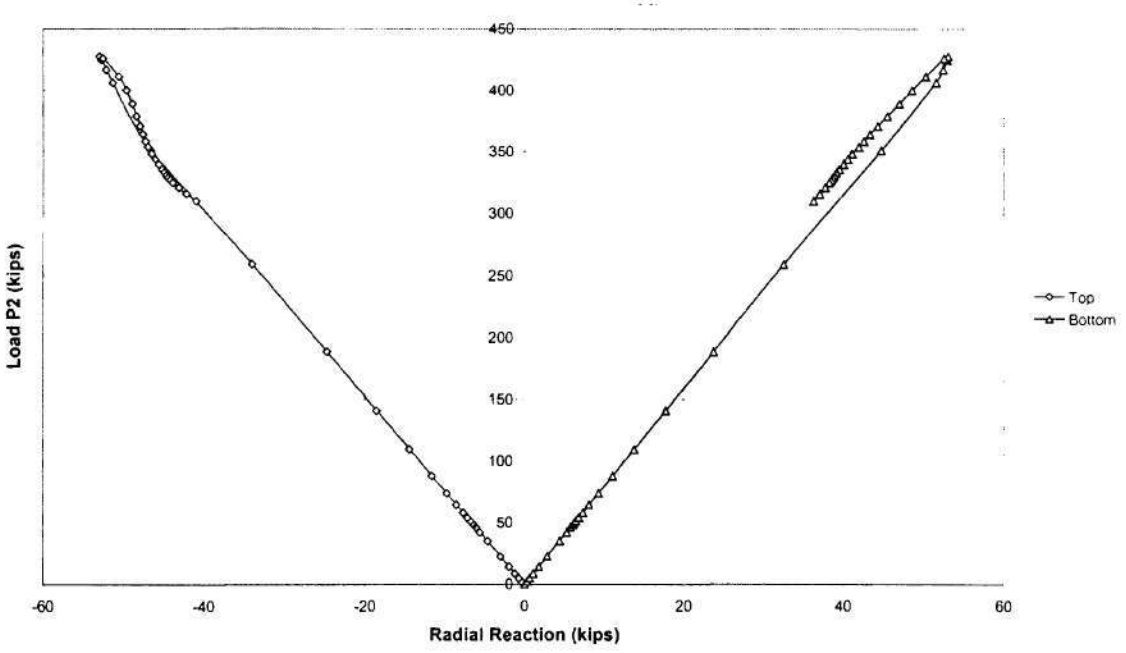

Figure 26. Load P_2 versus radial reactions at location 2 for Specimen MS2-0.10.

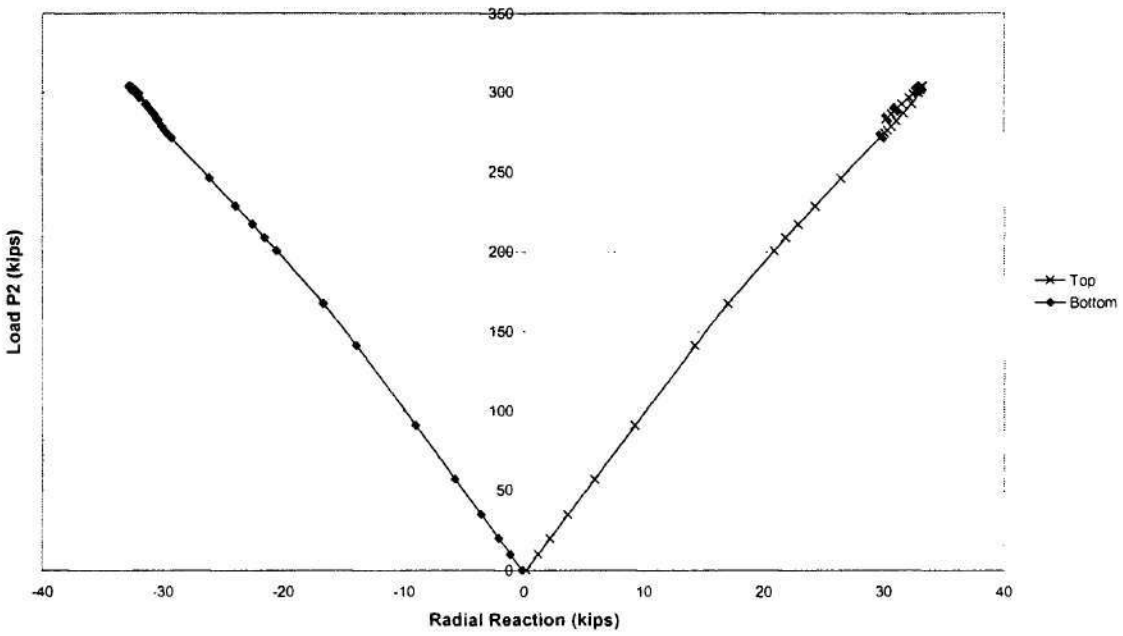

Figure 27. Load P_2 versus radial reactions at location 3 for Specimen MS1-S-0.06.

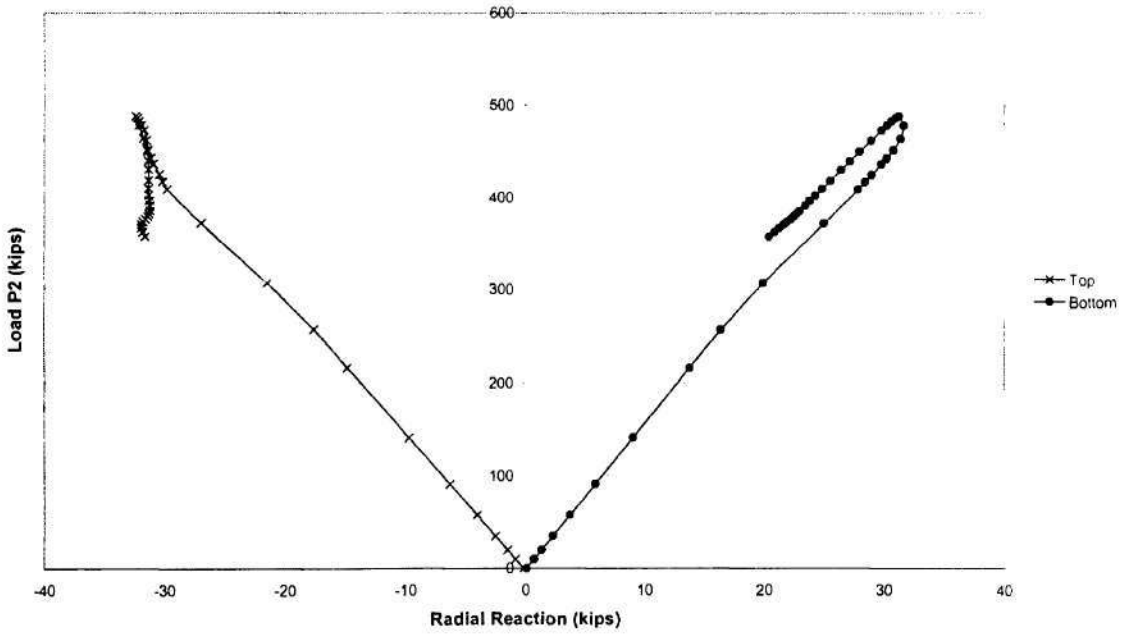

Figure 28. Load P_2 versus radial reactions at location 2 for Specimen MS2-S-0.06.

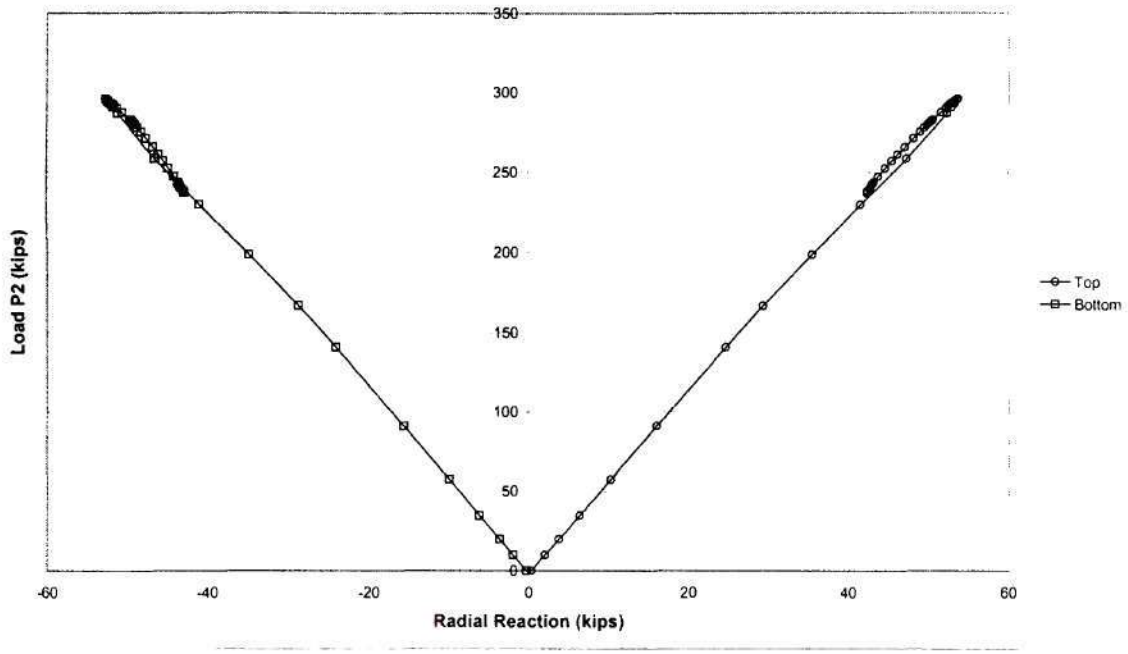

Figure 29. Load P_2 versus radial reactions at location 3 for Specimen MS1-S-0.10.

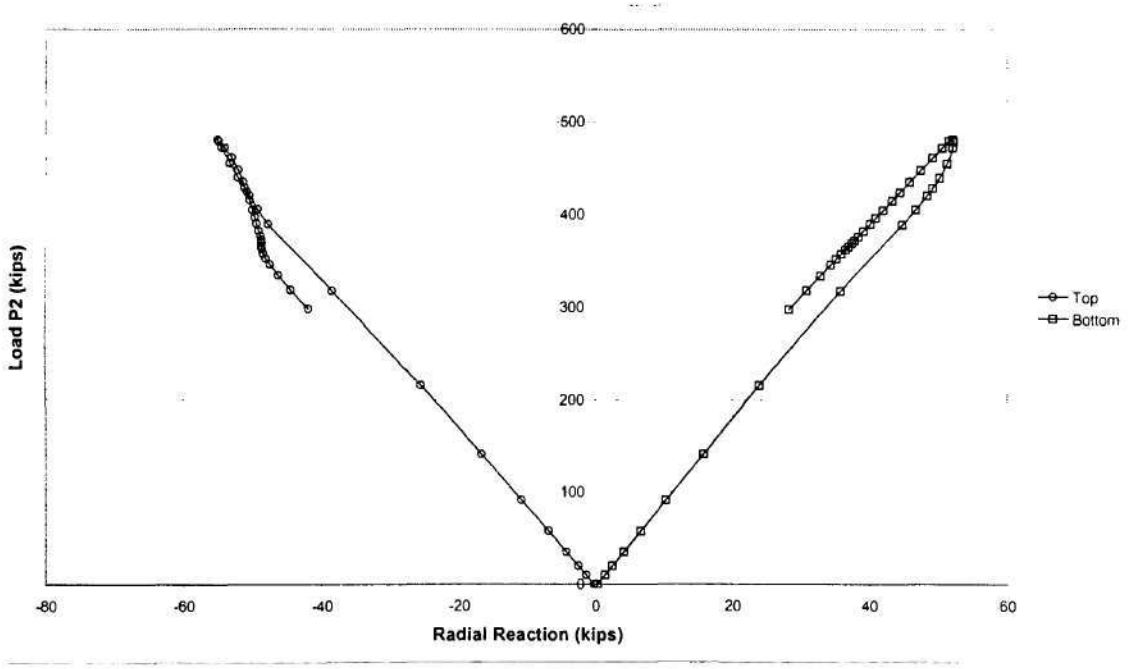

Figure 30. Load P_2 versus radial reactions at location 2 for Specimen MS2-S-0.10.

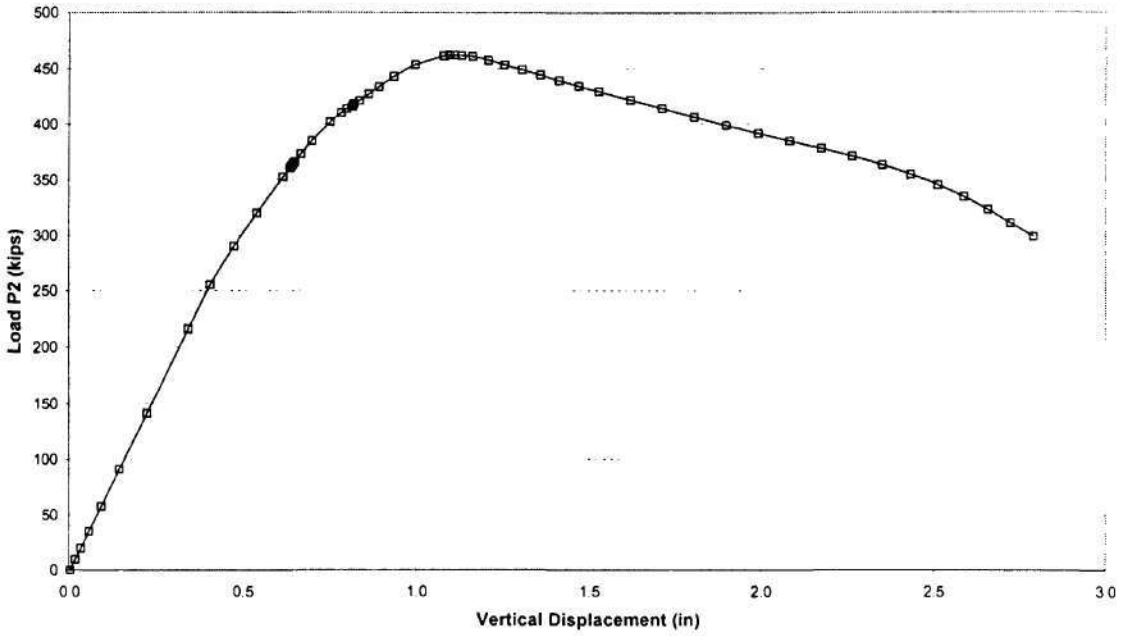

Figure 31. Load P_2 versus vertical displacement at the load location for Specimen MS1-0.06.

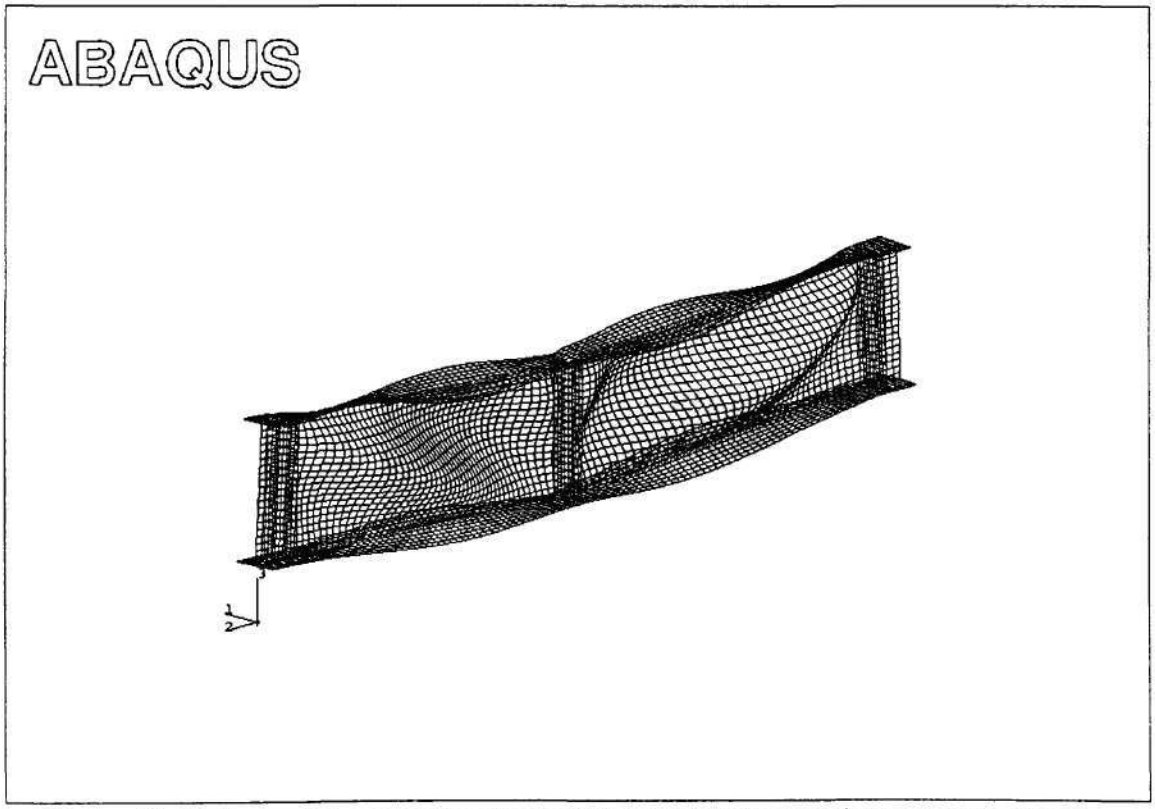

Figure 32. Deformed shape of Specimen MS1-0.06 at the maximum applied load.

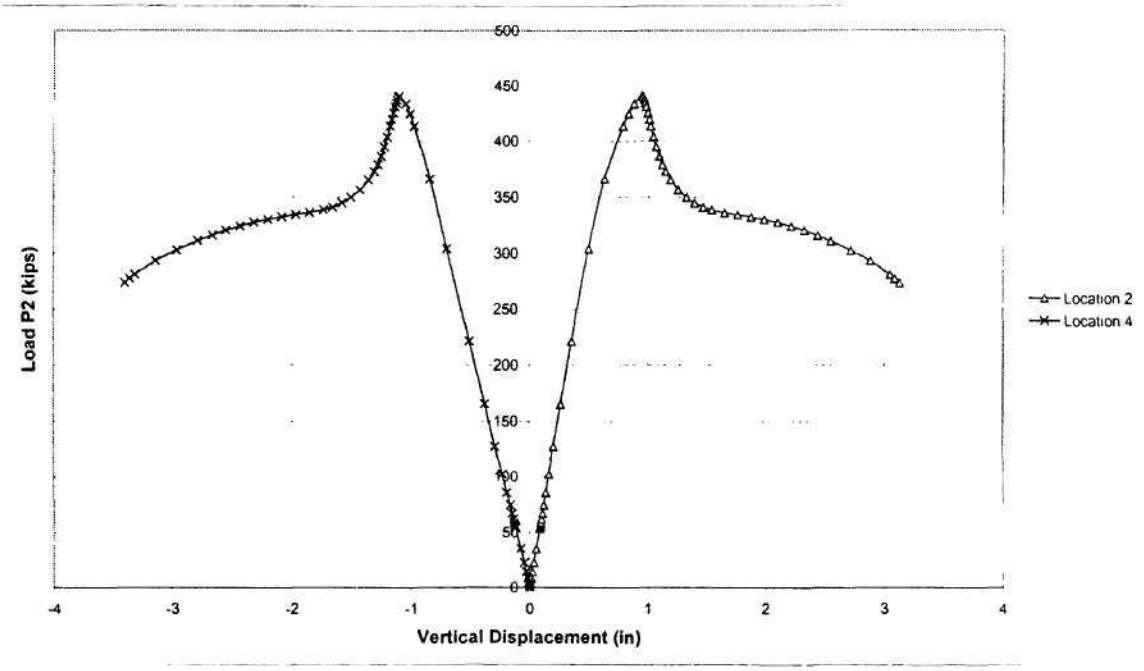

Figure 33. Load P_2 versus vertical displacements at the load locations for Specimen MS2-0.06.

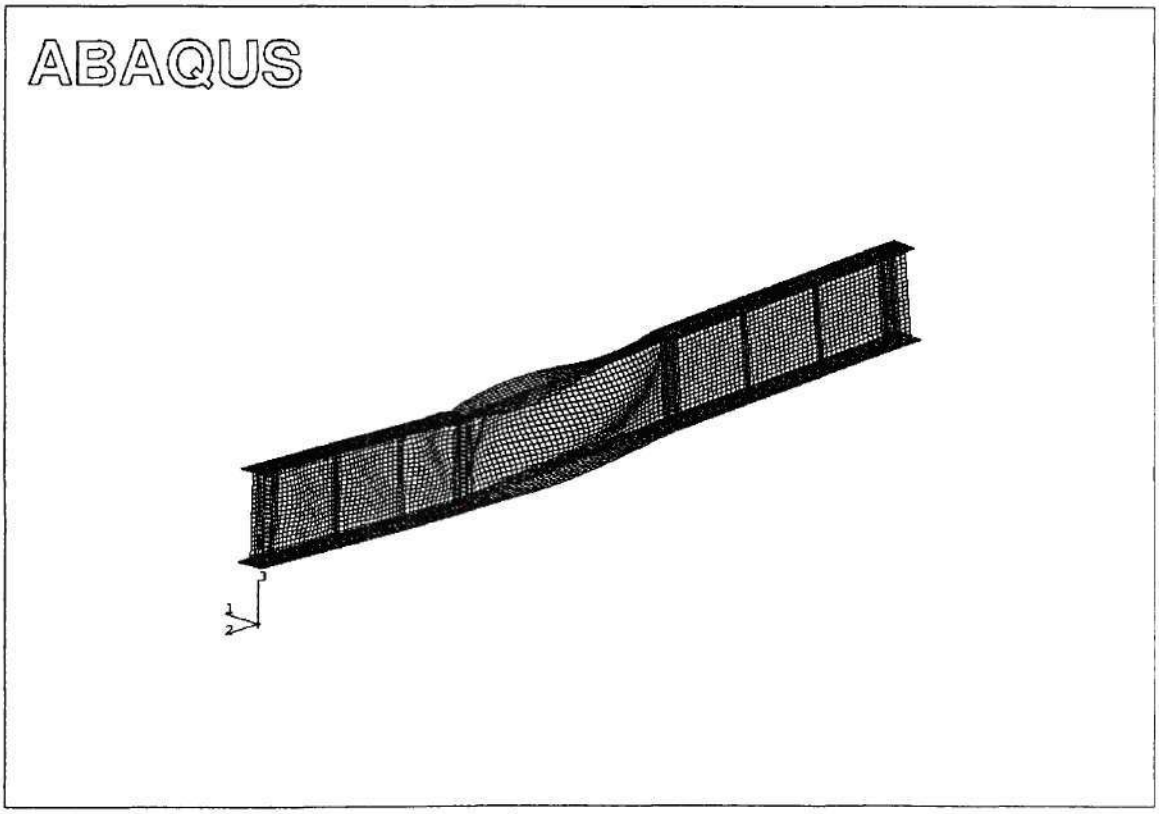

Figure 34. Deformed shape of Specimen MS2-0.06 at the maximum applied load.

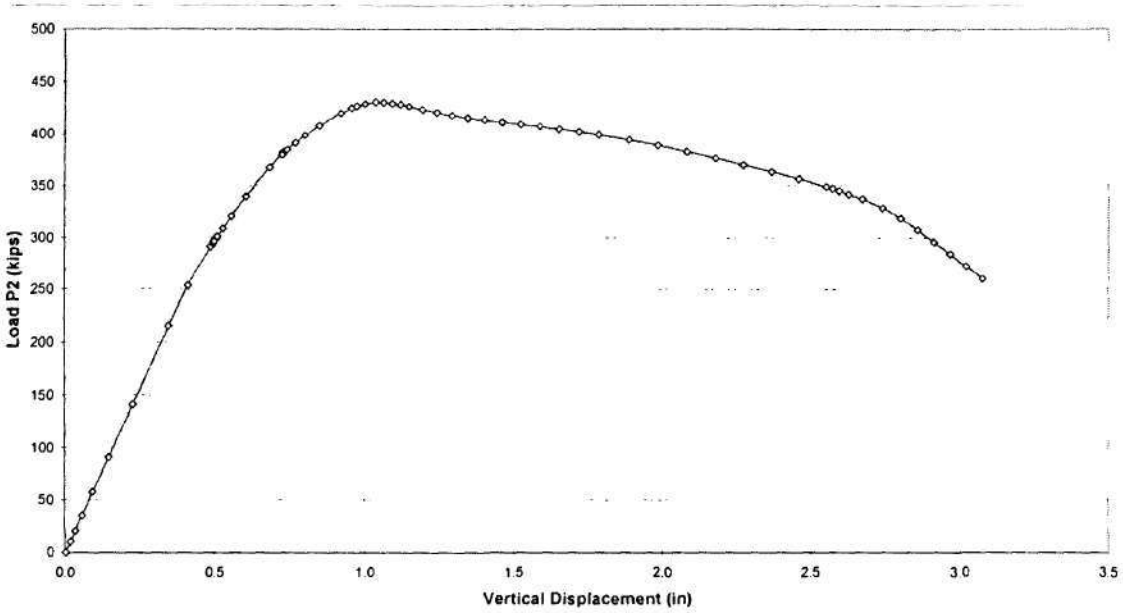

Figure 35. Load P_2 versus vertical displacement at the load location for Specimen MS1-0.10.

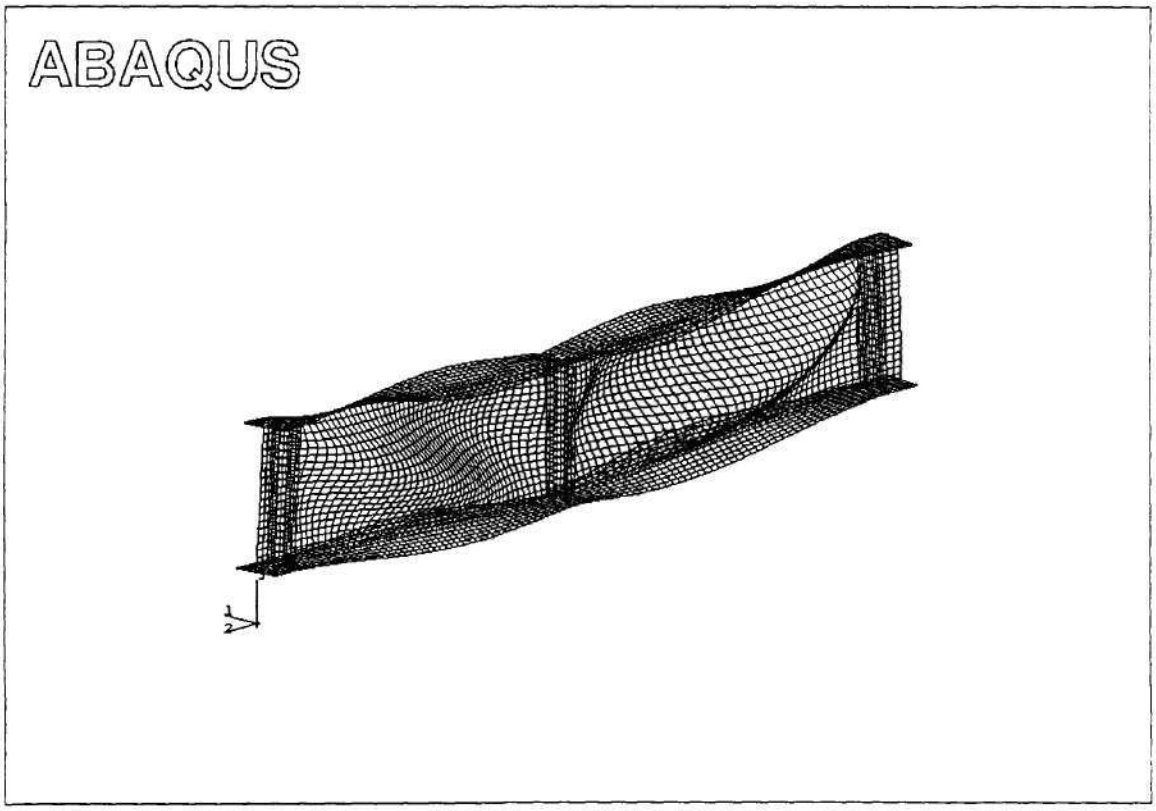

Figure 36. Deformed shape of Specimen MS1-0.10 at the maximum applied load.

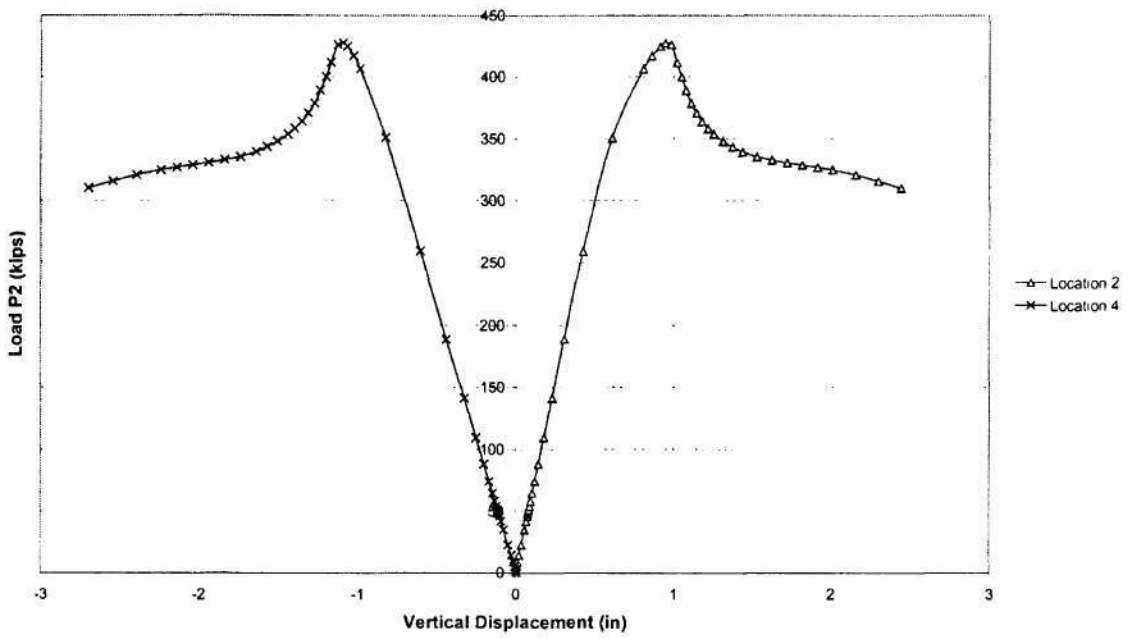

Figure 37. Load P_2 versus vertical displacements at the load locations for Specimen MS2-0.10.

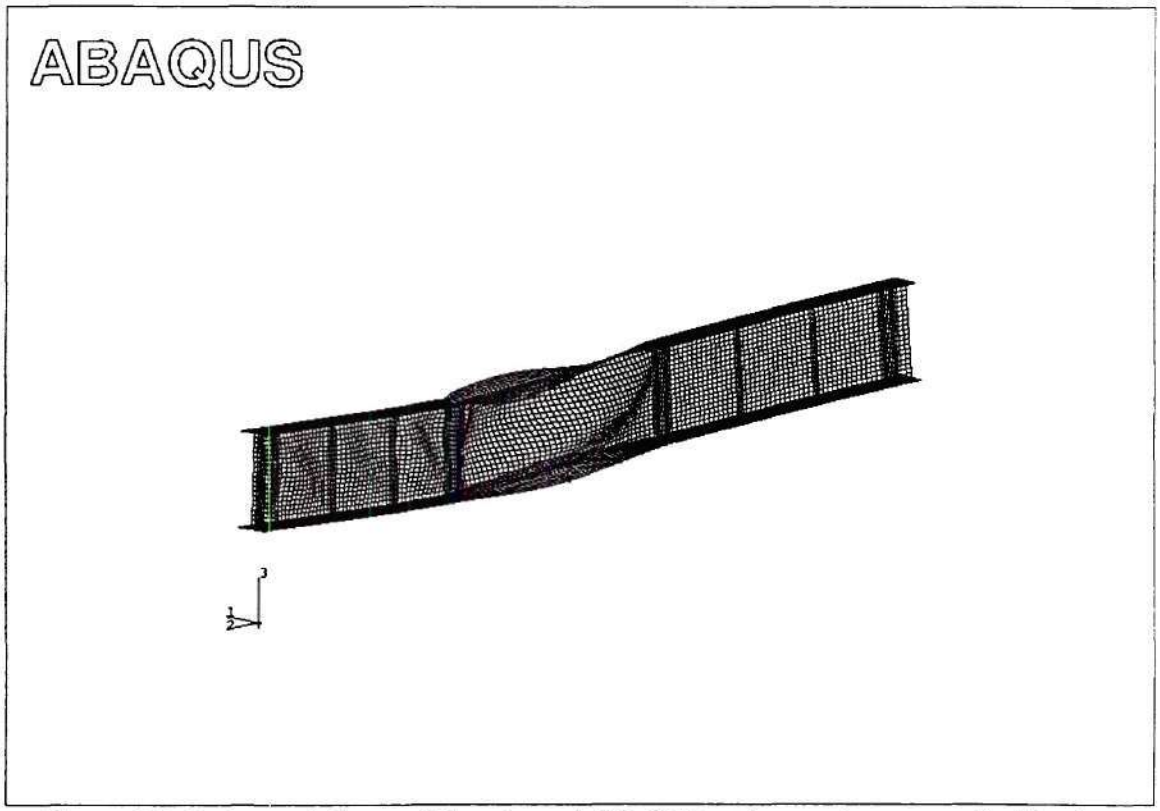

Figure 38. Deformed shape of Specimen MS2-0.10 at the maximum applied load.

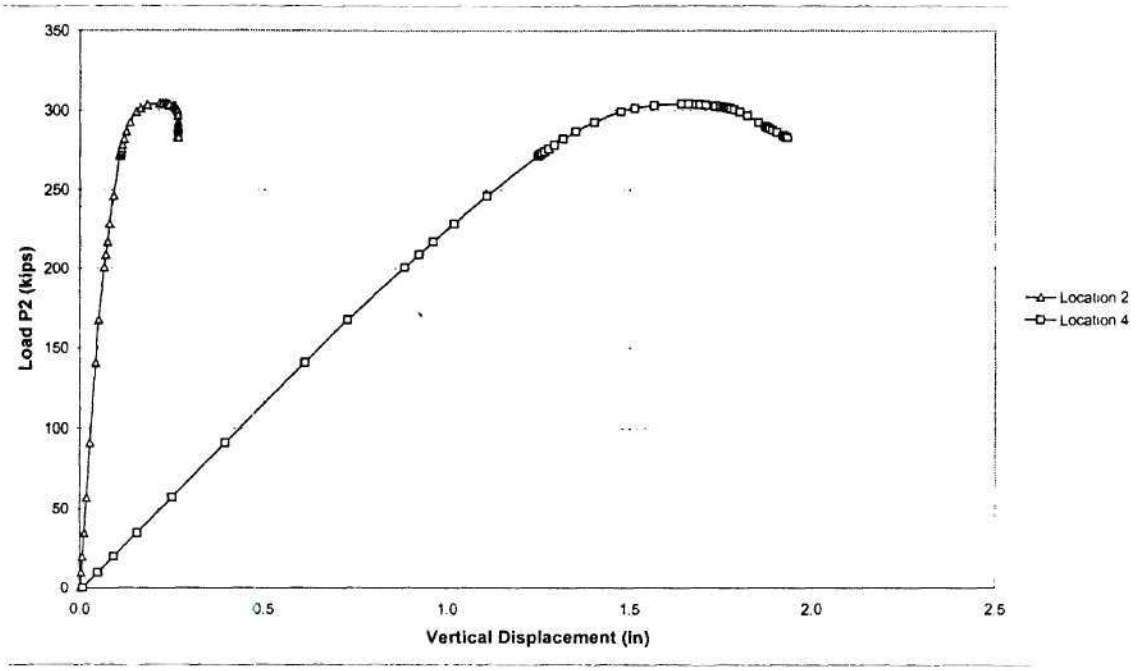

Figure 39. Load P_2 versus vertical displacements at the load locations for Specimen MS1-S-0.06.

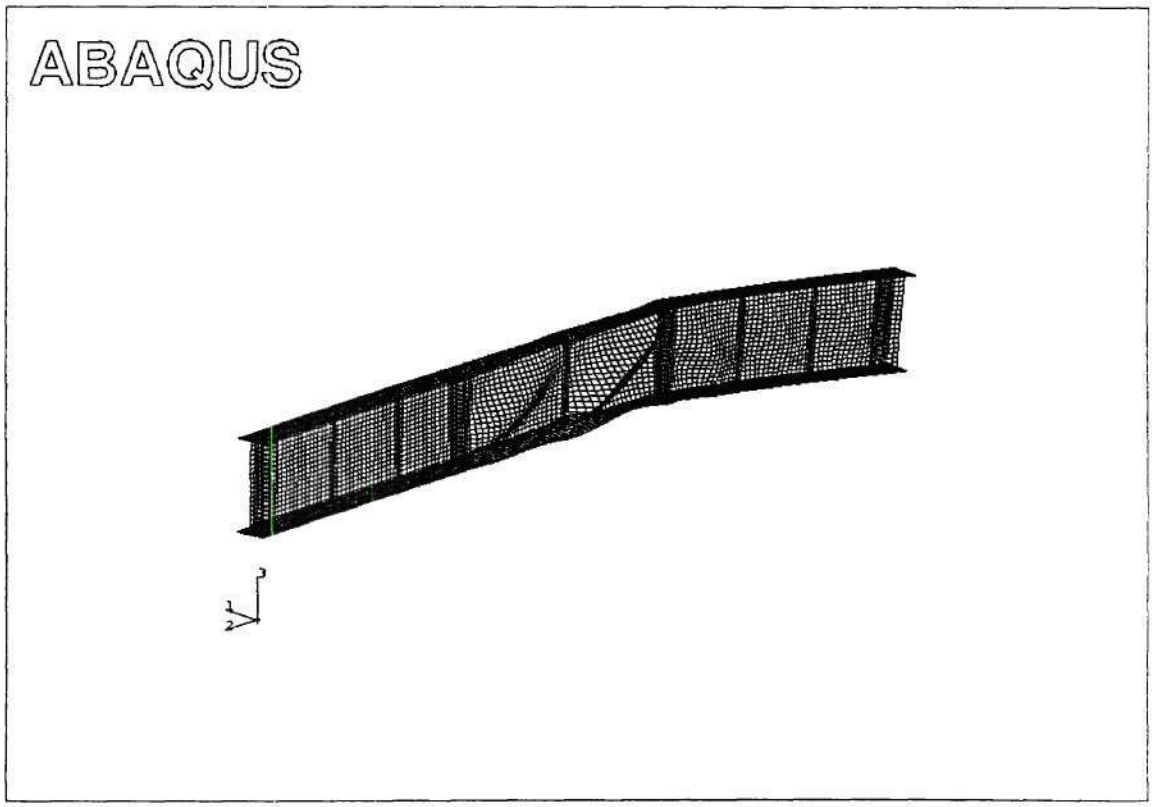

Figure 40. Deformed shape of Specimen MS1-S-0.06 at the maximum applied load.

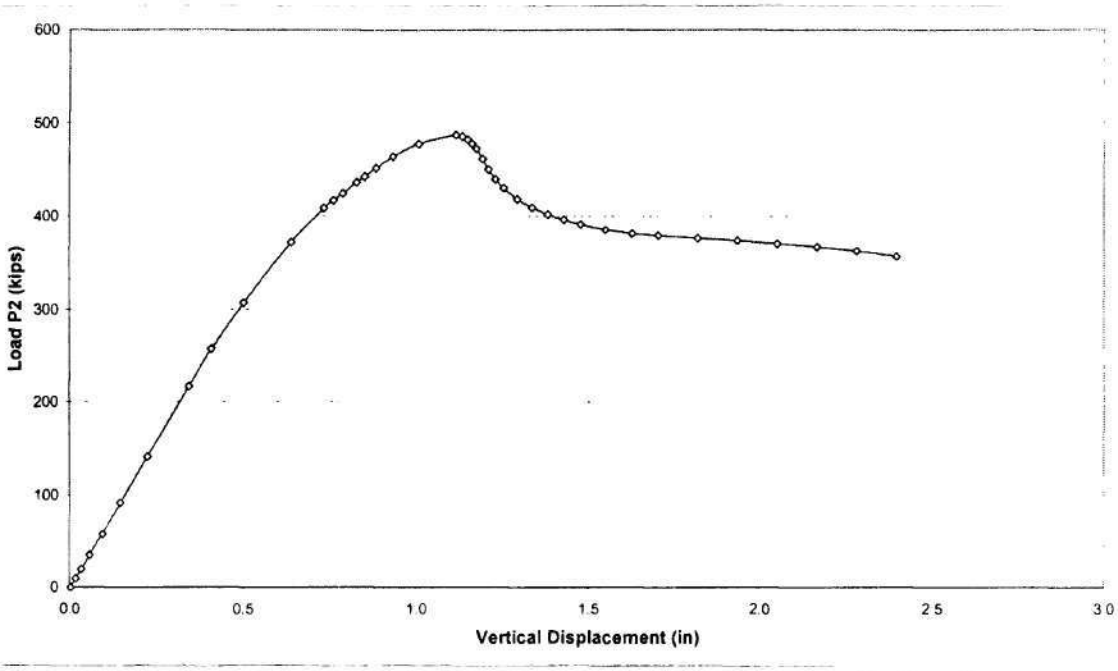

Figure 41. Load P_2 versus vertical displacement at the load location for Specimen MS2-S-0.06.

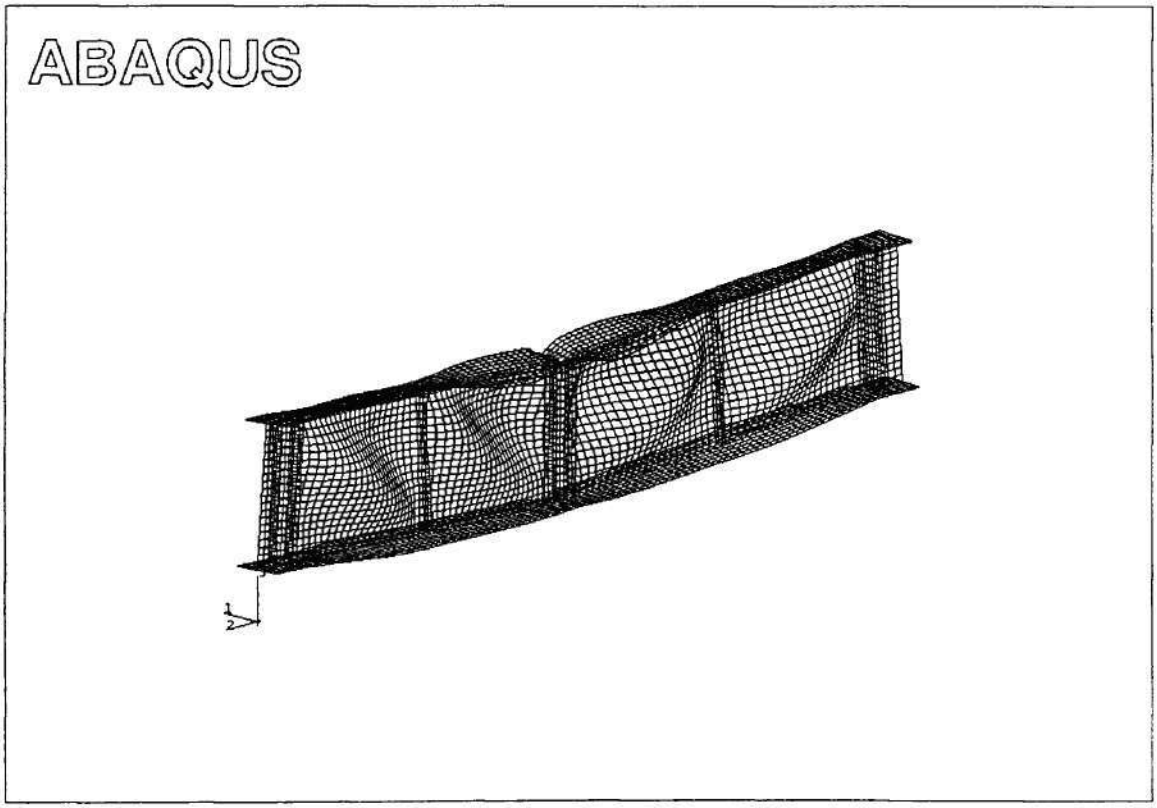

Figure 42. Deformed shape of Specimen MS2-S-0.06 at the maximum applied load.

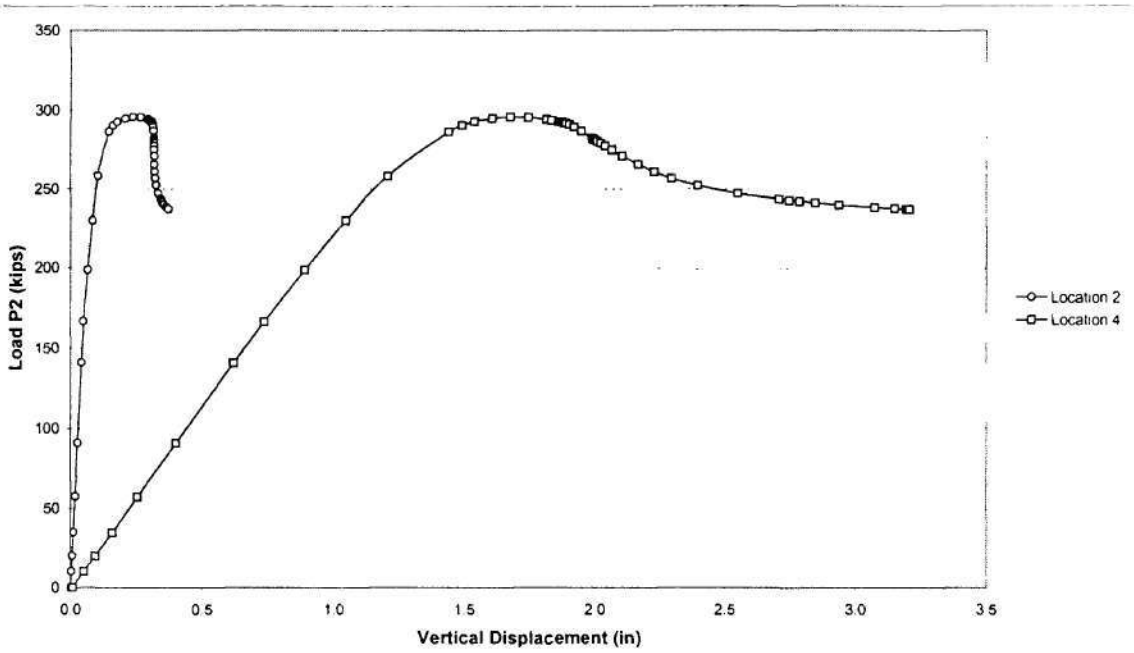

Figure 43. Load P_2 versus vertical displacements at the load locations for Specimen MS1-S-0.10.

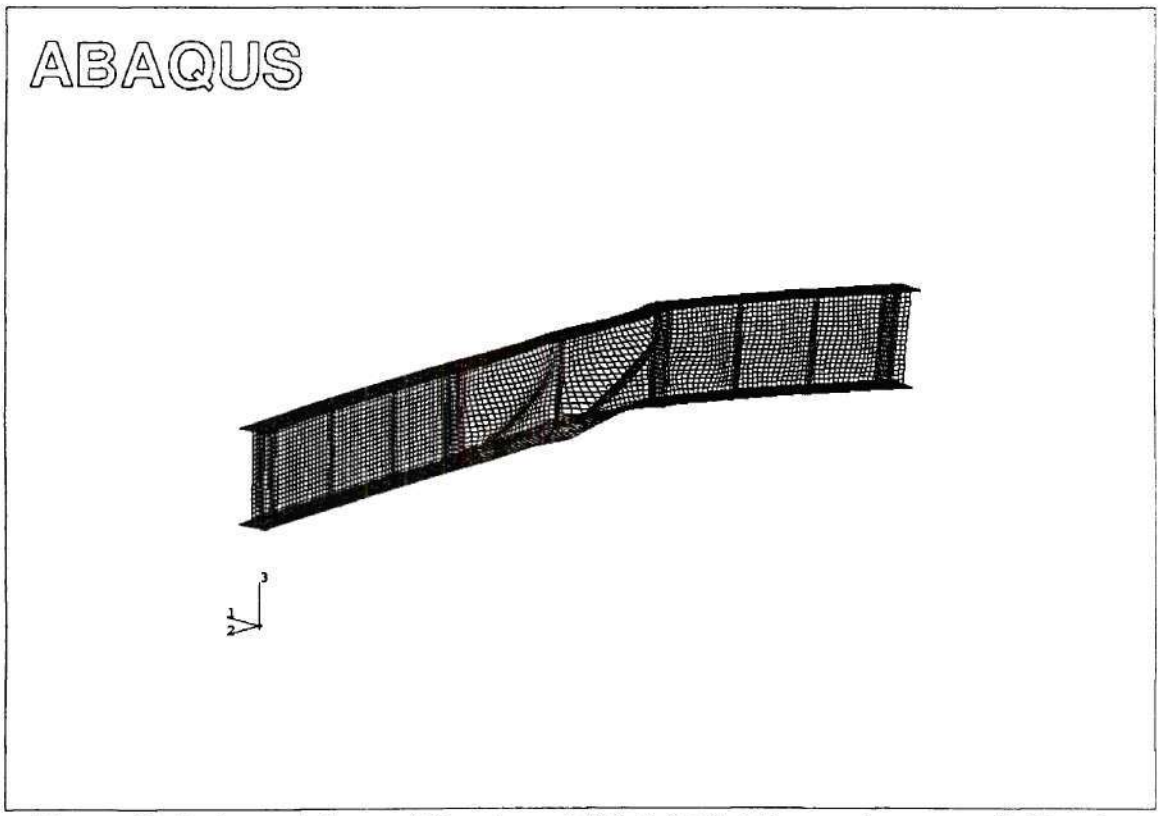

Figure 44. Deformed shape of Specimen MS1-S-0.10 at the maximum applied load.

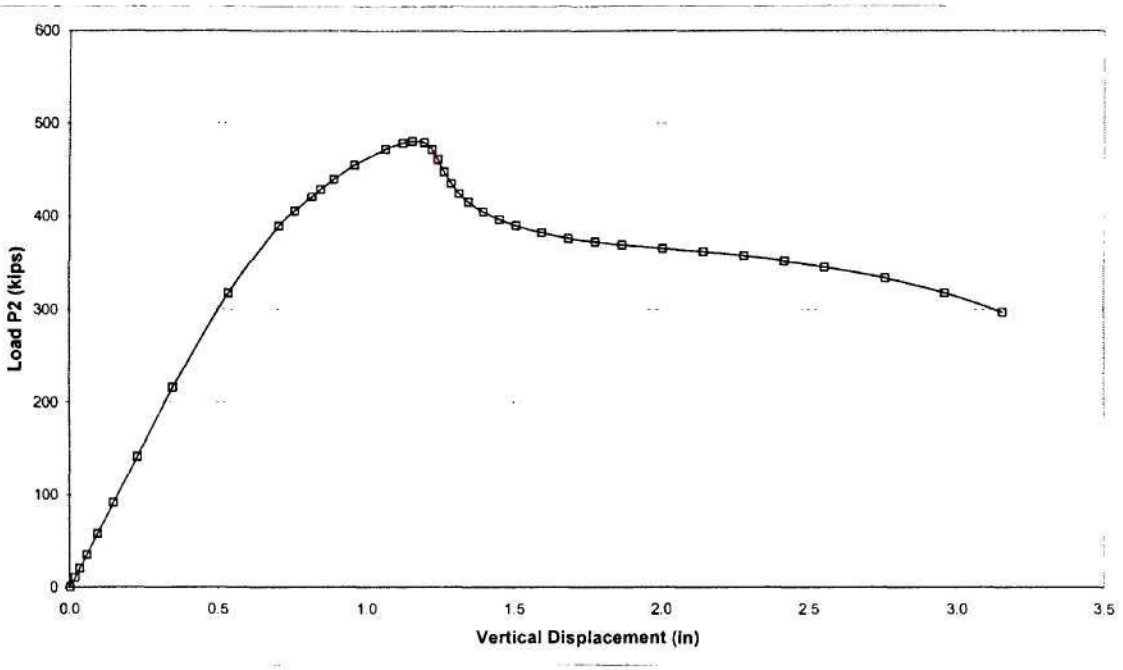

Figure 45. Load P_2 versus vertical displacement at the load location for Specimen MS2-S-0.10.

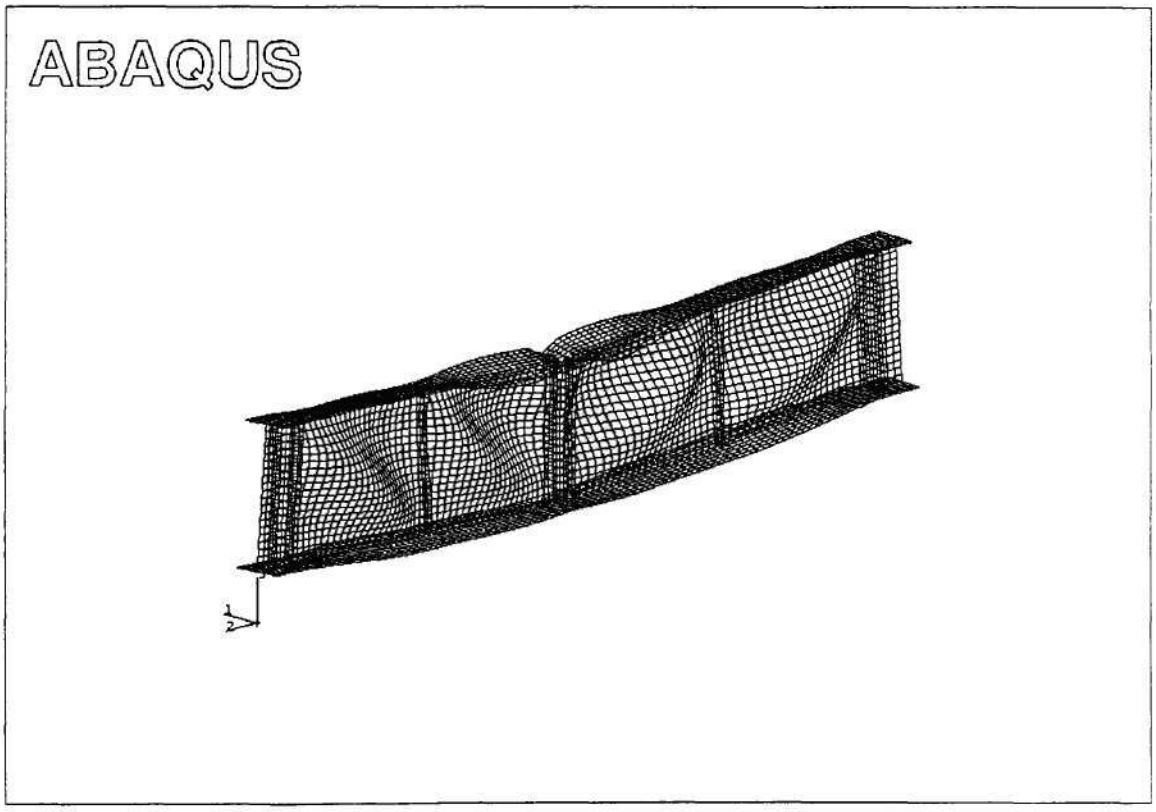

Figure 46. Deformed shape of Specimen MS2-S-0.10 at the maximum applied load.

APPENDIX 1

FINITE ELEMENT MODELING DECISIONS

The finite element models of shear test specimens all have the following attributes:

1. The ABAQUS analysis system is utilized for all of the studies.
2. The S4R shell element is used for all the plate components of the girders (i.e., the web, the top and bottom flanges, and the stiffeners). Five integration points are used through the thickness of the shell elements. Ten elements are used through the width of the flanges, and 20 elements are used through the depth of the web in all the studies. The elements at the ends of the bearing stiffeners (two-sided) are constrained to the top and bottom flange, whereas model of the transverse stiffeners (one-sided) is stopped one element short of the tension flange and is constrained to the compression flange.
3. The yield strength of the steel F_y is assumed to be 55 ksi. Also, the material is modeled as elastic-plastic-linear strain hardening, with a length of the yield plateau equal to 10 times the yield strain and a constant strain-hardening modulus of E_{st} = 800 ksi up to F_u = 70 ksi.
4. Residual stresses are not considered within the present studies. Finite element predictions for representative distributions of longitudinal residual stresses due to flame cutting and welding will be provided in a future report. Preliminary results indicate that primary effect of residual stresses is a "rounding" of the load deflection curves in the vicinity of the maximum load level. The load capacity can be reduced somewhat by the presence of residual stresses, but the preliminary results indicate that this effect is probably less than five percent.
5. The girders are rigidly restrained in the radial direction at the top and the bottom of the web at each of the locations 1 through 4. This represents the effect of radial bracing provided at these locations in the physical tests.
6. The vertical support at location 1 is modeled by restraining the displacements in the vertical direction along a line across the width of the bottom flange. That is, an ideal roller support is specified and the specimens are free to move along the tangential direction at this location. In the physical tests of these girders, a round bar will be placed under the girder at location 1.
7. The vertical support at location 3 is assumed to be rigid in compressive contact over the full area of the bearing plate, but uplift is allowed at any locations of the bottom flange that would tend to lift off of the bearing plate due to the deformations of the girder. The bearing plate is assumed to be 1" thick x 6" long x 21-7/16" wide.
8. Tangential displacements are assumed to be restrained across the entire width of the bottom flange at location 3. That is, it is assumed that the bearing plate prevents tangential displacements at this location.
9. In the physical tests, is desired to use an actuator that does not have swivels at the location of the applied load P_2. As a result, the actuator/loading frame provides some restraint against tangential movement of the top flange of the test specimens at this

location. Linear springs that are oriented in the tangential direction are provided across the flange width to model the effect of this restraint. By distributing the springs across the width of the flange, the model also simulates restraint against twisting of the top flange of the test girder about the axis of the actuator. The upper bound of the combined stiffness of the above springs against tangential movement is estimated as 250 kips/in while the lower bound is taken as 125 kips/in. The analyses presented in the body of the report are based on this upper bound stiffness. Analysis results based on a tangential stiffness of 125 kips/in and based on rigid and zero tangential restraint at location 2 are presented in Appendix 2. The primary source of flexibility within the actuator/loading frame system associated with the tangential movement of the test girders at the loading point (location 2) is twisting of the main loading beam (i.e., rigid body rotation of the actuator about an axis of the main loading beam).

APPENDIX 2

SENSITIVITY OF THE ANALYSIS RESULTS TO MODELING ASSUMPTIONS

A 2-1 EFFECT OF TANGENTIAL RESTRAINT OF THE TOP FLANGE AT LOCATION 2

As in the companion report (Phoawanich, et al 1999), it is believed that the actuator and loading frame provides some restraint against the tangential movement of the top flange of the test specimen at location of the applied load P_2. Also, due to the friction between the girder flange and the load application, there is some restraint of twisting of the girder flange about the axis of the actuator. The stiffnesses of these springs are estimated based on the upper bound of the elastic restraint of the actuator/loading frame against the tangential movement at location of applied load P_2. The above effects have been modeled by placing linear springs, which are oriented in the tangential direction of the girder, across the top-flange width at location 2. Two different models are considered for both the proposed unstiffened and stiffened Test Specimens:

1. Tangential Spring Stiffness, k = 250 kips/in. This value of stiffness represents a lower bound of the elastic restraint from the actuator/loading frame to the tangential displacement of the proposed test specimen at location 2.
2. Zero tangential restraint

The results from these analyses are summarized for L/R = 0.057 and 0.10 of both proposed moment-shear test specimens. The results for the proposed unstiffened test specimen and for the proposed stiffened test specimen are summarized in Table A1 and Table A2, respectively.

Table A1. Maximum shear forces of the proposed unstiffened test specimens with two different tangential restraint conditions.

L/R	Loading Configurations	Tangential Support of Top Flange at Location 2	V_{max} (k)	M_{max} (kips-ft)
0.057	Three-Point Bending	Tangential Spring with k = 250 kips/in	232	2784
		Zero Tangential Retraint	231	2770
	α = -0.125	Tangential Spring with k = 250 kips/in	193	2975
		Zero Tangential Retraint	191	2947
0.10	Three-Point Bending	Tangential Spring with k = 250 kips/in	215	2580
		Zero Tangential Retraint	212	2546
	α = -0.125	Tangential Spring with k = 250 kips/in	170	2624
		Zero Tangential Retraint	168	2589

Table A2. Maximum shear forces and maximum bending moment of the proposed stiffened test specimens with two different tangential restraint conditions.

L/R	Loading Configurations	Tangential Support of Top Flange at Location 2	V_{max} (k)	M_{max} (kips-ft)
0.057	Three-Point Bending	Tangential Spring with k = 250 kips/in	245	2944
		Zero Tangential Retraint	243	2920
	α = 0.8	Tangential Spring with k = 250 kips/in	273	2916
		Zero Tangential Retraint	271	2901
0.10	Three-Point Bending	Tangential Spring with k = 250 kips/in	241	2897
		Zero Tangential Retraint	238	2856
	α = 0.8	Tangential Spring with k = 250 kips/in	266	2832
		Zero Tangential Retraint	265	2829

From Table A1 and A2, the maximum shear forces for the models with zero tangential restraint and model with k = 250 kips/in are essentially the same. The maximum shear capacity and the maximum moment capacity from the model with zero tangential restraint decreases within only 2% compare to the model with k = 250 kips/in for both of the proposed moment-shear test specimen. The models based on the upper bound of the tangential spring stiffness and zero tangential restraint show that there is essentially no effect on the maximum shear capacity and maximum moment capacity of the stiffened test specimen due to the restraint of tangential movement from the actuator.

A 2-2 EFFECT OF MODELLING BRACING SYSTEM AS BRACING MEMBERS VERSUS ROLLER RADIAL SUPPORTS

In the companion report (Phoawanich, et al. 1999), the bracing system at the load locations and support locations was modeled as roller support. This type of bracing system restrained the web to remain vertical and allowed only the movement along the tangential and vertical direction only.

However, in the bracing system designed for this test, the bracing members are each connected to spherical bearings at their ends, such that each of the braces is a two-hinge mechanism. Therefore, the braces will resist radial movement of the girder (i.e., they hold the web of the test specimen in the vertical position at the braced cross-sections), while they allow free motions in the vertical and tangential directions. It should be noted that the small radial movement at the brace points may occurs because of the ends of the bracing members move through the arc of a circle while the braced cross-section deflects vertically and therefore.

To verify the effect of the bracing system modeling to the behavior of the test specimens, two different model of bracing systems are evaluated:

1. The bracing system at load locations and support locations is modeled as rollers
2. The bracing system at load locations and support locations is model to be the 4" ∅ standard weight pipes as in the bracing system designed for the shear test. This type of bracing system account for the small radial movements of the brace points that may occurred when the braced cross-section deflects vertically.

The maximum shear forces and the corresponding maximum bending moment from the FEA are summarized as follows. The results of the proposed unstiffened test specimens are summarized in Table A3. The results of the stiffened test specimens are summarized in Table A4.

Table A3. Maximum shear forces and the corresponding maximum bending moment for the proposed unstiffened test specimens for two bracing configurations.

L/R	Specimens	Bracing Configurations	V_{max} (k)	M_{max} (k-ft.)
0.057	MS1-0.06	Roller Radial Supports	232	2784
		Bracing Members	231	2772
	MS2-0.06	Roller Radial Supports	193	2978
		Bracing Members	192	2968
0.10	MS1-0.10	Roller Radial Supports	215	2580
		Bracing Members	215	2576
	MS2-0.10	Roller Radial Supports	180	2769
		Bracing Members	179	2762

Table A4. Maximum shear forces and the corresponding maximum bending moment for the proposed stiffened test specimens for two bracing configurations.

L/R	α	Bracing Configurations	V_{max} (k)	M_{max} (k-ft.)
0.057	MS1-S-0.06	Roller Radial Supports	273	2913
		Bracing Members	273	2912
	MS2-S-0.06	Roller Radial Supports	245	2940
		Bracing Members	245	2936
0.10	MS1-S-0.10	Roller Radial Supports	266	2837
		Bracing Members	266	2836
	MS2-S-0.10	Roller Radial Supports	241	2892
		Bracing Members	241	2888

REFERENCES

AASHTO (1993), *AASHTO Guide Specifications for Horizontally Curved Highway Bridges*, American Association of State and Highway Transportation Officials, Washington D.C.

AASHTO (1997), *Standard Specifications for Highway Bridges, 16th Edition*, American Association of State and Highway Transportation Officials, Washington D.C.

AASHTO (1998), *AASHTO LRFD Bridge Design Specifications 2nd Edition*, American Association of State and Highway Transportation Officials, Washington D.C.

Barth, K.E. and White, D.W. (1997), "Finite Element Evaluation of Pier Moment-Rotation Characteristics in Continuous-Span Steel I-Girders," *Engineering Structures*, Vol. 20, No. 8 1998, 761-778

Basler, K. and Thurlimann, B. (1961), " Strength of Plate Girders in Bending," *Journal of the Structural Division*, ASCE, 87, ST6 (August 1961), 153-181

Basler, K. (1961a), " Strength of Plate Girders in Shear," *Journal of the Structural Division*, ASCE, 87, ST7 (October 1961), 151-180

Basler, K. (1961b), " Strength of Plate Girders Under Combined Bending and Shear," *Journal of the Structural Division*, ASCE, 87, ST7 (October 1961), 181-197

Cooper, et al. (1978), "LRFD Criteria for Plate Girders", *Journal of the Structural Division*, ASCE 104, ST9 (September 1978), 1389-1407

Federal Highway Administration (1996), "Nominal Bending and Shear Strength", *Draft Report No. FHWA-RD-xx-yy: Task D – Nominal Bending and Shear Strength,* August 1996

Galambos, T.V. *Guide to Stability Design Criteria for Metal Structures 5th Edition*. New York: McGraw-Hill Book Company, Inc 1998

Hall, D.H. and Yoo, C.H. (1998), "Recommended Specifications for Steel Curved-Girder Bridge," Prepared for National Cooperative Highway Research Program, Transportation Research Board, National Research Council, July 1998, 103 pp.

Lee, S.C. and Yoo, C.H. (1998), "Strength of Plate Girder Web Panels Under Pure Shear", *Journal of Structural Engineering*, 124(2), 184-194.

Phoawanich, N., White, D.W., and Zureick, A.H., "Evaluation of Shear Test Specimens", *Report to FHWA*, July 1999, 25 pp.

Salmon C.G. and Johnson, J.E. (1996), *Steel Structures: Design and Behavior 4th Edition.* New York: HarperCollins College Publishers.

CURVED STEEL BRIDGE RESEARCH PROJECT

EVALUATION OF SHEAR TEST SPECIMENS

Narin Phoawanich, Donald W. White and Abdul Hamid Zureick
Georgia Institute of Technology
July 2, 1999

EXECUTIVE SUMMARY

The objective of this research is to determine the influence of shear on the strength of curved steel bridge I girders. This includes evaluation of: (1) shear capacity for high levels of shear in the presence of low bending moment, (2) interaction between flexural and shear strengths for high levels of combined bending and shear, in which case, the magnitude of the shear force may cause some reduction in the flexural capacity, and (3) influence of shear on the bending strength for low levels of shear combined with large moments, in which case, the moment gradient associated with the presence of shear can result in an increase in the capacity over that attained under pure bending.

This report focuses on the development and analysis of four experimental tests needed to verify and quantify the shear capacity of curved web panels – item (1) above. Two values of the web-panel aspect ratio d_0/D (3.0 and 1.5) and two values of L/R (0.057 and 0.10) are targeted. A symmetric girder cross-section with a D/t_w of 153.6, $b/t_f = 24.5$, and $A_f/A_w = 0.8$ is targeted in all of the suggested tests.

The significance of the above test variables is as follows. A d_0/D of 3.0 is implicitly defined as the limit between a stiffened and unstiffened web panel in the current *AASHTO Standard Specifications for Highway Bridges*. In the *Recommended Specifications for Steel Curved-Girder Bridges,* the limiting ratio for stiffened panels is 1.0. Also, L/R = 0.057 is just below the limit at which the *Recommended Specifications* suggest that curvature effects can be neglected in the analysis to determine primary vertical bending moments, and 0.10 is the current maximum L/R allowed in the *Recommended Specifications*. A D/t_w of 153.6 is selected largely because there have been no tests to date of curved unstiffened web panels subjected to high shear at web slenderness ratios larger than about 70. As a result, the *Recommended Specifications* limit the web slenderness to 100 for curved girders with unstiffened web panels and a radius of curvature less than or equal to 700 ft. The proposed studies will test the actual behavior of curved girders at the above limits and provide necessary verification of analytical finite element models to allow researchers to proceed confidently with a broad range of parametric studies.

This report incorporates material from previous project reports on the shear tests. It provides a complete assessment of the development and predicted behavior of the shear specimens, and in this regard, supercedes the previous reports.

1. INTRODUCTION

The presence of shear force can cause either a positive or a negative effect on the load capacity of a curved steel I girder. If the shear force is large but the concurrent bending moment is small, the strength can be governed by the shear capacity of the curved web panel. This situation can exist typically at end support locations, where the girder moment is zero.

Although there have been various important contributions to the state-of-the-art, including (FHWA, 1996) and (Lee and Yoo 1998), the shear capacity of curved steel I girders still is not well understood. For instance, at the present time, there have been no tests of curved unstiffened web panels subjected to high shear at web slenderness ratios greater than about 70. As a result, the *Recommended Specifications for Steel Curved-Girder Bridges* (Hall and Yoo, 1998) limit the web slenderness to 100 for girders with unstiffened web panels and a radius of curvature less than or equal to 700 ft. Also, the *Recommended Specifications* limit the aspect ratio of the web panels, d_o/D, to a maximum value of one for girders designed with stiffened web panels.

This report presents the development and analysis of four experimental tests needed to verify and quantify the shear capacity of curved web panels. Two values of the web-panel aspect ratio d_0/D (3.0 and 1.5) and two values of L/R (0.057 and 0.10) are targeted. The two girders with $d_o/D = 3.0$ are referred to as "unstiffened" and the two girders with $d_o/D = 1.5$ are referred to as "stiffened" girders for the purposes of the discussions. The corresponding tests are labeled as S1-0.06, S1-0.10, S1-S-0.06 and S1-S-0.10. A symmetric girder cross-section with D/t_w of 153.6, $b/t_f = 24.5$, and $A_f/A_w = 0.8$ is targeted in all of the suggested tests. The next section of the report discusses the overall layout and arrangement of the loads and the supports for these tests. Then, Section 3 describes the unstiffened test girder (S1) and presents the analysis results for this girder with both L/R = 0.057 and 0.10. The stiffened girder (S1-S) is addressed in a similar fashion in Section 4. Appendix 1 discusses detailed finite element modeling decisions behind the analysis predictions, and Appendix 2 summarizes various studies that have been conducted to investigate the sensitivity of the finite element predictions to variations or uncertainties in certain parameters.

2. OVERALL LAYOUT AND ARRANGEMENT OF THE TESTS

The layout and arrangement proposed for the shear tests is shown in Fig. 1. This is a three-span test configuration in which the center span (span 2-3) contains the "test girder span." Vertical loads of P_2 and $P_4 = P_2 / 3$ are applied at locations 2 and 4, and vertical supports are positioned at locations 1 and 3. Radial bracing is provided at the vertical

supports and at the load locations. This effectively simulates the limit-states behavior of an individual unsupported segment of a curved girder, including the constraint provided by the other portions of the bridge at the ends of this segment. These constraints are idealized as follows: the web of the girder is effectively held in the vertical position at the location of the crossframes, and the critical unsupported segment is continuous with the adjacent segments. The effect of vertical loadings that might be applied directly to the critical unsupported segment is not considered by this arrangement.

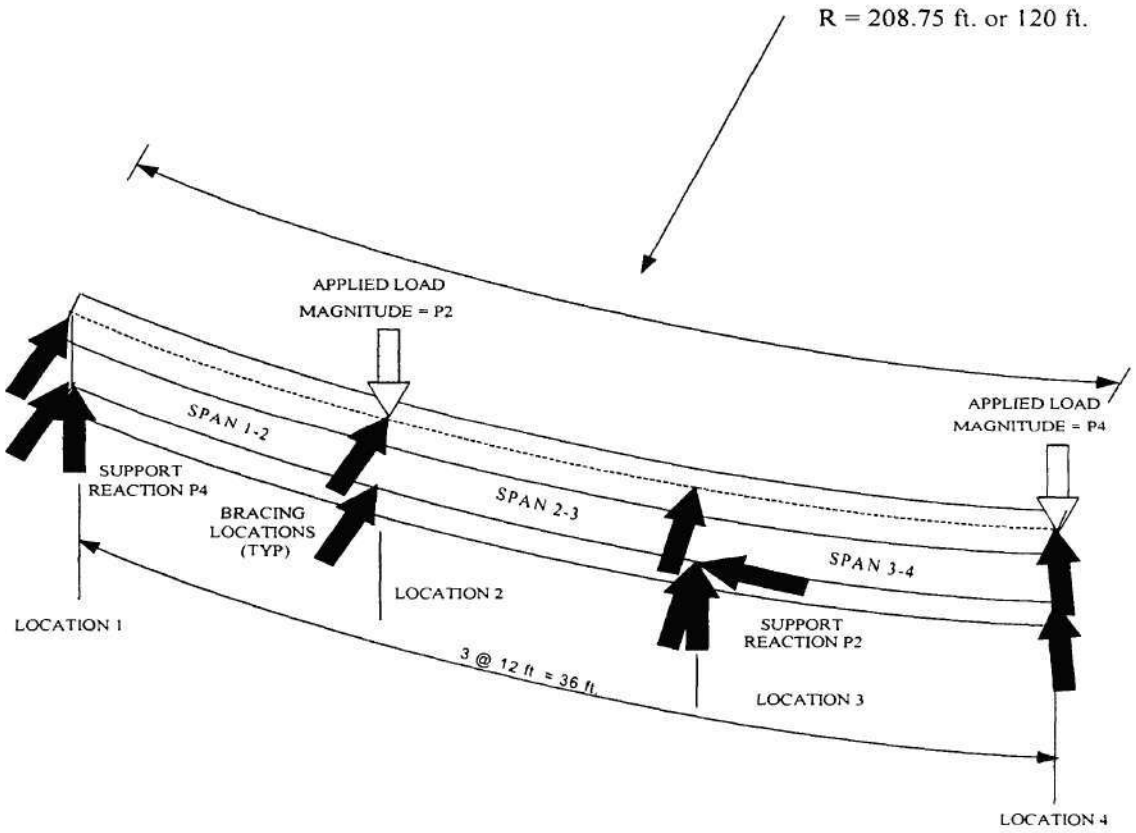

Figure 1. Shear test layout and arrangement.

Two values are considered for the radius of curvature in the proposed tests, R = 208.75 ft and 120 ft, and the unsupported span lengths are equal to 12 ft. in all of the tests. The value 208.75 is equal to the radius of curvature of the bending test specimens in the bridge test being conducted at the FHWA Turner-Fairbank Laboratory. However, the span length of 12 ft. is slightly shorter than the unsupported length of 15.65 ft employed for these bending specimens. This shorter length is necessary such that the web shear strength can be developed without generating excessive flange warping stresses. These selected L and R values give L/R ratios of 0.057 and 0.10 respectively. The value of L/R = 0.057 is just below the limit at which the *Recommended Specifications for Horizontally Curved Highway Bridges* (Hall and Yoo 1998) suggest that curvature effects can be neglected in the analysis to determine primary vertical

bending moment, and 0.10 is the current maximum L/R allowed in both the *AASHTO Guide Specifications for Horizontally Curved Highway Bridges* (AASHTO 1993) and the *Recommended Specifications*. All of the proposed tests have a web slenderness ratio, D/t_w, of 153.6. This value is selected largely because there have been no tests to date of curved unstiffened web panels subjected to high shear at web slenderness ratios larger than about 70. As a result, the *Recommended Specifications* limit the web slenderness to 100 for curved girders with unstiffened web panels and a radius of curvature less than or equal to 700 ft

The downward loads of P_2 and $P_4 = P_2/3$ at locations 2 and 4 produce a shear force of approximately P_2-$P_4 = 2P_2/3$ in the central test span of the girder (the reactions at locations 1 and 3 are slightly different than P_4 and P_2 respectively, due to the horizontal curvature of the girder; however, this difference is small). Also this loading minimizes the concurrent bending moment within the test span (the bending moment at the center of the length between locations 2 and 3 is approximately equal to zero).

3. UNSTIFFENED SHEAR TEST SPECIMENS (S1-0.06 AND S1-0.10)

3.1 DESCRIPTION

An elevation of the unstiffened test specimens is shown in Fig. 2. The primary purpose of these tests is to determine the shear capacity of curved unstiffened web panels with a web slenderness ratio of approximately 150.

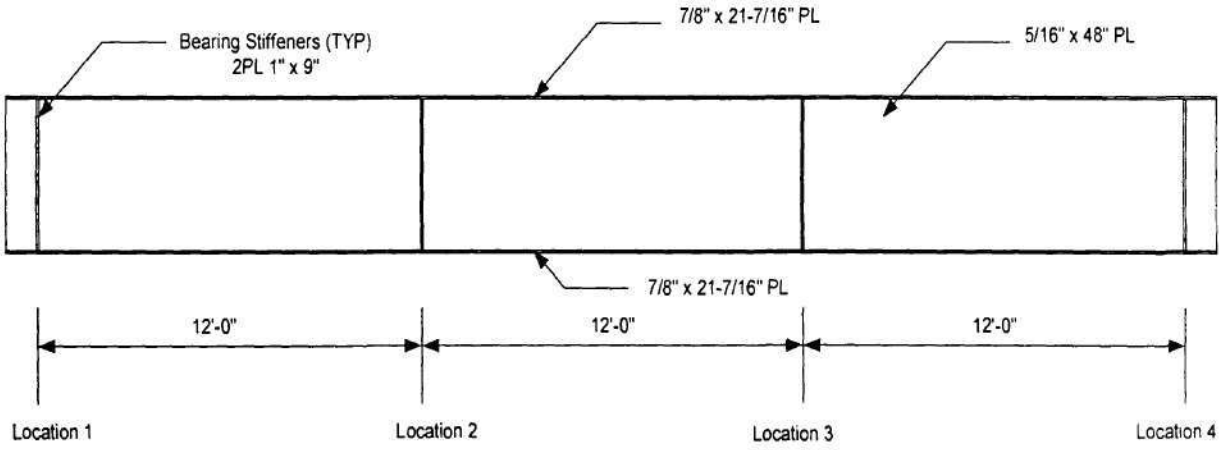

Figure 2. Unstiffened test Specimens S1-0.06 and S1-0.10.

3.2 ANALYSIS RESULTS

The predicted shear capacities (V_{max}) from the FEA solutions are shown for Specimens S1-0.06 and S1-0.10 in Table 1. These predicted capacities are compared to the following estimates of shear capacity:

1. The equations recommended by Lee and Yoo (1998)
2. The shear capacity formulas in the current *AASHTO Guide Specifications for Horizontally Curved Highway Bridges* (AASHTO 1993).
3. The current *AASHTO Guide Specifications*, but using the shear buckling coefficient (k) proposed by Lee and Yoo (1998), which accounts more realistically for the restraint provided by the flanges against web buckling.
4. The theoretical plastic shear capacity of the web (V_p)

Table 1. Maximum shear force for Specimens S1-0.06 and S1-0.10.

Methods	Shear Force	Specimens	
		S1-0.06	S1-0.10
FEA	V_{max} (k)	253	238
Lee and Yoo (1998)	V_u (k) V_{max}/V_u	279 0.907	279 0.853
AASHTO Guide Specifications for Horizontally Curved Highway Bridges	V_u (k) V_{max}/V_u	191 1.325	191 1.246
AASHTO Guide Specifications (1993) but using the shear buckling coefficient proposed by Lee and Yoo (1998)	V_u (k) V_{max}/V_u	238 1.063	238 1.000
Plastic Shear Capacity	V_u (k) V_{max}/V_P	478.5 0.529	478.5 0.497

Full nonlinear finite element analyses are utilized to obtain the predicted shear capacities (V_{max}). The results from Table 1 show that the *AASHTO Guide Specifications* (1993) give a good prediction when used with the shear buckling coefficient proposed by Lee and Yoo (1998). However, the shear capacities calculated from the complete design equations proposed by Lee and Yoo (1998) are quite different from the value obtained by FEA (about 10-15%). In the equations proposed by Lee and Yoo (1998), the shear capacity is proportional to $0.6V_{cr} + 0.4\ V_p$ for all cases, where V_{cr} is the elastic shear

buckling capacity of the web, and 0.4 V_p is taken as the contribution from post buckling strength. Therefore, the contribution from post-buckling does not depend on the panel aspect ratio in the Lee and Yoo equations. Also, as the web panel approaches unstiffened conditions (for a large d_o/D), the strength of a noncompact web should be related to V_{cr}, but this relationship is not a constant 0.6. As a result, while the Lee and Yoo equations appear to be accurate for smaller d_o/D values, they do not appear to be a reliable predictor of the shear capacity for $d_o/D = 3.0$. This conclusion is confirmed by results shown in the Lee and Yoo paper.

The flange warping to bending stress ratios (f_w/ f_b) at locations 2 and 3, at the maximum load level, are shown for Specimens S1-0.06 and S1-0.10 in Table 2.

Table 2. Warping to bending stress ratios at the maximum load level for Specimens S1-0.06 and S1-0.10.

Specimens	L/R	f_w/f_b			
		Location 2		Location 3	
		Top	Bottom	Top	Bottom
S1-0.06	0.057	0.205	0.462	0.452	0.185
S1-0.10	0.10	0.255	0.609	0.615	0.269

The f_w/ f_b values for Specimen S1-0.06 (L/R = 0.057) are less than the AASHTO Guide Specification (1993) limit of 0.5. However, for L/R = 0.10, the f_w /f_b ratios are greater than 0.50 at the bottom flange of location 2 and at the top flange of location 3. This increase in the warping to bending stress ratio is likely to be a key cause for the decrease in the predicted shear capacity from Specimen S1-0.06 to Specimen S1-0.10 (see Table 1). However, it should be noted that the flanges remain elastic throughout the girder lengths in these tests.

The maximum applied loads P_2 and P_4 for the unstiffened specimens are shown in Table 3, and the vertical displacements at the load locations at this load level are shown in Table 4.

Table 3. Maximum applied loads P_2 and P_4 for Specimens S1-0.06 and S1-0.10.

Specimens	Load P2 (k)	Load P4 (k)
S1-0.06	380	127
S1-0.10	357	119

Table 4. Vertical displacements at load locations for Specimens S1-0.06 and S1-0.10 at the maximum load level.

Specimens	L/R	Vertical Displacement (in)	
		Location 2	Location 4
S1-0.06	0.057	0.409	0.415
S1-0.10	0.10	0.391	0.385

The radial reactions at each of lateral bracing locations, at the maximum load level, are summarized for each of the models in Table 5.

Table 5. Radial reactions at the maximum load level for Specimens S1-0.06 and S1-0.10.

Specimens	L/R	Radial Reactions (kips)							
		Location 1		Location 2		Location 3		Location 4	
		Top	Bottom	Top	Bottom	Top	Bottom	Top	Bottom
S1-0.06	0.057	-2.177	2.435	-16.889	16.581	16.835	-16.920	2.520	-2.212
S1-0.10	0.10	-3.777	4.078	-26.197	25.499	25.56	-25.443	4.026	-3.508

The maximum radial reactions in both of the tests are well below the capacity of the bracing system designed for this test, which is 86 k in compression and 97 k in tension.

The total applied load P_2 versus the radial reactions at location 2, which is the location that has largest radial reaction, is shown for specimens S1-0.06 and S1-0.10 in Figs. 3 and 4 respectively

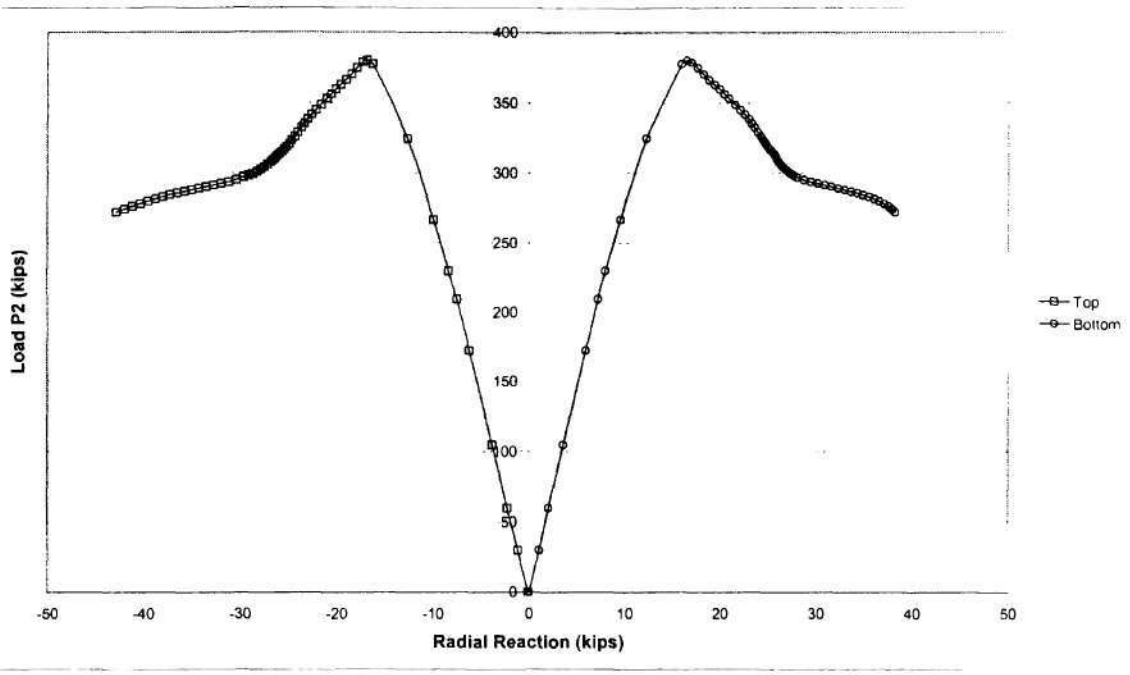

Figure 3. Load P_2 versus radial reactions at location 2 for Specimen S1-0.06.

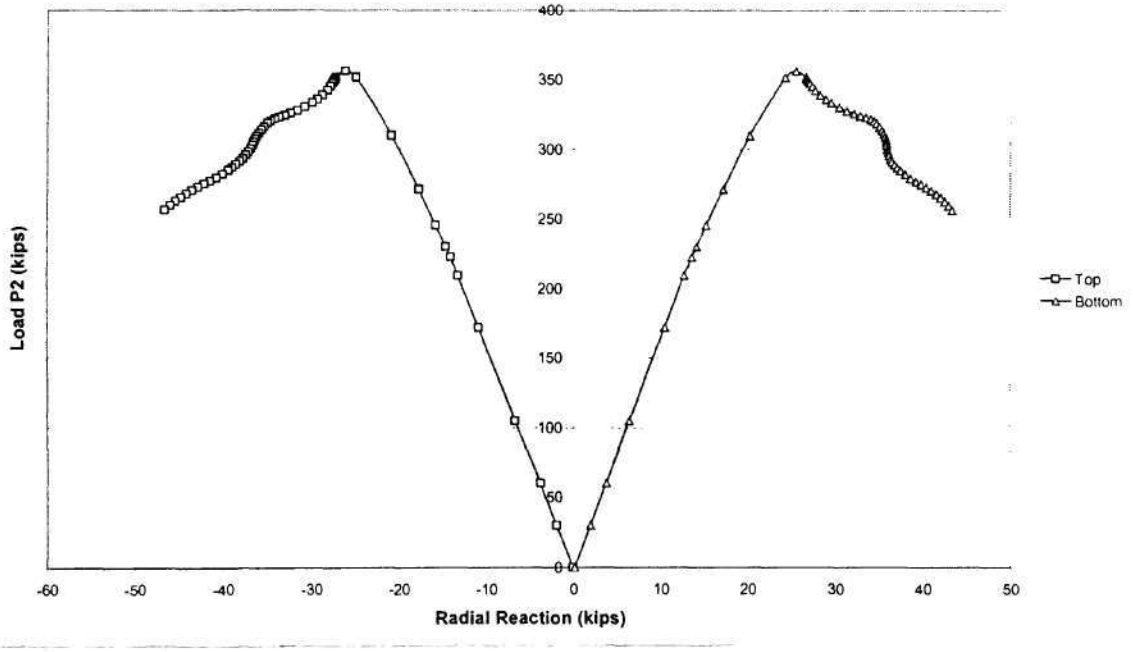

Figure 4. Load P_2 versus radial reactions at location 2 for Specimen S1-0.10.

The total applied load P_2 versus the vertical displacement at each of the load points and the deformed shape of Specimen S1-0.06 at its peak load are shown in Figs. 5 and 6. These results are shown for Specimen S1-0.10 in Figs 7 and 8.

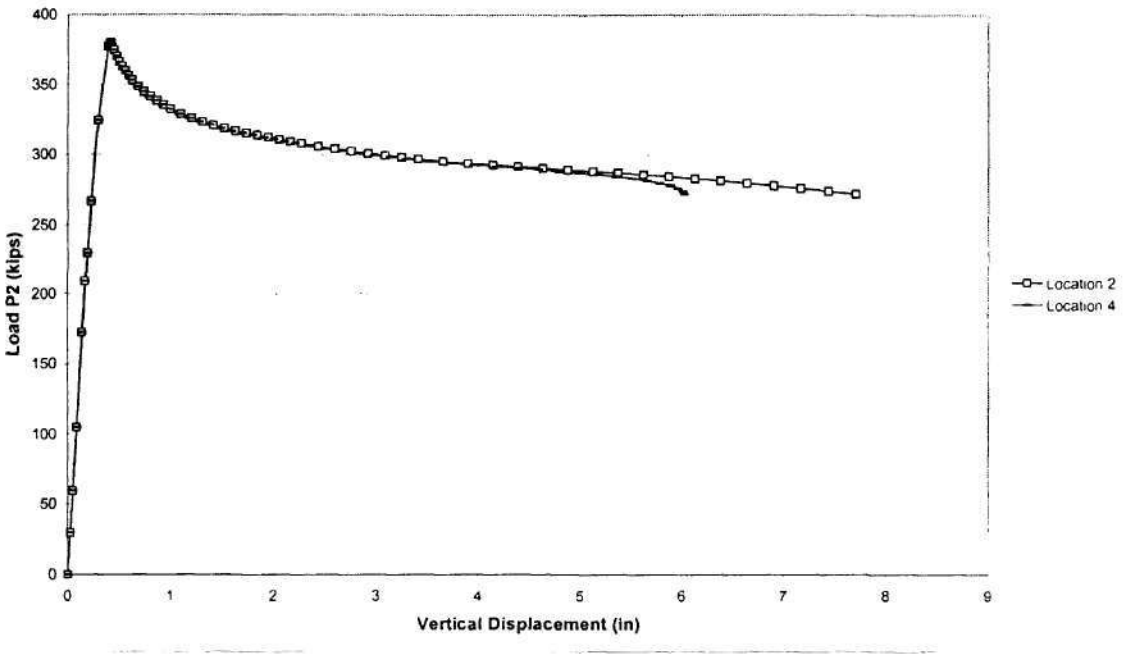

Figure 5. Load P_2 versus vertical displacements at the load locations for Specimen S1-0.06.

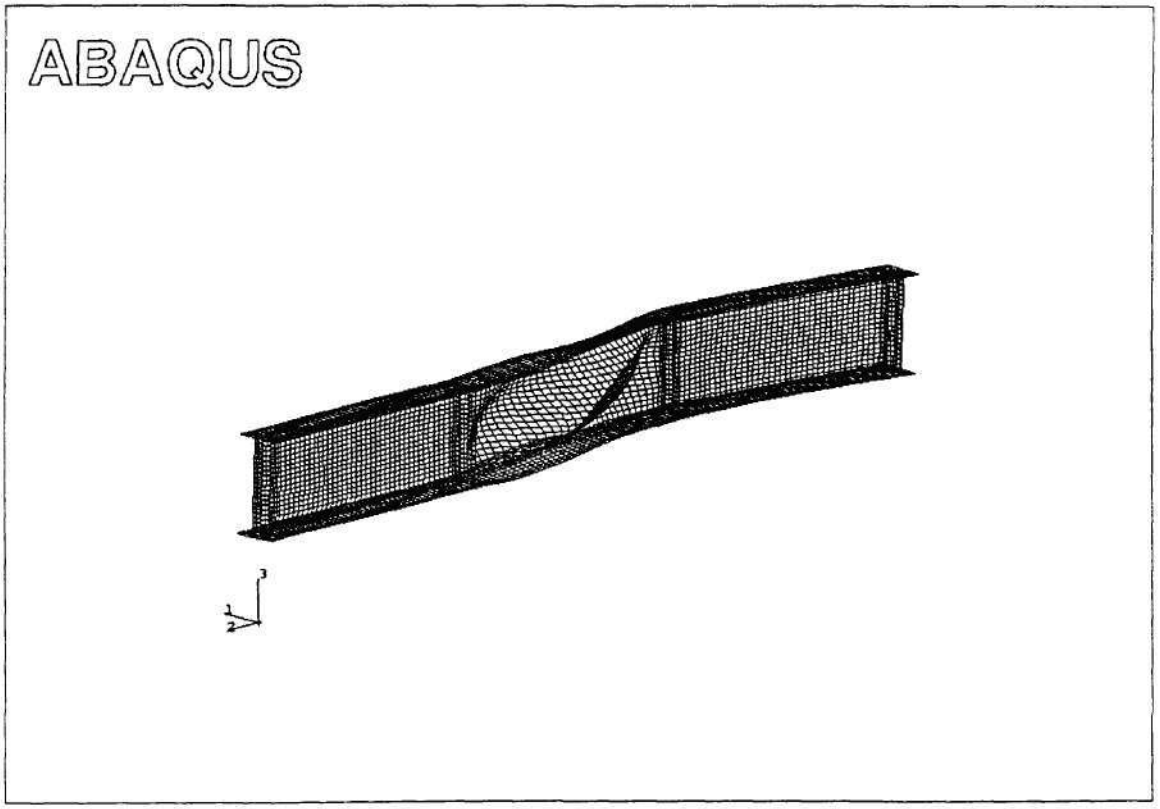

Figure 6. Deformed shape of Specimen S1-0.06 at the maximum applied load.

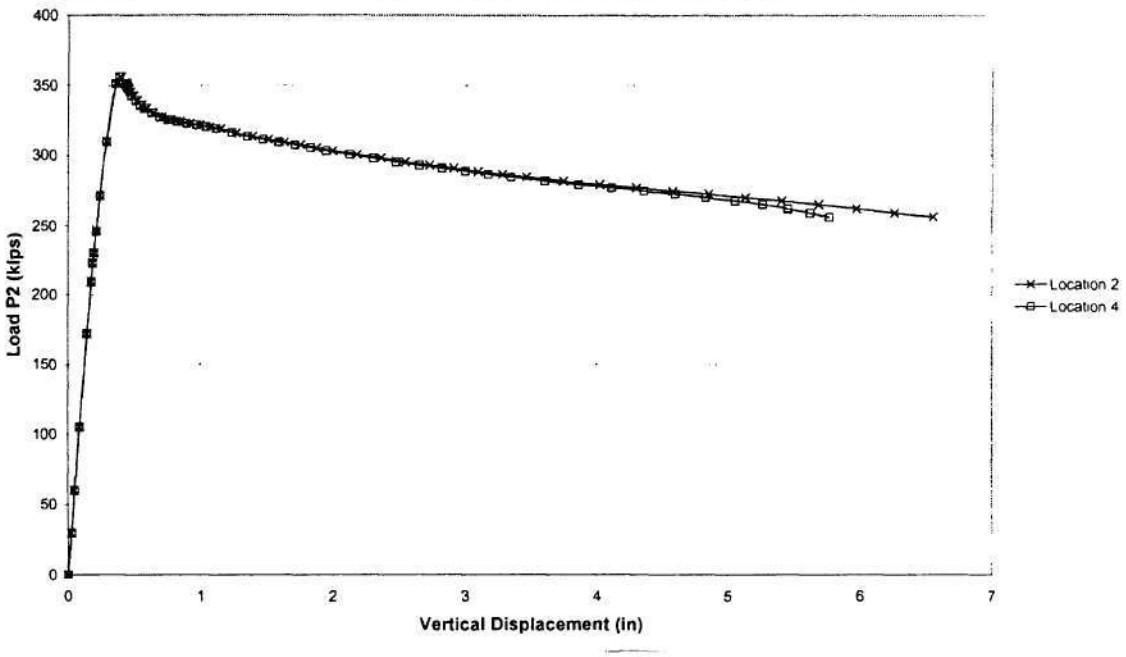

Figure 7. Load P_2 versus vertical displacements at the load locations for Specimen S1-0.10.

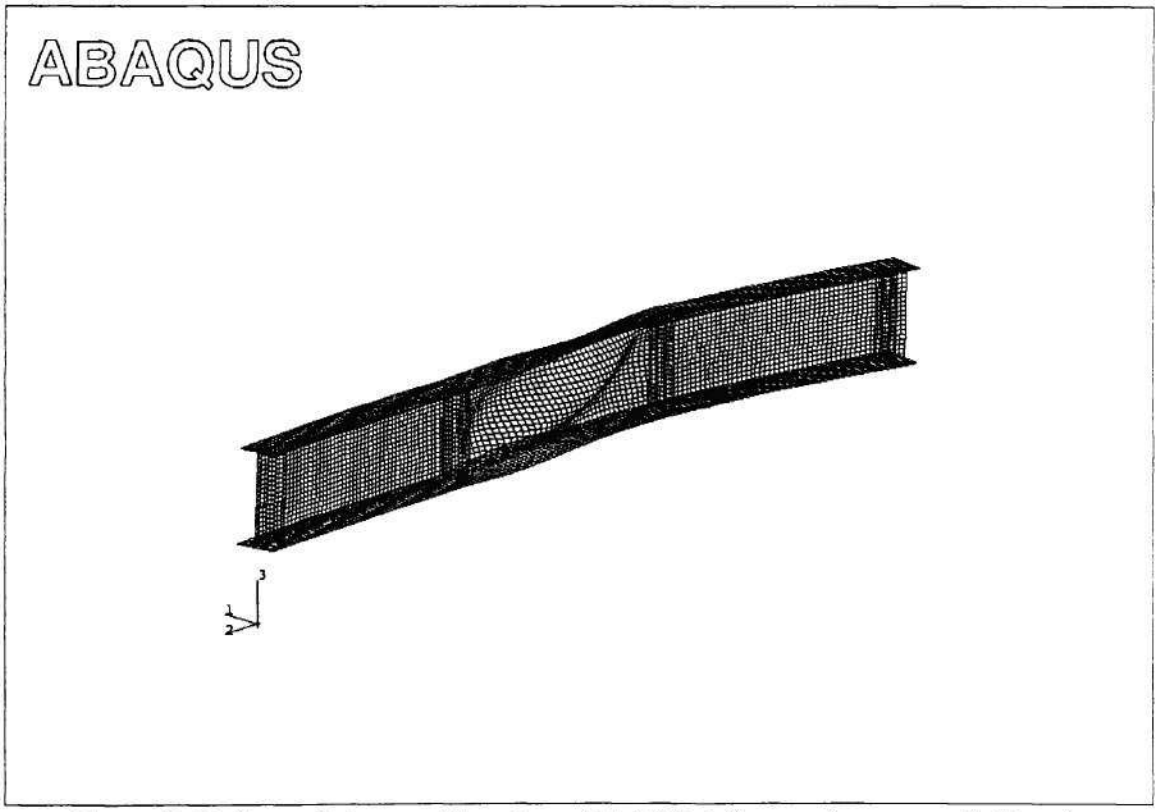

Figure 8. Deformed shape of Specimen S1-0.10 at the maximum applied load.

4. STIFFENED SHEAR TEST SPECIMENS (S1-S-0.06 AND S1-S-0.10)

4.1 DESCRIPTION

The stiffened shear test specimens are configured by placing a single transverse stiffener at the center of the panels in the layout of the unstiffened girders. This produces a web panel aspect ratio of $d_o/D = 1.5$. Otherwise, the stiffened test specimens have the same cross-section geometry and overall layout as the unstiffened specimens (see Fig. 9). The current limit on transverse stiffener spacing given in the *Recommended Specifications* is equal to the web depth D (i.e., $d_0/D = 1.0$). The web slenderness ratio D/t_w of this test specimen is slightly higher than the limit of 150 for transversely stiffened girders given in the *Recommended Specifications*.

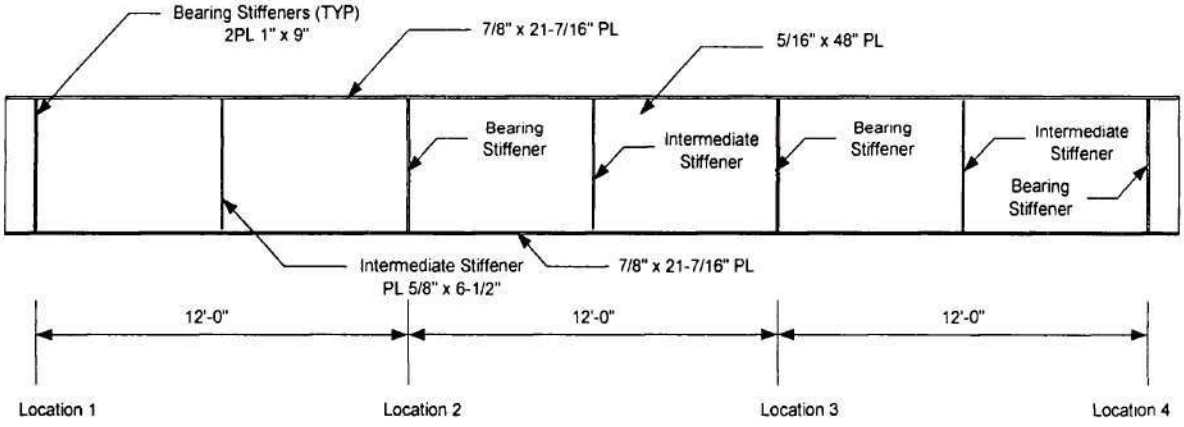

Figure 9. Stiffened test Specimens S1-S-0.06 and S1-S-0.10.

4.2 ANALYSIS RESULTS

The predicted shear capacities (V_{max}) from the finalized FEA solutions are shown for Specimens S1-S-0.06 and S1-S-0.10 in Table 6. These predicted capacities are compared to design estimates from the same references as considered in Table 1.

Table 6. Maximum shear force for Specimens S1-S-0.06 and S1-S-0.10.

Methods	Shear Force	Specimens	
		S1-S-0.06	S1-S-0.10
FEA	V_{max} (k)	302	295
Lee and Yoo (1998)	V_u (k) V_{max}/V_u	292 1.034	292 1.010
AASHTO Guide Specifications for Horizontally Curved Highway Bridges	V_u (k) V_{max}/V_u	285 1.060	285 1.035
AASHTO Guide Specifications (1993) but using the shear buckling coefficient proposed by Lee and Yoo (1998)	V_u (k) V_{max}/V_u	310 0.974	310 0.952
Plastic Shear Capacity	V_u (k) V_{max}/V_P	478.5 0.631	478.5 0.617

The Lee and Yoo (1998) formulas provide the best prediction of the shear capacity for these tests (one to three percent conservative), although the AASHTO Guide Specifications (1993) when used with the shear buckling coefficient proposed by Lee and Yoo also provide a reasonably accurate prediction of the shear strength (3.5 to 6 percent unconservative).

The flange warping to bending stress ratios (f_w/ f_b) at locations 2 and 3, at the maximum load level, are shown for Specimens S1-S-0.06 and S1-S-0.10 in Table 7. Similar to the behavior for the unstiffened girders, it should be noted that, the flanges remain elastic throughout the girder lengths in these tests

Table 7. Warping to bending stress ratios for Specimens S1-S-0.06 and S1-S-0.10.

Specimens	L/R	f_w/f_b			
		Location 2		Location 3	
		Top	Bottom	Top	Bottom
S1-S-0.06 S1-S-0.10	0.057 0.10	0.16 0.224	0.137 0.216	0.01 0.217	0.011 0.202

In contrast with the results for the unstiffened test specimens, the f_w/f_b values are less than the AASHTO limit of 0.5 for both L/R = 0.057 and 0.10. It is apparent that the "frame action" from the transverse stiffeners helps to reduce the flange warping stresses. It is believed that that the small f_w/f_b values for both L/R values shown in Table 7 are a major contributor to the result that the shear capacity is reduced by only 2.3 percent in going from Specimen S1-S-0.06 to Specimen S1-S-0.10 in Table 6. The maximum applied loads P_2 and P_4 for the stiffened specimens are shown in Table 8, and the vertical displacements at the load locations at this load level are shown in Table 9.

Table 8. Maximum applied loads P_2 and P_4 for Specimens S1-0.06 and S1-0.10.

L/R	Specimens	Load P1 (k)	Load P2 (k)
0.057	S1-S-0.06	453	151
0.10	S1-S-0.10	442	147

Table 9. Vertical displacements at the load locations, at the maximum load level, for Specimens S1-S-0.06 and S1-S-0.10.

Specimens	L/R	Vertical Displacement (in)	
		Location 2	Location 4
S1-S-0.06	0.057	2.363	2.621
S1-S-0.10	0.10	2.426	2.664

The radial reactions at each of the lateral bracing locations, at the maximum load level, are summarized for each of the models in Table 10.

Table 10. Radial reactions at the maximum load level for Specimens S1-S-0.06 and S1-S-0.10.

Specimens	L/R	Radial Reactions (kips)							
		Location 1		Location 2		Location 3		Location 4	
		Top	Bottom	Top	Bottom	Top	Bottom	Top	Bottom
S1-S-0.06	0.057	-2.346	2.997	-22.476	26.267	20.274	-25.02	4.443	-2.473
S1-S-0.10	0.10	-4.409	4.083	-36.05	42.698	31.916	-38.874	6.554	-4.104

The total applied load P_2 versus the radial reactions at location 2, which is the location that has the maximum radial reaction, is shown for the stiffened test specimens in Figs. 10 and 11. It can be observed from Figs. 10 and 11 that the maximum radial reaction is well below the capacity of the bracing system designed for this test, which is 86 k in compression and 97 k in tension.

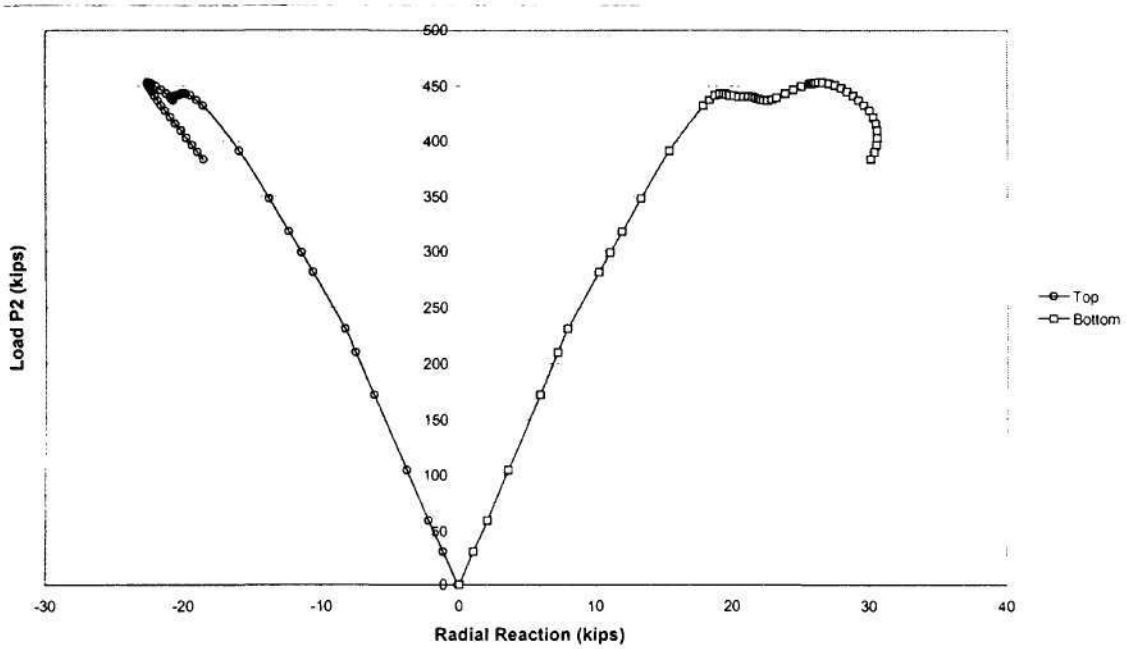

Figure 10. Load P_2 versus radial reactions at location 2 for Specimen S1-S-0.06.

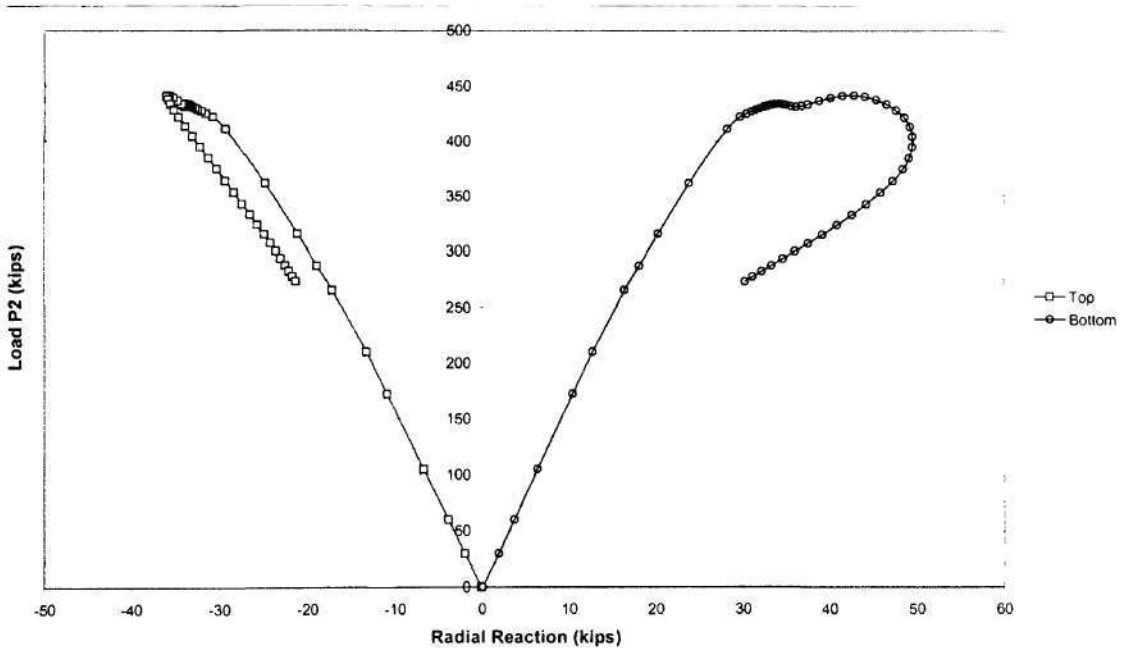

Figure 11. Load P_2 versus radial reaction at location 2 for Specimen S1-S-0.10.

The total applied load P_2 versus the vertical displacement at each of the load points and the deformed shape of Specimen S1-S-0.06 at its peak load are shown in Figs. 12 and 13. Also, these results are shown for Specimen S1-S-0.10 in Figs. 14 and 15.

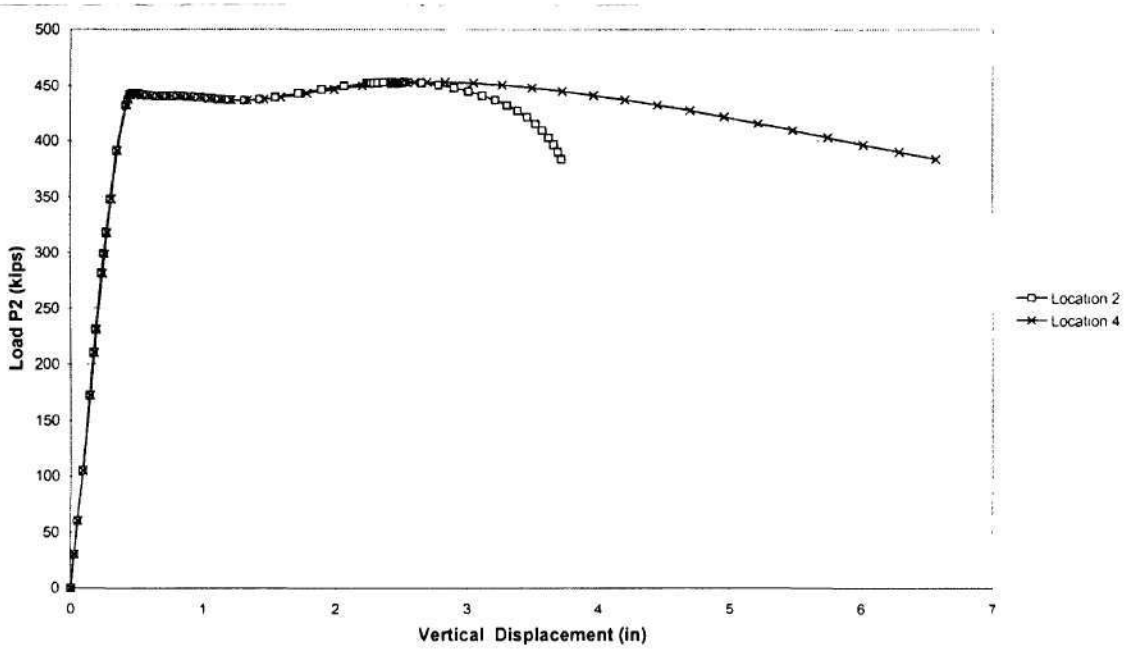

Figure 12. Load P_2 versus vertical displacements at the load locations for Specimen S1-S-0.06.

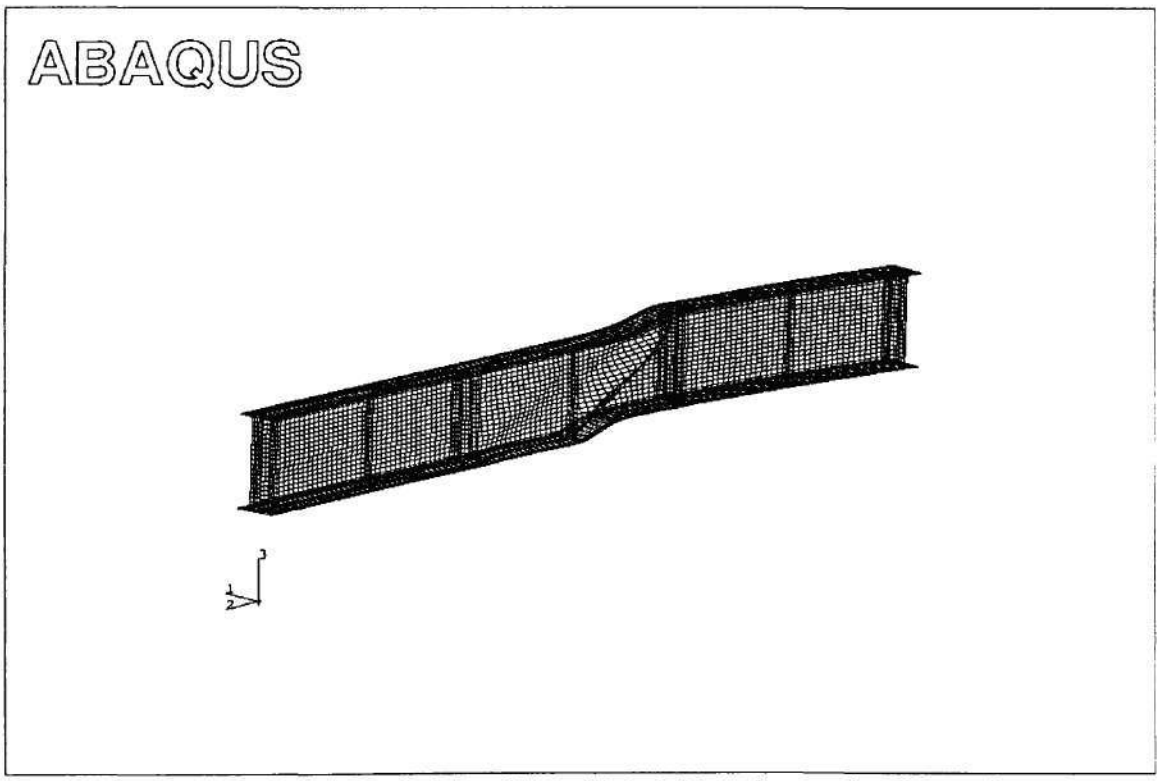

Figure 13. Deformed shape of Specimen S1-S-0.06 at the maximum applied load.

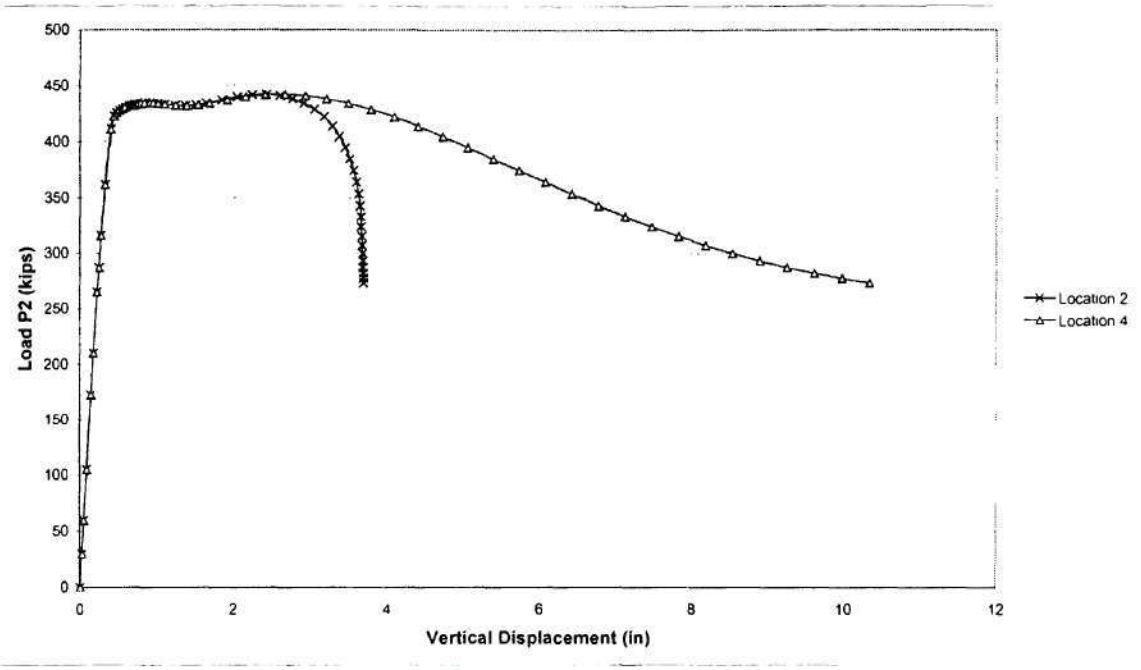

Figure 14. Load P_2 versus vertical displacements at the load locations for Specimen S1-S-0.10.

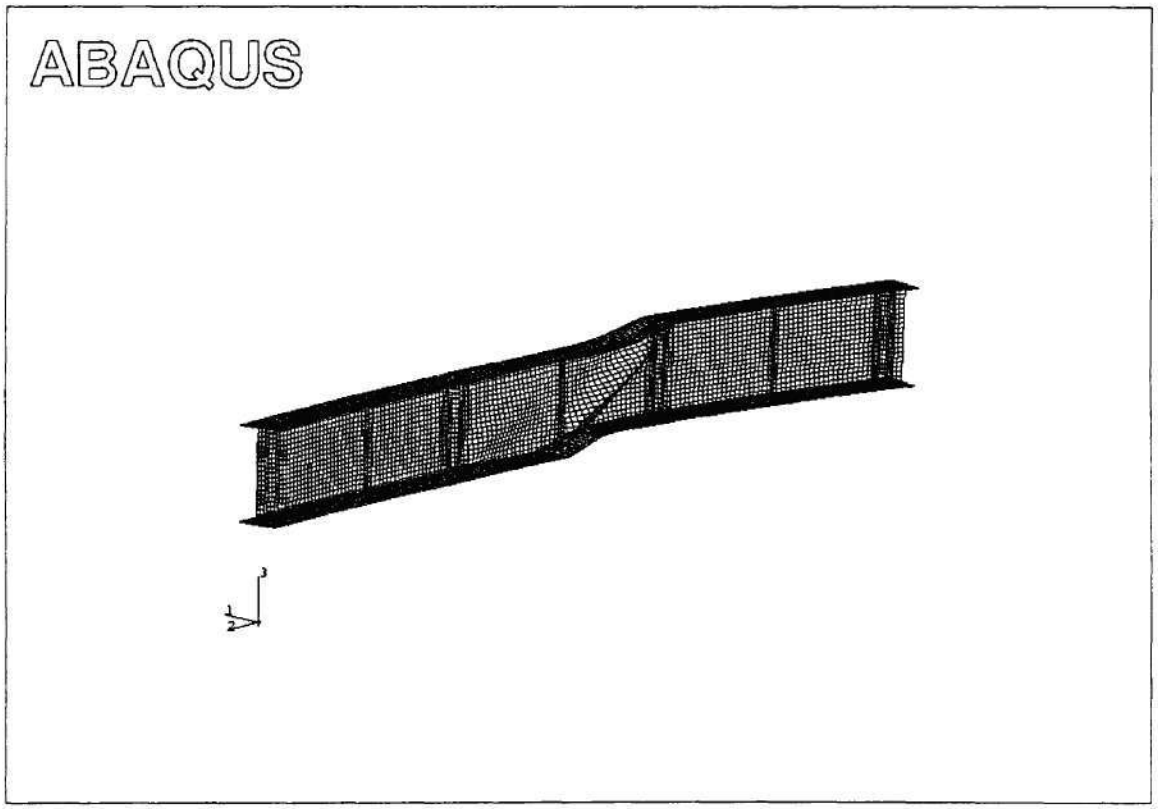

Figure 15. Deformed shape of Specimen S1-S-0.10 at the maximum applied load.

APPENDIX 1
FINITE ELEMENT MODELING DECISIONS

The finite element models of shear test specimens all have the following attributes:

1. The ABAQUS analysis system is utilized for all of the studies.
2. The S4R shell element is used for all the plate components of the girders (i.e., the web, the top and bottom flanges, and the stiffeners). Five integration points are used through the thickness of the shell elements. Ten elements are used through the width of the flanges, and 20 elements are used through the depth of the web in all the studies. The elements at the ends of the bearing stiffeners (two-sided) are constrained to the top and bottom flange, whereas the element at the ends of the transverse stiffeners (one-sided) are stopped one element short of the tension flange and is constrained to the compression flange.
3. The yield strength of the steel F_y is assumed to be 55 ksi. Also, the material is modeled as elastic-plastic-linear strain hardening, with a length of the yield plateau equal to 10 times the yield strain and a constant strain-hardening modulus of E_{st} = 800 ksi up to F_u = 70 ksi.
4. Residual stresses are not considered within the present studies. Finite element predictions for representative distributions of longitudinal residual stresses due to flame cutting and welding will be provided in a future report. Preliminary results indicate that primary effect of residual stresses is a "rounding" of the load deflection curves in the vicinity of the maximum load level. The load capacity can be reduced somewhat by the presence of residual stresses, but the preliminary results indicate that this effect is probably less than five percent.
5. The girders are rigidly restrained in the radial direction at the top and the bottom of the web at each of the locations 1 through 4. This represents the effect of radial bracing provided at these locations in the physical tests.
6. The vertical support at location 1 is modeled by restraining the displacements in the vertical direction along a line across the width of the bottom flange. That is, an ideal roller support is specified and the specimens are free to move along the tangential direction at this location. In the physical tests of these girders, a round bar will be placed under the girder at location 1.
7. The vertical support at location 3 is assumed to be rigid in compressive contact over the full area of the bearing plate, but uplift is allowed at any locations of the bottom flange that would tend to lift off of the bearing plate due to the deformations of the girder. The bearing plate is assumed to be 1" thick x 6" long x 21-7/16" wide.
8. Tangential displacements are assumed to be restrained across the entire width of the bottom flange at location 3. That is, it is assumed that the bearing plate prevents tangential displacements at this location.
9. In the physical tests, is desired to use an actuator that does not have swivels at the location of the applied load P_2. As a result, the actuator/loading frame provides some restraint against tangential movement of the top flange of the test specimens at this location. Linear springs that are oriented in the tangential direction are provided across the flange width to model the effect of this restraint. By distributing the springs

across the width of the flange, the model also simulates restraint against twisting of the top flange of the test girder about the axis of the actuator. The upper bound of the combined stiffness of the above springs against tangential movement is estimated as 250 kips/in while the lower bound is taken as 125 kips/in. The analyses presented in the body of the report are based on this upper bound stiffness. Analysis results based on a tangential stiffness of 125 kips/in and based on rigid and zero tangential restraint at location 2 are presented in Appendix 2. The primary source of flexibility within the actuator/loading frame system associated with the tangential movement of the test girders at the loading point (location 2) is twisting of the main loading beam (i.e., rigid body rotation of the actuator about an axis of the main loading beam).

APPENDIX 2
SENSITIVITY OF THE ANALYSIS RESULTS TO MODELING ASSUMPTIONS

Variations in the actual test conditions from those assumed within the finite element models, as well as a number of modeling assumptions and approximations, can have an influence on the accuracy of the finite element predictions. In the sections below, three specific issues are investigated:

1. As noted in Appendix 1, it is desired to use an actuator at location 2 that does not have swivels. In the finite element models used to produce the results presented in the body of this report, the tangential restraint conditions imposed on the test girder by this actuator have been modeled by a line of springs across the with of the top flange at location 2 with a total combined stiffness of 250 kips/in. Analysis results based on a tangential stiffness of 125 kips/in and based on rigid and zero tangential restraint at location 2 are considered in Section A2.1. These results indicate that the tangential restraint induced by the above actuator does not have any significant influence on the girder behavior.
2. In the design of the test specimens, consideration was given to whether multiple stiffeners should be utilized at locations 2 and 3 to eliminate any possible effect of the transverse load from the actuator at location 2 or the vertical support at location 3 on the strength of the test panels. Analysis results are summarized in Section A2.2 which indicate that the use of single or multiple stiffeners at these locations should have a negligible influence on the test results.
3. In the physical layout of the shear tests, it is desired to brace the girders radially at the top and bottom of the web by "pin-ended" struts (with spherical bearings at each of their ends) that will be tied to a reaction wall within the testing laboratory. This bracing arrangement can potentially influence the test results due to the fact that the ends of the braces attached to the top and bottom of the girder web will tend to move through the arc of a circle as the loading points (locations 2 and 4) are deflected vertically. However, it was initially felt that the vertical deflections of the proposed tests would be small enough such that the horizontal deflections induced by the

bracing system would be negligible. Section A2.3 presents the results of preliminary calculations which indicate that the elastic lateral bending stresses in the girder flanges are small for the complete range of deflections that are expected within the proposed shear tests. Section A2.4 then presents results that show that the maximum strengths of the girders are essentially unaffected by the proposed bracing arrangement, although in one of the tests, the post-peak behavior appears to be affected.

A2.1 EFFECT OF TANGENTIAL RESTRAINT FROM THE ACTUATOR AT THE TOP FLANGE AT LOCATION 2

It is desired to use an actuator that does not have swivels at location 2 in the tests. As a result, the actuator and loading frame provides some restraint against the tangential movement of the top flange of the test specimen at this location. It was felt that the effect of this restraint must be quantified before the loading arrangement for the physical tests could be finalized. Also, due to the friction between the girder flange and the load application, there is some restraint of twisting of the girder flange about the axis of the actuator. The above effects have been modeled by placing linear springs, which are oriented in the tangential direction of the girder, across the top-flange width at location 2. The stiffnesses of these springs are estimated based on the elastic restraint of the actuator/loading frame against tangential movement at location 2. Three different models with different degrees of tangential restraints are of tangential restraints considered below for specimen S1-S-0.06:

1. Zero tangential restraint at location 2.
2. A sum of the tangential spring stiffnesses of k = 125 kips/in. This value of stiffness represents a lower bound of the elastic restraint from the actuator/loading frame to the tangential displacement of the test specimen at location 2.
3. A sum of the tangential spring stiffnesses of k = 250 kips/in. This value of stiffness represents an upper bound of the elastic restraint from the actuator to the tangential displacement of the test specimen at location 2.
4. Rigid tangential restraint along the top flange of the test specimen at location 2.

The results from these analyses are summarized in Table A2.1.

Table A2.1. Maximum applied loads and shear force for Specimen S1-S-0.06 with four different tangential restraint conditions at location 2.

Model	Tangential Support of Top Flange at Location 2	Load P2 (k)	Load P4 (k)	V_{max} (k)
S1S-S-6	Zero Tangential Restraint	449	150	299
S1S-S-7	Tangential Spring with k = 125 kips/in	453	151	302
S1S-S-8	Tangential Spring with k = 250 kips/in	453	151	302
S1S-S-9	Rigid Tangential Restraint	605	202	403

From Table A2.1, the predicted shear capacity for the models with zero tangential restraint, k = 125 kips/in and k = 250 kips/in are all essentially the same. The maximum shear capacity decreases by only one percent, from V_{max} = 302 kips to V_{max} = 299 kips if zero tangential restraint is assumed at location 2. However, when a rigid tangential restraint is assumed at the top flange of the girder at location 2, the maximum shear force is increased by 33% to V_{max} = 403 kips. This was the first case that was considered, and subsequently, it was decided that the flexibility of the supports needed to be modeled. The rigid tangential restraint does not realistically represent the actual restraint conditions that would be present in the physical test. This is due mainly to the torsional flexibility of the main loading beam in the test frame. In contrast, the models based on the upper and lower bounds of the tangential stiffness show that there is essentially no effect on the maximum shear capacity of the stiffened test specimen due to the restraint of tangential movement from the actuator. Since the stiffened test specimen S1-S-0.06 has the largest vertical displacement at the maximum load level, it also has the largest tangential movement of the top flange at location 2. Therefore, it can be concluded that the effect of tangential restraint conditions from the actuator also should not have any significant effect on the behavior for all of the shear tests.

It should be noted that the primary effect of the tangential restraint at location 2 is that the primary "shear buckling" mode of failure occurs in the test panel adjacent to location 3 (see Figs. 13 and 15).

4.2 EFFECT OF SINGLE VERSUS MULTIPLE BEARING STIFFENERS AT LOCATIONS 2 AND 3 ON THE STRENGTH OF THE TEST SPECIMENS

It is possible that the transverse loads applied to the girder web by the actuator at location 2 and by the vertical support at location 3 may have some influence on the capacity of the test specimens. Therefore, it is necessary to investigate the behavior of the girders with single and with multiple bearing stiffeners at these locations, to ascertain whether multiple stiffeners should be used to "isolate" the test web panels from the locations where the transverse loads are applied. The use of double bearing stiffeners was considered, but this option was eliminated since it was desired to connect the radial braces into a bearing stiffener at the centerline of the loading and vertical support locations. Table A2.2 compares the results for the analysis of Specimen S1-S-0.06 with a single bearing stiffener (2 PL 1" x 9") at the support and loading locations, and with three bearing stiffeners (2 PL 1" x 9"), spaced at 6" apart, at these locations. In each of these analyses, a tangential spring stiffness of k =250 kip/in is assumed.

Table A2.2. Maximum shear force for shear test Specimen S1-S-0.06 with two different sizes of stiffeners.

Model	Bearing Stiffeners at the End of Test Panel	Vmax (k)
S1S-S-8	Single Bearing Stiffeners size 2PL 1" x 9"	302
S1S-S-10	Triple Bearing Stiffeners size 2PL 1" x 9" each	310

The maximum shear force predicted by the model with triple bearing stiffeners is only 3% higher than that obtained with single bearing stiffeners. This and hand calculations of the approximate stresses that would be induced in the web due to the transverse loads indicates that the use of a single bearing stiffener at the loading and support locations should be sufficient. The use of triple bearing stiffeners would increase the fabrication cost, plus the use of these stiffeners introduces potential extra warping restraint to the flanges at locations 2 and 3. It is expected that this additional warping restraint is a key cause of the increase in the capacity for the model with triple bearing stiffeners (see the discussion regarding the f_w/f_b values for the stiffened versus the unstiffened test specimens in Section 4.2). Also, the use of triple stiffeners might be perceived as looking rather odd to a design engineer. Therefore, it is suggested that the test girders should be fabricated with single bearing stiffeners at each of locations1 through 4.

A2.3 EFFECT OF RADIAL DISPLACEMENTS AT THE BRACING LOCATIONS -- FLANGE ELASTIC BENDING STRESSES

In the bracing system designed for this test, the bracing members are each connected to the test specimens and to a reaction wall by spherical bearings at their ends, such that each of the braces is a two-hinge mechanism. Therefore, the braces resist radial movement of the girder (i.e., they hold the web of the test specimen approximately in a vertical position at the braced cross-sections), while they allow free motions in the vertical and tangential directions.

However, for this bracing arrangement, the ends of the bracing members move through the arc of a circle when a braced cross-section deflects vertically. It is necessary to check the effect of these radial displacments on the behavior of the test specimen for the range of vertical displacements expected in the tests.

The maximum elastic lateral bending moments and the corresponding bending stresses in the flanges of the test specimen induced by the radial displacements of the brace points is shown for three different levels of vertical displacement at the load points (locations 2 and 4) in Table A2.3. The maximum force induced in the braces is equal to 1.5M/12, where M is the lateral moment shown in the table. The vertical displacements at locations 2 and 4 are assumed to be the same for this analysis. This is approximately true

until the girder is loaded well into post-collapse. The procedure for obtaining the results shown in the table is as follows: the corresponding radial displacements of the brace points are calculated for the specified vertical displacements at locations 2 and 4, then these displacements are imposed on the test girder and a linear elastic analysis is conducted.

It should be noted that in the physical tests, the braces will be inclined vertically at one-half of the total desired vertical displacement prior to the start of the test. This doubles the range of vertical motion that the test specimen can be subjected to for a given radial displacement of the brace points. Also, the test girders can be "pre-loaded." by pulling the girders at the brace points for locations 2 and 4 in the opposite direction that the brace points will move due to the braces swinging through a circular arc, to cut the maximum induced forces in the test specimen by one-half. The values listed in Table A2.3 assume that the braces are inclined by one-half of the maximum vertical displacement at the start of the test, but the effect of a possible initial "pre-loading" of the girders at the brace points is not included. It should be noted that the radial displacements shown in the table are "reasonably small".

Table A2.3. Vertical displacements at load points and the corresponding lateral bending stresses for shear test specimens.

Vertical Displacement (in)	Corresponding Radial Displacement (in)	Lateral Moment (kips-ft)	Lateral Bending Stress (ksi)	% of F_y
4	0.037	12.641	1.132	2.057
5	0.057	19.608	1.756	3.192
6	0.083	28.104	2.516	4.574

A2.4 EFFECT OF RADIAL DISPLACEMENTS AT THE BRACING LOCATIONS – NONLINEAR FINITE ELEMENT ANALYSIS RESULTS

As noted in Appendix 1, the analysis results presented in the body of this report assume that the web of the test girders is held vertical at the loading and vertical support locations by perfectly rigid radial supports. In this section, analysis results are presented in which the "pin-ended" bracing members, and their attachment to the "rigid" reaction wall are modeled directly within the finite element model.

Tables A2.4 and A2.5 compare the shear capacities predicted based on the perfectly rigid radial supports versus the explicit modeling of the bracing members. The proposed bracing members are 4" diameter standard weight pipes, and they are modeled using truss finite elements.

Table A2.4. Maximum shear forces for Specimens S1-0.06 and S1-0.10 for two bracing models.

Specimens	L/R	Bracing Configurations	V_{max} (k)	M_{max} (k-ft.)
S1-0.06	0.057	Roller Radial Supports	253	1012
		Bracing Members	253	1010
S1-0.10	0.10	Roller Radial Supports	238	952
		Bracing Members	237	950

Table A2.5. Maximum shear forces for Specimens S1-S-0.06 and S1-S-0.10 for two bracing models.

Specimens	L/R	Bracing Configurations	V_{max} (k)	M_{max} (k-ft.)
S1-S-0.06	0.057	Roller Radial Supports	302	1210
		Bracing Members	302	1208
S1-S-0.10	0.10	Roller Radial Supports	295	1180
		Bracing Members	294	1178

It can be observed from these tables that there is practically zero difference in the maximum predicted capacities for the two models. With one exception, the load-vertical deflection curves for the two models also are practically indistinguishable. Figure A2.1 shows example results for Specimen S1-0.10, in which the load-vertical deflection curves practically match for the two models. The one exception is Specimen S1-S-0.10. For this test, the predicted load deflection curves, shown in Figs. A2.2 and A2.3, practically match for the pre-peak portion of the load-deflection curves. However, for the post-peak

portion of the load-deflection curves, the model in which the bracing members are included shows a rapid unloading behavior for the load-displacement at location 2 and a "snap-back" type of response at location 4.

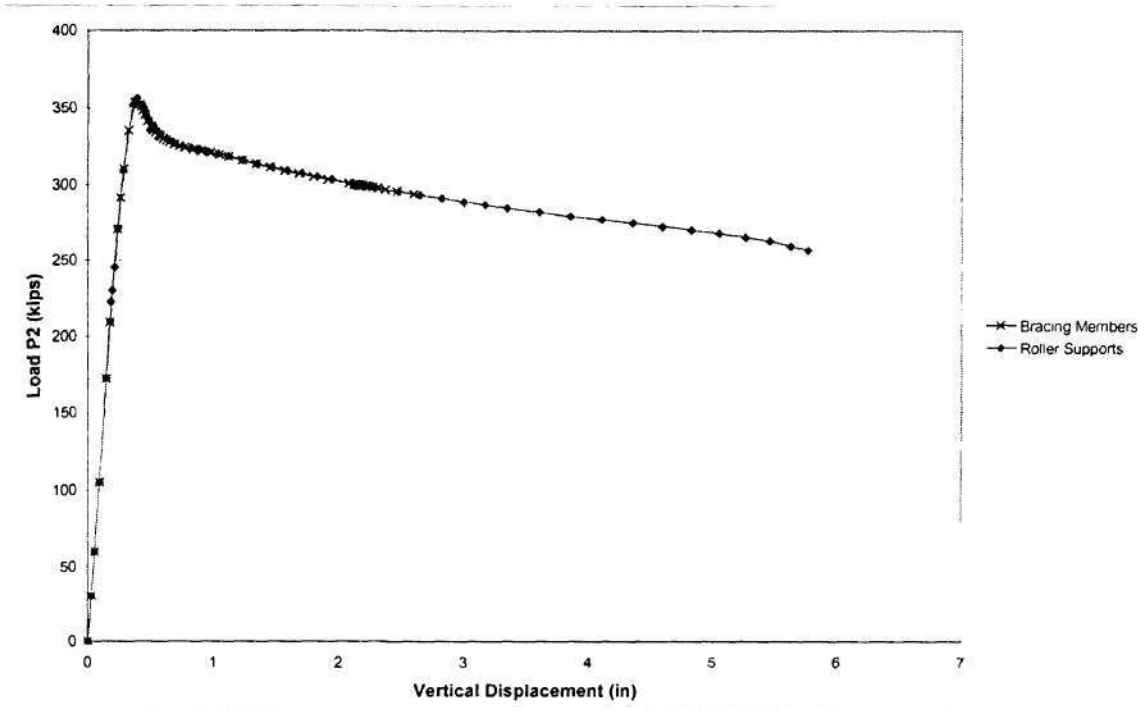

Figure A2.1 Load P_2 versus vertical displacement at location 2 for Specimen S1-0.10.

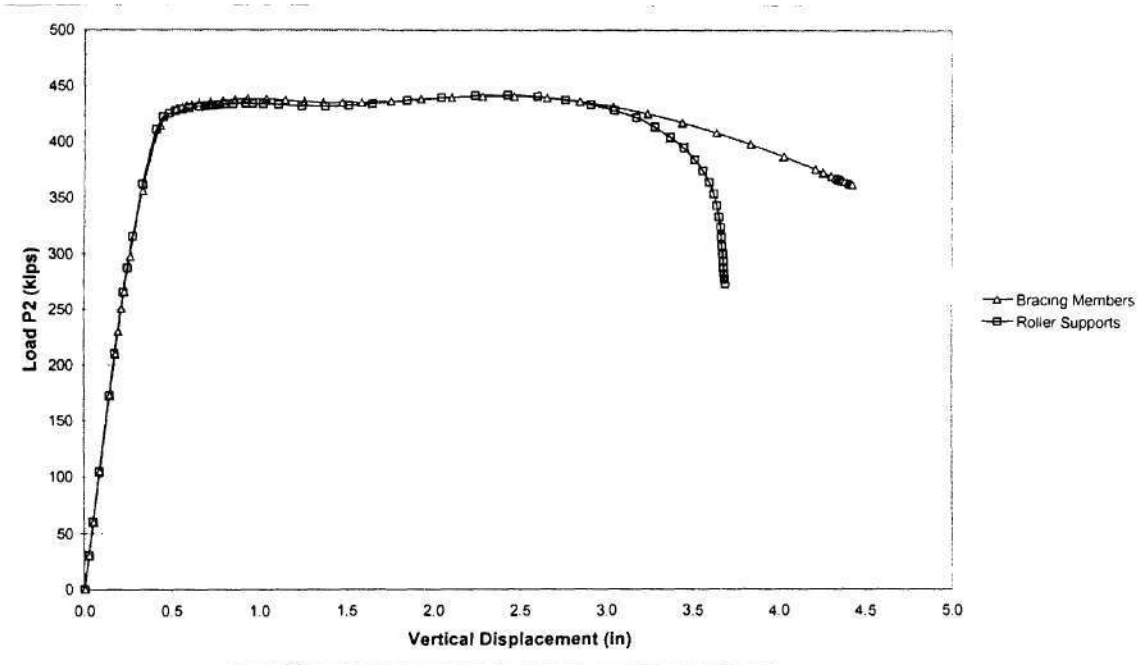

Figure A2.2 Load P_2 versus vertical displacement at location 2 for Specimen S1-S-0.10.

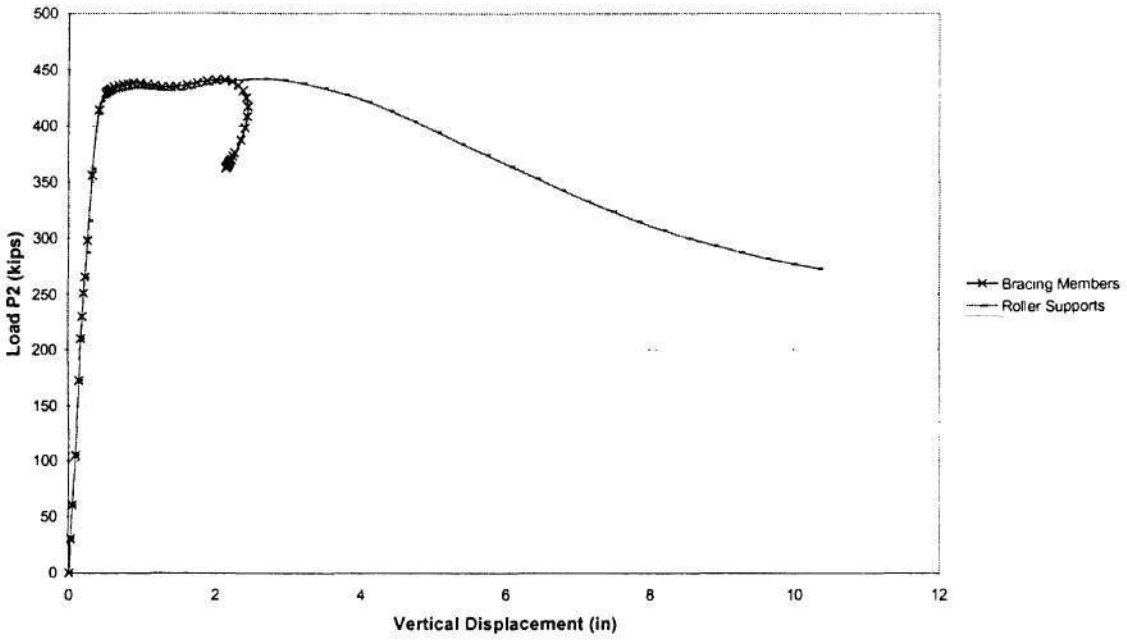

Figure A2.3 Load P_2 versus vertical displacement at location 4 for Specimen S1-S-0.10.

REFERENCES

AASHTO (1993), *AASHTO Guide Specifications for Horizontally Curved Highway Bridges*, American Association of State and Highway Transportation Officials, Washington D.C.

Federal Highway Administration (1996), "Nominal Bending and Shear Strength", *Draft Report No. FHWA-RD-xx-yy: Task D – Nominal Bending and Shear Strength,* August 1996

Hall, D.H. and Yoo, C.H. (1998), "Recommended Specifications for Steel Curved-Girder Bridge," Prepared for National Cooperative Highway Research Program, Transportation Research Board, National Research Council, July 1998, 103 pp.

Lee, S.C. and Yoo, C.H. (1998), "Strength of Plate Girder Web Panels Under Pure Shear", *Journal of Structural Engineering*, 124(2), 184-194

CURVED STEEL BRIDGE RESEARCH PROJECT

EVALUATION OF RESIDUAL STRESS EFFECTS ON STRENGTHS OF TEST SPECIMENS

Narin Phoawanich, Donald W. White and Abdul Hamid Zureick
Georgia Institute of Technology
September 20, 1999

EXECUTIVE SUMMARY

The developments and analyses of both shear test and moment-shear test specimens are presented in the previous reports by authors (Phoawanich, et al. 1999a&b). However, in these studies, residual stresses are not considered. This report summarizes and discusses the results of the finite element predictions for representative distributions of longitudinal residual stresses due to flame cutting and welding in the test specimens.

The analysis results show that the presence of residual stresses has effect on the strengths of all the test specimens less than five percent. The effect of residual stresses on the strength of the test specimens is less pronounced in the case of the stiffened specimens than in the case of unstiffened specimens. In terms of curvature effects, there are no significant differences in residual stress effects for the different L/R ratios. Furthermore, in the case of shear test specimens, the presence of residual stresses, practically, does not cause any difference in both pre-peak and post-peak behavior of the load versus vertical deflection curves. The only difference between the models including residual stresses and models excluding residual stresses is the reduction in the maximum shear strength mentioned above. For the case of the three-point bending moment-shear test specimens, the pre-peak and post-peak behavior of the test specimens including and excluding residual stresses is practically the same. However, for the other case of the moment-shear test, i.e., $\alpha \neq 0$, the presence of residual stresses tends to somewhat increase the vertical deflection in the pre-peak range.

All the analysis studies presented in this report are based on the same finite element modeling decisions as in the previous reports by authors (Phoawanich, et al. 1999a&b), except that residual stresses are considered. The residual stresses are modeled in accordance with the equations of the *ECCS Manual on Stability of Steel Structures* (ECCS 1976).

1. INTRODUCTION

In the previous reports by authors (Phoawanich, et al 1999a&b), the authors stated that residual stresses would be addressed in a subsequent report. It is known that residual stresses can have a major impact on stability and strength of steel structures. However, by the presence of residual stresses, the softening of the load versus vertical deflection may have an impact on member deflection. Therefore, finite element analyses of the test specimens with the representative longitudinal residual stress distribution included should be conducted to observe the effect of residual stresses that may have on the behavior of the proposed test specimens.

Residual stresses can be introduced into the test specimens by the processes of flame cutting and welding. Generally, the residual stresses are essentially equal to the yield stress of the material in tension within a small width of the heat affected zones, and a smaller constant self-equilibrating stress in compression is generated within the other regions of the plates.

This report presents the finite element predictions for representative distributions of longitudinal residual stresses due to flame cutting and welding for the complete set of the proposed test specimens, four shear test specimens and eight moment-shear test specimens. The next section of the report discusses the overall layout and arrangement of the loads and the supports for these tests. Then, Section 3 describes the residual stress distribution according to equations of the *ECCS Manual on Stability of Steel Structures* (ECCS 1976). Section 4 presents the analysis results for presence of residual stresses in the shear test specimens (S1 and S1-S). The moment-shear test specimens (MS1, MS2, MS1-S, and MS2-S) are addressed in similar fashion in Section 5. Appendix 1 discusses detailed finite element modeling decisions behind the analysis predictions, and Appendix 2 describes the determination of the residual stress distribution.

2. OVERALL LAYOUT AND ARRANGEMENT OF THE TESTS

The layout and arrangements proposed for the tests are shown in Figs. 1 and 2. Figure 1 is a three-span test configuration in which the center span (span 2-3) contains the "test girder". Vertical loads of P_2 and P_4 are applied at locations 2 and 4, and vertical supports are positioned at locations 1 and 3. Radial bracing is provided at the vertical supports and at the load locations. This test configuration is used for testing the shear test specimens in which $\alpha = 1/3$ as well as for the moment-shear test specimens with $\alpha \neq 0$ (MS1 and MS2-S). In addition, a three-point bending test configuration in which will be used to test Specimen MS2, and MS1-S is shown in Fig 2.

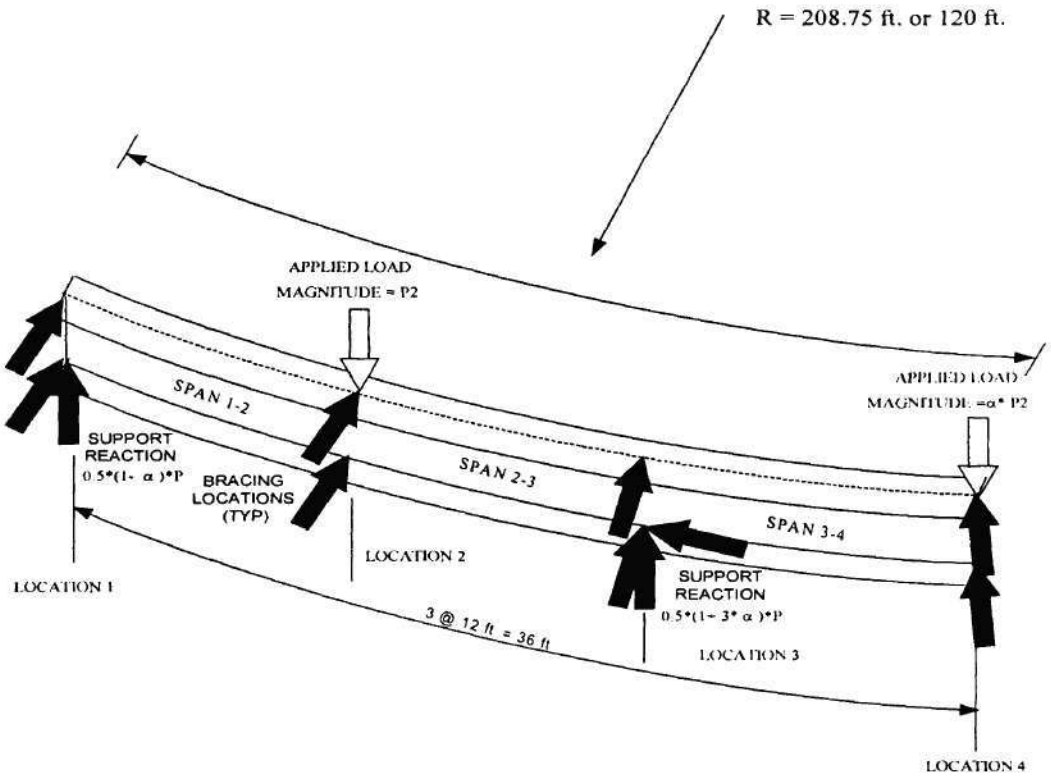

Figure 1. Test configuration for shear test and moment-shear test when $\alpha \neq 0$

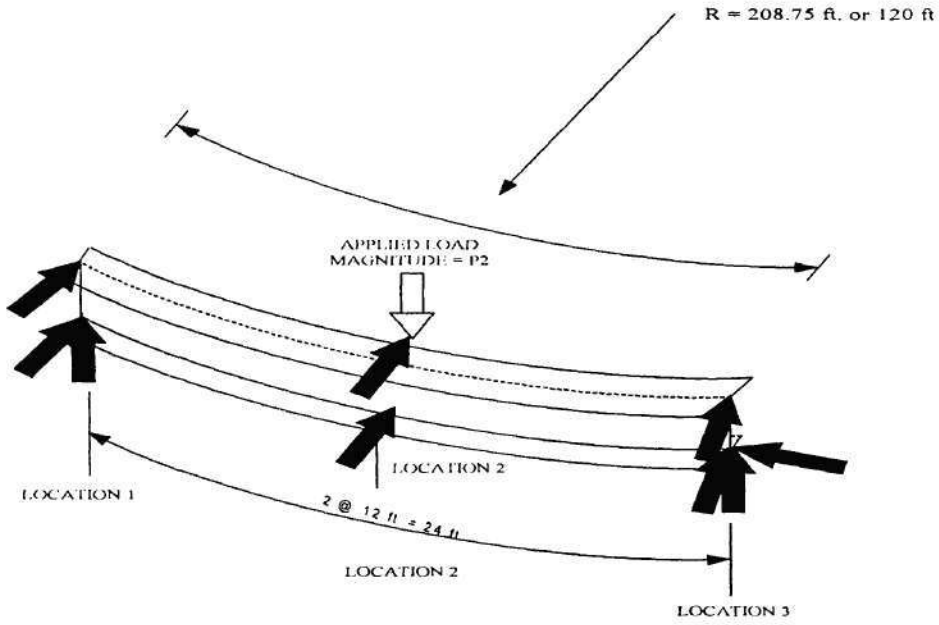

Figure 2. Three-point bending test configuration

Two values are considered for the radius of curvature in the tests, R = 208.75 ft and 120 ft, and the unsupported span lengths are equal to 12 ft. in all of the tests. These selected L and R values give L/R ratios of 0.057 and 0.10 respectively.

3.REPRESENTATIVE DISTRIBUTIONS OF LONGITUDINAL RESIDUAL STRESSES

Residual stresses in the test specimens are modeled by specifying initial stress conditions at the beginning of the analyses. The residual stress distribution is idealized based on the fact that when the section is free of external forces, the resultant forces, due to the sum of residual stresses over the entire cross-section, must be zero. The stresses in the flanges and web are assumed in accordance with the equations of the *Manual on Stability of Steel Structures* (ECCS 1976) which includes the residual stresses due the both welding and flame cutting as shown in Fig 2. The detailed calculations of residual stresses are described in Appendix 2.

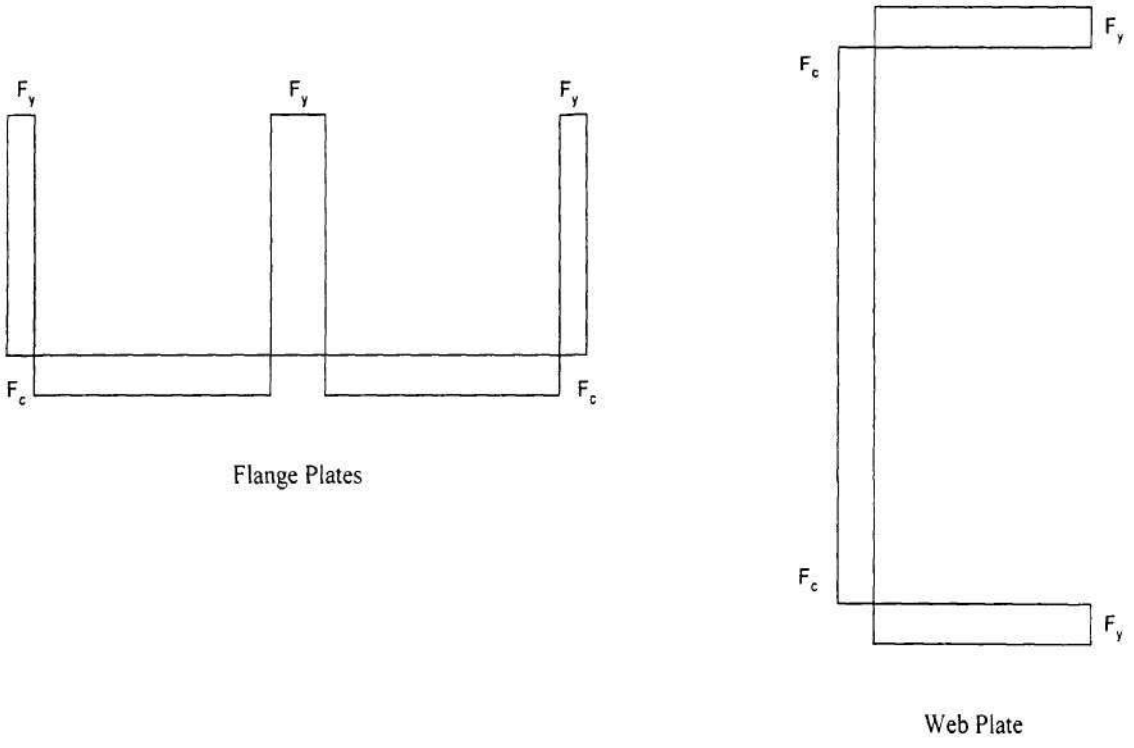

Figure 2. Residual stress pattern in welded girder according to (ECCS 1976) equations.

4. SHEAR TEST SPECIMENS

4.1 DESCRIPTION

The elevations of the unstiffened test specimens are the same as previous report by authors (Phoawanich, et al. 1999a) as shown in Fig. 3.

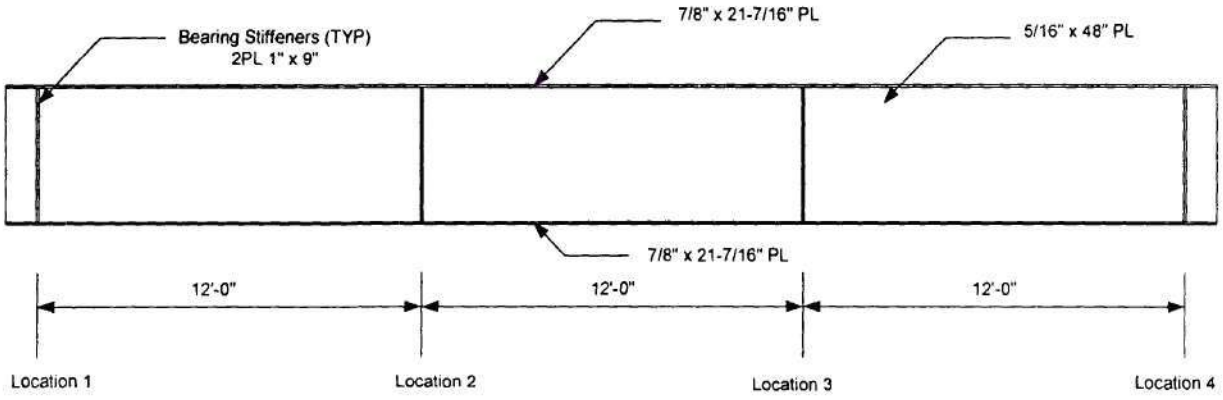

Figure 3. Unstiffened test Specimens S1-0.06 and S1-0.10.

The stiffened shear test specimens are configured by placing a single transverse stiffener at the center of the panels in the layout of the unstiffened girders. This produces a web panel aspect ratio of $d_o/D = 1.5$. Otherwise, the stiffened test specimens have the same cross-section geometry and overall layout as the unstiffened specimens (see Fig. 4).

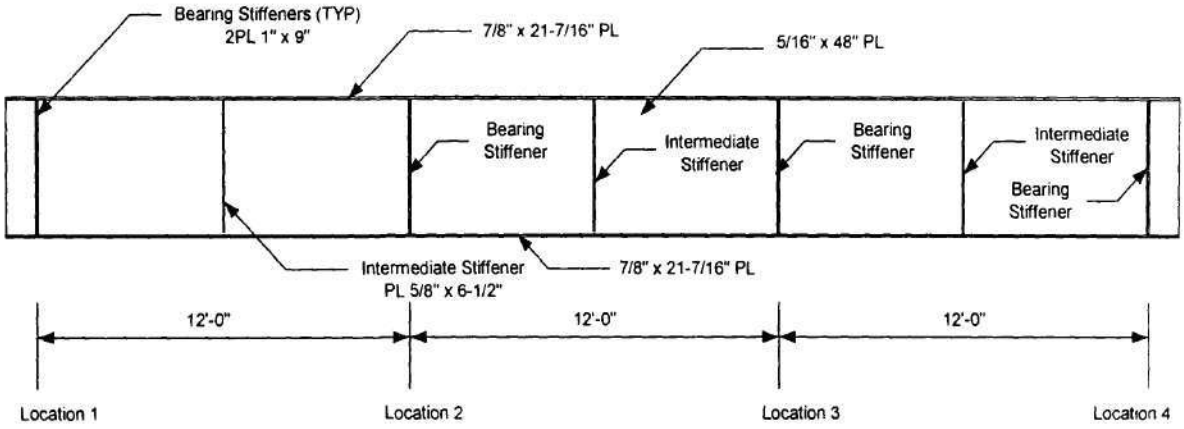

Figure 4. Stiffened test Specimens S1-S-0.06 and S1-S-0.10.

4.2 ANALYSIS RESULTS

The comparisons between shear capacities (V_{max}) from the FEA solutions, for stiffened and unstiffened specimens including and excluding residual stresses, are shown in Table 1. The predicted shear capacities (V_{max}) from the FEA solutions for both stiffened and unstiffened specimens including and excluding residual stresses are compared to other estimates of shear capacities in Table 2.

Table 1. Maximum shear force for stiffened and unstiffened test specimens including and excluding residual stresses.

d_0/D	Specimens	Maximum shear force (V_{max})		
		Residual Stresses		Difference
		Excluded	Included	%
3.0	S1-0.06	253	243	-3.95
	S1-0.10	238	227	-4.62
1.5	S1-S-0.06	302	296	-1.99
	S1-S-0.10	295	289	-2.03

Table 2. Maximum shear force for Specimens S1-0.06 and S1-0.10.

Methods	Shear Force	Unstiffened Test Specimens				Stiffened Test Specimens			
		S1-0.06		S1-0.10		S1-S-0.06		S1-S-0.10	
		Residual Stresses		Residual Stresses		Residual Stresses		Residual Stresses	
		Included	Excluded	Included	Excluded	Included	Excluded	Included	Excluded
FEA	V_{max} (k)	243	253	227	238	296	302	289	295
Lee and Yoo (1998)	V_u (k)	279	279	279	279	292	292	292	292
	V_{max}/V_u	0.871	0.907	0.814	0.853	1.014	1.034	0.990	1.010
AASHTO Guide Specifications for Horizontally Curved Highway Bridges	V_u (k)	191	191	191	191	285	285	285	285
	V_{max}/V_u	1.272	1.325	1.188	1.246	1.039	1.060	1.014	1.035
AASHTO Guide Specifications (1993) but using the shear buckling coefficient proposed by Lee and Yoo (1998)	V_u (k)	238	238	238	238	310	310	310	310
	V_{max}/V_u	1.021	1.063	0.954	1.000	0.955	0.974	0.932	0.952
Plastic Shear Capacity	V_u (k)	478.5	478.5	478.5	478.5	478.5	478.5	478.5	478.5
	V_{max}/V_p	0.508	0.529	0.474	0.497	0.619	0.631	0.604	0.617

It can be seen from Table 1 that the presence of residual stresses causes some reductions in the maximum shear forces, and these reductions are less than 5%. The effect of the residual stresses appears to be less pronounced in the stiffened specimens than in the unstiffened specimens. The maximum shear forces are reduced by a maximum of only 2% for the stiffened specimens while the reduction in the shear strength is within 5% for the case of unstiffened specimens when the residual stresses are included in the model. Furthermore, the increase in L/R ratio appears to be insignificant to the reduction of maximum shear force when residual stresses are included in the models. The increase in L/R ratio from 0.057 to 0.10, the decrease in maximum shear force changes from 3.9% to 4.6 % for the unstiffened specimens whereas, the decrease is almost constant at approximately 2% for the two ratio of L/R in the case of stiffened specimen.

From Table 2, for the unstiffened specimens, similar to previous report by authors (Phoawanich, et al. 1999a), the AASHTO Guide Specifications (1993) when used with the shear buckling coefficient proposed by Lee and Yoo (1998) give the best prediction compared to other methods. In the case of stiffened specimens, the equations proposed by Lee and Yoo (1998) provide the best predictions for both the models with including and excluding of residual stresses (within 1.5% and 3% conservative for models with and without residual stresses, respectively). However, the *AASHTO Guide Specifications* (1993) when used with the shear buckling coefficient proposed by Lee and Yoo also provide a reasonably good prediction (within 6.8% and 4.8% unconservative for the models that exclude include residual stress, respectively). In addition to the above two methods, the *AASHTO Guide Specifications* (1993) also give a reasonably accurate estimate (less than 6 % conservative and less than 3.9% conservative for model without residual stresses and model that include residual stresses, respectively).

The total applied load P_2 versus radial reaction at location 2, the location of maximum radial reaction, for the models including and excluding residual stresses of both stiffened and unstiffened specimens are shown in Figs. 5 through 8. In addition, the total applied load P_2 versus the vertical displacement at location 2 of the two models for both stiffened and unstiffened girders are shown in Figs. 9 through 12.

It can be observed from the plots that there is no significant difference between the models that include and exclude residual stresses in both pre-peak and post-peak behavior of both stiffened and unstiffened specimens. The only difference between the models including residual stresses and model excluding residual stresses is the reduction in the maximum applied load.

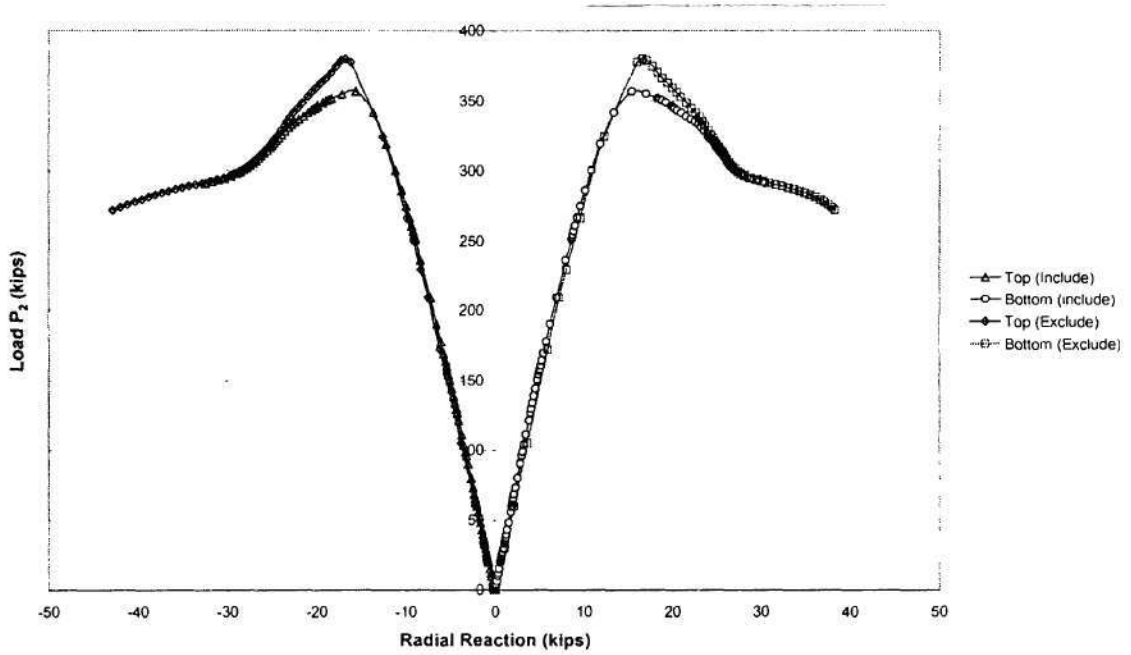

Figure 5. Load P_2 versus radial reaction at location 2 for Specimen S1-0.06 including and excluding residual stresses.

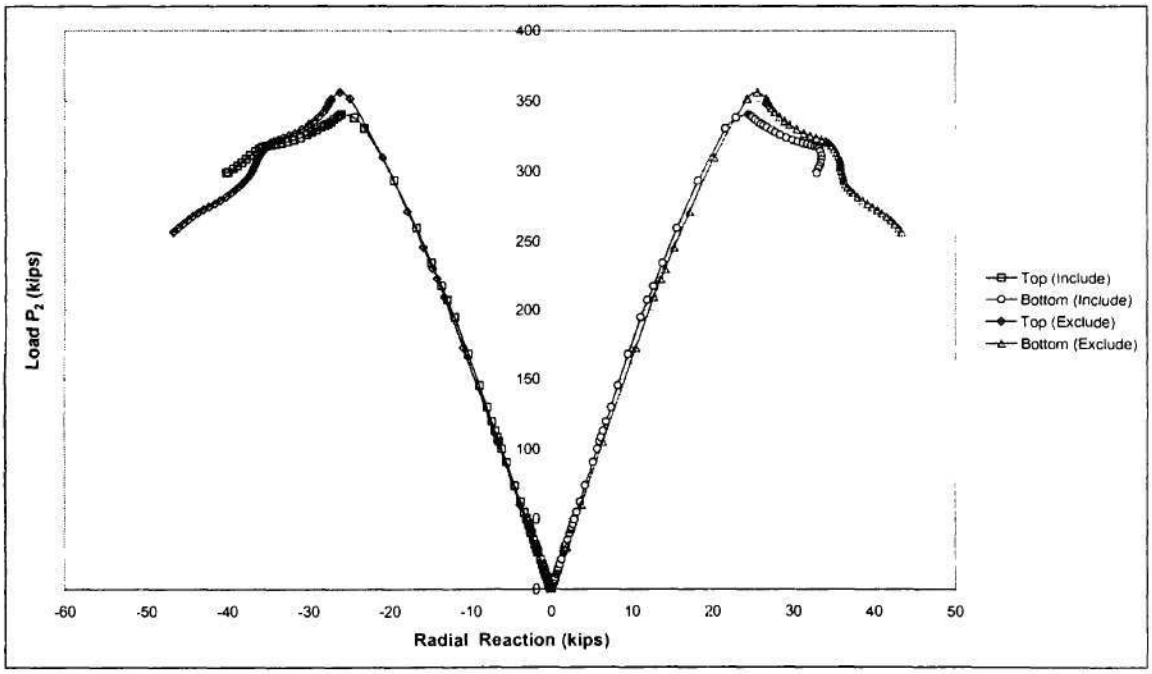

Figure 6. Load P_2 versus radial reaction at location 2 for Specimen S1-0.10 including and excluding residual stresses.

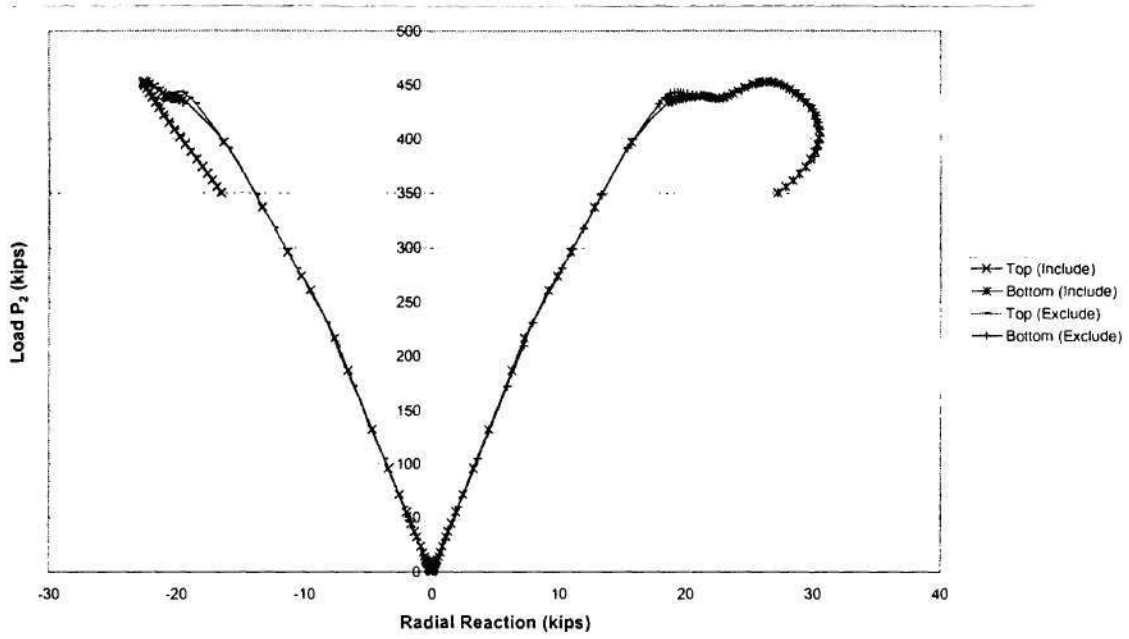

Figure 7. Load P_2 versus radial reaction at location2 for Specimen S1-S-0.06 including and excluding residual stresses.

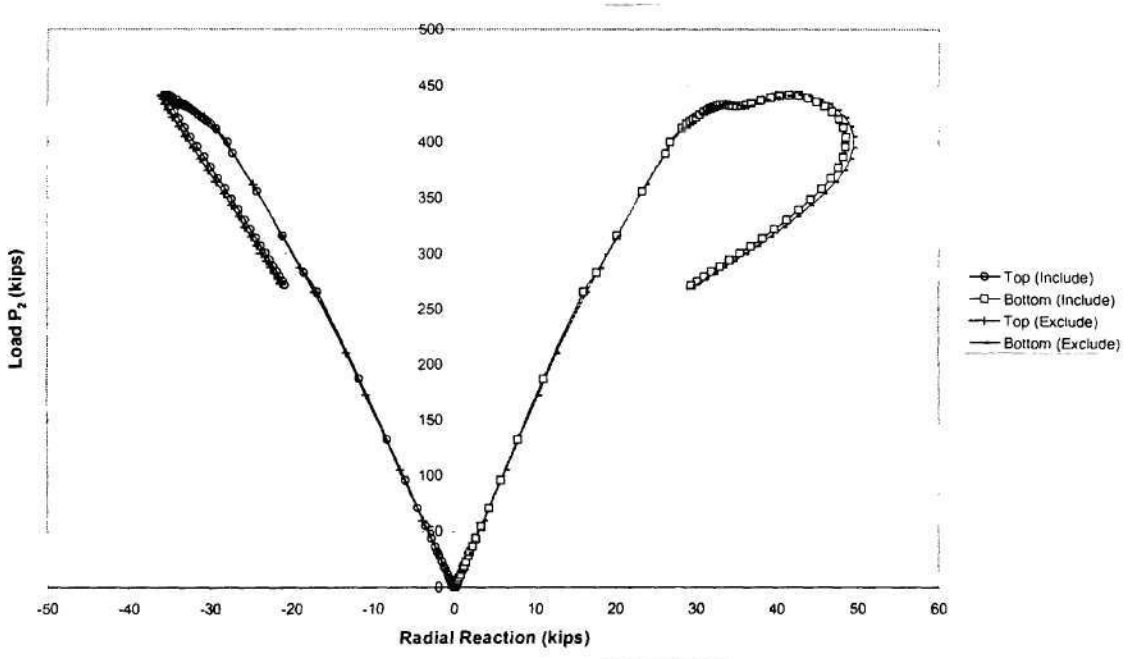

Figure 8. Load P_2 versus radial reaction at location2 for Specimen S1-S-0.10 including and excluding residual stresses.

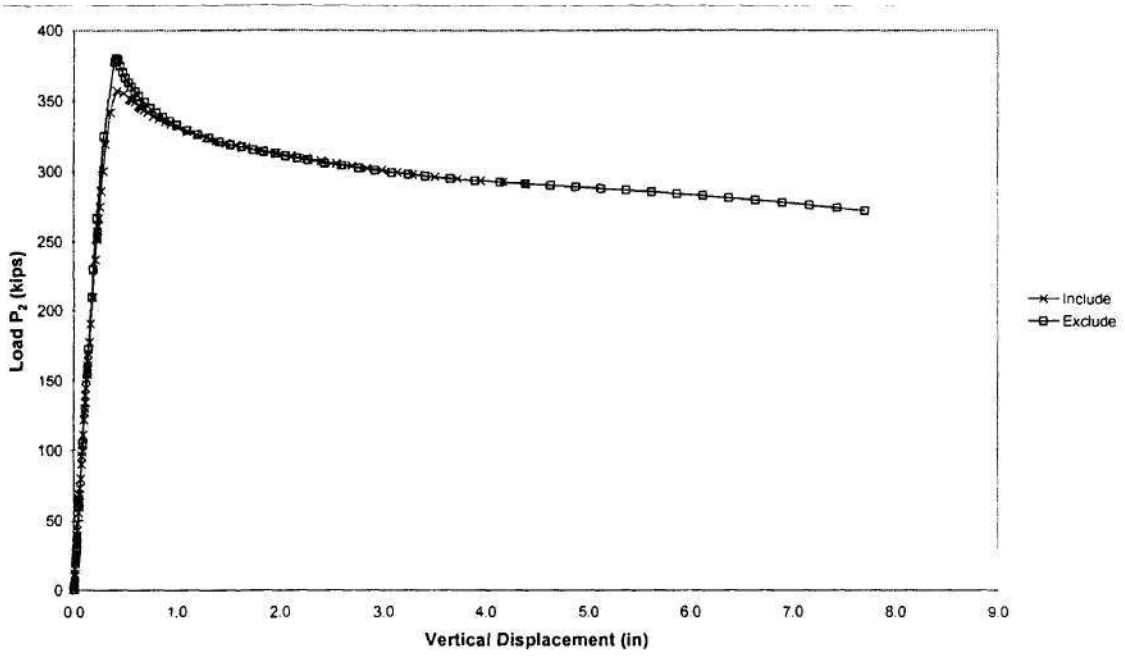

Figure 9. Load P_2 versus vertical displacement at location 2 for Specimen S1-0.06 including and excluding residual stresses.

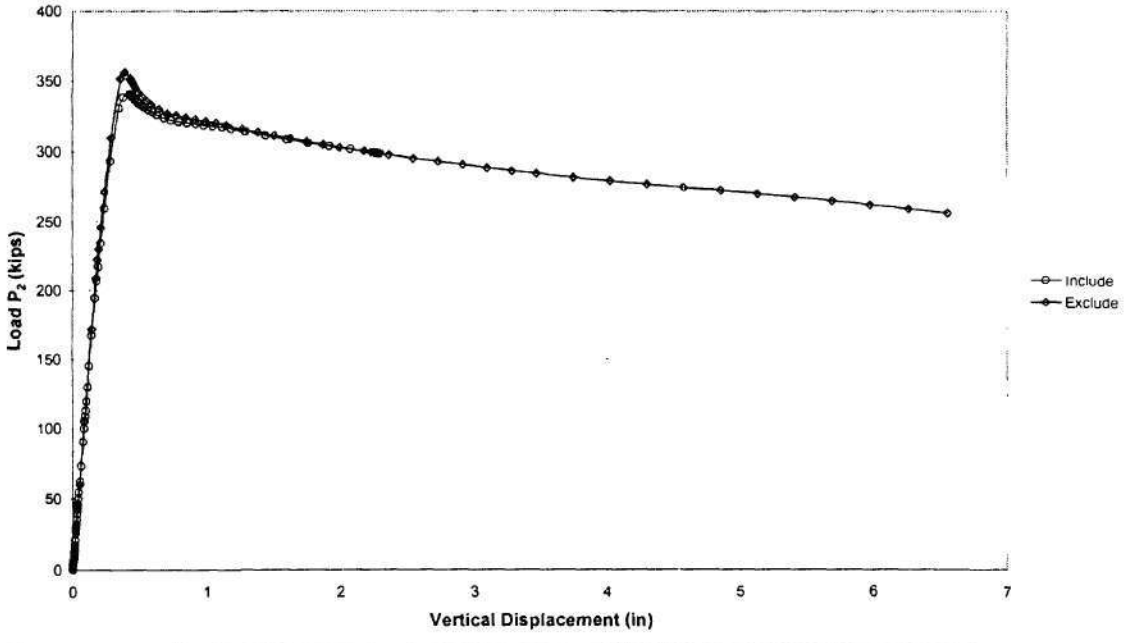

Figure 10. Load P_2 versus vertical displacement at location 2 for Specimen S1-0.10 including and excluding residual stresses.

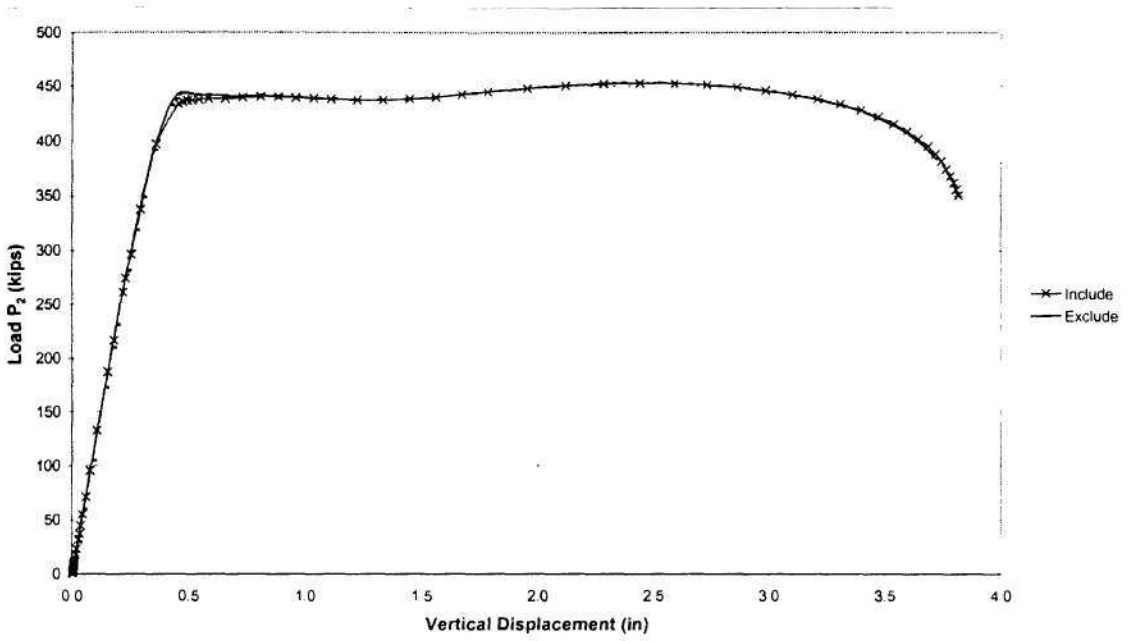

Figure 11. Load P_2 versus vertical displacement at location 2 for Specimen S1-S-0.06 including and excluding residual stresses.

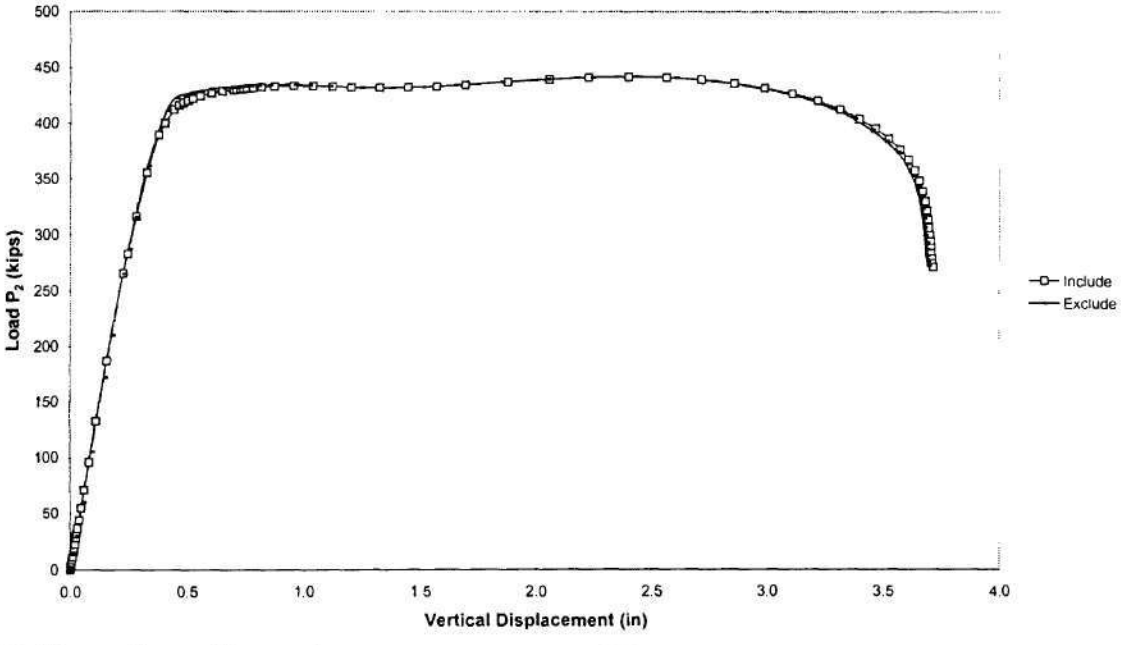

Figure 12. Load P_2 versus vertical displacement at location 2 for Specimen S1-S-0.10 including and excluding residual stresses.

5. MOMENT-SHEAR TEST SPECIMENS

5.1 OVERVIEW OF MOMENT-SHEAR TEST SPECIMENS

5.1.1 UNSTIFFENED TEST SPECIMENS

An elevation of the unstiffened three-point bending test specimens (MS1-0.06 and MS1-0.10) is shown in Fig. 13 whereas an elevation of the three-span test with α = -0.125 of the unstiffened test specimens (MS2-0.06 and MS2-0.10) is shown in Fig. 14. Spans 1-2 and 2-4 are reinforced for the moment-shear test to prevent the outer spans from failing before the test span reaches its capacity for some values of α.

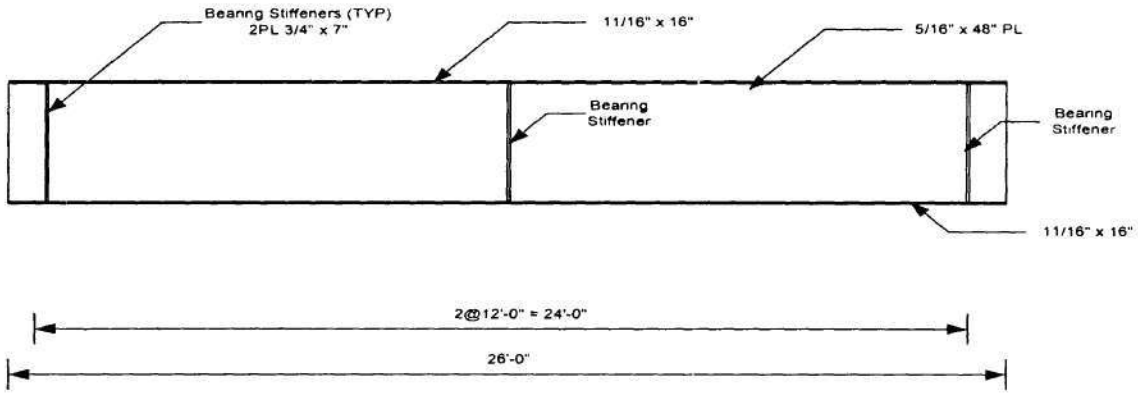

Figure 13. Unstiffened test Specimens MS1-0.06 and MS1-0.10.

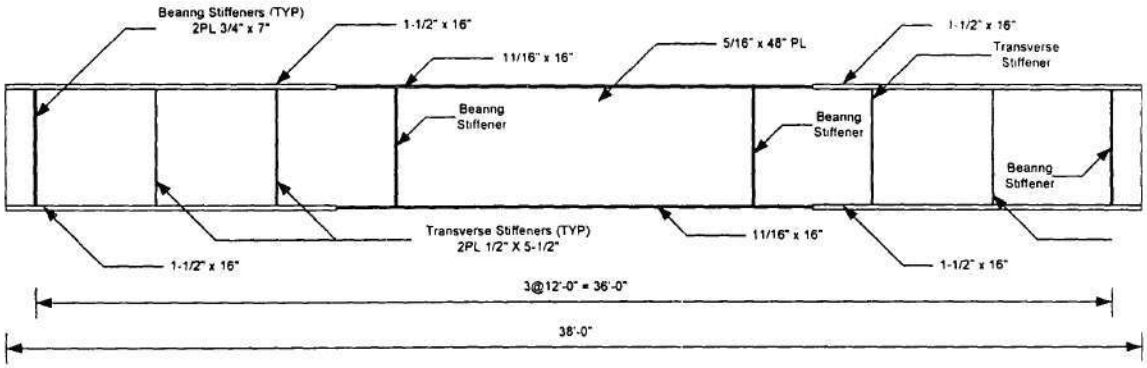

Figure 14. Unstiffened test Specimens MS2-0.06 and MS2-0.10.

5.1.2 STIFFENED TEST SPECIMENS

The stiffened moment-shear test specimens are configured by placing a single transverse stiffener at the center of the test panel of the unstiffened test specimens (see Figs. 15 and 16). This produces a web panel aspect ratio of $d_0/D = 1.5$. Otherwise, the stiffened test specimens have the same cross-section geometry and overall layout as the unstiffened test specimens.

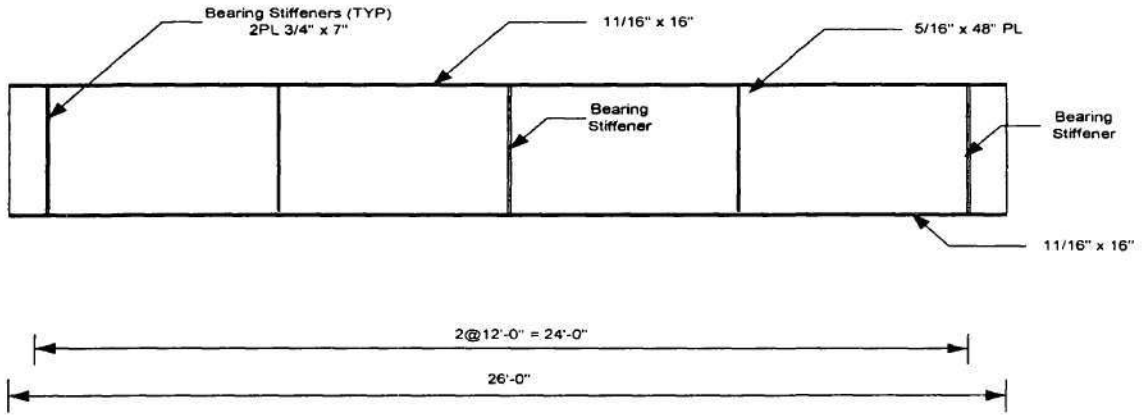

Figure 15. Stiffened test specimens MS2-S-0.06 and MS2-S-0.10.

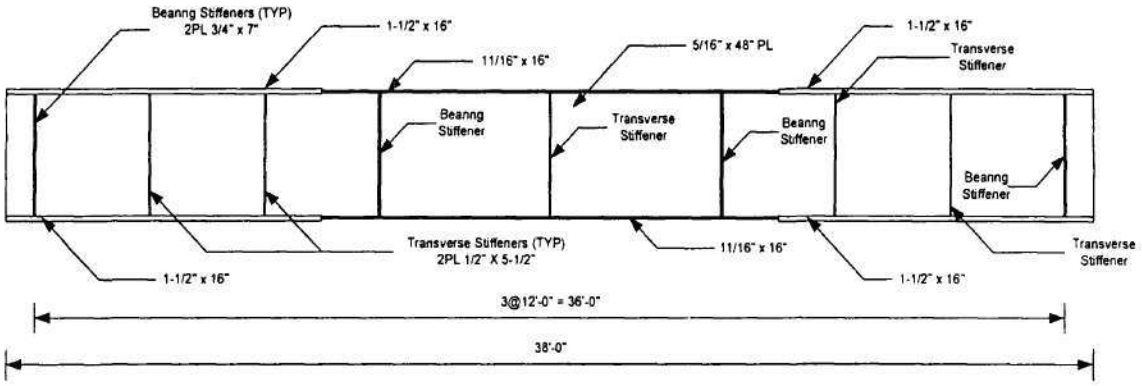

Figure 16. Stiffened test specimens MS1-S-0.06 and MS1-S-0.10.

5.2 ANALYSIS RESULTS

The maximum applied forces and maximum support reactions of the test specimens are summarized in Table 3. The maximum shear forces and the corresponding maximum bending moment of the proposed moment-shear test specimens including and excluding residual stresses are summarized in Table 4.

Table 3. Maximum applied forces and maximum support reactions.

d_0/D	L/R	Specimens	M_{max}/V_{max}	Loading Configuration	P_{max} (k)		Maximum Support Reaction (k)		% Difference
					Residual Stress		Residual Stress		
					Included	Excluded	Included	Excluded	
3.0	0.057	MS1-0.06	12.0	Three-Point Bending	452	464	226	232	-2.59
		MS2-0.06	15.4	α = -0.125	432	441	243	248	-2.02
	0.10	MS1-0.10	12.0	Three-Point Bending	422	430	211	215	-1.86
		MS2-0.10	15.4	α = -0.125	398	409	224	230	-2.79
1.5	0.057	MS1-S-0.06	10.7	α = 0.8	303	304	514	516	-0.37
		MS2-S-0.06	12.0	Three-Point Bending	483	491	241	245	-1.63
	0.10	MS1-S-0.10	10.7	α = 0.8	292	295	496	502	-1.13
		MS2-S-0.10	12.0	Three-Point Bending	474	482	237	241	-1.66

Table 4. Maximum shear forces and the corresponding maximum bending moments.

d_0/D	L/R	Specimens	M_{max}/V_{max}	Loading Configuration	V_{max} (k)		M_{max} (k-ft)		% Difference
					Residual Stress		Residual Stress		
					Included	Excluded	Included	Excluded	
3.0	0.057	MS1-0.06	12.0	Three-Point Bending	226	232	2712	2784	-2.59
		MS2-0.06	15.4	α = -0.125	189	193	2915	2975	-2.02
	0.10	MS1-0.10	12.0	Three-Point Bending	211	215	2532	2580	-1.86
		MS2-0.10	15.4	α = -0.125	174	179	2684	2761	-2.79
1.5	0.057	MS1-S-0.06	10.7	α = 0.8	272	273	2910	2921	-0.37
		MS2-S-0.06	12.0	Three-Point Bending	241	245	2892	2940	-1.63
	0.10	MS1-S-0.10	10.7	α = 0.8	263	266	2814	2846	-1.13
		MS2-S-0.10	12.0	Three-Point Bending	237	241	2844	2892	-1.66

From Tables 3 and 4, the strengths of the test specimens are reduced by the presence of residual stresses. However, the reduction appears to be small (less than 3 %). Similar to the case of shear test specimens, the effect of residual stresses to the strengths of the specimens decreases as the ratio of panel aspect ratio, d_0/D, increases. The reductions in the maximum shear force when residual stresses are included range from 1.86-2.79% in the case of unstiffened specimens while the reductions are between 0.37-1.66% for the stiffened specimens. Furthermore, the effect of residual stresses to strengths of the test specimens does not significantly change as the L/R ratios increase from 0.057 to 0.10. For example, Specimen MS1, as L/R ratio increases from 0.057 to 0.10, the reductions in the strengths change from 2.59% to 1.86% while in the case of specimen MS1-S, the strength reductions change from 0.37 % to 1.13%.

The total applied load P_2 versus radial reaction at the locations that have the largest values for specimens including and excluding residual stresses are shown in Figs 17-24. Furthermore, the total applied load P_2 versus vertical displacement at location 2, the location of maximum applied load, are shown in Figs. 25-32. From the figures, it can be seen that the presence of residual stresses can cause small differences in pre-peak or post-peak behavior in addition to the reduction in maximum applied load P_2. The effects of residual stresses to the pre-peak and post-peak behaviors seem to be very small for the case of three-point bending test especially for the case of stiffened specimens (see Figs. 30 and 32). For the unstiffened specimens, the differences are more pronounced than the stiffened specimens, but the differences are still small (see Figs. 25 and 27). However, residual stresses introduce somewhat significant effect in both the pre-peak and the post-peak behavior of the stiffened and unstiffened specimens for the case of $\alpha \neq 0$. For $\alpha \neq 0$, residual stresses tend to soften the load versus vertical deflection curves of the specimens especially in the pre-peak range, i.e., the vertical displacements are higher than models without residual stresses at the same applied load level (see Figs. 26, 28, 29 and 31).

Although the differences in the load versus vertical deflection curves of the moment-shear test specimens between the models including and excluding residual stresses are small, it should be noted that, however, the presence of residual stresses results in more noticeable changes in pre-peak or post-peak behavior of the moment-shear test specimens than in the case of shear test specimens.

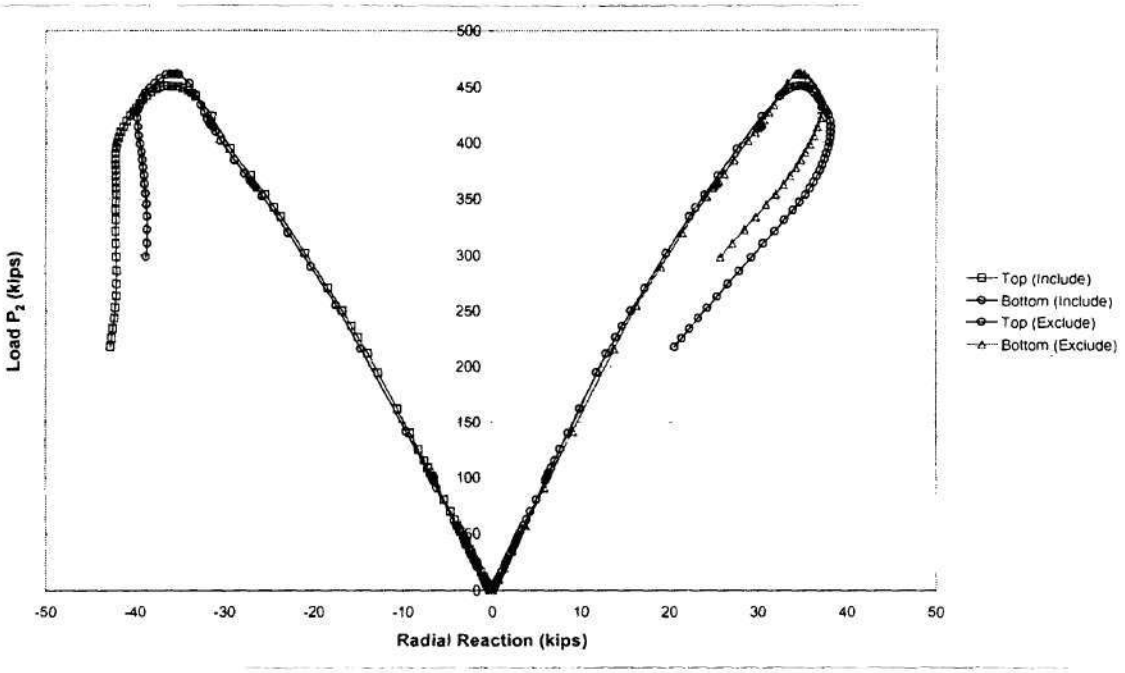

Figure 17. Load P_2 versus radial reaction at location 2 for Specimen MS1-0.06 including and excluding residual stresses.

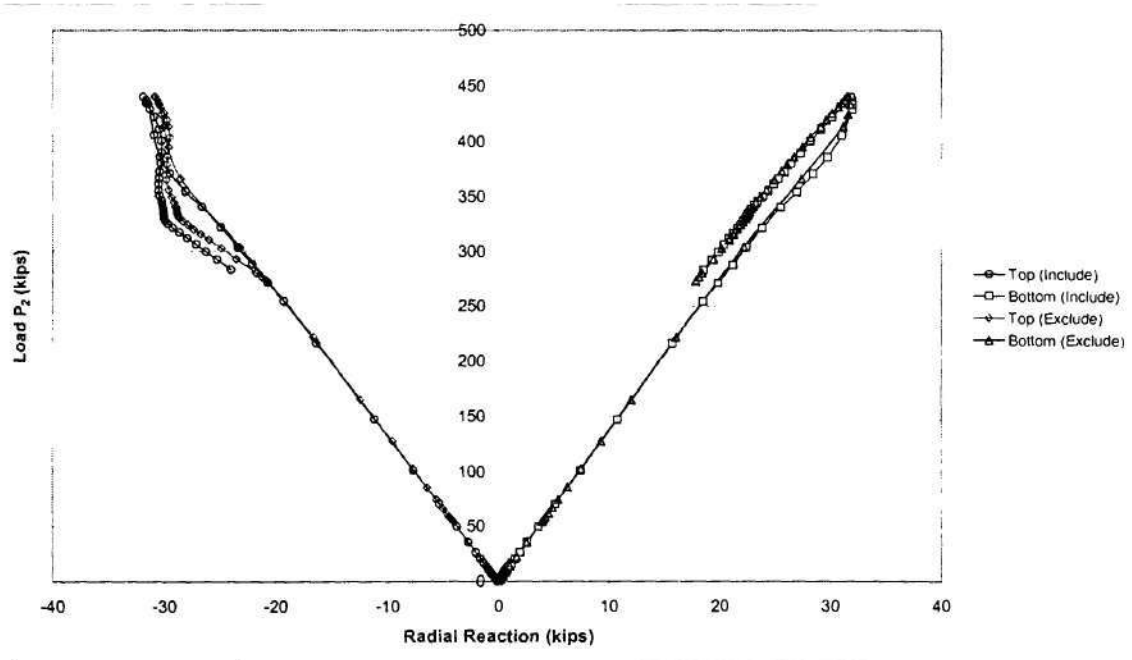

Figure 18. Load P_2 versus radial reaction at location 2 for Specimen MS2-0.06 including and excluding residual stresses.

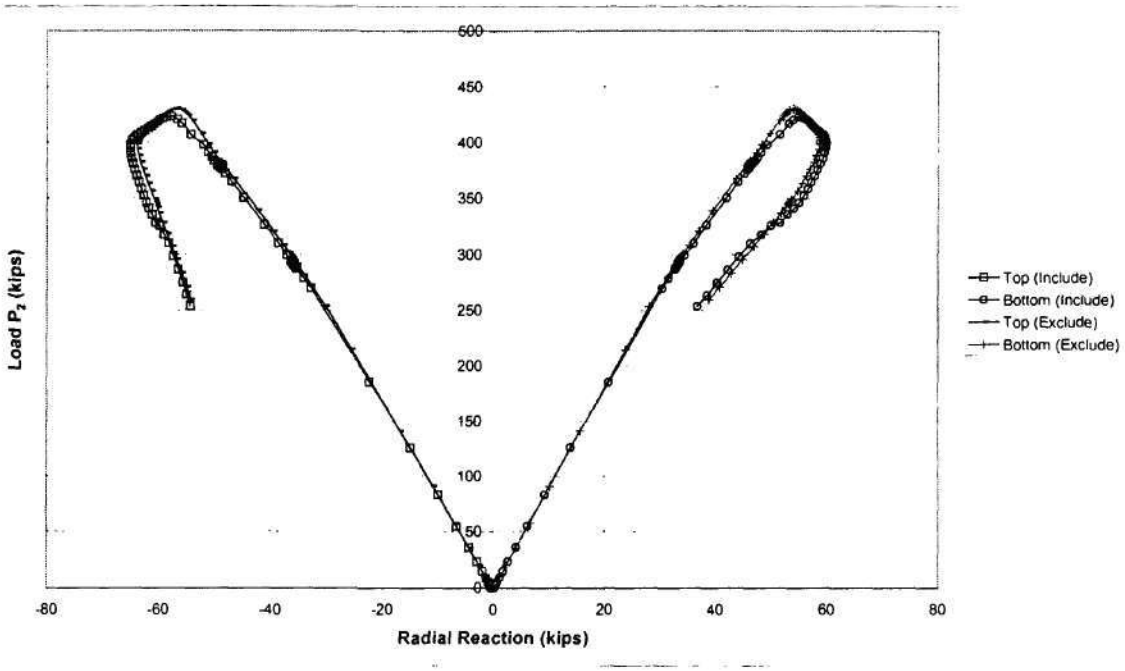

Figure 19. Load P_2 versus radial reaction at location 2 for Specimen MS1-0.10 including and excluding residual stresses.

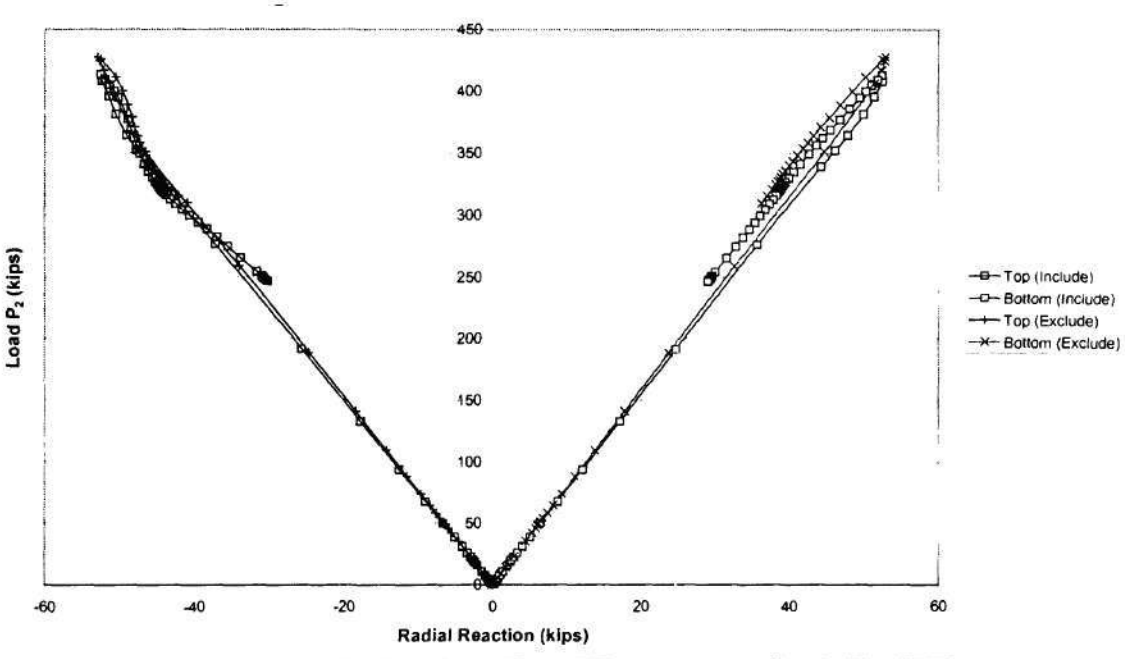

Figure 20. Load P_2 versus radial reaction at location 2 for Specimen MS2-0.10 including and excluding residual stresses.

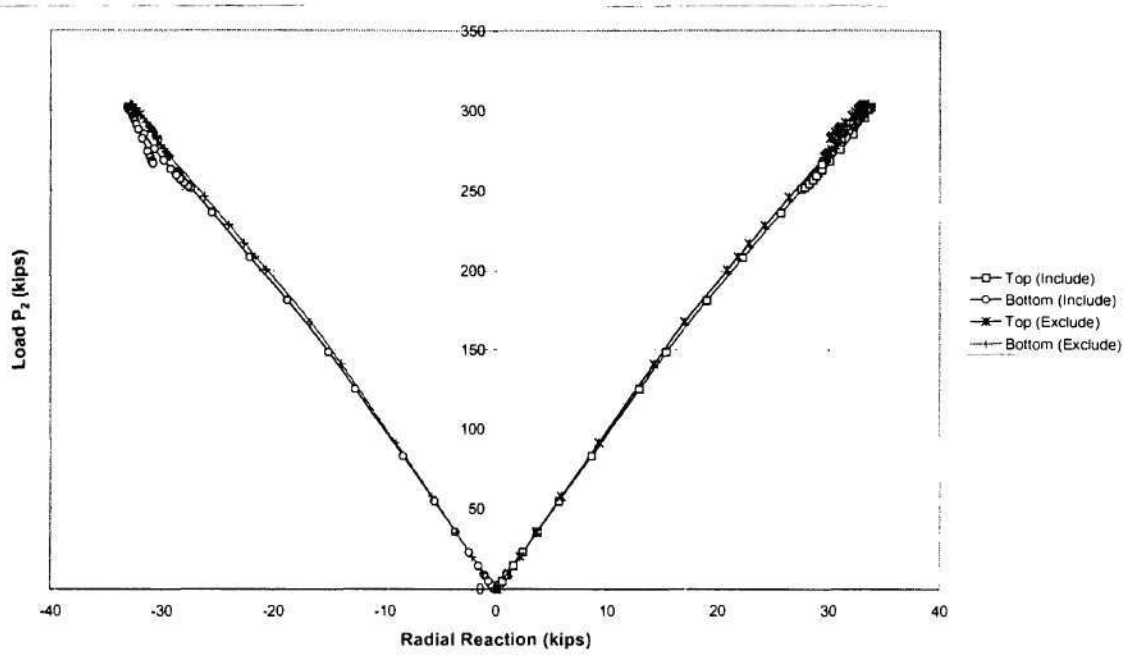

Figure 21. Load P_2 versus radial reaction at location 3 for Specimen MS1-S-0.06 including and excluding residual stresses.

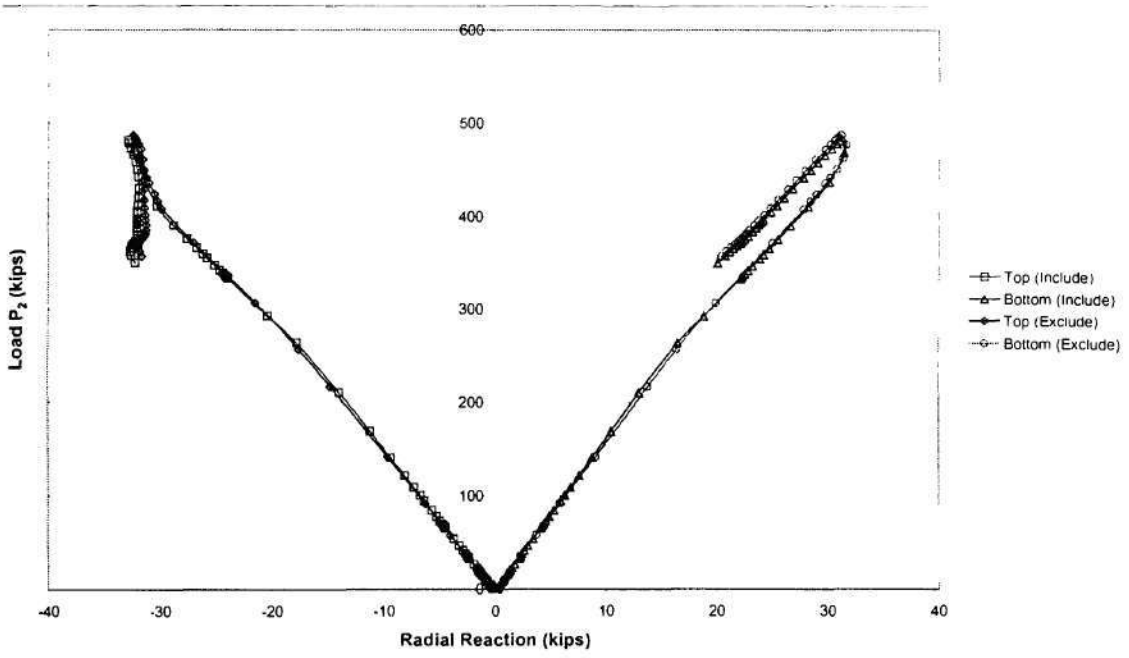

Figure 22. Load P_2 versus radial reaction at location 2 for Specimen MS2-S-0.06 including and excluding residual stresses.

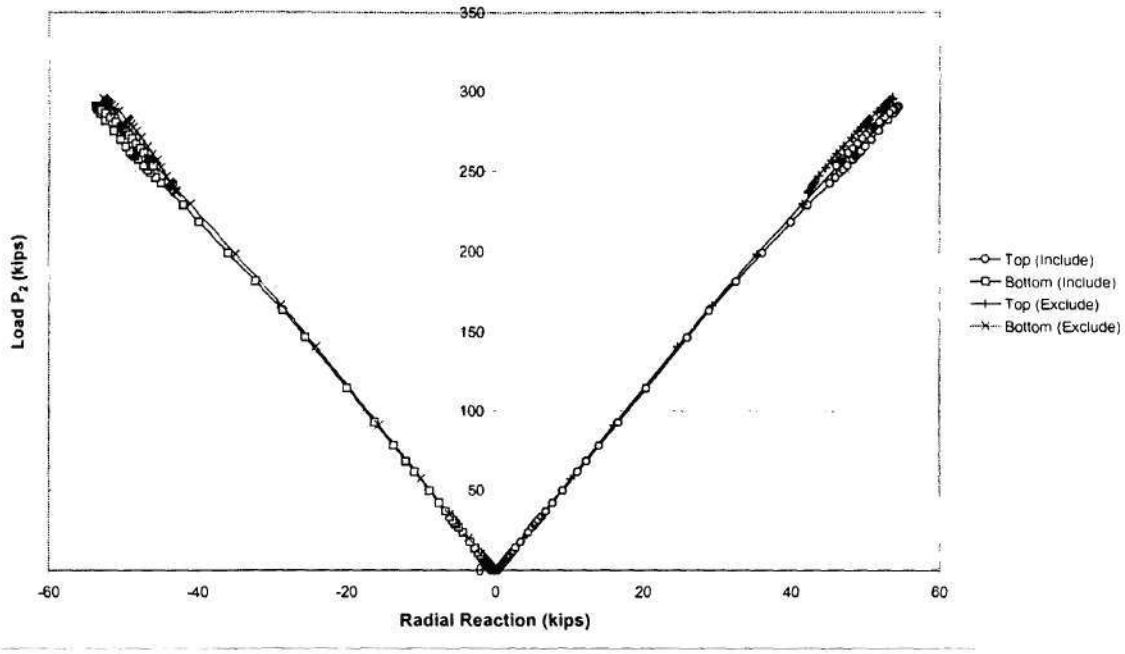

Figure 23. Load P_2 versus radial reaction at location 2 for Specimen MS1-S-0.10 including and excluding residual stresses.

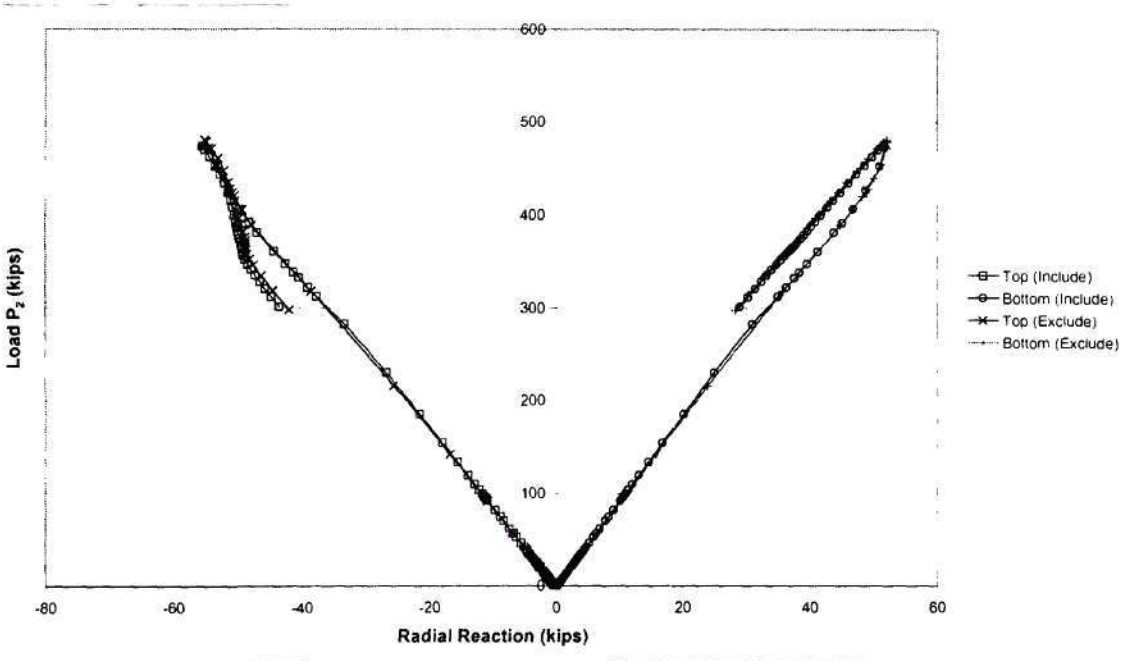

Figure 24. Load P_2 versus radial reaction at location 2 for Specimen MS2-S-0.10 including and excluding residual stresses.

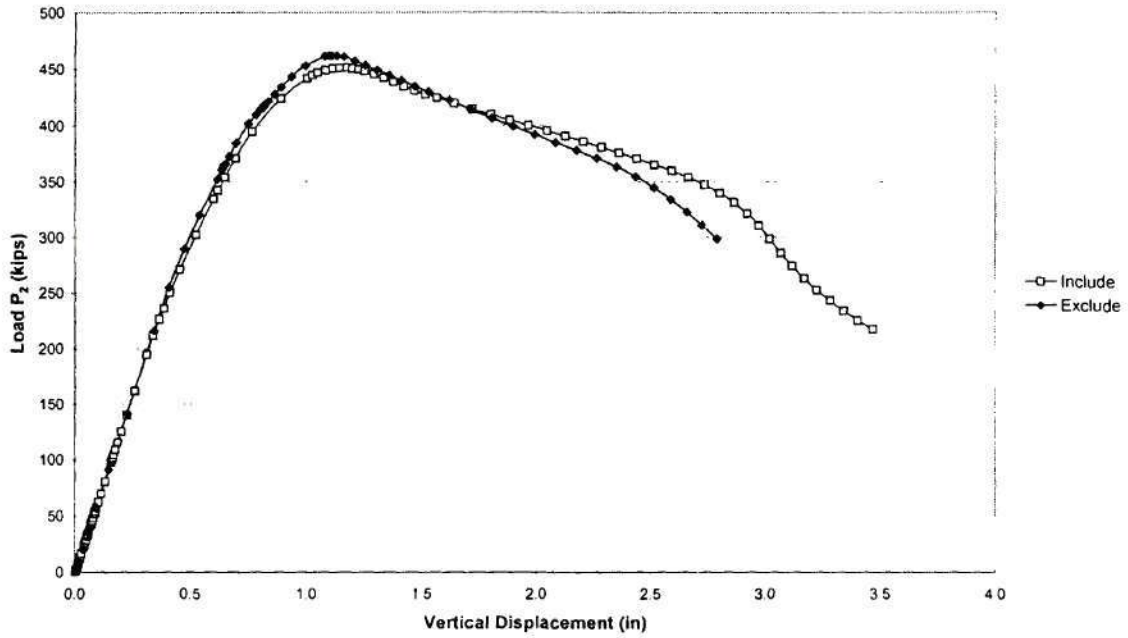

Figure 25. Load P_2 versus vertical displacement at location 2 for Specimen MS1-0.06 including and excluding residual stresses.

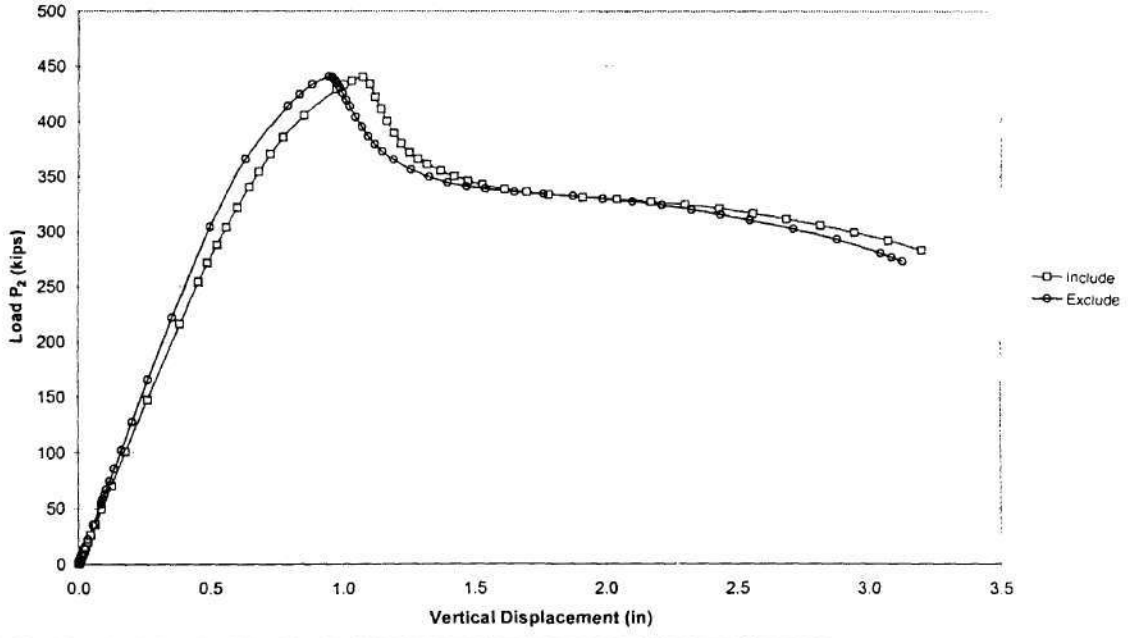

Figure 26. Load P_2 versus vertical displacement at location 2 for Specimen MS2-0.06 including and excluding residual stresses.

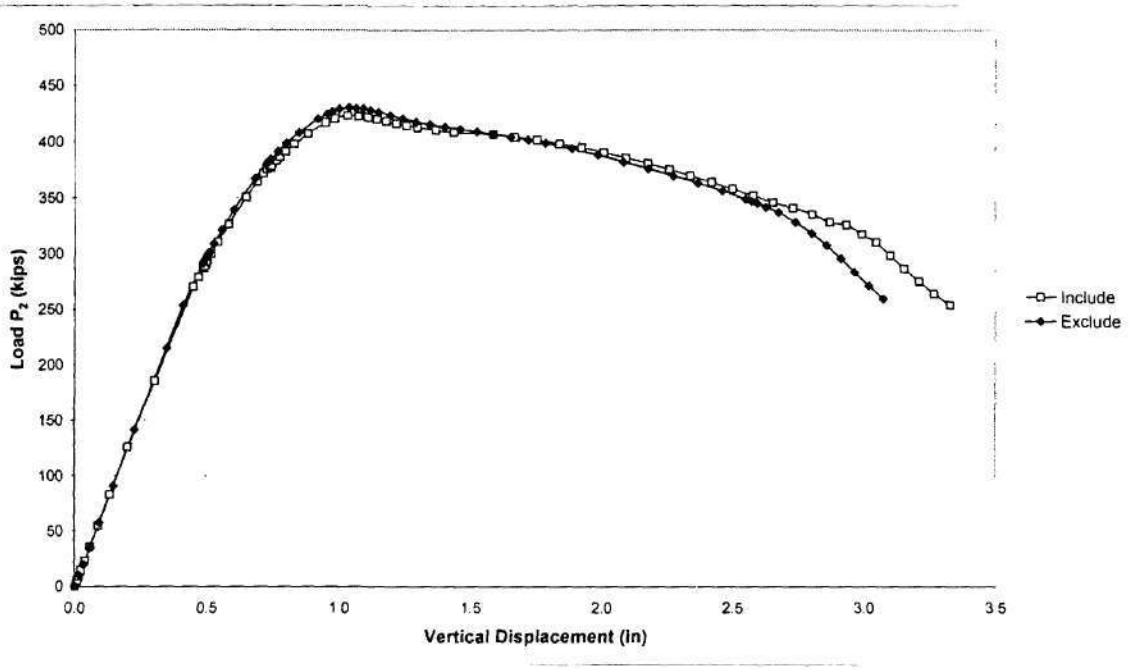

Figure 27. Load P_2 versus vertical displacement at location 2 for Specimen MS1-0.10 including and excluding residual stresses.

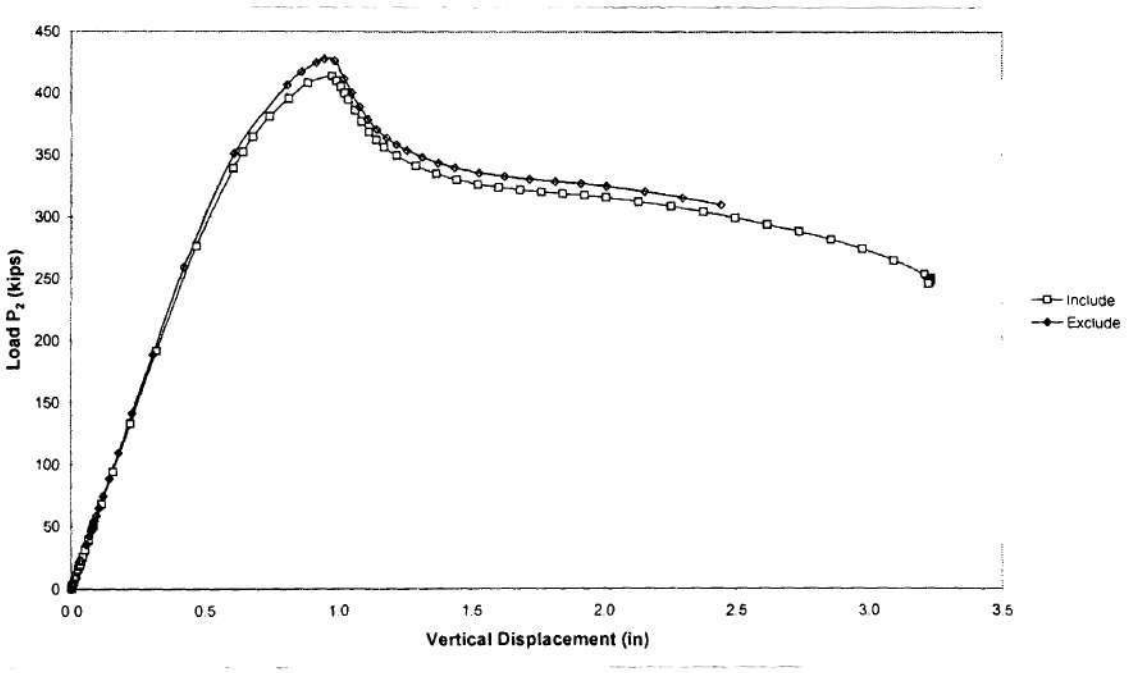

Figure 28. Load P_2 versus vertical displacement at location 2 for Specimen MS2-0.10 including and excluding residual stresses.

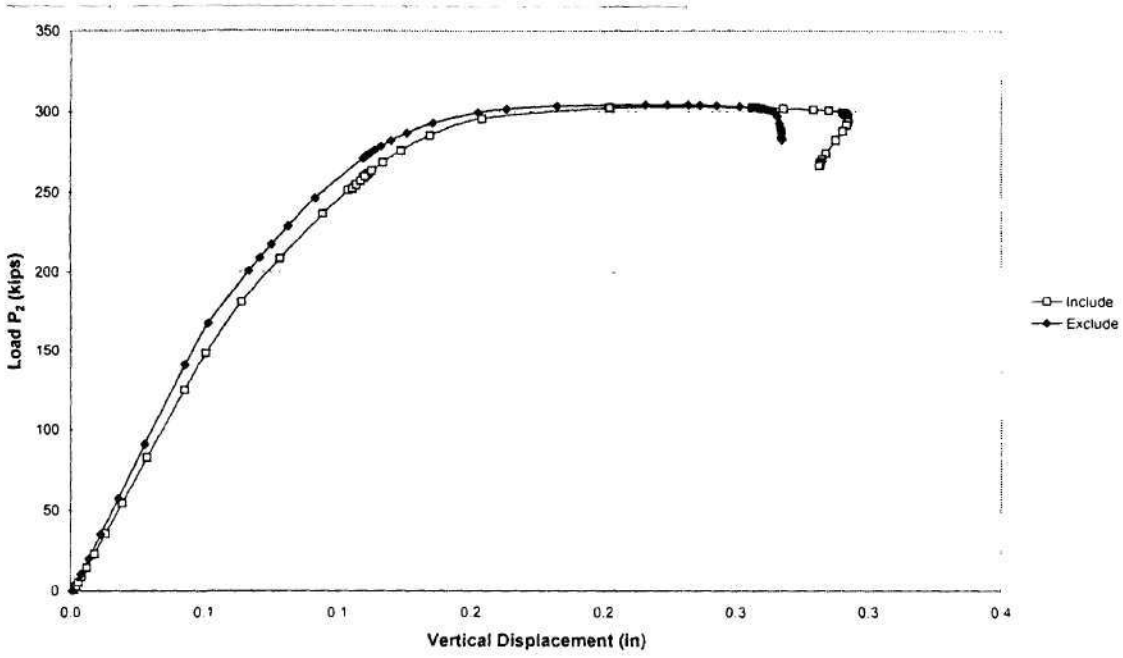

Figure 29. Load P_2 versus vertical displacement at location 2 for Specimen MS1-S-0.06 including and excluding residual stresses.

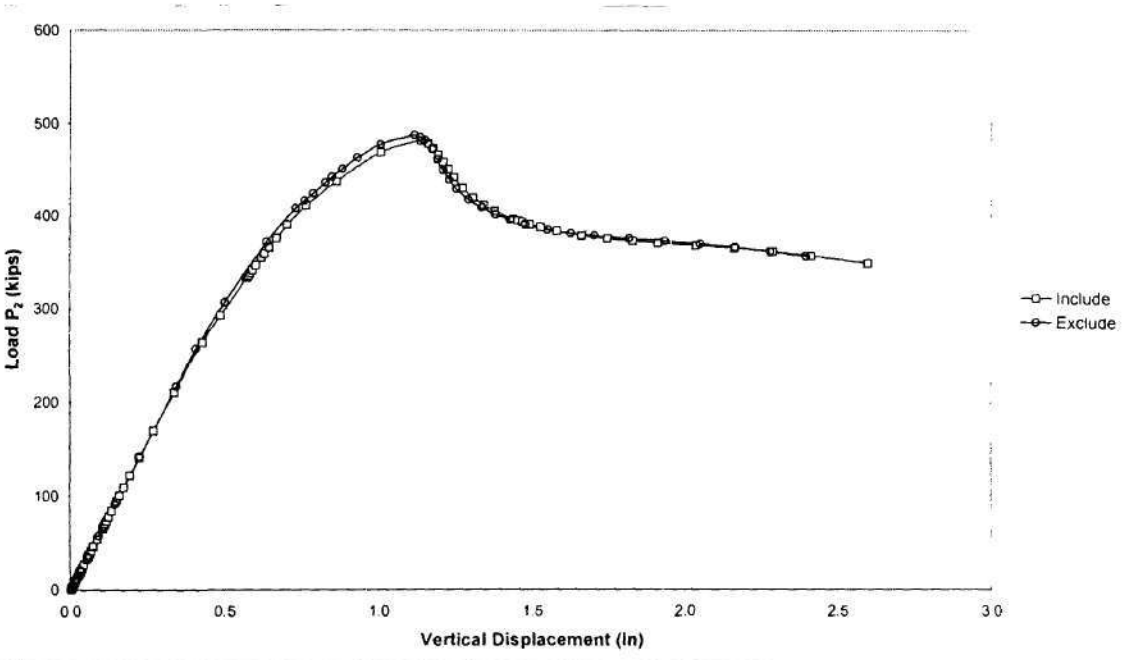

Figure 30. Load P_2 versus vertical displacement at location 2 for Specimen MS2-S-0.06 including and excluding residual stresses.

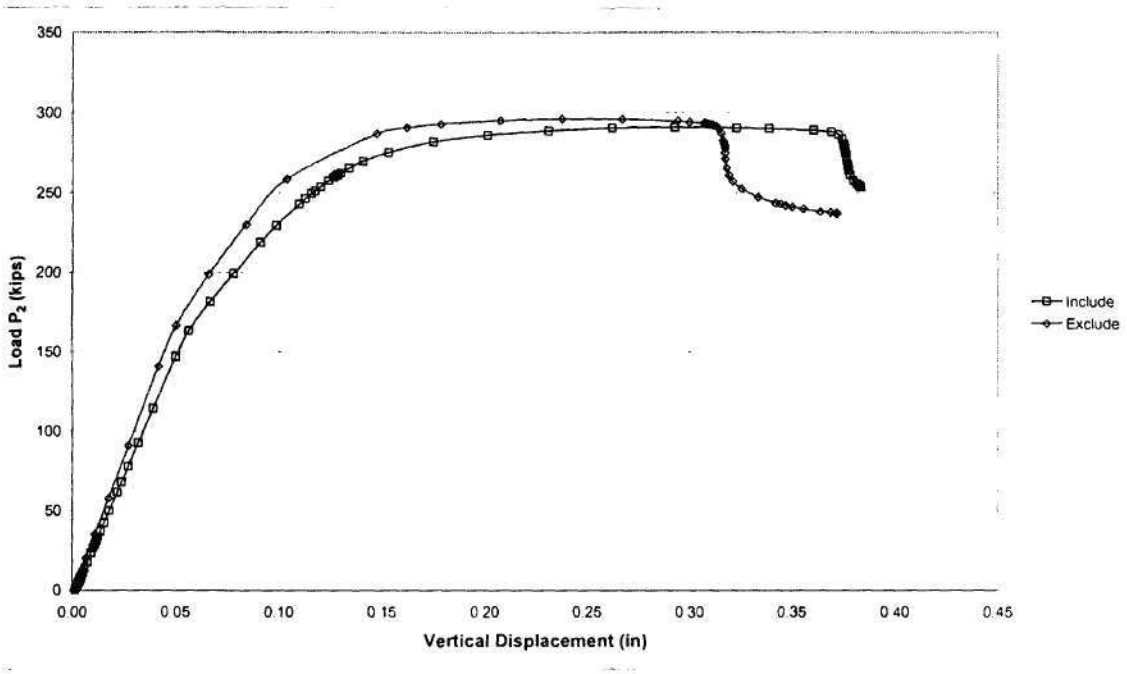

Figure 31. Load P_2 versus vertical displacement at location 2 for Specimen MS1-S-0.10 including and excluding residual stresses.

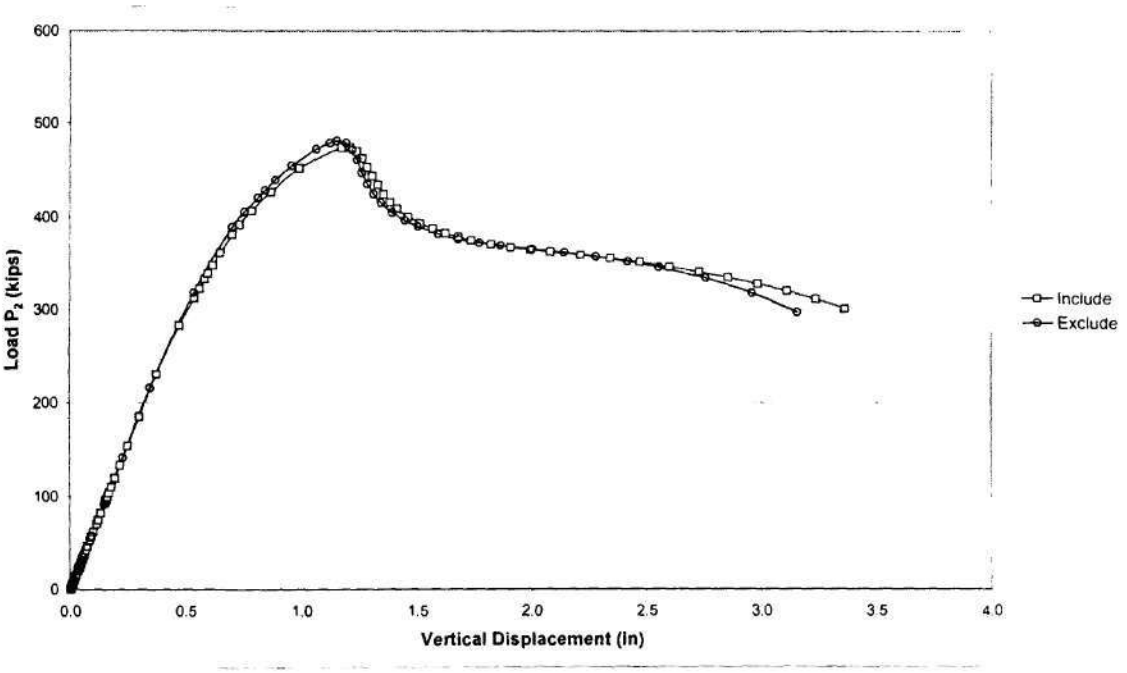

Figure 32. Load P_2 versus vertical displacement at location 2 for Specimen MS2-S-0.10 including and excluding residual stresses.

APPENDIX 1
FINITE ELEMENT MODELING DECISIONS

The finite element models of shear test specimens all have the following attributes:

1. The ABAQUS analysis system is utilized for all of the studies.
2. The S4R shell element is used for all the plate components of the girders (i.e., the web, the top and bottom flanges, and the stiffeners. Five section points are used through the thickness of the shell elements. Ten elements are used through the width of the flanges, and 20 elements are used through the depth of the web in all the studies. The elements at the ends of the bearing stiffeners (two-sided) are constrained to the top and bottom flange, whereas model of the transverse stiffeners (one-sided) is stopped one element short of the tension flange and is constrained only to the compression flange.
3. The yield strength of the steel F_y is assumed to be 55 ksi. Also, the material is modeled as elastic-plastic-linear strain hardening, with a length of the yield plateau equal to 10 times the yield strain and a constant strain-hardening modulus of E_{st} = 800 ksi up to F_u = 70 ksi.
4. Residual stresses are considered within the present studies based on the ECCS equations for estimating residual stresses (ECCS 1976). The detailed calculations of the residual stress distribution are described in Appendix 2.
5. The girders are rigidly restrained in the radial direction at the top and the bottom of the web at each of the locations 1 through 4. This represents the effect of radial bracing provided at these locations in the physical tests.
6. The vertical support at location 1 is modeled by restraining the displacements in the vertical direction along a line across the width of the bottom flange. That is, an ideal roller support is specified and the specimens are free to move along the tangential direction at this location. In the physical tests of these girders, a round bar will be placed under the girder at location 1.
7. The vertical support at location 3 is assumed to be rigid in compressive contact over the full area of the bearing plate, but uplift is allowed at any locations of the bottom flange that would tend to lift off of the bearing plate due to the deformations of the girder. The bearing plate is assumed to be 1" thick x 6" long x 21-7/16" wide.
8. Tangential displacements are assumed to be restrained across the entire width of the bottom flange at location 3. That is, it is assumed that the bearing plate prevents tangential displacements at this location.
9. In the physical tests, is desired to use an actuator that does not have swivels at the location of the applied load P_2. As a result, the actuator/loading frame provides some restraint against tangential movement of the top flange of the test specimens at this location. Linear springs that are oriented in the tangential direction are provided across the flange width to model the effect of this restraint. By distributing the springs across the width of the flange, the model also simulates restraint against twisting of the top flange of the test girder about the axis of the actuator. The upper bound of the combined stiffness of the above springs against tangential movement is estimated as 250 kips/in while the lower bound is taken as 125 kips/in. The analyses presented in

the body of the report are based on this upper bound stiffness. Analysis results based on a tangential stiffness of 125 kips/in and based on rigid and zero tangential restraint at location 2 are presented in Appendix 2. The primary source of flexibility within the actuator/loading frame system associated with the tangential movement of the test girders at the loading point (location 2) is twisting of the main loading beam (i.e., rigid body rotation of the actuator about an axis of the main loading beam).

APPENDIX 2
DETERMINATION OF RESIDUAL STRESSES DUE TO FLAME CUTTING AND WELDING

Residual stresses can have a significant effect on the stability, strength, and deflection of the steel structures. A combination of applied and residual stresses will induce inelastic behavior in a member cross-section at earlier levels of applied load.

The ECCS Manual on Stability of Steel Structures (ECCS 1976) provides a comprehensive summary of simplified equations for estimating residual stresses. These equations reflect the two primary causes of the longitudinal stress in welded I girders:

1. flame-cutting
2. welding between the flanges and the web

The residual stresses are essentially equal to the yield stress in a narrow strip of plate near the heat affected zone and a smaller almost constant self-equilibrating compression stress is generated within the other regions of the plate. ECCS (1976) provides the width of the equivalent tension block (c) for a plate that is flame-cut to be given by

$$c_f = \frac{1100\sqrt{t}}{F_y}$$

where t is the plate thickness in mm and F_y is the plate yield stress in MPa. In addition, based on the assumption of continuous single pass weld between the web and the flange, the resulting tension block on each side of the centerline of the weld in the flange plate and at the top and bottom edge of the web plate is given by

$$c = \frac{12000\,pA_w}{F_y \sum t}$$

where p is the process efficiency factor depends on the welding process adopted and is equal to 0.90 for submerged arc welding, A_w is the cross-sectional area of the added weld metal in mm^2, and Σt is the sum of the plate thickness meeting at the weld in mm.

The effect of welding and previously flame-cut edges does not result in the algebraic sum of the tension block widths since the weld heat tends to relieve the tension block due to cutting. The ECCS Manual (1976) suggested that the final tension block width (c_{fw}) can be calculated by

$$c_{fw}^{\ 4} = c_f^{\ 4} + c_w^{\ 4}$$

where c_f is the tension block width due to flame-cutting alone and c_w is the tension block width due to welding alone.

If it is assumed that the web is fillet weld on each side to the flange plates, (ECCS 1976) proposes that the effective width of the tension block width on each side of the centerline of the web-flange juncture is given by

$$c_2 = c_w + 0.5d \quad for\ t_w \leq 2c_w$$

From the widths that have stress equal to yield stress (F_y), c_f and c_2 at the edge and interior of the flange plates, and c_{fw} at both edges of the web plate, and by neglecting the reduction in the residual stresses at the flange tips due to the compressive residual stresses caused by the welding, the smaller constant self-equilibrating compressive stress within the majority of the plate area can be calculated based on the equilibrium of the longitudinal residual stresses in each of the plates. The typical residual stresses pattern for the flange and the web plates are shown in Fig. A2-1.

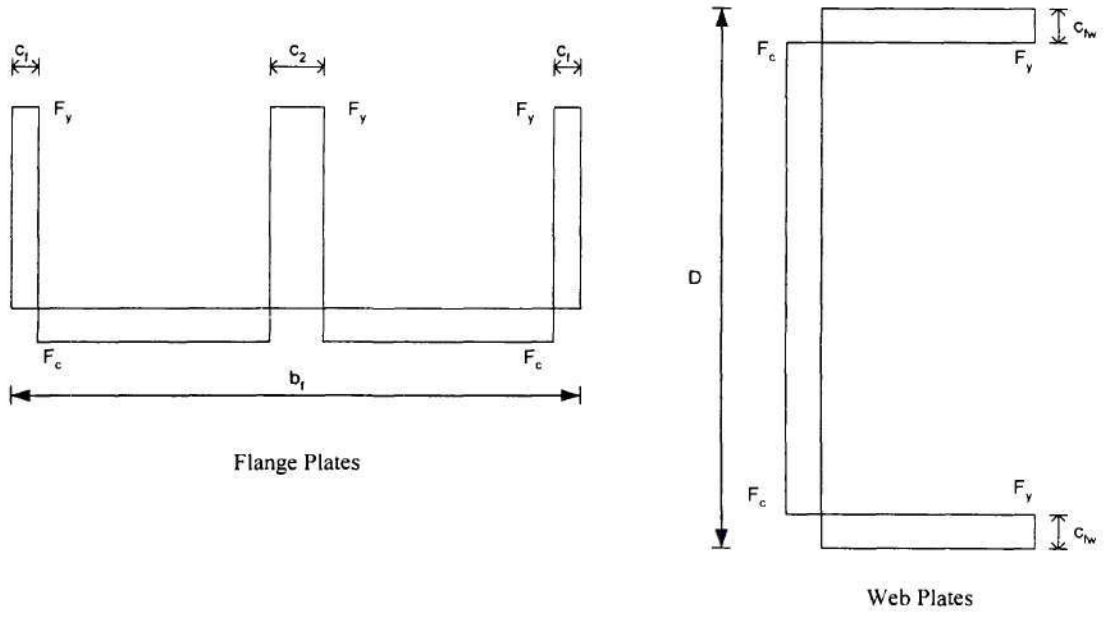

Figure A2-1. Typical residual stresses distribution in flange and web plates.

For the type of element used in the FEA, S4R, one point Gauss integration rule is employed within each element. Ten elements are used through the width of the top and bottom flanges while twenty elements are used through the depth of the web, therefore, there are ten integration points across the width of both top and bottom flanges and twenty integration points along the depth of the web.

Based on the equations in the *ECCS Manual* (1976) it is found that the width of the tension blocks is narrower than the width of an individual finite element. Therefore, in each of the elements that have residual stresses in tension, it is required to sum the residual stresses that are applied over each of the elements, compression and tension, to obtain the net residual stresses that will be applied to the single integration point. Figures A2-2 and A2-3 illustrate the self-equilibrating Gauss point residual stresses specified for the FEA conducted in this report.

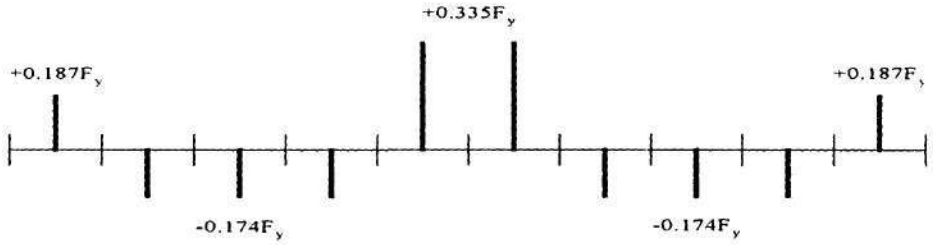

Figure A2-2. Gauss point residual stresses in top and bottom flanges.

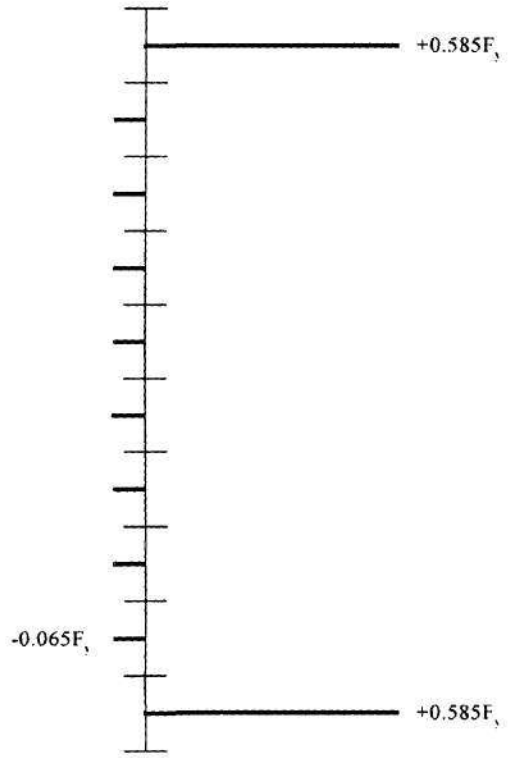

Figure A2-3. Gauss point residual stresses in web.

The compressive stresses applied in the web, $0.065F_y$, is also equal to the compressive residual stresses proposed by (Barth and White 1997) which is specified as 80 percent of the elastic buckling stresses of the web plate, assuming uniform longitudinal compression and simply supported edges (the elastic buckling stress of the web plate of the test specimens assuming simply supported edges is equal to $0.081F_y$).

It should be pointed out that the residual stresses shown in Figs. A2-2 and A2-3 are actually in equilibrium only within perfectly flat plates. Also, the stresses at the end cross-sections of the girders must be zero. Therefore, in the FEA conducted in this report, zero load is applied in the first step of the analyses, and the residual stresses are allowed to equilibrate.

REFERENCES

AASHTO (1993), *AASHTO Guide Specifications for Horizontally Curved Highway Bridges*, American Association of State and Highway Transportation Officials, Washington D.C.

Barth, K.E. and White, D.W. (1997), "Finite Element Evaluation of Pier Moment-Rotation Characteristics in Continuous-Span Steel I-Girders," *Engineering Structures*, Vol. 20, No. 8 1998, 761-778

ECCS (1976), *Manual on Stability of Steel Structures*, 2nd Edition, ECCS – Committee 8 – Stability, European Convention for Constructional Steelwork, Publication No. 22, 328 pp.

Federal Highway Administration (1996), "Nominal Bending and Shear Strength", *Draft Report No. FHWA-RD-xx-yy: Task D – Nominal Bending and Shear Strength,* August 1996

Hall, D.H. and Yoo, C.H. (1998), "Recommended Specifications for Steel Curved-Girder Bridge," Prepared for National Cooperative Highway Research Program, Transportation Research Board, National Research Council, July 1998, 103 pp.

Lee, S.C. and Yoo, C.H. (1998), "Strength of Plate Girder Web Panels Under Pure Shear", *Journal of Structural Engineering*, 124(2), 184-194

Phoawanich, N., White, D.W., and Zureick, A.H. (1999a), "Evaluation of Shear Test Specimens", *Report to FHWA*, July 1999, 25 pp.

Phoawanich, N., White, D.W., and Zureick, A.H.(1999b), "Evaluation of Moment-Shear Test Specimens", *Report to FHWA*, July 1999, 43 pp.

Compression and Tension Tests on Tubular Members

INTRODUCTION

This report presents the results of experiments conducted on steel pipes having the same dimensions and material properties as those used for the construction of the cross-frames, shown in figure 1, of a three curved steel girder bridge system tested at the Federal Highway Administration 's Turner Fairbank Highway Research Center. These pipes were tested under concentric and eccentric tension and compression loading conditions with the objective of determining the most efficient means of instrumenting these pipes so that axial forces and moments can be deduced during the full scale experiment of the three-girder system. Another important objective is to determine the maximum load or strain level below which the pipes remain elastic when subjected to the combined axial loading and bending. Schematics of the tested pipe configurations are shown in figure 2. All tests were conducted in a Riehle Universal Testing Machine located in the Structural Testing Laboratory at the Georgia Institute of Technology.

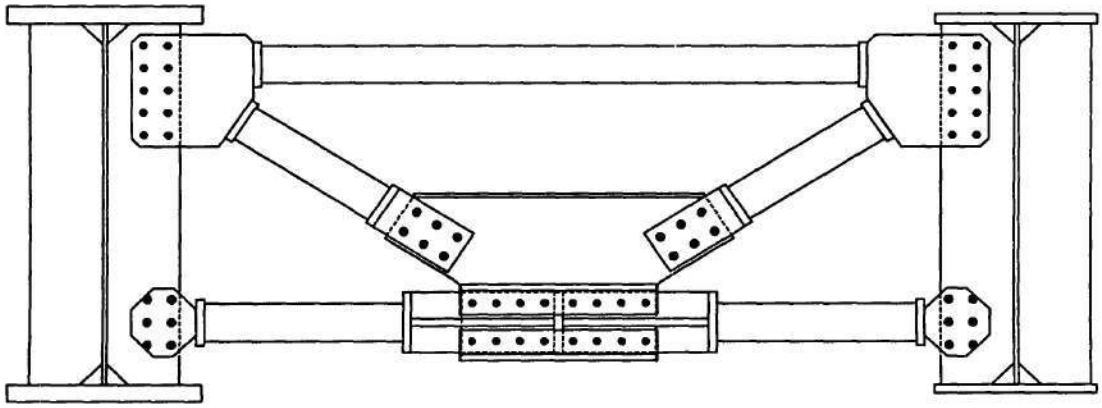

Figure 1: Elevation of Typical Cross Frame (not to scale)

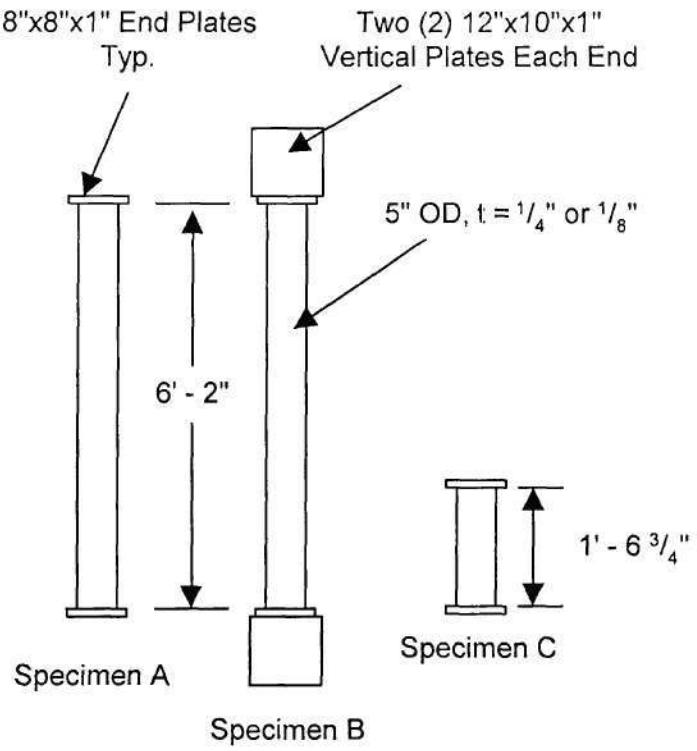

Figure 2: Cross Frame Specimens (not to scale)

A summary of the completed tests, including the support and loading conditions, the active instrumentation, and a description of the load history, can be found in table 1.

An independent series of material tests were performed at the Georgia Institute of Technology to verify the values given in the manufacturer's reports, which contained yield and ultimate stress values from tensile tests of the 1/8" and 1/4" thick tubes. A summary of the values is shown in table 2. This was accomplished by testing stub columns according to the procedure outlined in SSRC Technical Memorandum No. 3 (1998). Stub column tests were selected because their size gave an accurate representation of residual stress distributions in the full-scale cross frame members. A total of three tests were completed, two on 1/8" thick specimens and one on a 1/4" specimen. A schematic of stub column test specimen dimensions is shown in figure 3 followed by representative photos of one of the tests before and after completion. Resulting stress-strain curves are shown in figures 6 through 8. Results are also incorporated into table 2 for comparative purposes.

Table 1: Cross Frame Member Testing Summary

Test	Member	Tube Thick-ness (in)	Load	Instrumentation	Load History
1C	Top Chord	1/8	Conc.	*Load* - load cell at top *Strain* - 4 single-arm, 4 rosettes at midht	1. Load at 10 kips/min past proportional limit to 125 kips 2. Unload to initial conditions
2C/3C	Top Chord	1/8	Conc.	*Load* - load cell at top *Strain* - 4 single-arm, 4 rosettes at midht *Displacement* - LVDT at midht., LVDT at top *Rotation* - inclinometer at top	1. Load at 10 kips/min past proportional limit to 120 kips (2C), 115 kips (3C) 2. Unload to 10 kips 3. Load to 110 kips (2C), 100 kips (3C) 4. Unload to initial conditions
4C	Top Chord	1/8	1" Ecc. Conc.- Post yield	*Load* - load cell at top *Strain* - 4 single-arm, 4 rosettes at midht. *Displacement* - LVDT at midht., LVDT at top *Rotation* - inclinometer at top	(ECCENTRIC) - Terminated due to lack of bending 1. (CONCENTRIC) Post yield - load at 10 kips/min past proportional limit to 110 kips 2. (CONCENTRIC) Unload to initial conditions
5C	Top Chord	1/8	2" Ecc.	*Load* - load cell at top *Strain* - 4 single-arm, 4 rosettes at midht. *Displacement* - LVDT at midht., potentiometer at midht., LVDT at top *Rotation* - inclinometer at top	1. Align with elastic cycles to 20 kips 2. Load at 10 kips/min past proportional limit to 55 kips 3. Unload to 3 kips 4. Cycle twice to 40 kips
6C	Top Chord	1/4	Conc.	*Load* - load cell at top *Strain* - 4 single-arm, 4 rosettes at midht. *Displacement* - LVDT at midht., potentiometer at midht., LVDT at top *Rotation* - inclinometer at top	1. Load at 10 kips/min past proportional limit to 245 kips 2. Unload to 5 kips 3. Cycle twice to 200 kips
7C	Top Chord	1/4	2" Ecc.	*Load* - load cell at top *Strain* - 4 single-arm, 4 rosettes at midht. *Displacement* - 2 potentiometers at midht., LVDT at top *Rotation* - inclinometer at top	1. Load at 10 kips/min past proportional limit to 100 kips 2. Unload to 10 kips 3. Seven cycles to 100 kips 4. Eighth cycle to 110 kips
8C	Top Chord	1/4	1" Ecc.	*Load* - load cell at top *Strain* - 4 single-arm, 4 rosettes at midht. *Displacement* - 2 potentiometers at midht., LVDT at top *Rotation* - inclinometer at top	1. Load at 10 kips/min past proportional limit to 140 kips 2. Unload to 10 kips 3. Seven cycles to 100 kips 4. Eighth cycle to 145 kips
9C1	Diagonal	1/4	Conc.	*Load* - load cell at top *Strain* - 4 single-arm, 4 rosettes at midht. *Displacement* - 2 potentiometers at midht., LVDT at top, LVDT on loading machine head	1. Load at 10 kips/min past proportional limit to 280 kips 2. Unload to 3 kips 3. Eight cycles to 200 kips
9C2	Diagonal	1/4	Conc.	*Load* - load cell at top *Strain* - 4 rosette longitudinal arms at midht.	1. Load at 10 kips/min to 50 kips with "post gain" at 2 2. Unload to original conditions 3. Load at 10 kips/min to 50 kips with "post gain" at 4 4. Unload to original conditions 5. Load at 10 kips/min to 50 kips with "post gain" at 8 6. Unload to original conditions
10C	Top Chord	1/4	1" Ecc.	*Load* - load cell at top *Strain* - 4 single-arm, 4 rosettes at midht., 4 single-arm at quarter pts., 4 single-arm at 1.5* dia. from ends *Displacement* - 2 potentiometers at midht., potentiometers at quarter pts., potentiometer on loading machine head, LVDT at top *Rotation* - inclinometer at top	1. Align with elastic cycles to 100 kips 2. Load at 10 kips/min past proportional limit at quarter pts.to 170 kips 3. Unload to 5 kips 4. Eight cycles to 150 kips
1T	Top Chord	1/4	Conc.	*Load* - load cell at top *Strain* - 4 single-arm, 4 rosettes at midht. *Displacement* - LVDT at midht., potentiometer at midht., LVDT at bottom *Rotation* - inclinometer at bottom	1. Load at 10 kips/min past proportional limit to 220 kips 2. Unload to 5 kips 3. Load at 10 kips//min to 225 kips 4. Unload to 5 kips 5. Load at 10 kips/min to 235 kips 6. Unload to initial conditions
2T	Top Chord	1/4	1.5" Ecc	*Load* - load cell at top *Strain* - 4 single-arm, 4 rosettes at midht. *Displacement* - LVDT at midht., potentiometer at midht., LVDT at bottom *Rotation* - inclinometer at bottom	1. Align with elastic cycle to 20 kips 2. Load at 10 kips/min past proportional limit to 130 kips 3. Unload to 2 kips 4. Cycle eight times to 65 kips (25% higher than anticipated peak cross frame member load)

Table 2: Cross Frame Member Material Properties

Specimen	Measured Average Tube Thickness (in)	Proportional Limit	Yield Stress			Ultimate Stress	Modulus of Elasticity	
		Stub Column Tests (ksi)	Manuf Cert. Reports (ksi)	Stub Column Tests (ksi)	% Diff.	Manuf Cert. Reports (ksi)	Manuf Cert. Reports (ksi)	Stub Column Tests (ksi)
SC1	0.128	47	71.9	74	+2.8	82.2	--	30000
SC2	0.129	46	71.9	73	+1.5	82.2	--	30000
SC3	0.253	60	84.5	80	-5.3	98.4	--	29268

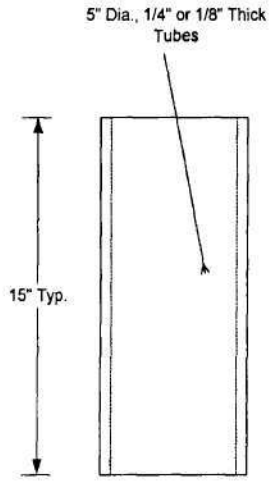

Figure 3: Stub Column Specimen Schematic

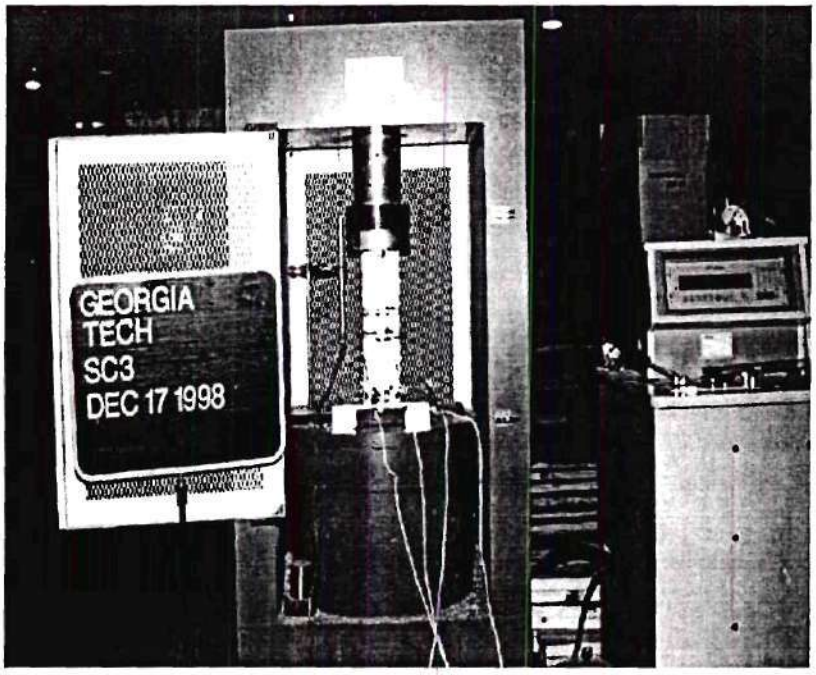

Figure 4: Stub Column Specimen SC3, Before Testing

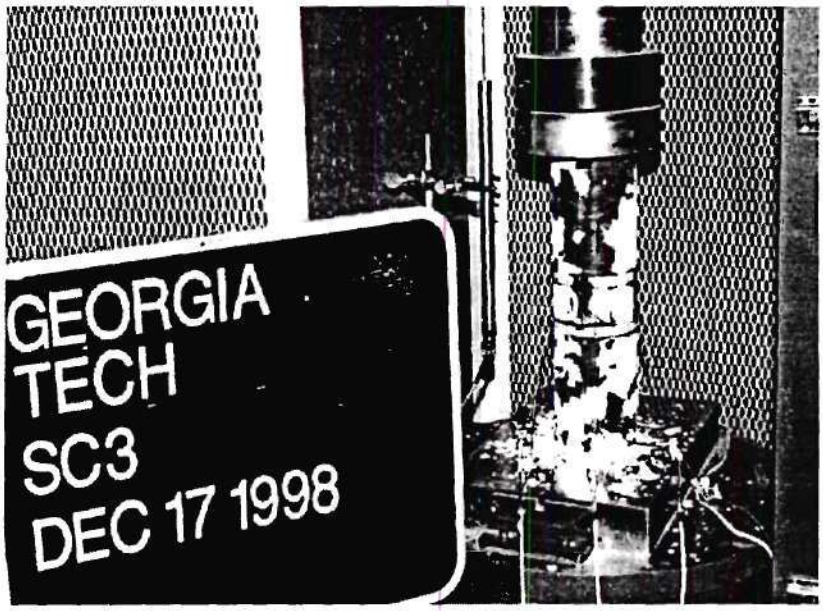

Figure 5: Stub Column Specimen SC3, After Testing

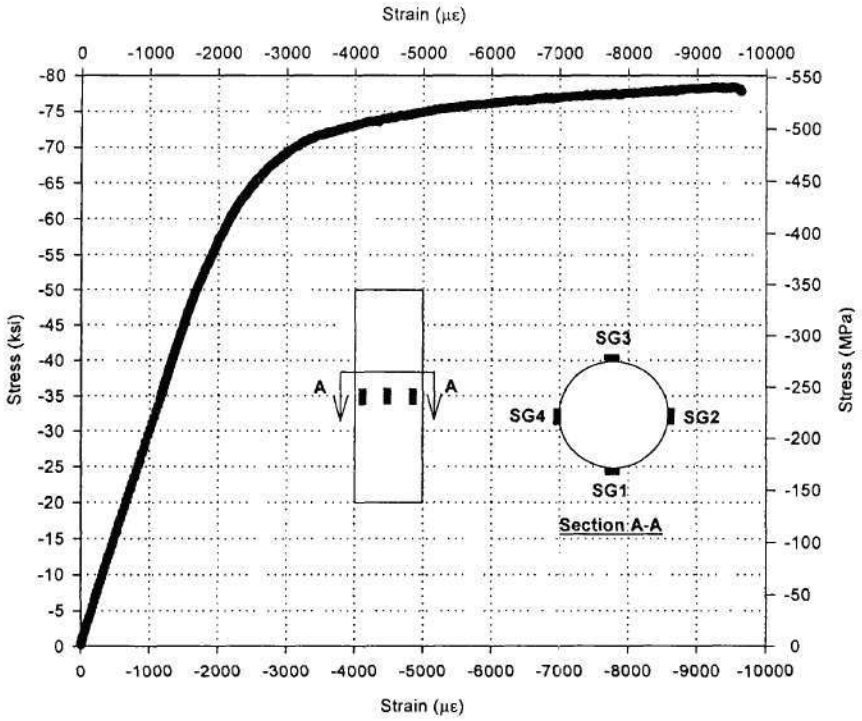

Figure 6: Stub Column Test SC1, Stress vs. Average Strain

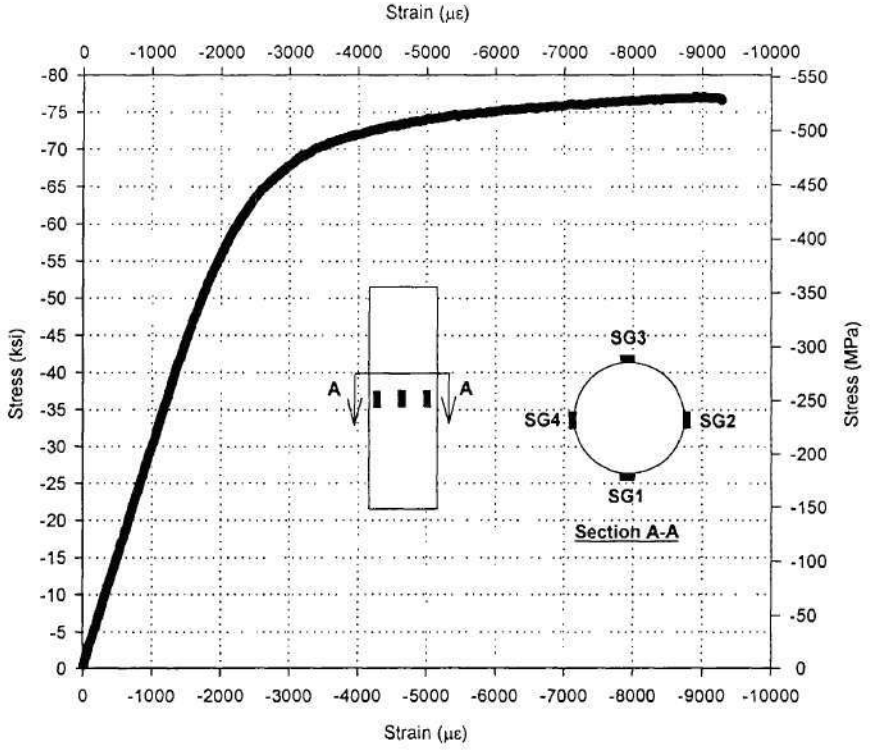

Figure 7: Stub Column Test SC2, Stress vs. Average Strain

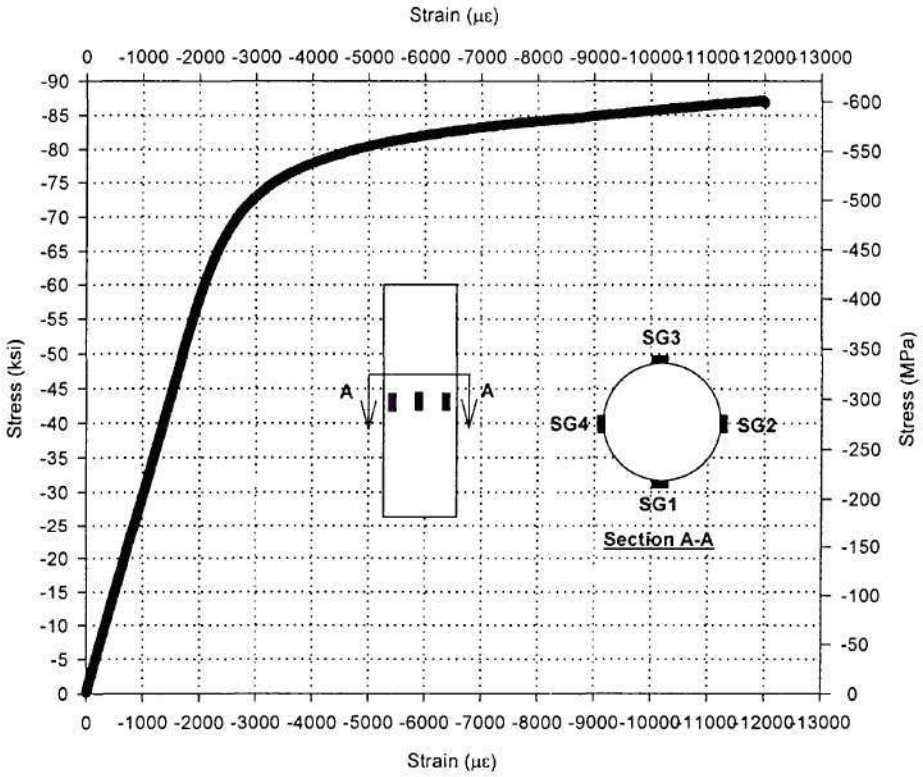

Figure 8: Stub Column Test SC3, Stress vs. Average Strain

As the table and plots indicate, comparisons between yield stresses from the certification reports and the stub column tests showed good agreement with differences below 5 percent. Stub column yield stress magnitudes were larger for the 1/8" specimens but smaller for the 1/4" specimen. The remaining information shown in table 2 was supplied by either the certification reports or the stub column tests.

Compression Series

For all compression tests, loads were applied to each specimen through as direct a path as possible, with a minimal amount of additional material being used to transfer forces from the testing machine to the specimen. End conditions used for each specimen test are explained within the test discussion sections.

Instrumentation

There are two possible approaches to the problem of obtaining axial force, bending moments, and torques in a tubular member. In the first approach each component is measured separately, requiring two full bridge strain gage configurations to find the axial loads and torques along with an additional four gages to calculate bending effects. The arrangements for each gage configuration are presented by Dally, et al. (1993). One full bridge would be arranged as a link-type load cell shown in figure 9 to determine axial force while the other full bridge would be arranged as shown in figure 10 to obtain torque about the tube's longitudinal axis. The additional four strain gages would be affixed as shown in figure 11. Values from the four gages would be placed into "dummy" channels within the acquisition systems to calculate the bending moments while the two full bridges would produce axial force and torque directly. The "dummy" channels would be used to form numerical Wheatstone bridge circuits from which the desired bending components would be determined. This instrumentation scheme would require twelve strain gages and six channels to correctly acquire and reduce the data.

The second approach would use four separate gages, two of which aligned along the member's longitudinal axis and two at +/- 45° degrees with respect to that axis as shown in figure 10 for the torque load cell. "Dummy" channels would again be used to calculate all of the desired force components using numerical Wheatstone bridge circuits. This arrangement would require four strain gages and the same number of acquisition channels. The major trade-off between the two approaches is that the first required many more gages, with the associated costs and vulnerability to individual gage failure. However, the full-bridge configurations would produce higher resolution outputs (by a factor of four over single-arm strain gages) and would therefore give more accurate results.

To study the effects of different combinations of single gages and bridges, specimens were heavily instrumented at mid-height using a combination of single-arm resistance strain gages and rosettes. Figure 12, which corresponds to Specimen 1C, shows a typical instrumentation scheme. Eight gages were placed every 45° around the tube's periphery and alternated between single-arm gages and rosettes. As can be seen in figure 12, rosettes were aligned so that their center arms fell on the specimen's longitudinal axis while single-arm gages were placed at alternating 0° and 45° angles with this axis. The heavy distribution of instrumentation made it possible to obtain a detailed set of measurements for the test. Once testing was completed, several of the theoretical configurations described above could be checked by combining output from different strain gages.

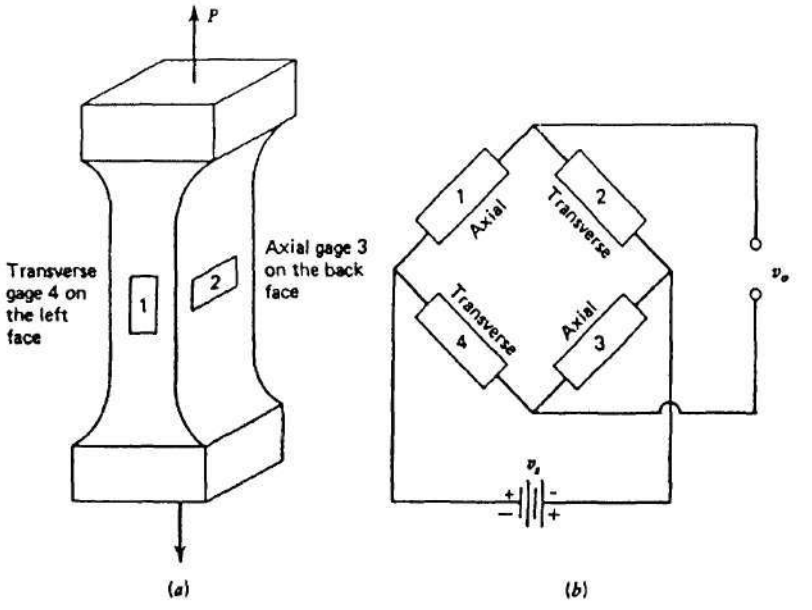

Figure 9: Link-Type Load Cell Gage Placement Schematic, from Dally et al. (1993)

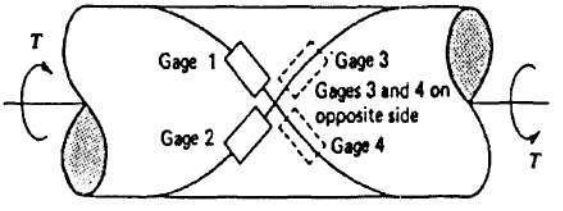

Figure 10: Torque Load Cell Gage Placement Schematic, from Dally et al. (1993)

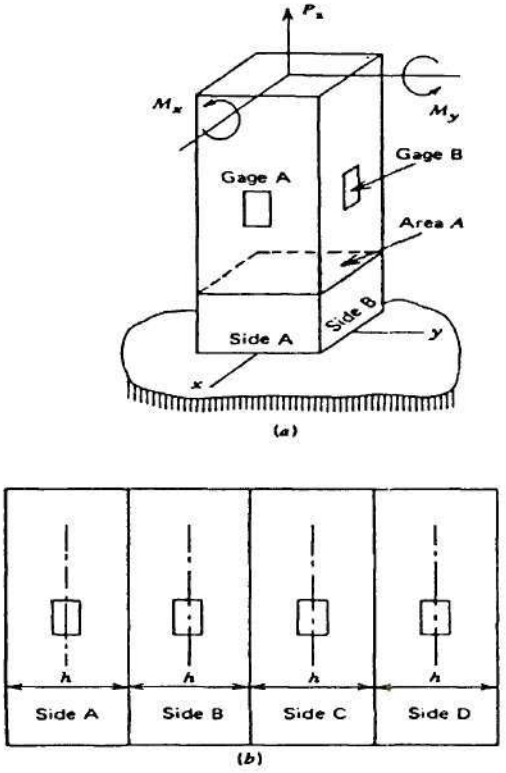

Figure 11: Bending Moment Gage Placement Schematic, from Dally et al. (1993)

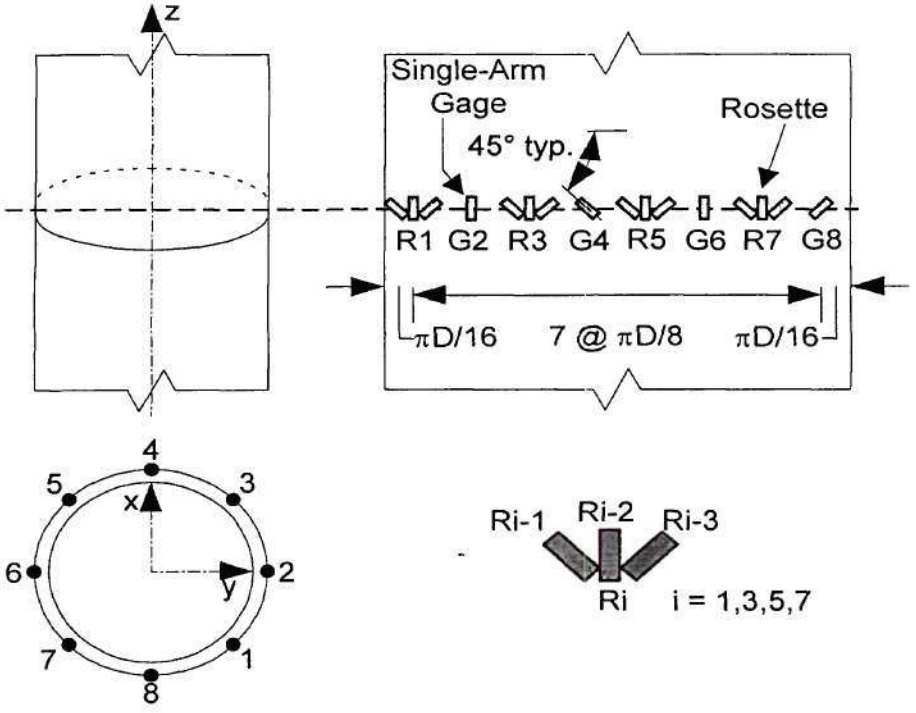

Figure 12: Mid-Height Strain Gaging Detail

The internal axial forces were calculated utilizing strains recorded from longitudinally oriented single-arm and longitudinally oriented rosette gages. Longitudinal gage pairs, both single-arm and rosette center-arm, positioned directly across from each other (e.g. gage 2 and 6 in figure 12) were averaged and substituted into the following equation:

$$P_A = \frac{AE}{2}(\varepsilon_{G2} + \varepsilon_{G6}) \tag{1}$$

where:
ε_{G2} and ε_{G6} = opposite single-arm gage strains (see figure 26)
A = cross-sectional area
E = modulus of elasticity.

Using equation (1), an internal force in the specimen for each longitudinal gage pair was found. Results were compared as individual quantities or averaged together and compared to the applied load. Nondimensionalized ratios, obtained by dividing the forces derived from the strain gages by those obtained from the load cell, were utilized to complete the comparisons. Values of 1.0 indicate perfect correlation between applied and calculated axial forces.

Additional equations, based on linear stress-strain relationships and coordinate transfor-mation laws, were introduced to calculate internal mid-height bending and torsional moments. These equations involved the four single-arm gages, G2, G4, G6, and G8 in figure 12, and appear as:

$$M_x = \frac{EI}{2r_o}(\varepsilon_{G2} - \varepsilon_{G6}) \tag{2}$$

$$M_y = \frac{EI}{(1-\nu)r_o}(\varepsilon_{G4} - \varepsilon_{G8}) \tag{3}$$

$$T_z = \frac{EI}{4r_o(1+\nu)}[2(\varepsilon_{G4} + \varepsilon_{G8}) - (1-\nu)(\varepsilon_{G2} + \varepsilon_{G6})] \tag{4}$$

where:
E = modulus of elasticity
A = cross frame tube area
I = cross frame tube moment of inertia
J = cross frame tube torsion constant
r_o = tube outside radius
ν = Poisson's ratio
ε_{G2} to ε_{G8} = single-arm gage strains (see figure 24).

Equations (5) and (6) from Dally et al. (1993) converted resistance changes in each gage to changes in output voltage for a constant current source or for a constant voltage source:

$$\Delta v_o = \frac{i_s R_1 R_3}{\Sigma R + \Sigma \Delta R}\left(\frac{\Delta R_1}{R_1} - \frac{\Delta R_2}{R_2} + \frac{\Delta R_3}{R_3} - \frac{\Delta R_4}{R_4} + \frac{\Delta R_1}{R_1}\frac{\Delta R_3}{R_3} - \frac{\Delta R_2}{R_2}\frac{\Delta R_4}{R_4}\right) \tag{5}$$

$$\Delta v_o = \frac{R_1 R_2}{(R_1 + R_2)^2}\left(\frac{\Delta R_1}{R_1} - \frac{\Delta R_2}{R_2} + \frac{\Delta R_3}{R_3} - \frac{\Delta R_4}{R_4}\right) v_s \tag{6}$$

where:
Δv_o = change in output voltage,
i_s = source current,
$\Delta R_1, \ldots, \Delta R_4$ = change in gage resistance,
$R_1, \ldots, R_4$ = gage resistance,
v_s = source voltage.

Various combinations of active and inactive arms within the Wheatstone bridge were used with equation (6) to develop formulas providing internal axial force and bending moments directly from resistance changes in the gages (Measurements Group, Inc. (1988)) which allowed strain gages to be used as measurement transducers. This procedure was closely followed for the remaining cross frame member tests to calculate internal force, moment, and torque equations when the Wheatstone bridge was under constant current or voltage excitation.

A different method of calculating internal forces and bending moments was also investigated starting with test 6C. The data acquisition system used in this investigation utilized a constant current source, so initial derivations were performed for this type of excitation. Different resistances in figure 13 were placed into the half-bridge depending upon which information was desired. For internal axial force, resistance R_2 and resistance R_4 in the Wheatstone bridge were kept constant while R_1 and R_3, which correspond to a longitudinally oriented gage pair such as G2 and G6 in figure 12, were used to calculate axial force. Eliminating appropriate terms from equation (5) and substituting the following relationship between the change in resistance and subsequent change in strain for a single gage:

$$\Delta R_i = R S_g \varepsilon_i \tag{7}$$

gave the following equation for change in output voltage:

$$\Delta v_o = v_o = \frac{i_s R^2}{R(4 + S_g \varepsilon_{G2} + S_g \varepsilon_{G6})}(S_g \varepsilon_{G2} + S_g \varepsilon_{G6} + S_g{}^2 \varepsilon_{G2} \varepsilon_{G6}) \tag{8}$$

where:
v_o = change in output voltage = Δv_o (initially $v_o = 0$ for a balanced circuit),
i_s = source current,

$R = R_i$ = gage resistance,
S_g = gage factor,
ε_i = strain in i^{th} gage,
ε_{G2} = strain in gage G2 (see figure 26),
ε_{G6} = strain in gage G6.

Substituting the equation relating axial force and longitudinal strain for an isotropic material and solving for the axial force gives the following Wheatstone bridge based equation:

$$P_z = 2AE\left(\frac{\varepsilon_{G2} + \varepsilon_{G6} + S_g\varepsilon_{G2}\varepsilon_{G6}}{4 + S_g\varepsilon_{G2} + S_g\varepsilon_{G6}}\right) \tag{9}$$

where:
P_z = axial force,
A = cross-sectional area,
E = Young's modulus
and the remaining terms were defined in equation (8).

Determination of the equation for internal bending moment with constant current excitation used resistances R_1 and R_4 in figure 13. Removing terms related to R_2 and R_3 in equation (5) and substituting strain-resistance and strain-bending moment relations gave the following equation for internal bending moment:

$$M = \frac{EI}{r_o}\left(\frac{\varepsilon_{G2} - \varepsilon_{G6}}{2 + S_g\varepsilon_{G6}}\right) \tag{10}$$

where:
M = internal bending moment about axis orthogonal to opposite gage pair,
d_o, d_i = tube outer, inner diameter,
I = cross frame tube moment of inertia
r_o = cross frame tube outer radius.

The remaining terms are as defined for equation (8).

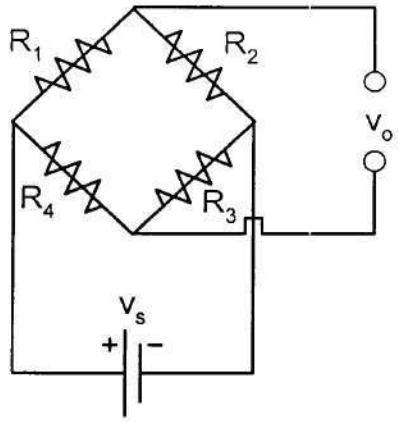

V_s = source voltage

V_o = output voltage

Figure 13: Constant Voltage Wheatstone Bridge Circuit

Since acquisition systems involved in the CSBRP may use a constant voltage source, equations (9) and (10) were re-derived for this situation using equation (6). The resulting Wheatstone bridge based formulas are:

$$P_z = \frac{AE}{2}(\varepsilon_{G2} + \varepsilon_{G6}) \tag{11}$$

and

$$M = \frac{EI}{2r_o}(\varepsilon_{G2} - \varepsilon_{G6}) \tag{12}$$

All terms were defined for the earlier constant current equations. Note that the constant current equations contain a non-linear term while the ones associated with a constant voltage excitation contained purely linear relationships between internal forces and the strains. It is also noted that both of the above equations are identical to equations (1) and (2), which were derived using solely engineering mechanics principles.

Loading Scheme

For this test and all that followed numerous small elastic loading cycles were run to ensure that the specimens were correctly aligned and that the desired eccentricities, or lack thereof, were maintained throughout the test. Once they were properly aligned, specimens were generally tested monotonically, with a loading rate of approximately 10 kips per minute up to and past the proportional limit. These forces were then removed at a similar rate until initial conditions were reached. In several cases, as will be noted in the individual descriptions, more than one cylce was applied. Load histories were previously described in table 1.

Data Acquisition

Applied forces and resulting strains were recorded every half-second using an Optim Megadac 3100 data acquisition system for Specimen 1C. This rate was decreased to one reading per second for all remaining tests.

Test 1C

The objective of this test was to examine the performance of 1/8" thick tubes under concentric loading (figure 9) The specimen was aligned in the testing machine with the load cell button applied directly onto the specimen's top end plate while the bottom end plate rested on testing machine's base plate. Test 1C involved a single loading and unloading cycle before being terminated.

Plots of applied loads versus longitudinal strains and nondimensionalized load ratios versus applied loads are shown for the first load cycle of test 1C in figures 15 and 16. Figure 15 presents the strain readings from each longitudinally oriented gage against the applied axial force and indicates that the 1/8" thick cross frame specimen reached its proportional limit at approximately 90 kips of concentric compression force. The proportional limit load values were found based upon a method outlined in the SSRC Technical Memorandum No. 3 (1998) for stub column tests. Each opposite longitudinal strain gage pair was averaged and plotted against the applied load. Figure 15 also indicates that the ultimate load for specimen 1C is approximately 130 kips.

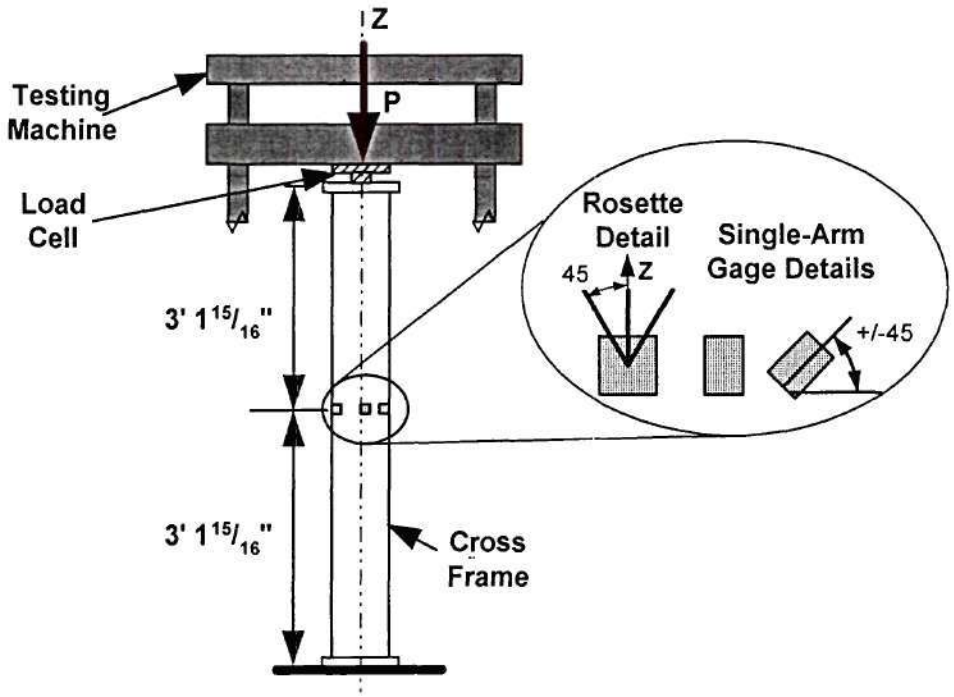

Figure 14: Elevation and Details for Test 1C (not to scale)

Figures 16 and 17 compare applied and average calculated axial forces computed from the rosette and the single-arm gage data. Rosette values were taken from longitudinal center-arm gage pairs and the single-arm values from the single opposite longitudinal pair (see figure 24). The gages were used as active arms within a Wheatstone bridge to calculate the axial forces, with all four bridge arms being active for the rosettes and two arms being active for the single-arm gages. Convergence of the results to nondimensionalized ratios near 1.0 would indicate that the strain gages could be used reliably to predict axial loads. Note, however, that the average nondimensionalized ratio was 0.93, with a standard deviation of 0.01 rather than 1.0 within the bounded range on the plots. Actual values fell between 0.92 and 0.96 within the envelope that was used. These values are based on nominal areas for the tubes. After completion of the tests, the average thickness of the specimens were measured and found to be closer to 0.27" than to the nominal 0.25". When the ratios are recalculated using the measured values, the ratios are very close to 1. Note that the calculations are all elastic and thus bounds had to be establsihed for the nondimensionalized ratio. In the plots, the lower bound was typically set where nondimensionalized ratios fell between 0.9 and 1.1 (10 percent error) while the proportional limit was determined using a 0.01 percent offset from the average longitudinal strain. The results show, in general, very good agreement between measured loads from the load cell and forces computed from the strain gages. Means very close to 1 with standard deviations approaching 0.02 are reasonable for axial load ratios using these

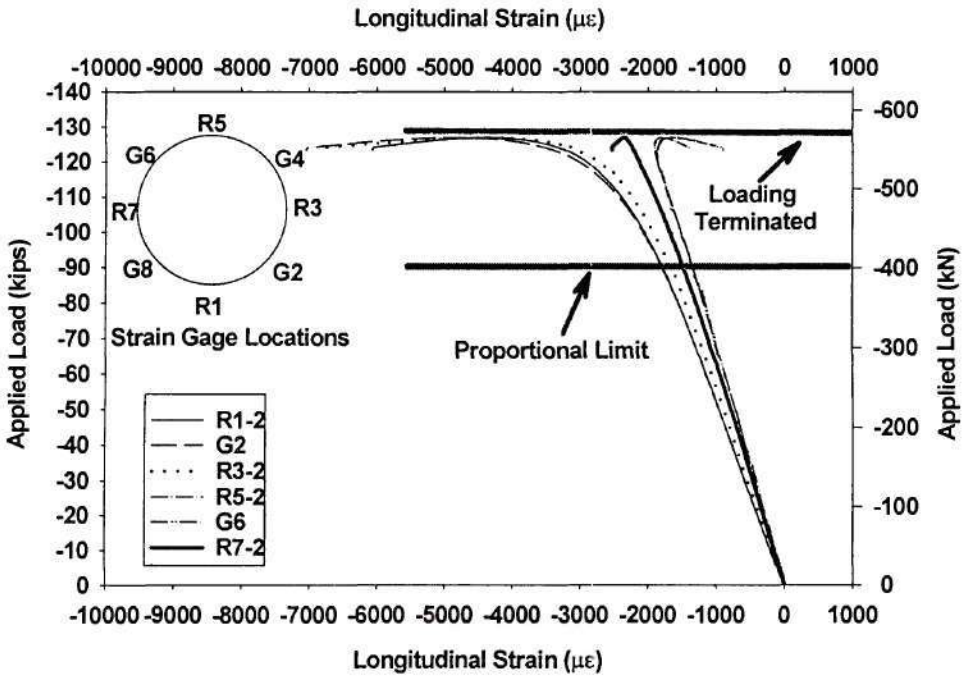

Figure 15: Applied Load vs. Longitudinal Strain, First Loading Cycle, Test 1C

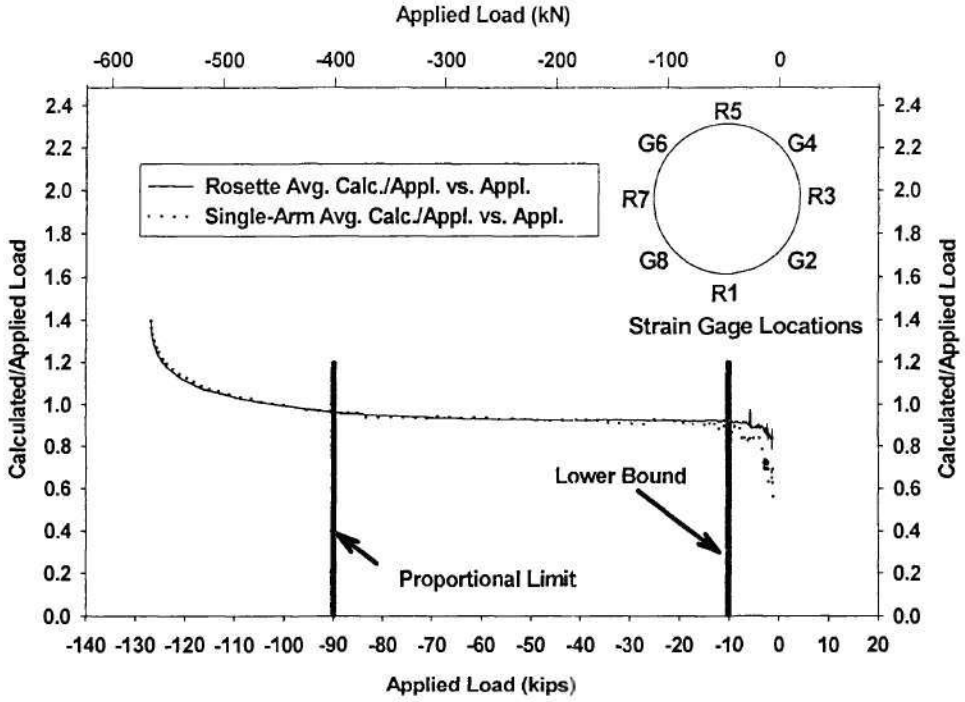

Figure 16: Average Calculated/Applied Load Ratios, First Loading Cycle, Test 1C

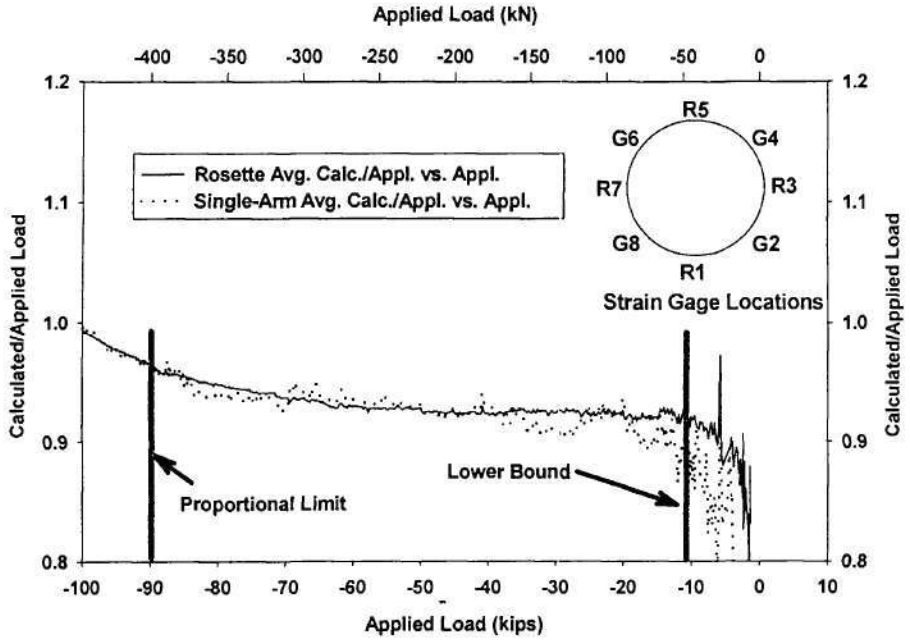

Figure 17: Average Calculated/Applied Load Ratios - Lower End of Loading Range, First Loading Cycle, Test 1C

Test 2C & 3C

The second and third concentric cross frame tests of 1/8" thick specimens were conducted with simulated pinned-pinned boundary conditions using knife-edges as shown in figure 18. Differences between these two tests were in fabrication procedures used for the specimens. The specimen for test 2C had its end plates welded to the tubular member using groove welds, which had been originally specified in the design plans but can be expensive to produce. The specimen for test 3C was fabricated with less costly fillet welds to determine if overall capacity would be compromised.

The only change in instrumentation from test 1C was the addition of a mid-height horizontal displacement LVDT, a vertical displacement LVDT at the top, and an inclinometer to measure end rotations. Testing was terminated after completion of two loading cycles.

Graphical methods were again used to evaluate each specimen's capacity and check the accuracy of equations (1) through (4). Figures 19 to 21 show variations within specimen 2C of applied load versus longitudinal strain, average axial load ratios versus applied load, and calculated moment and torque versus applied load. Figure 19 indicates that during the first loading cycle, 2C reached its proportional limit at approximately 90 kips, and had an ultimate capacity of approximately 125 kips. These values closely matched those from test 1C, although the boundary conditions differed. Figure 20 shows that the applied to calculated load ratios had an average ratio of 0.96 with a standard deviation of 0.02 between the lower bound and the proportional limit, using nominal dimensions. Since no external moments or torques were explicitly applied to this specimen, figure 21 checked relative magnitudes calculated using equations (2) through (4). Values for moment and torque relative to a local axis system through the four single-arm gages were typically less than 2 k-ft and appeared reasonable for a concentrically loaded specimen.

Figures 22 to 24 detail the same variations in load, strain, and calculated internal forces as those shown for test 2C, but this time they're for the fillet-welded specimen from test 3C. Figure 22 indicates a proportional limit near 80 kips with an ultimate load approximating 115 kips. These capacity marks were on the average 10 kips lower than corresponding values for the groove welded specimen in test 2C. While different fabrication methods may have caused the drop in capacity, a slight misalignment of specimen 3C may be a better explanation behind this discrepancy.

Figures 23 shows the nondimensionalized load ratios, and 23 indicates good correlation between calculated and applied loads. The mean was 0.95 and the standard deviation was 0.02 in the bounded range, based on nominal areas. Figure 24 showed bending moment and torque magnitudes that appeared reasonable with magnitudes less than 2 k-ft in the elastic range. Comparisons between both sets of results, combined with visual inspections of the welds after the tests, indicated that using the less expensive fillet welded specimens would not appreciably affect the capacity of individual cross frame members under compressive loads.

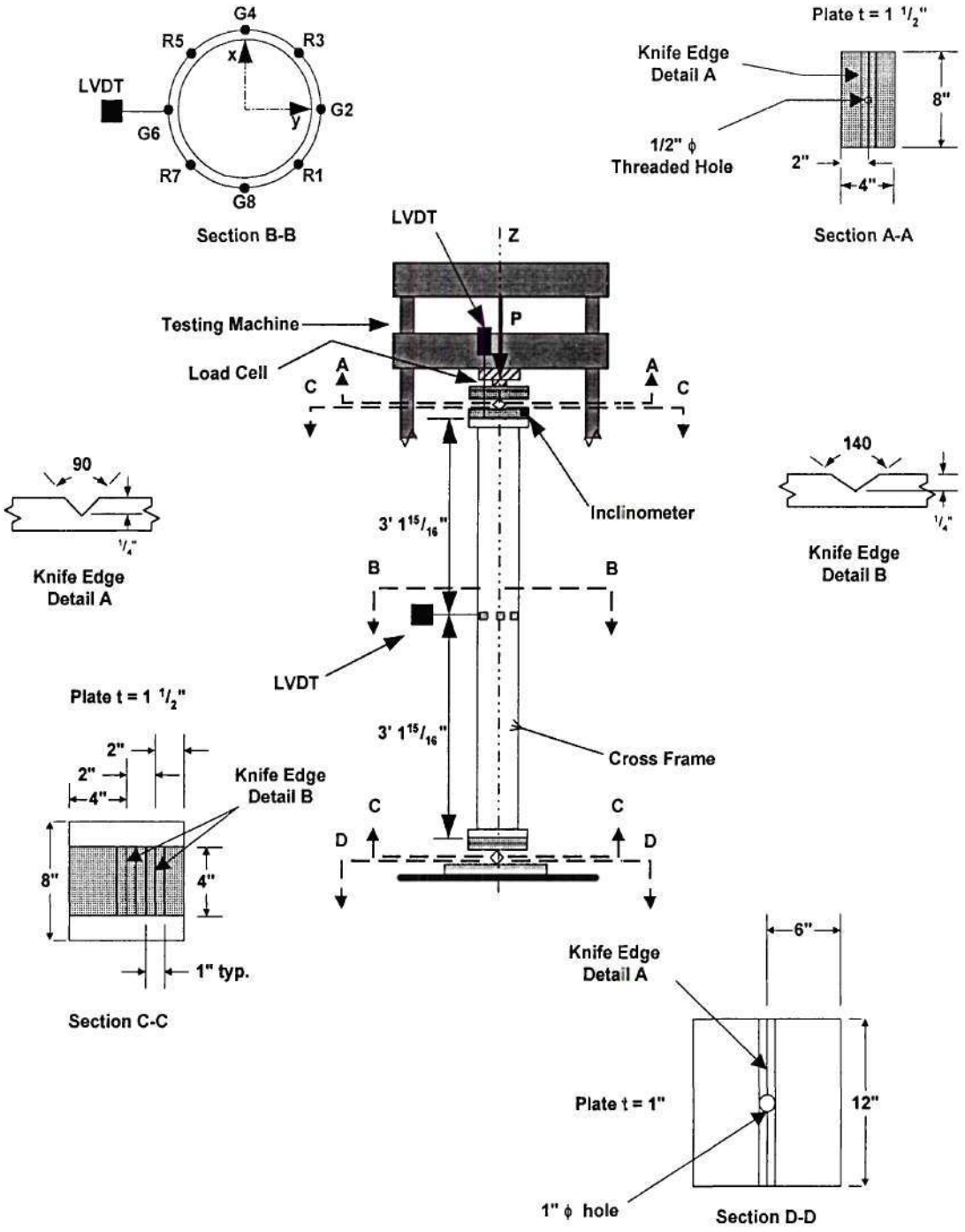

Figure 18: Elevation and Details for Tests 2C and 3C (not to scale)

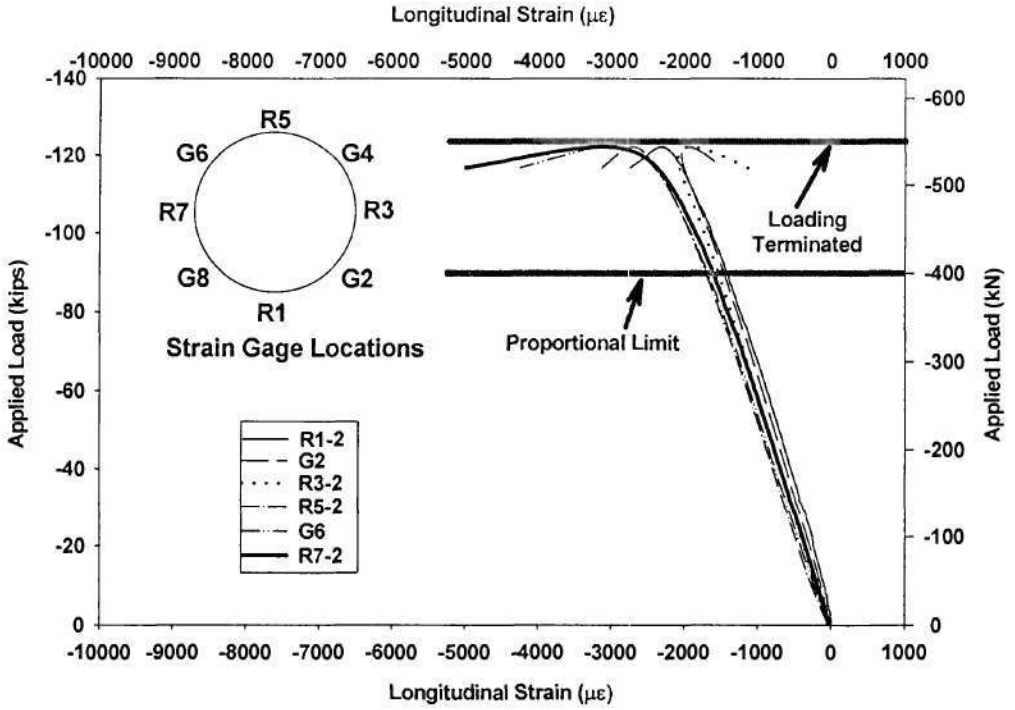

Figure 19: Applied Load vs. Longitudinal Strain, First Loading Cycle, Test 2C

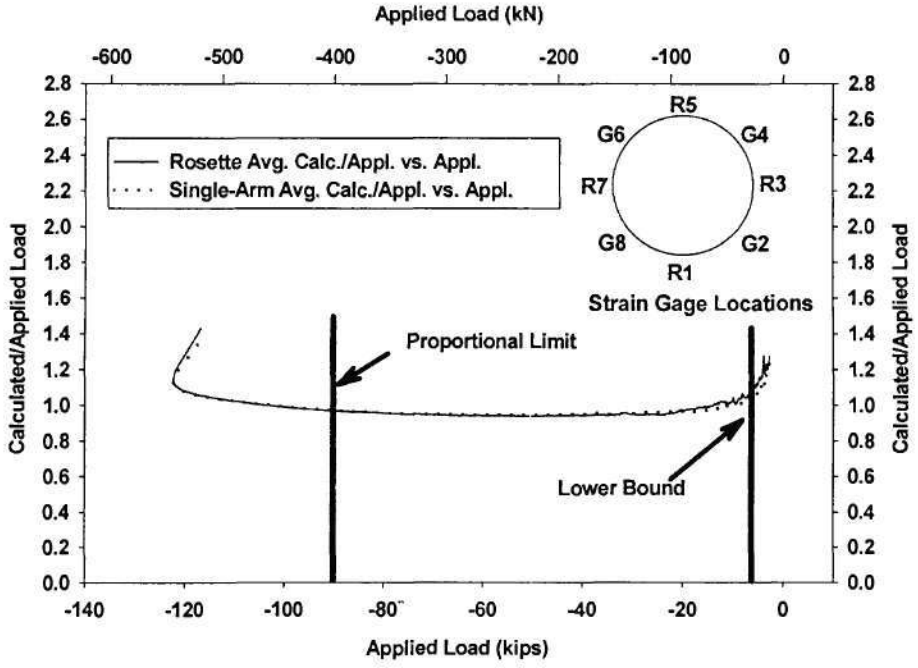

Figure 20: Average Calculated/Applied Load Ratios, First Loading Cycle, Nominal Thickness, Test 2C

- Either single-arm gage configuration, with two gages oriented longitudinally and two oriented at 45° or with all four gauges oriented longitudinally, would be sufficient to compute the axial loads and the moments in the cross frame members. Thus, it is recommended that the strain gauge configuration shown in figure 66 be used for the purpose of deducing the axial load and moments in each cross-frame member of the three-girder bridge system.

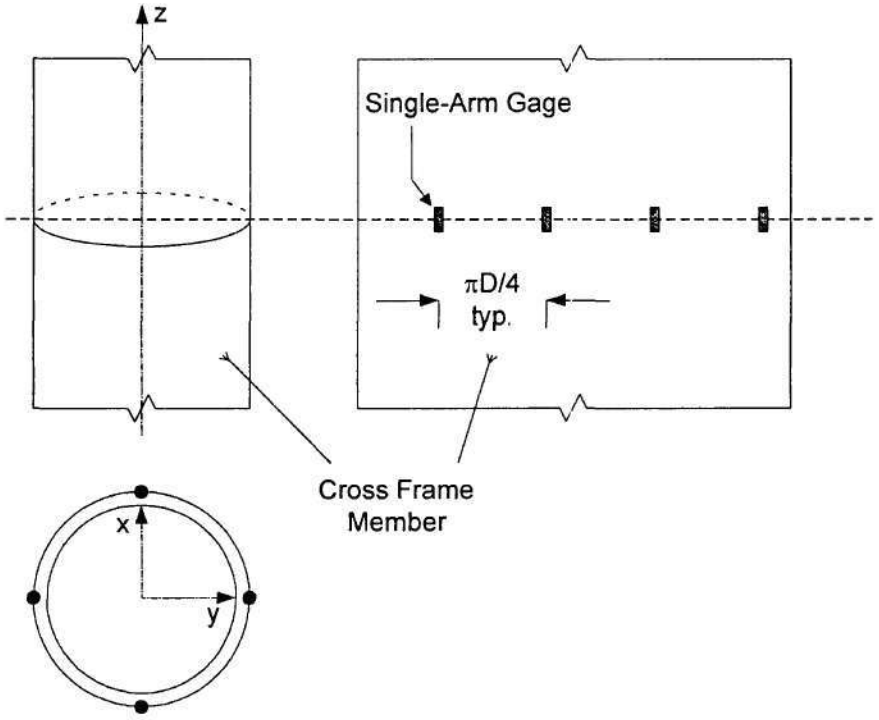

Figure 66: Cross Frame Member Strain Gage Configuration

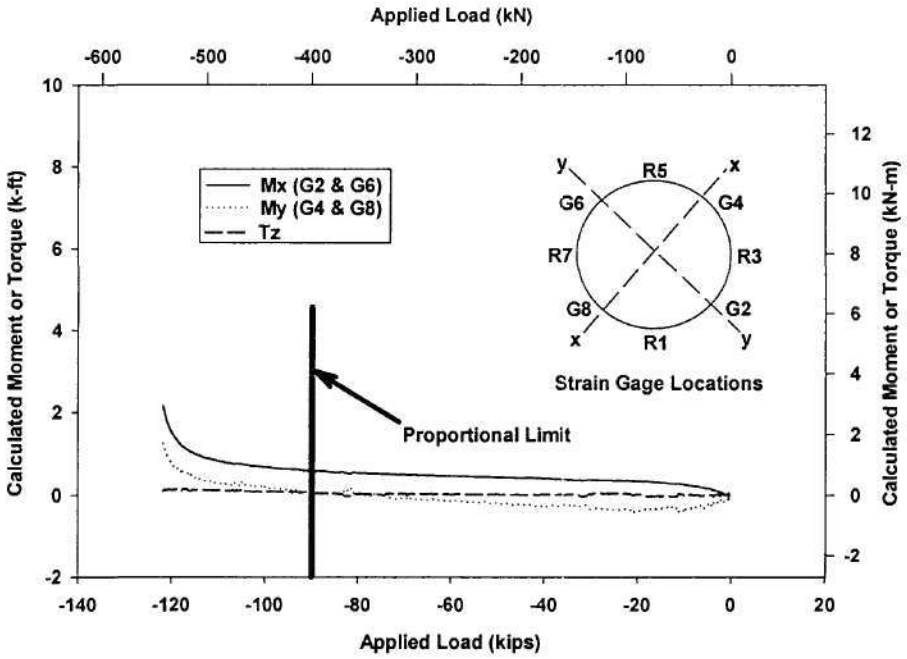

Figure 21: Calculated Internal Moments and Torque vs. Applied Load, First Loading Cycle, Nominal Thickness, Test 2C

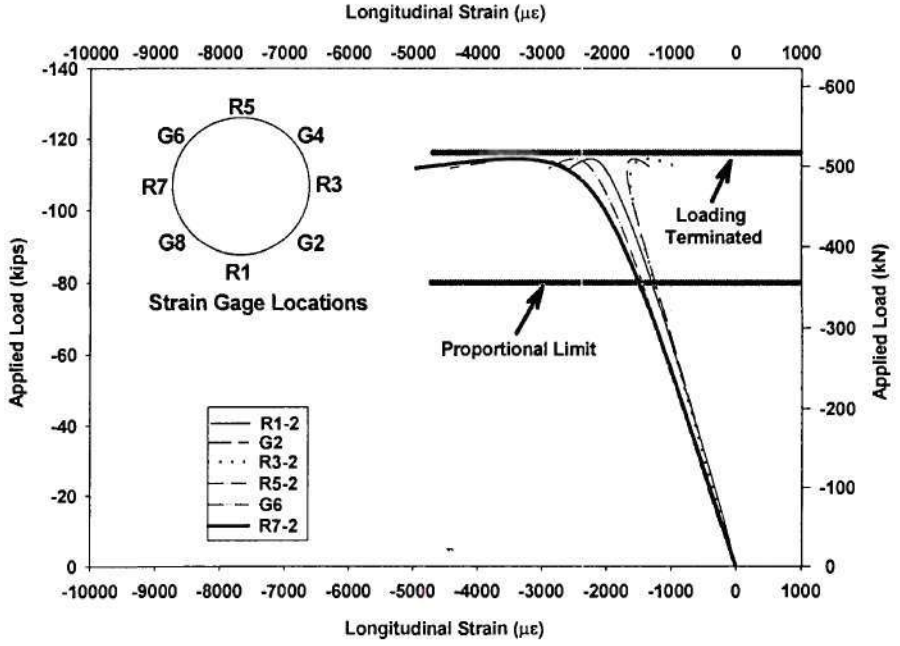

Figure 22: Applied Load vs. Longitudinal Strain, First Loading Cycle, Test 3C

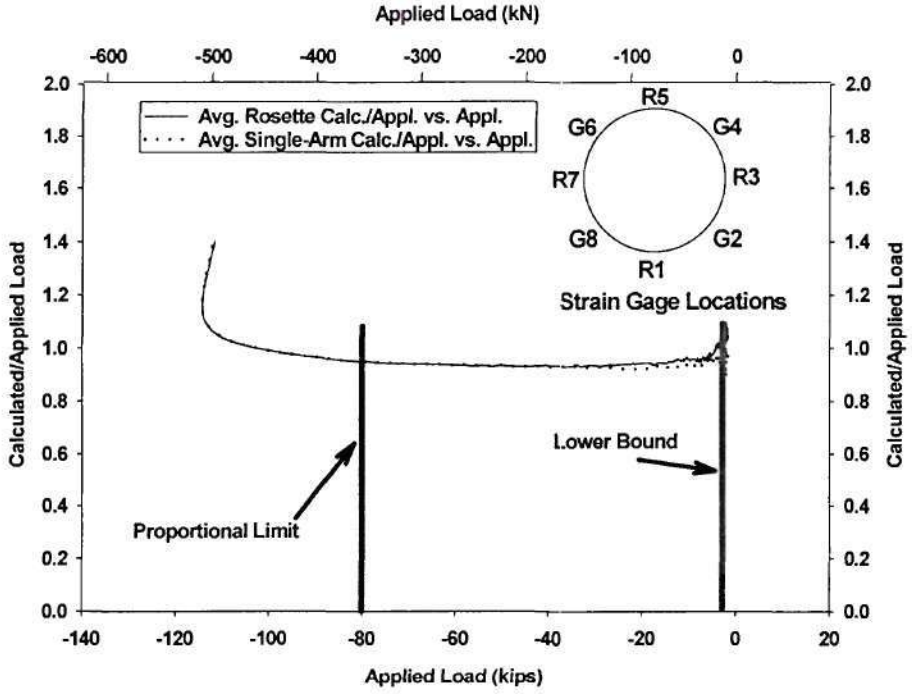

Figure 23: Average Calculated/Applied Load Ratios vs. Applied Load, First Loading Cycle, Nominal Thickness, Test 3C

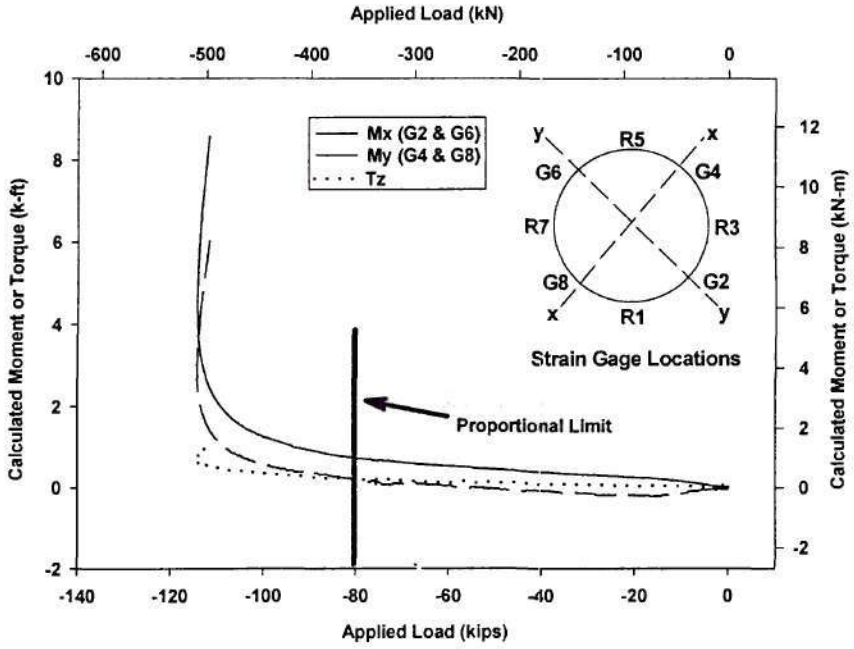

Figure 24: Calculated Internal Moments and Torque vs. Applied Load, First Loading Cycle, Nominal Thickness, Test 3C

Test 4C

Test 4C was the first compression test where loads were applied at a known eccentricity. The load fixture at the top consisted of a fabricated steel "double-T" (figure 25). If the testing machine head remained perfectly horizontal, this configuration would have imposed a 1" eccentricity onto the cross frame member. Instrumentation was identical to that of the previous two experiments.

Two loading cycles were intended, the first being used to obtain a capacity value and the second used to investigate post-yield behavior. However, during the first cycle little or no bending within the cross frame specimen was measured. It appeared that the bottom end plate's bearing surface was large enough to allow the reaction force resultant to shift exactly as the eccentrically applied load did. This, in effect, forced the entire system back to a concentrically loaded case. Since the proposed test fixture would require extensive modifications to impose bending forces, it was decided to conduct a post-yield investigation on specimen 4C in the same manner used for the final load cycles for tests 2C and 3C. Figure 26 shows that internal axial force calculations using equation (1) gave nondimensionalized ratios averaging 0.92 with a standard deviation of 0.01 using nominal dimensions.

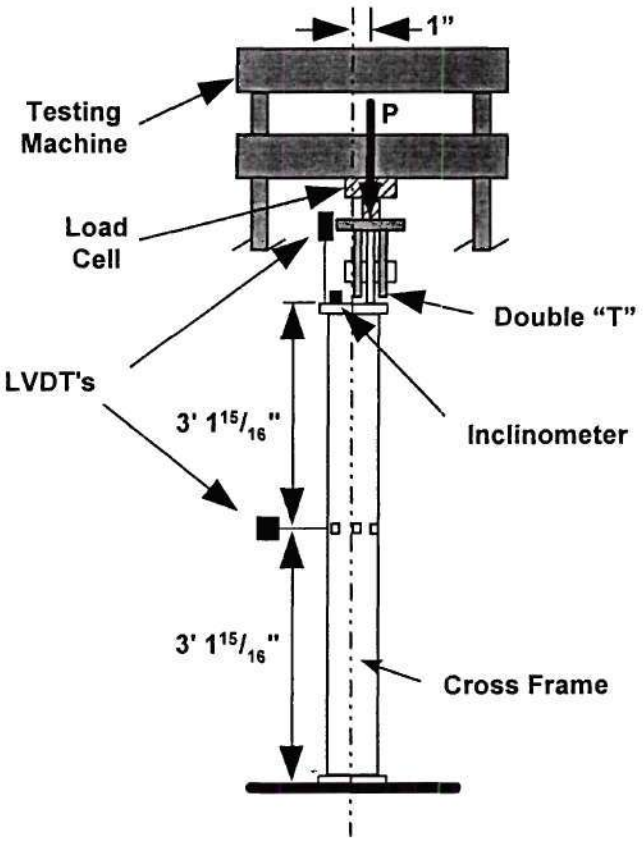

Figure 25: Set-up of Test 4C (not to scale)

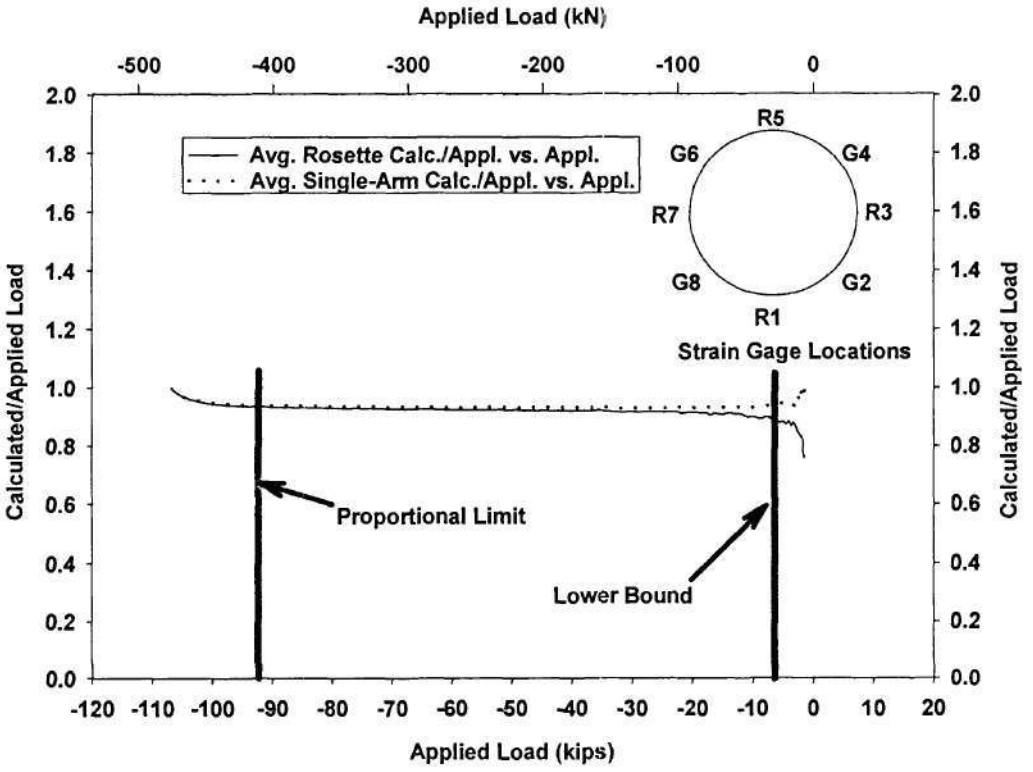

Figure 26: Average Calculated/Applied Load Ratios vs. Applied Load, Post-Yield Investigation, Nominal Thickness, Test 4C

Test 5C

Test 5C re-addressed the performance of a 1/8" thick cross frame specimen under an applied eccentric compressive load. For this test, pinned-pinned boundary conditions were simulated with the use of top and bottom knife edges placed eccentrically at 2" with respect to the longitudinal axis of the specimen (figure 34). Instrumentation was identical to that of the previous tests. In addition, both an LVDT and a potentiometer were used to measure the mid-height lateral deflection.

Figure 27 shows that, when subjected to a 2" load eccentricity, the proportional limit was reached at a load of approximately 40 kip, and that the ultimate load was approximately 60 kips. Both of these values were less than half those observed for the earlier, concentrically loaded cases. Figure 28 shows that the internal axial force equation again provided reasonably accurate results within the elastic range with nondimensionalized ratios averaging 0.91 with a standard deviation of 0.01. Figure 29 contains plots of the calculated internal bending moments and torque equations (2) through (4), along with two plots estimating the applied external moment. The first external moment plot multiplies the applied load times its 2" eccentricity while the second more accurately depicts the external moment as the product of the applied load times the 2"

eccentricity plus the amount of lateral deflection that had occurred at mid-height. The calculated internal moments indicate that bending predominates about the local x-axis with y-axis moments and torques were near zero. Figure 29 indicates that the internal and external moments agree reasonably well within the linear range of the test, and figure 30 reinforces this through the use of nondimensionalized ratios. The ratios average 0.91, with a standard deviation of 0.01 in the linear range using nominal dimensions. Differences between experimental and nominal thickness values, in addition to a potential slight misalignment of the specimen, explain the differences between the values reported in the figure and the desired ratio of 1.0

Combined results from the first five compression tests showed that an adequate measure of internal axial force, bending moment, and torque within each cross frame member could be obtained using only four single-arm strain gages and simple mechanics equations. While internal force results obtained from the equations appeared to give reasonable results, some improvement could still be made and future tests were necessary. As shown in figure 24, the gage configuration that would be used based upon these tests would consist of one pair of oppositely positioned gages oriented along the member's longitudinal axis with the other pair positioned at +/- 45° angles with that axis.

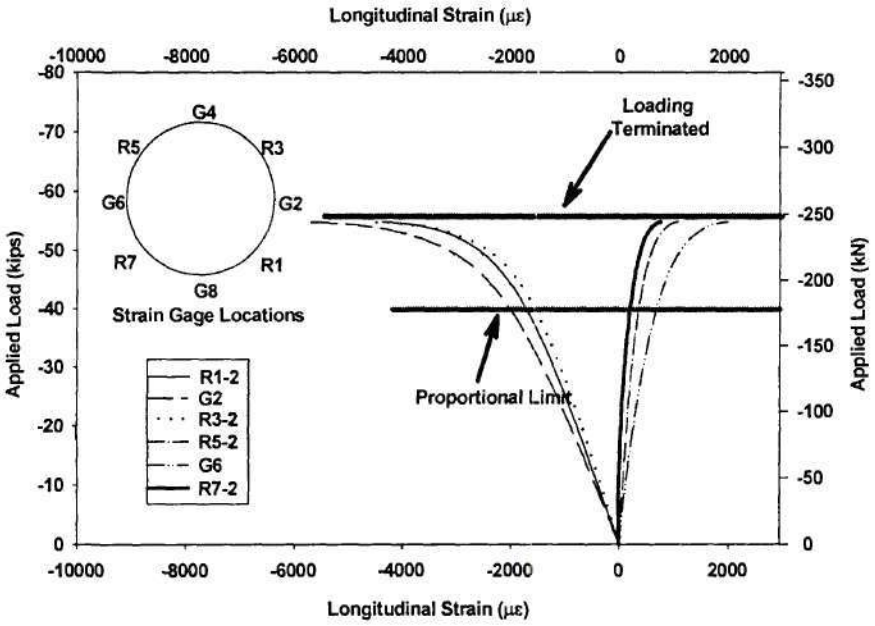

Figure 27: Applied Load vs. Longitudinal Strain, First Loading Cycle, Test 5C

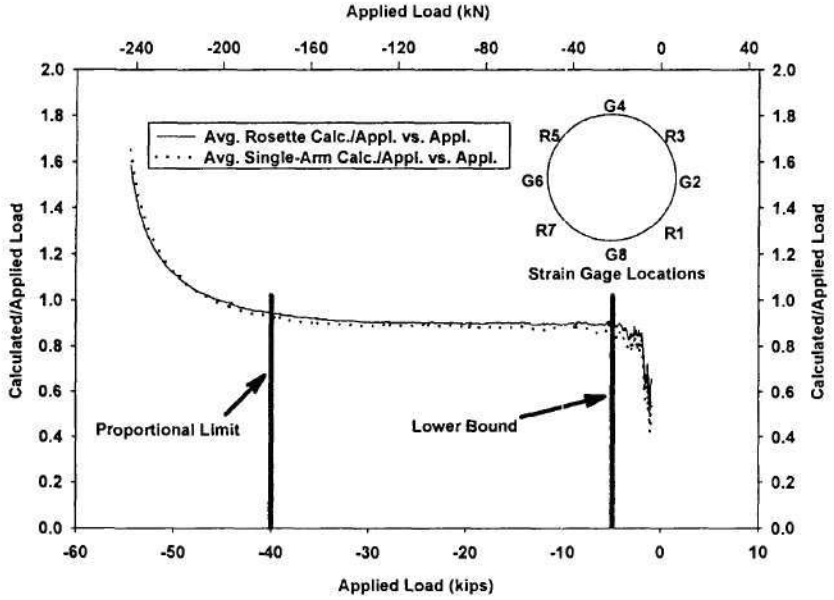

Figure 28: Average Calculated/Applied Load Ratios vs. Applied Load, First Loading Cycle, Nominal Thickness, Test 5C

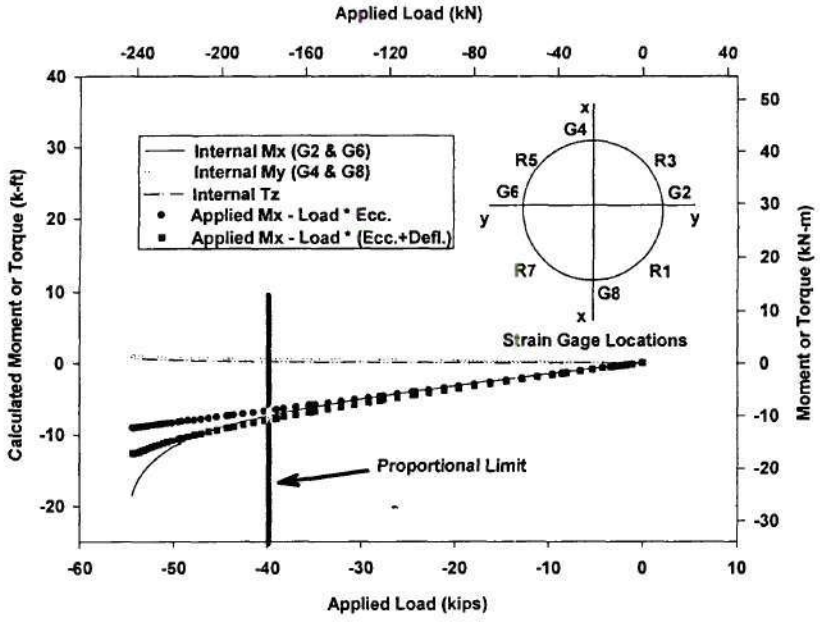

Figure 29: Calculated Internal Moments and Torque vs. Applied Load, First Loading Cycle, Nominal Thickness, Test 5C

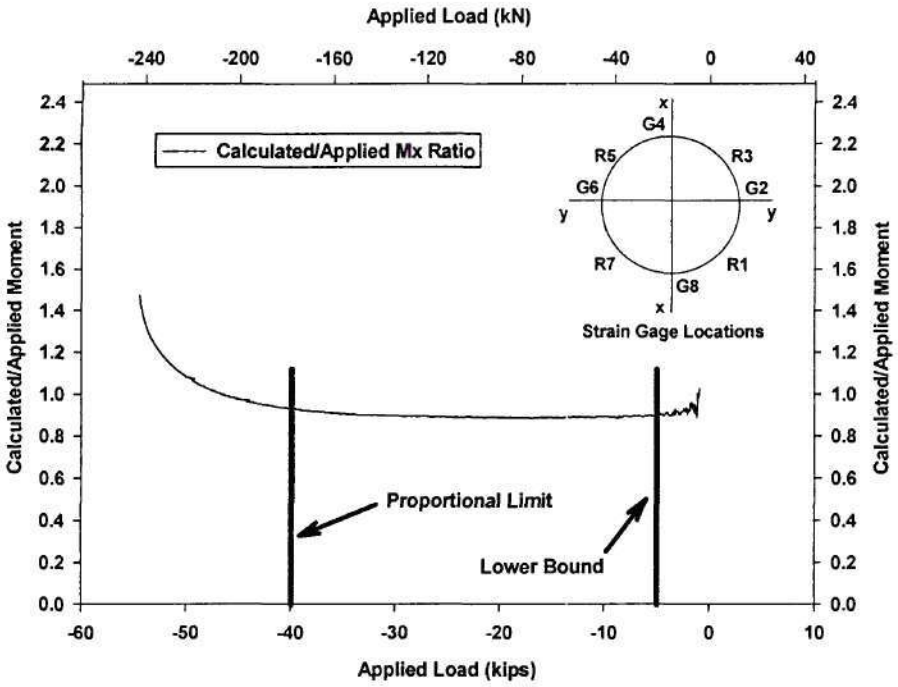

Figure 30: Calculated/Applied Moment Ratios (Mx) vs. Applied Load, First Loading Cycle, Nominal Thickness, Test 5C

Test 6C

This is a 1/4" thick specimen examined under concentric loading with simulated pin-pin boundary conditions using top and bottom knife edge supports as shown in figure 18. Since previous tests provided some verification of the accuracy of internal axial force, equation (1), this test was completed to ascertain a 1/4" thick cross frame specimen's concentric load capacity.

Figure 31 shows the longitudinal strain variation during the first loading cycle and indicates a proportional limit near 220 kips with an ultimate load of approximately 250 kips. These values were nearly double concentric capacities for the 1/8" thick specimens examined in tests 1C through 3C.

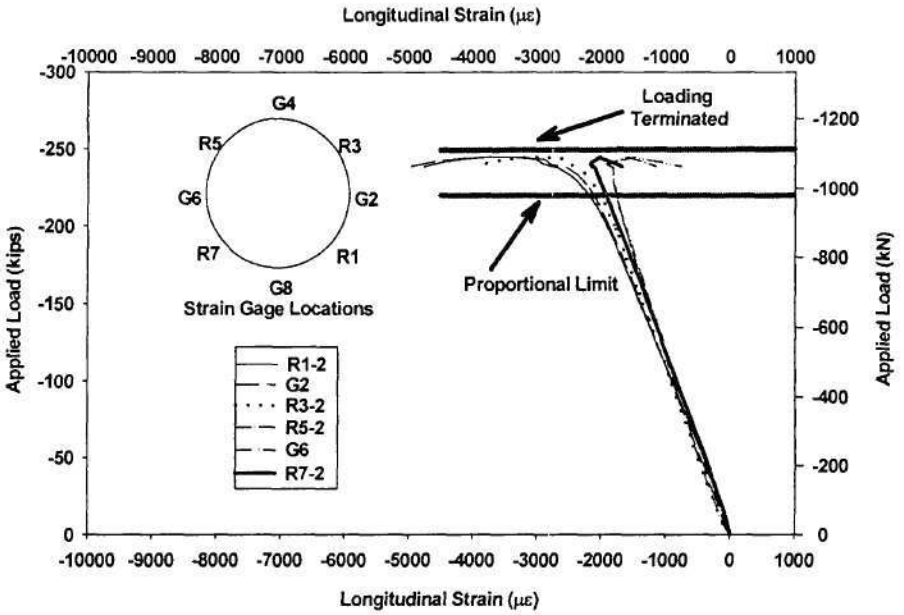

Figure 31: Applied Load vs. Longitudinal Strain, First Loading Cycle, Test 6C

Test 6C was used to check the accuracy of equation (9) in the same manner that equation (1) was evaluated with earlier concentric tests. Figure 32 is a plot of calculated internal axial force to applied external force for the first load cycle for both mechanics based equation (1) and Wheatstone bridge based equation (9). As had occurred with equation (1), equation (9) produced reasonably accurate internal force values within the elastic region when nominal dimensions were used. The small magnitudes that additional nonlinear terms in equation (9) add to the solution did not appreciably enhance results within the linear range. Thickness measurements were taken after completion of test 9C2, which examined a portion of the member tested for 6C. The average measured thickness was 0.27" and its effects on the calculated to applied load ratios is shown in figure 33. The figure indicates that convergence for both the mechanics based and the Wheatstone bridge based equations was improved with values approaching 1.0 within the bounded loading range, as noted earlier.

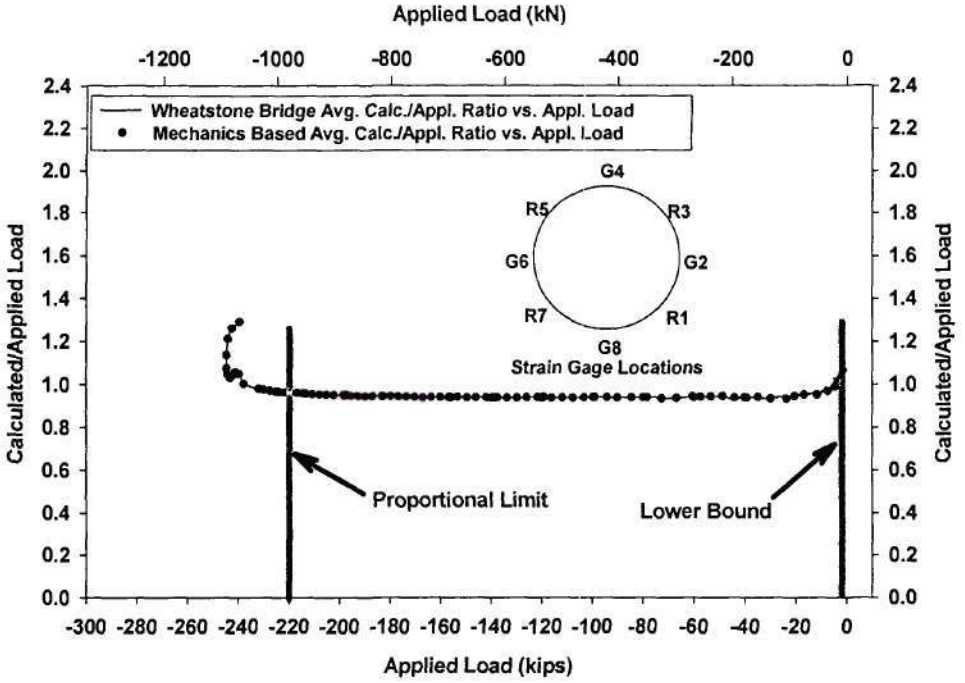

Figure 32: Average Calculated/Applied Load Ratios vs. Applied Load, First Loading Cycle, Nominal Thickness, Test 6C

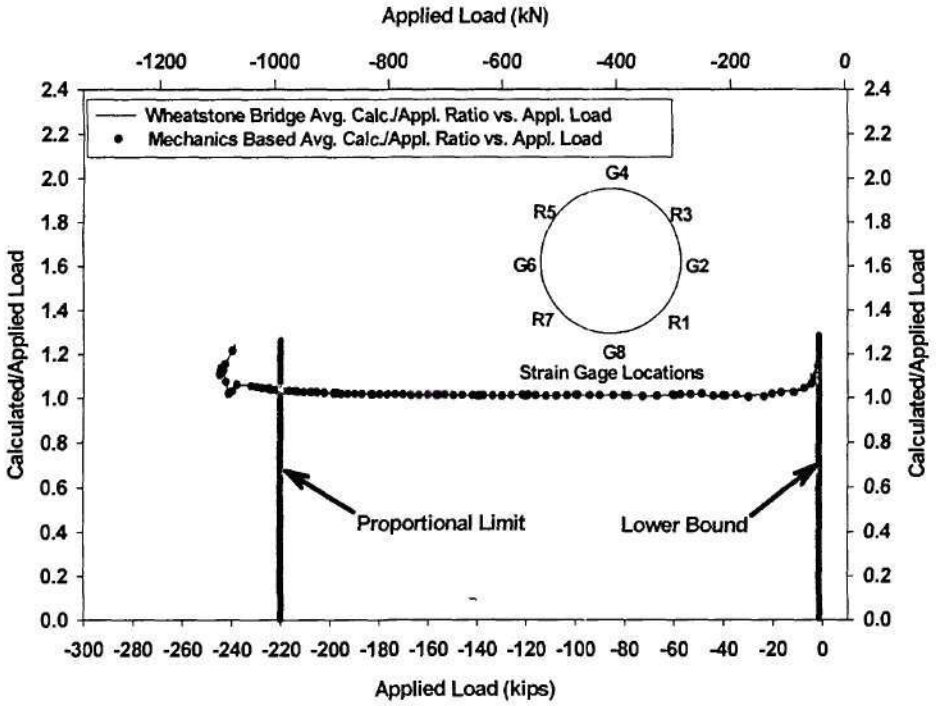

Figure 33: Average Calculated/Applied Load Ratios vs. Applied Load, First Loading Cycle, Measured Thickness, Test 6C

Tests 7C & 8C

Cross frame member compressive tests 7C and 8C were used to examine the response of of 1/4" thick specimens under 2" and 1" load eccentricities. The test set-up is identical to that of 5C and shown in figure 34. Instrumentation was identical to that of Tests 5C and 6C. Here, however, the LVDT at the mid-height of the specimen was replaced by a potentiometer due to space restrictions. A photo of test 7C is shown in figure 35. Each specimen had a total of nine loading cycles applied.

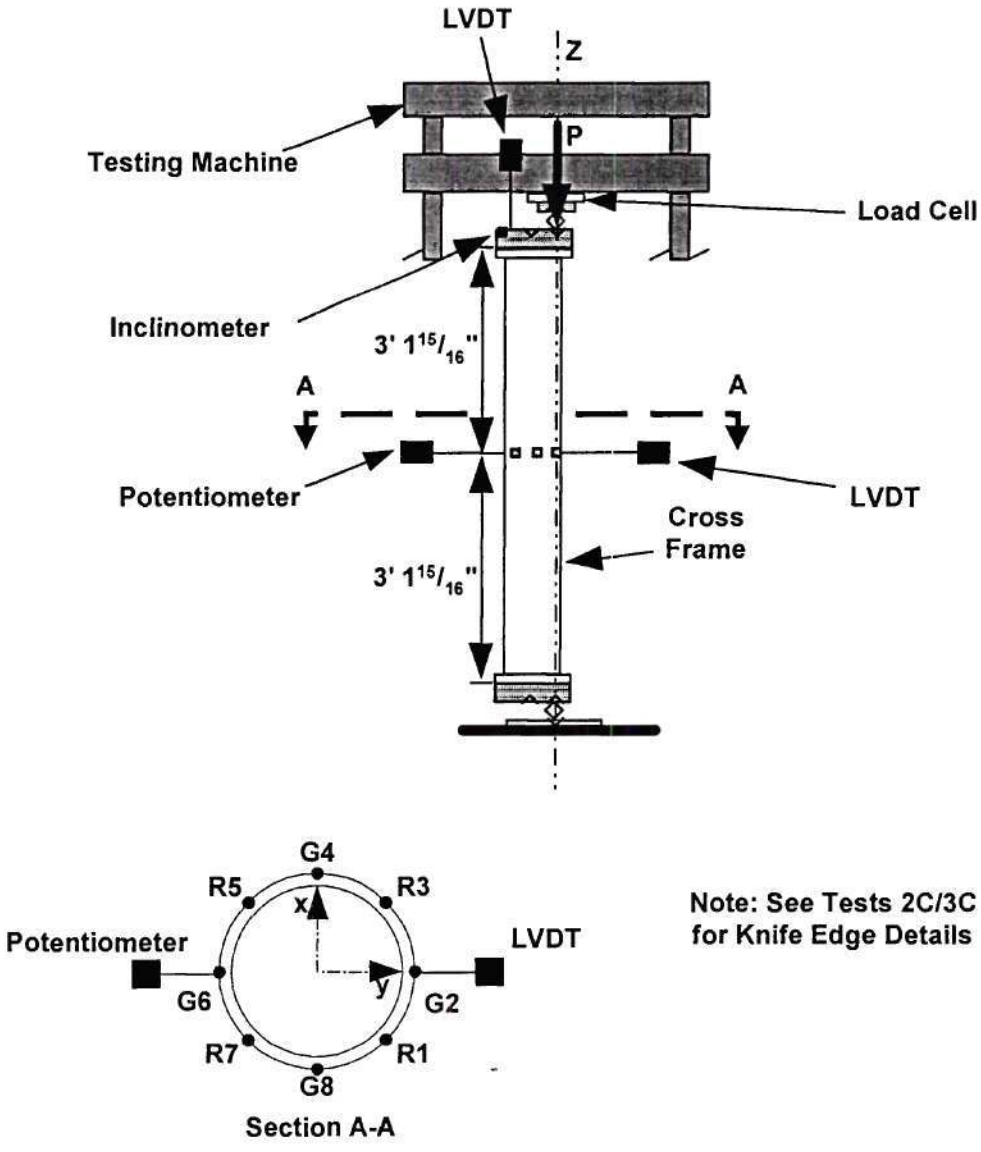

Figure 34: Elevation and Details for Test 5C (not to scale)

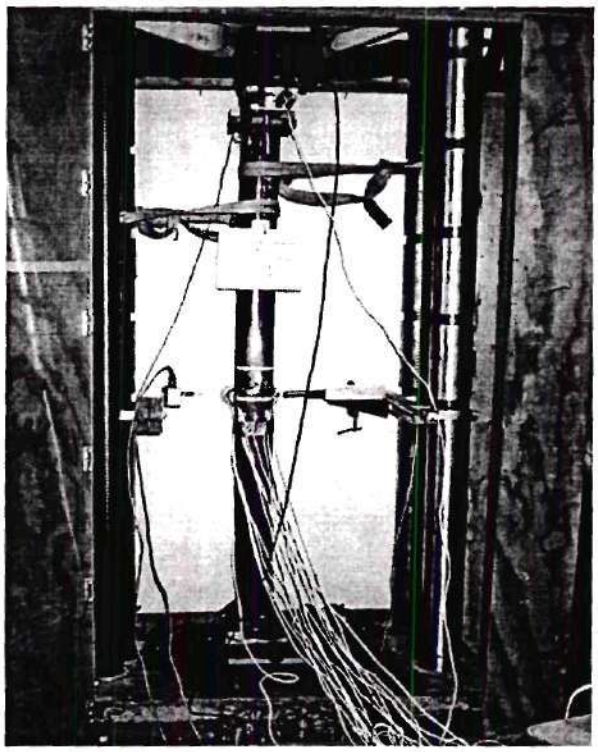

Figure 35: Photo of Test 7C

Figures 36 through 38 detail capacity values and calculated to applied moment comparisons for test 7C, the 2" eccentric case. Figure 36 indicates a proportional limit of around 80 kips, which is nearly double the value for the 1/8" thick specimen examined in test 5C. Although an ultimate load was not reached due to concerns about the capacity of the gripping mechanism, figure 36 indicates that the value would be near 120 kips. Figures 37 and 38 help to verify accuracy of internal moment and torque equations for the single-arm gage configuration with one pair mounted at 45°. Figure 37 shows bending about the x-axis, as was intended, and figure 38 indicates that applied and calculated moments about the that axis are very near one another within the elastic region with average nondimensionalized ratios of 0.94 and a standard deviation of 0.01. Error in the convergence can again be attributed to the use of nominal thickness values.

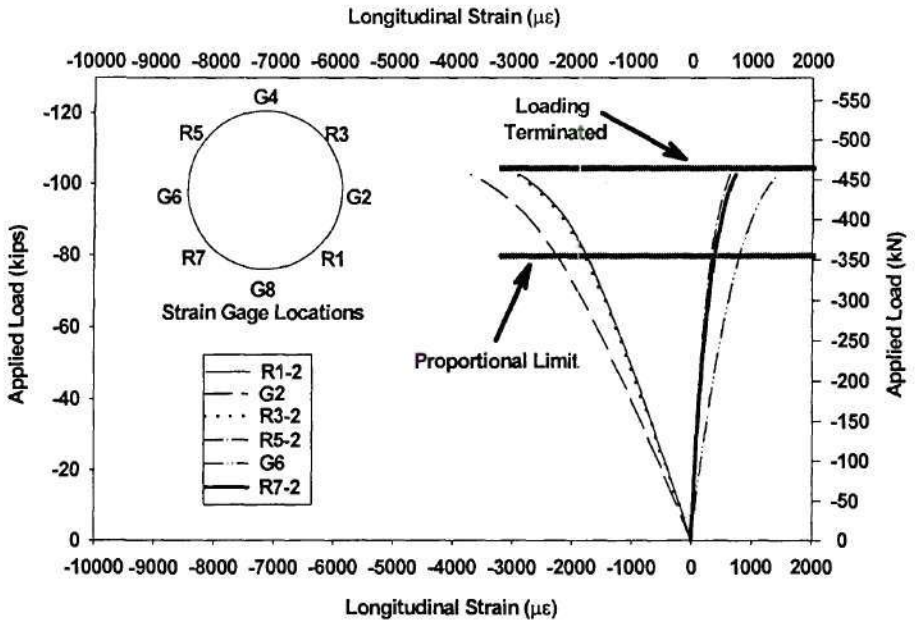

Figure 36: Applied Load vs. Longitudinal Strain, First Loading Cycle, Test 7C

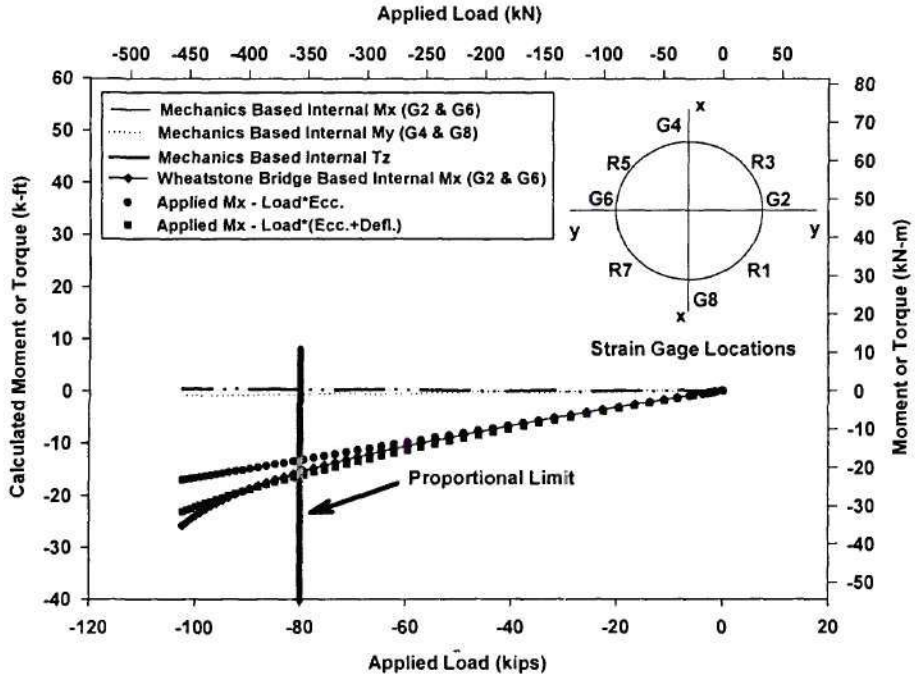

Figure 37: Calculated Internal Moments and Torque Using Equations (1) through (4), First Loading Cycle, Nominal Thickness, Test 7C

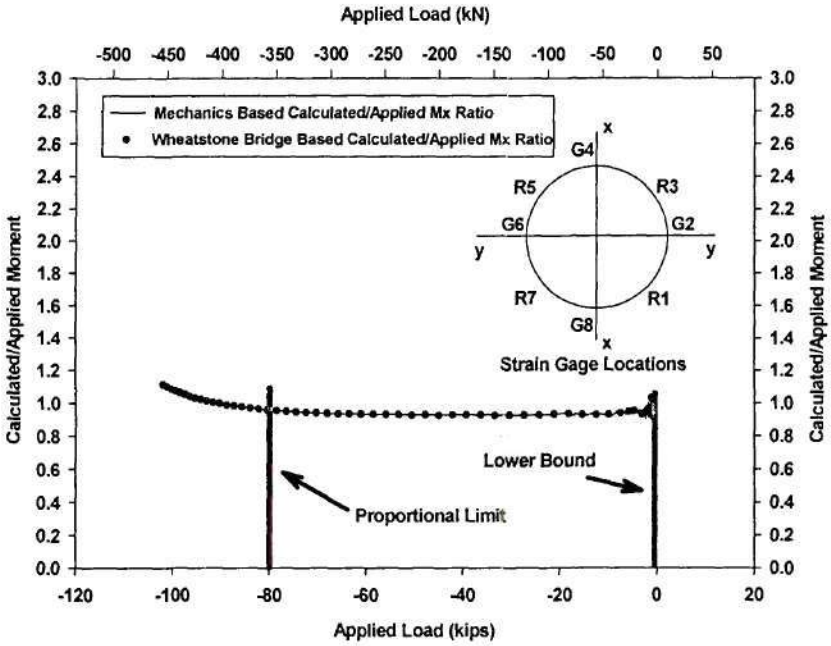

Figure 38: Calculated/Applied Moment Ratios (Mx) Using Equation (2) vs. Applied Load, First Loading Cycle, Nominal Thickness, Test 7C

Test 8C

The results of test 8C, which had a 1" load eccentricity, can be observed in figure 39 and showed yielding initiating at around 120 kips with an ultimate load near 150 kips. Comparisons between internal moment and torque calculation methods produced similar results to those in figures 37 and 38 and are not shown.

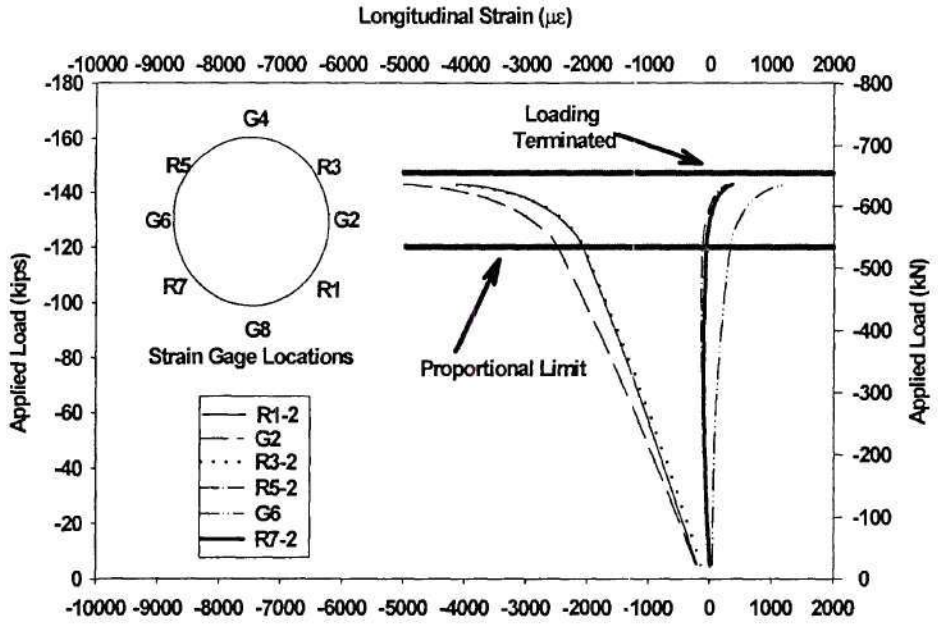

Figure 39: Applied Load vs. Longitudinal Strain, Final Loading Cycle, Test 8C

Tests 9C1 and 9C2

Because of the short lengths of the lower chord and also for the diagonal members, it was deemed necessary to examine these members under compressive loading to ensure that end effects will not influence the strain readings required for the computation of the axail load and moments of these members. Therefore, tests on replicas of the shortest cross frame member were performed.

Test 9C1 was the initial investigation of a 1/4" thick short cross frame member. The specimen had 1" thick end plates attached as shown in Fig. 2. Since end effects on internal force calculations was the primary focus of this test, the specimen was placed into the testing machine in a manner similar to what is shown in figure 14 for test 1C. Therefore, fixed and pinned boundary conditions were approximated which permitted concurrent examination their effects on results. Instrumentation matched that for the majority of the previous tests but the inclinometer measuring end rotation was replaced with an additional LVDT located on top of the loading head. Incompatibilities between movement of the head and vertical deflections experienced by the specimen could then be investigated. A photo of the testing configuration is shown in figure40.

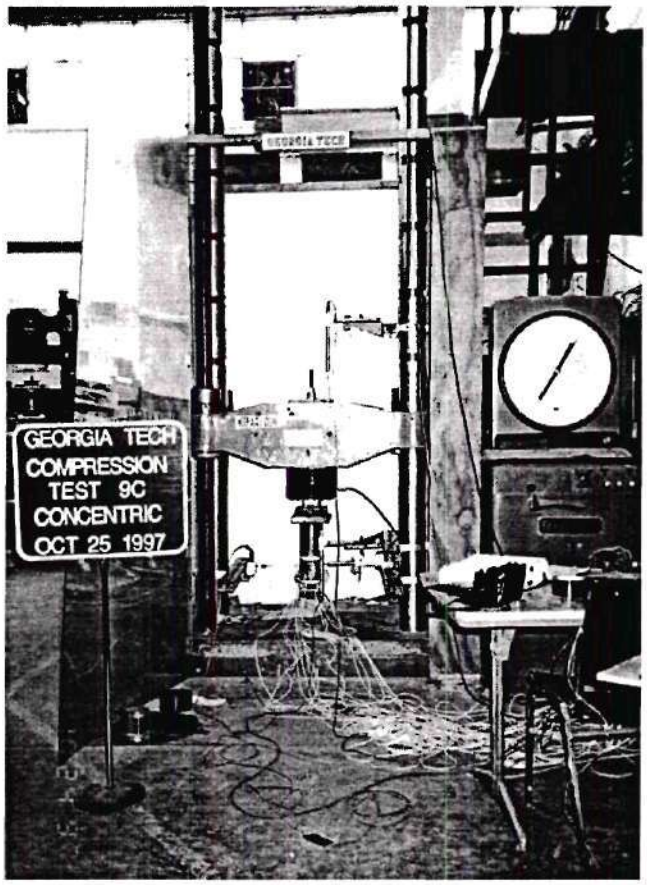

Figure 40: Photo of Test 9C1

Test 9C2 addressed two of problems that became evident during the first compression tests. The first of these problems was that at a low range of loads (between 0 and 10 kips), results indicated significant deviations between internal forces calculated from the strain gages with those external forces measured directly from the load cell. These variations were of concern because bending component analyses indicated many cross frame members would experience maximum compressive and tensile loads that fell within that range. At least two sources, the data acquisition and the loading system, could contribute to this error. The first source was related to the inherent accuracy of the data acquisition system, linked to the electronics themselves and their sensitivity to drift and to random noise coming from poor connections, grounding, shielding, and other sources. In all initial tests, the range of strains to be measured by the system was set at its largest value since the intent was to measure strains well into the inelastic range. For the 16-bit Optim Megadac 3100 data acquisition system with a single-arm configuration and an excitation of 2 volts, the largest recordable strain range was nominally +/- 32768 με with a 1 με resolution. Electronic "noise" in the system at this range was believed to be +/- 2 με. Thus it was expected that the readings would be accurate to +/- 5 με. Given this assumption, it would be expected that significant errors would result when the strain gages were measuring less than 100 με. To see if the low end resolution problem was linked to the electronics in the data acquisition software, the recordable range was varied systematically in test 9C2

.

The second possible source of error was the inability to maintain the load accurately at low levels. This is inherent in the open-loop architecture of the Riehle testing machine that was used and would be magnified at lower loads. There was no possible solution to this problem since more stable machines for the load range and dimensions being tested were not available.

Test 9C1 investigated end effects on internal force results from equations (1) through (4) and equations (9) and (10). Figure 41 shows the load versus strain variation for the first load cycle. The proportional limit was reached at around 240 kips and the test was terminated at 280 kips, near the upper end of the load cell's range (300 kips). The trend observed near the upper strain range in figure 41 indicates that the specimen's ultimate load would be at least 290 kips. Figure 42 shows average calculated/applied load ratios using both equations (1) and (9) for the first loading cycle. End effects do not appear to affect results over the elastic range and good correlation for both equations was evident until the proportional limit was reached. Therefore, placement of strain gages at mid-length of the diagonal and lower chord cross frame members was shown to provide acceptable data.

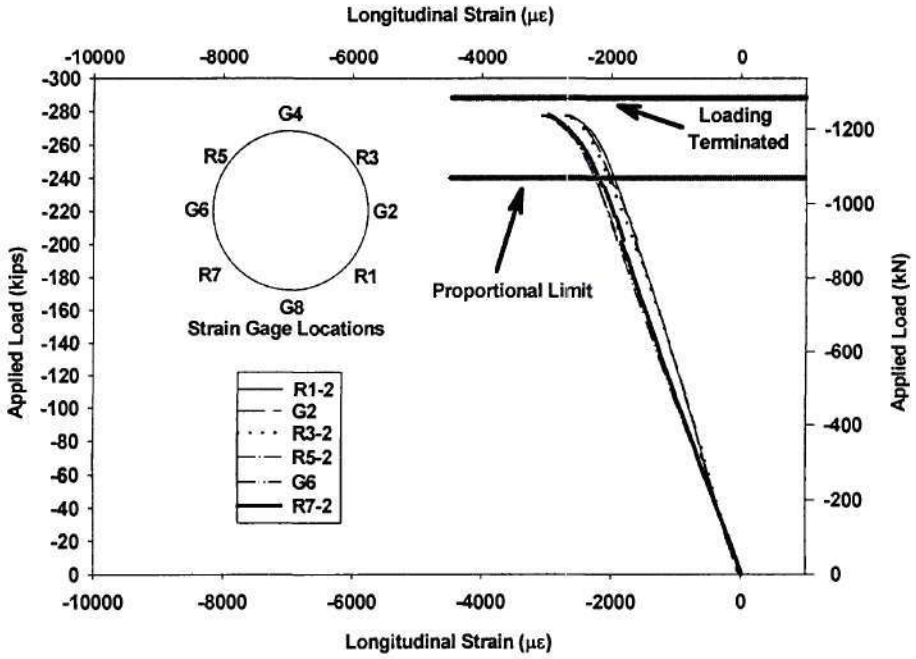

Figure 41: Applied Load vs. Longitudinal Strain, First Loading Cycle, Test 9C1

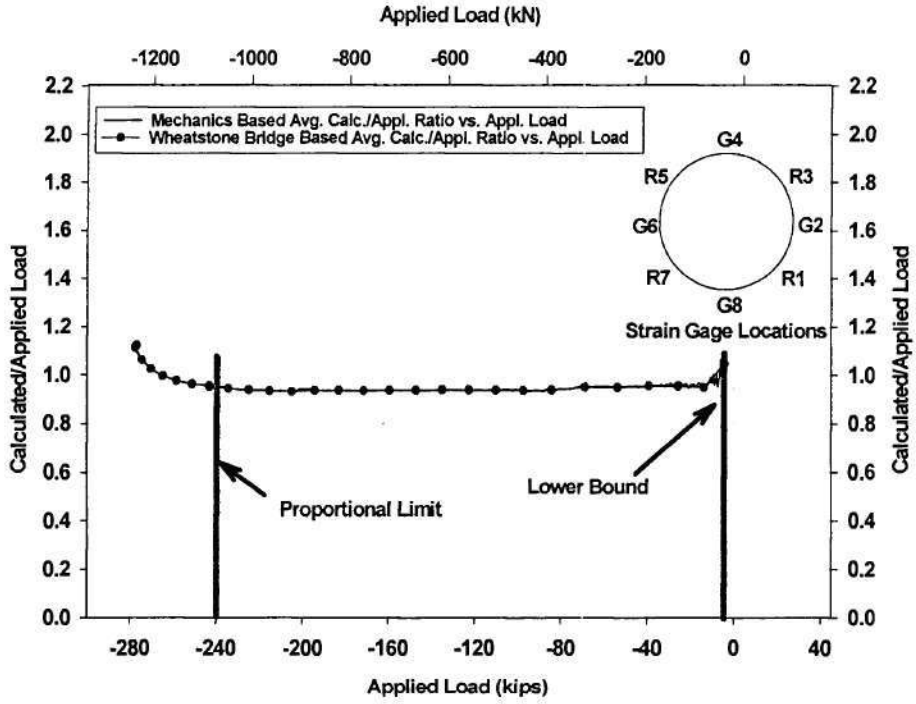

Figure 42: Average Calculated/Applied Load Ratios vs. Applied Load, First Loading Cycle, Test 9C1

Figure 42 is representative of most of the previous comparisons between calculated internal and applied loads which show variations in results occurring over the lower end of the testing range with convergence of nondimensionalized ratios between 0.91 and 0.97.

Test 9C2 addressed the variation and convergence problems with a series of elastic investigations. The specimen was placed into the universal testing machine with the four rosette gage longitudinal arms active. Figure 43 details results for the first investigation, where the strain gage "post gain" was set at two. This permitted strain readings over a range of 17300 microstrain, instead of the full gage operating range of 34600 microstrain which would theoretically improve the resolution of the readings by a factor of two. Excessive variation in average nondimensionalized ratios, which was defined as greater than a 5 percent deviation to either side of the converged value (e.g. outside of the range of 0.95 to 1.05 if the converged value was 1.0), was still evident for results up to an applied load of near 5 kips. While variation in results at the lower end of the loading range was not appreciably enhanced with the refined strain range, load ratio convergence was improved with an average of 1.0 and a standard deviation of 0.01 when a measured wall thickness of 0.27" was used. The measured thickness was obtained from a series of micrometer readings taken at the cut end of the specimen prior to attachment of an end plate.

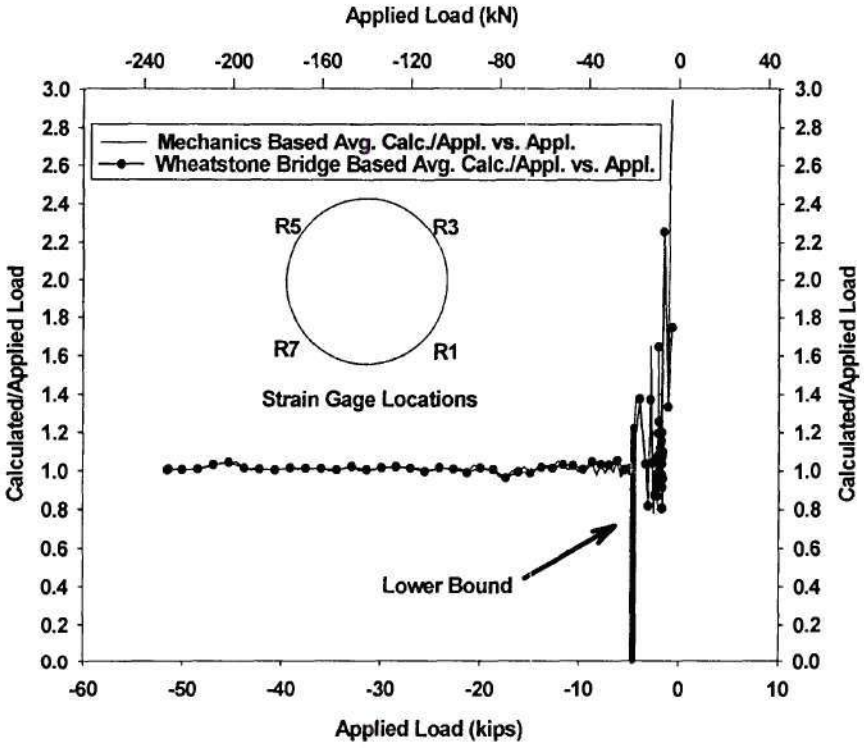

Figure 43: Average Calculated/Applied Load Ratios Using Equations (1) and (8) vs. Applied Load, Post Gain = 2, Strain Range = 17300 με, Measured Thickness, Test 9C2

The second and third investigations incorporated further strain range refinement. Figure 44 contains results for a "post gain" of four, which limited the range to 8650 microstrain. Figure 45 contains values for a setting of eight, which limited the range to 4325 microstrain. For both cases, appreciable variation in load ratios was evident until approximately 5 kips of axial force was applied. These results indicated that improved strain gage resolution did not significantly enhance the accuracy of calculated internal forces. Therefore, errors were most likely caused by variations in loads applied by the testing machine, which could come from "seating" of various parts of the screw driven loading system onto one another, rather than errors in the instrumentation or acquisition system. The use of measured tube wall thickness values was again shown to improve convergence of nondimensionalized load ratios in figures 44 and 45. Using measured thickness to reexamine results from 9C1 would improve the average nondimensionalized ratio calculated from Figure 42 to a value of 1.0.

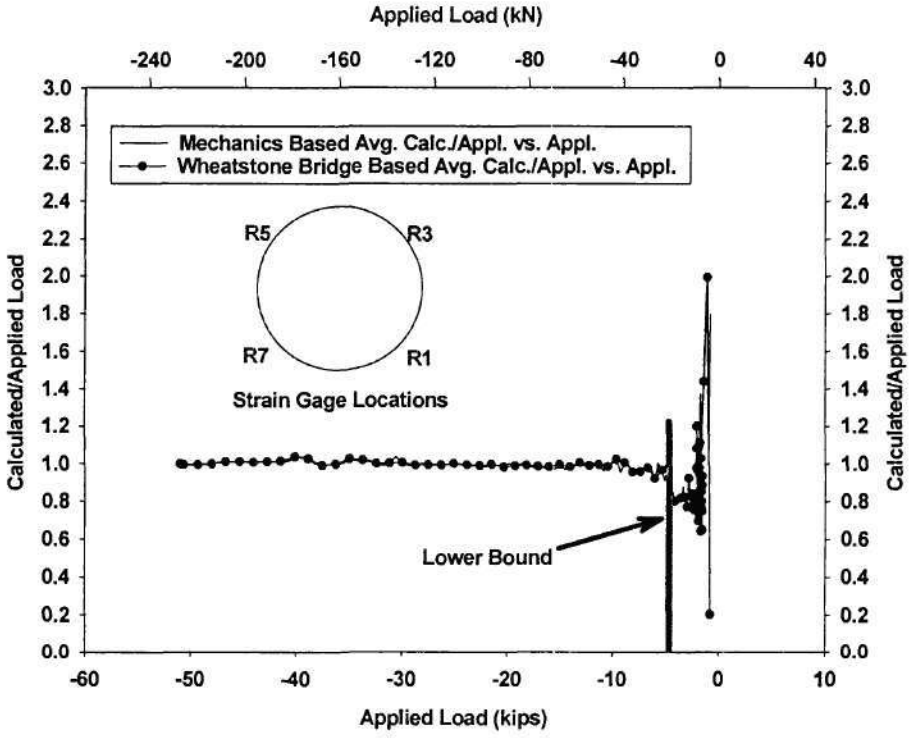

Figure 44: Average Calculated/Applied Load Ratios Using Equations (1) and (8) vs. Applied Load, Post Gain = 4, Strain Range = 8650 με, Measured Thickness, Test 9C2

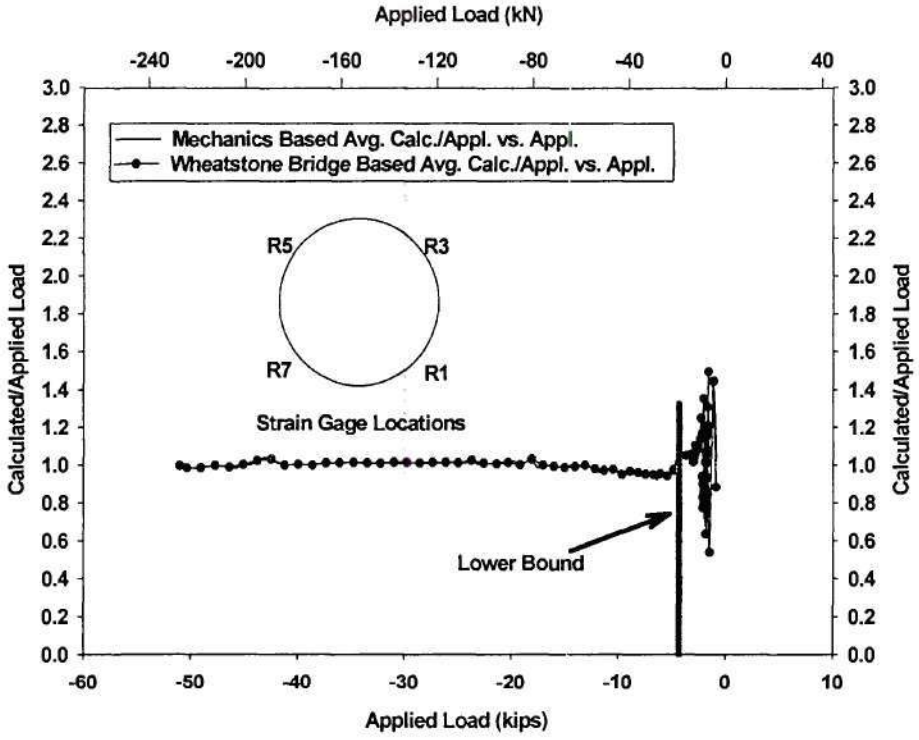

Figure 45: Average Calculated/Applied Load Ratios Using Equations (1) and (8) vs. Applied Load, Post Gain = 8, Strain Range = 4325 με, Measured Thickness, Test 9C2

Test 10C

The final cross frame specimen compression test involved a 1/4" top chord member under eccentric compressive loads causing double curvature behavior. Loads were applied to the specimen using knife edges, as was done with earlier compressive tests. To produce double curvature behavior, knife edges were shifted in opposite directions from the tube centerline as shown in figure 55. Inherent instability within this type of load system limited eccentricities to 1".

Mid-height strain gage instrumentation matched that for the majority of the earlier investigations with the addition of a potentiometer that measured deflections orthogonal to the plane of bending. Since maximum bending effects would theoretically occur at the quarter points, additional strain gages and potentiometers were placed at these sections. At L/4 from either end, four longitudinally oriented single-arm gages were placed at 90° intervals around the tube periphery. One gage pair was positioned in the plane of bending and the other orthogonal to that plane. In addition to these two additional instrumented sections, four single-arm gages were attached at 1.5 times the outer diameter from each end which allowed end effects to be reexamined.

The specimen was aligned utilizing a series of preliminary tests within the linear range, limited to 100 kips of applied load. The goal of these tests was to obtain uniaxial behavior at mid-height

and equal and opposite quarter point deflections. When the trials were performed, it was noticed that strain readings at mid-height and the quarter points were somewhat indicative of a double-curvature state of bending while deflection readings were not. It was determined that base shears generated at the top end of the specimen caused lateral movement of the testing machine head. Therefore, an additional potentiometer was attached to the head as shown in figure 55, and its readings were used to correct specimen lateral deflection values. While the use of corrected lateral deflection values did help with alignment, the system was still quite sensitive to subtle changes in load eccentricity and a pure mid-height uniaxial loading condition was never attained at 100 kips. However, discrepancies between gages within the specimen's plane of bending, which fell through G2 and G6 in section A-A of figure 55, were around 100 με and they decreased as compressive loads greater than 100 kips were applied. The specimen was tested under a series of nine loading cycles. A photo of the configuration is shown in figure 56.

Figures 46 through 53 detail results from the first loading cycle for test 10C. Figure 46 shows the variation of mid-height longitudinal strains with applied load, while figures 47 and 48 contain similar comparisons at the quarter points and at 1-1/2 times the diameter from each end. These plots show that while a double-curvature state was achieved, slightly more bending occurred at 1-1/2 times the diameter from the ends than at the quarter points. This indicated that knife edges permitted rotation but also provided a certain amount of fixity at the ends. The results also indicated that the proportional limit was observed at an applied compressive load of 140 kips.

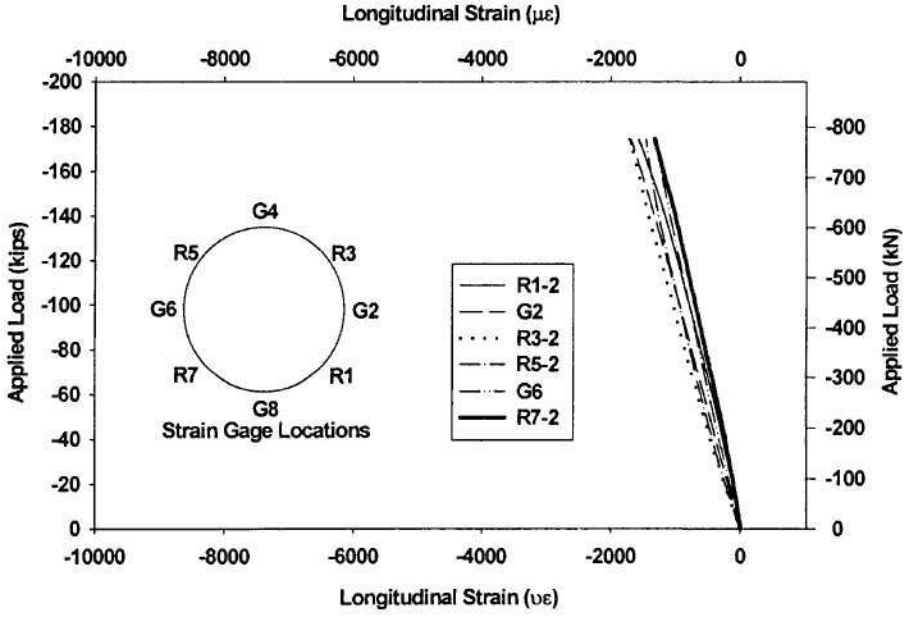

Figure 46: Applied Load vs. Longitudinal Strain at Mid-Height, First Loading Cycle, Test 10C

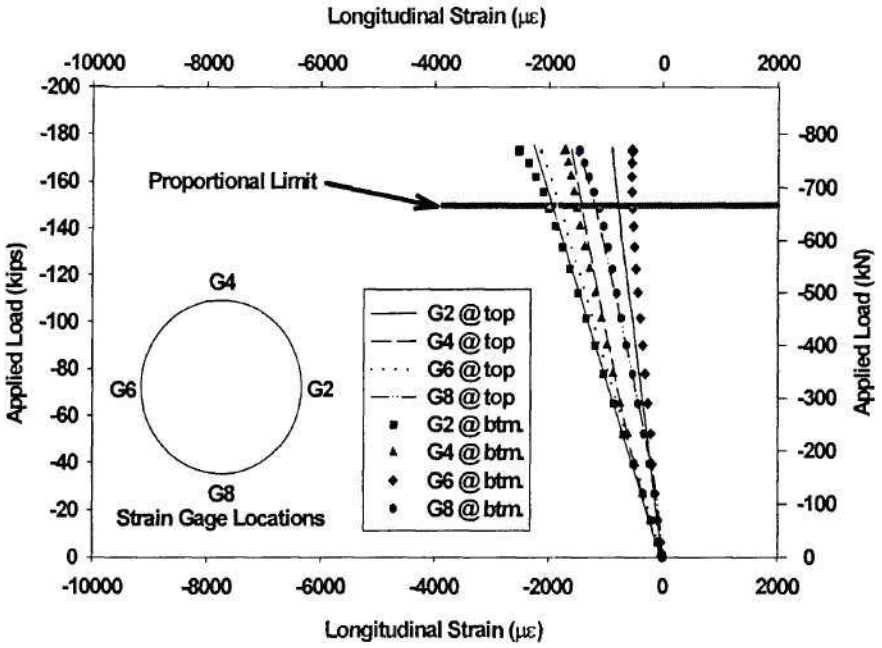

Figure 47: Applied Load vs. Longitudinal Strain at Quarter Points, First Loading Cycle, Test 10C

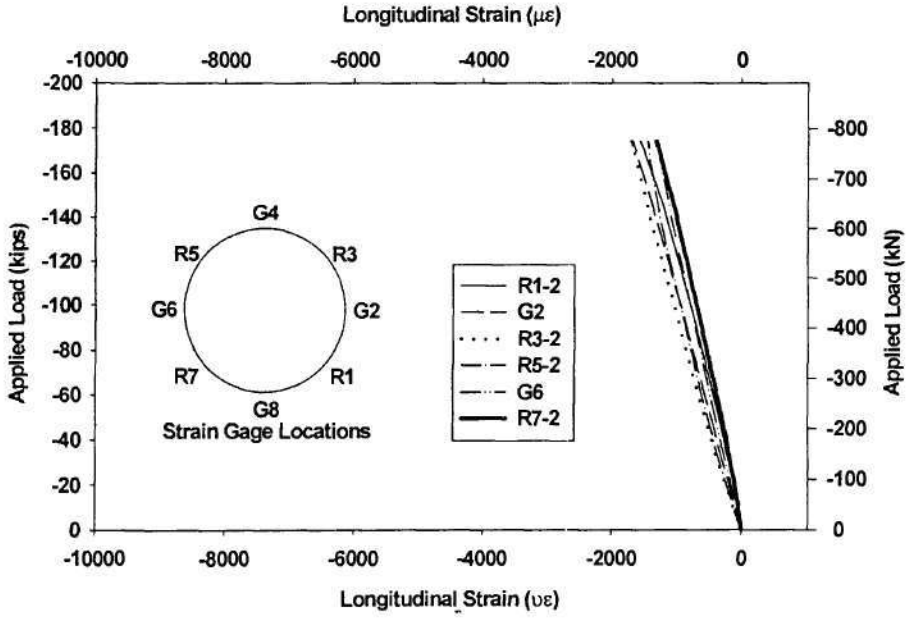

Figure 48: Applied Load vs. Longitudinal Strain at (1.5*ϕ), First Loading Cycle, Test 10C

Figure 49 depicts the effects of correcting in-plane mid-height and quarter point deflections using lateral shift values experienced by the loading head of the testing machine. Corrections were made at each lateral deflection measurement point using linear extrapolation. Similar triangles were used to determine the amount of shift at mid-height or the quarter points based upon readings at the head, as shown in figure 50. It can be seen in figure 49 that, while not exact, corrected quarter point deflections were somewhat equal and opposite and corrected mid-height deflections were near zero.

Figure 51 checks the accuracy of axial load values calculated using equation (9) for four single-arm gages oriented longitudinally. Correlation was poor at low loads and was again attributed to the testing apparatus and not the acquisition system. Convergence error was also evident, but it would be corrected if actual thickness measurements replaced nominal values. For instance, if the average thickness from the ultrasonic measurements was used, the average ratio would improve to 0.99.

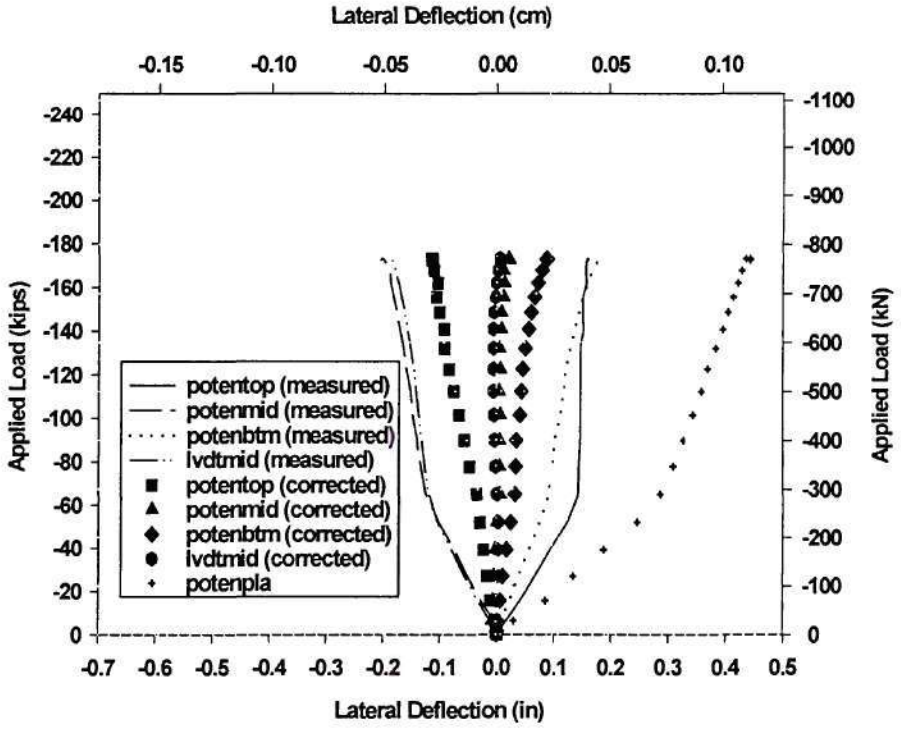

Figure 49: Recorded and Corrected Lateral Deflection at Mid-Height and Quarter Points vs. Applied Load, First Loading Cycle, Test 10C

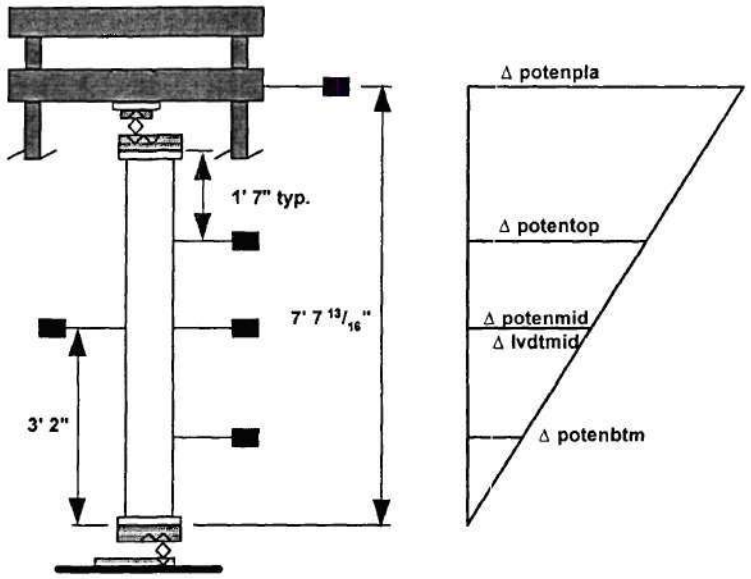

Figure 50: Test 10C Lateral Deflection Correction Schematic (not to scale)

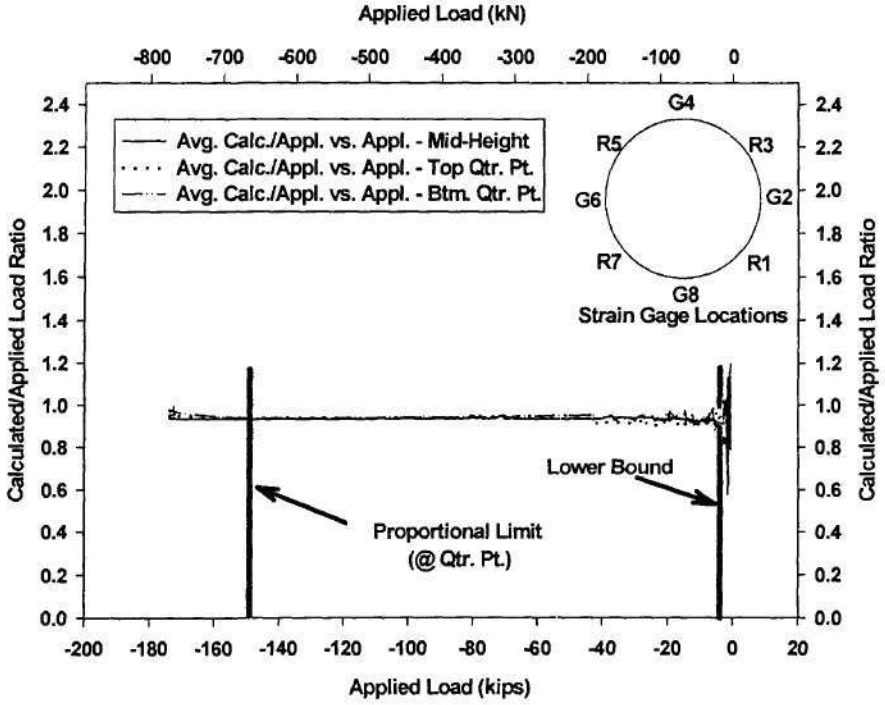

Figure 51: Calculated/Applied Load Ratios Using Equation (9) vs. Applied Load, First Loading Cycle, Nominal Thickness, Test 10C

The final three figures, figures 52, 53, and 54, examine in-plane moments generated within the cross frame specimen. Figure 52 shows that equations (2) and (10) produce internal moment values quite close to one another during the first loading cycle. Figure 53 compares calculated in-plane internal moments at the quarter points using equations (2) and (10) to applied external moments found from corrected deflections. Although agreement between the two calculation methods appears quite good, the nondimensionalized ratios did not converge to values approaching 1.0 until a rather large amount of external load was applied. The reason for these discrepancies most likely relates to the use of corrected lateral deflections to calculate applied moments at each quarter point. The corrected values induce some error into the deflection magnitudes which is, in turn, reflected in the nondimensionalized ratios. Note that no lower bound is shown on the plot due to the lack of convergence until application of a higher external load (20 kips) than that shown in figure 51. Figure 54 shows variations in internal moments about the local x-axis at four load steps during the test. Note that for all cases, the moment variations remained linear with the highest values located at 1.5 times the diameter away from the tube ends. These results reinforce the hypothesis that the knife edges provided a certain amount of fixity. It can also be seen that the moment intercept was typically located around 2" away from mid-length of the tube. This showed that the bottom knife edge provided slightly more restraint against rotation than the top knife edge.

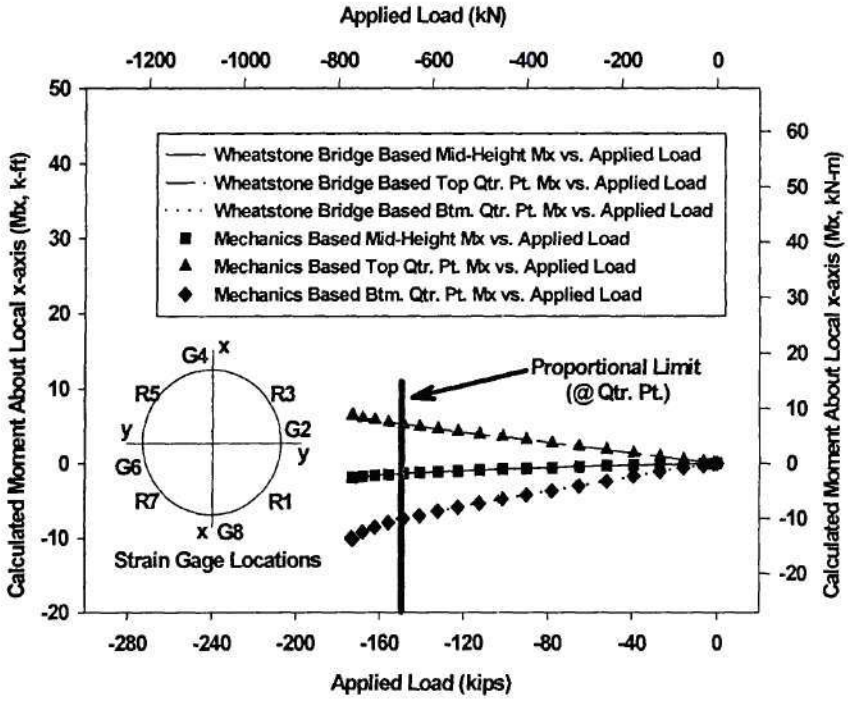

Figure 52: Calculated Internal Moments (Mx) Using Equations (2) and (10) vs. Applied Load, First Loading Cycle, Nominal Thickness, Test 10C

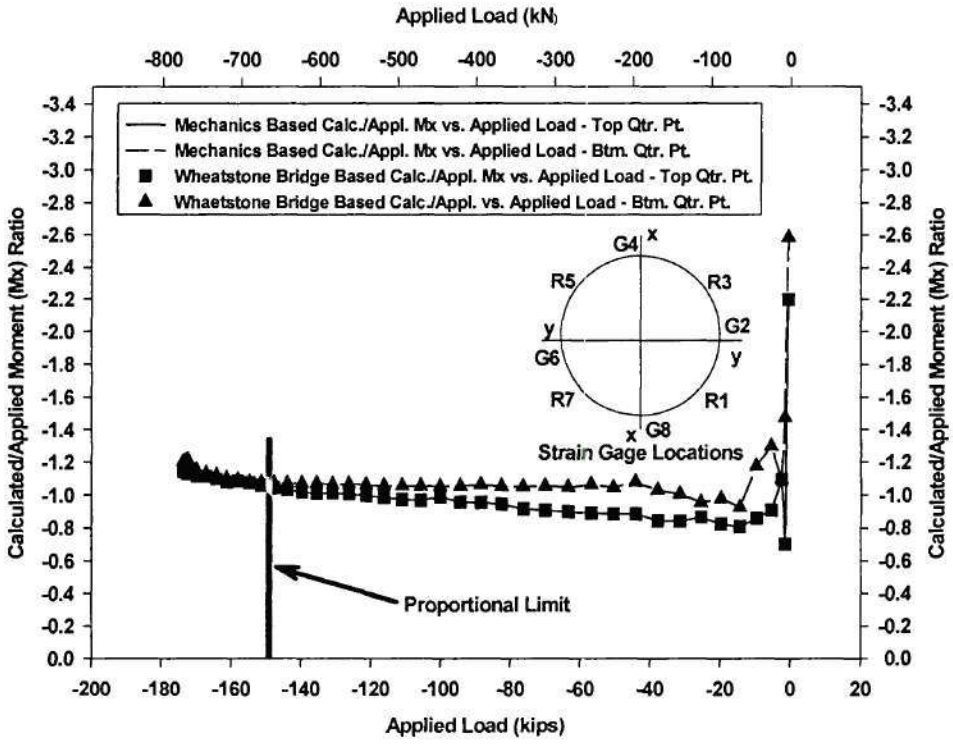

Figure 53: Calculated/Applied Quarter Point Moment Ratios (Mx) Using Equations (2) and (10) vs. Applied Load, First Loading Cycle, Nominal Thickness, Test 10C

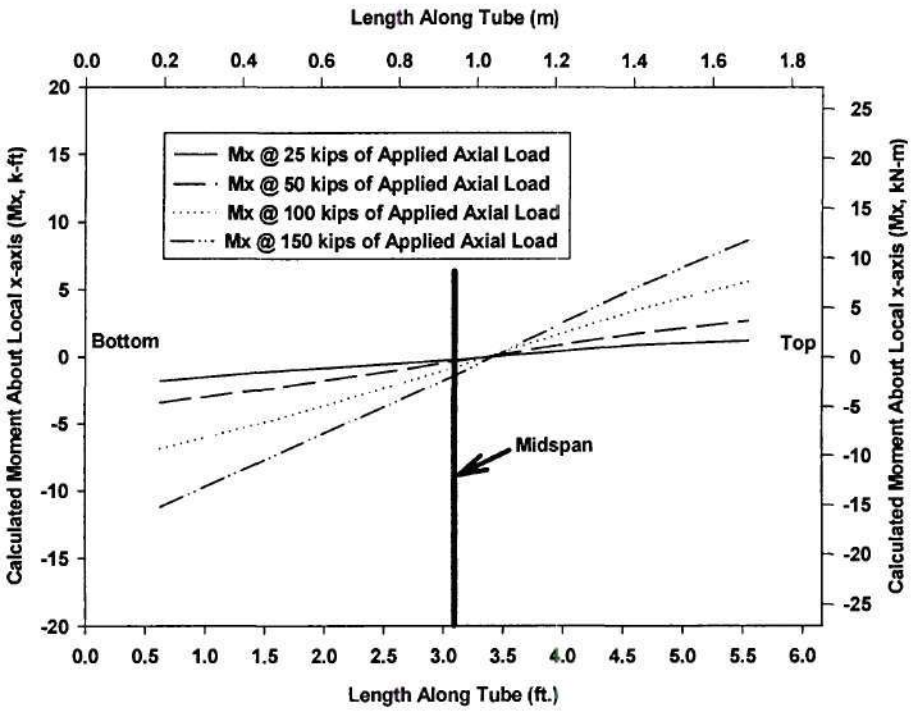

Figure 54: Calculated Moments (Mx) Using Equation (2) vs. Location Along Tube, First Loading Cycle, Nominal Thickness, Test 10C

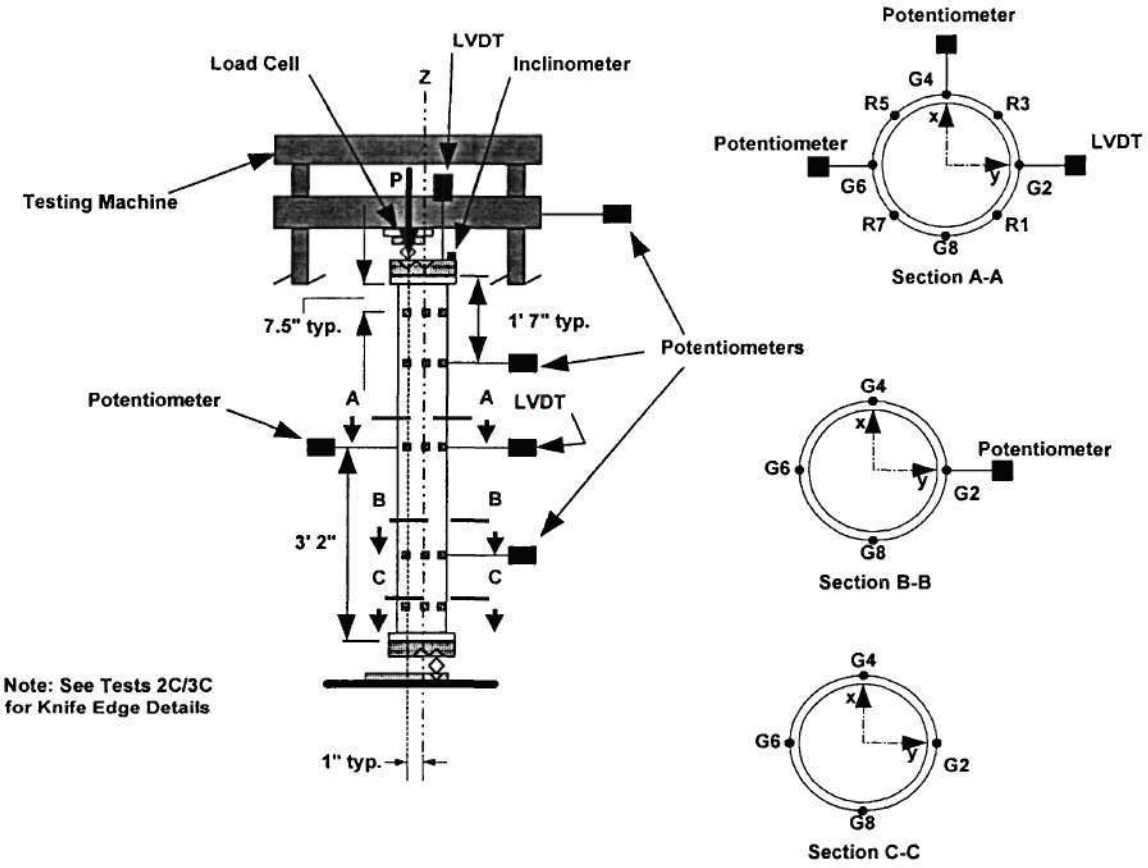

Figure 55: Elevation and Details for Test 10C (not to scale)

The specimen was aligned utilizing a series of preliminary tests within the linear range, limited to 100 kips of applied load. The goal of these tests was to obtain uniaxial behavior at mid-height and equal and opposite quarter point deflections. When the trials were performed, it was noticed that strain readings at mid-height and the quarter points were somewhat indicative of a double-curvature state of bending while deflection readings were not. It was determined that base shears generated at the top end of the specimen caused lateral movement of the testing machine head. Therefore, an additional potentiometer was attached to the head as shown in figure 55, and its readings were used to correct specimen lateral deflection values. While the use of corrected lateral deflection values did help with alignment, the system was still quite sensitive to subtle changes in load eccentricity and a pure mid-height uniaxial loading condition was never attained at 100 kips. The minimal difference in longitudinal strain gage readings at mid-height while approximating equal and opposite quarter point deflections was around 300 με. However, discrepancies between gages within the specimen's plane of bending, which fell through G2 and G6 in section A-A of figure 55, were around 100 με and they decreased as compressive loads greater than 100 kips were applied. The specimen was tested under a series of nine loading cycles. A photo of the configuration is shown in figure 56.

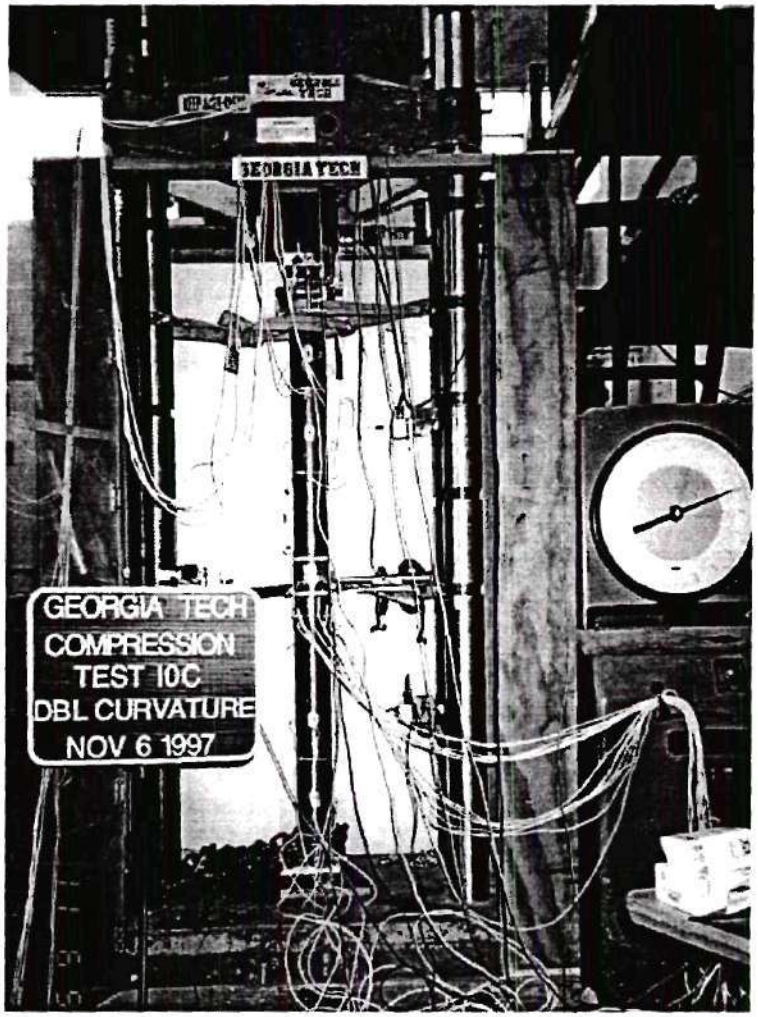

Figure 56: Photo of Test 10C

Tension series

One concentrically and one eccentrically tensile load tests were conducted on 1/4" thick tubular members having the configuration of Specimen B in figure 2. These tests are described below.

Test 1T

The test set-up of the first concentric tension test is shown in figure 57. The specimen was connected to the testing machine by means of 3 1/2" diameter pins inserted through vertical plates at each end. Instrumentation was similar to that used for the majority of the compression tests. The specimen was first loaded monotonically up to approximetely 220 kips, a value below the estimated ultimate tensile strength of 314 kips obtained by multiplying the nominal area by the experimentally found yield strength of 80 ksi. The load-strain curves are shown in figure 58. The proprortional load limit is approximately 160 kips. The ratios of the calculated tensile load from

the strain gauge data ((1) through (4)) and the Wheatstone bridge based equations ((9) and (10)) are presented in figure 59. It is clear that if the member were loaded concentrically below a value of 160 kips, strain gauge data can be used to compute the force in the top chord member of the cross frame with reasonable accuracy. In figure 60, values of the bendingmoments about the x- and y-axis as well as the torque are presented and shown to be very small.

Test 2T

The test set-up of the eccentrically loaded tensile test is shown in figure 61. Load eccentricity was achieved by using the same testing apparatus for Test 1T and shifting the specimen in one direction along the pins. Loads were applied to these pins away from the centerline of the tubular cross-section, resulting in externally applied end moments. The load transfer apparatus limited the eccentricity to a maximum value of 1.5". This specimen was loaded monotonically at the rate of 10 kips/minute to a load of 130 kips. The load-strain curves are shown in figure 63. The specimen was subjected to a total of nine loading cycles.

Figures 63 through 65 show results from the first load cycle for eccentric test 2T. Figure 63 indicates that, with a 1-1/2" eccentricity, the proportional limit was reached at around 100 kips of tensile load. Figure 64 shows most bending occurring about the y-axis and helps validate internal bending moment equations (2), (3), and (10) using two gages at 45°. Since gages G4 and G8 shown in the legend of figure 64 were oriented at 45°, comparisons between applied moments about the y-axis and results from equation (10) could not occur. Figure 65 does indicate reasonably good agreement between applied and calculated bending moments about the y-axis. The agreement would be improved if measured thickness values were used for the internal moment calculations. If the average ultrasonic value of 0.26" was used for the thickness, the average nondimensionalized ratio would become 1.0.

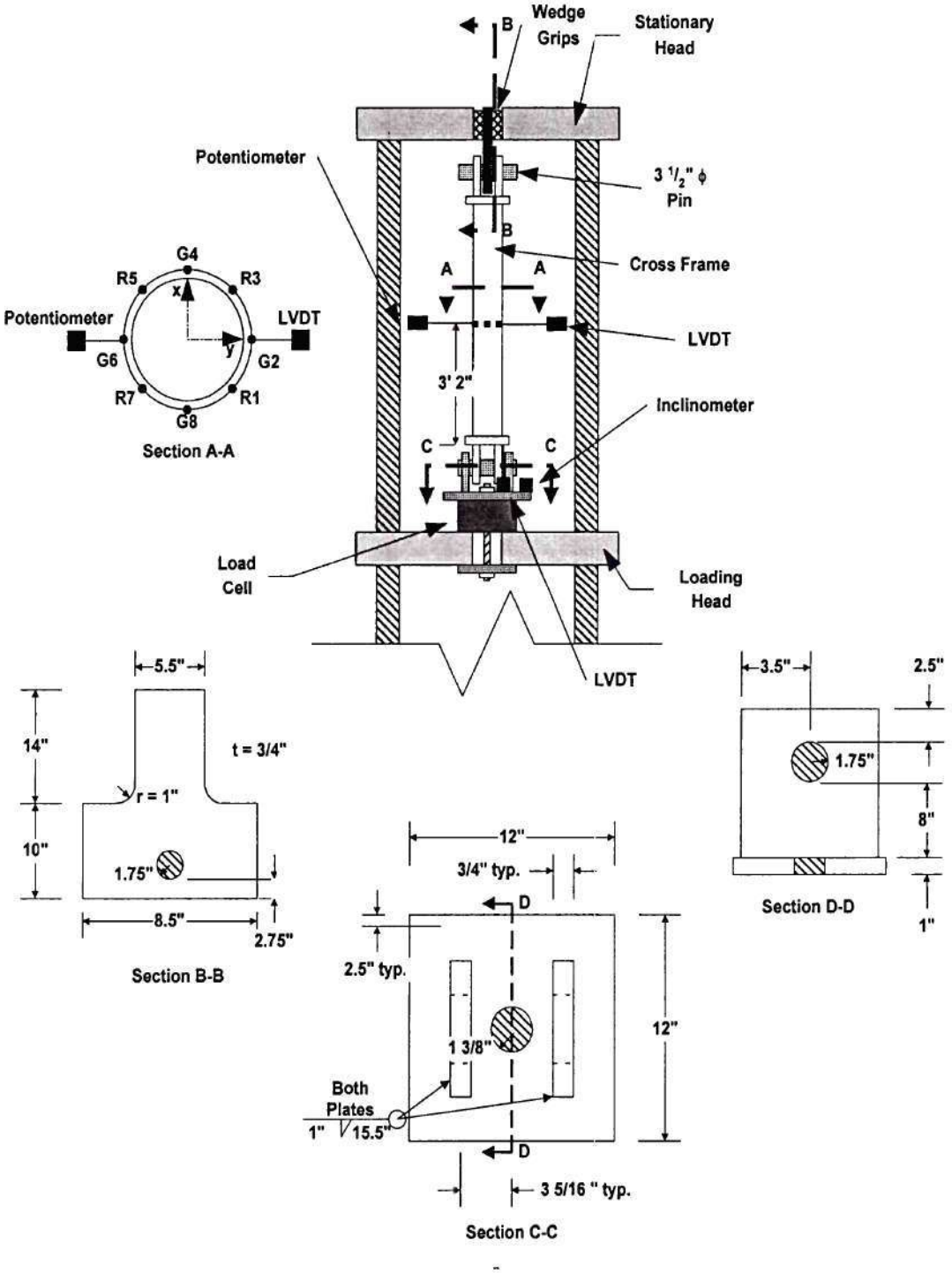

Figure 57: Elevation and Details for Test 1T (not to scale)

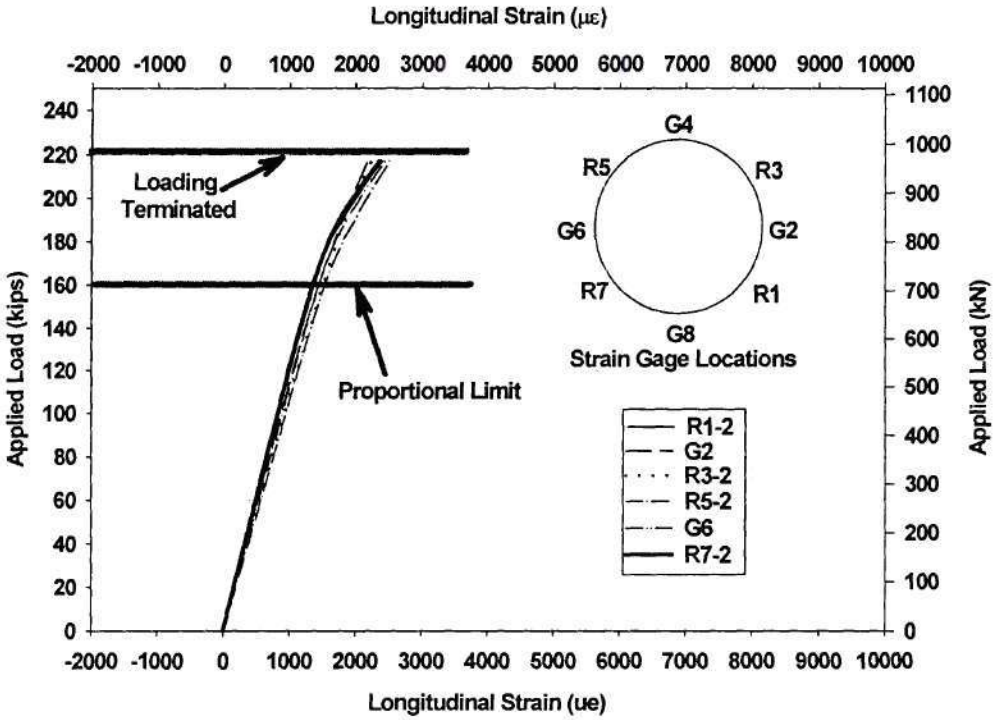

Figure 58: Applied Load vs. Longitudinal Strain, First Loading Cycle, Test 1T

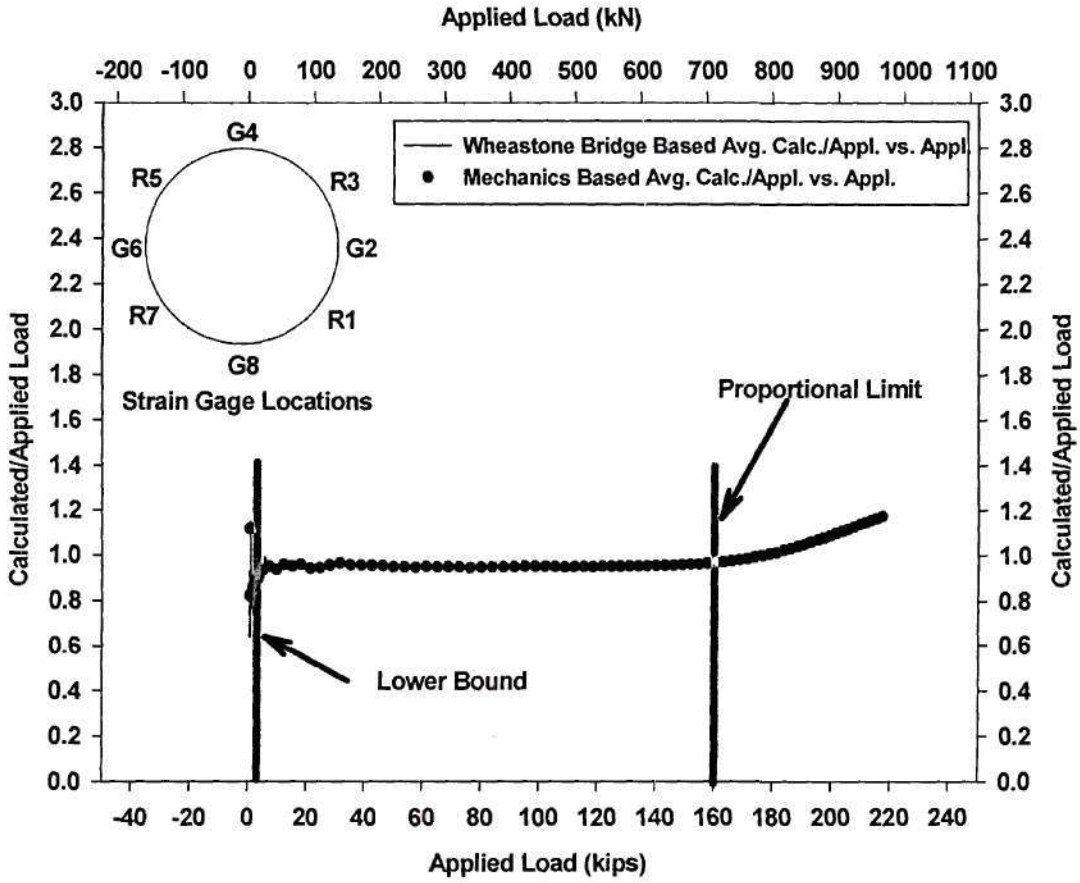

Figure 59: Average Calculated/Applied Load Ratios Using Equations (1) and (9) vs. Applied Load, First Loading Cycle, Nominal Thickness, Test 1T

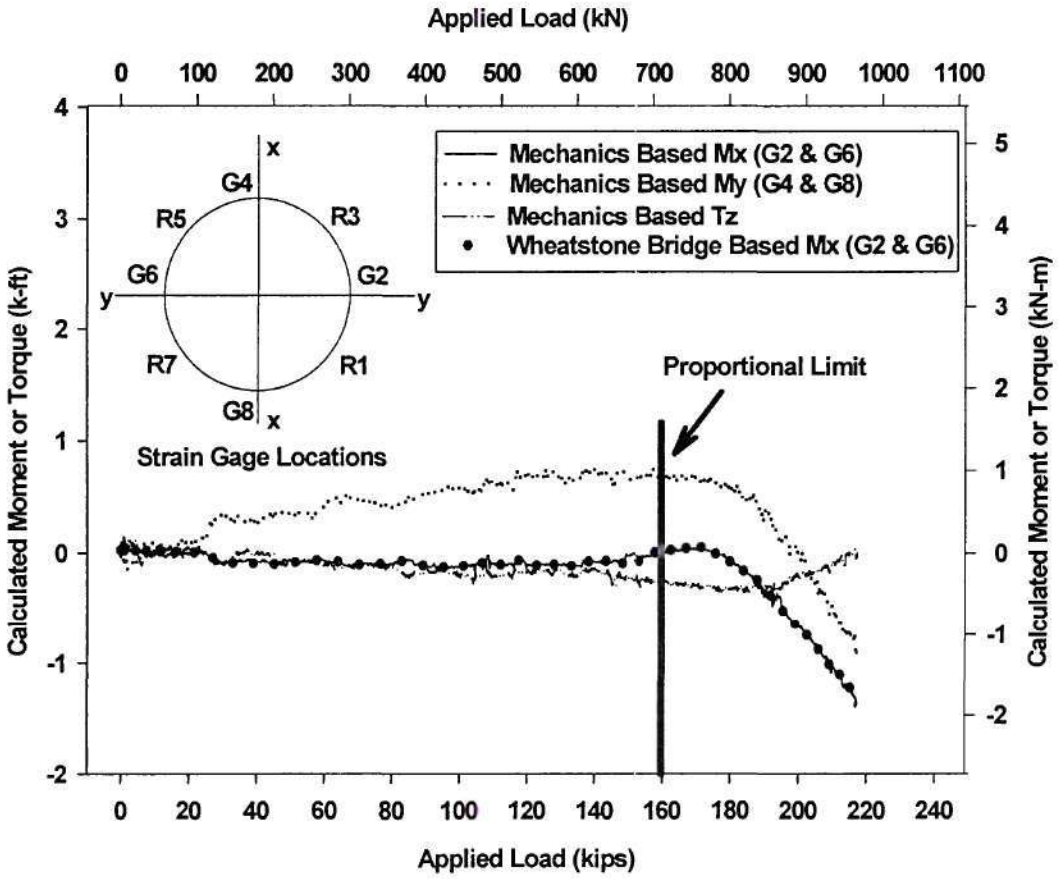

Figure 60: Calculated Internal Moments and Torque Using Equations (2) to (4) and (10) vs. Applied Load, First Loading Cycle, Nominal Thickness, Test 1T

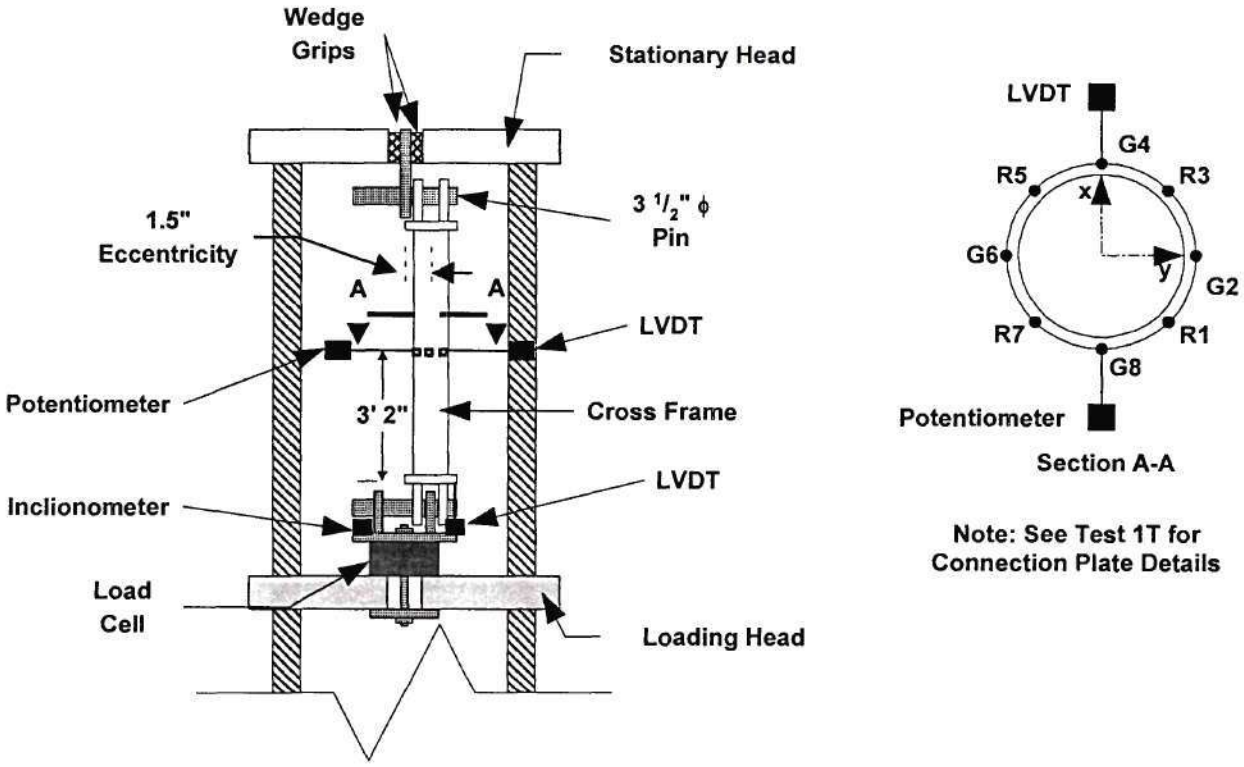

Figure 61: Eccentrically loaded tensile test 2T set-up (not to scale)

Figure 62: Photo of Test 2T

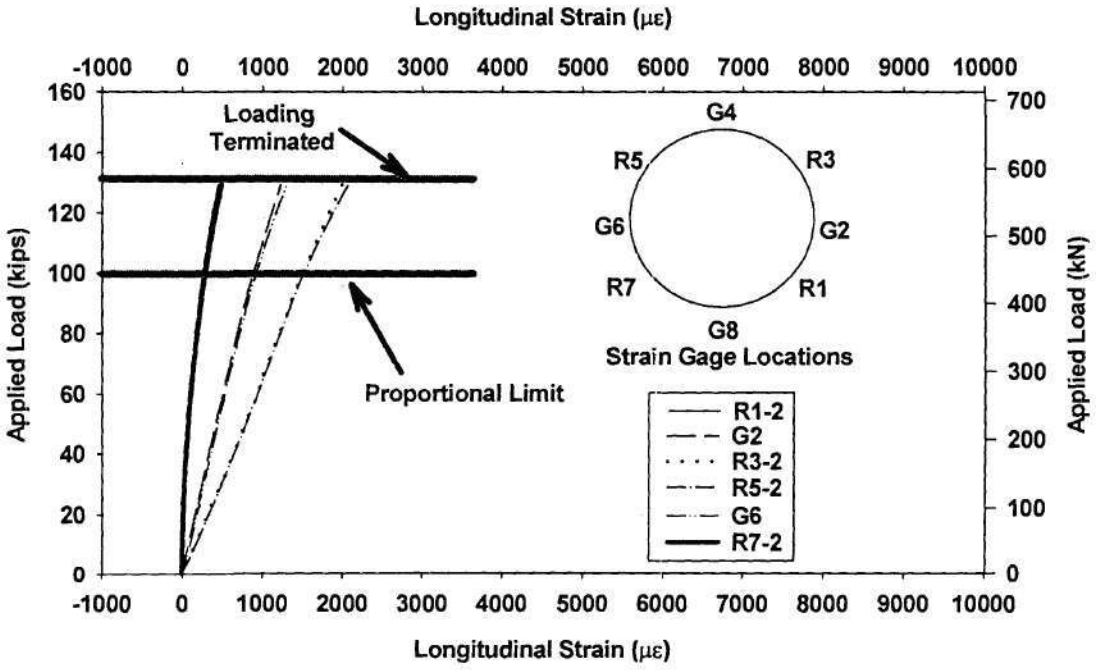

Figure 63: Applied Load vs. Longitudinal Strain, First Loading Cycle, Test 2T

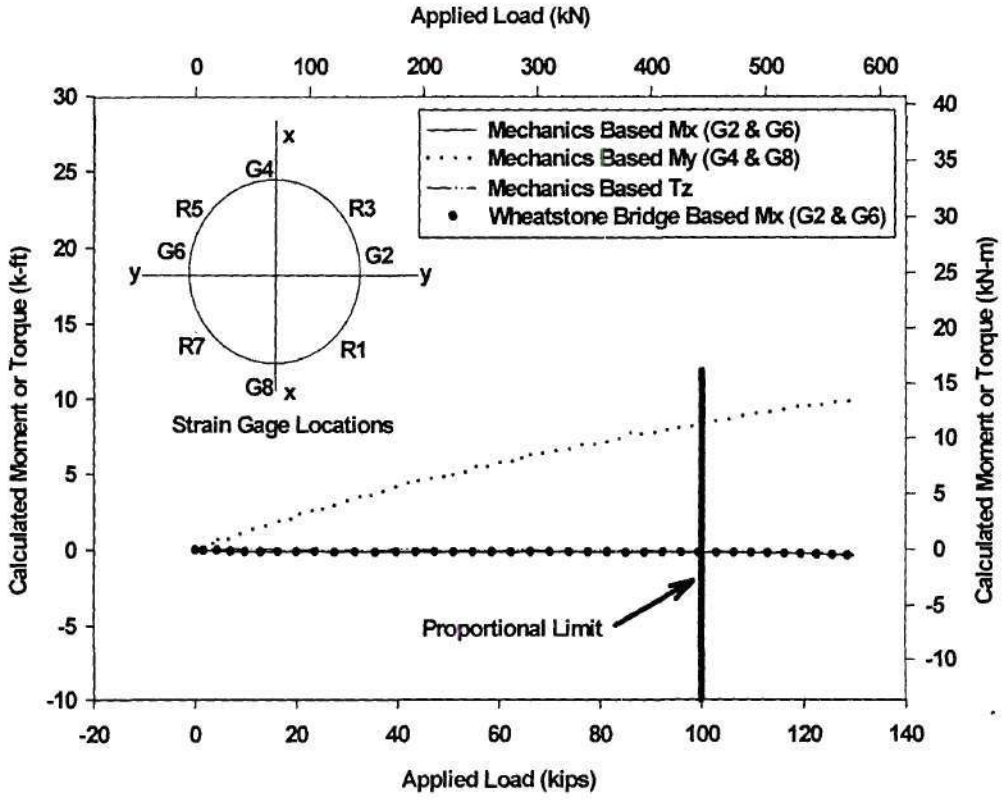

Figure 64: Calculated Internal Moments and Torque Usingm Equations (2) to (4) and Equation (10) vs. Applied Load, First Loading Cycle, Nominal Thickness, Test 2T

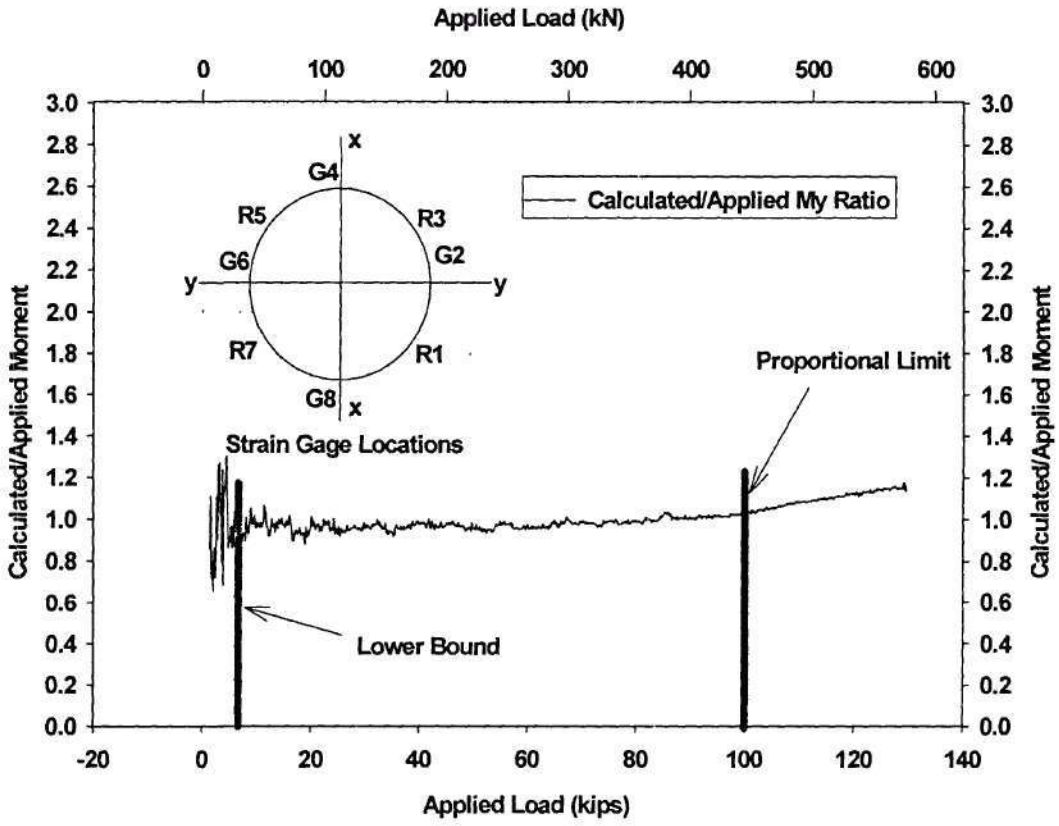

Figure 65: Calculated/Applied Moment Ratios (My) Using Equation (3) vs. Applied Load, First Loading Cycle, Nominal Thickness, Test 2T

Conclusion

Based on the results of compression and tension tests, the following conclusions are made:

- No appreciable difference in the strength of the groove and fillet welds was observed. Both welding techniques can be used for the fabrication of the cross-frame members.
- It is recommneded that 1/4" thick tubular members be used for in the construction of the cross-frame members of the the three-girder bridge system. This will ensure that the pipes remain elastic during the full-scale testing of ihe system as the test components reach their ultimate capacity.
- Improvement of results from the Wheatstone bridge based equations, (9) and (10), that account for the type of excitation over those from the mechanics based equations, (1) to (4), is negligible in the elastic range for a constant current excitation.

- Either single-arm gage configuration, with two gages oriented longitudinally and two oriented at 45° or with all four gauges oriented longitudinally, would be sufficient to compute the axial loads and the moments in the cross frame members. Thus, it is recommended that the strain gauge configuration shown in figure 66 be used for the purpose of deducing the axial load and moments in each cross-frame member of the three-girder bridge system.

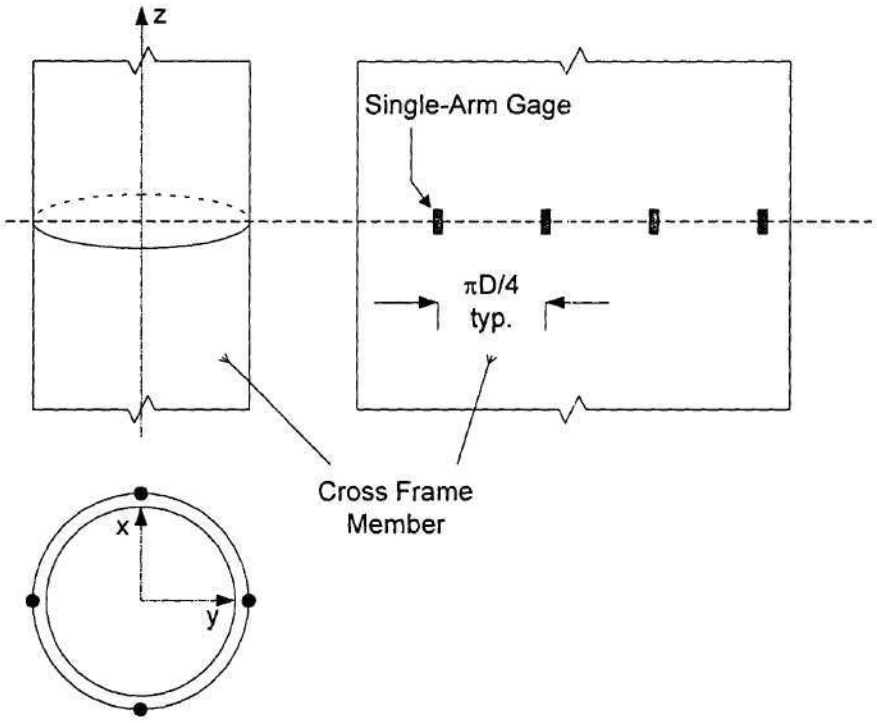

Figure 66: Cross Frame Member Strain Gage Configuration

Finite Element Model Description

Presented in this chapter is a description of the Finite Element Model (FEM) of the test frame, which includes a discussion of the model organization, coordinate system, boundary conditions, geometry of the test frame and bending specimens, finite element descriptions, element connectivity, and constitutive relationships.

Overview

Presented in Figure 4-1 is the typical mesh refinement of the FEM used during the evaluation of the three-girder test configuration. The model shown was developed using the solid modeling package PATRAN Version 3.0, which was then converted to ABAQUS/Aqua Version 5.5 for the detailed analyses.

Model organization

Examination of Figure 4 - 1 indicates that the FEM is organized into two major components consisting of:

1) Bending Test Specimens:
   B1 through B6
2) Support Test Frame:
   Support Girders G1, G2, and G3
   Cross Frames (Pipe Sections, Brackets, Center Gusset Assembly)
   Bottom Flange Lateral Bracing
   Loading Fixture
   Bearings

The Bending Specimens are bolted into the outside girder of the test frame, indicated as support girder G3, through a field splices and laterally supported by the cross frames at stations 6L and 6R. The test frame, however consists of several components, which can be futher broken

and 6R. The test frame, however consists of several components, which can be futher broken down into subcomponents. The major components of the test frame consist of the three support girders G1, G2, and G3, the loading fixture, cross frames, bottom flange bracing system, and the bearings which are supported by concrete abutments.

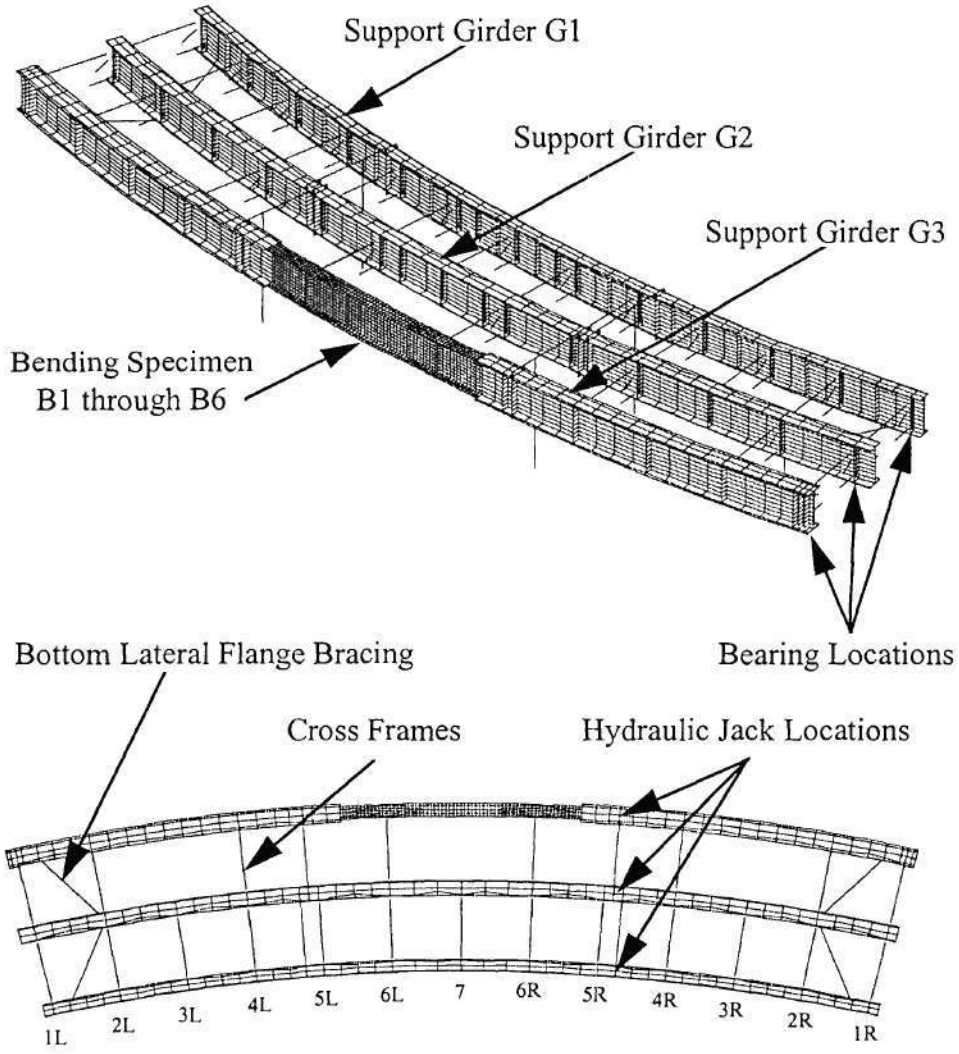

Figure 33 Three girder test configuration finite element model

Coordinate system

The geometry of the three-girder test configuration lends itself naturally to being described within a cylindrical coordinate system whose orgin is located at the center of curvature of the three concentric girders as indicated in Figure 4 - 2. The global **Z** axis defines the vertical direction with the **R**-θ plane (**Z** = 0.0) passing through the midheight of the three girders. Midspan of the three girders coincide with θ = 0.0, with θ having a positive orientation from midspan toward station 1L.

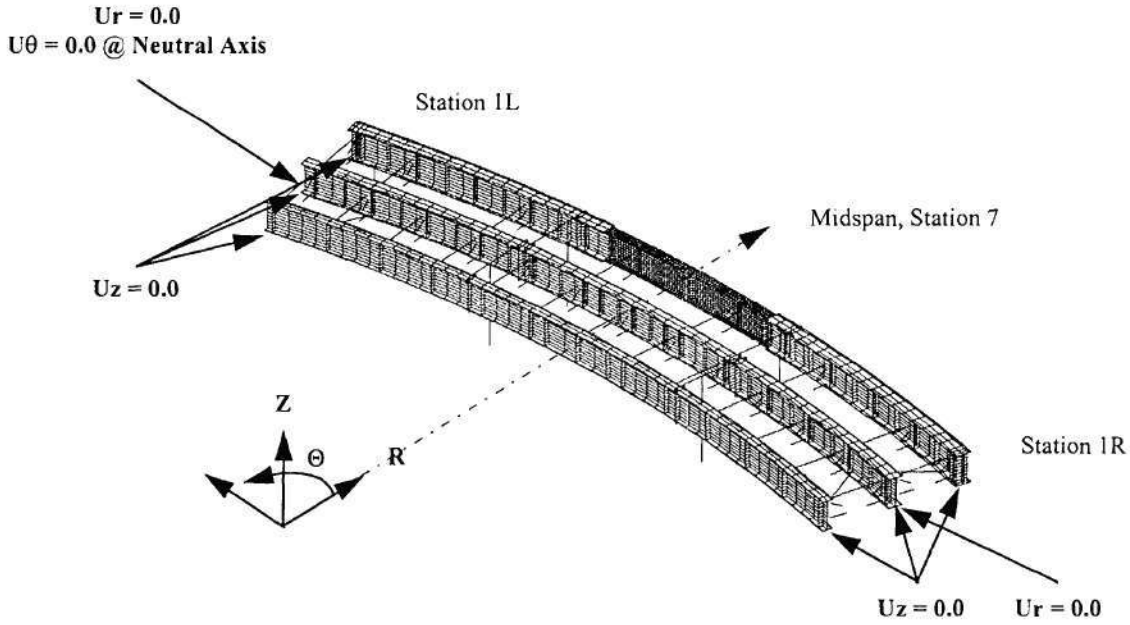

Figure 34 Coordinate system and boundary conditions

Boundary conditions

Boundary conditions, Figure 4 -2, imposed on the three-girder test configuration consist of vertical restraints at the six (6) bearing locations, radial restraints applied at both ends of the center support girder G2, and a tangential restraint at the neutral axis of support girder G2 at station 6L. The bearings, spherical and radial, are modeled using unidirectional gap elements with a

coulomb friction of 5%, thus making it is possible to account for the radial and tangential forces experienced at each of the bearings. The bearings are mounted into concrete abutments which are assumed to relatively stiff and are not specifically included in the model.

Test frame

SUPPORT GIRDER G1

The basic geometry of the inside support girder G1 is illustrated in Figure 4 -3. The dimensions presented are summarized below:

R - Radius of curvature, measured to the centerline of the web.

L_{G1} - Arc length between the bearing supports.

L_{lf} - Arc length between midspan and the load fixture stiffener plates.

L_{cf} - Arc length between cross frame connection plates

L_{wb} - Arc length between intermediate web stiffener plates

Figures 4 - 4 and 4 - 5 present exploded views of support girder G1 and indicate the individual components of the girder. The paranthetic descriptions refer to element group names used in ABAQUS to associate the element and material properties to a particular set of elements. Finally, Table 4 -1 summarizes the dimensions of the components, material properties, and weight.

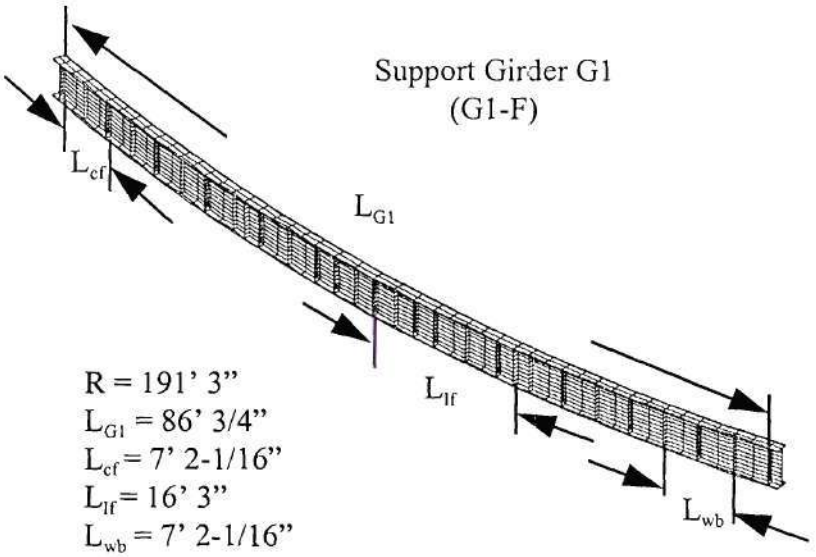

Figure 35 Support girder G1 geometry

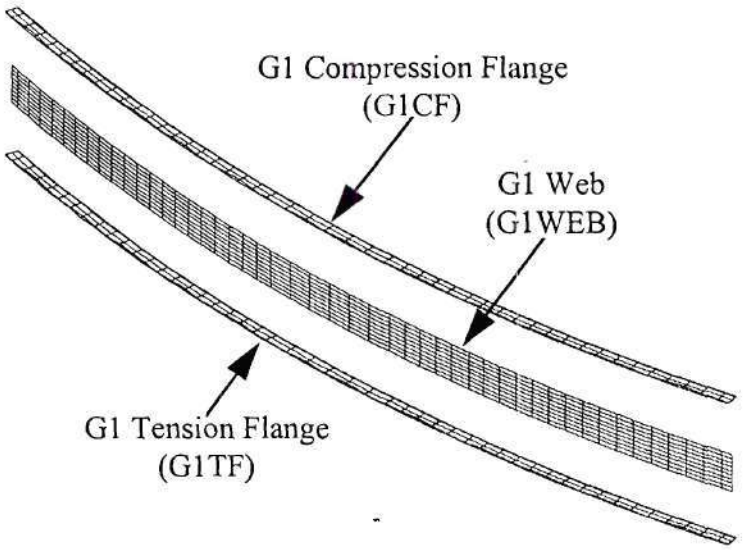

Figure 36 Exploded view of support girder G1 flanges and web

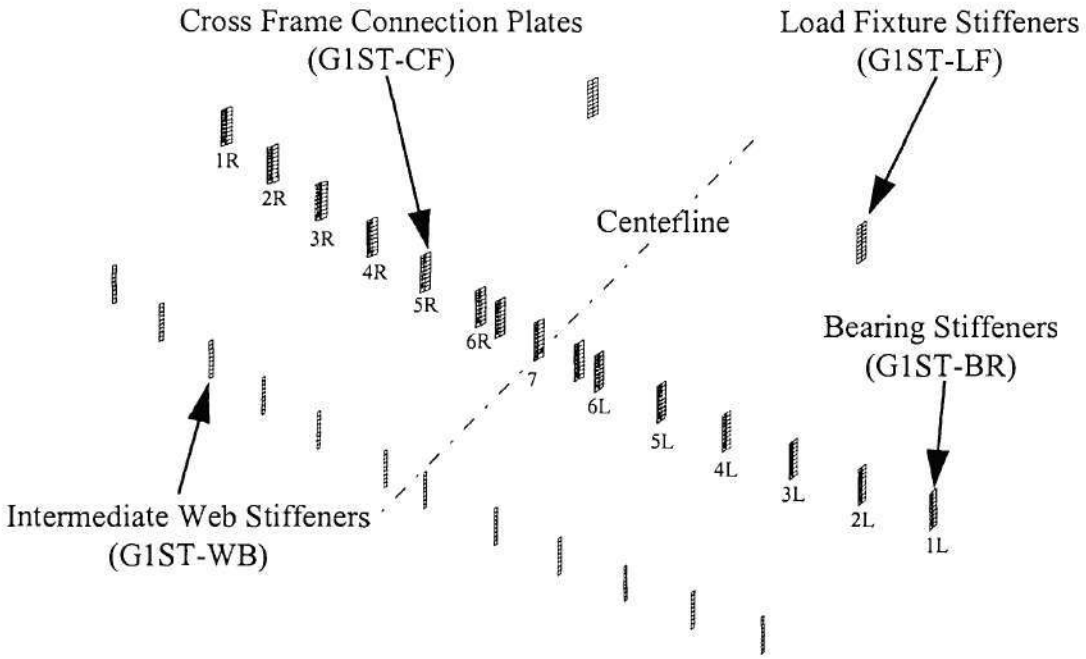

Figure 37 Exploded view of support girder G1 stiffeners

Table 20 Support girder G1 component summary

Component (Element Set)	Quantity	Dimension (in)	Material	Weight (lbf)
G1 Top Flange Plate (G1WEB)	1	L=1057 h=48 t=7/16	Steel 57ksi	6,293
G1 Top Flange Plate (G1TF)	1	L=1057 b=16 t=1 1/16	Steel 57ksi	5.094
G1 Bottom Flange Plate (G1BF)	1	L=1057 b=16 t=1 1/16	Steel 57ksi	5.094
G1 Web Stiffner Plate (G1ST-WB)	12	h=48 b=5 t=7/16	Steel 57ksi	29.8

G1 Cross Frame Connection Plate (G1ST-CF)	26	h=48 b=7 t=5/8	Steel 57ksi	59.5
G1 Load Fixture Stiffner Plate (G1ST-LF)	4	h=48 b=7 t=5/8	Steel 57ksi	59.5
G1 Bearing Stiffner Plate (G1ST-BR)	4	h=48 b=7 t=3/4	Steel 57ksi	71.5
G1 Support Girder			(17.87 lbf/in)	Total Weight 18,910

SUPPORT GIRDER G2

The basic geometry of the center support girder G2 is illustrated in Figure 4 -6. The dimensions presented are summarized below:

R - Radius of curvature, measured to the centerline of the web

L_{G2} - Arc length between the bearing supports

$L_{lf\text{-}1}$ - Arc length between midspan and the first set of load fixture stiffener plates

$L_{lf\text{-}2}$ - Arc length between midspan and the second set of load fixture stiffener plates

L_{cf} - Arc length between cross frame connection plates

L_{wb} - Arc length between intermediate web stiffener plates

Figures 4 - 7 and 4 - 8 present exploded views of support girder G2 and indicate the individual components of the girder. The paranthetic descriptions refer to element group names used in ABAQUS to associate the element and material properties to a particular set of elements. Finally Table 4 -2 summarizes the dimensions of the components, material properties, and weight.

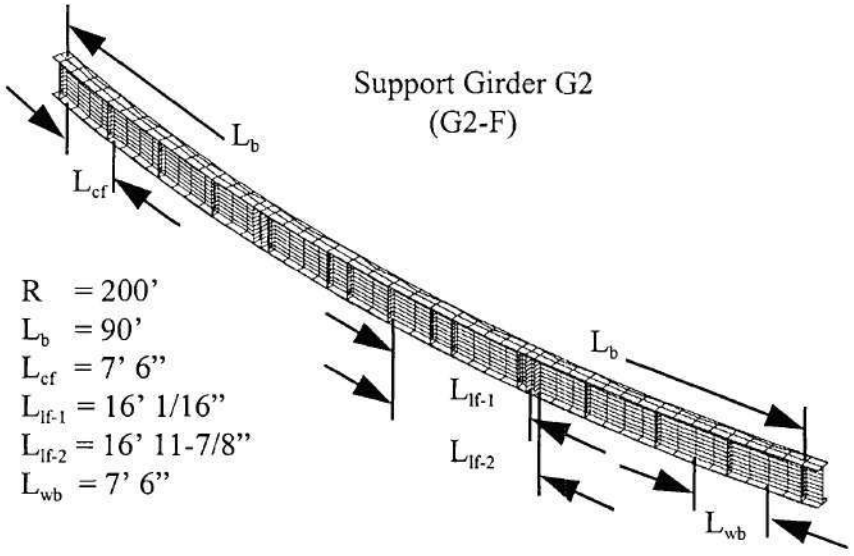

Figure 38 Support girder G2 geometry

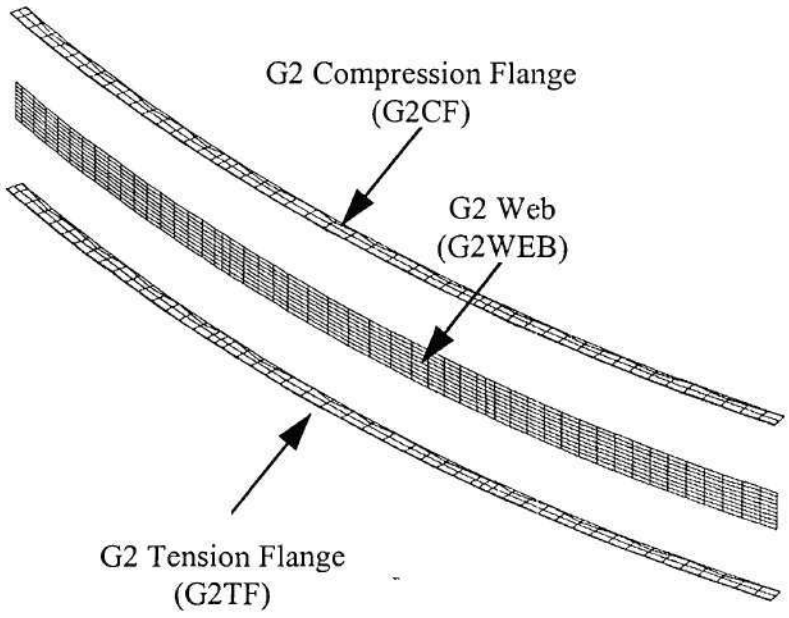

Figure 39 Exploded view of support girder G2 flanges and web

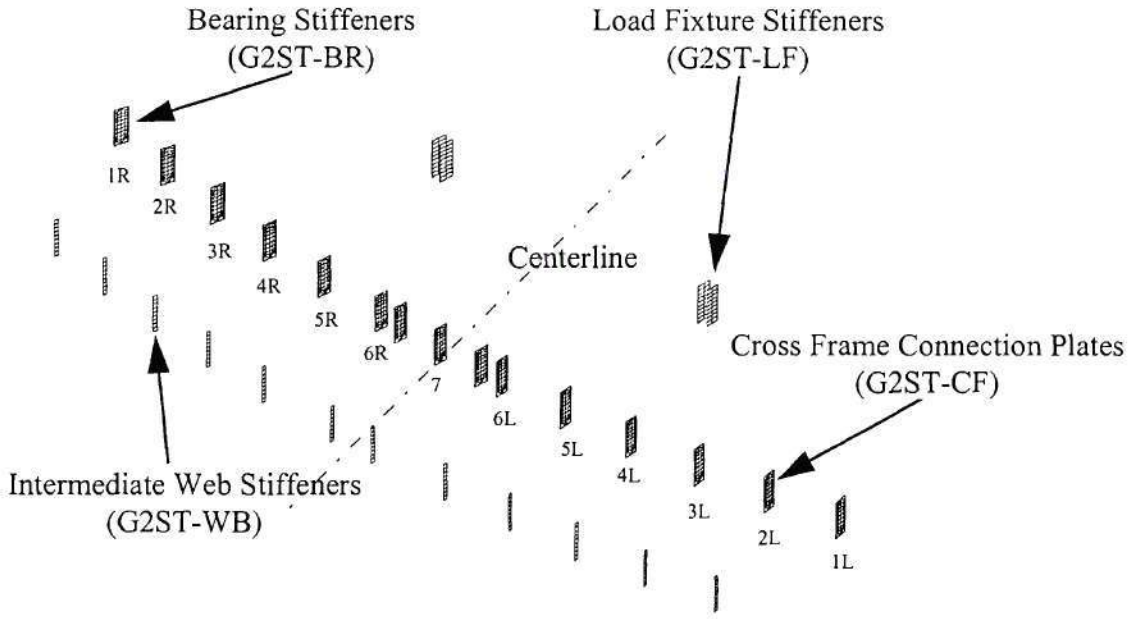

Figure 40 Exploded view of support girder G2 stiffeners

Table 21 Support girder G2 component summary

Component (Element Set)	Quantity	Dimension (in)	Material	Weight (lbf)
G2 Top Flange Plate (G2WEB)	1	L=1112 h=48 t=1/2	Steel 70ksi	7,568
G2 Top Flange Plate (G2TF)	1	L=1112 b=20 t=1 3/16	Steel 70ksi	7,489
G2 Bottom Flange Plate (G2BF)	1	L=1112 b=20 t=1 31/16	Steel 70ksi	7,489
G2 Web Stiffner Plate (G2ST-WB)	12	h=48 b=5 t=7/16	Steel 70ksi	29.8

G2 Cross Frame Connection Plate (G2ST-CF)	26	h=48 b=9 t=13/16	Steel 70ksi	99.5
G2 Load Fixture Stiffner Plate (G2ST-LF)	8	h=48 b=9 t=13/16	Steel 70ksi	99.5
G2 Bearing Stiffner Plate (G2ST-BR)	4	h=48 b=9 t=1	Steel 70ksi	122.5
G2 Support Girder			(24.08 lbf/in)	Total Weight 26,780

SUPPORT GIRDER G3

The basic geometry of the outside support girder G3 is illustrated in Figure 4 -9. The dimensions presented are summarized below:

R - Radius of curvature, measured to the centerline of the web

L_b - Arc length between the bearing supports

L_{lf} - Arc length between midspan and the load fixture stiffener plates

L_{cf} - Arc length between cross frame connection plates

L_{wb} - Arc length between intermediate web stiffener plates

Figures 4 - 10 and 4 - 11 present exploded views of support girder G3 and indicate the individual components of the girder. The paranthetic descriptions refer to element group names used in ABAQUS to associate the element and material properties to a particular set of elements. Finally Table 4 -3 summarizes the dimensions of the components, material properties, and weight.

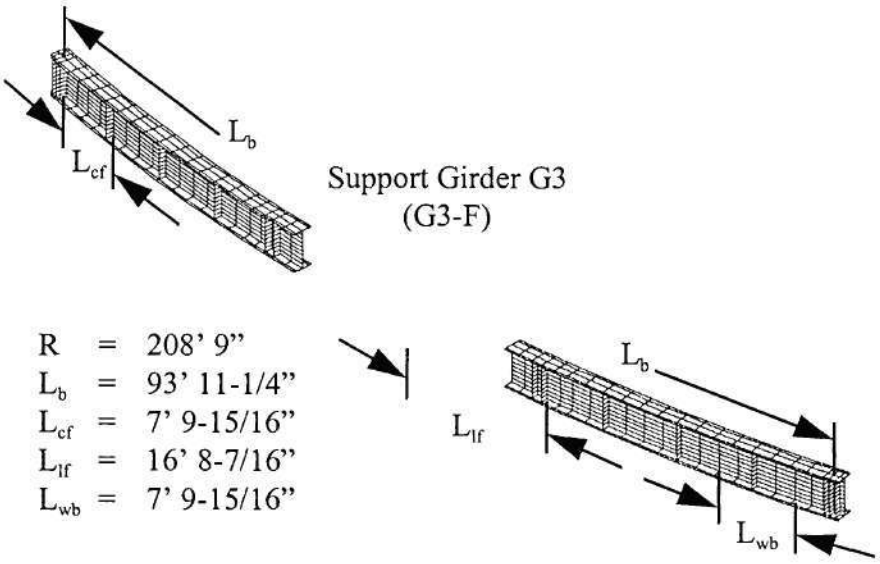

Figure 41 Support girder G3 geometry

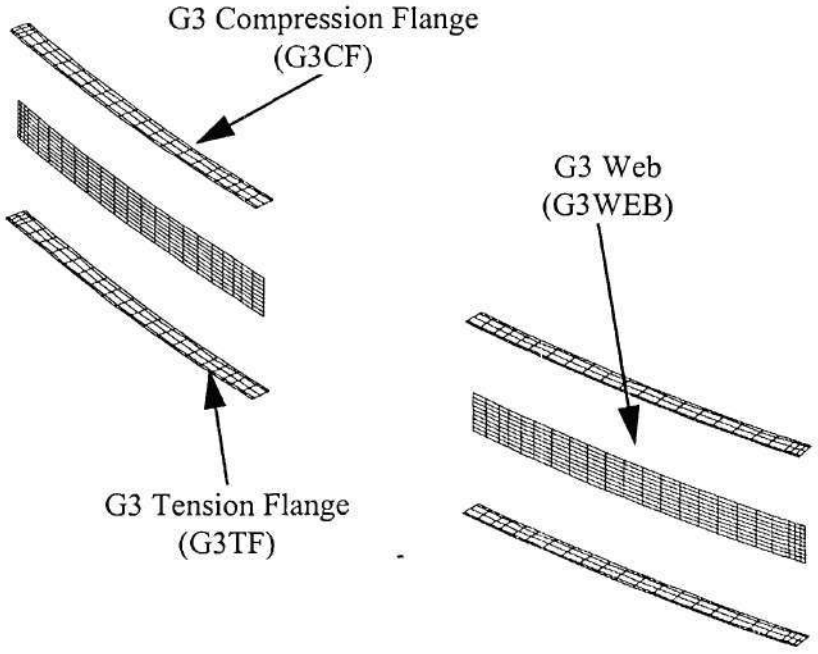

Figure 42 Exploded view of support girder G3 flanges and web

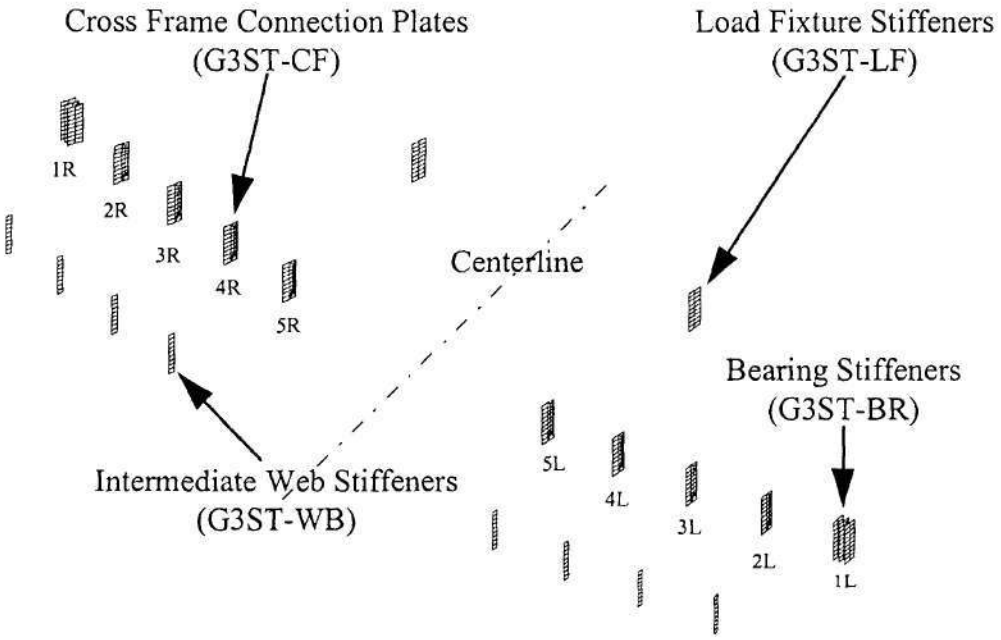

Figure 43 Exploded view of support girder G3 stiffeners

Table 22 Support girder G3 component summary

Component (Element Set)	Quantity	Dimension (in)	Material	Weight (lbf)
G3 Top Flange Plate (G3WEB)	2	L=411.25 h=48 t=1/2	Steel 57ksi	2,799
G3 Top Flange Plate (G3TF)	2	L=411.25 b=24 t=2 1/4	Steel 57ksi	6,295
G3 Bottom Flange Plate (G3BF)	2	L=411.25 b=24 t=2 1/4	Steel 57ksi	6,295
G3 Web Stiffner Plate (G3ST-WB)	12	h=48 b=7 t=5/8	Steel 57ksi	59.5
G3 Cross Frame Connection Plate (G3ST-CF)	16	h=48 b=9 t=13/16	Steel 57ksi	99.5
G3 Load Fixture Stiffner Plate (G3ST-LF)	4	h=48 b=9 t=13/16	Steel 57ksi	99.5
G3 Bearing Stiffner Plate (G3ST-BR)	12	h=48 b=9 t=1	Steel 57ksi	122.5
G3 Support Girder			(24.08 lbf/in)	Total Weight 34,720

Comparison Between Analysis(B1h_3) and Test(4-2-99) for B1
Vertical Reactions at the East Supports

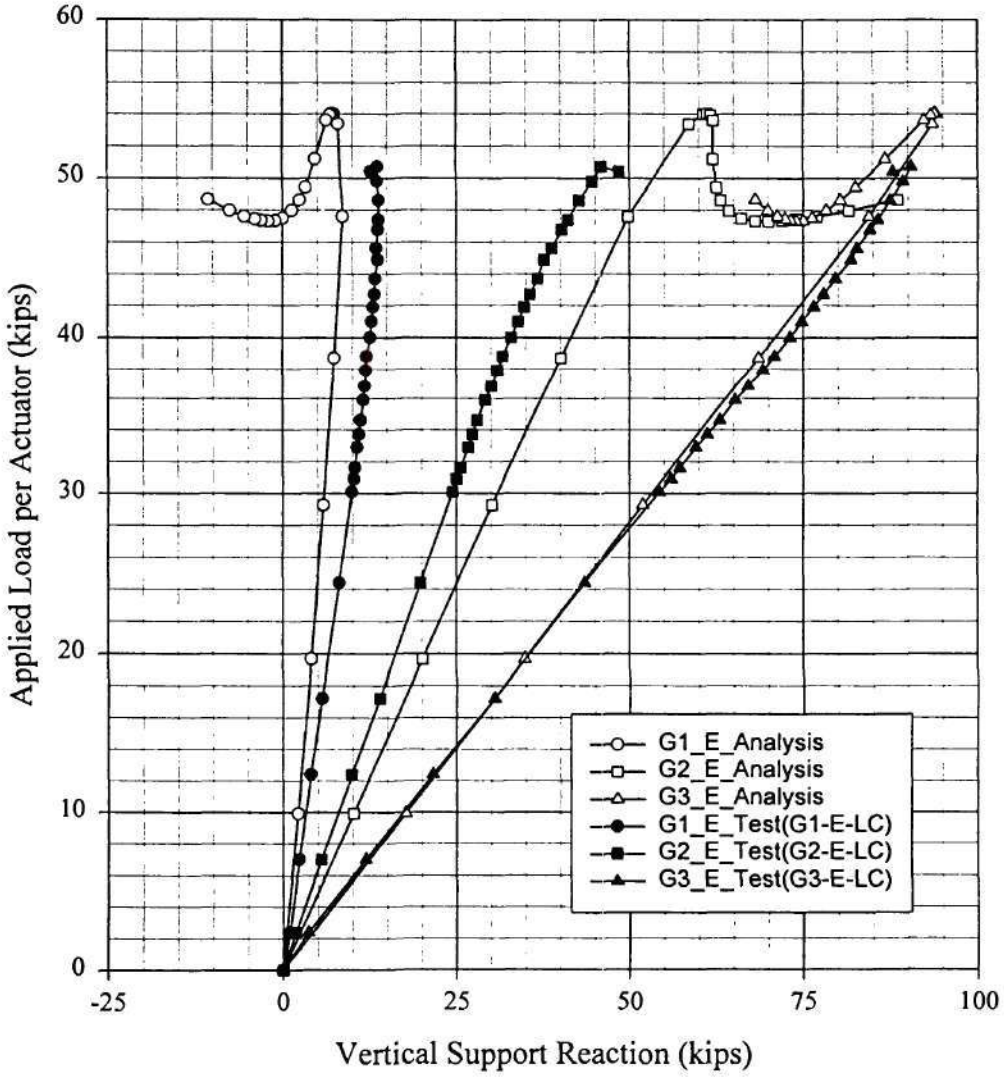

Comparison Between Analysis(B1h_3) and Test(4-2-99) for B1
Vertical Reactions at the West Supports

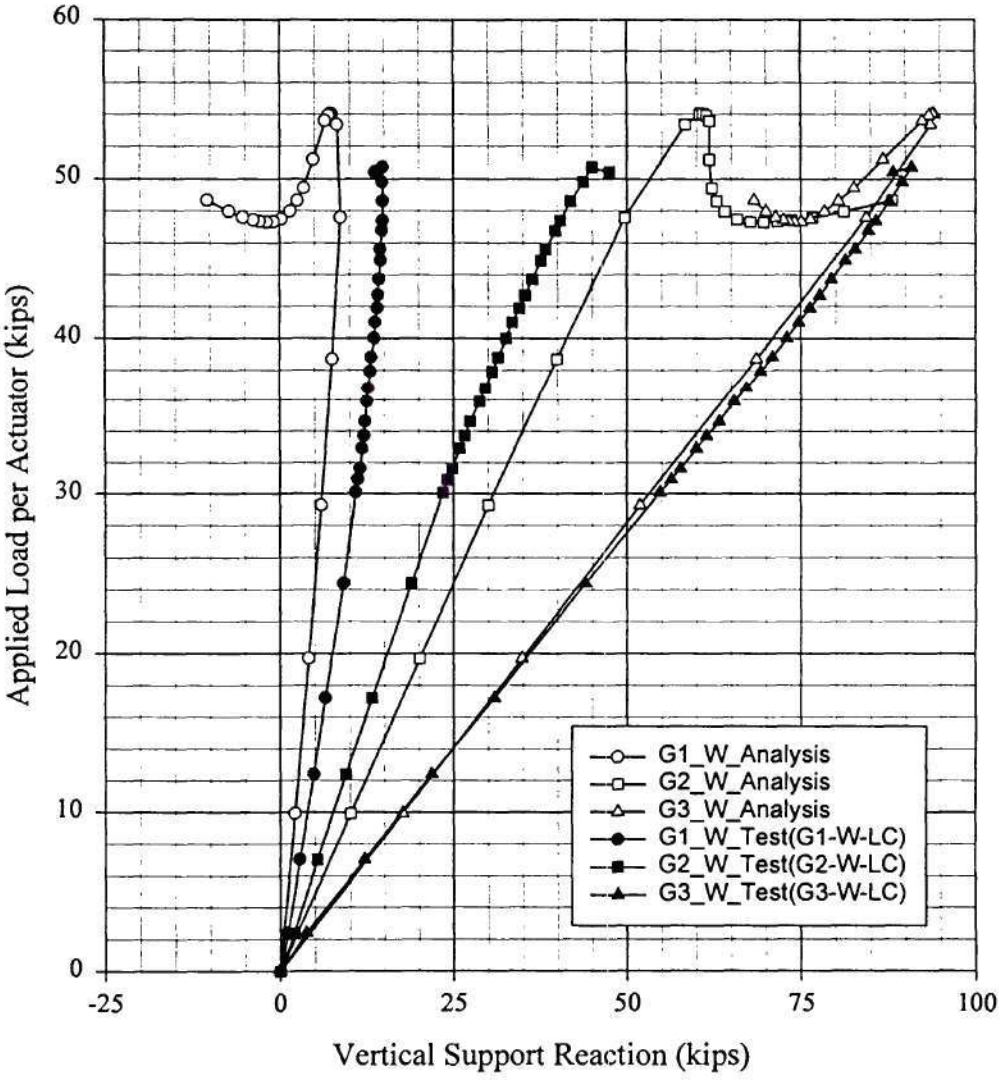

Comparison Between Analysis(B1h_3) and Test(4-2-99) for B1
Vertical Displacement of Bottom Flange (Outside) at Midspan

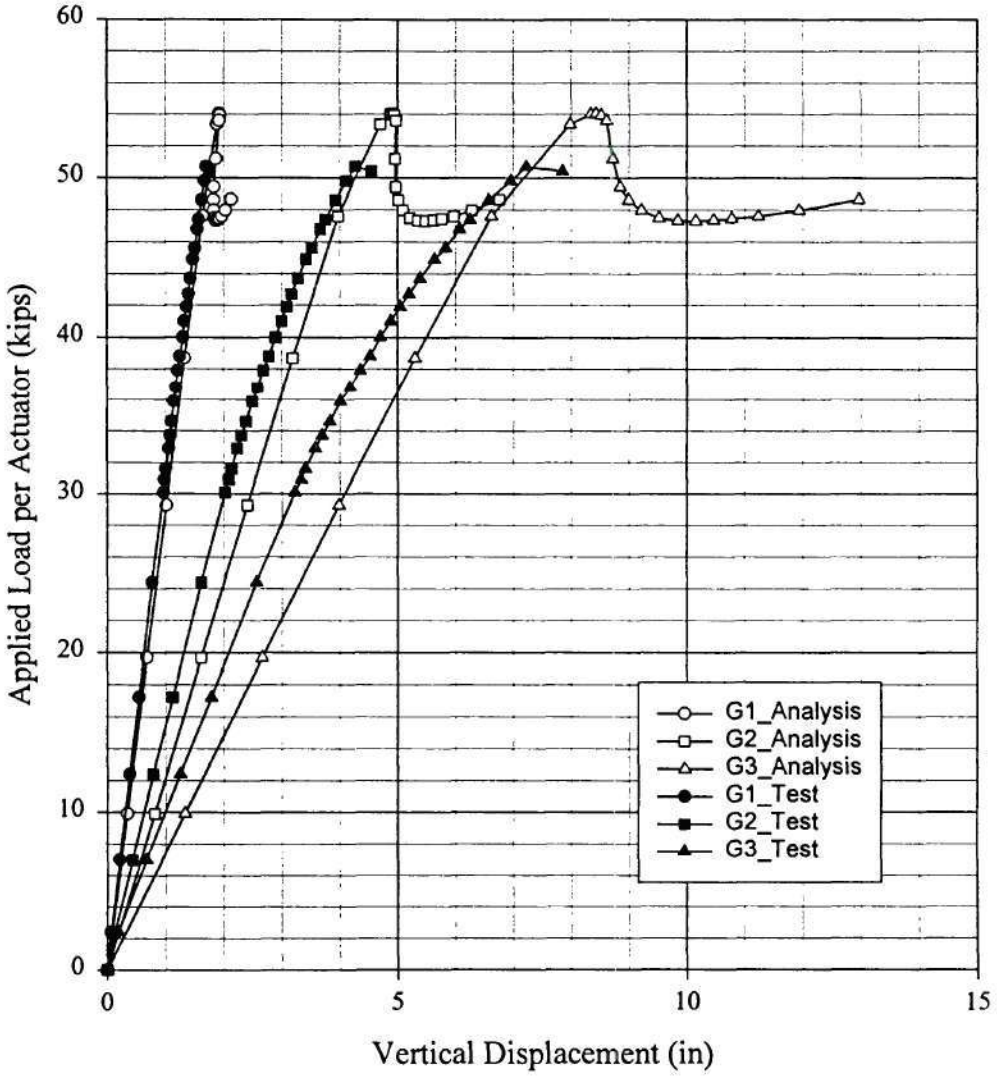

Comparison Between Analysis(B1h_3) and Test(4-2-99) for B1
Radial Displacement of Top Flange (Outside) at Midspan

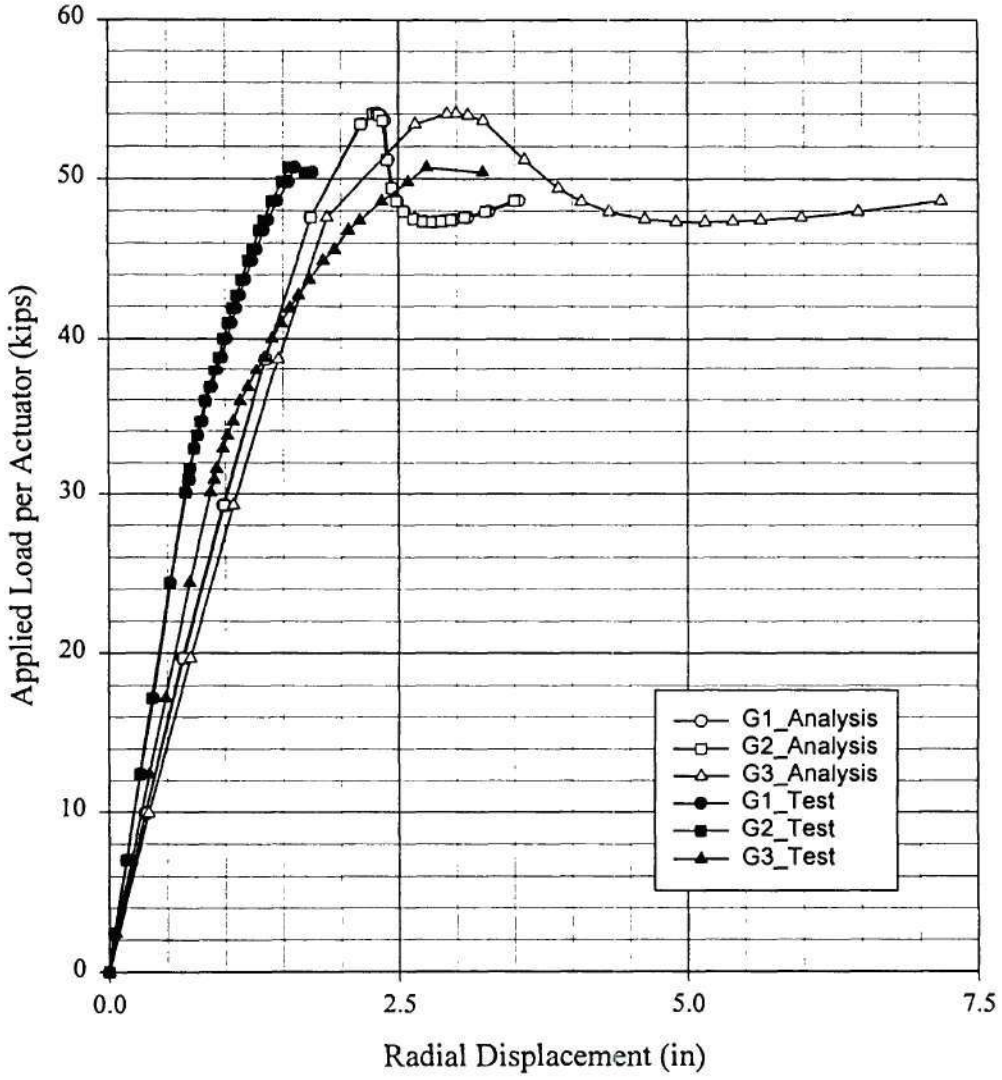

Comparison Between Analysis(B1h_3) and Test(4-2-99) for B1
Radial Displacement of Bottom Flange (Outside) at Midspan

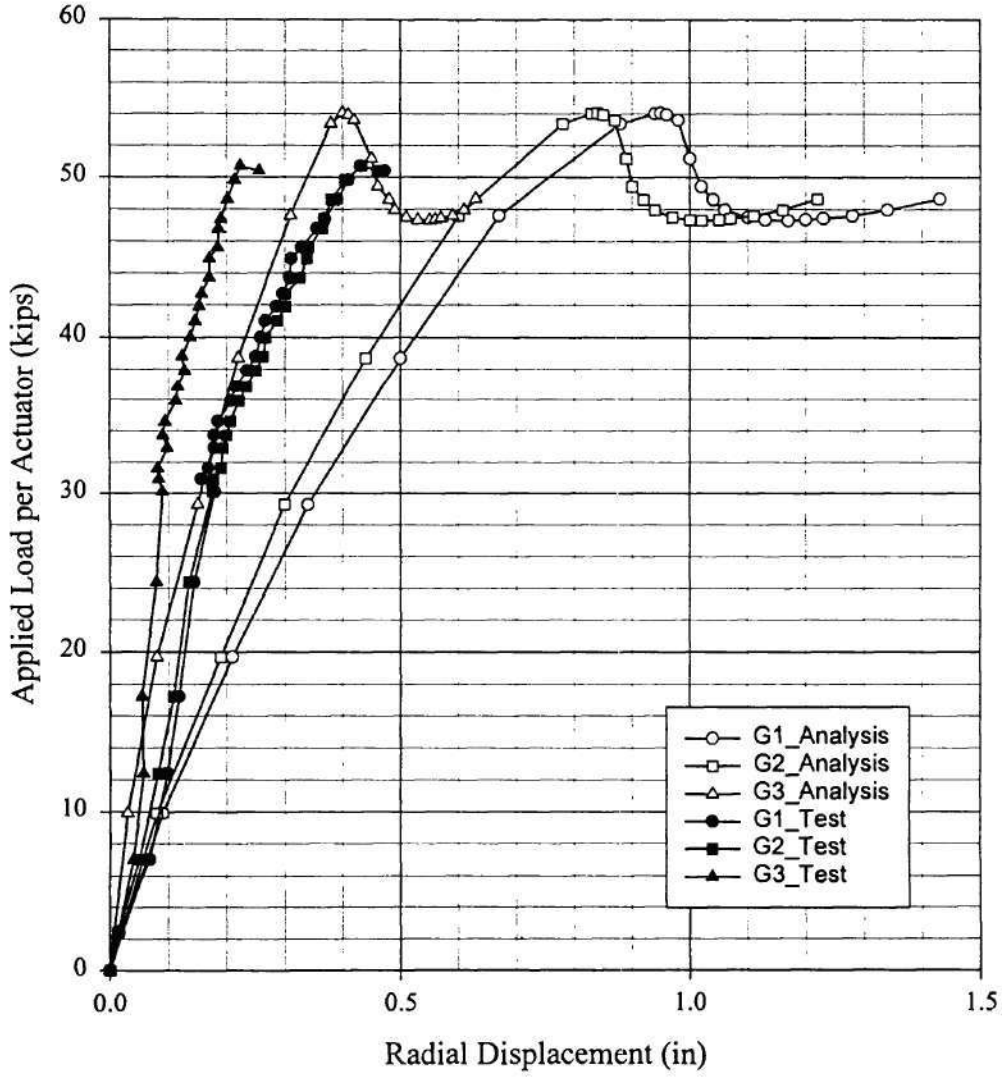

Comparison Between Analysis(B1h_3) and Test(4-2-99) for B1
Axial Force of Cross Frame at 6R Between G2 and G3

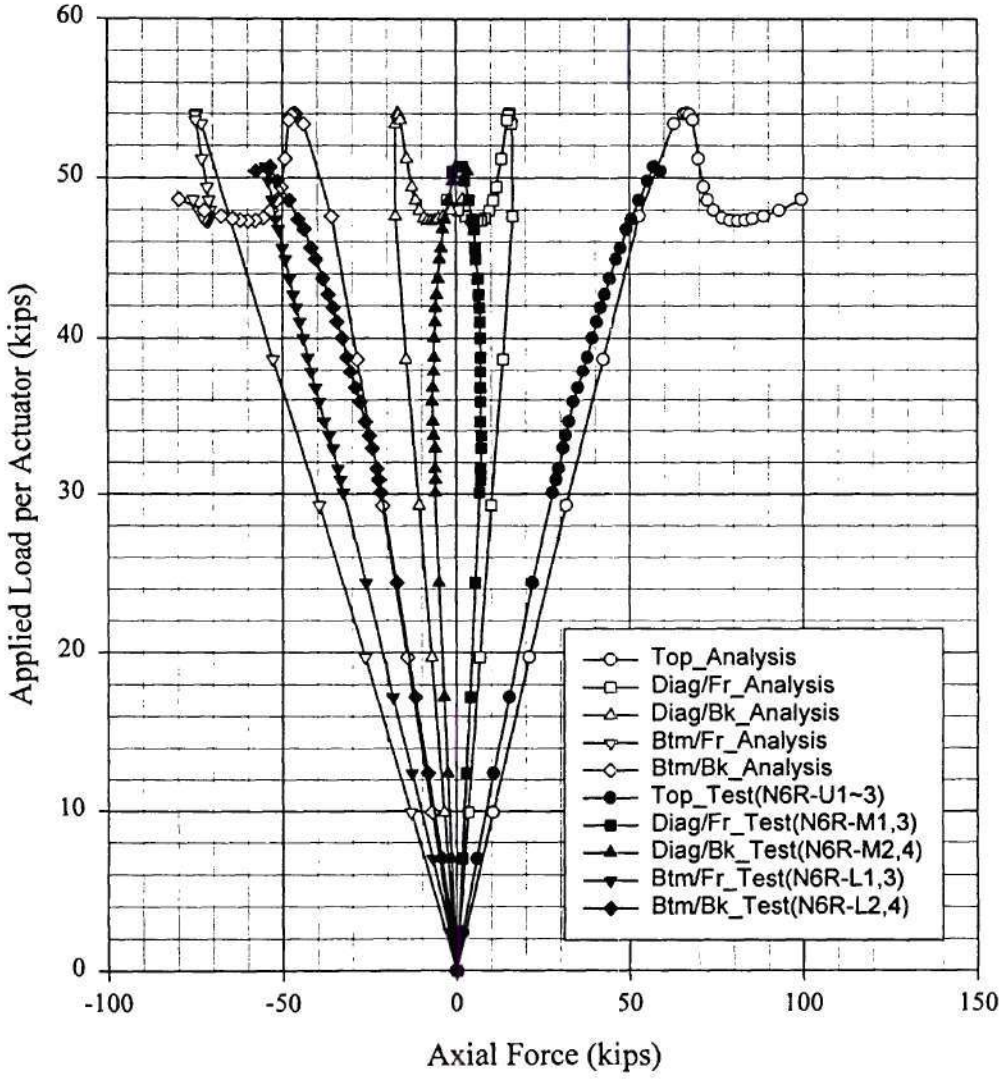

Comparison Between Analysis(B1h_3) and Test(4-2-99) for B1
Axial Force of Cross Frame at 6L Between G2 and G3

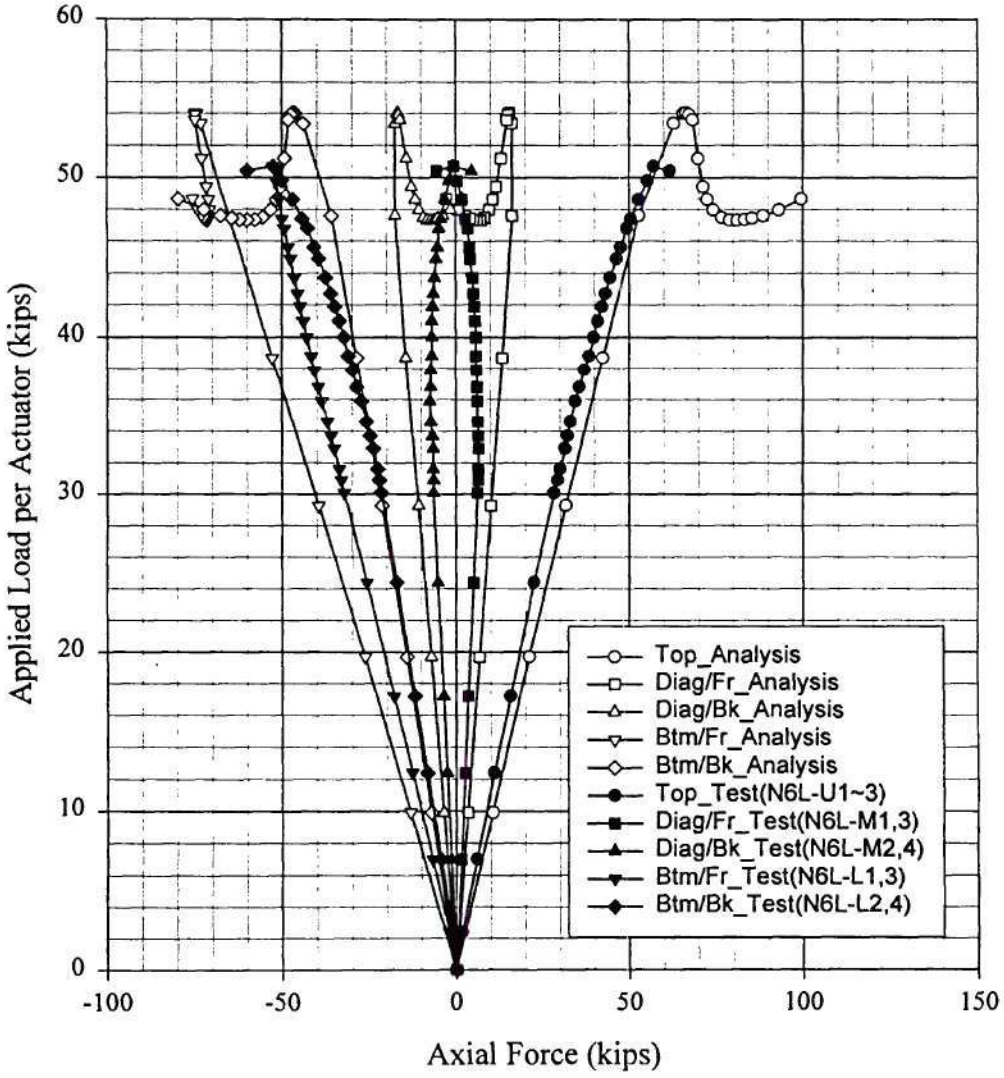

Comparison Between Analysis(B1h_3) and Test(4-2-99) for B1
Bending Moment at Midspan

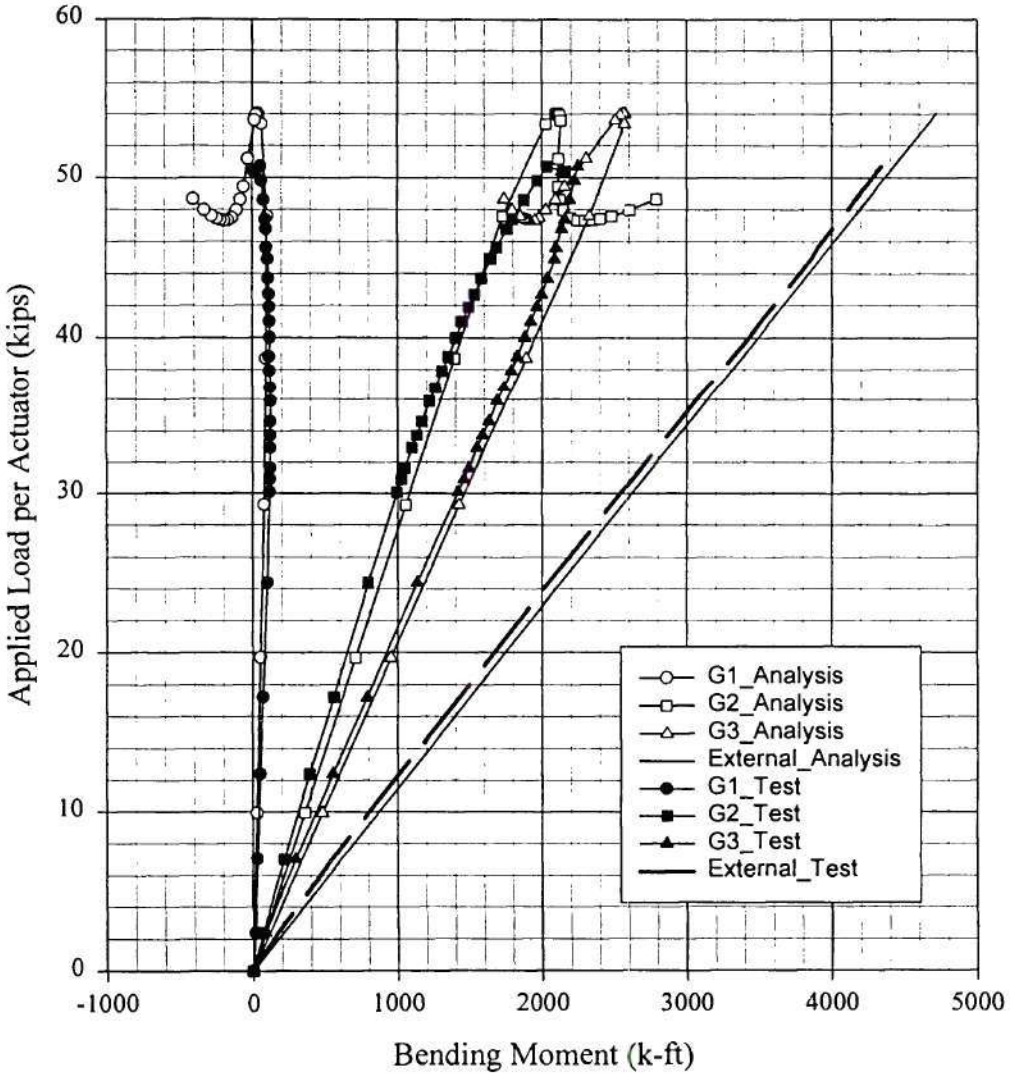

Comparison Between Analysis(B1h_3) and Test(4-2-99) for B1
Normal Strain of the Web Inside at the Location G1_B

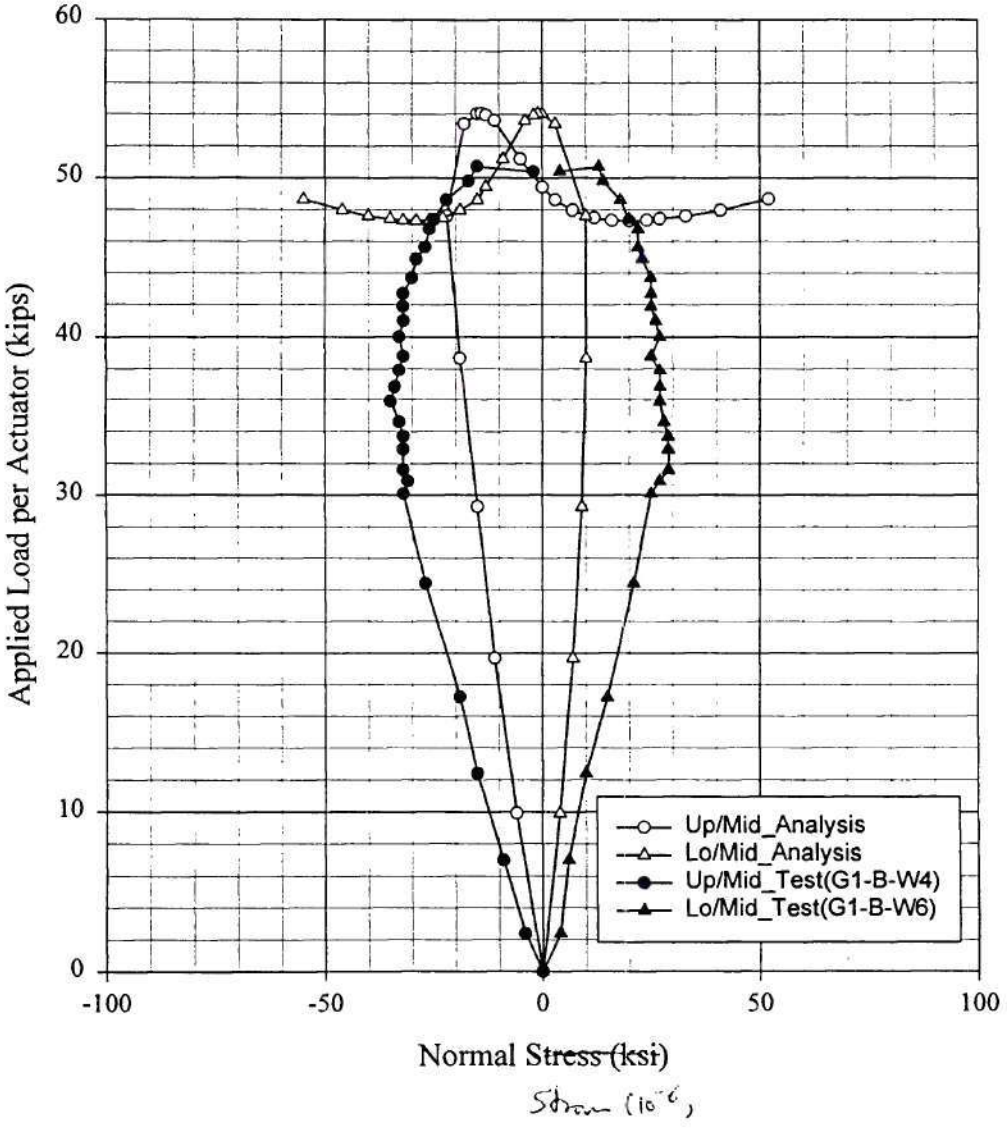

Comparison Between Analysis(B1h_3) and Test(4-2-99) for B1
Normal Strain of the Top Flange Topside at the Location G1_B

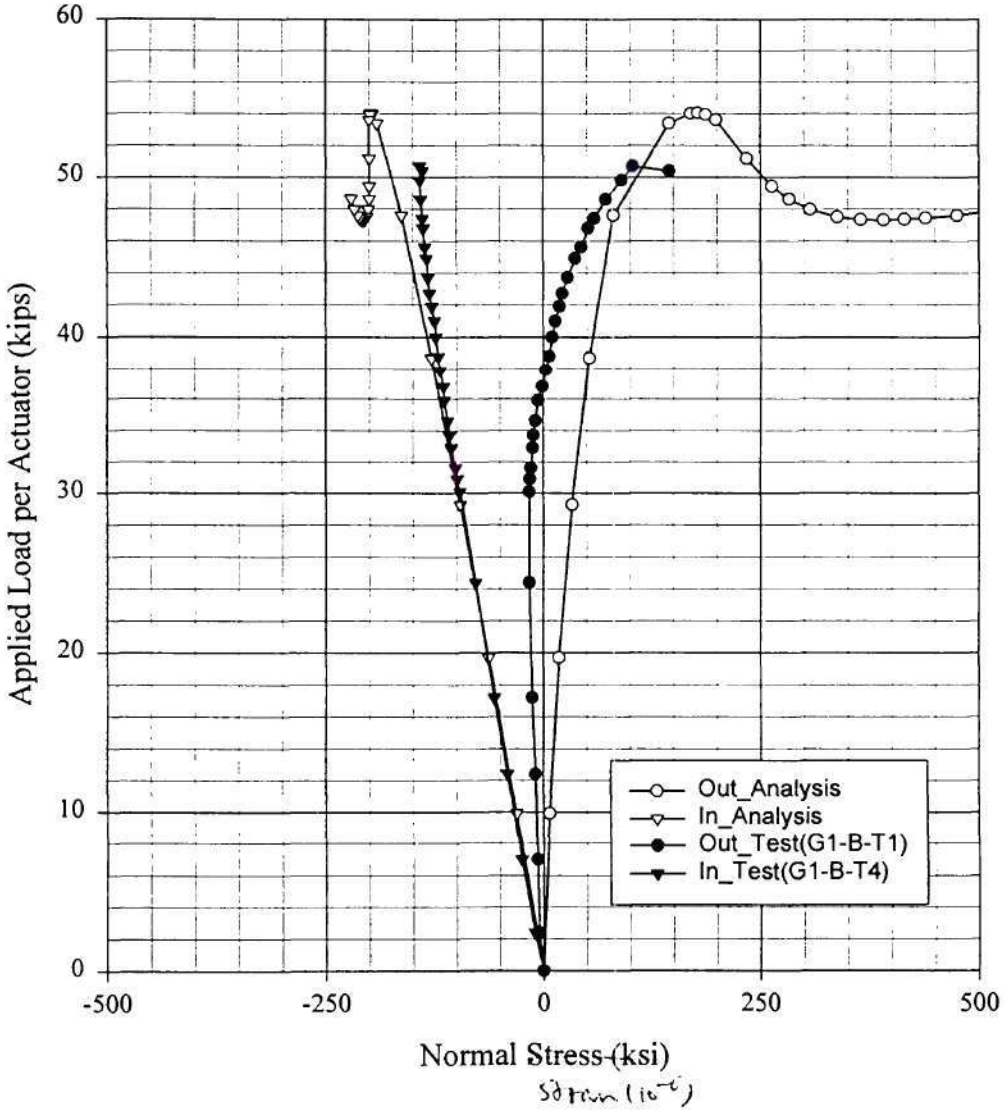

Comparison Between Analysis(B1h_3) and Test(4-2-99) for B1
Normal Strain of the Top Flange Btmside at the Location G1_B

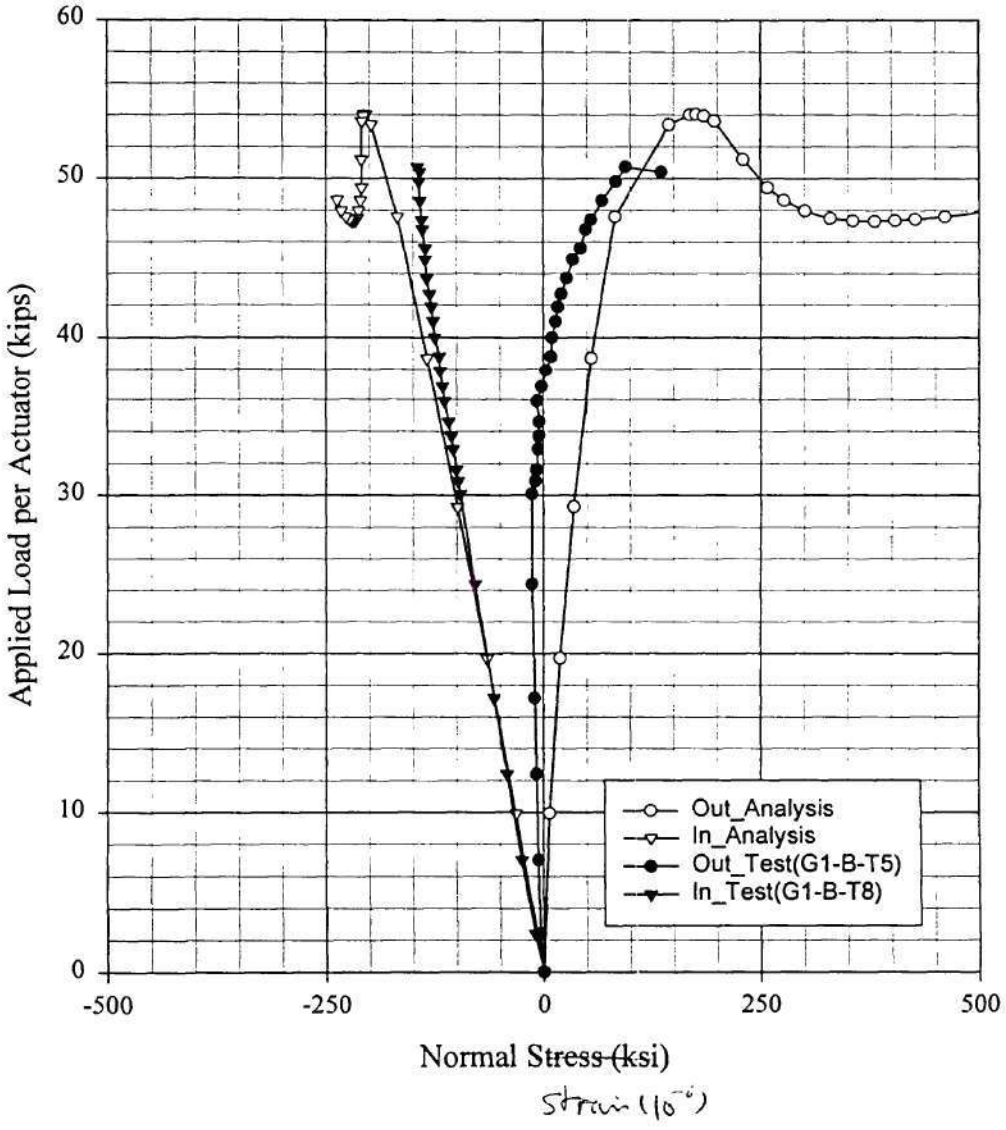

Comparison Between Analysis(B1h_3) and Test(4-2-99) for B1
Normal Strain of the Btm Flange Topside at the Location G1_B

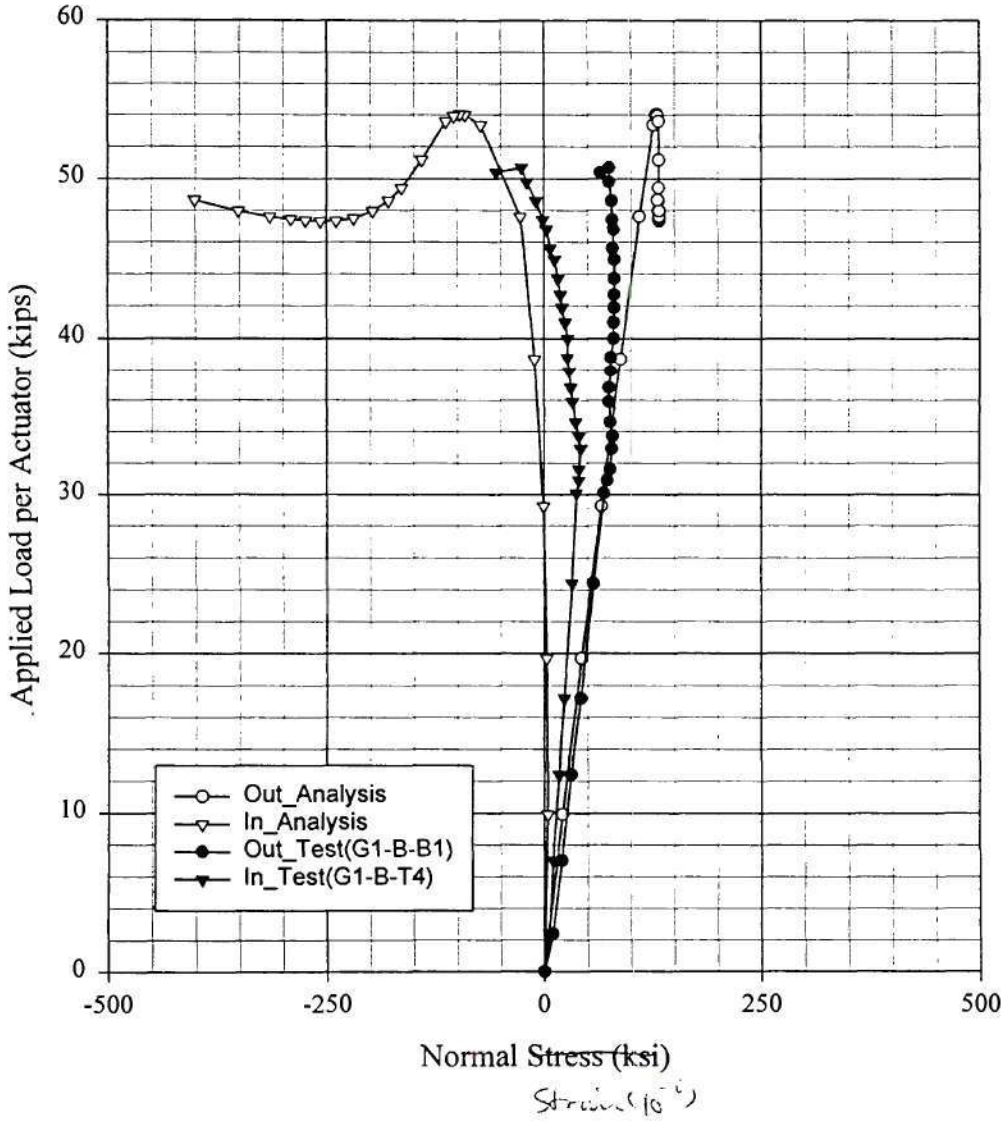

Comparison Between Analysis(B1h_3) and Test(4-2-99) for B1
Normal Strain of the Btm Flange Btmside at the Location G1_B

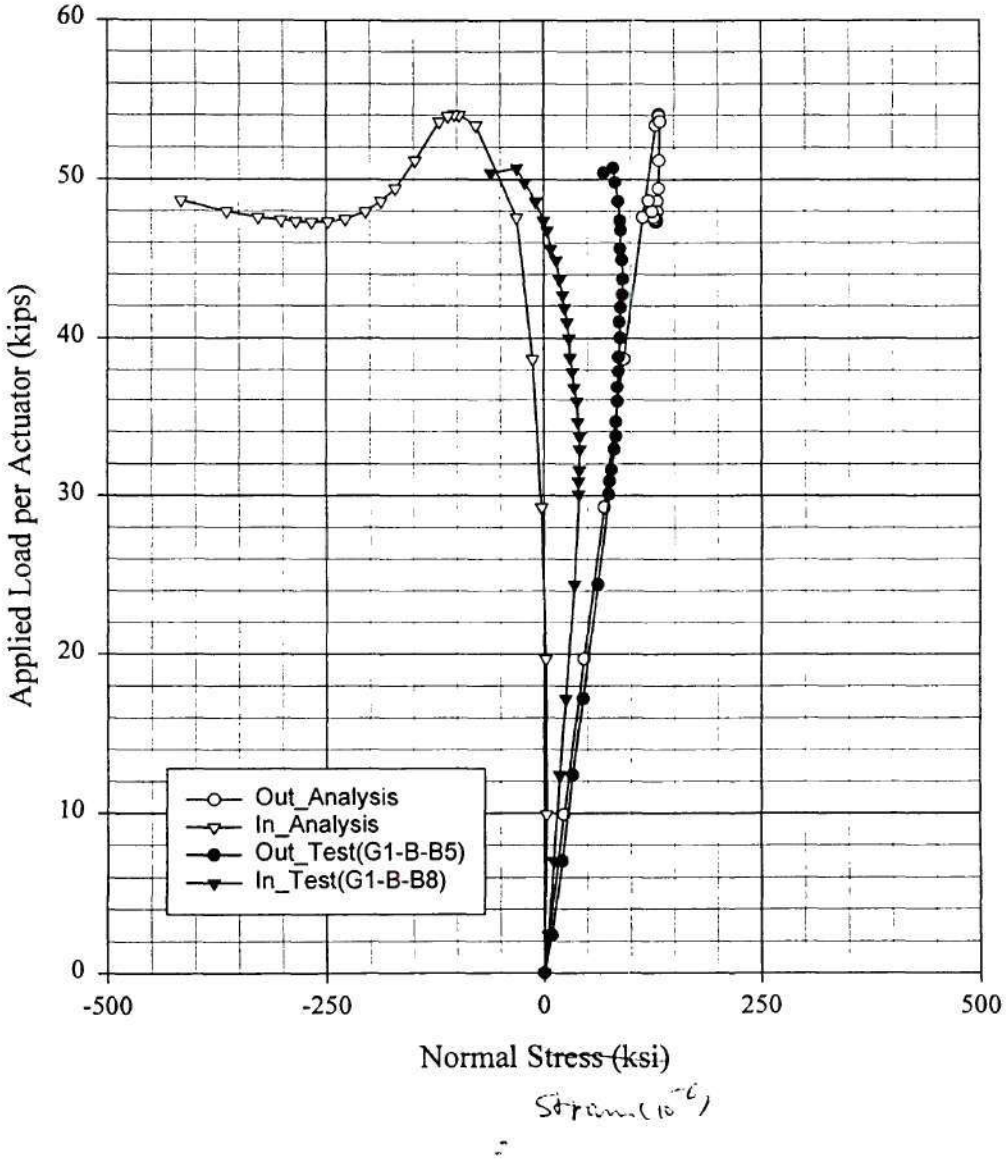

Comparison Between Analysis(B1h_3) and Test(4-2-99) for B1
Normal Strain of the Web Inside at the Location G2_B

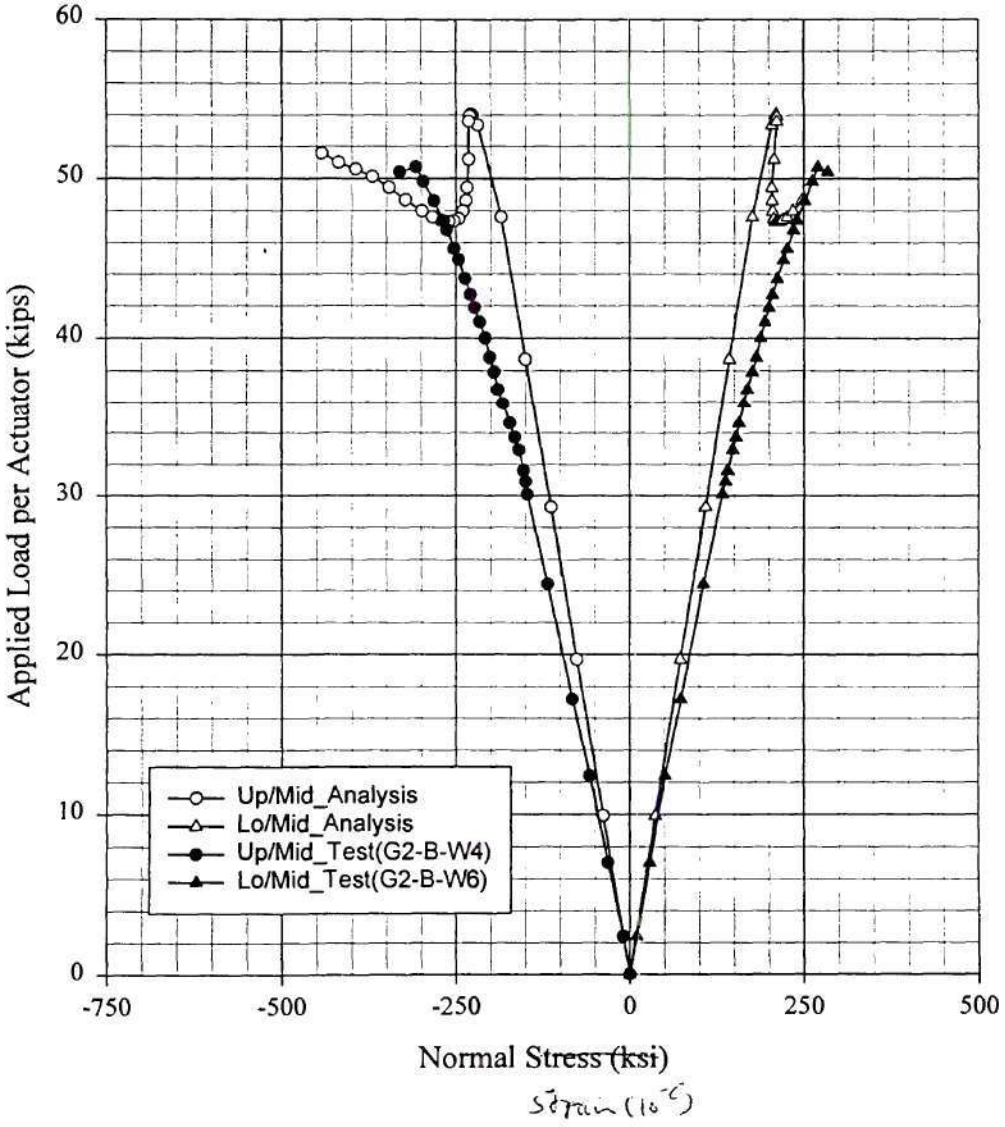

Comparison Between Analysis(B1h_3) and Test(4-2-99) for B1
Normal Strain of the Top Flange Topside at the Location G2_B

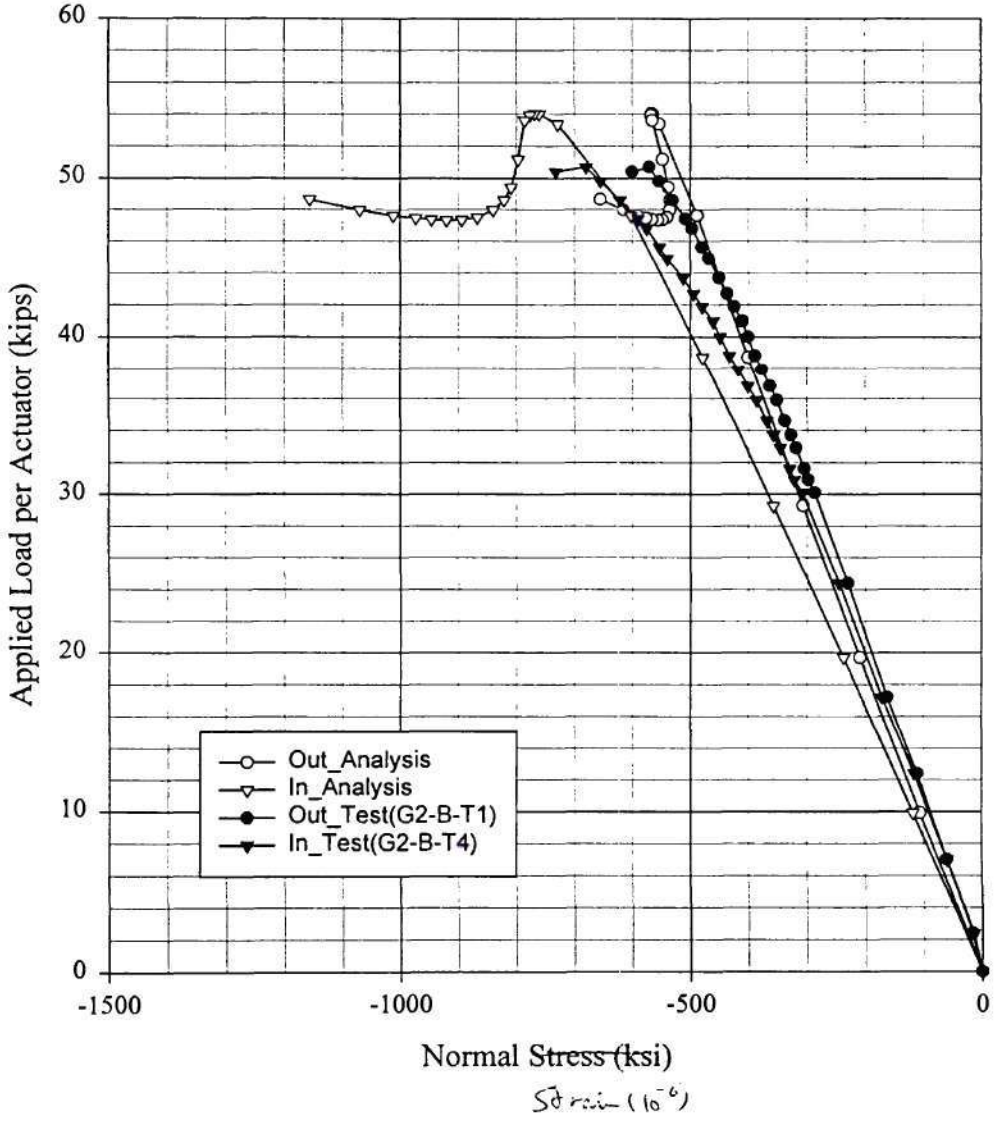

Comparison Between Analysis(B1h_3) and Test(4-2-99) for B1
Normal Strain of the Top Flange Btmside at the Location G2_B

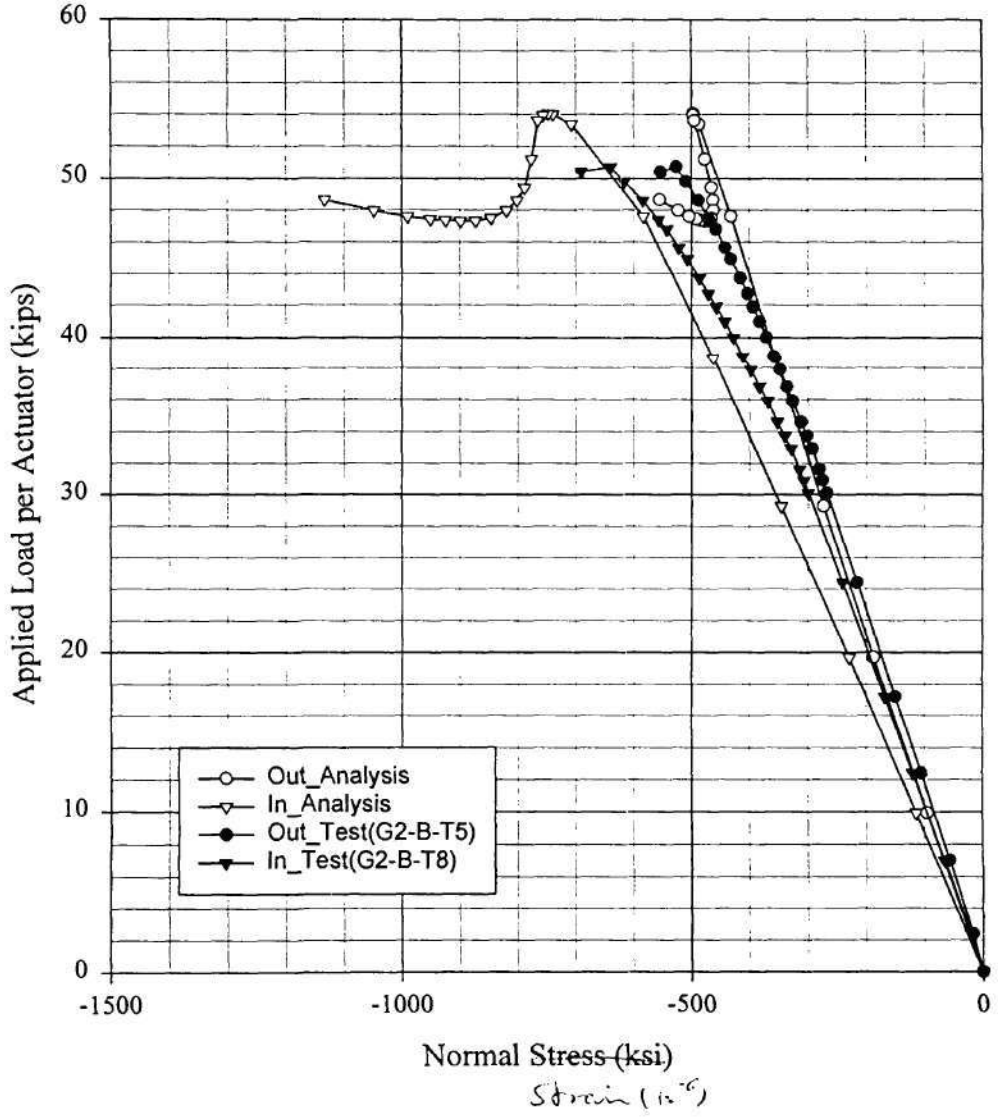

Comparison Between Analysis(B1h_3) and Test(4-2-99) for B1
Normal Strain of the Btm Flange Topside at the Location G2_B

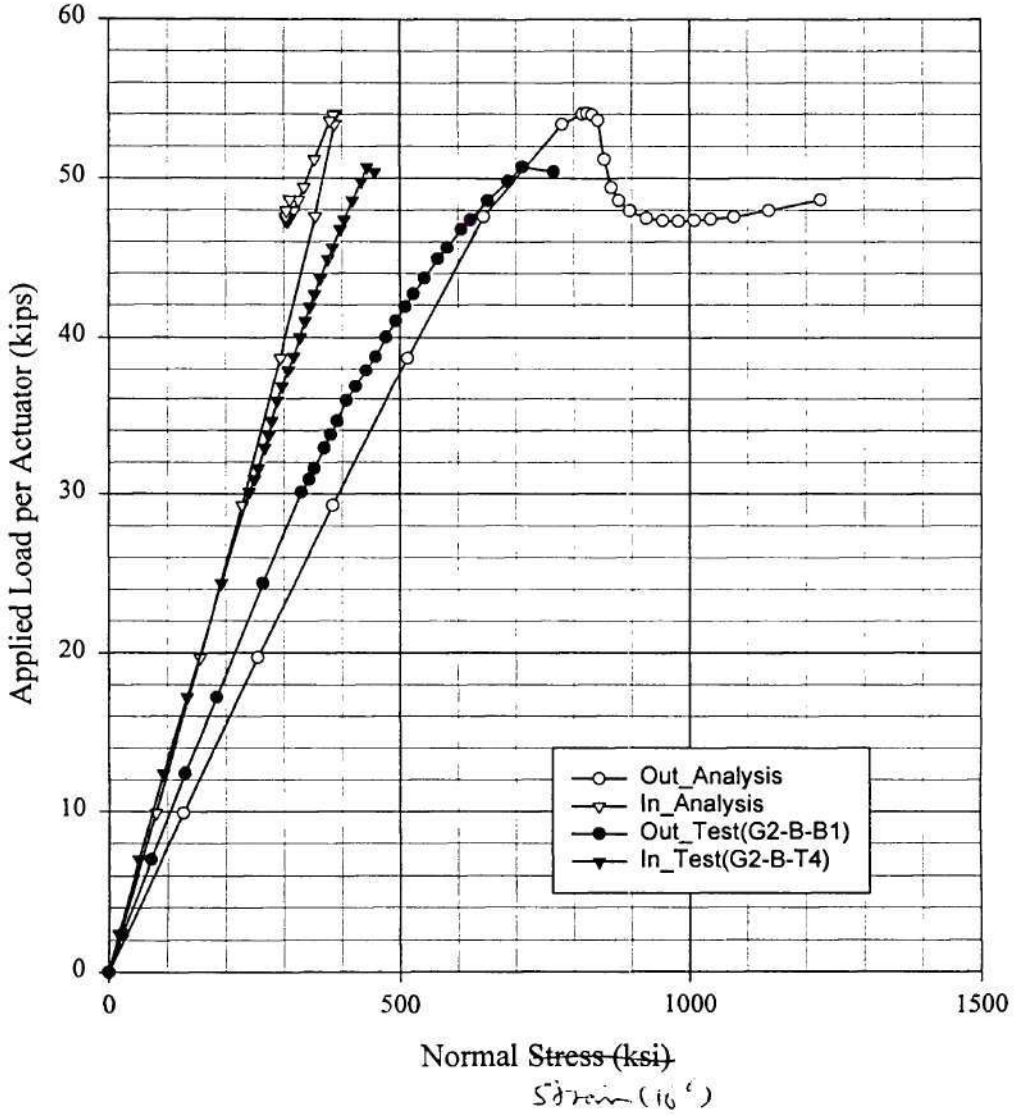

Comparison Between Analysis(B1h_3) and Test(4-2-99) for B1
Normal Strain of the Btm Flange Btmside at the Location G2_B

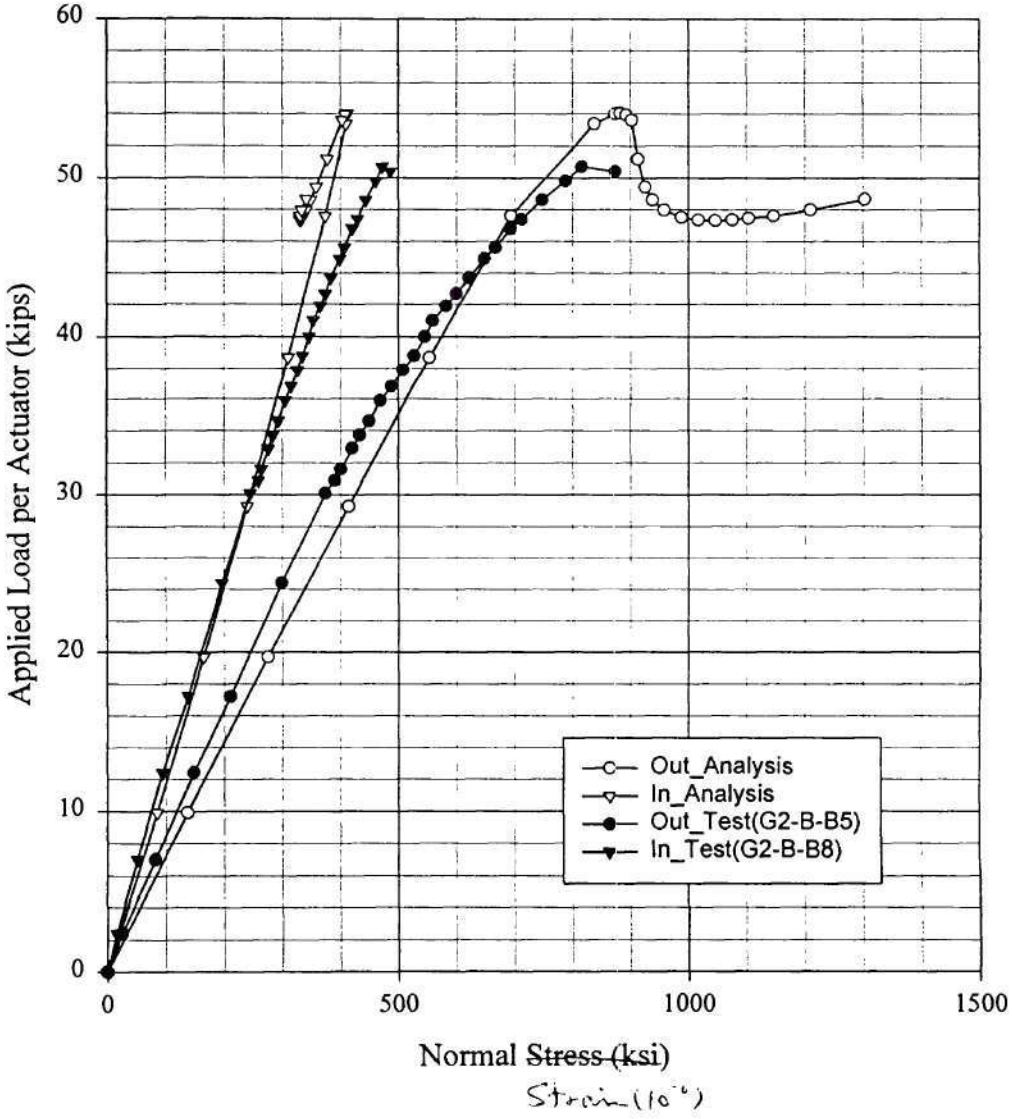

Comparison Between Analysis(B1h_3) and Test(4-2-99) for B1
Normal Strain of the Web Inside at the Location G3_E

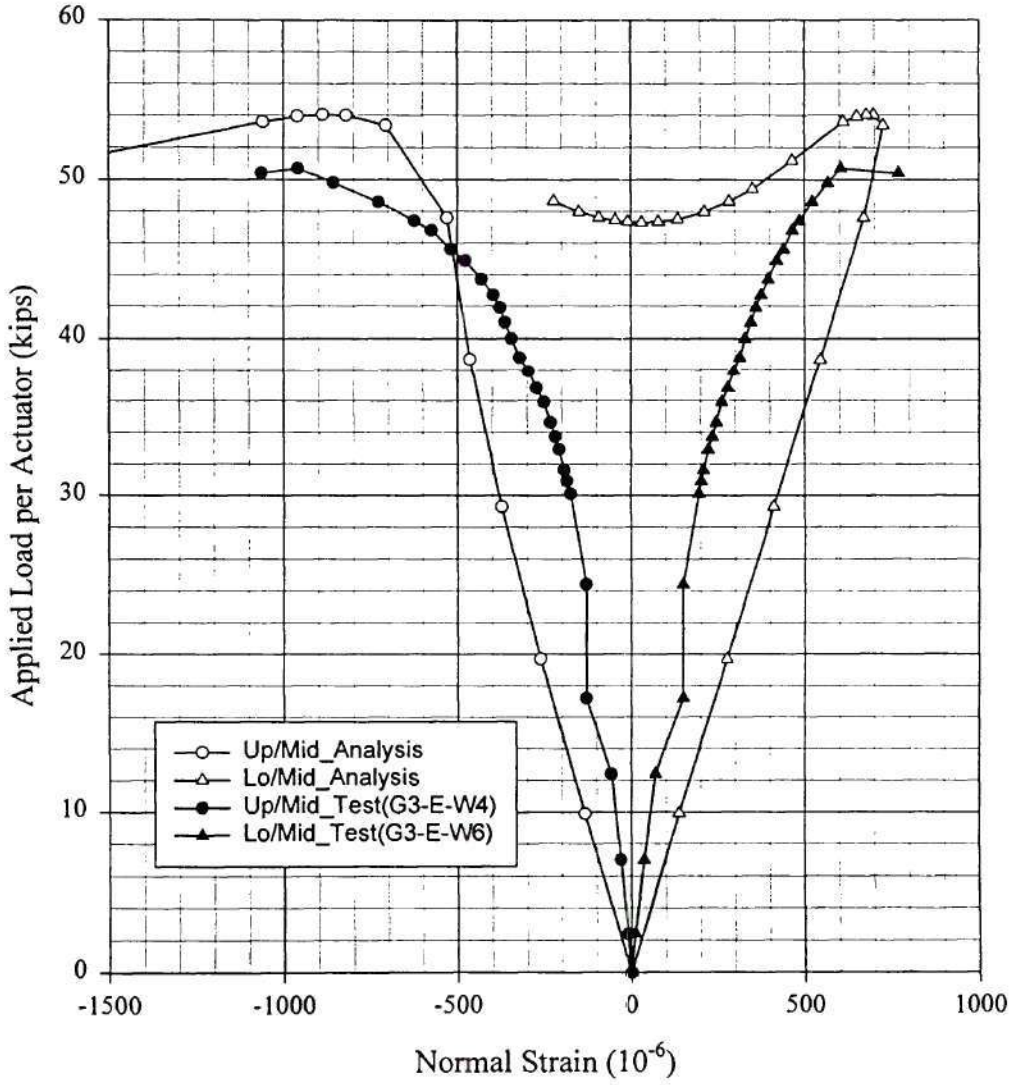

Comparison Between Analysis(B1h_3) and Test(4-2-99) for B1
Normal Strain of the Web Outside at the Location G3_E

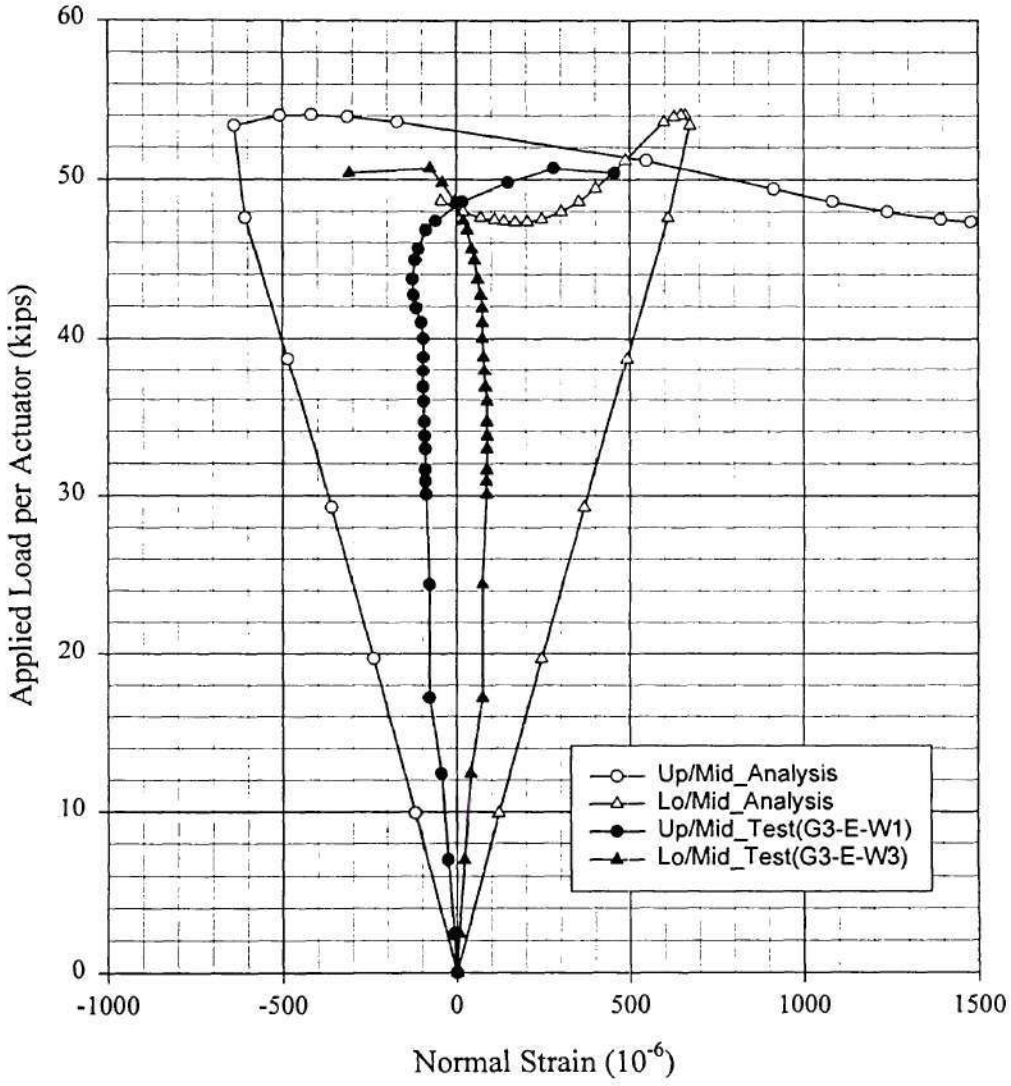

Comparison Between Analysis(B1h_3) and Test(4-2-99) for B1
Normal Strain of the Top Flange Topside at the Location G3_E

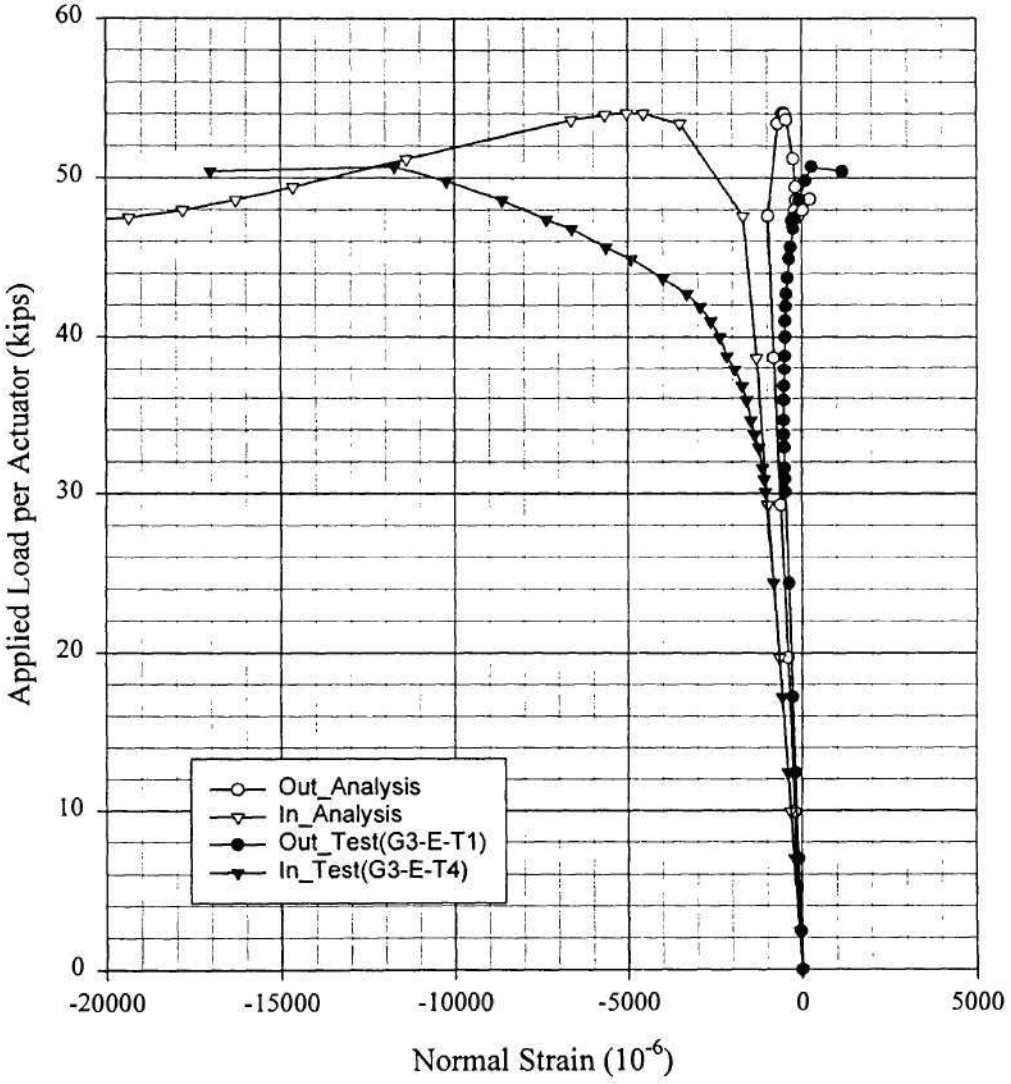

Comparison Between Analysis(B1h_3) and Test(4-2-99) for B1
Normal Strain of the Top Flange Btmside at the Location G3_E

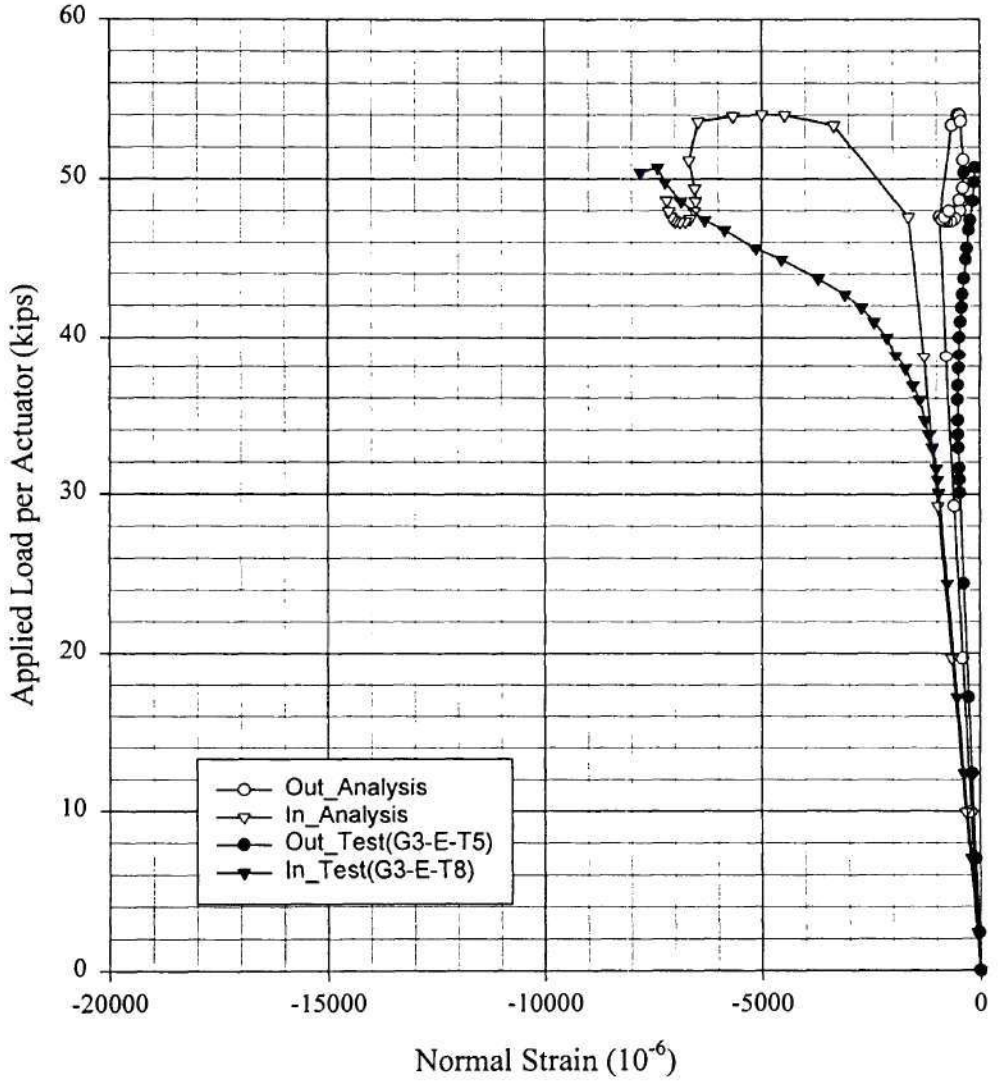

Comparison Between Analysis(B1h_3) and Test(4-2-99) for B1
Normal Strain of the Btm Flange Topside at the Location G3_E

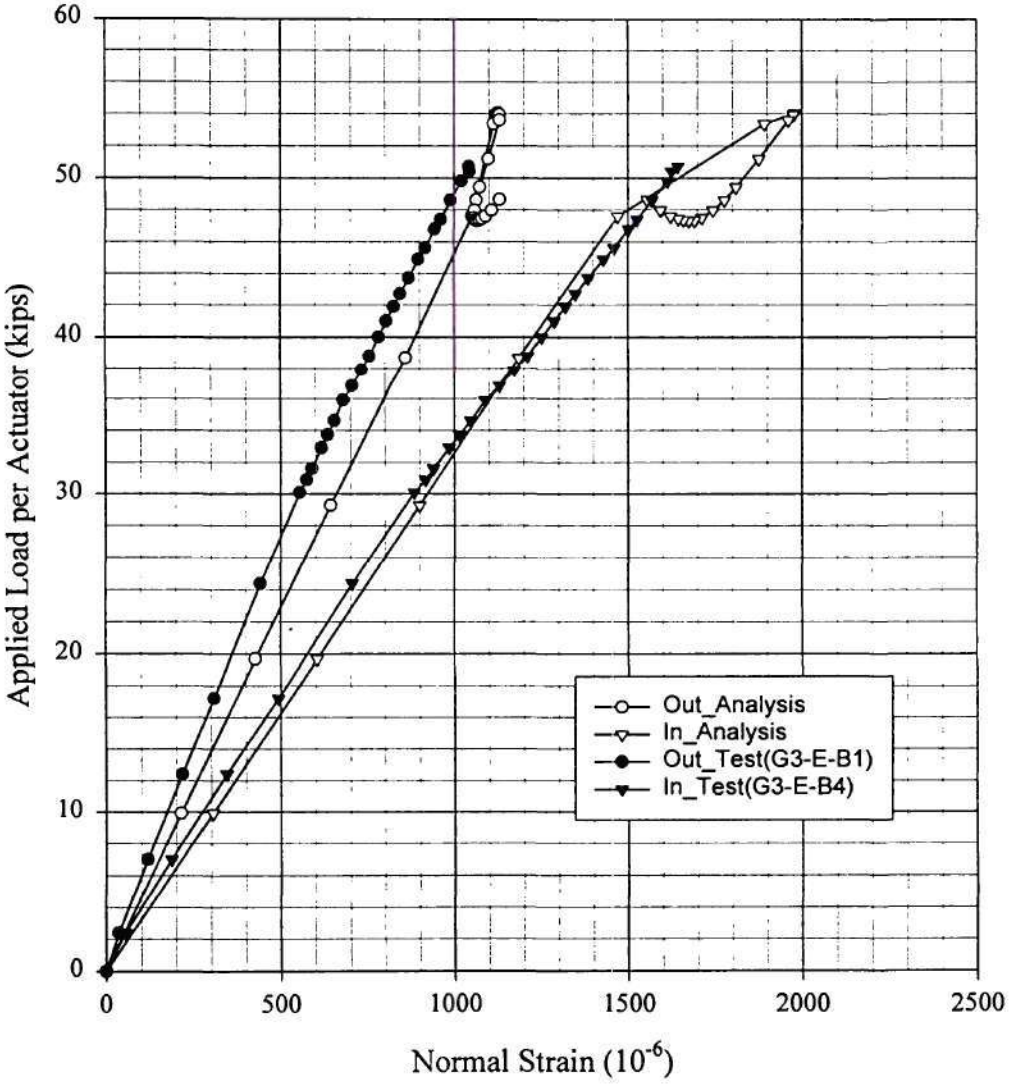

Comparison Between Analysis(B1h_3) and Test(4-2-99) for B1
Normal Strain of the Btm Flange Btmside at the Location G3_E

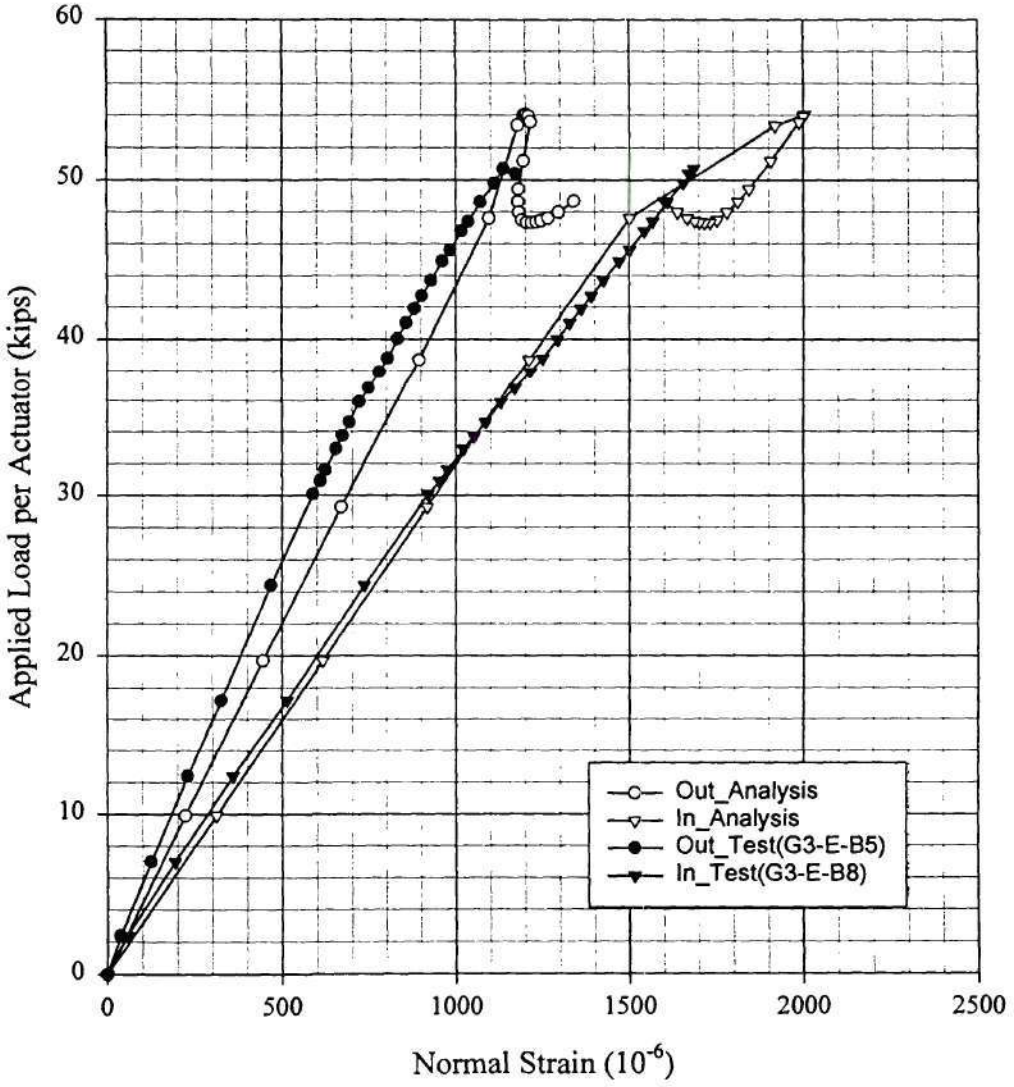

Test(4-2-99) for B1
Normal Strain of the Web at the Location G3_E

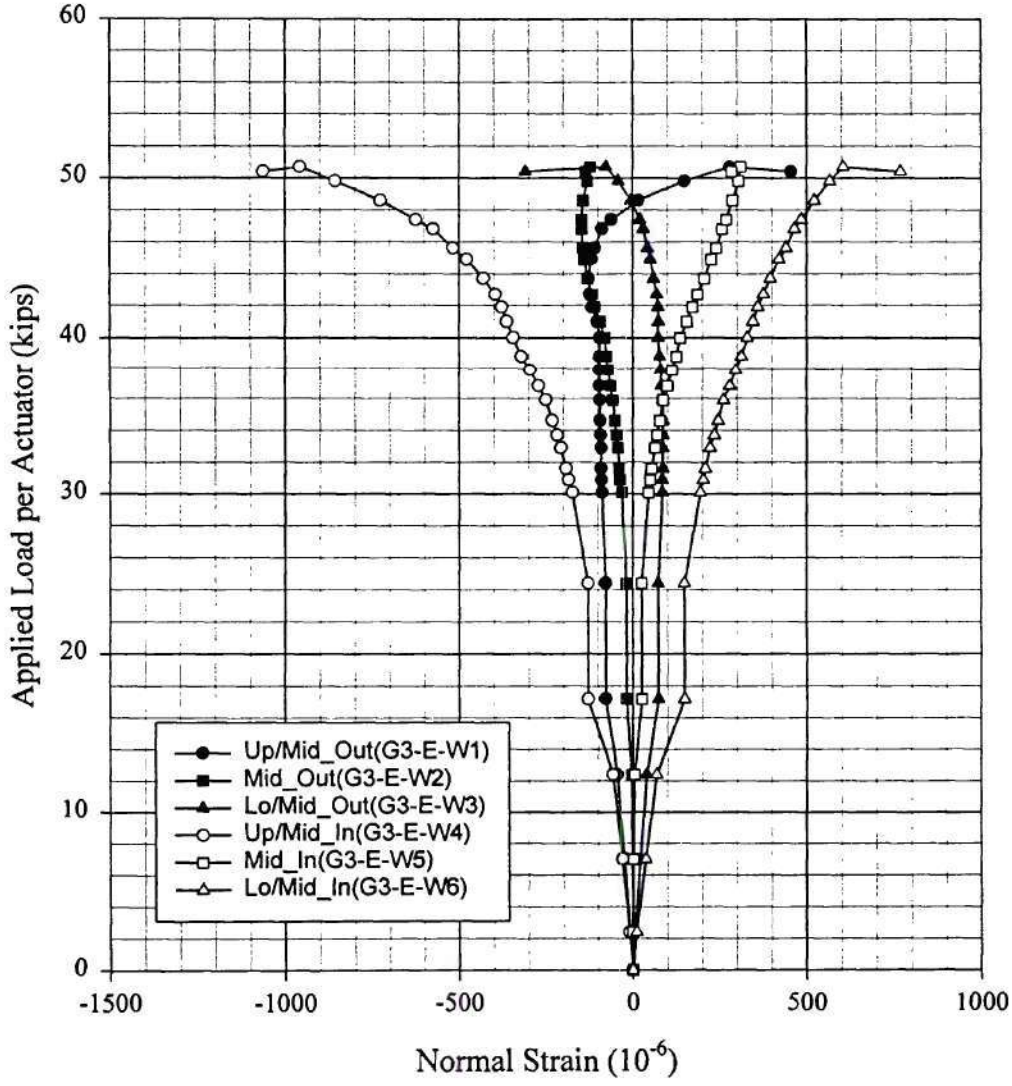

Test(4-2-99) for B1
Normal Strain of the Top Flange at the Location G3_E

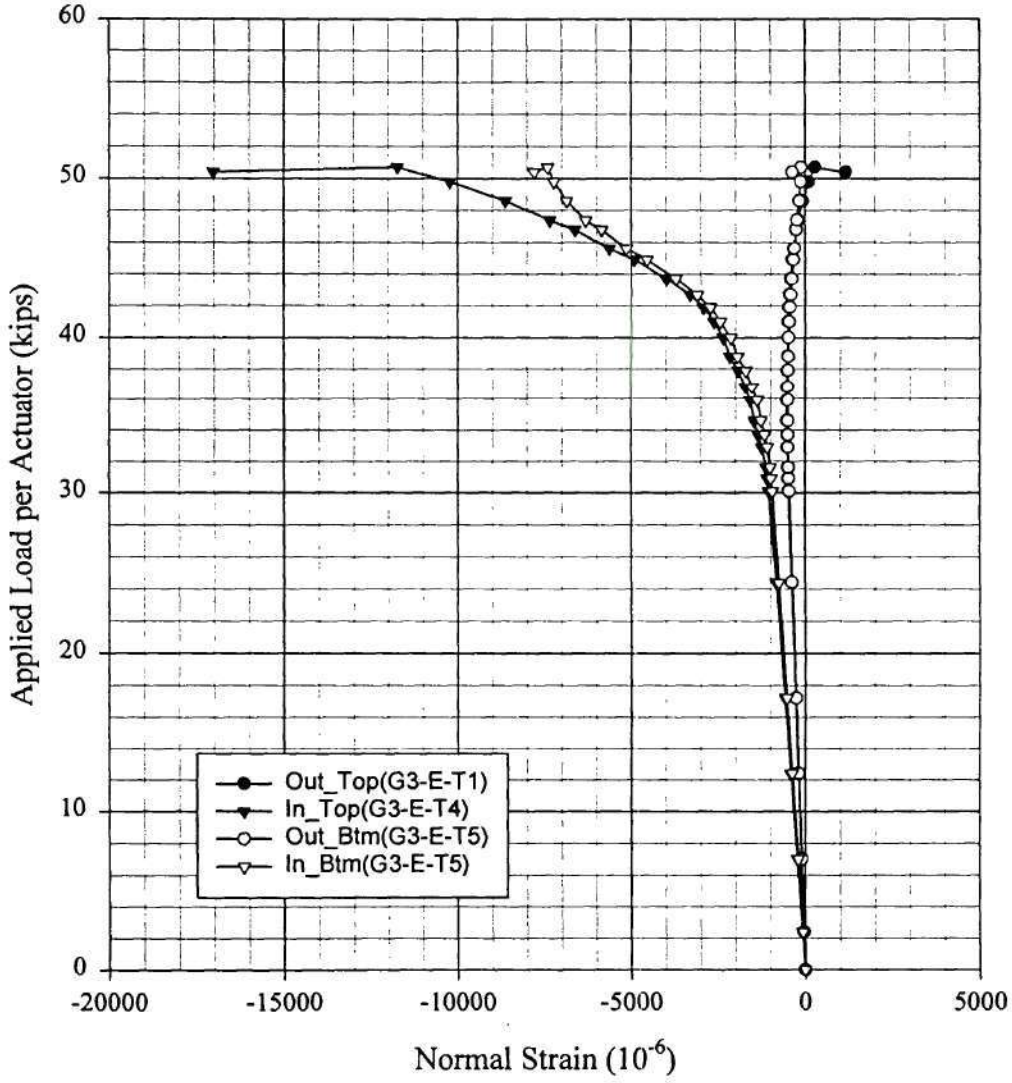

Test(4-2-99) for B1
Normal Strain of the Bottom Flange at the Location G3_E

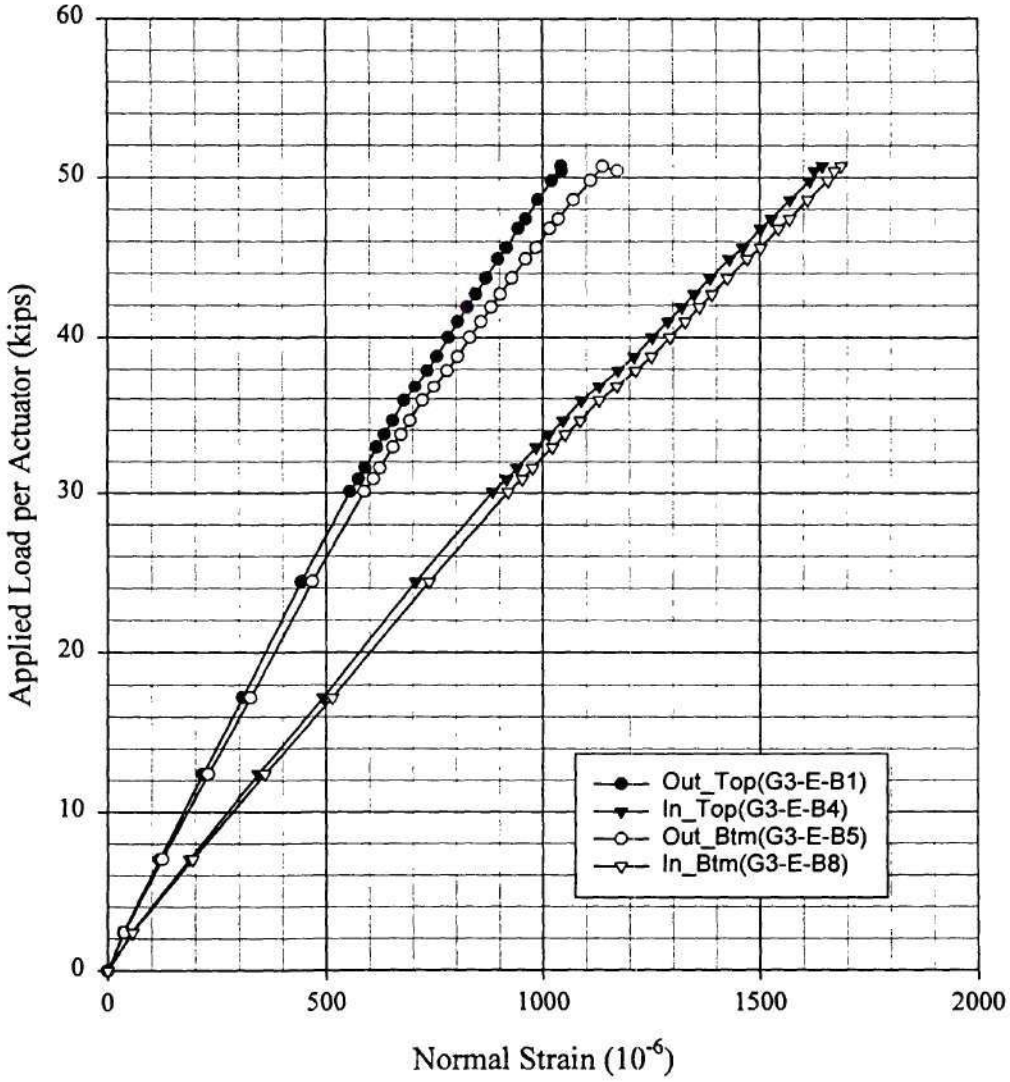

Comparison Between Analysis(B2h_3) and Test(5-21-99) for B2
Vertical Reactions at the East Supports

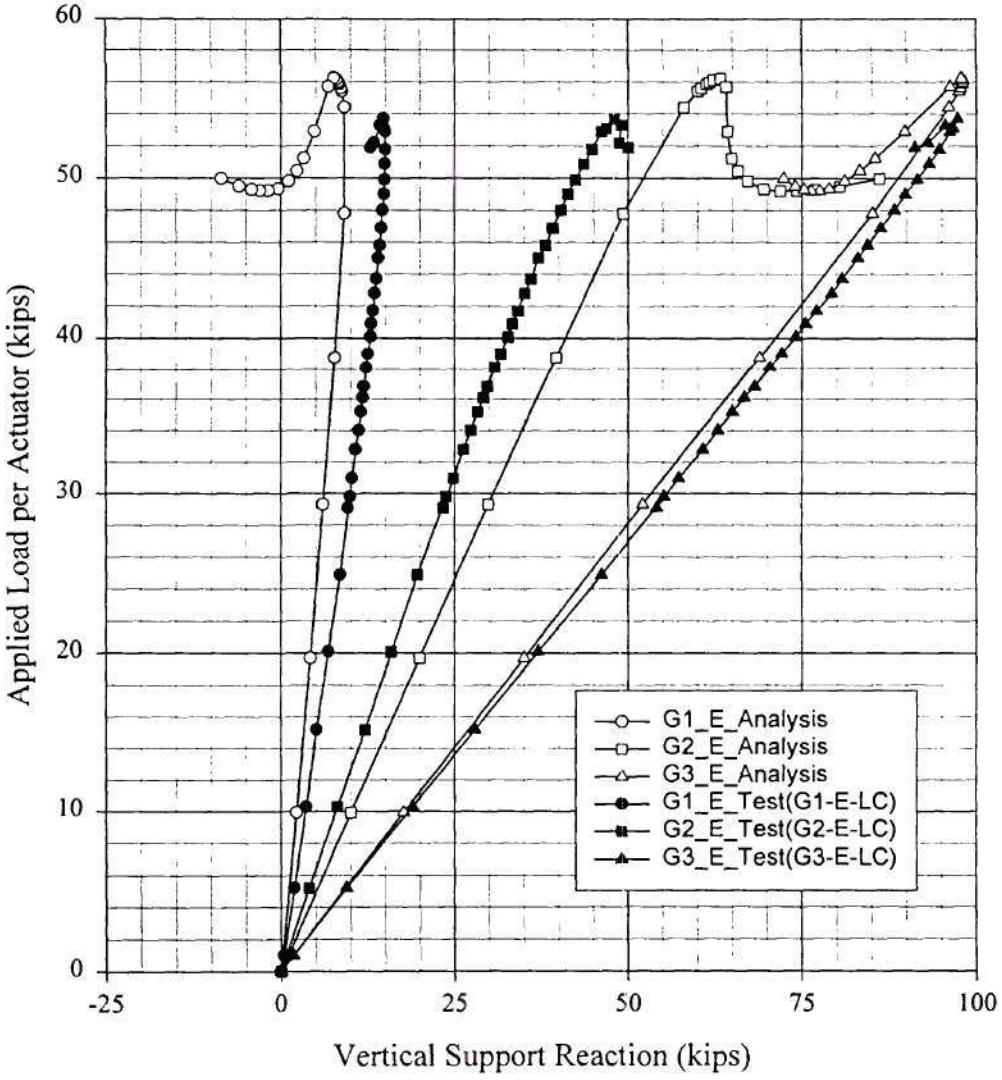

Comparison Between Analysis(B2h_3) and Test(5-21-99) for B2
Vertical Reactions at the West Supports

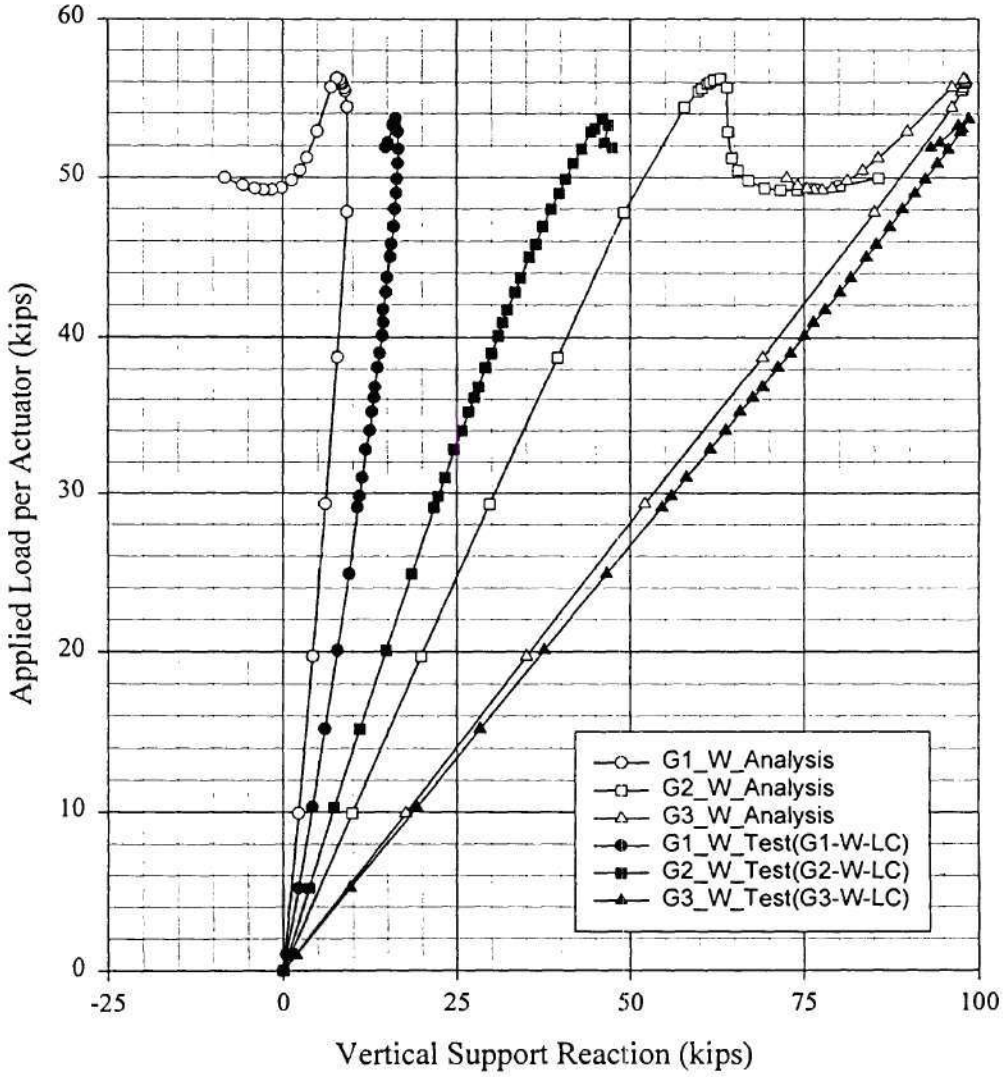

Comparison Between Analysis(B2h_3) and Test(5-21-99) for B2
Vertical Displacement of Bottom Flange (Outside) at Midspan

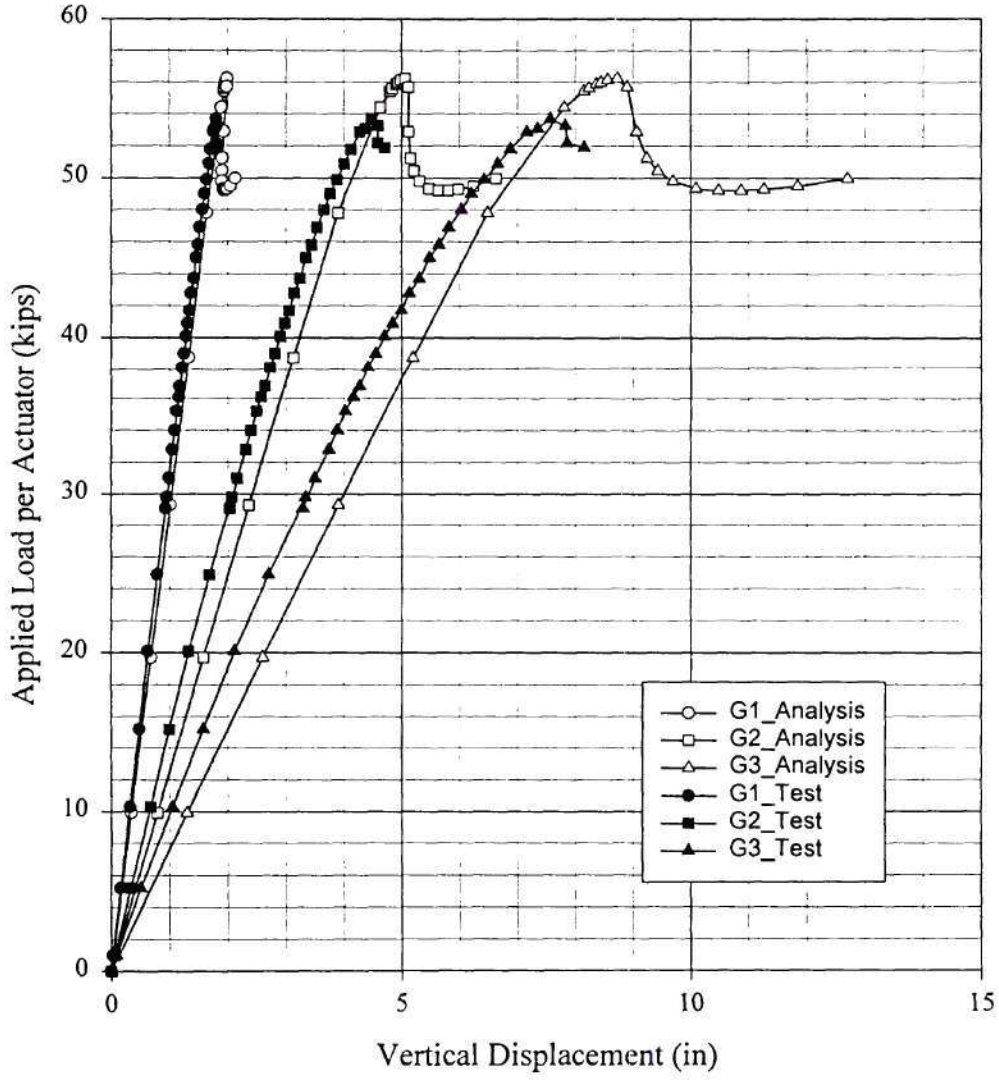

Comparison Between Analysis(B2h_3) and Test(5-21-99) for B2
Radial Displacement of Top Flange (Outside) at Midspan

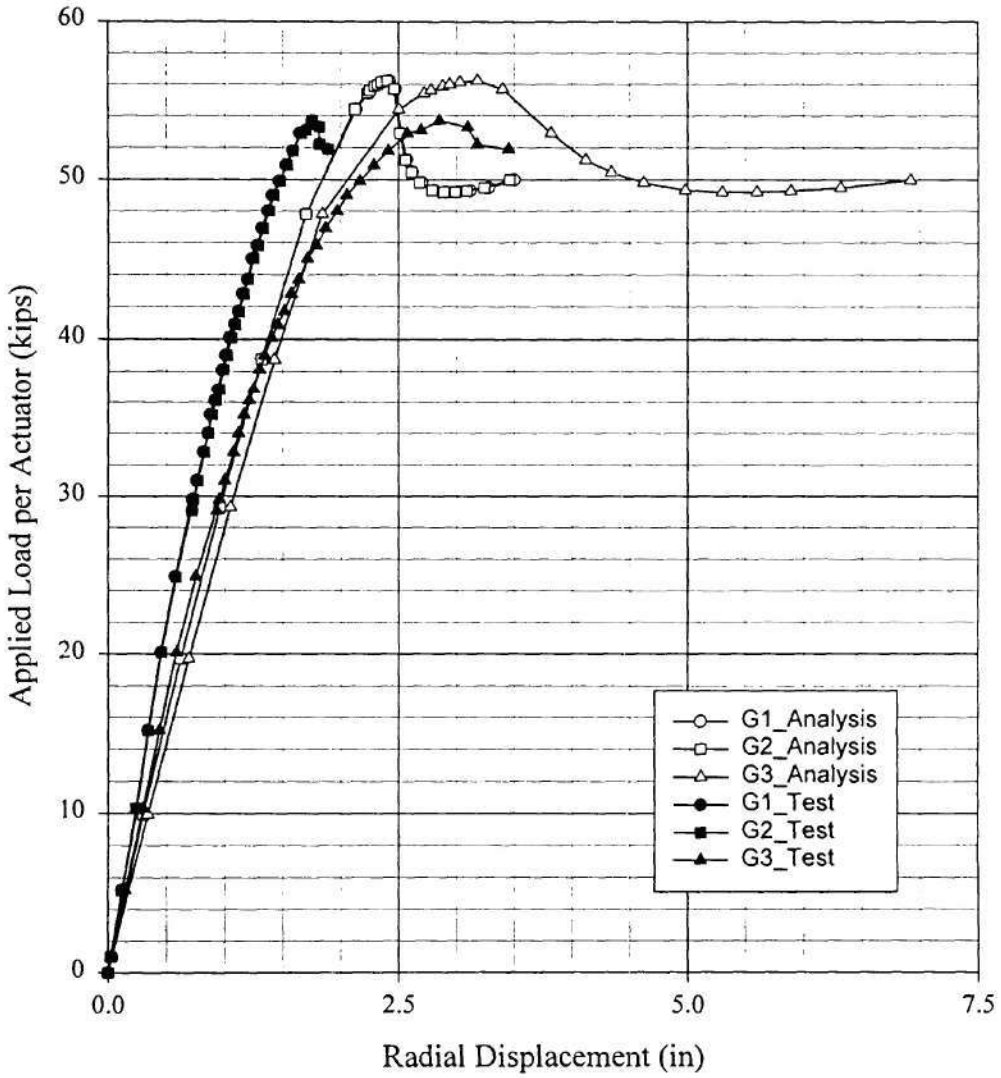

Comparison Between Analysis(B2h_3) and Test(5-21-99) for B2
Radial Displacement of Bottom Flange (Outside) at Midspan

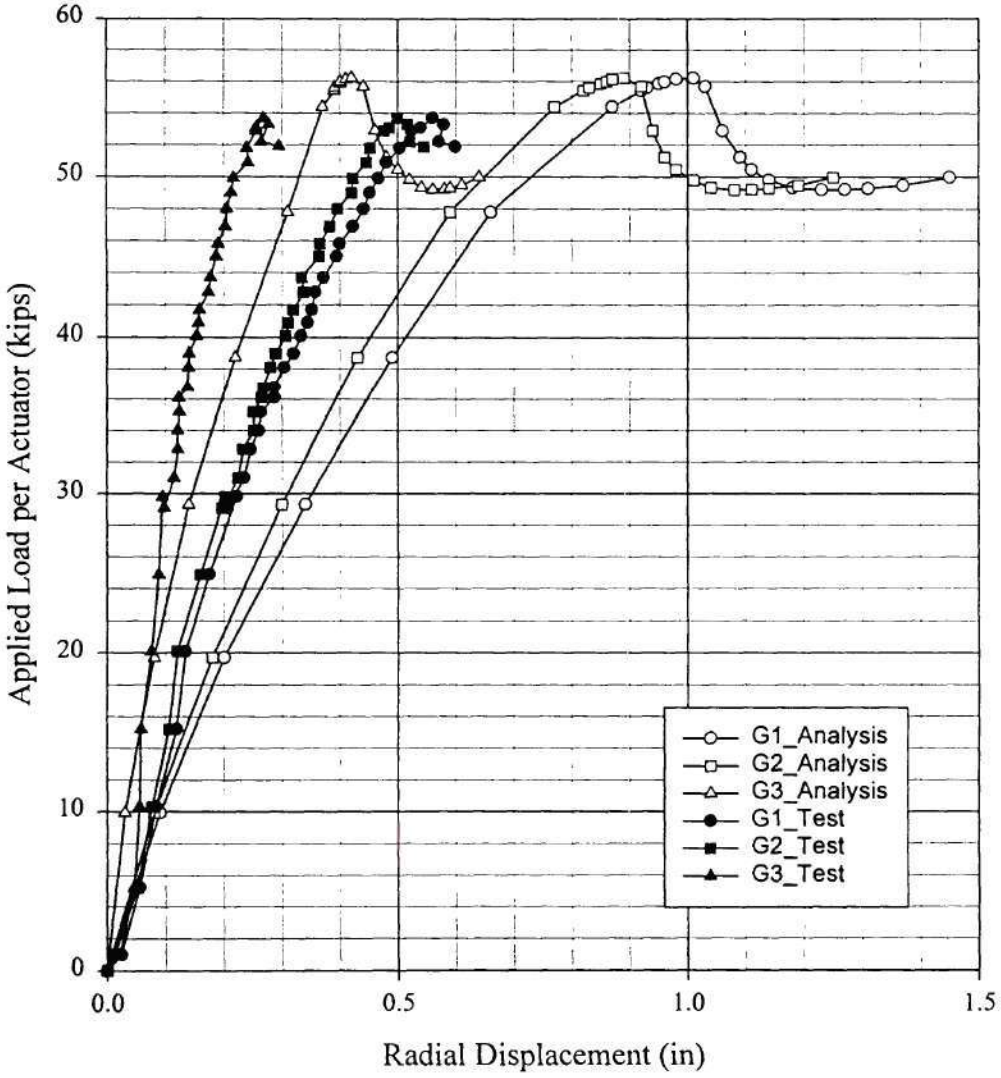

Comparison Between Analysis(B2h_3) and Test(5-21-99) for B2
Axial Force of Cross Frame at 6R Between G2 and G3

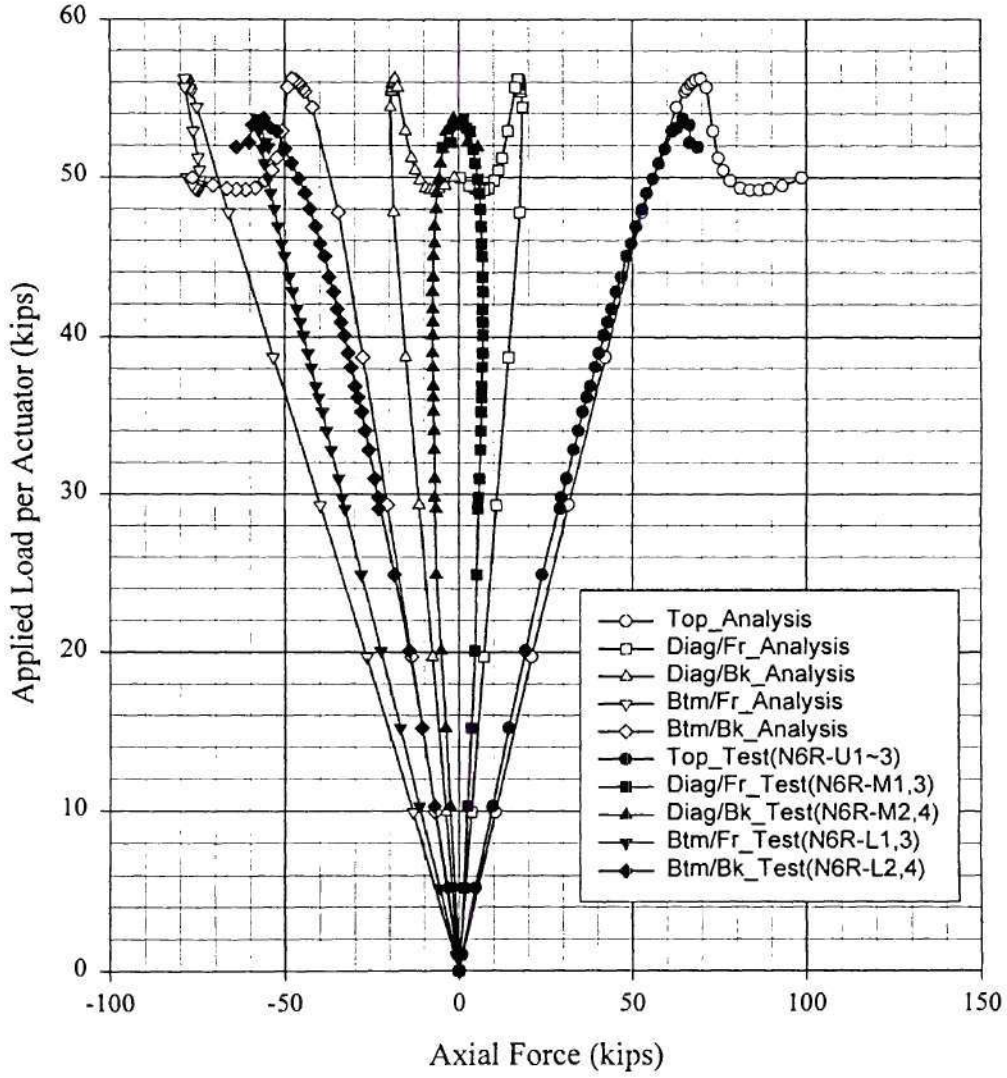

Comparison Between Analysis(B2h_3) and Test(5-21-99) for B2
Axial Force of Cross Frame at 6L Between G2 and G3

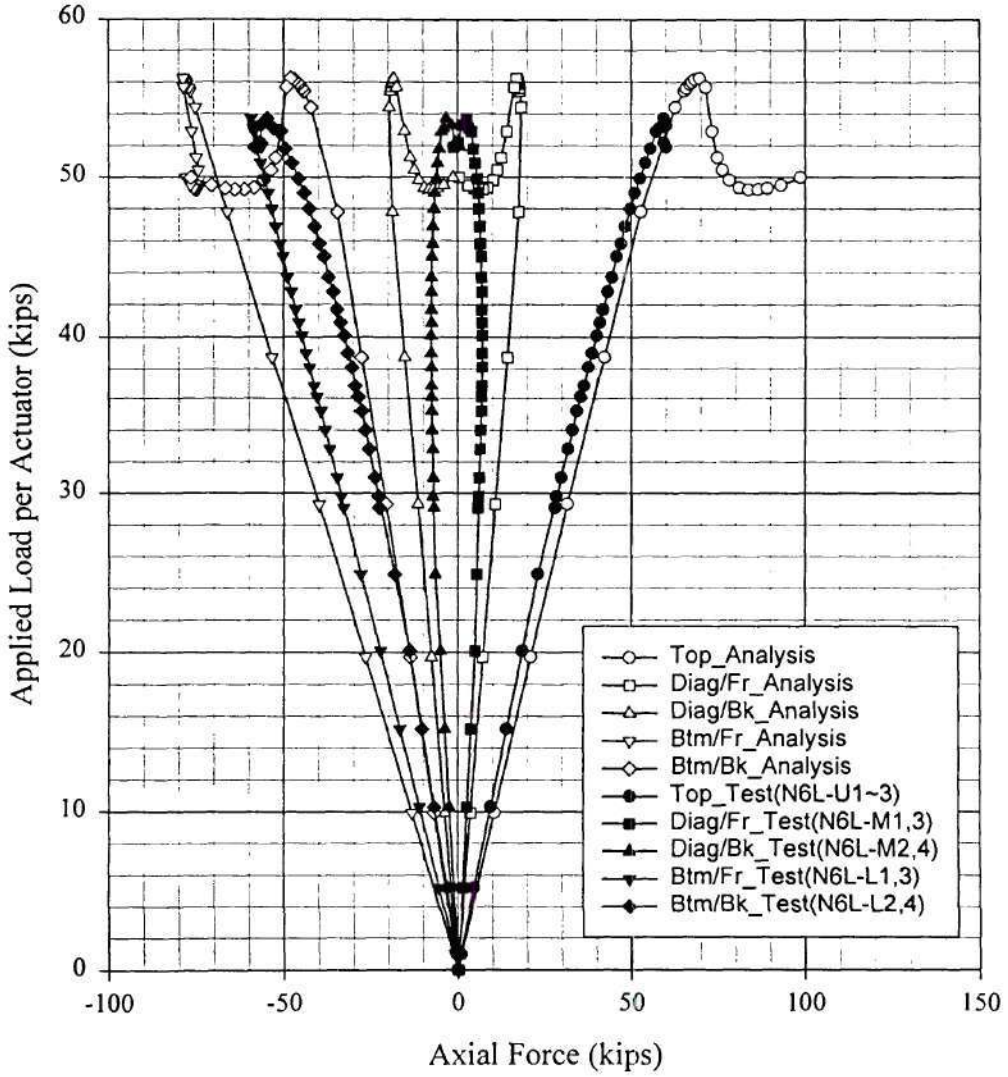

Comparison Between Analysis(B2h_3) and Test(5-21-99) for B2
Bending Moment at Midspan

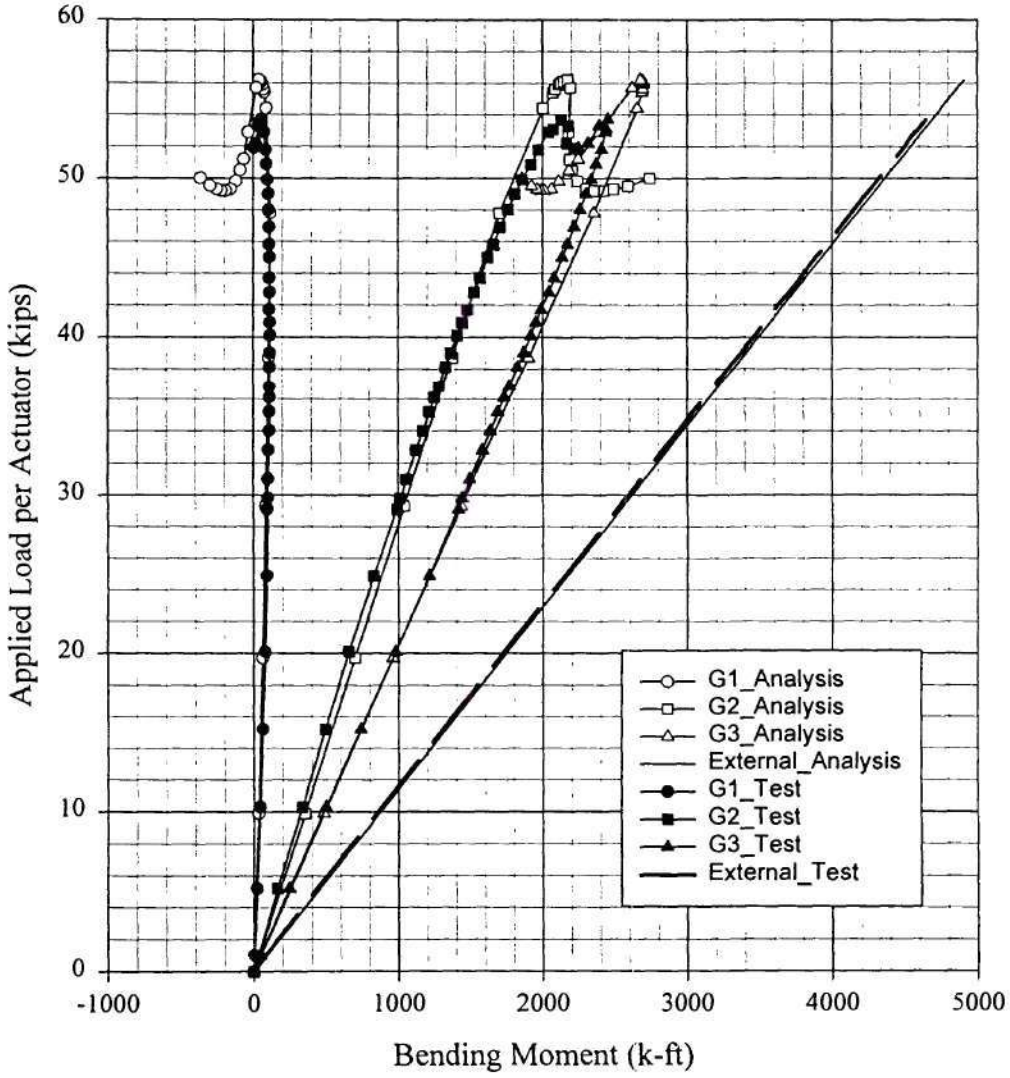

Comparison Between Analysis(B2h_3) and Test(5-21-99) for B2
Normal Strain of the Web Inside at the Location G1_B

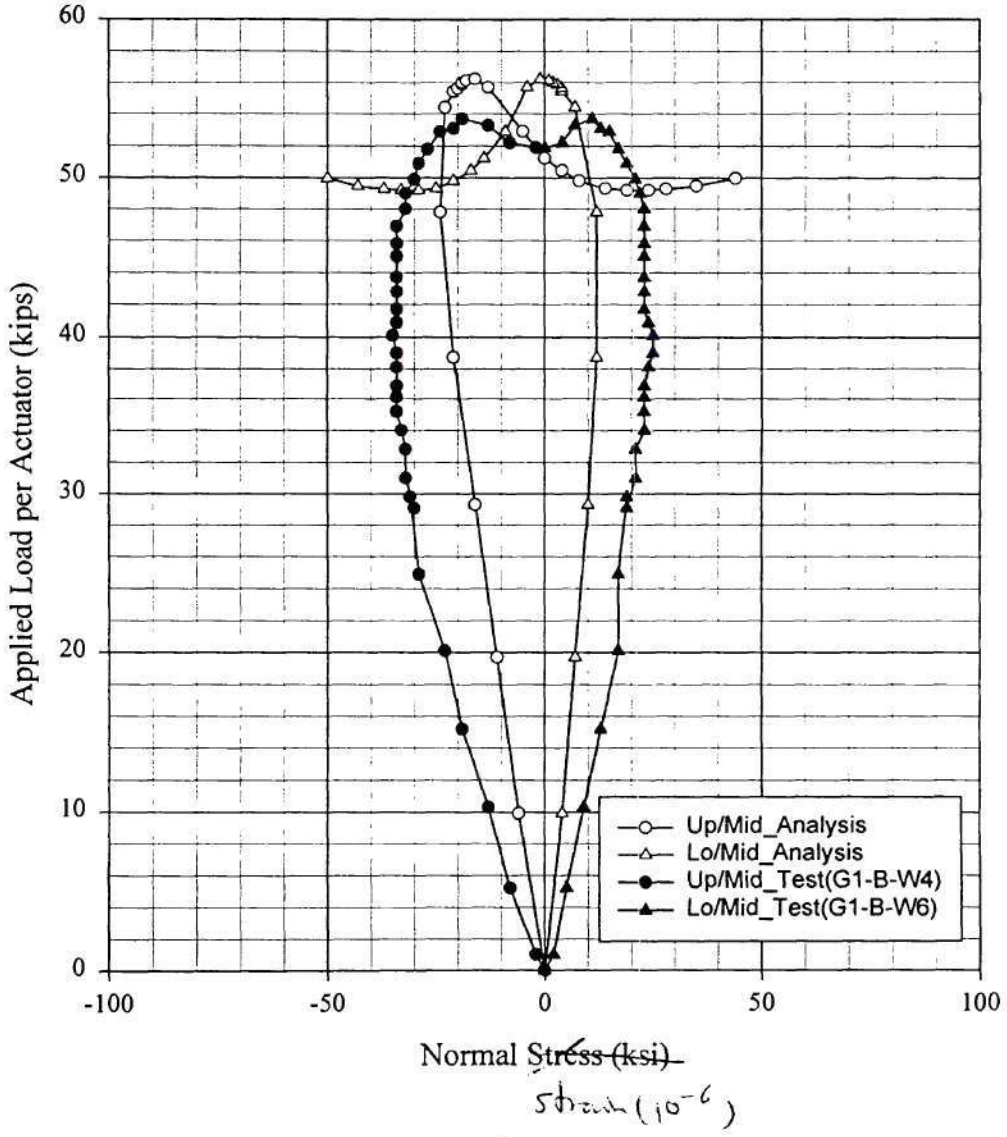

Comparison Between Analysis(B2h_3) and Test(5-21-99) for B2
Normal Strain of the Top Flange Topside at the Location G1_B

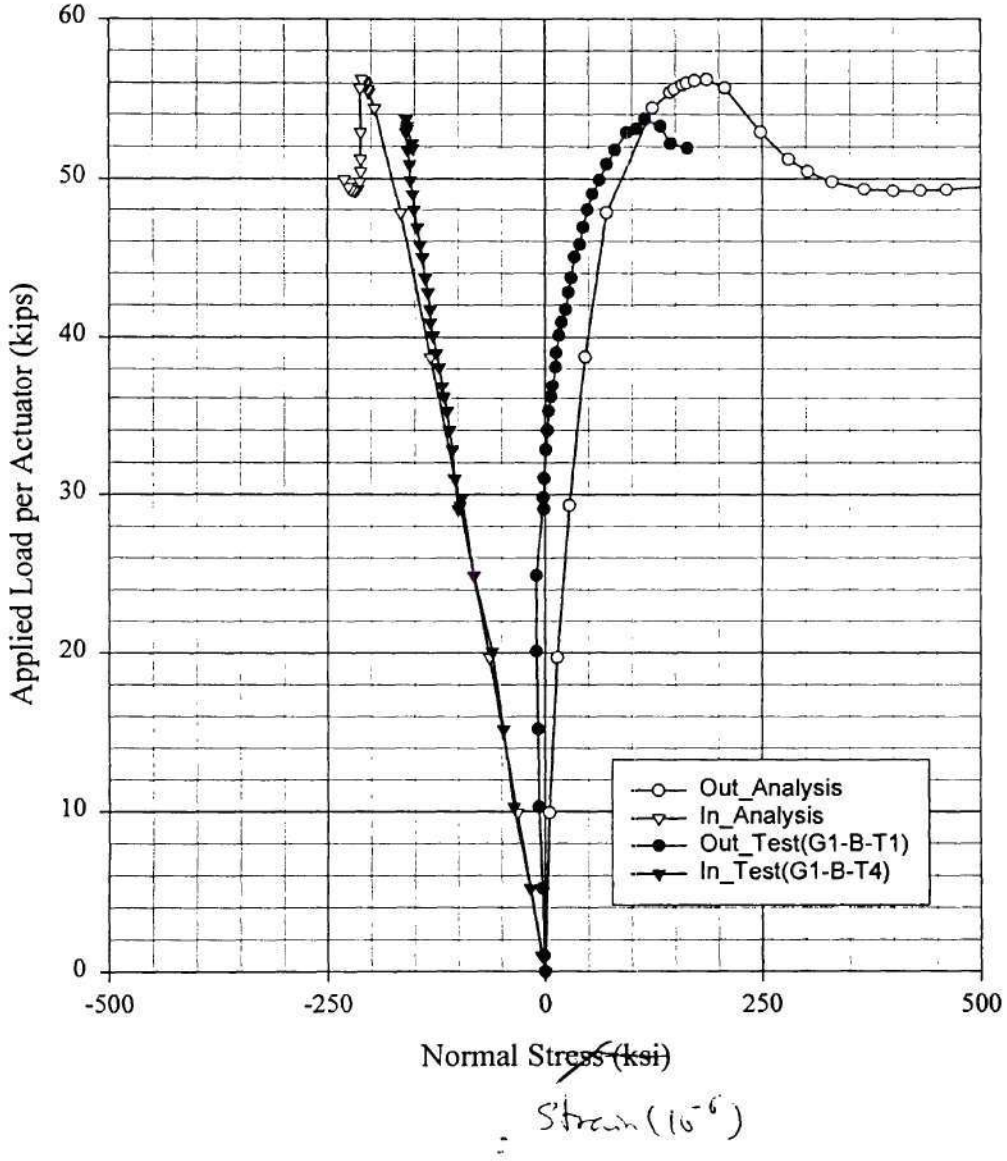

Comparison Between Analysis(B2h_3) and Test(5-21-99) for B2
Normal Strain of the Top Flange Btmside at the Location G1_B

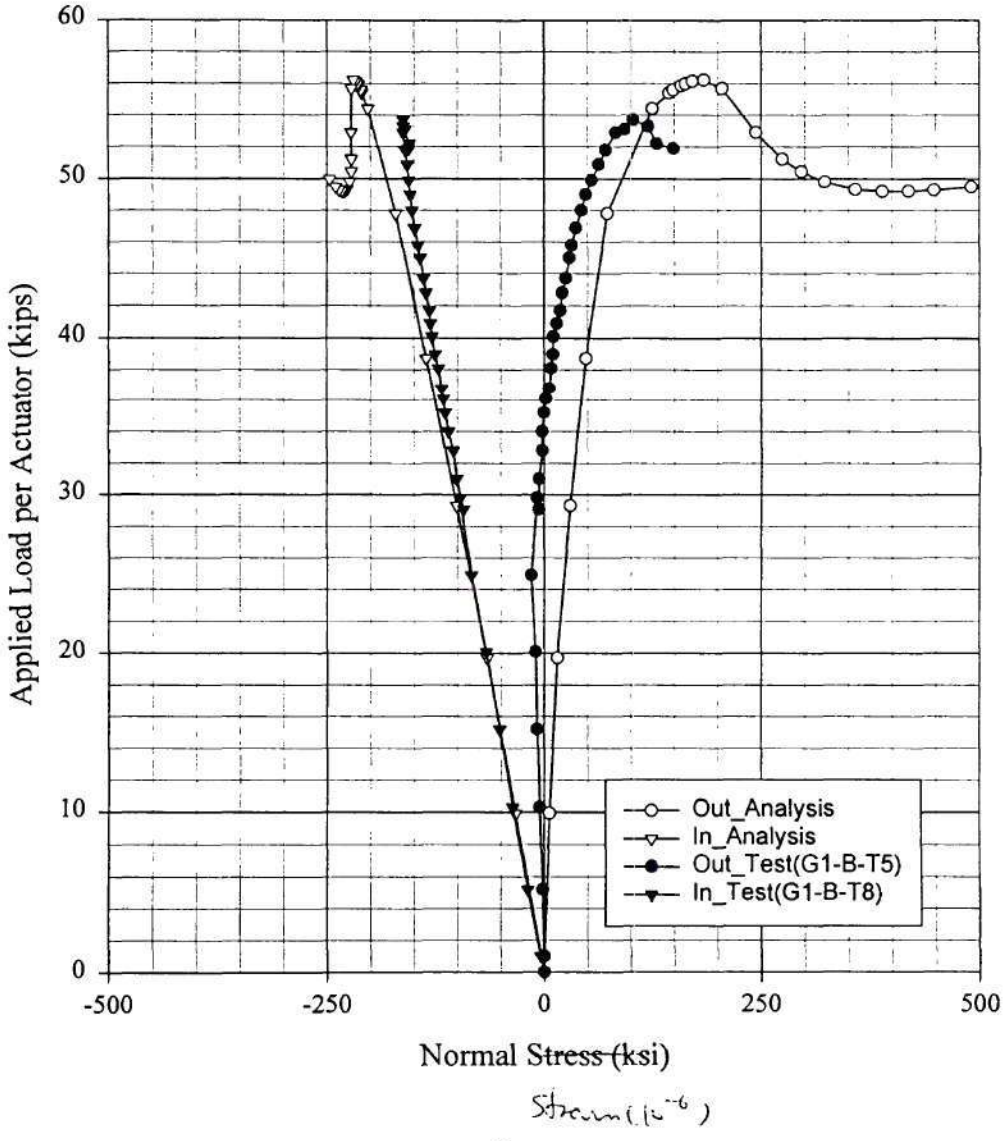

Comparison Between Analysis(B2h_3) and Test(5-21-99) for B2
Normal Strain of the Btm Flange Topside at the Location G1_B

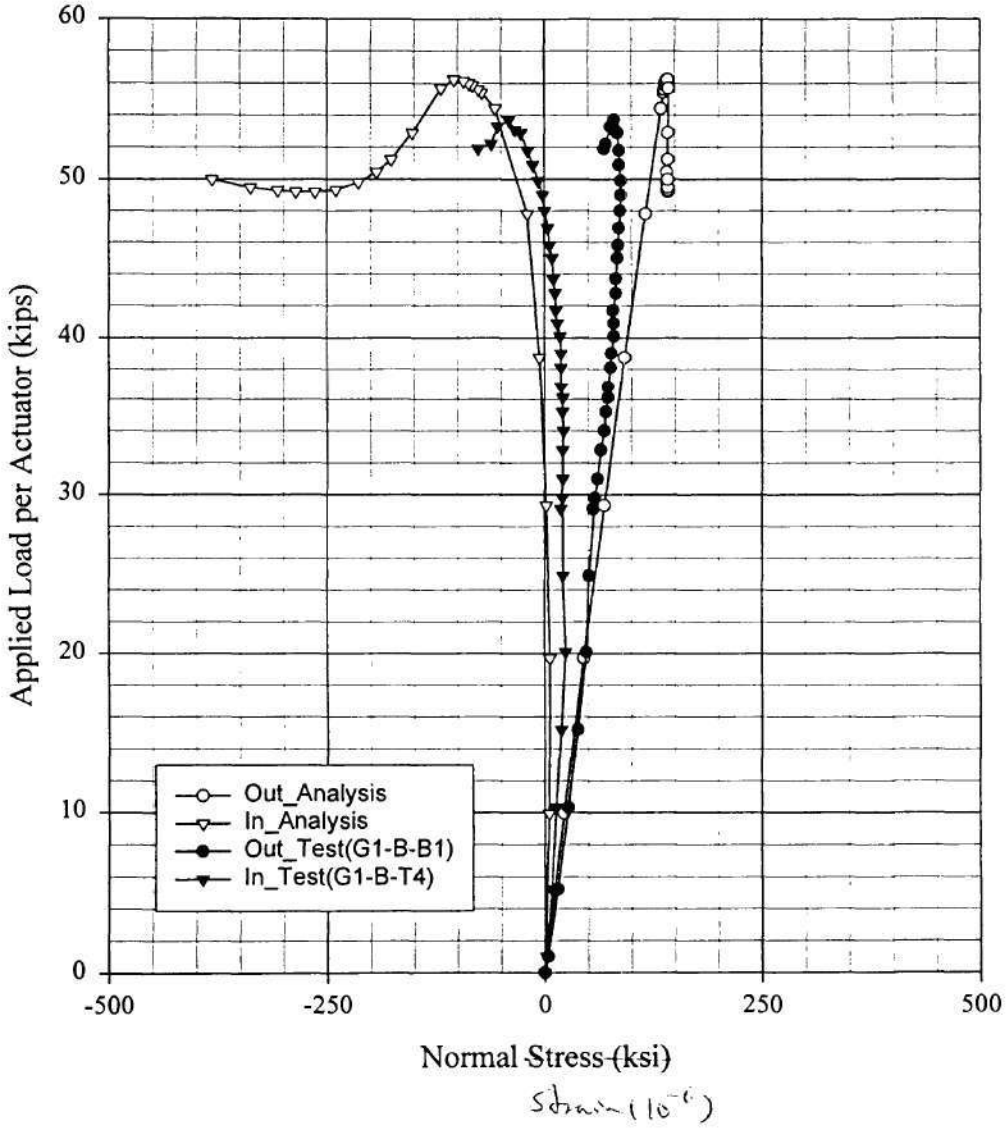

Comparison Between Analysis(B2h_3) and Test(5-21-99) for B2
Normal Strain of the Btm Flange Btmside at the Location G1_B

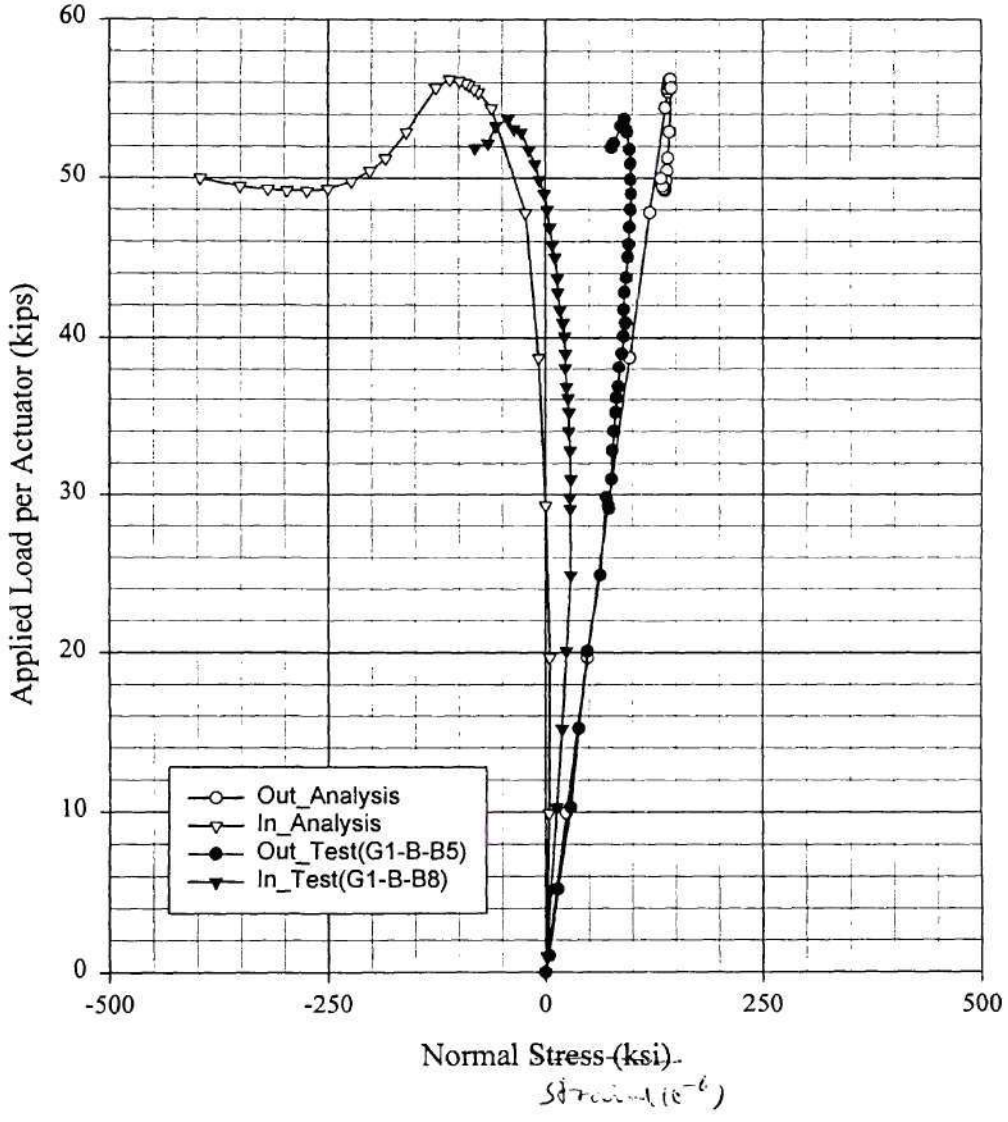

Comparison Between Analysis(B2h_3) and Test(5-21-99) for B2
Normal Strain of the Web Inside at the Location G2_B

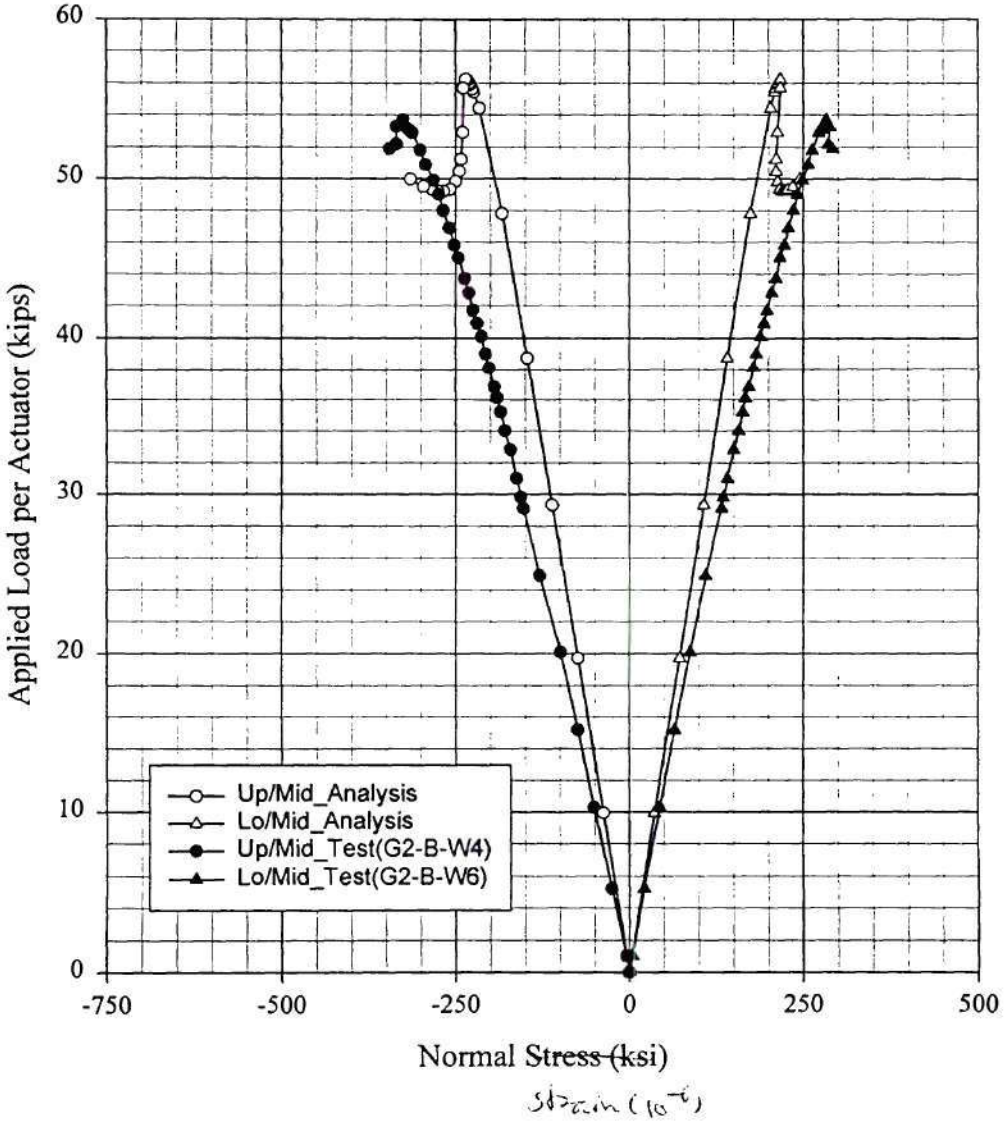

Comparison Between Analysis(B2h_3) and Test(5-21-99) for B2
Normal Strain of the Top Flange Topside at the Location G2_B

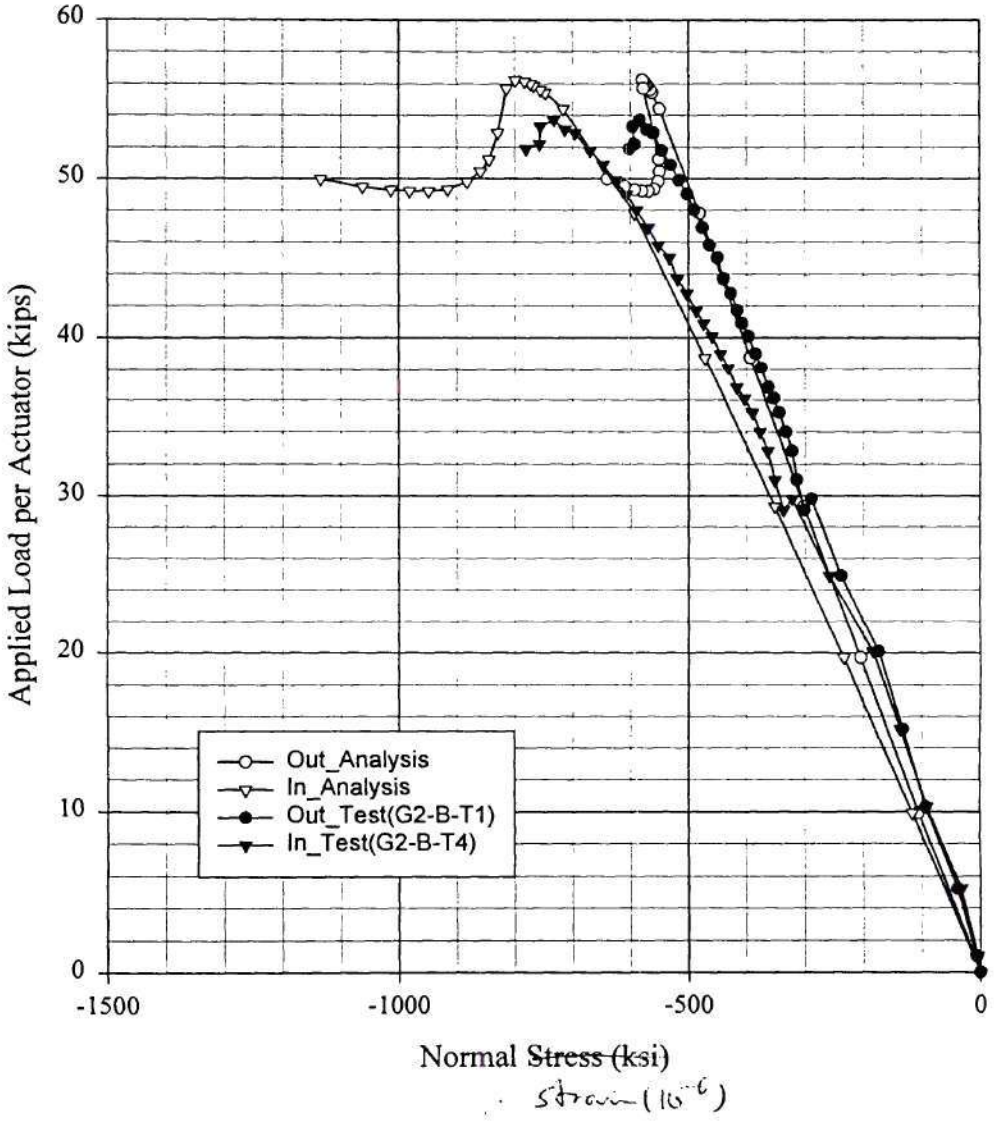

Comparison Between Analysis(B2h_3) and Test(5-21-99) for B2
Normal Strain of the Top Flange Btmside at the Location G2_B

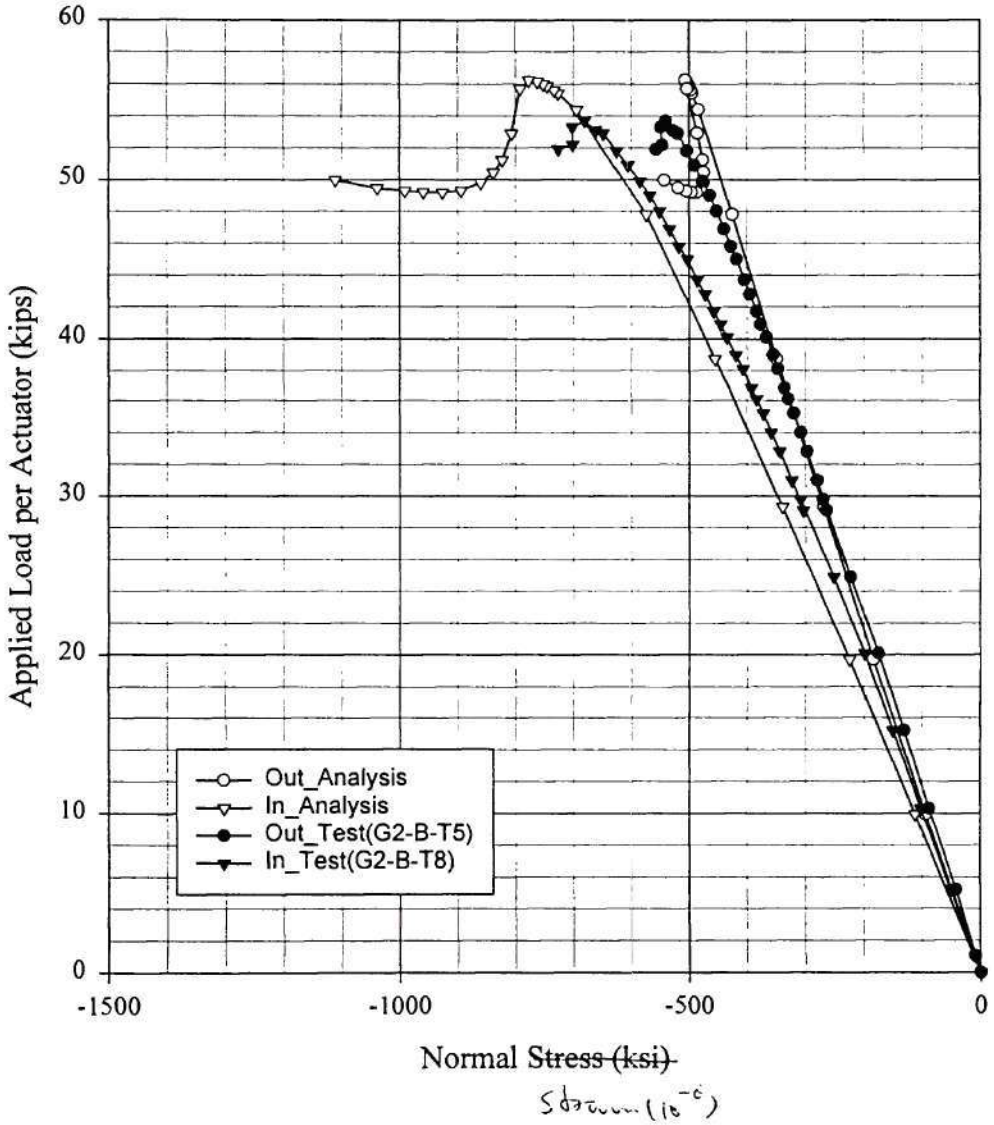

Comparison Between Analysis(B2h_3) and Test(5-21-99) for B2
Normal Strain of the Btm Flange Topside at the Location G2_B

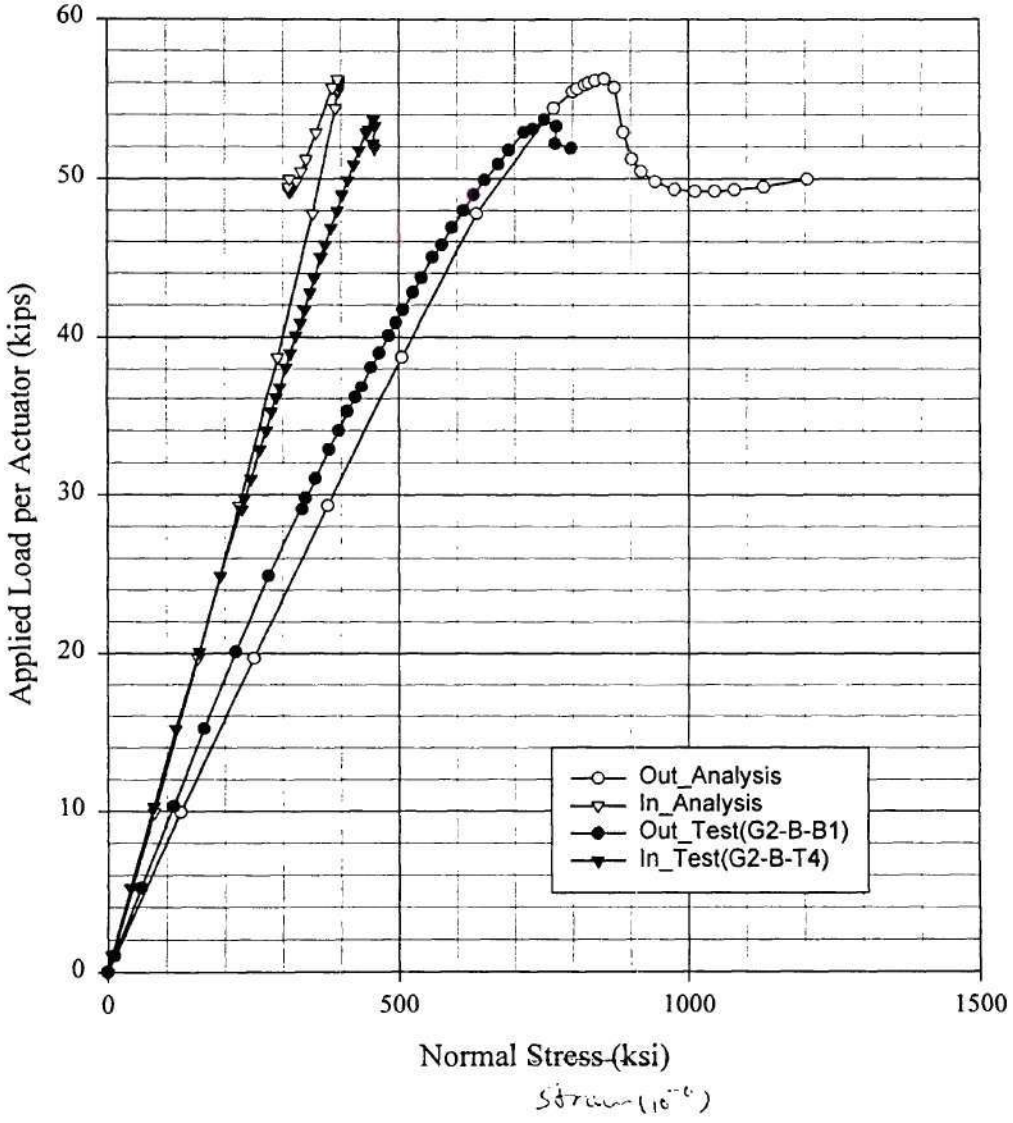

Comparison Between Analysis(B2h_3) and Test(5-21-99) for B2
Normal Strain of the Btm Flange Btmside at the Location G2_B

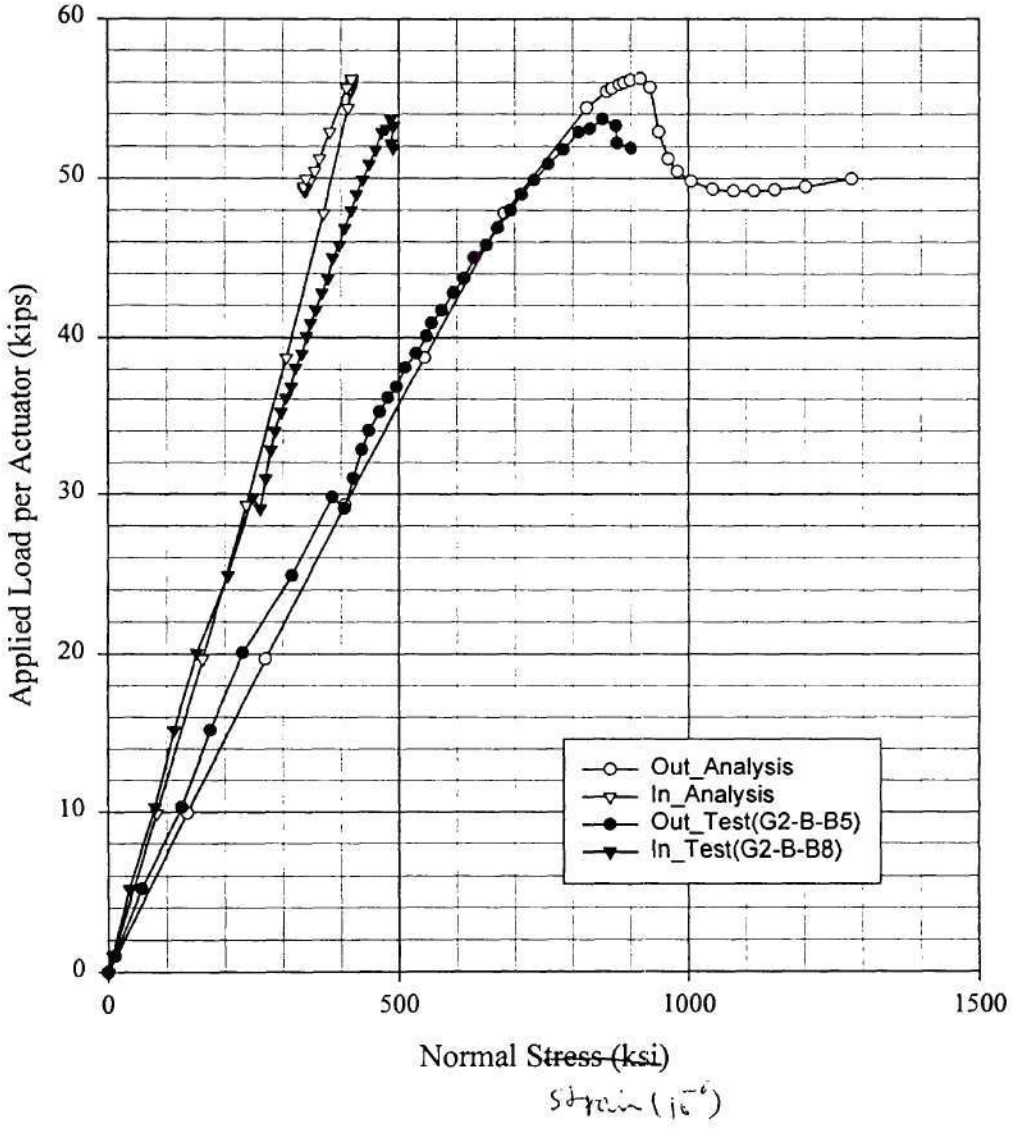

Comparison Between Analysis(B2h_3) and Test(5-21-99) for B2
Normal Strain of the Web Inside at the Location G3_E

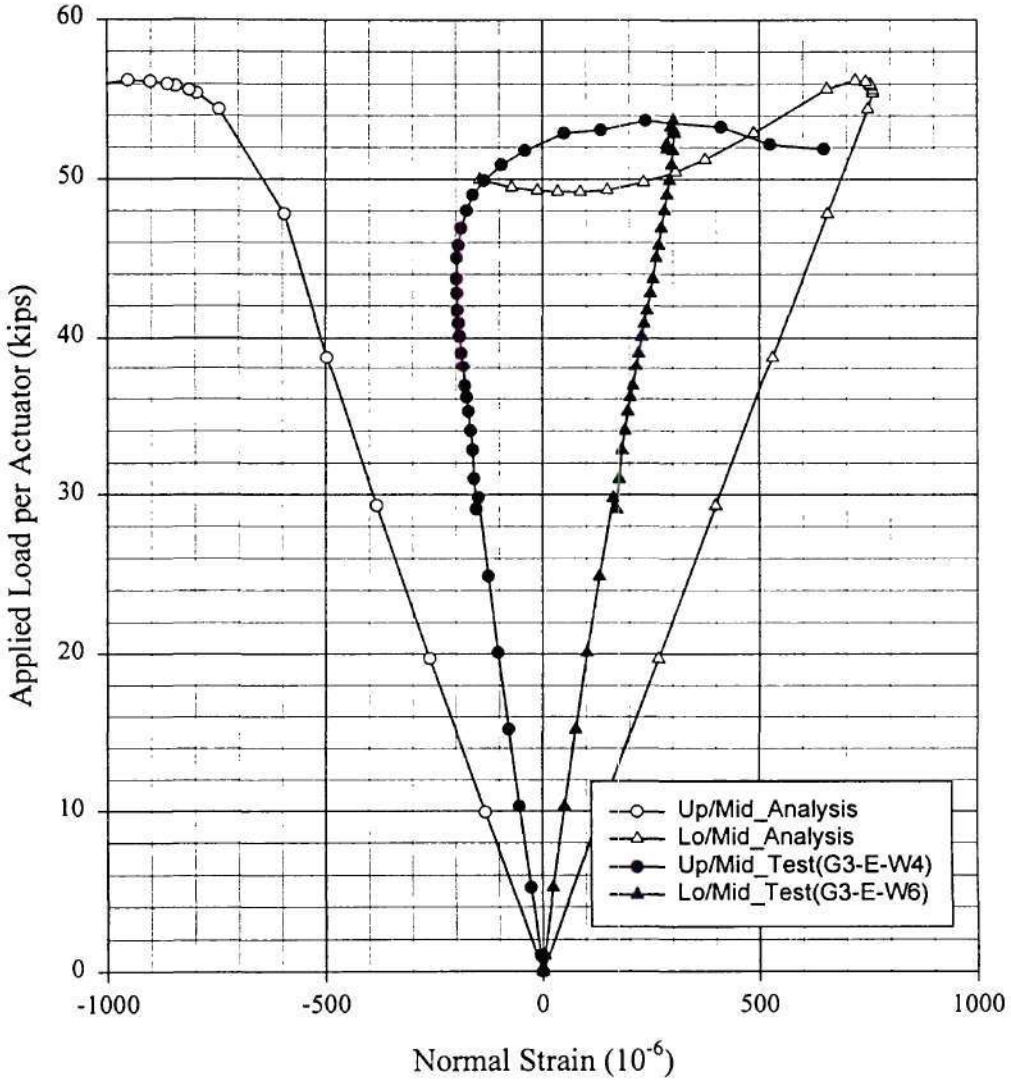

Comparison Between Analysis(B2h_3) and Test(5-21-99) for B2
Normal Strain of the Web Outside at the Location G3_E

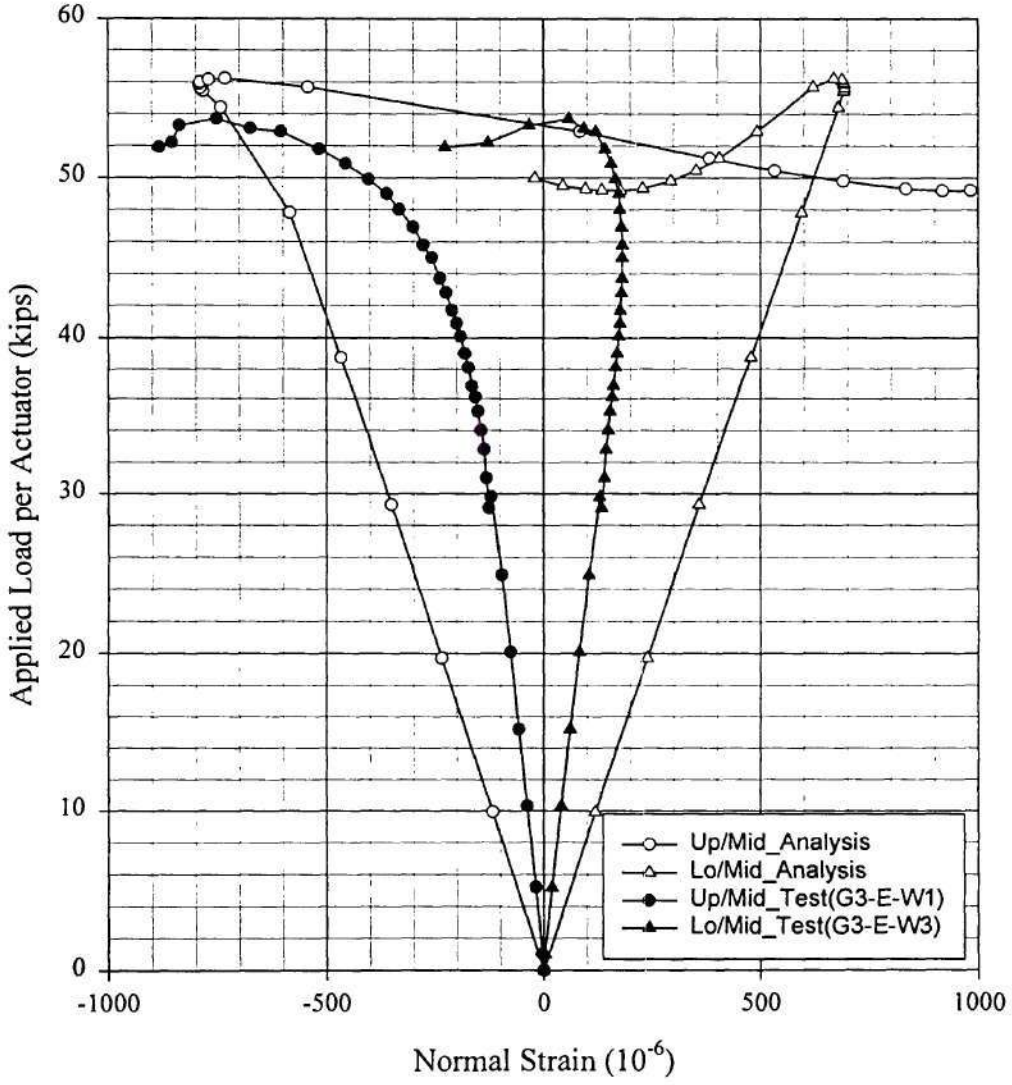

Comparison Between Analysis(B2h_3) and Test(5-21-99) for B2
Normal Strain of the Top Flange Topside at the Location G3_E

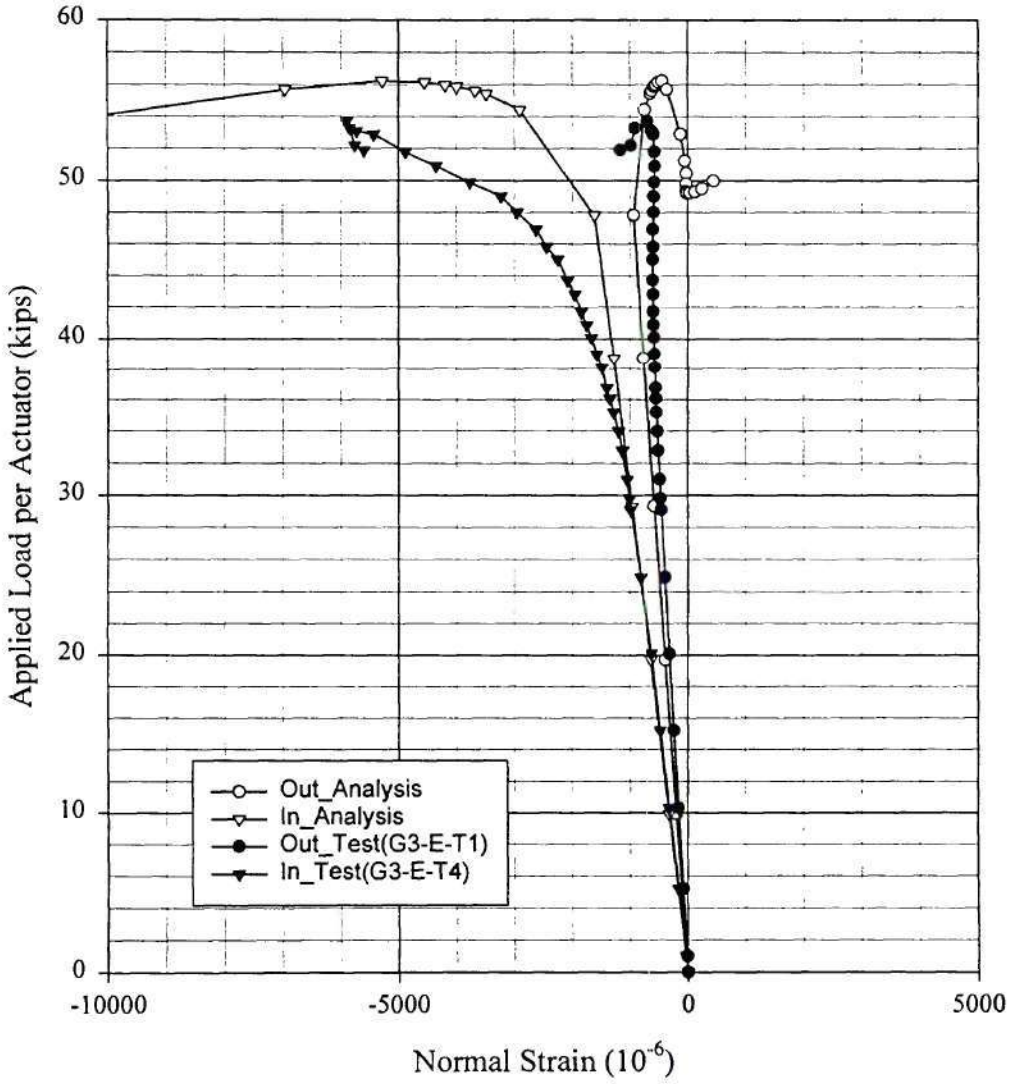

Comparison Between Analysis(B2h_3) and Test(5-21-99) for B2
Normal Strain of the Top Flange Btmside at the Location G3_E

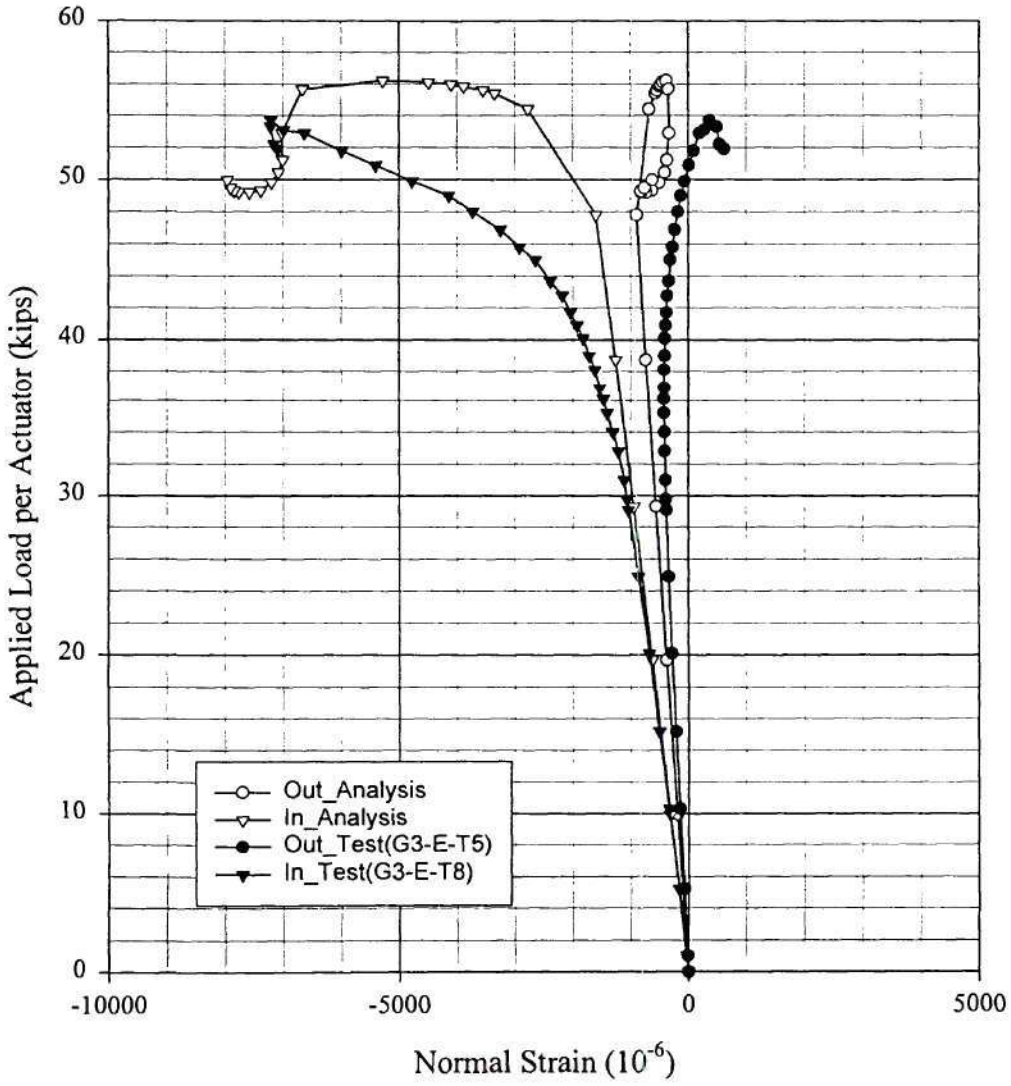

Comparison Between Analysis(B2h_3) and Test(5-21-99) for B2
Normal Strain of the Btm Flange Topside at the Location G3_E

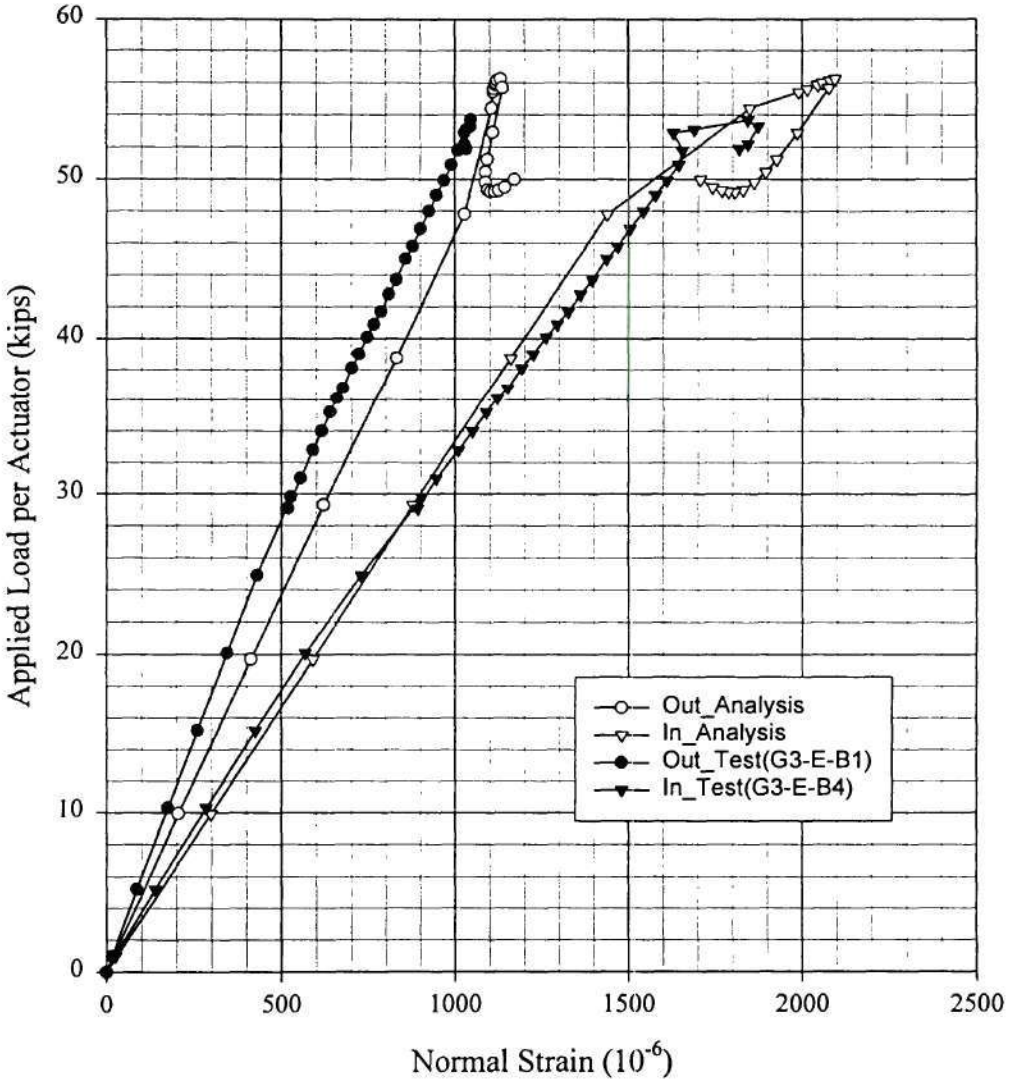

Comparison Between Analysis(B2h_3) and Test(5-21-99) for B2
Normal Strain of the Btm Flange Btmside at the Location G3_E

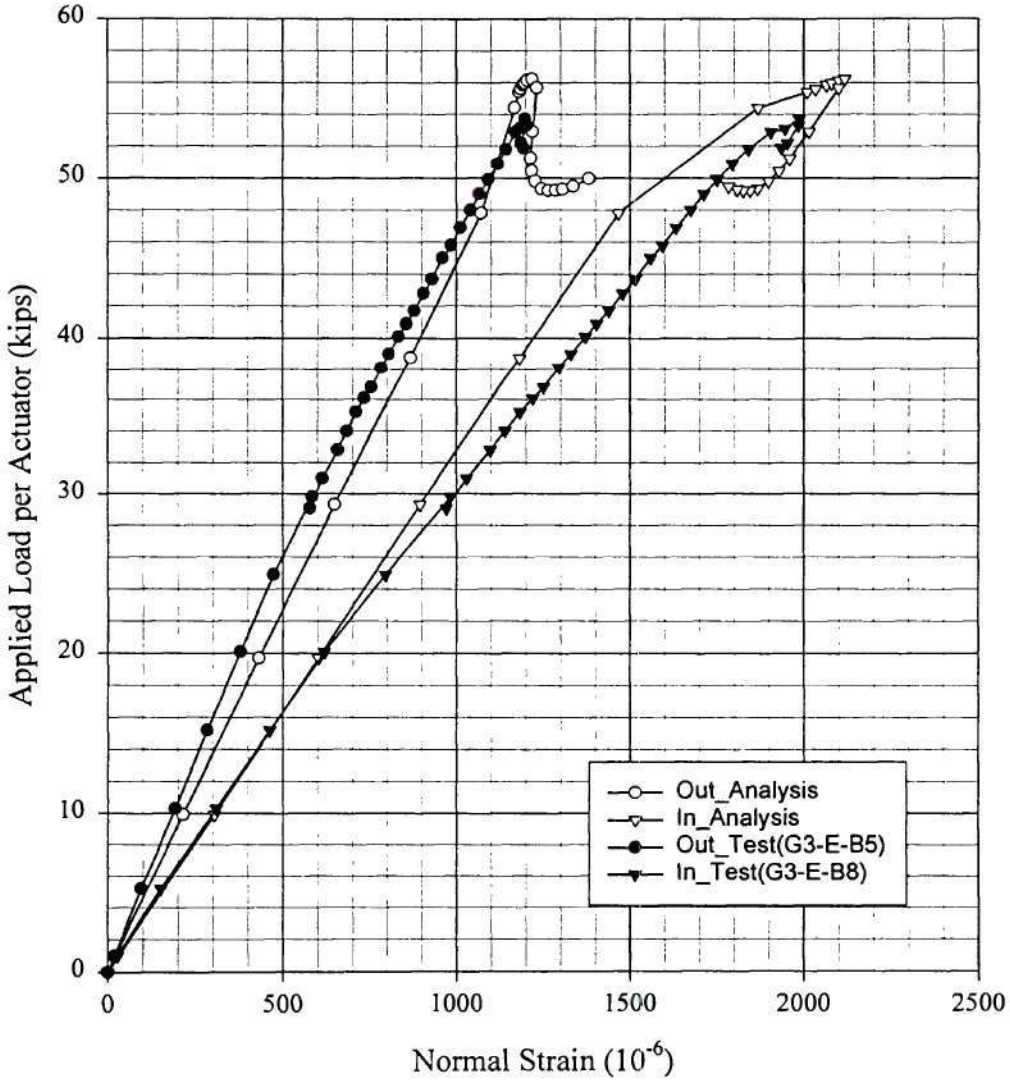

Test(5-21-99) for B2
Normal Strain of the Web at the Location G3_E

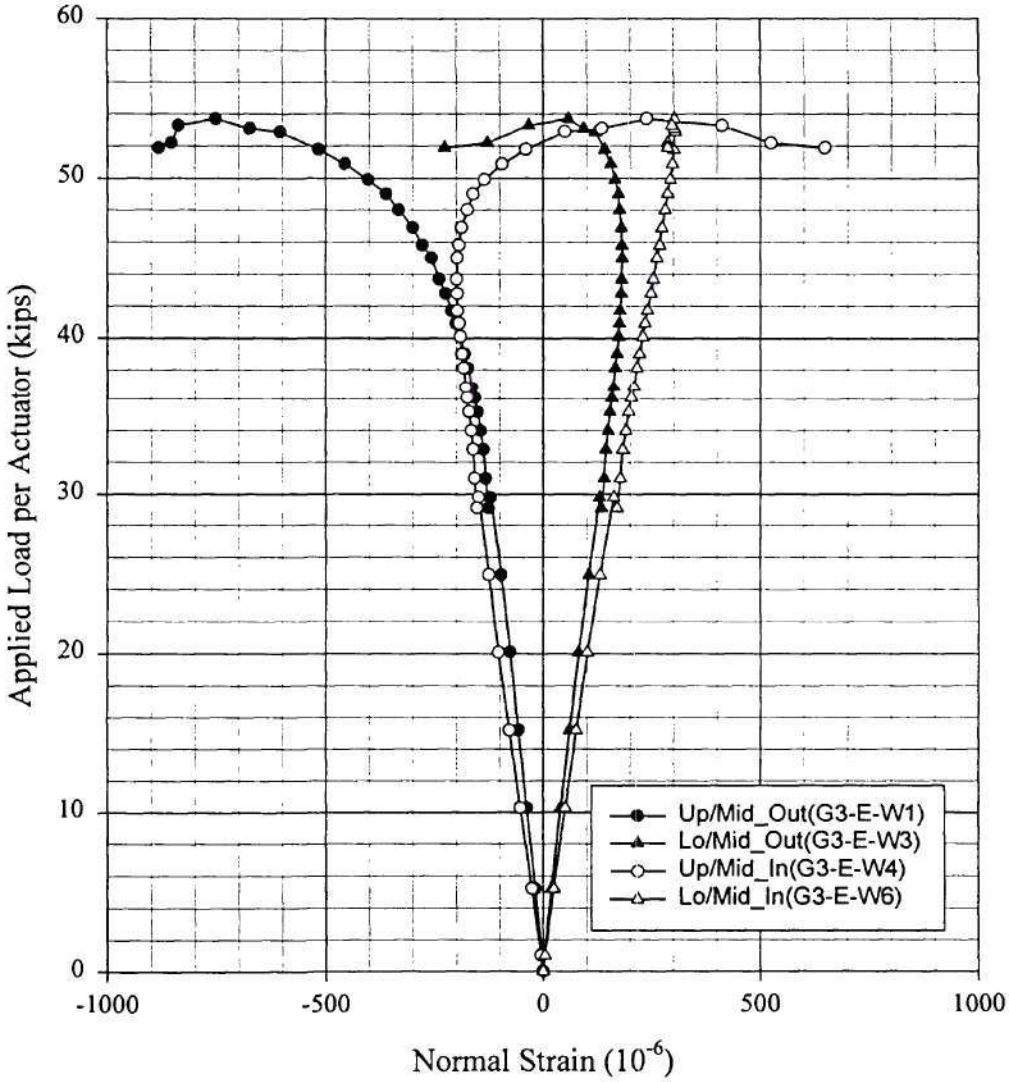

Test(5-21-99) for B2
Normal Strain of the Top Flange at the Location G3_E

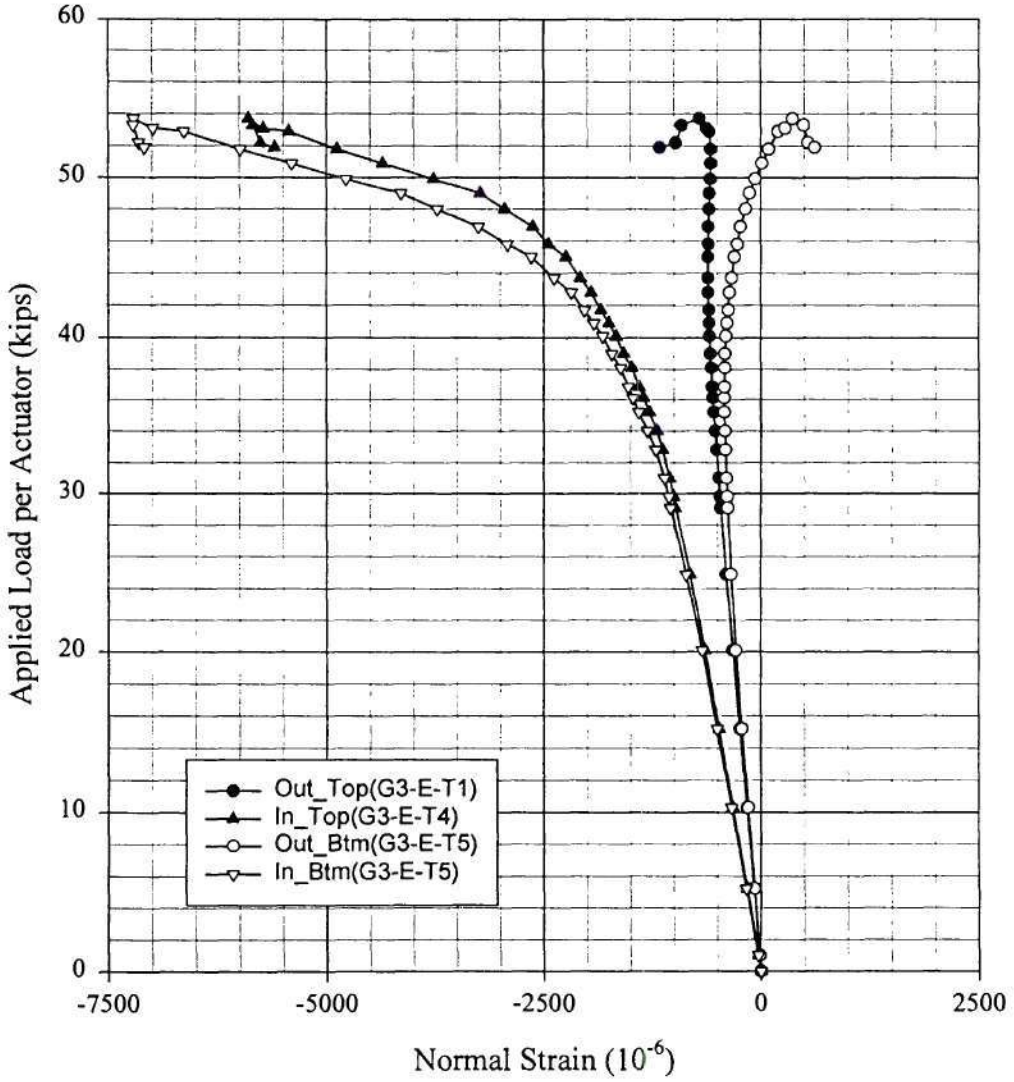

Test(5-21-99) for B2
Normal Strain of the Bottom Flange at the Location G3_E

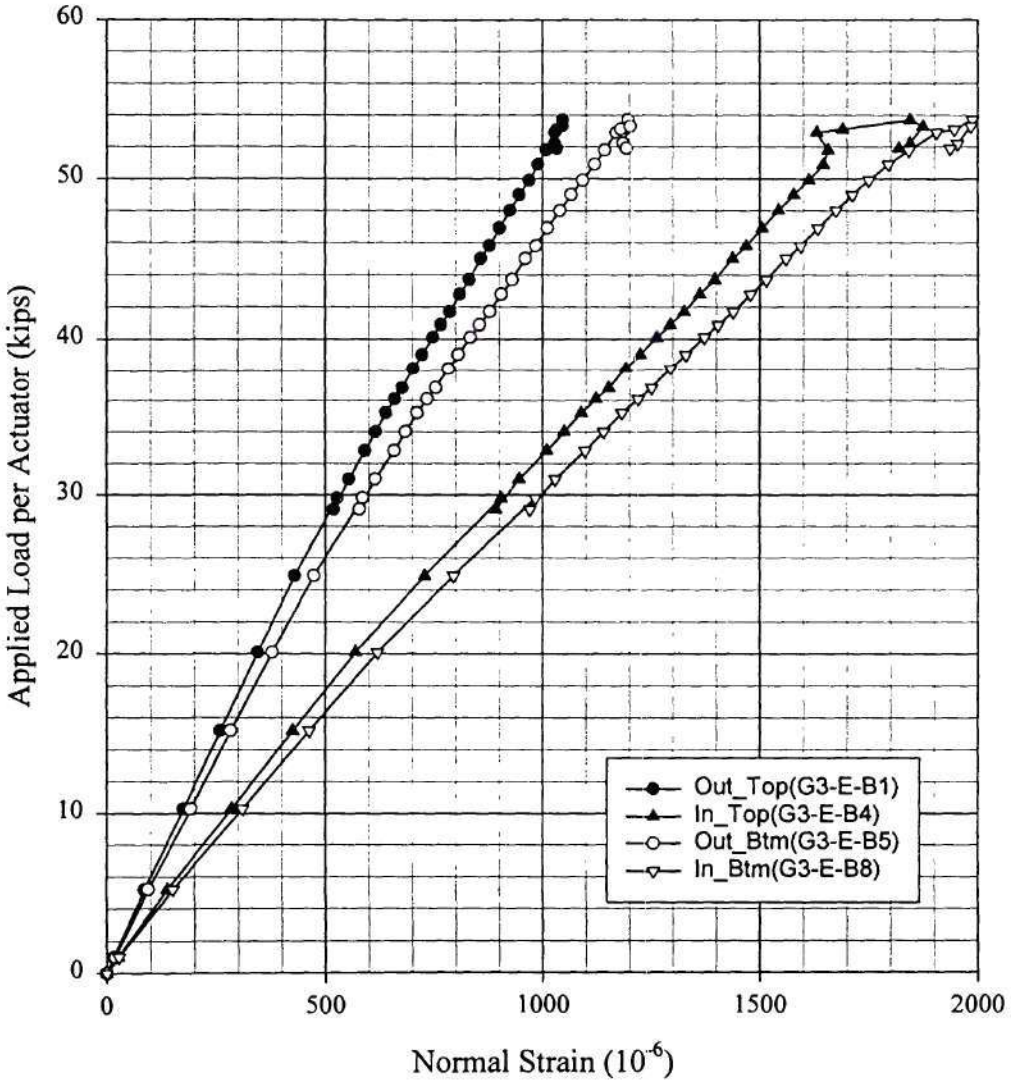

Comparison Between Analysis(B3h_3) and Test(6-24-99) for B3
Vertical Reactions at the East Supports

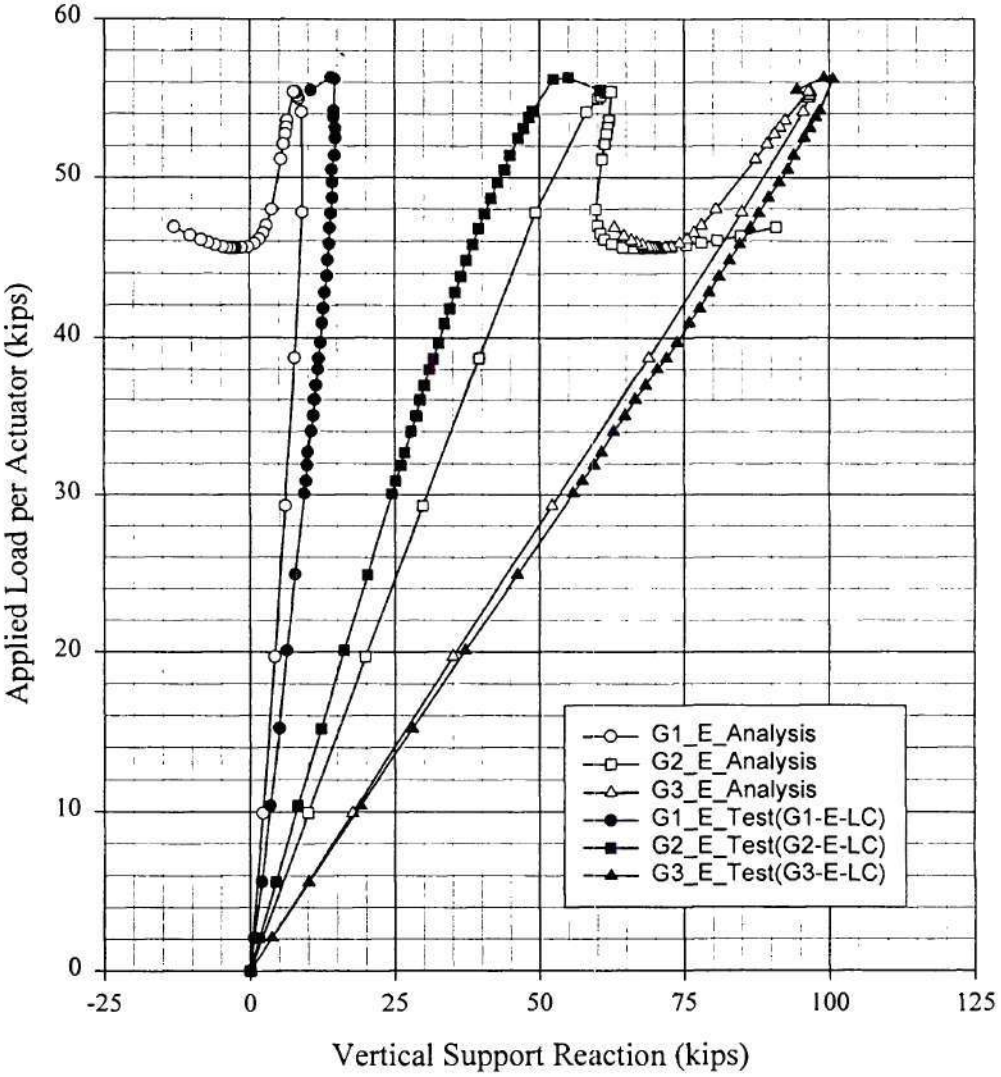

Comparison Between Analysis(B3h_3) and Test(6-24-99) for B3
Vertical Reactions at the West Supports

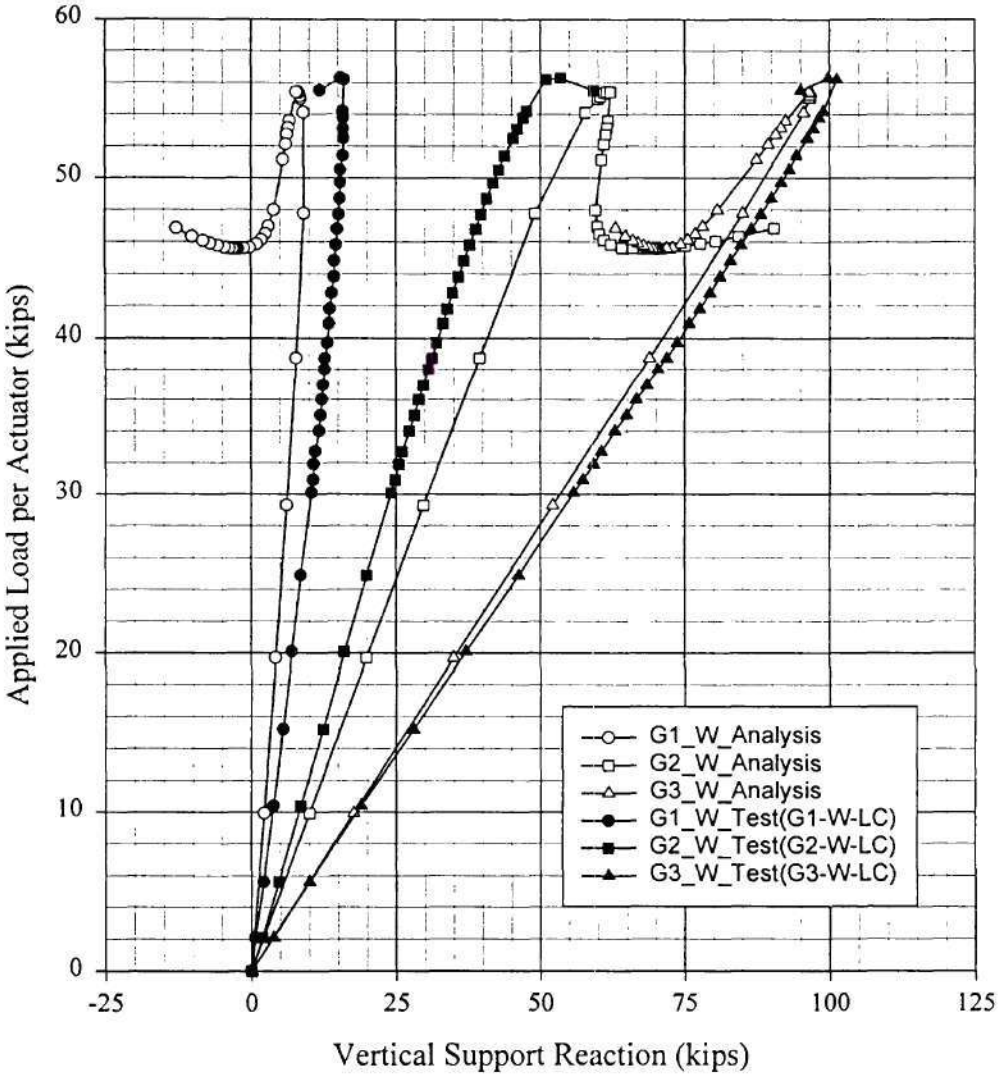

Comparison Between Analysis(B3h_3) and Test(6-24-99) for B3
Vertical Displacement of Bottom Flange (Outside) at Midspan

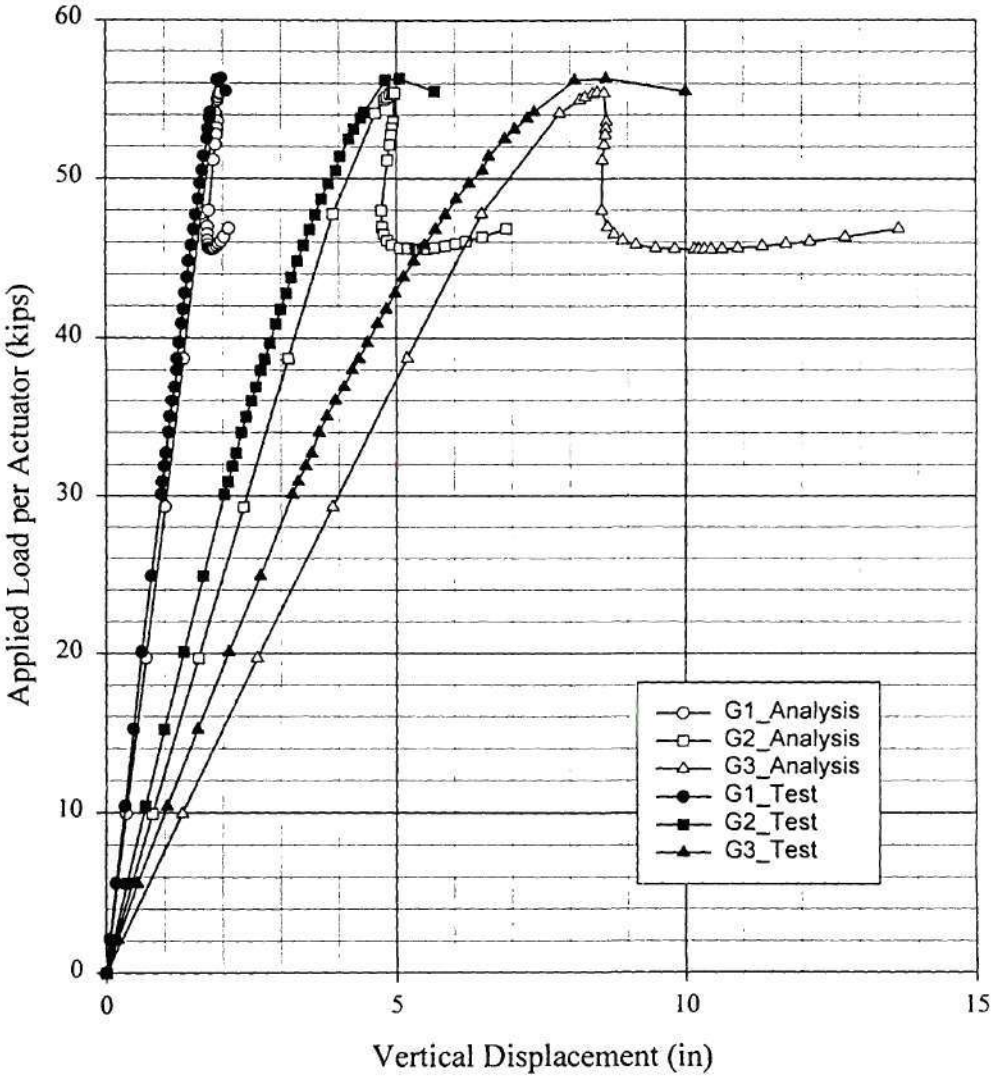

Comparison Between Analysis(B3h_3) and Test(6-24-99) for B3
Radial Displacement of Top Flange (Outside) at Midspan

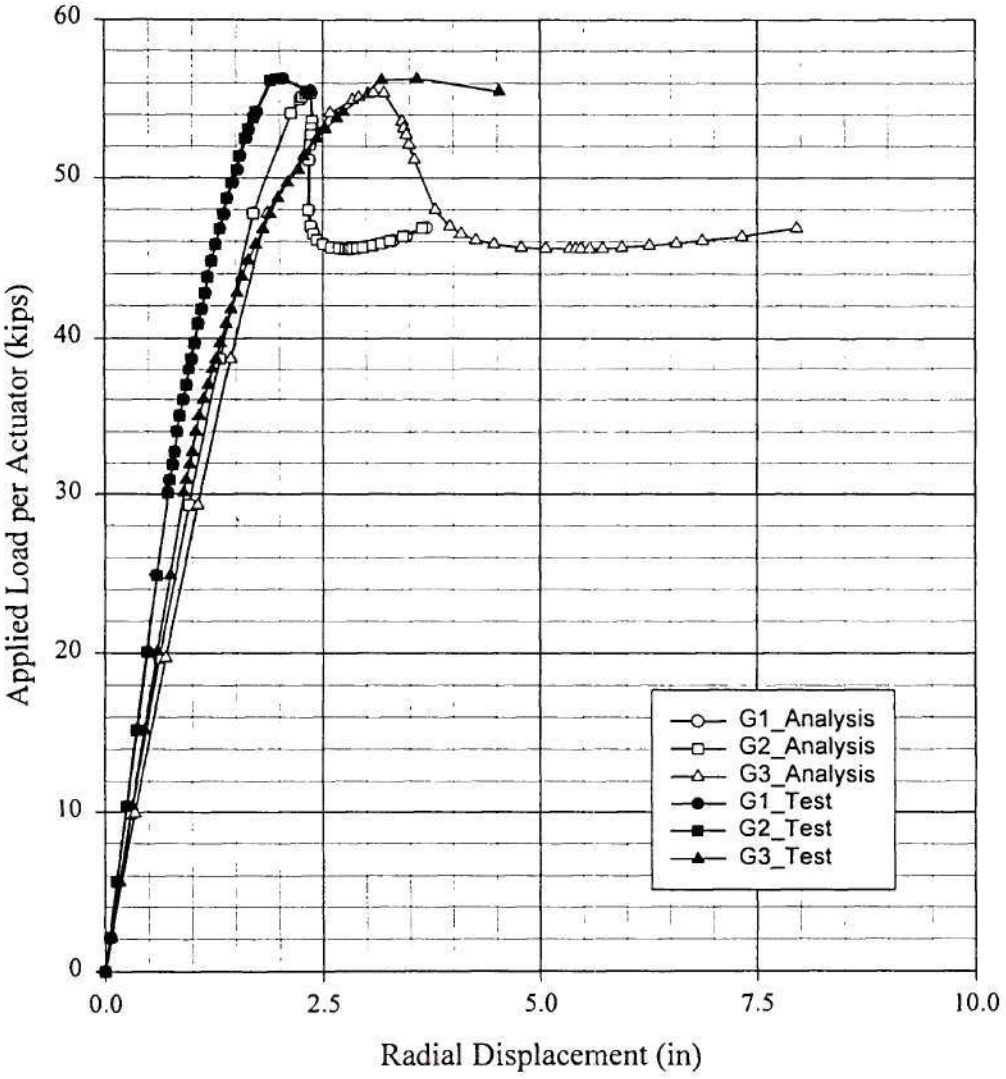

Comparison Between Analysis(B3h_3) and Test(6-24-99) for B3
Radial Displacement of Bottom Flange (Outside) at Midspan

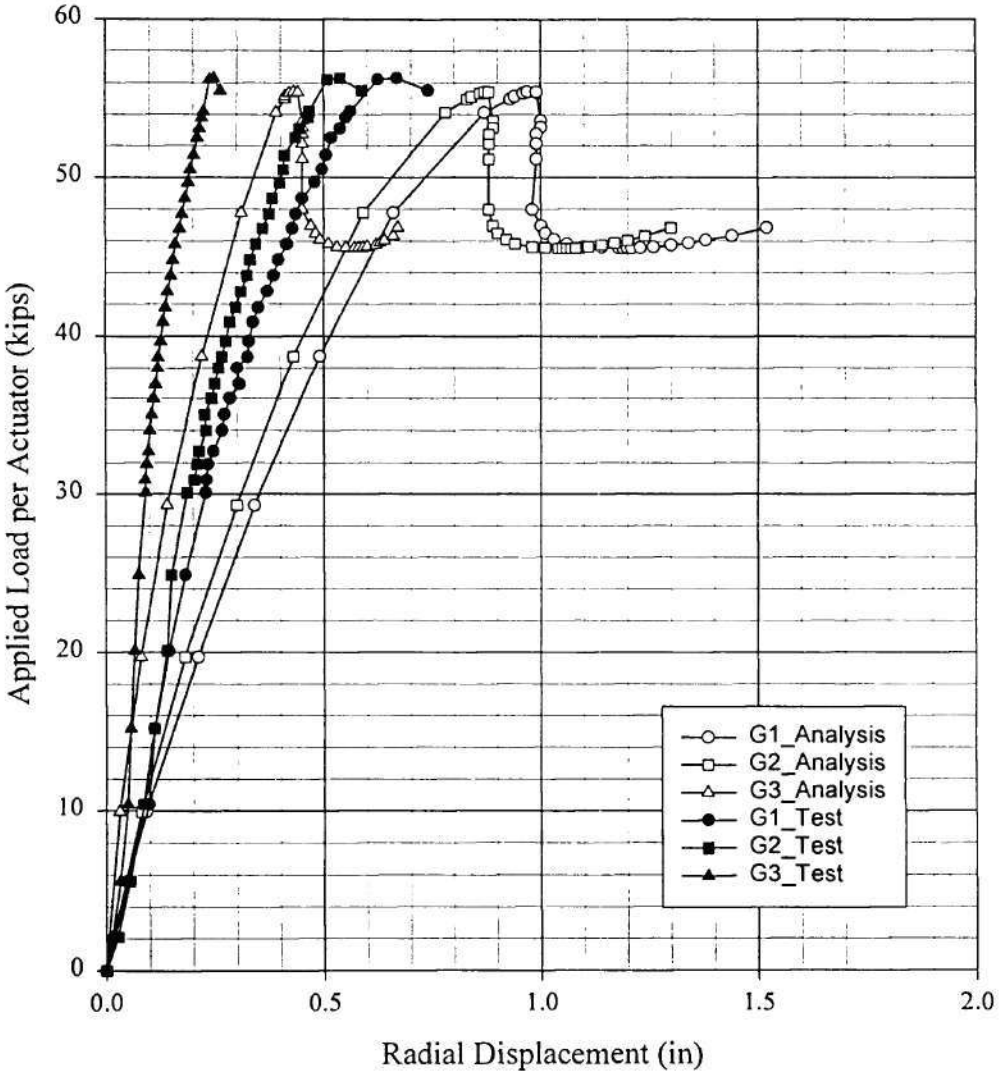

Comparison Between Analysis(B3h_3) and Test(6-24-99) for B3
Axial Force of Cross Frame at 6R Between G2 and G3

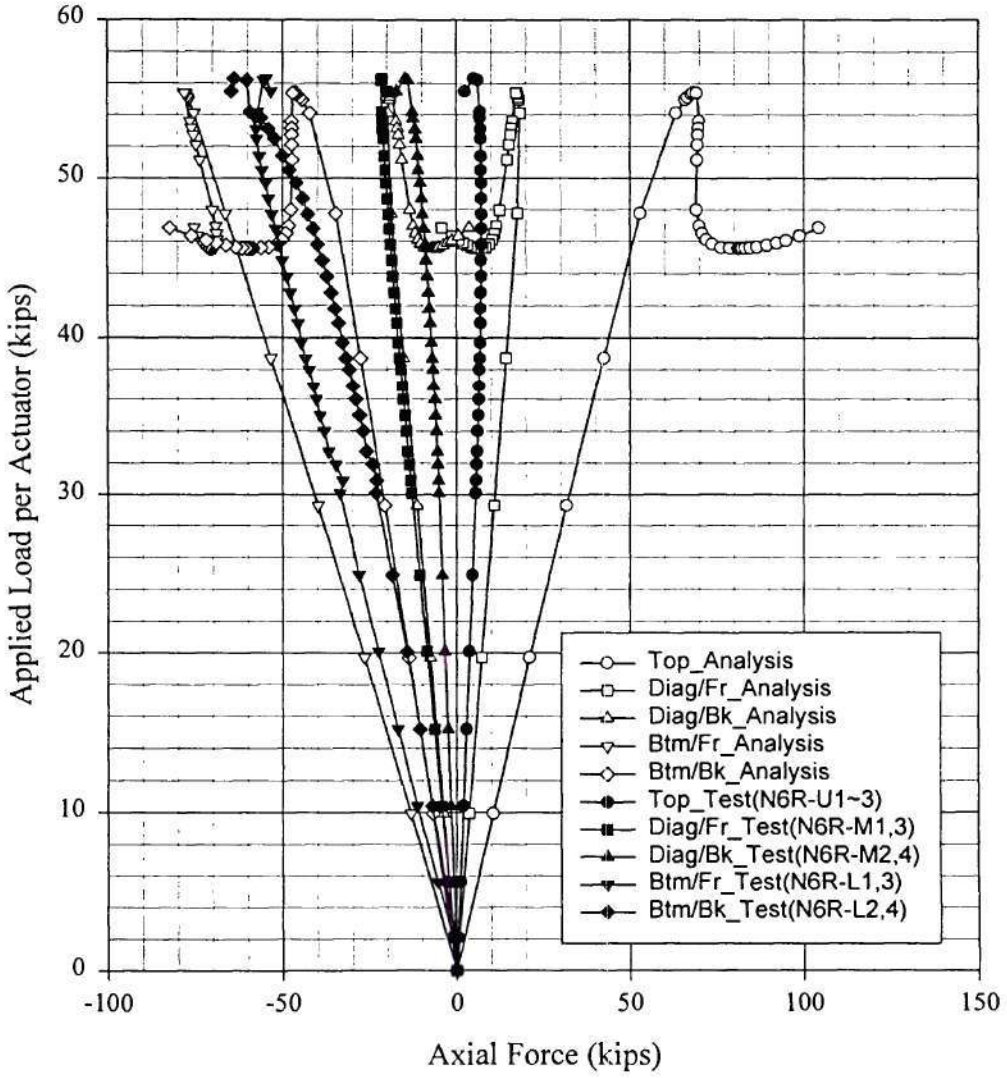

Comparison Between Analysis(B3h_3) and Test(6-24-99) for B3
Axial Force of Cross Frame at 6L Between G2 and G3

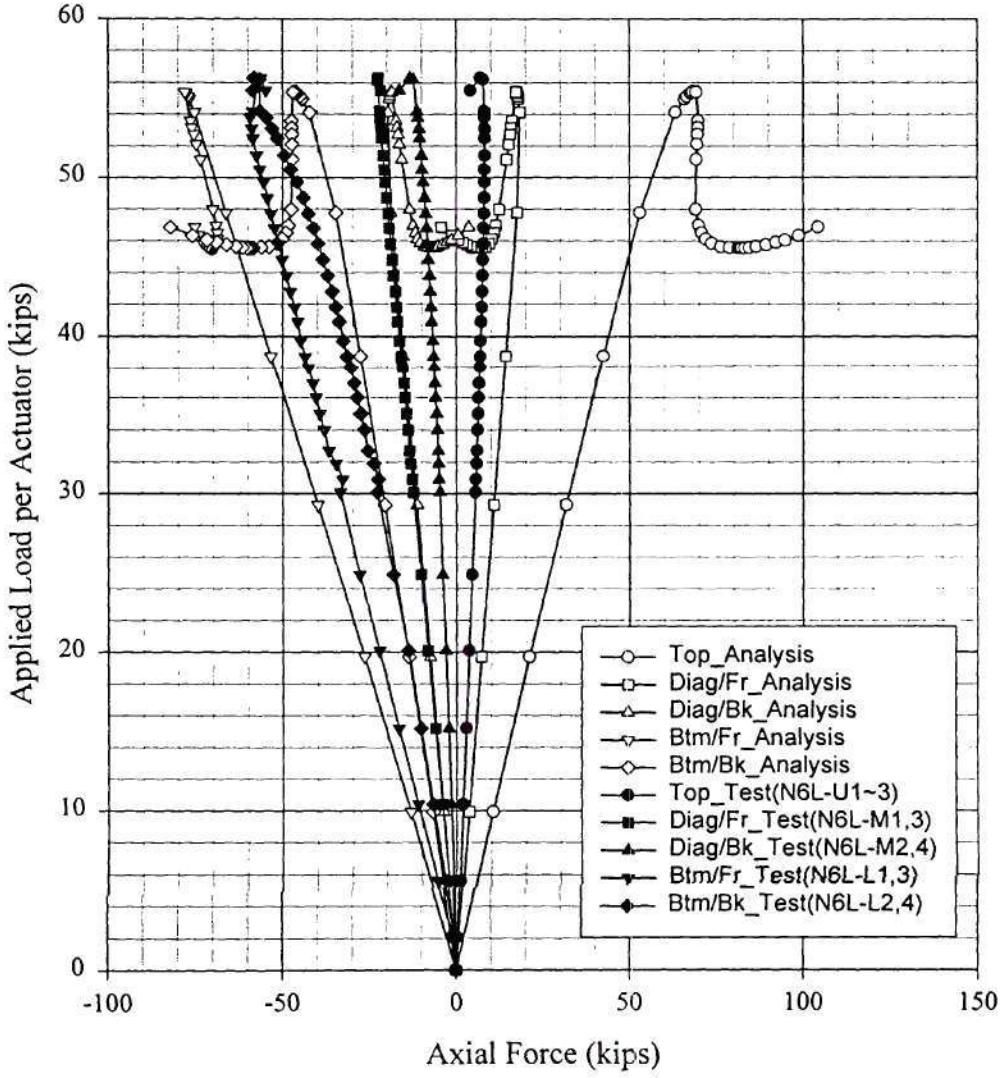

Comparison Between Analysis(B3h_3) and Test(6-24-99) for B3
Bending Moment at Midspan

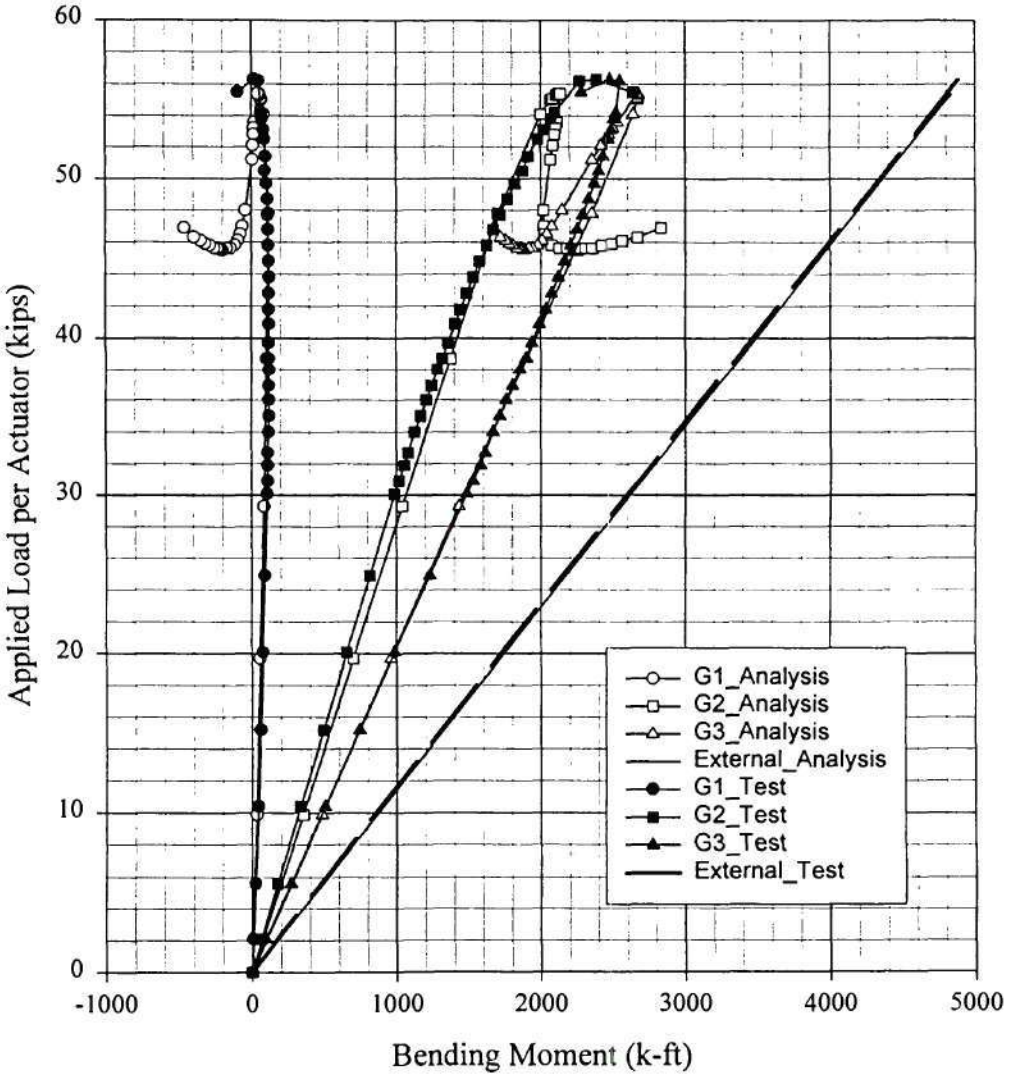

Comparison Between Analysis(B3h_3) and Test(6-24-99) for B3
Normal Strain of the Web Inside at the Location G1_B

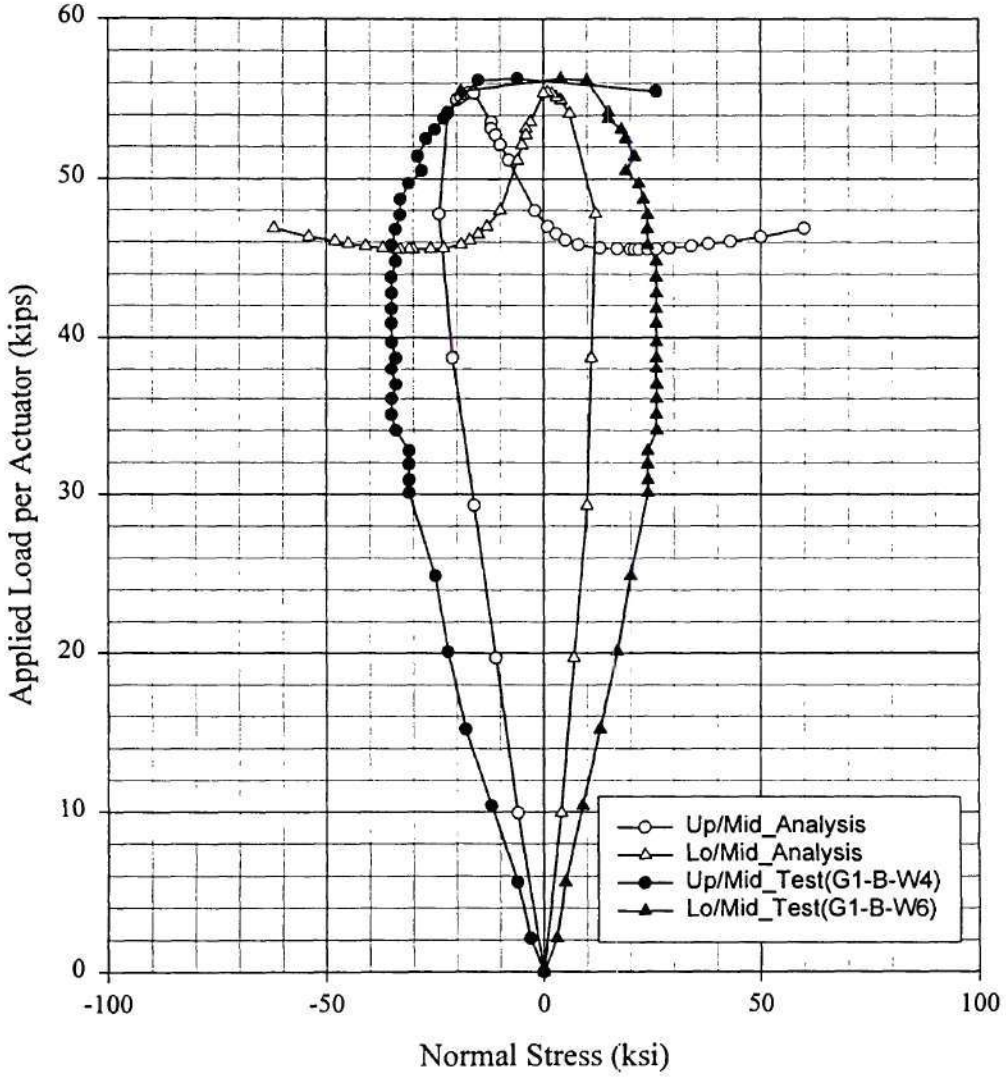

Comparison Between Analysis(B3h_3) and Test(6-24-99) for B3
Normal Strain of the Top Flange Topside at the Location G1_B

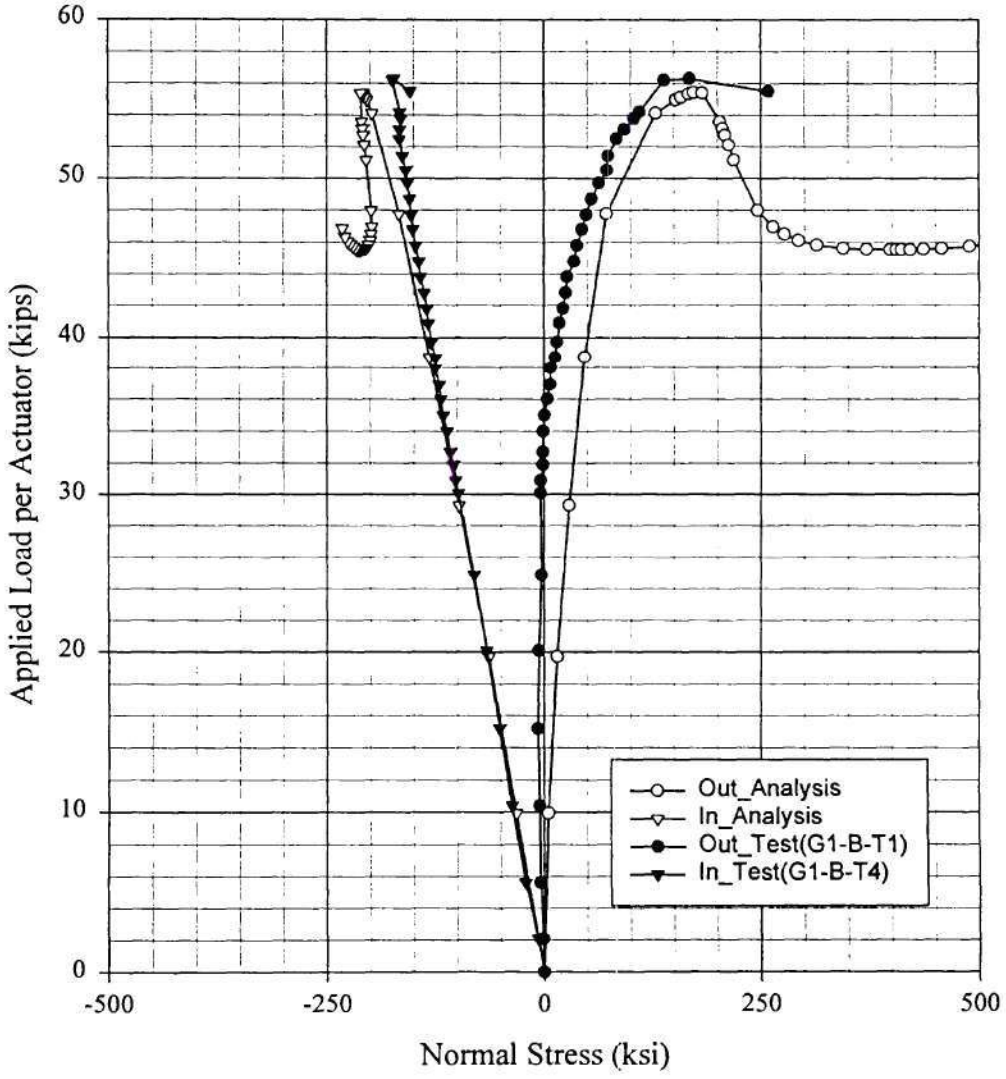

Comparison Between Analysis(B3h_3) and Test(6-24-99) for B3
Normal Strain of the Top Flange Btmside at the Location G1_B

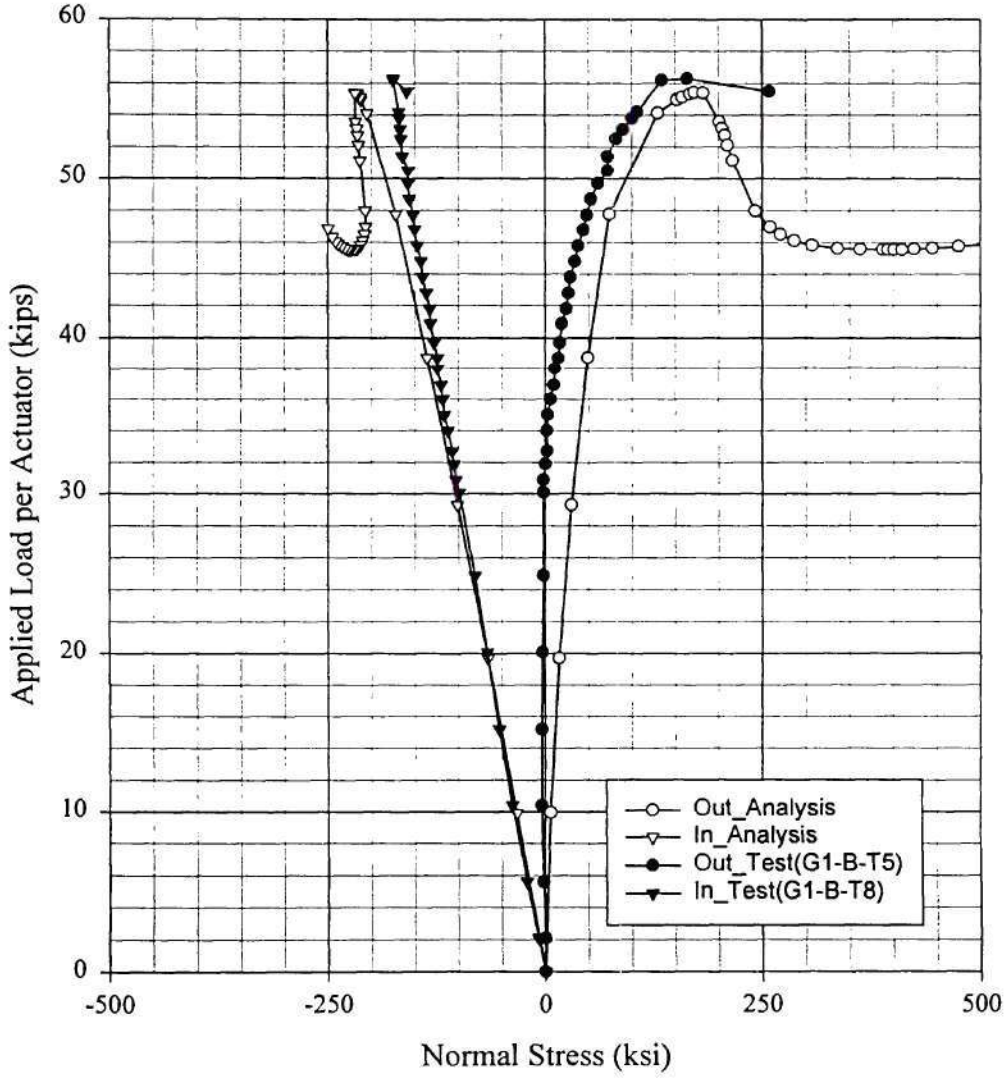

Comparison Between Analysis(B3h_3) and Test(6-24-99) for B3
Normal Strain of the Btm Flange Topside at the Location G1_B

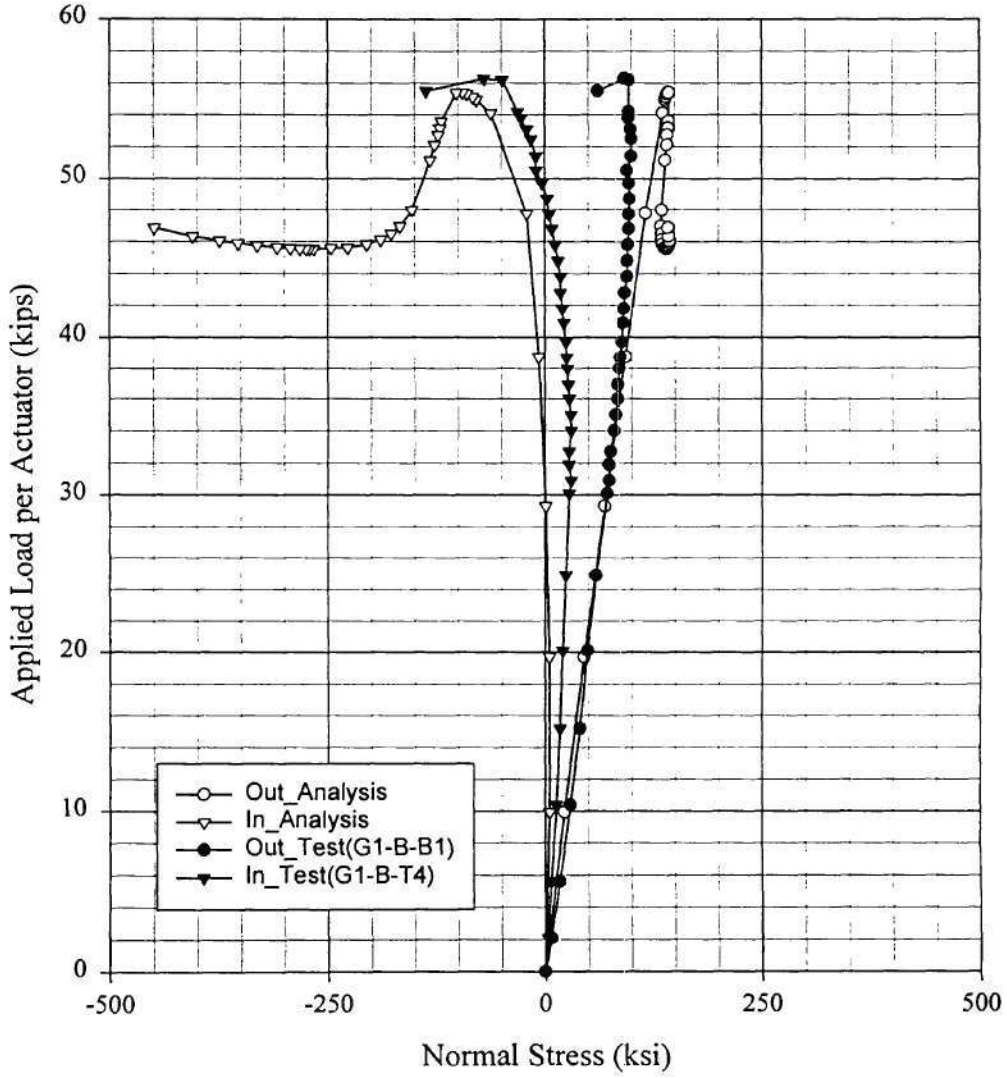

Comparison Between Analysis(B3h_3) and Test(6-24-99) for B3
Normal Strain of the Btm Flange Btmside at the Location G1_B

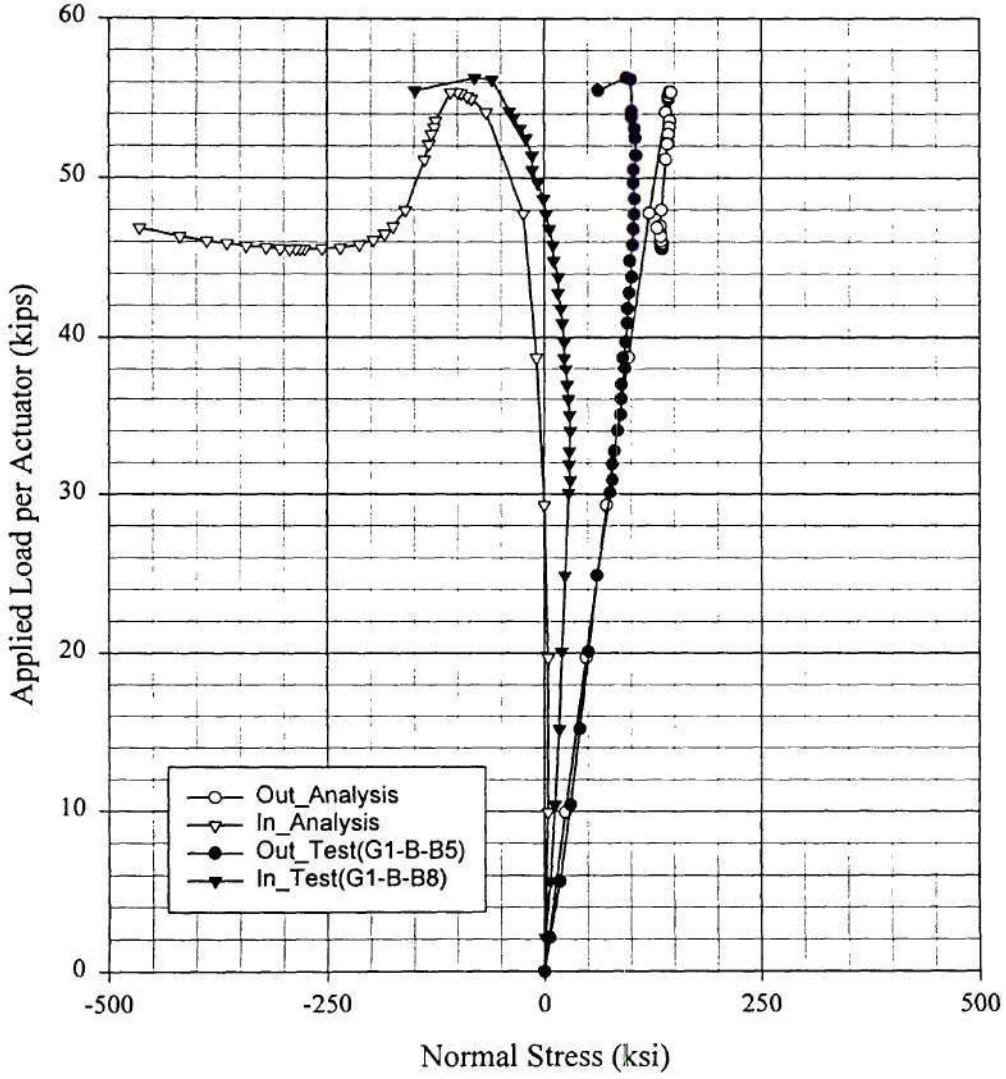

Comparison Between Analysis(B3h_3) and Test(6-24-99) for B3
Normal Strain of the Web Inside at the Location G2_B

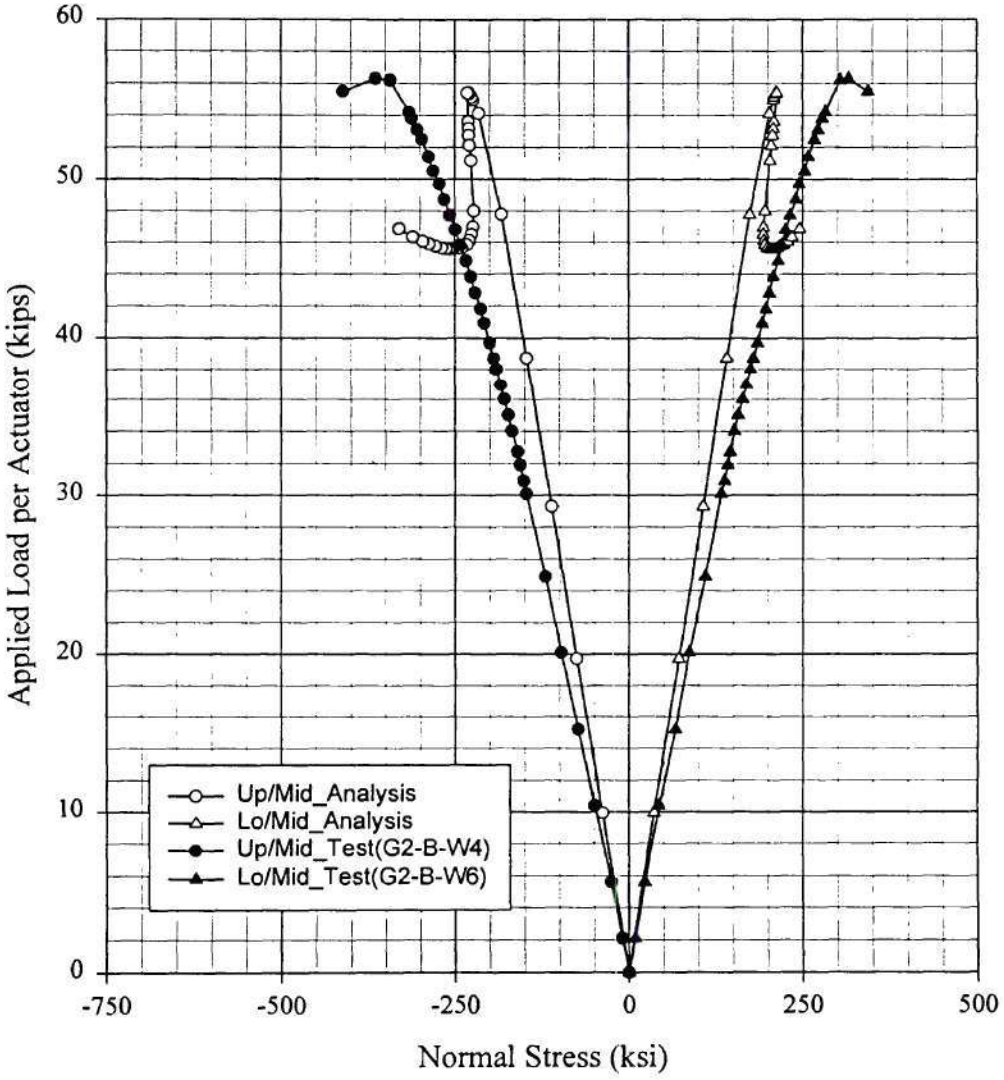

Comparison Between Analysis(B3h_3) and Test(6-24-99) for B3
Normal Strain of the Top Flange Topside at the Location G2_B

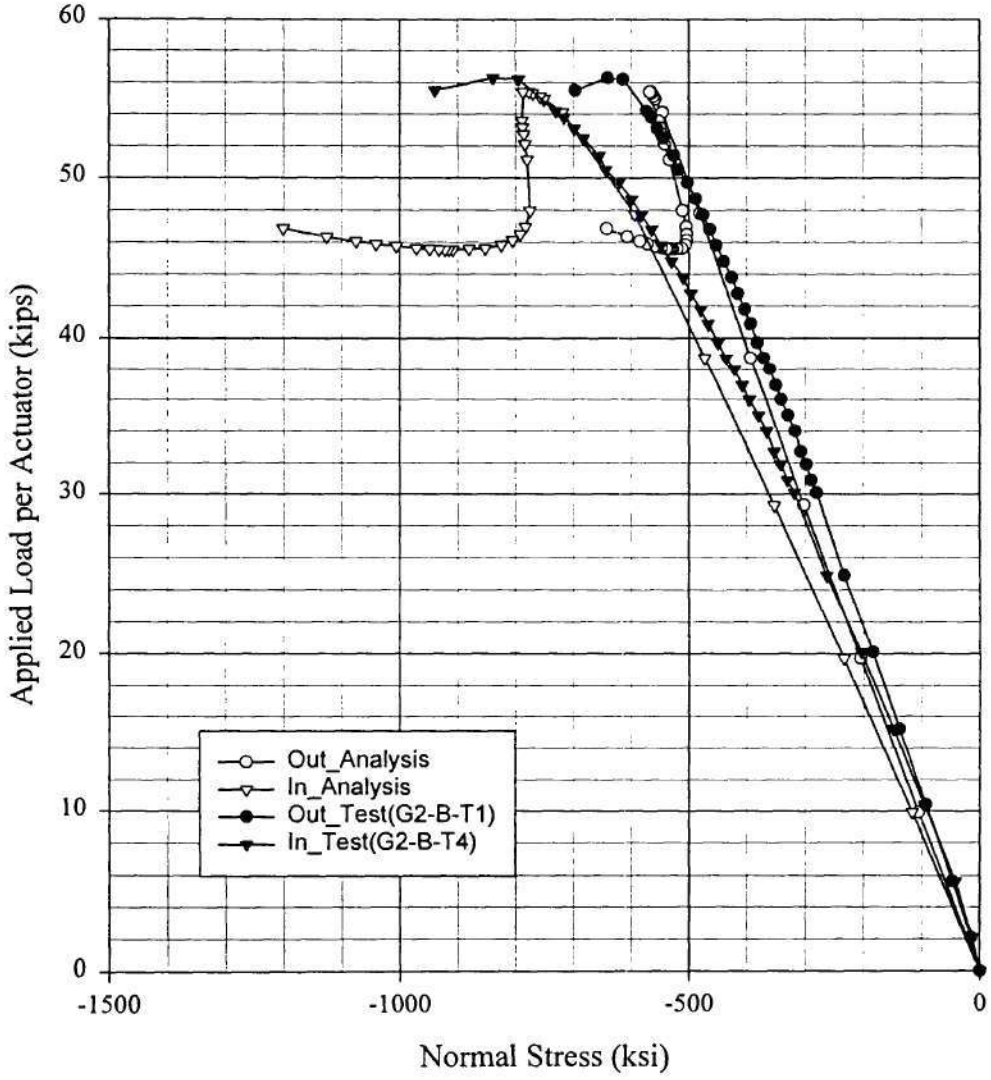

Comparison Between Analysis(B3h_3) and Test(6-24-99) for B3
Normal Strain of the Top Flange Btmside at the Location G2_B

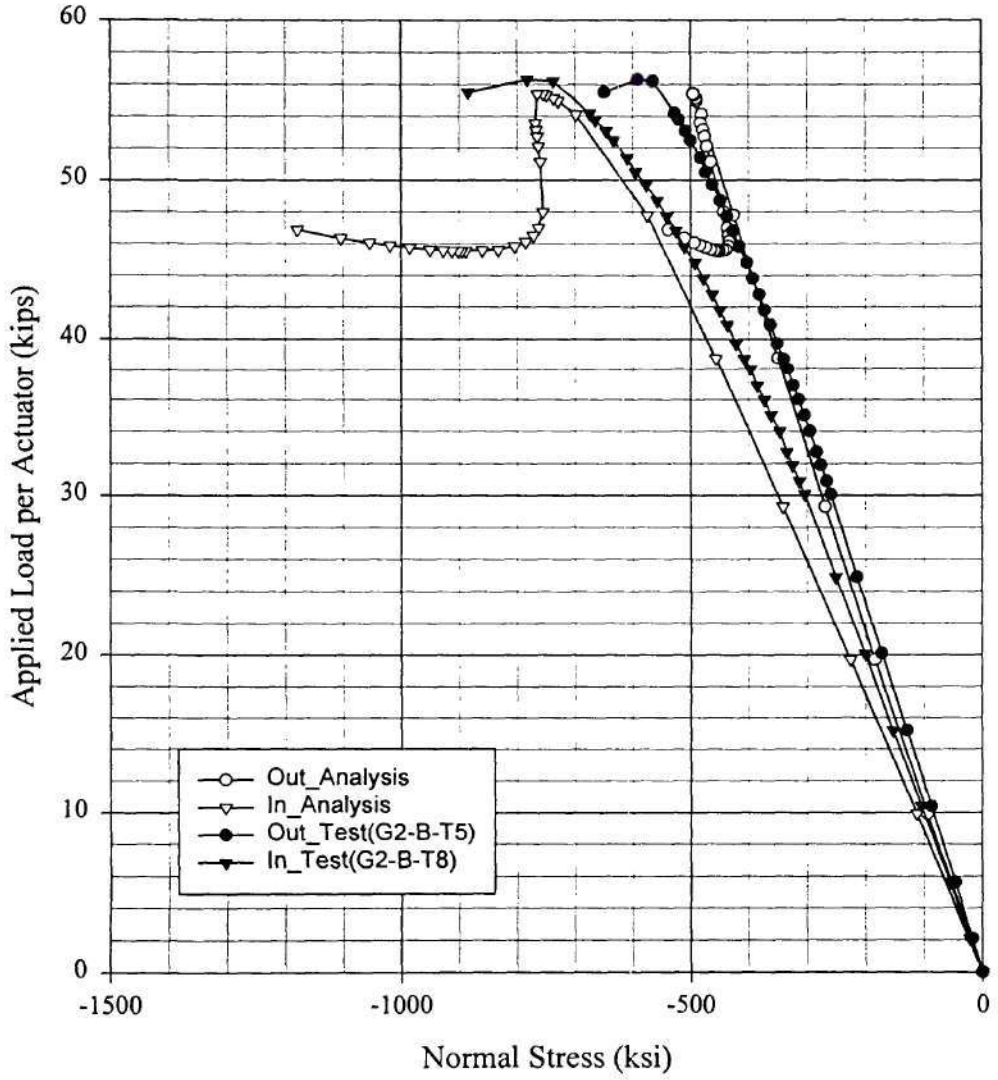

Comparison Between Analysis(B3h_3) and Test(6-24-99) for B3
Normal Strain of the Btm Flange Topside at the Location G2_B

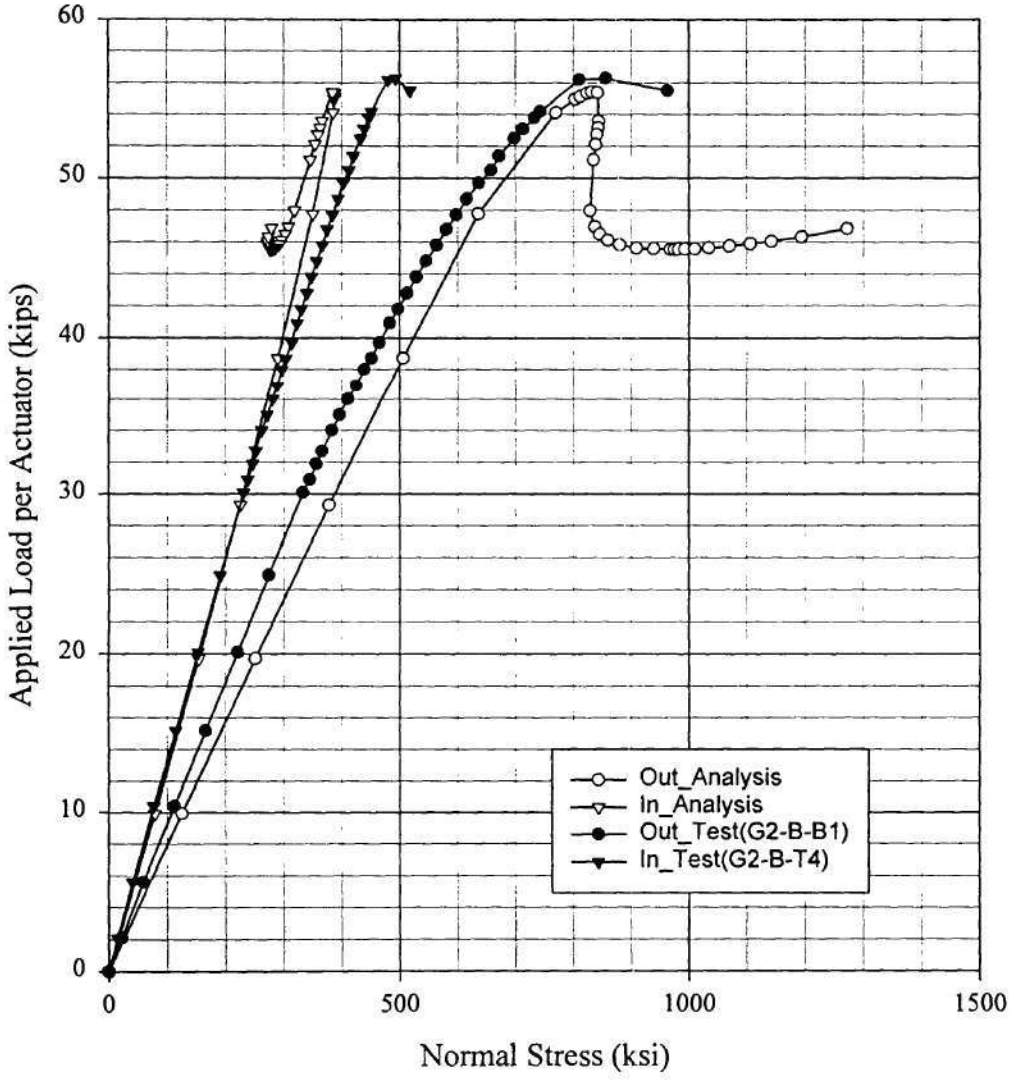

Comparison Between Analysis(B3h_3) and Test(6-24-99) for B3
Normal Strain of the Btm Flange Btmside at the Location G2_B

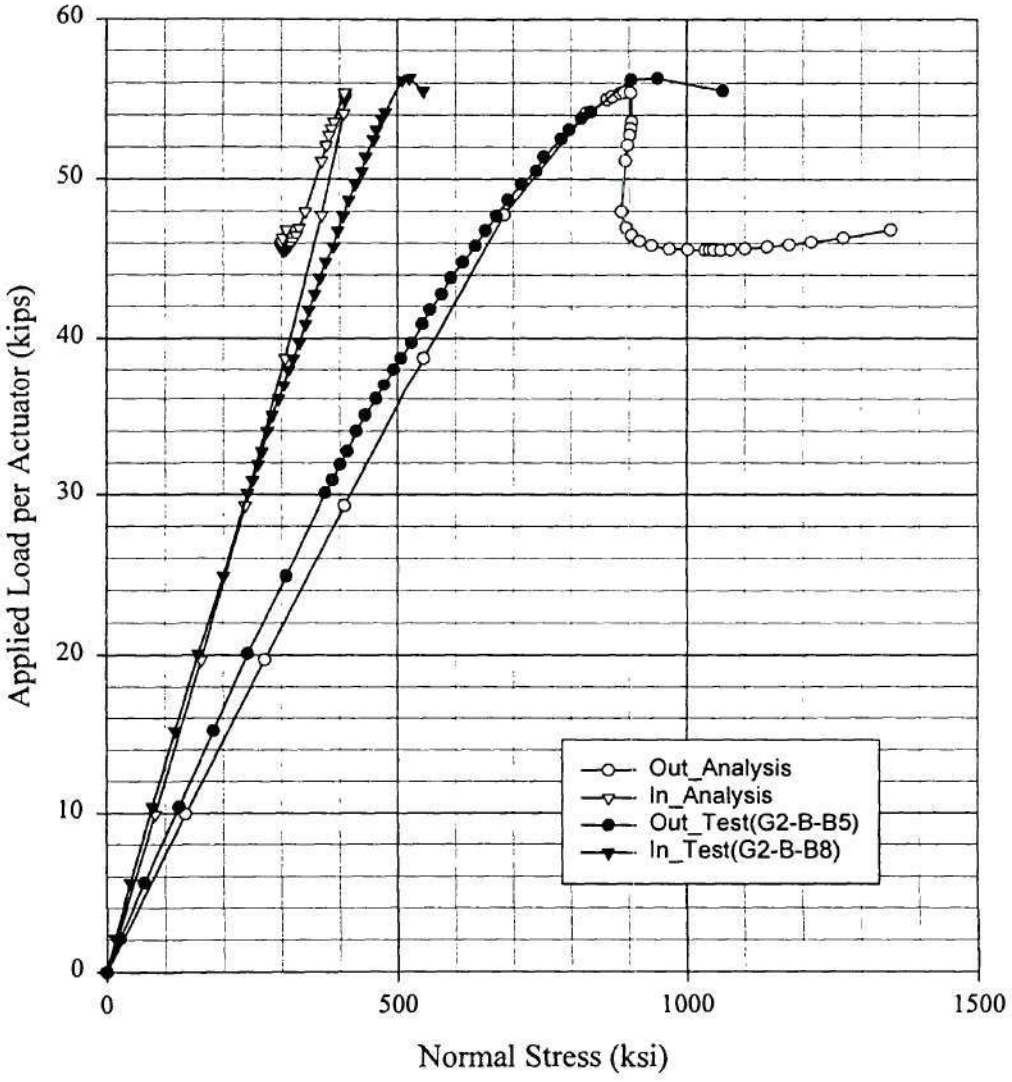

Comparison Between Analysis(B3h_3) and Test(6-24-99) for B3
Normal Strain of the Web Inside at the Location G3_E

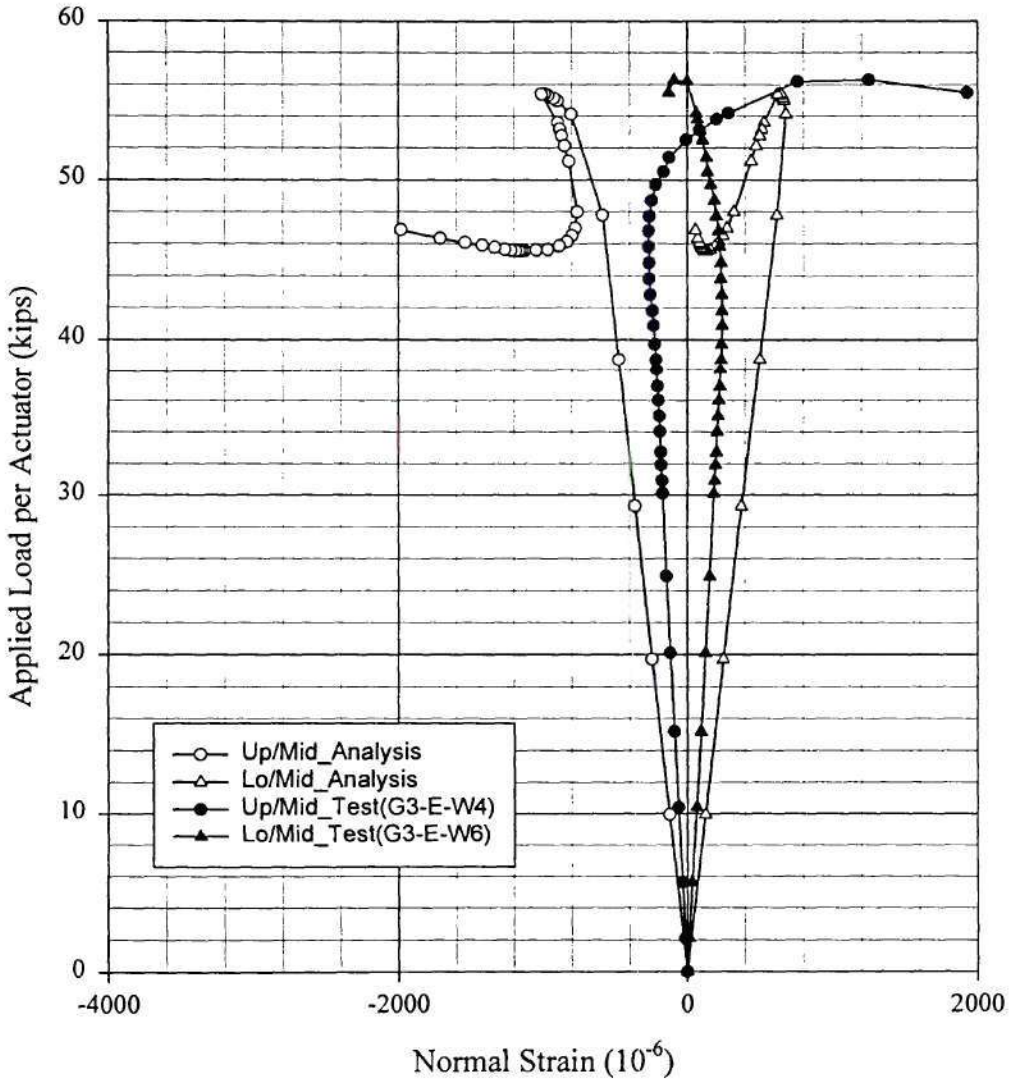

Comparison Between Analysis(B3h_3) and Test(6-24-99) for B3
Normal Strain of the Web Outside at the Location G3_E

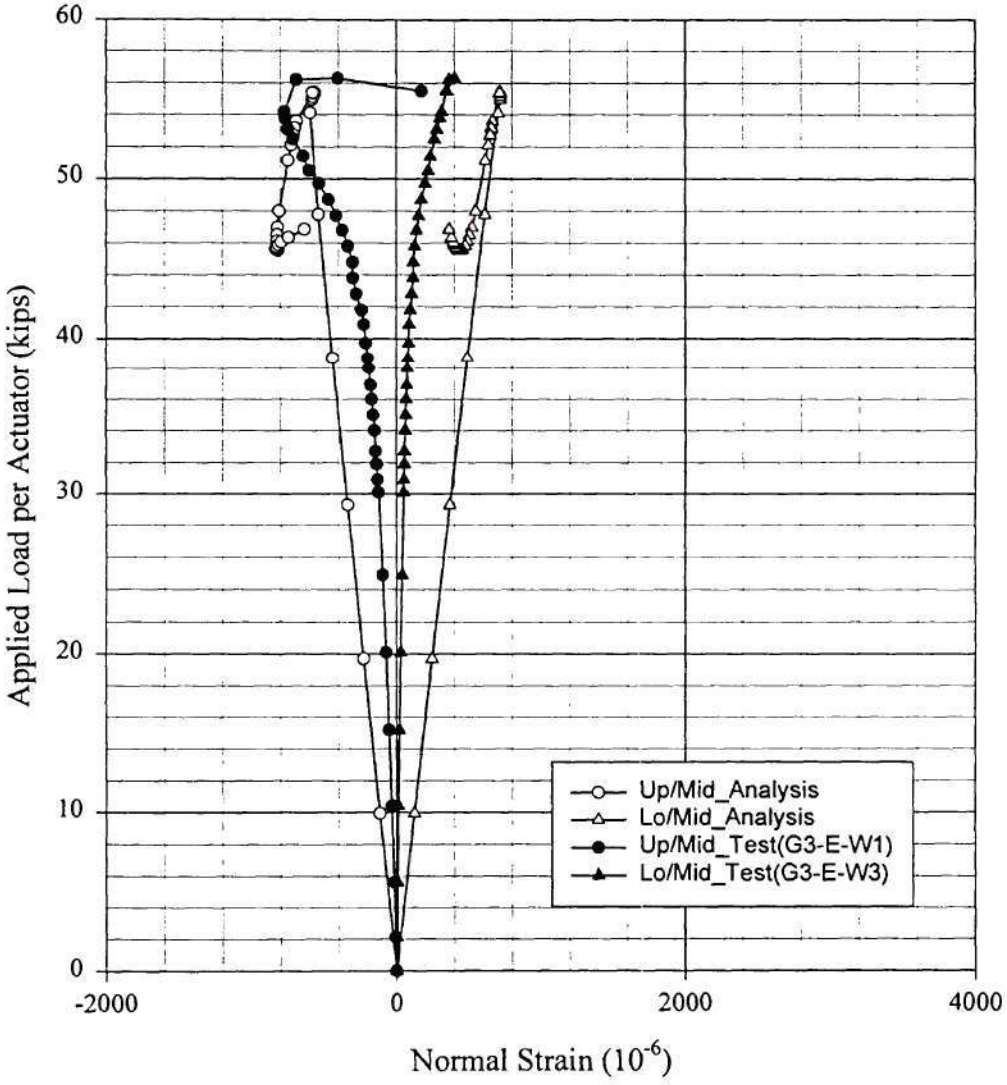

Comparison Between Analysis(B3h_3) and Test(6-24-99) for B3
Normal Strain of the Top Flange Topside at the Location G3_E

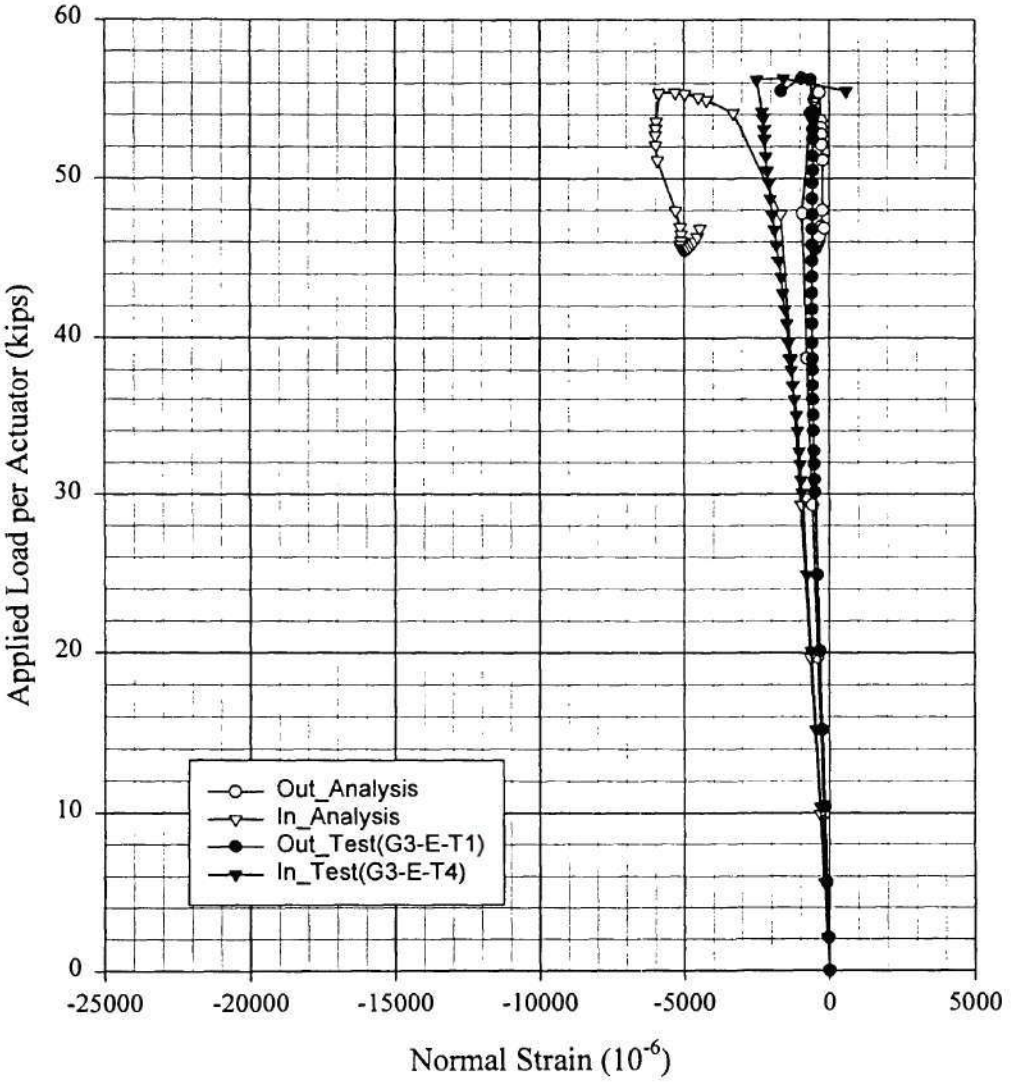

Comparison Between Analysis(B3h_3) and Test(6-24-99) for B3
Normal Strain of the Top Flange Btmside at the Location G3_E

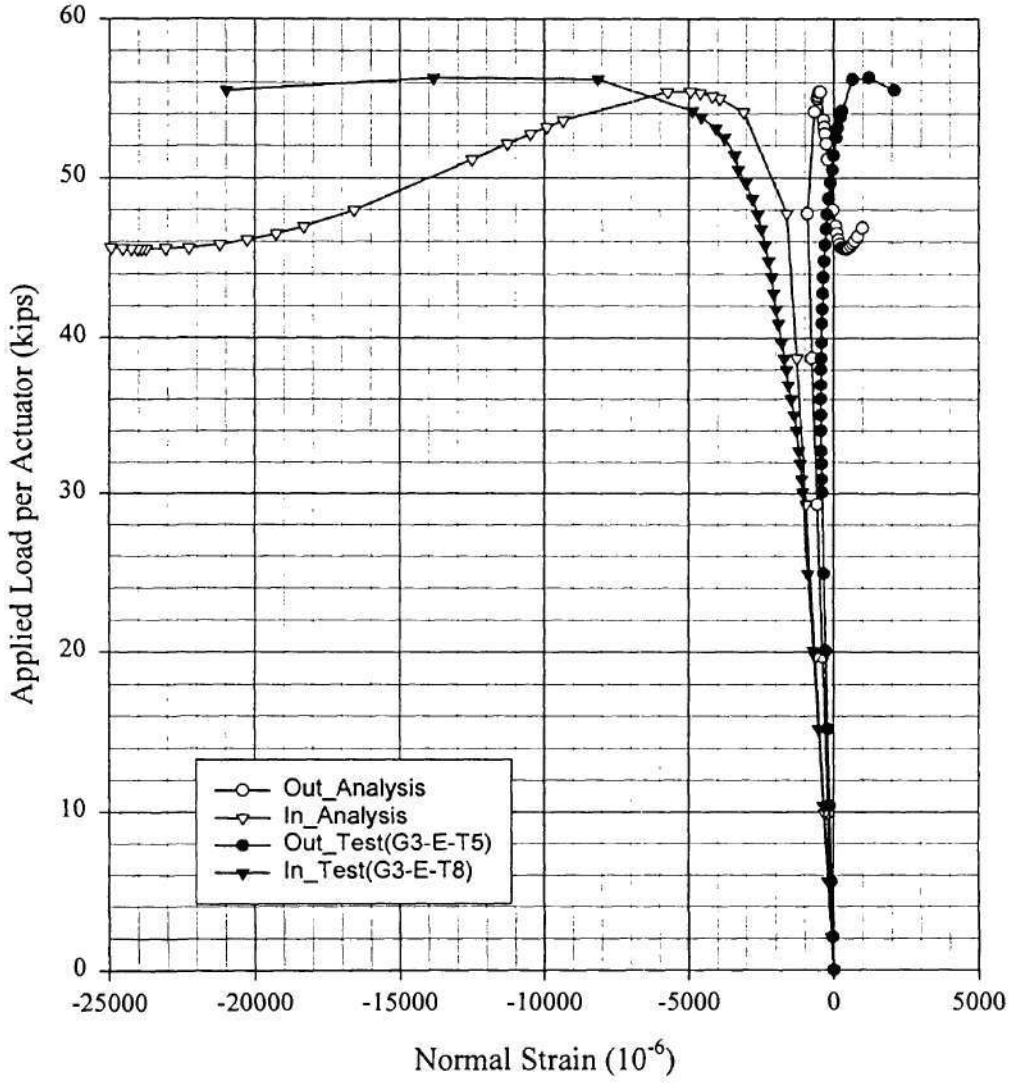

Comparison Between Analysis(B3h_3) and Test(6-24-99) for B3
Normal Strain of the Btm Flange Topside at the Location G3_E

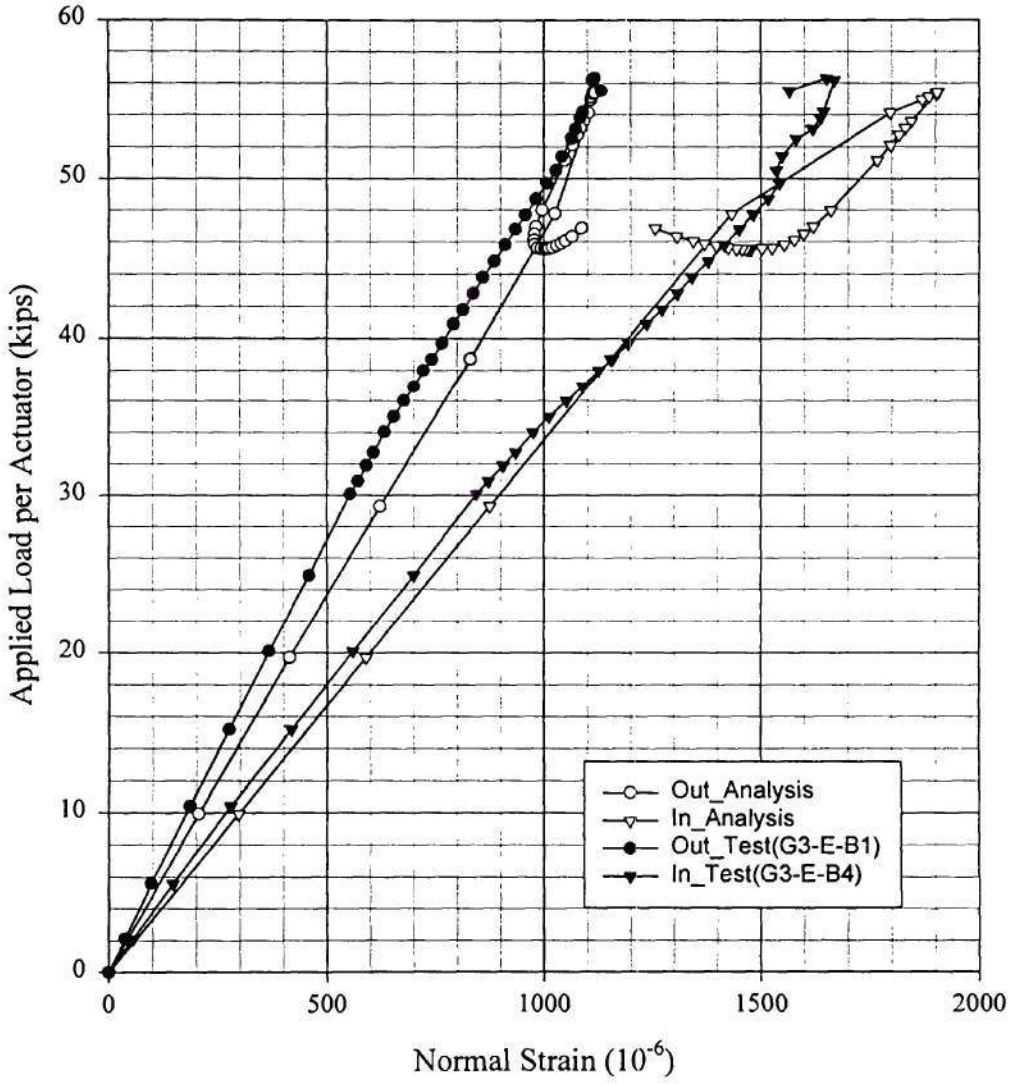

Comparison Between Analysis(B3h_3) and Test(6-24-99) for B3
Normal Strain of the Btm Flange Btmside at the Location G3_E

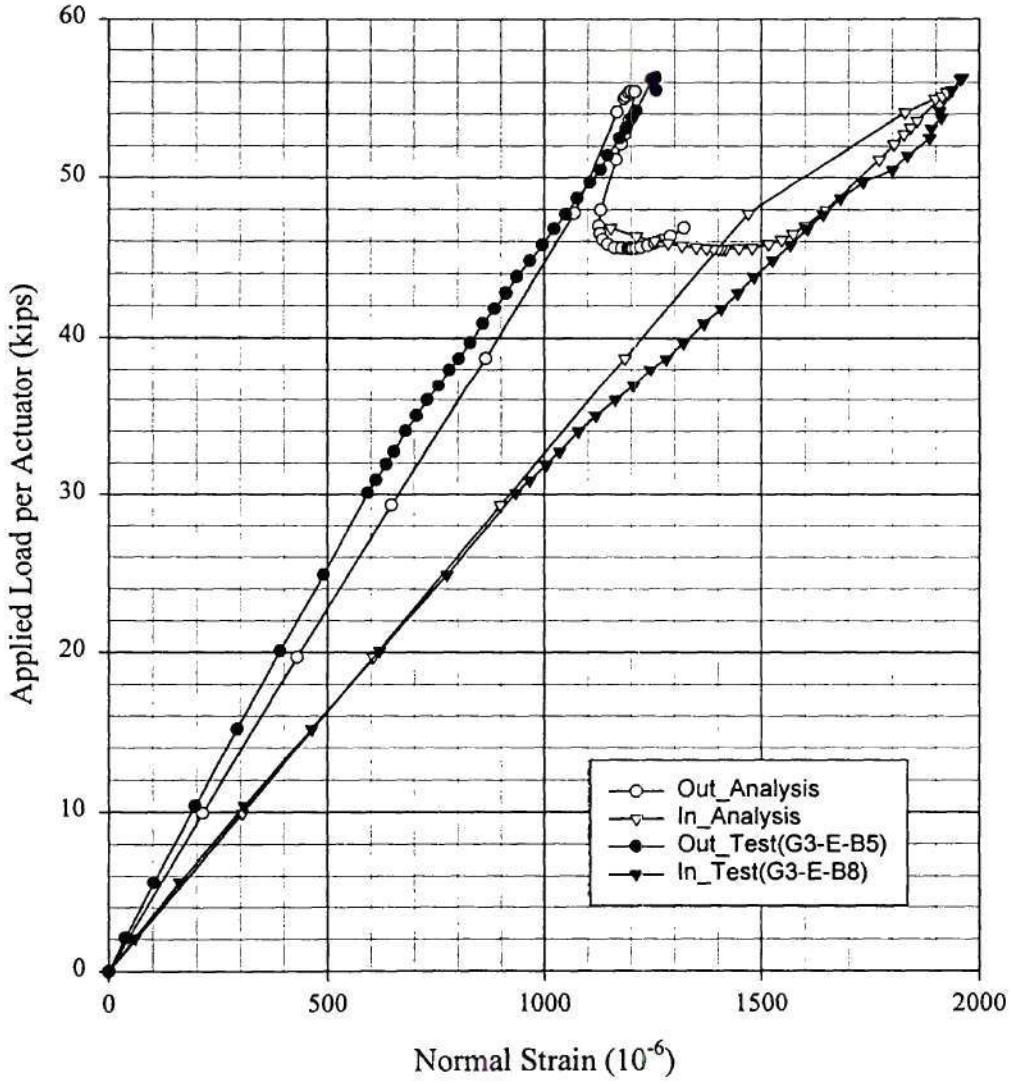

Test(6-24-99) for B3
Normal Strain of the Web at the Location G3_E

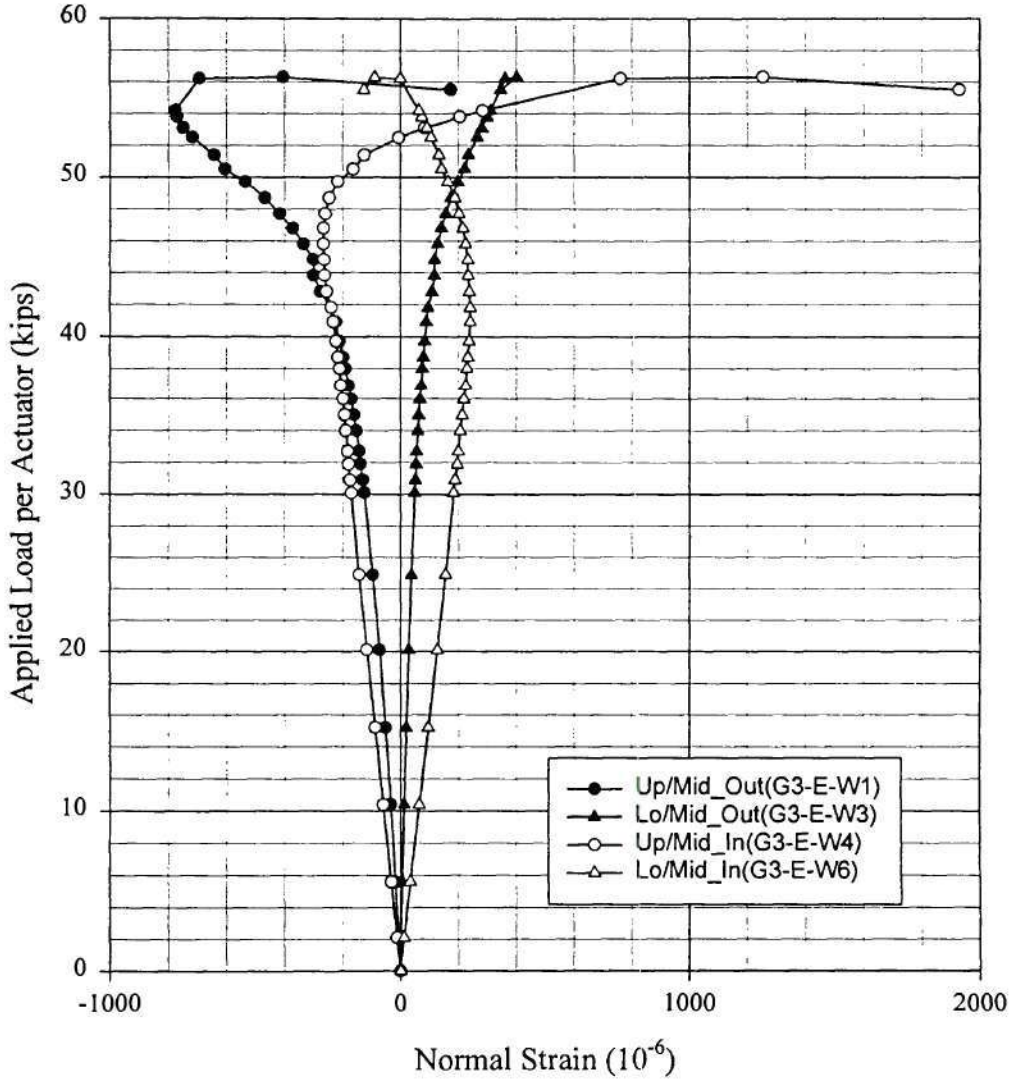

Test(6-24-99) for B3
Normal Strain of the Top Flange at the Location G3_E

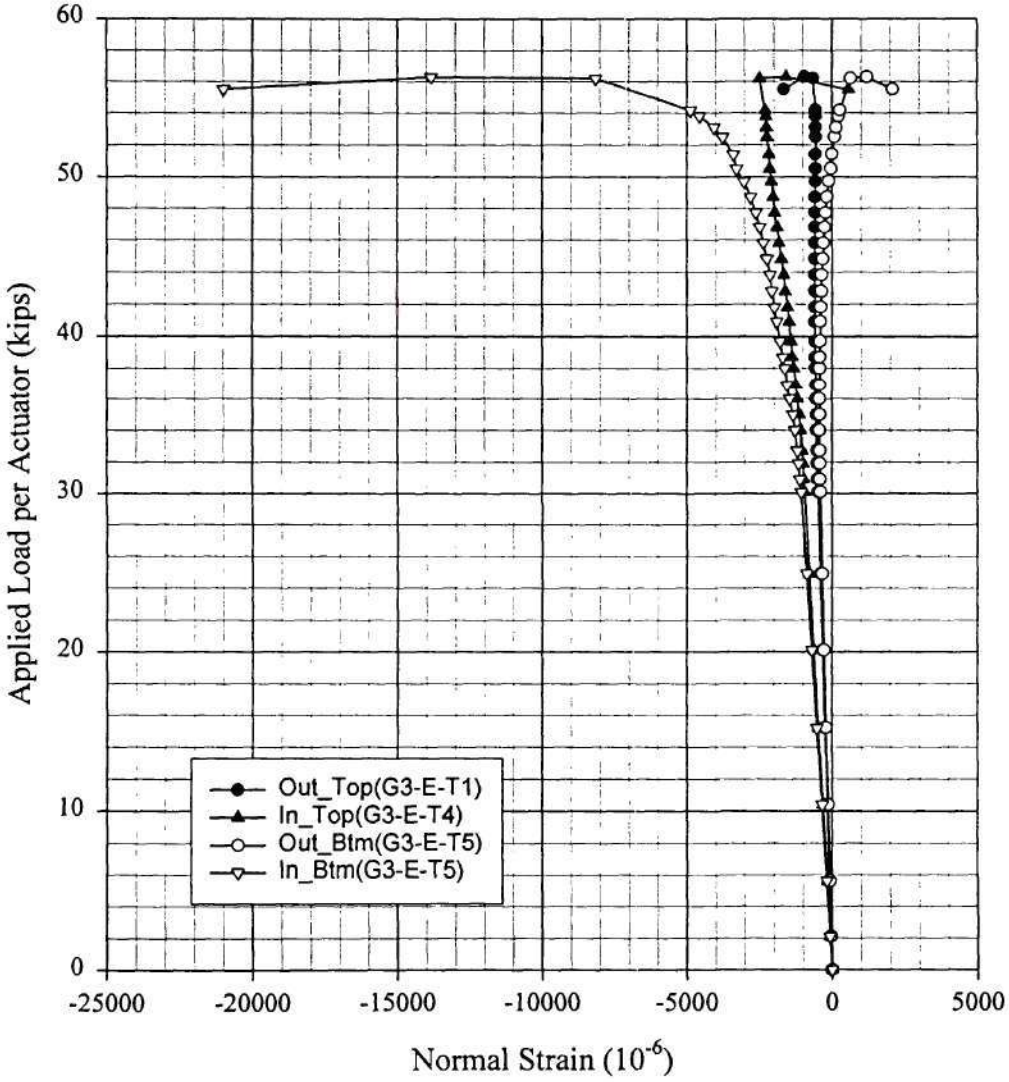

Test(6-24-99) for B3
Normal Strain of the Bottom Flange at the Location G3_E

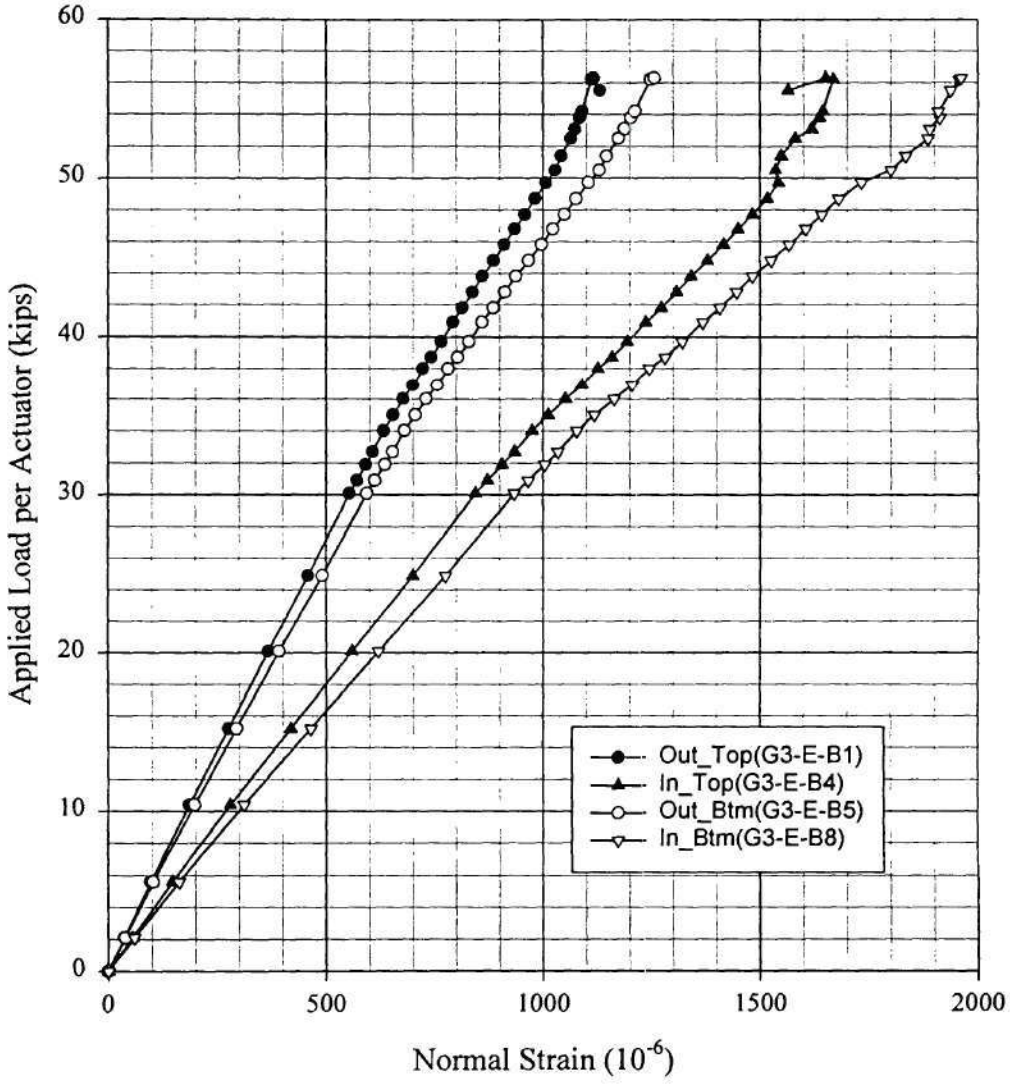

Comparison Between Analysis(B4h_3) and Test(7-26-99) for B4
Vertical Reactions at the East Supports

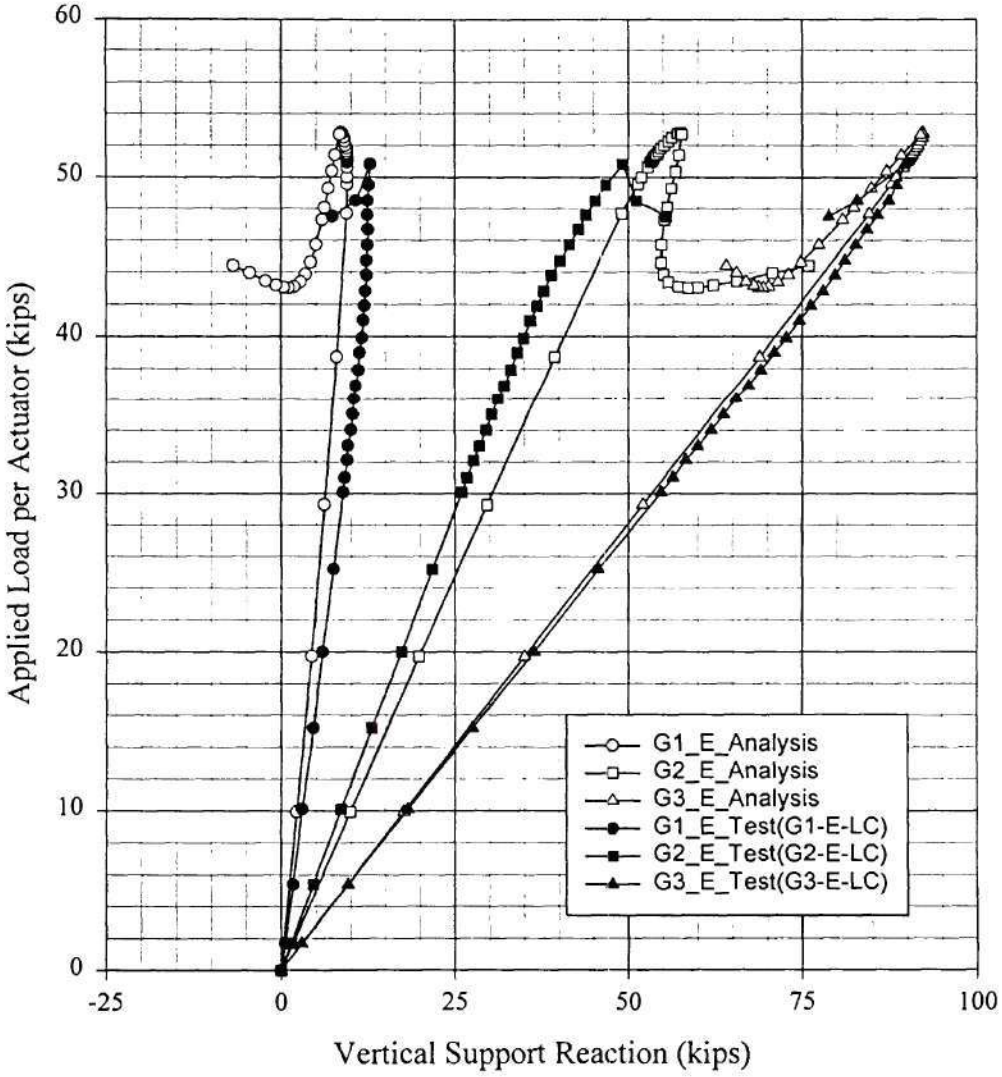

Comparison Between Analysis(B4h_3) and Test(7-26-99) for B4
Vertical Reactions at the West Supports

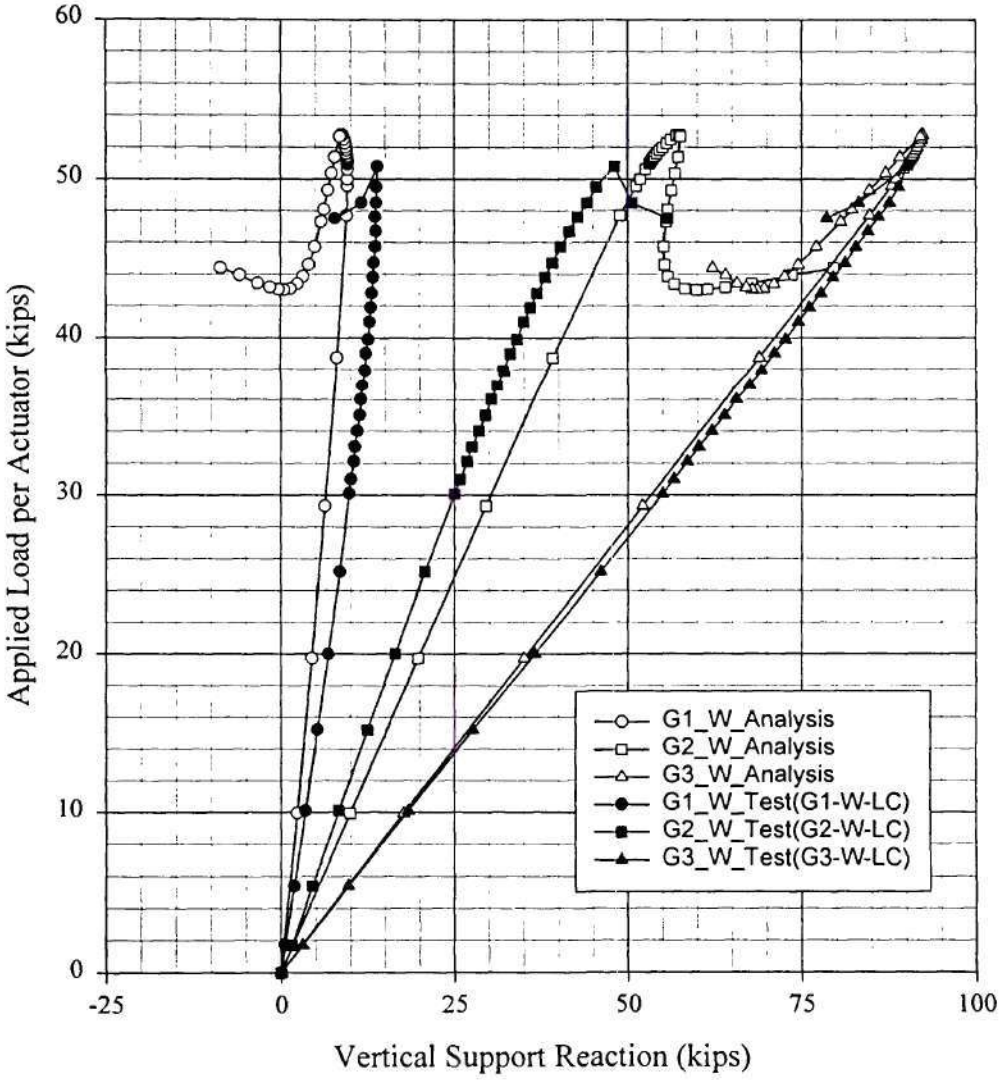

Comparison Between Analysis(B4h_3) and Test(7-26-99) for B4
Vertical Displacement of Bottom Flange (Outside) at Midspan

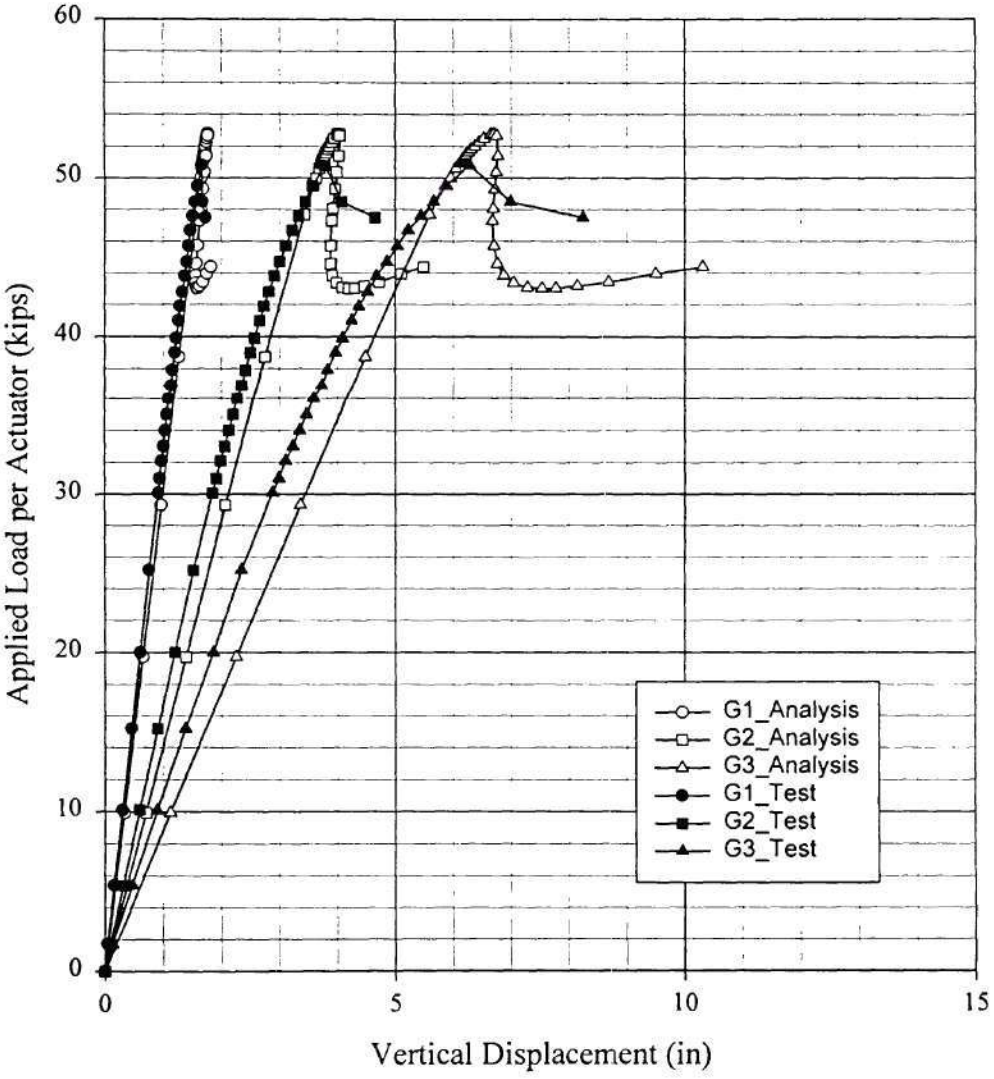

Comparison Between Analysis(B4h_3) and Test(7-26-99) for B4
Radial Displacement of Top Flange (Outside) at Midspan

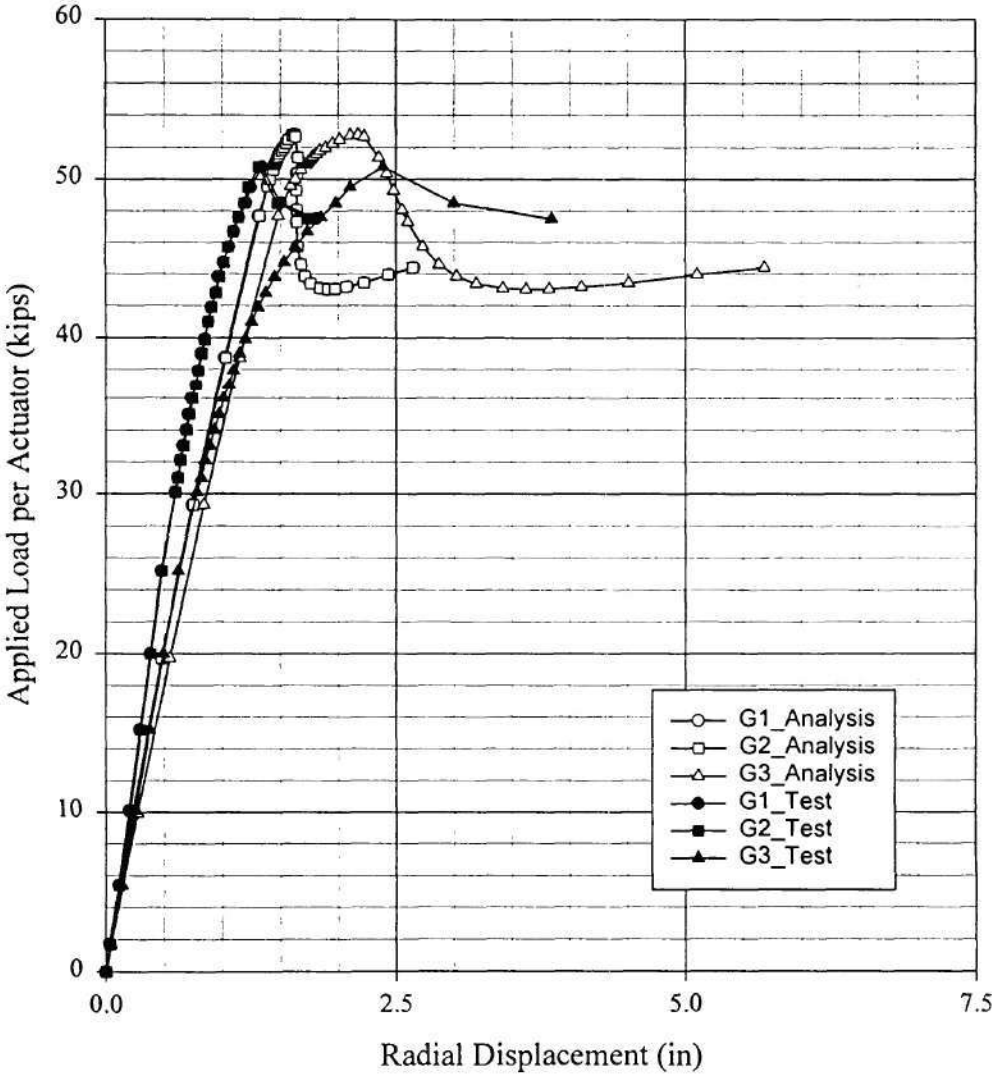

Comparison Between Analysis(B4h_3) and Test(7-26-99) for B4
Radial Displacement of Bottom Flange (Outside) at Midspan

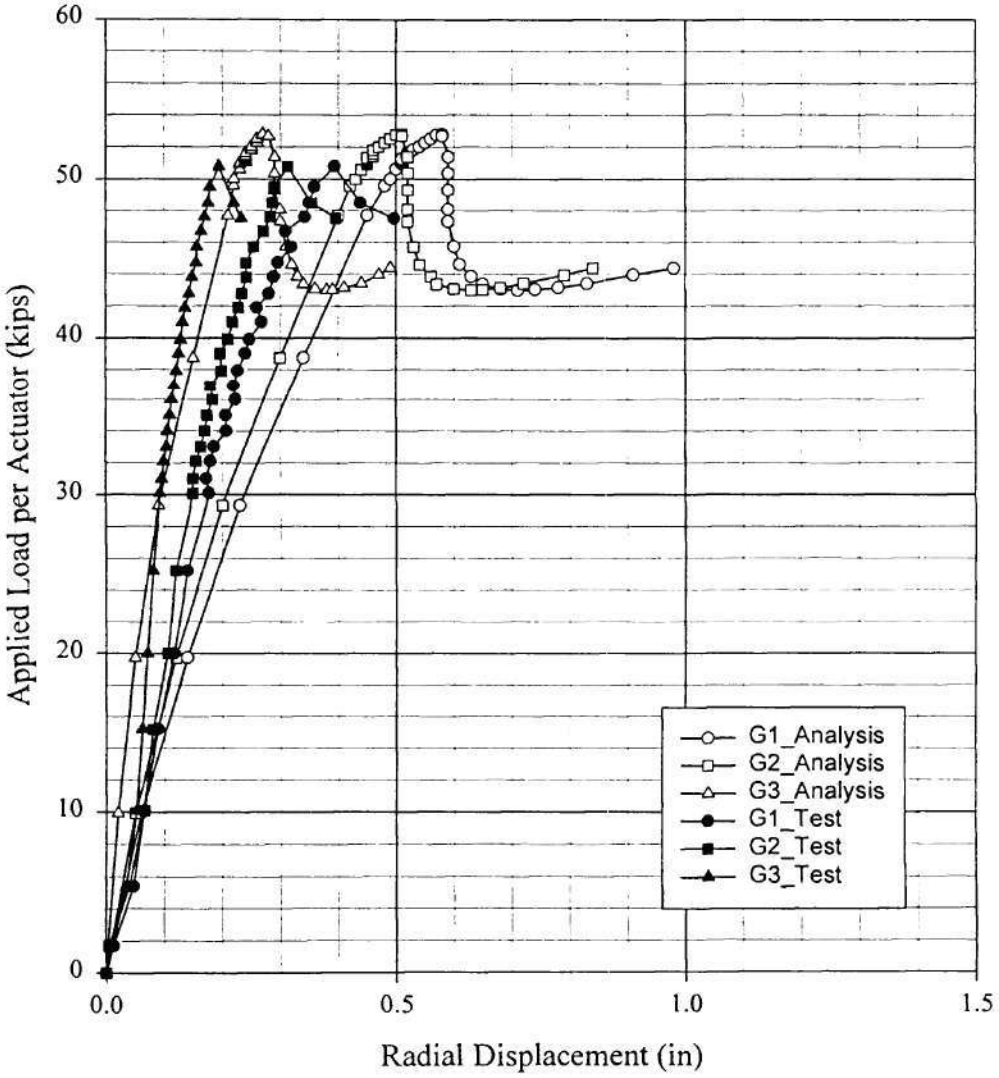

Comparison Between Analysis(B4h_3) and Test(7-26-99) for B4
Axial Force of Cross Frame at 6R Between G2 and G3

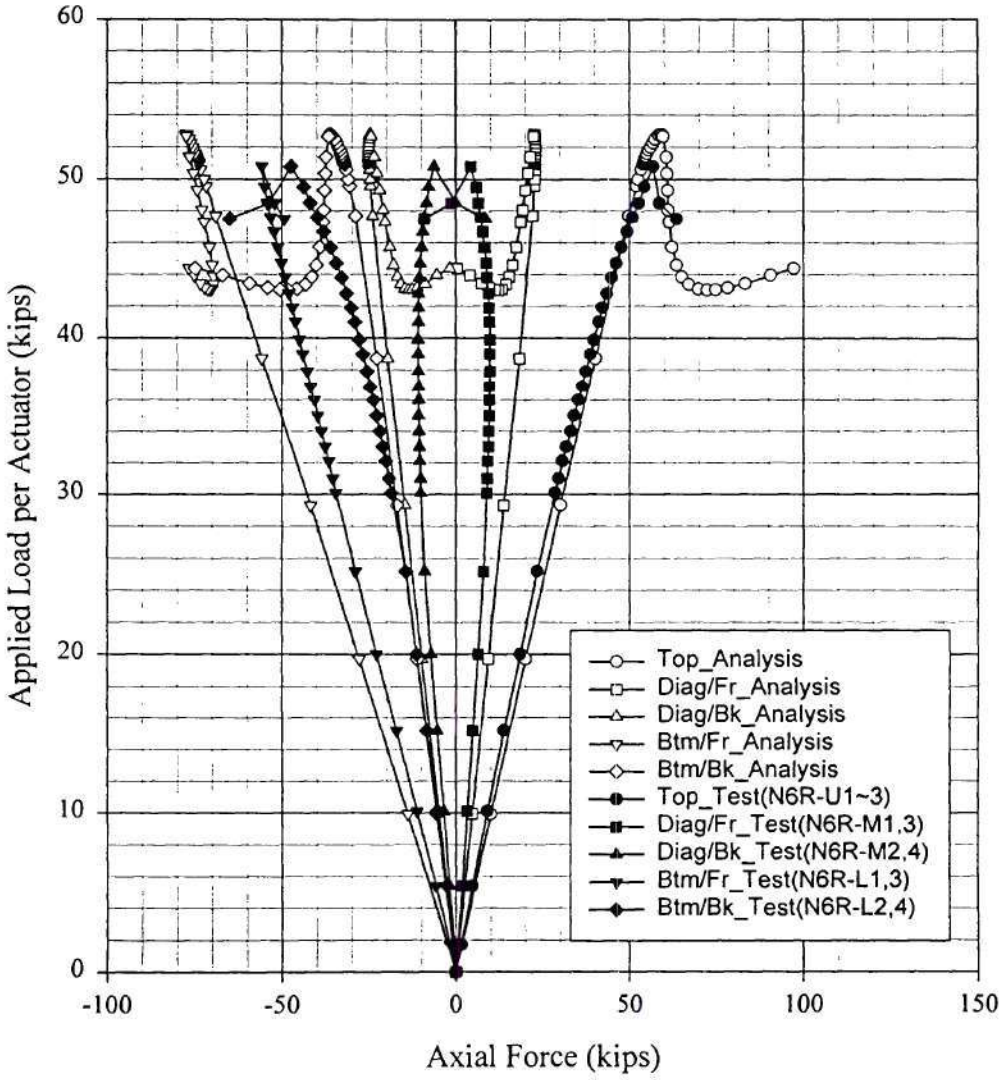

Comparison Between Analysis(B4h_3) and Test(7-26-99) for B4
Axial Force of Cross Frame at 6L Between G2 and G3

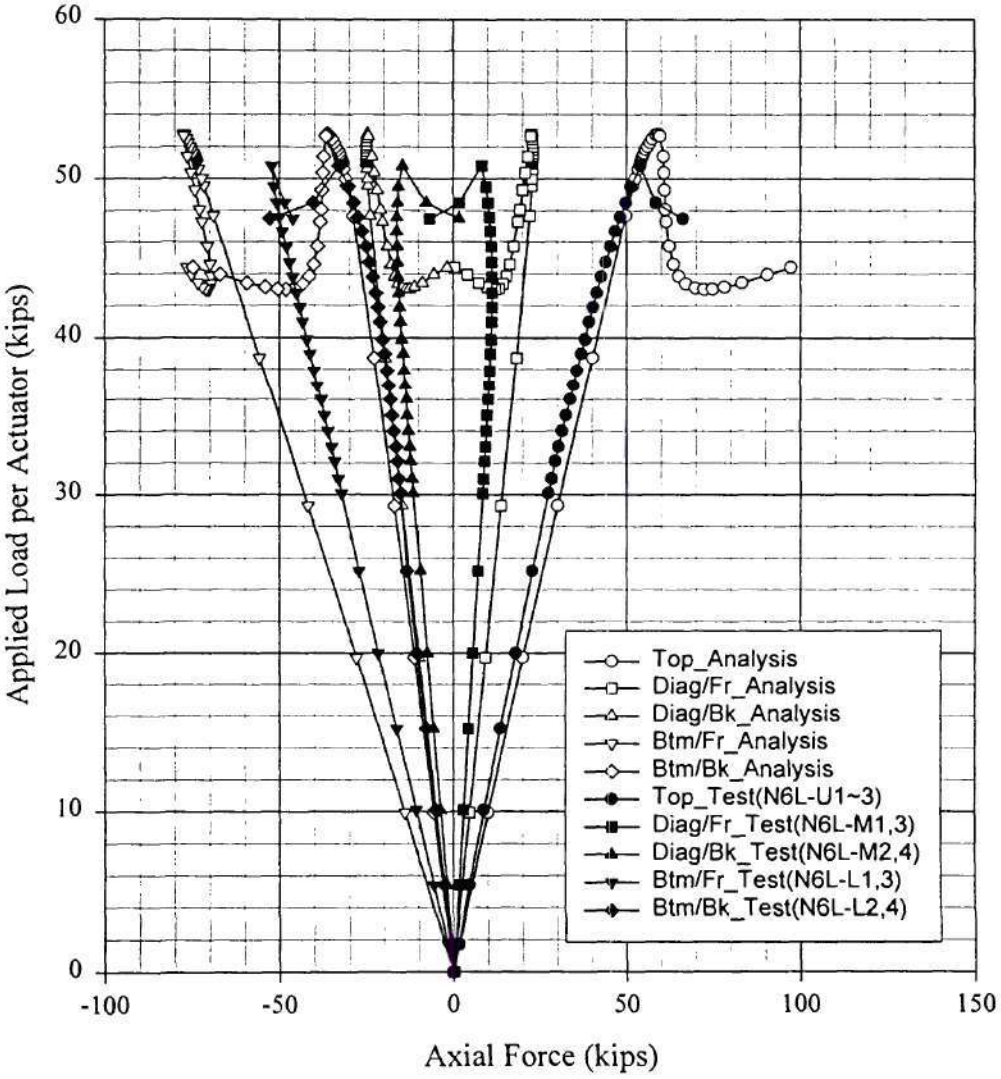

Comparison Between Analysis(B4h_3) and Test(7-26-99) for B4
Bending Moment at Midspan

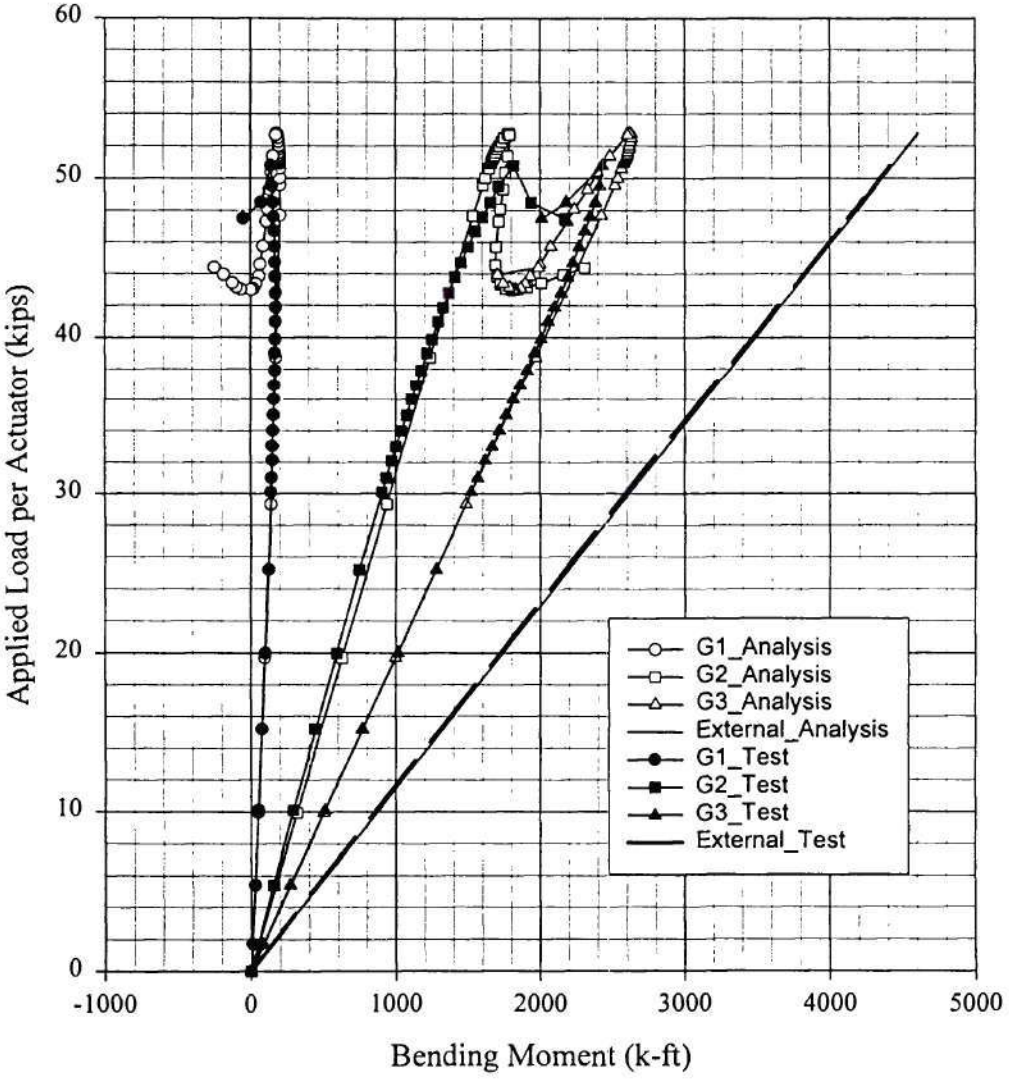

Comparison Between Analysis(B4h_3) and Test(7-26-99) for B4
Normal Strain of the Web Inside at the Location G1_B

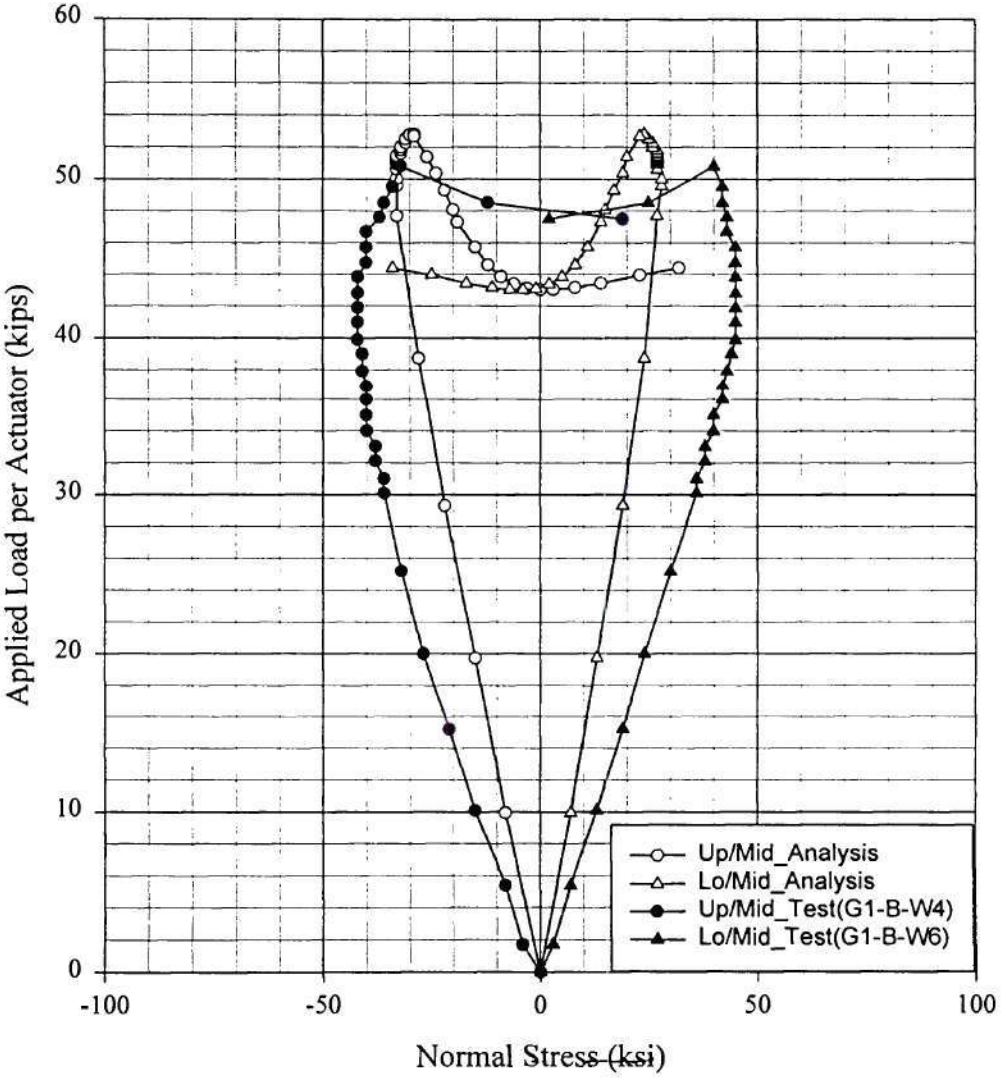

Comparison Between Analysis(B4h_3) and Test(7-26-99) for B4
Normal Strain of the Top Flange Topside at the Location G1_B

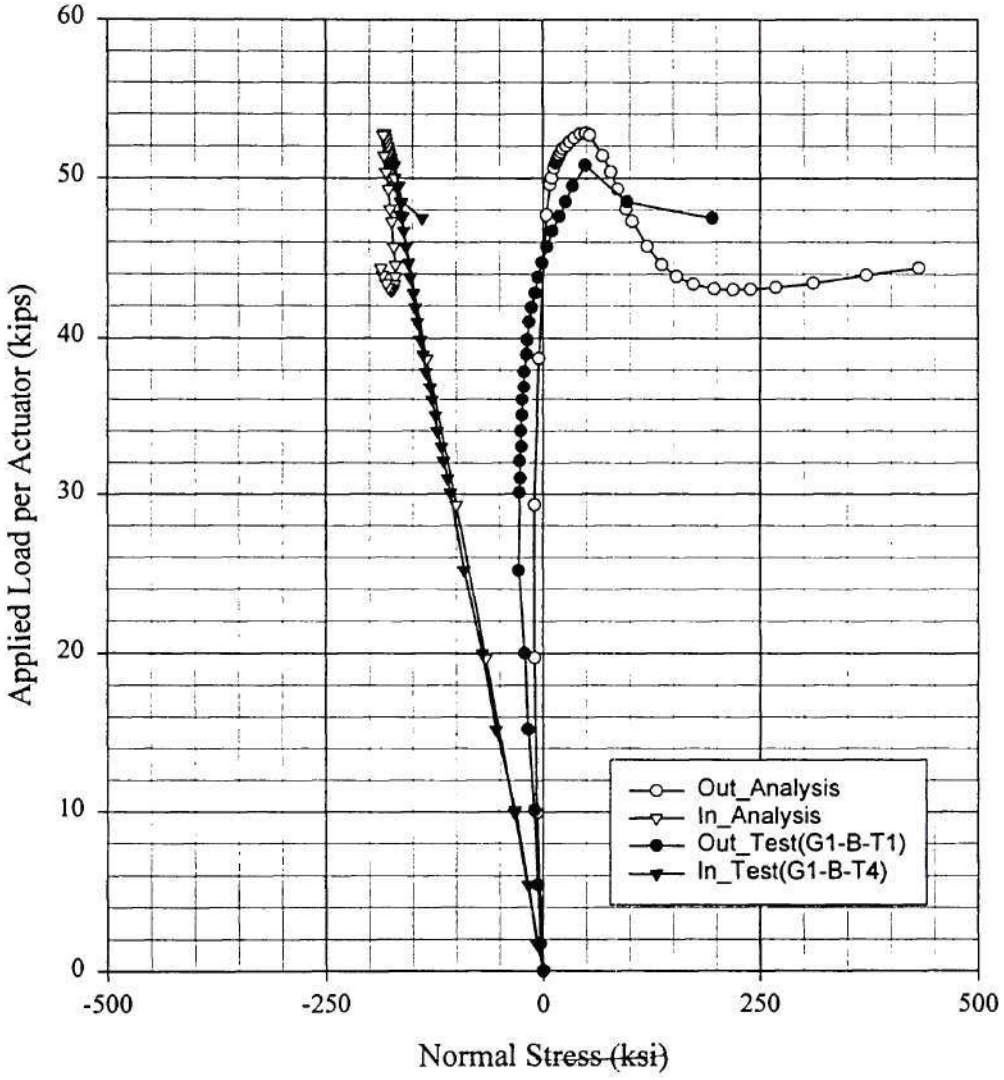

Comparison Between Analysis(B4h_3) and Test(7-26-99) for B4
Normal Strain of the Top Flange Btmside at the Location G1_B

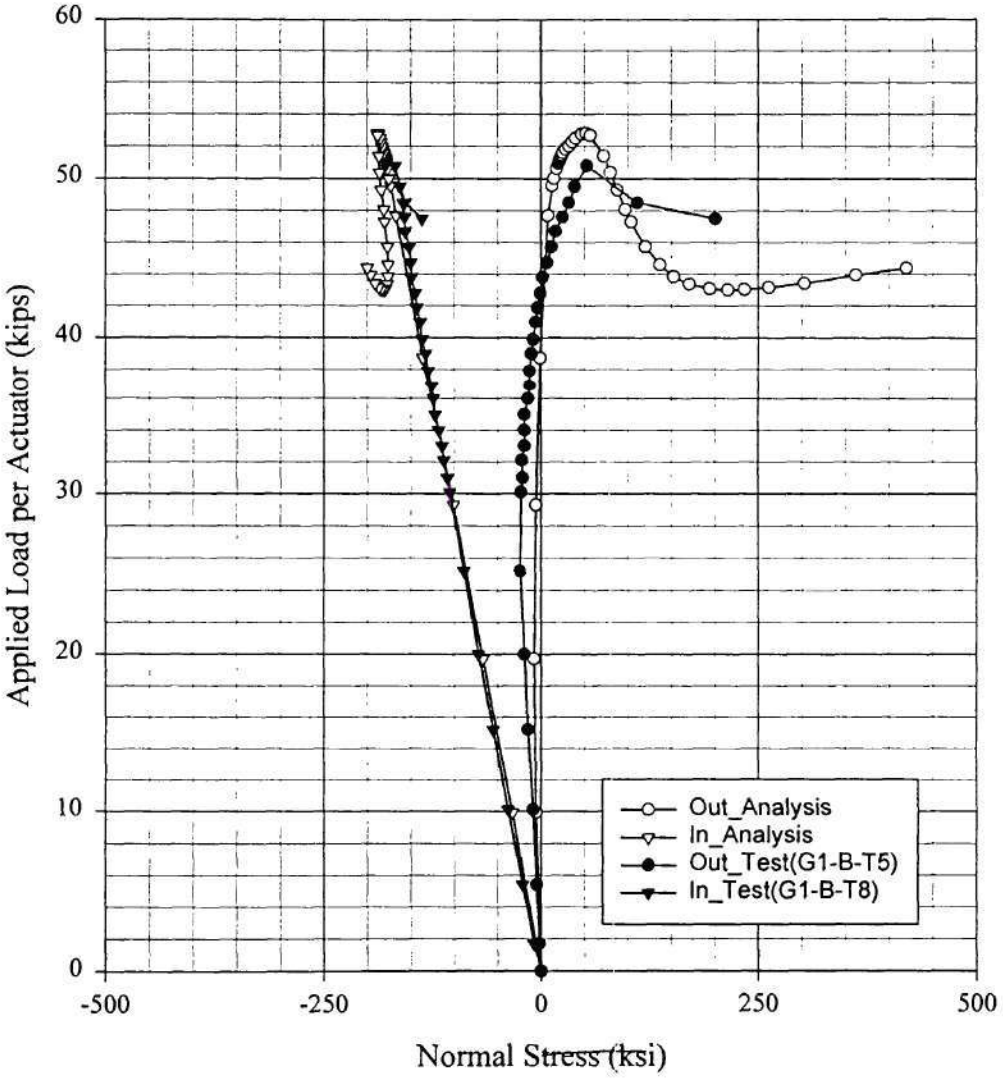

Comparison Between Analysis(B4h_3) and Test(7-26-99) for B4
Normal Strain of the Btm Flange Topside at the Location G1_B

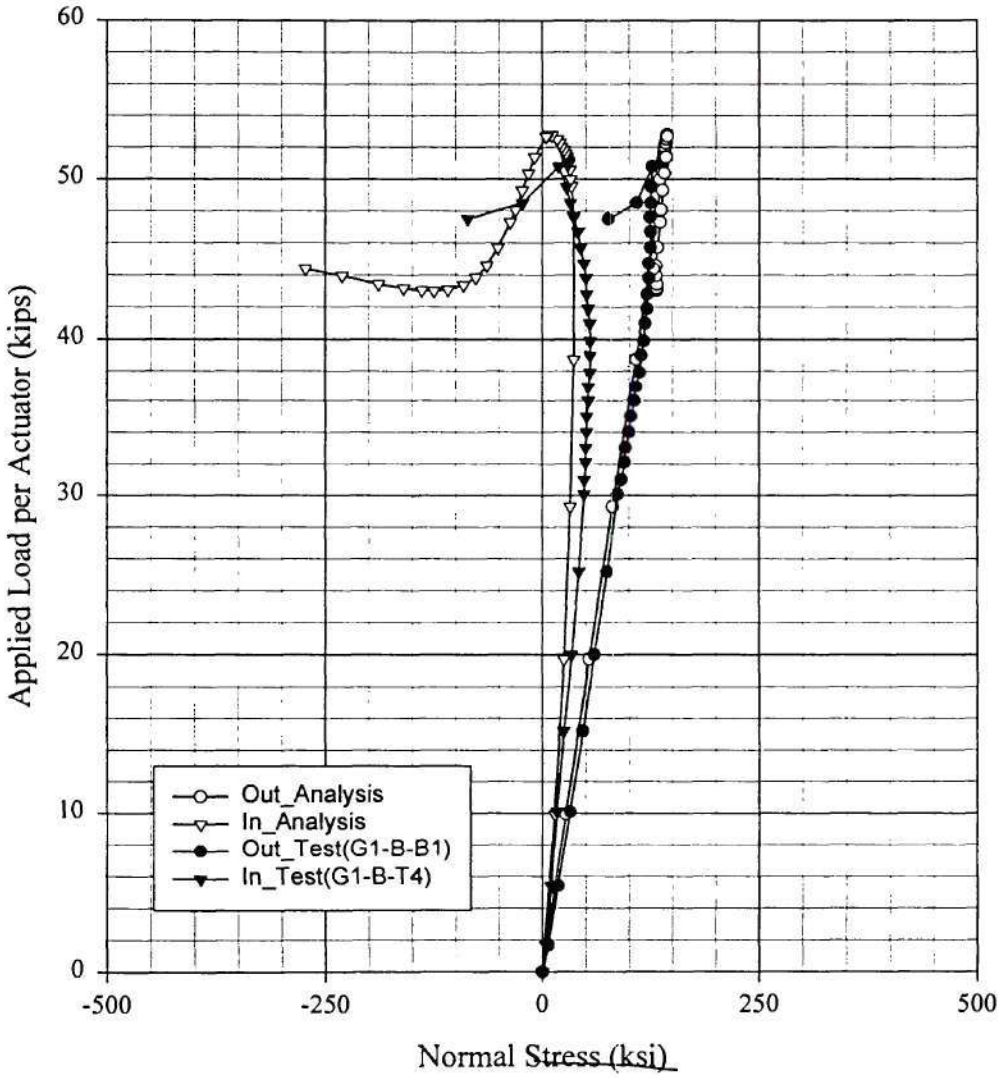

Comparison Between Analysis(B4h_3) and Test(7-26-99) for B4
Normal Strain of the Btm Flange Btmside at the Location G1_B

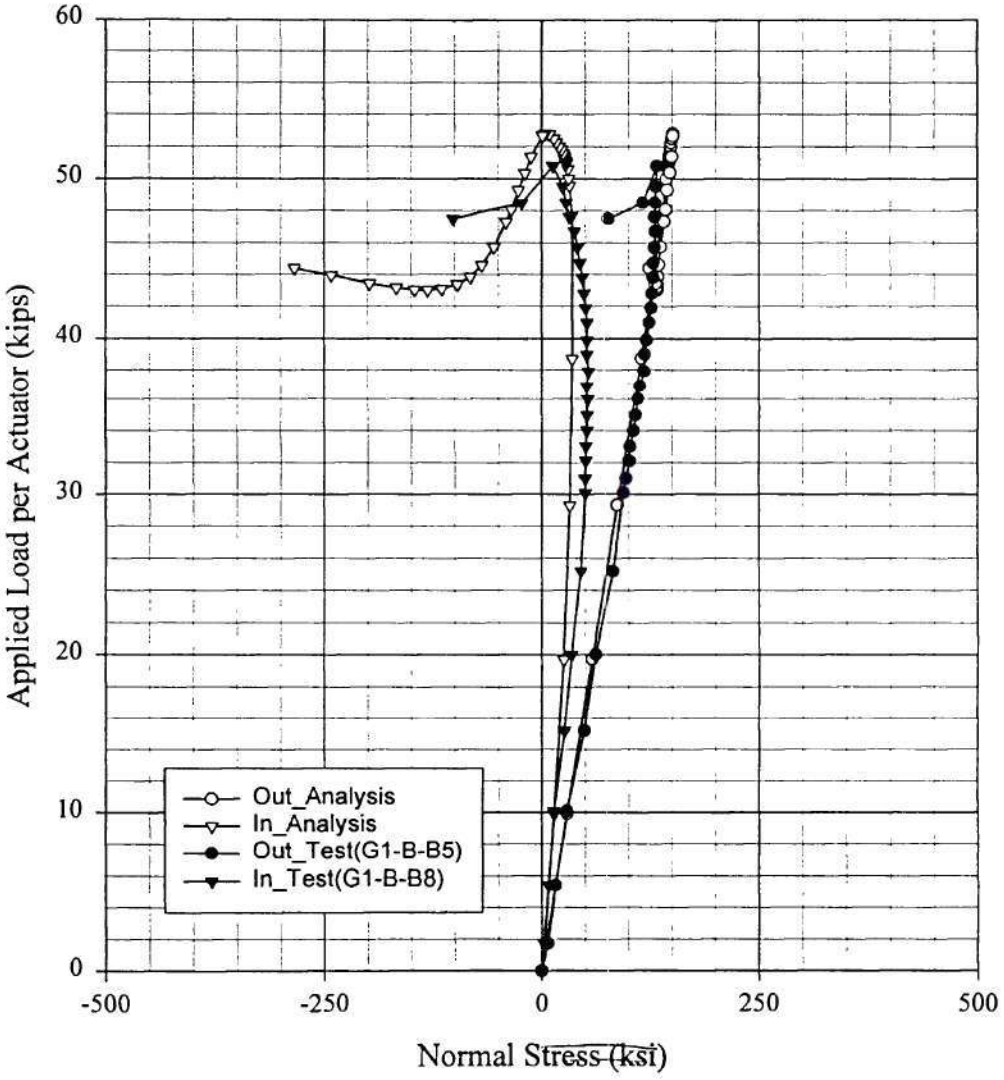

Comparison Between Analysis(B4h_3) and Test(7-26-99) for B4
Normal Strain of the Web Inside at the Location G2_B

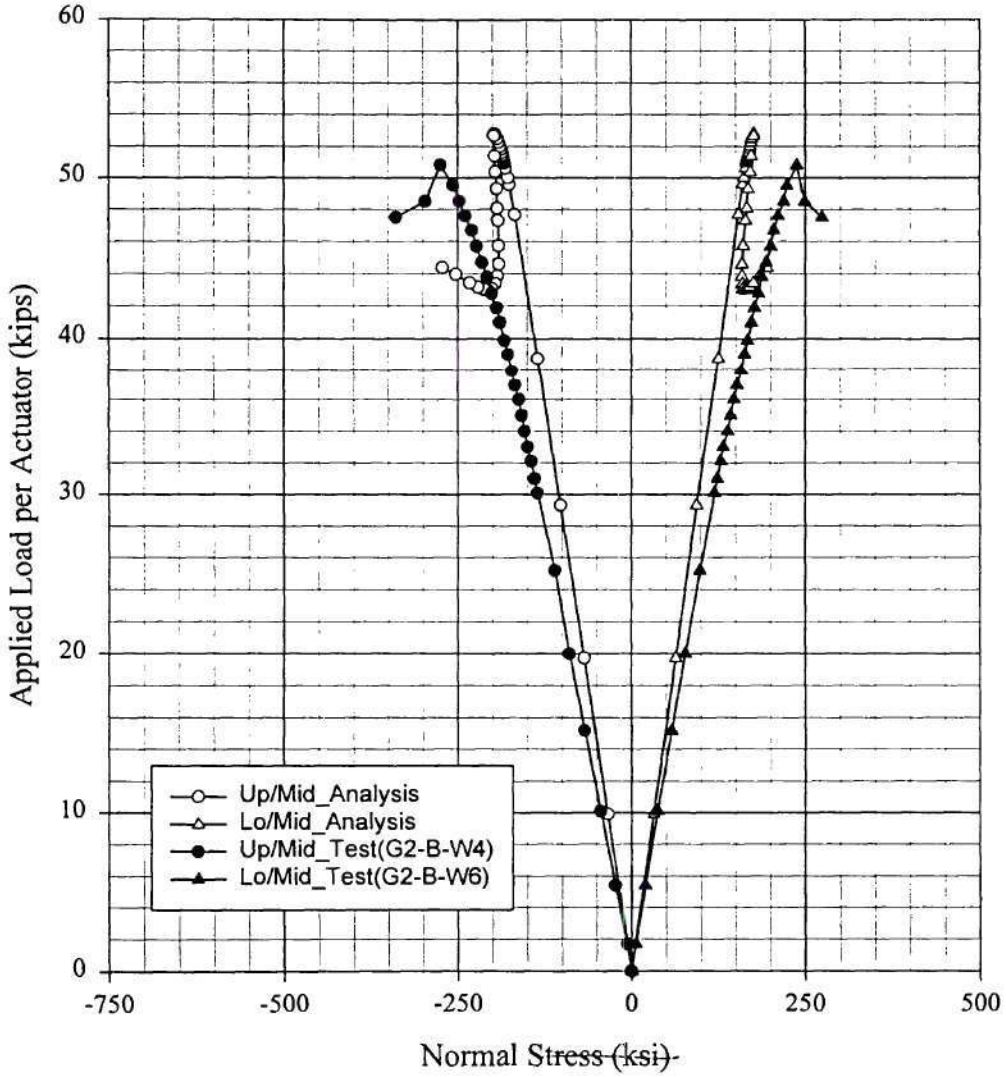

Comparison Between Analysis(B4h_3) and Test(7-26-99) for B4
Normal Strain of the Top Flange Topside at the Location G2_B

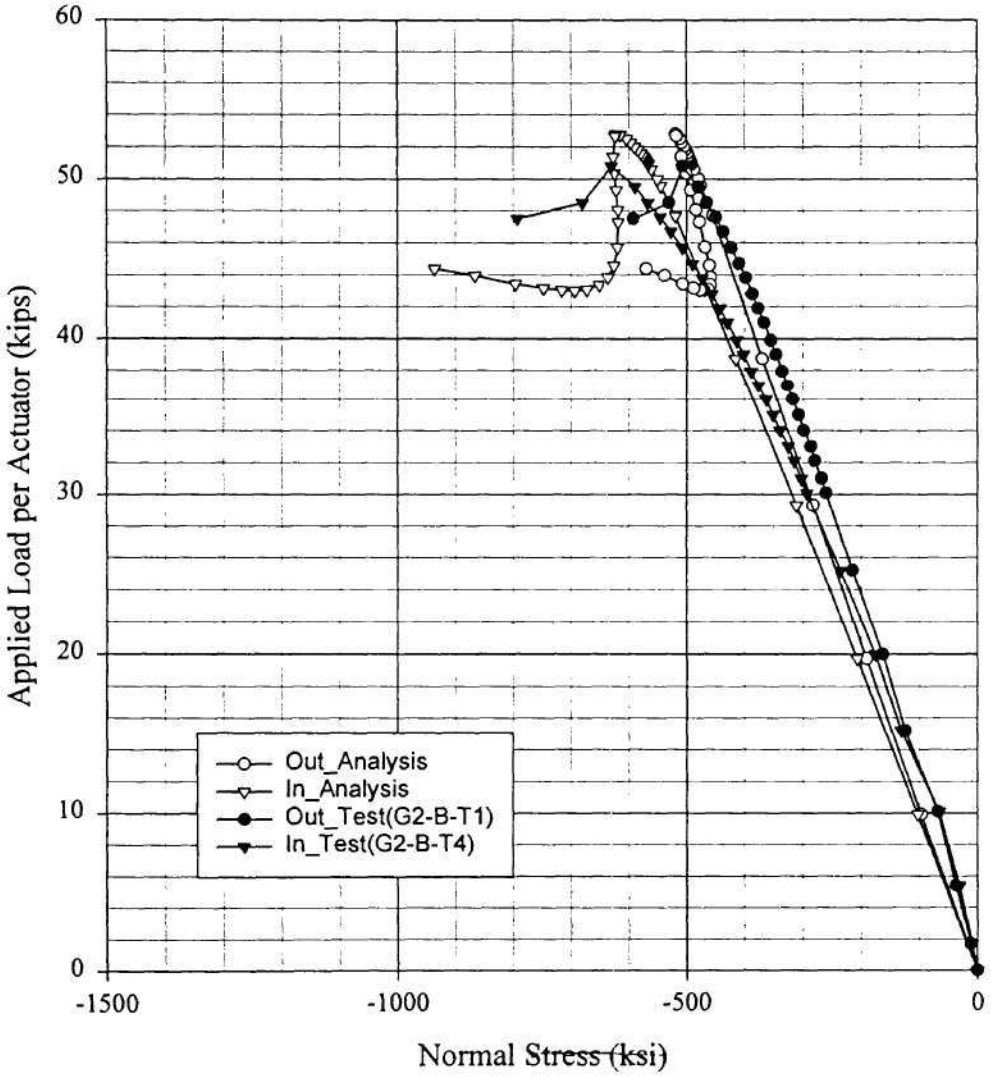

Comparison Between Analysis(B4h_3) and Test(7-26-99) for B4
Normal Strain of the Top Flange Btmside at the Location G2_B

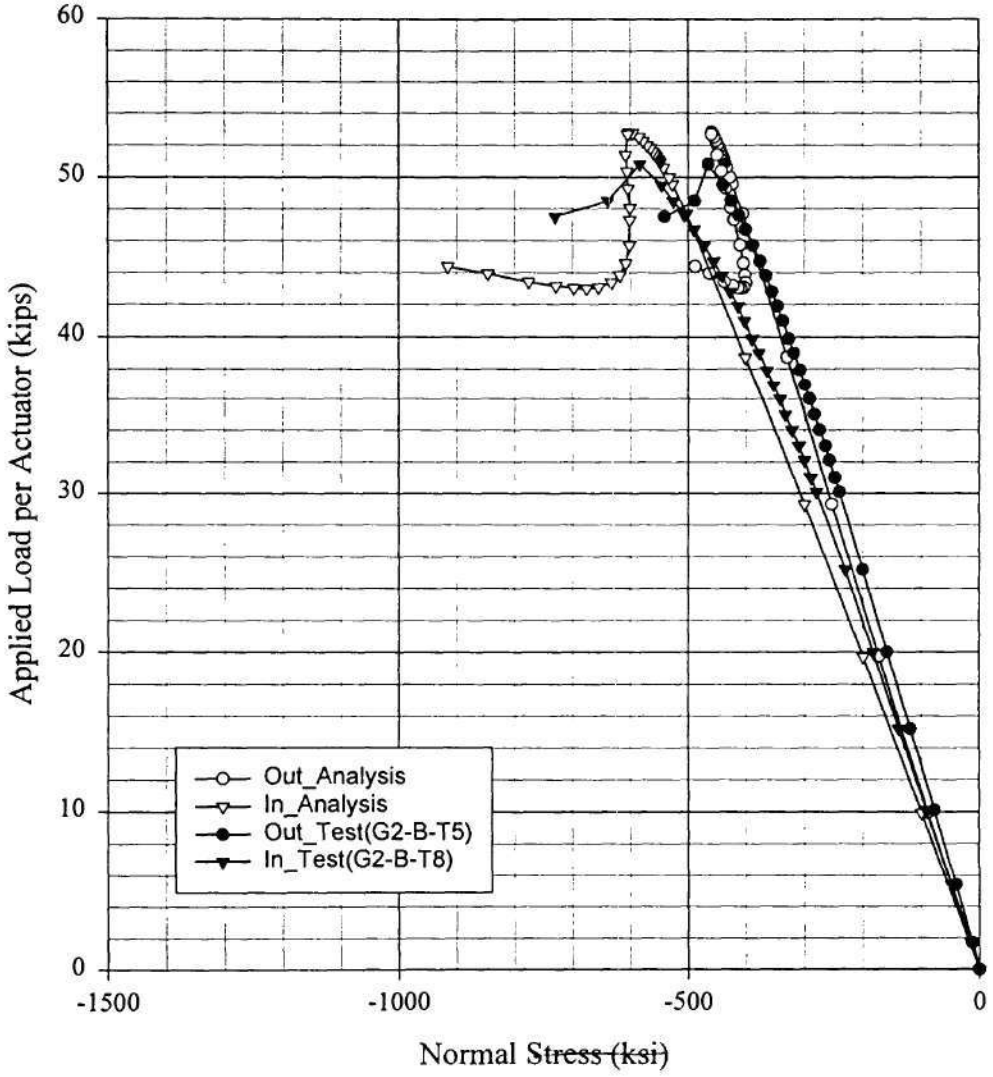

Comparison Between Analysis(B4h_3) and Test(7-26-99) for B4
Normal Strain of the Btm Flange Topside at the Location G2_B

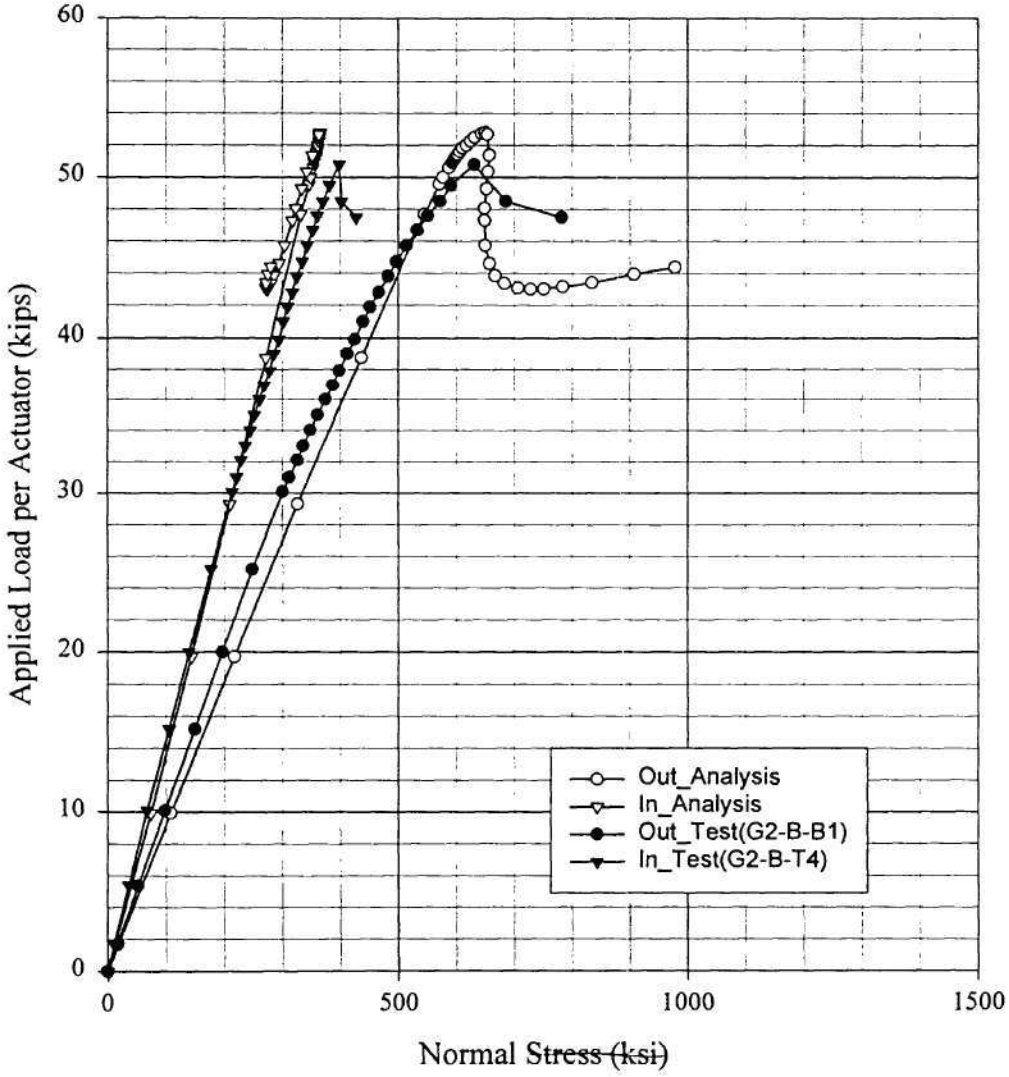

Comparison Between Analysis(B4h_3) and Test(7-26-99) for B4
Normal Strain of the Btm Flange Btmside at the Location G2_B

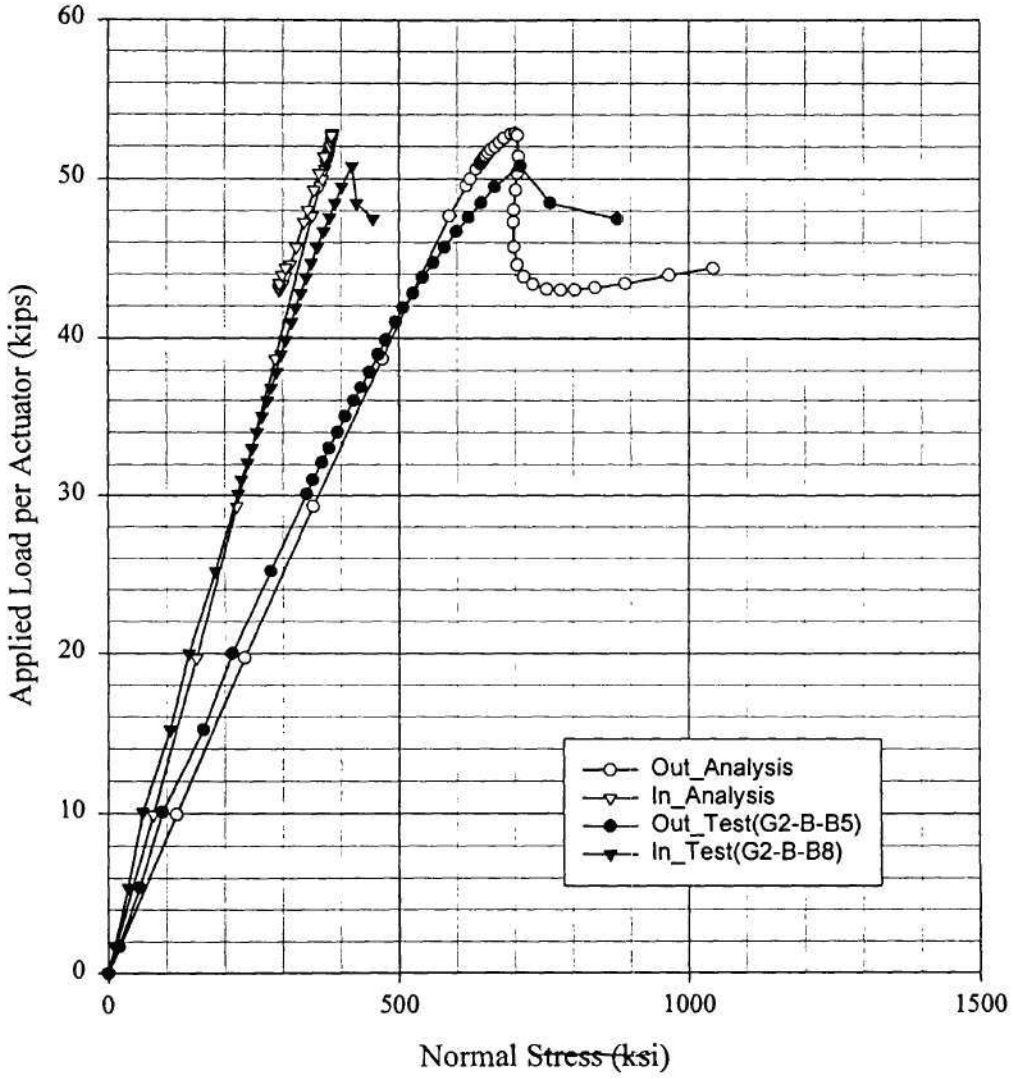

Comparison Between Analysis(B4h_3) and Test(7-26-99) for B4
Normal Strain of the Web Inside at the Location G3_E

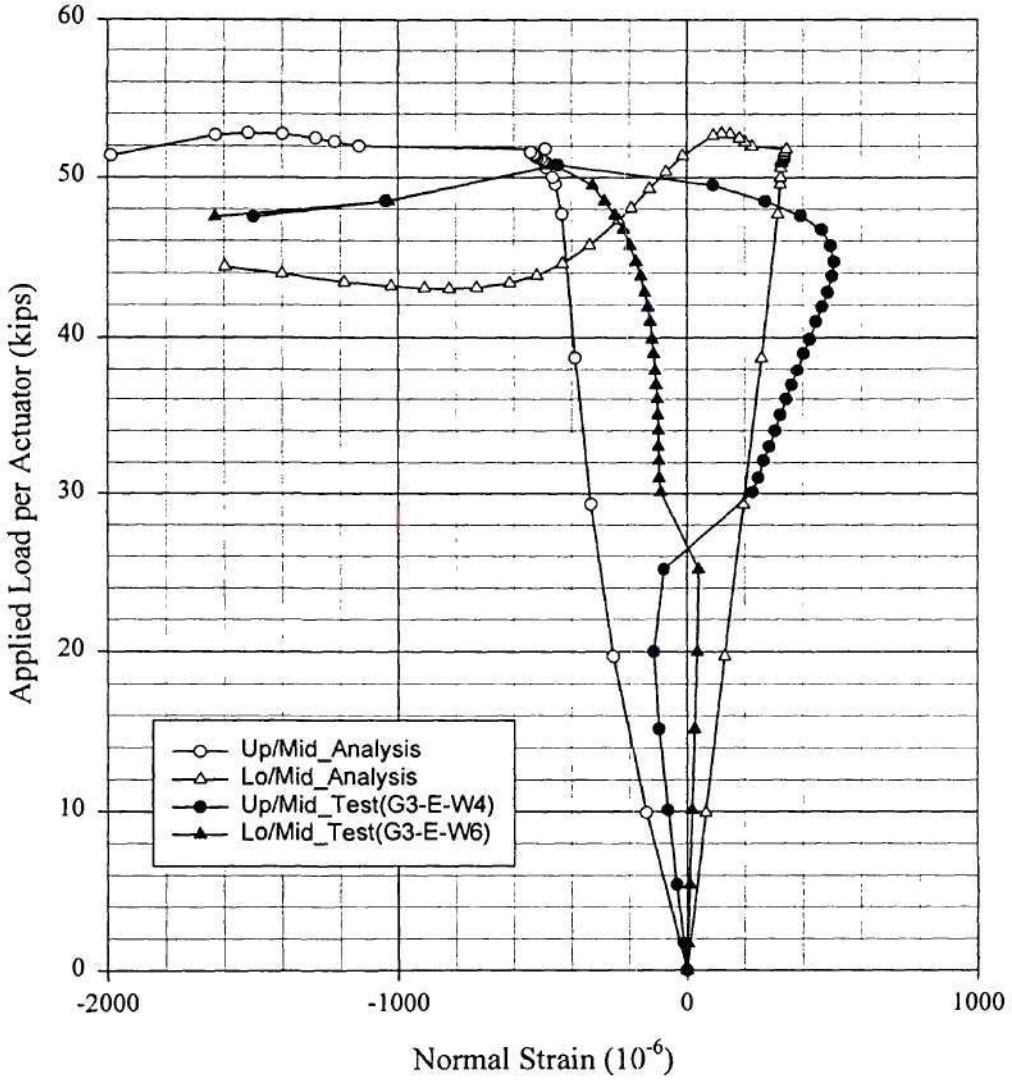

Comparison Between Analysis(B4h_3) and Test(7-26-99) for B4
Normal Strain of the Web Outside at the Location G3_E

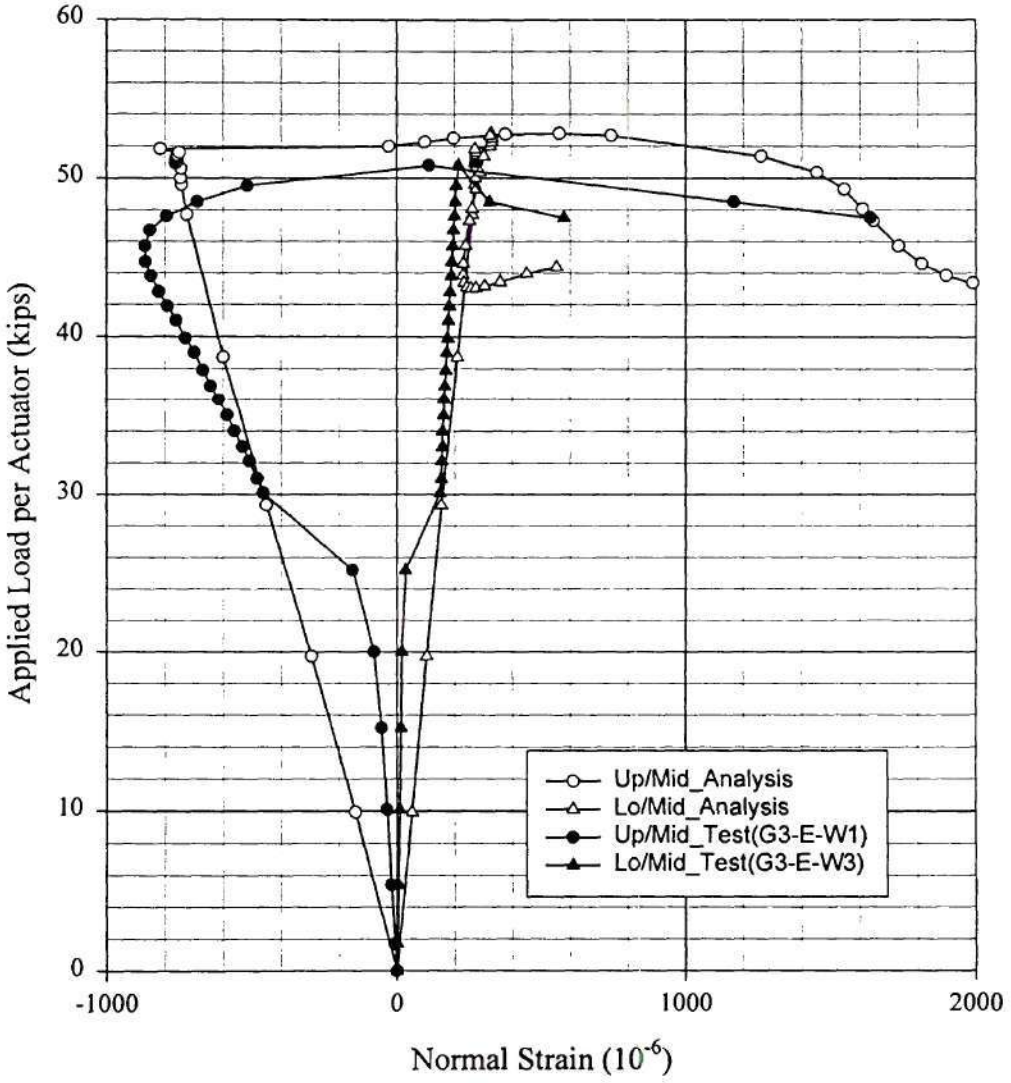

Comparison Between Analysis(B4h_3) and Test(7-26-99) for B4
Normal Strain of the Top Flange Topside at the Location G3_E

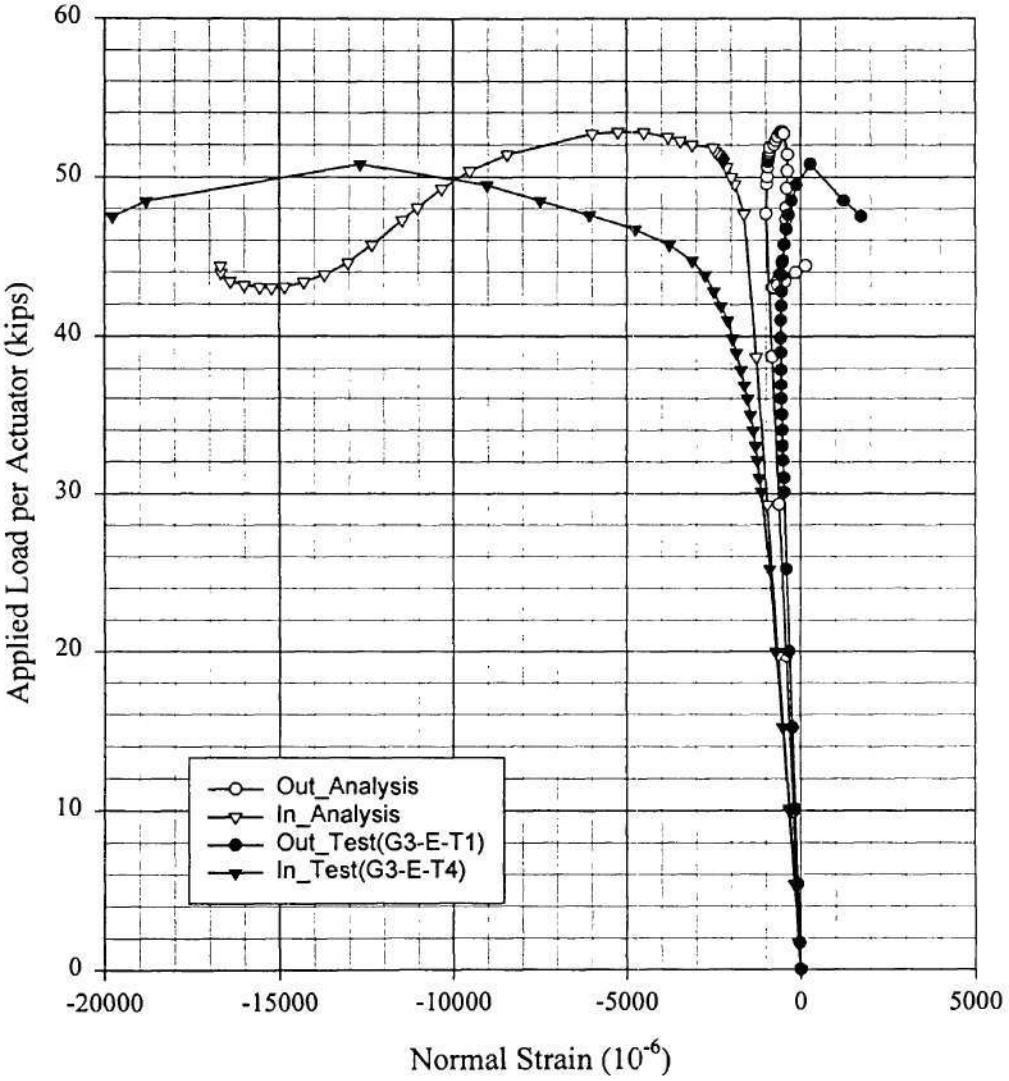

Comparison Between Analysis(B4h_3) and Test(7-26-99) for B4
Normal Strain of the Top Flange Btmside at the Location G3_E

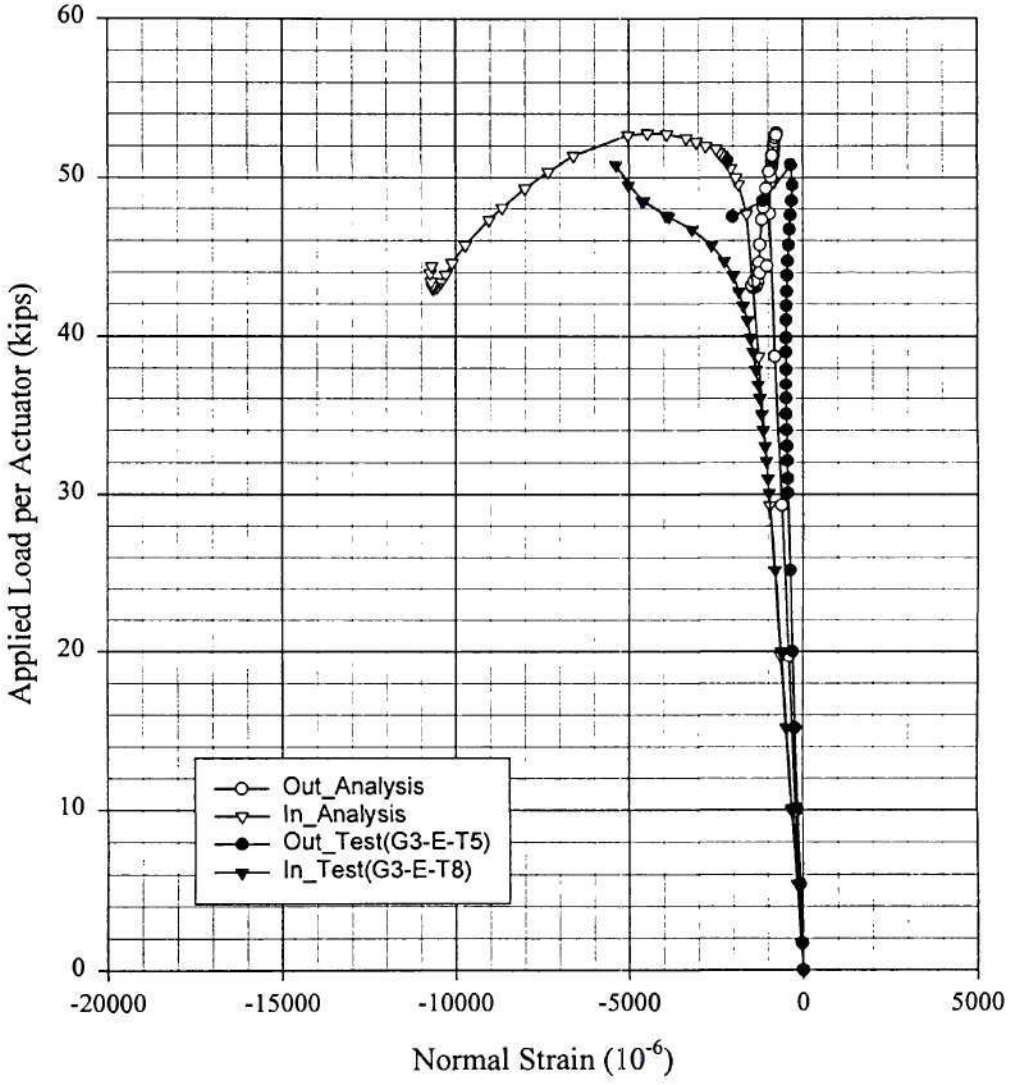

Comparison Between Analysis(B4h_3) and Test(7-26-99) for B4
Normal Strain of the Btm Flange Topside at the Location G3_E

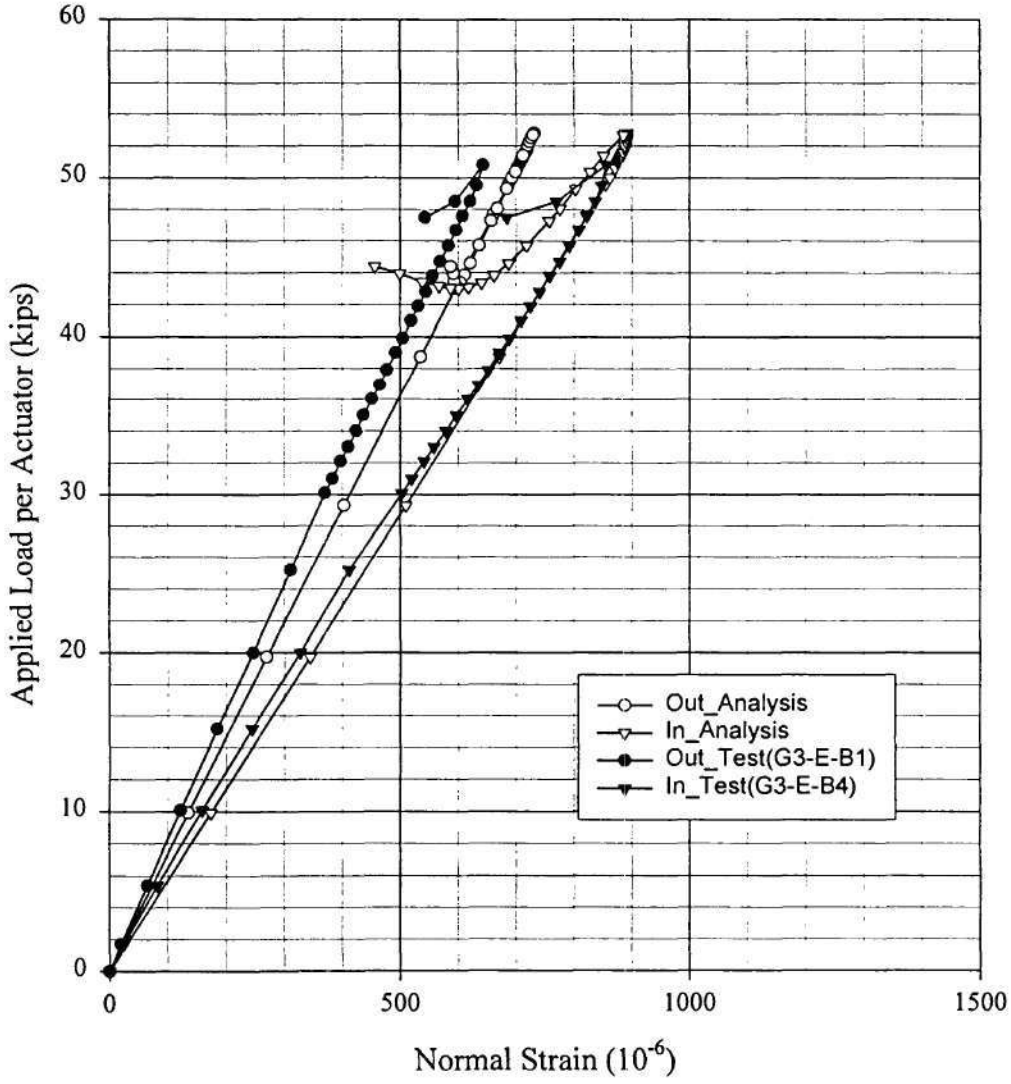

Comparison Between Analysis(B4h_3) and Test(7-26-99) for B4
Normal Strain of the Btm Flange Btmside at the Location G3_E

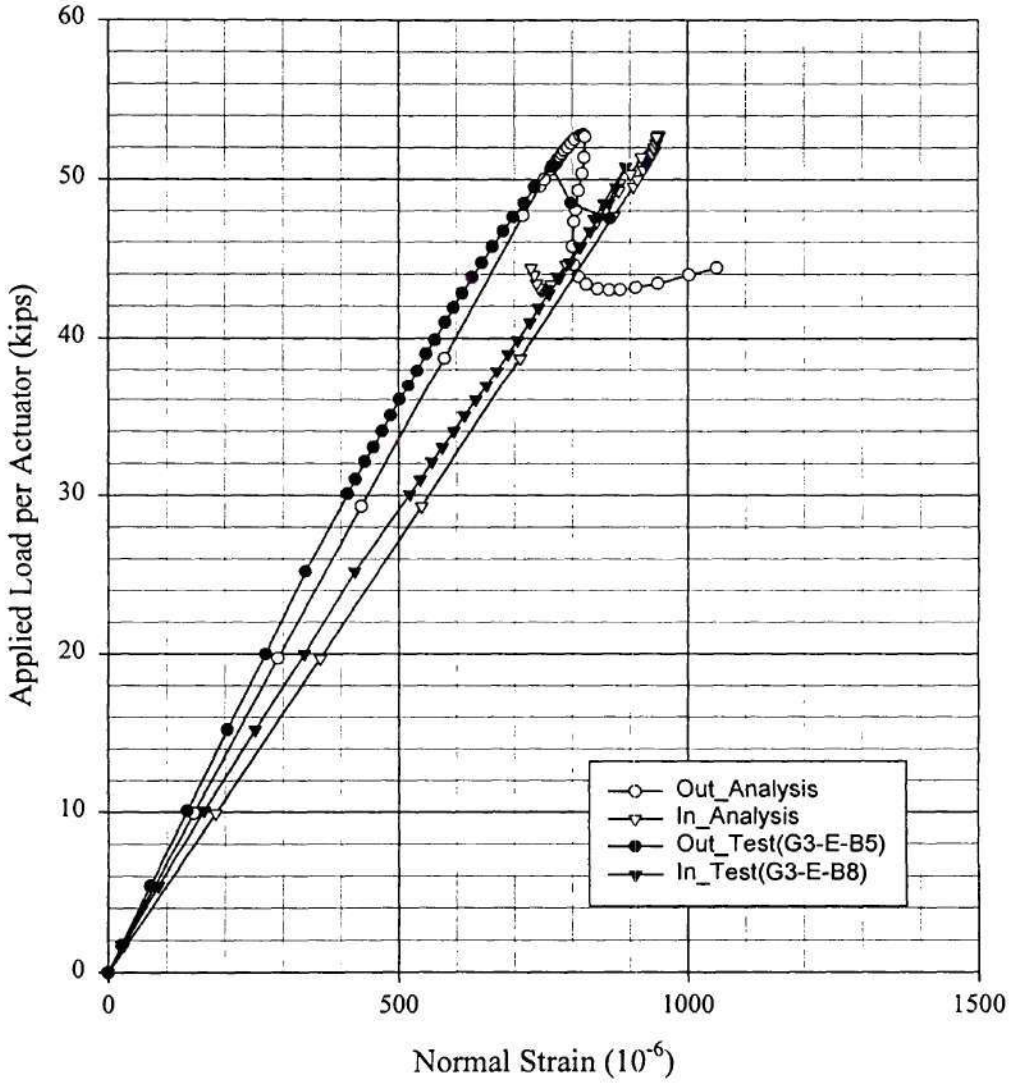

Test(7-26-99) for B4
Normal Strain of the Web at the Location G3_E

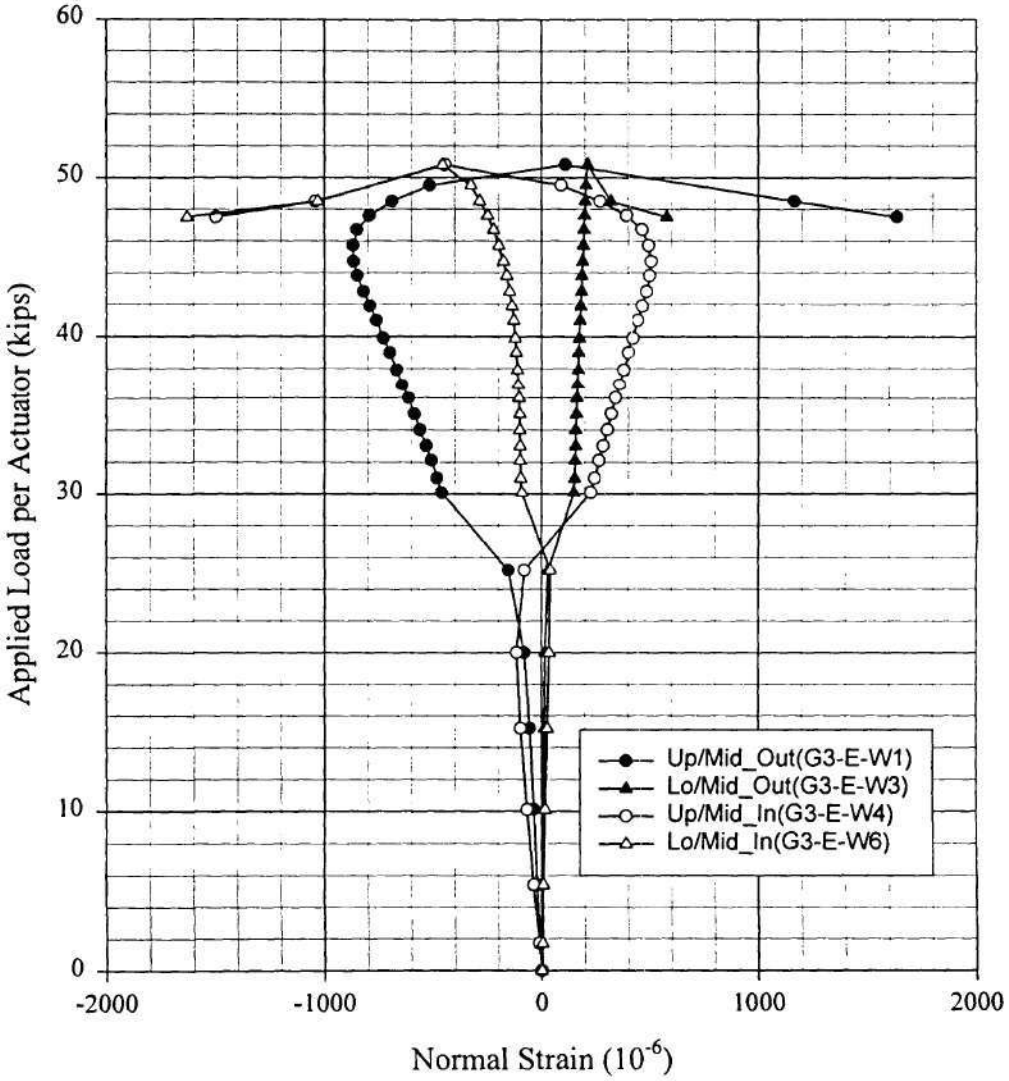

Test(7-26-99) for B4
Normal Strain of the Top Flange at the Location G3_E

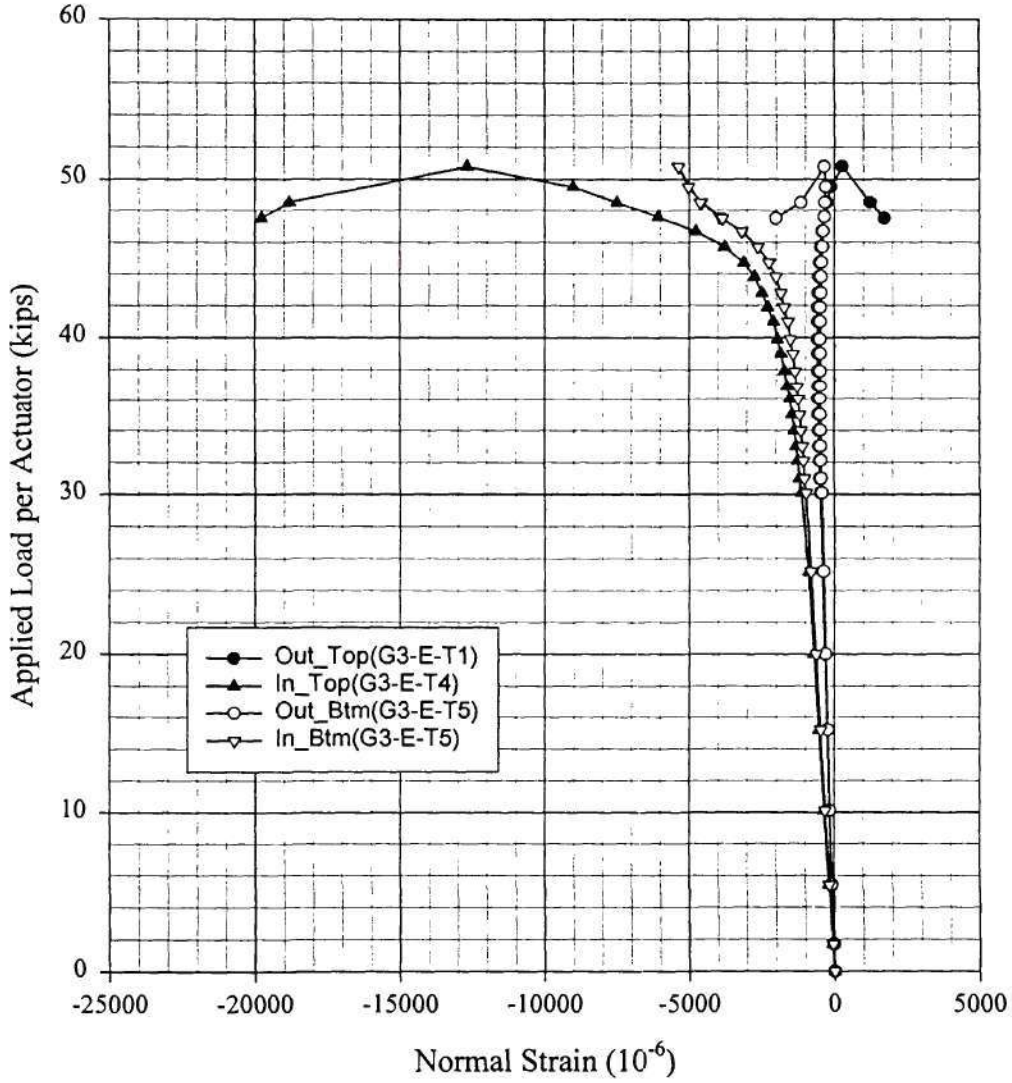

Test(7-26-99) for B4
Normal Strain of the Bottom Flange at the Location G3_E

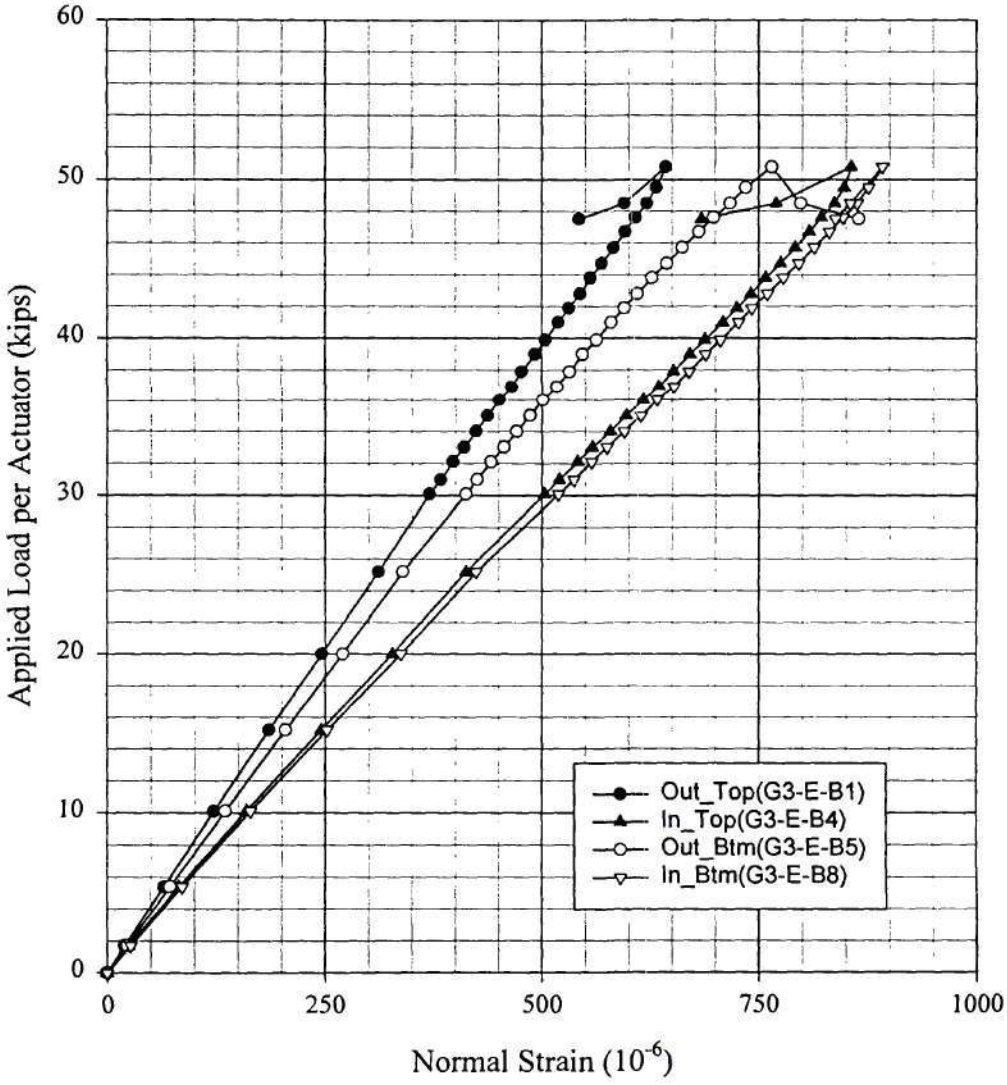

Comparison Between Analysis(B5h_3) and Test(9-30-99) for B5
Vertical Reactions at the East Supports

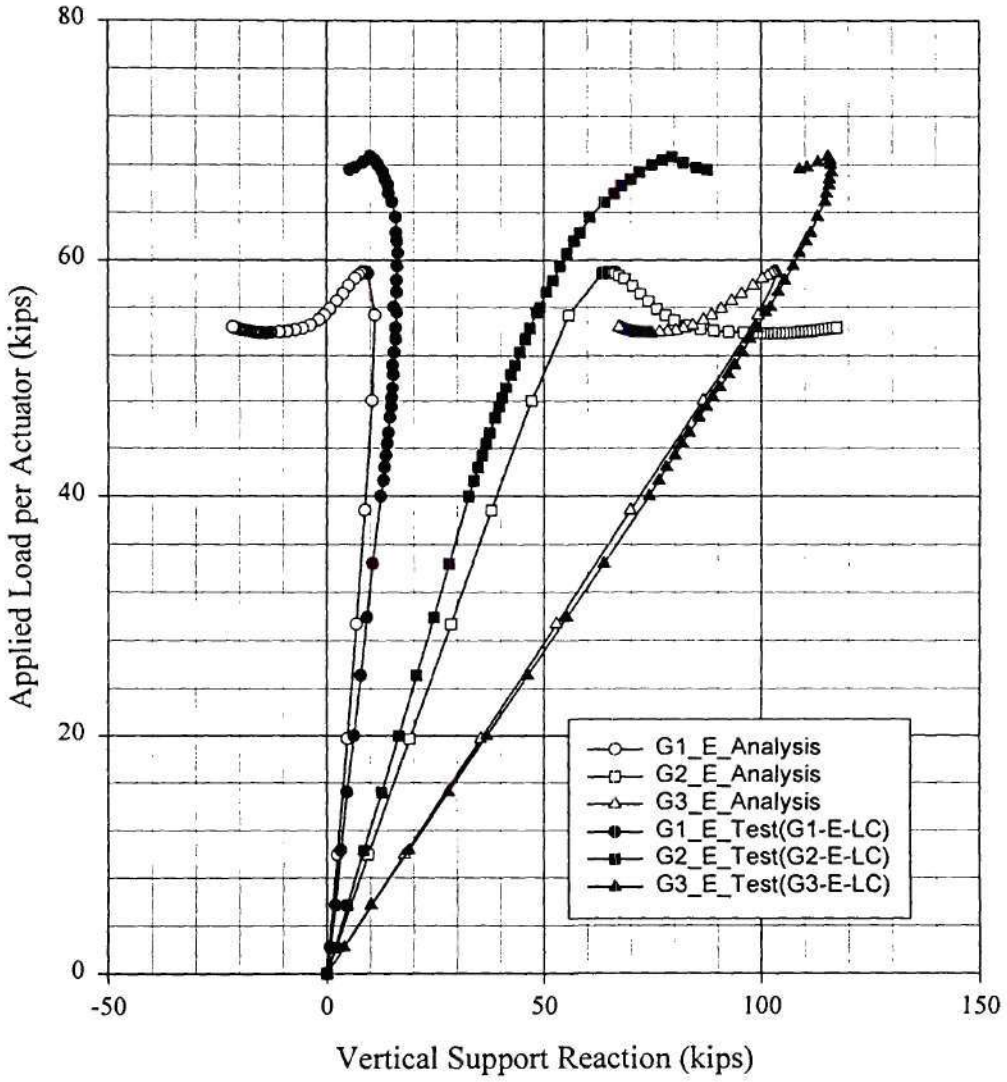

Comparison Between Analysis(B5h_3) and Test(9-30-99) for B5
Vertical Reactions at the West Supports

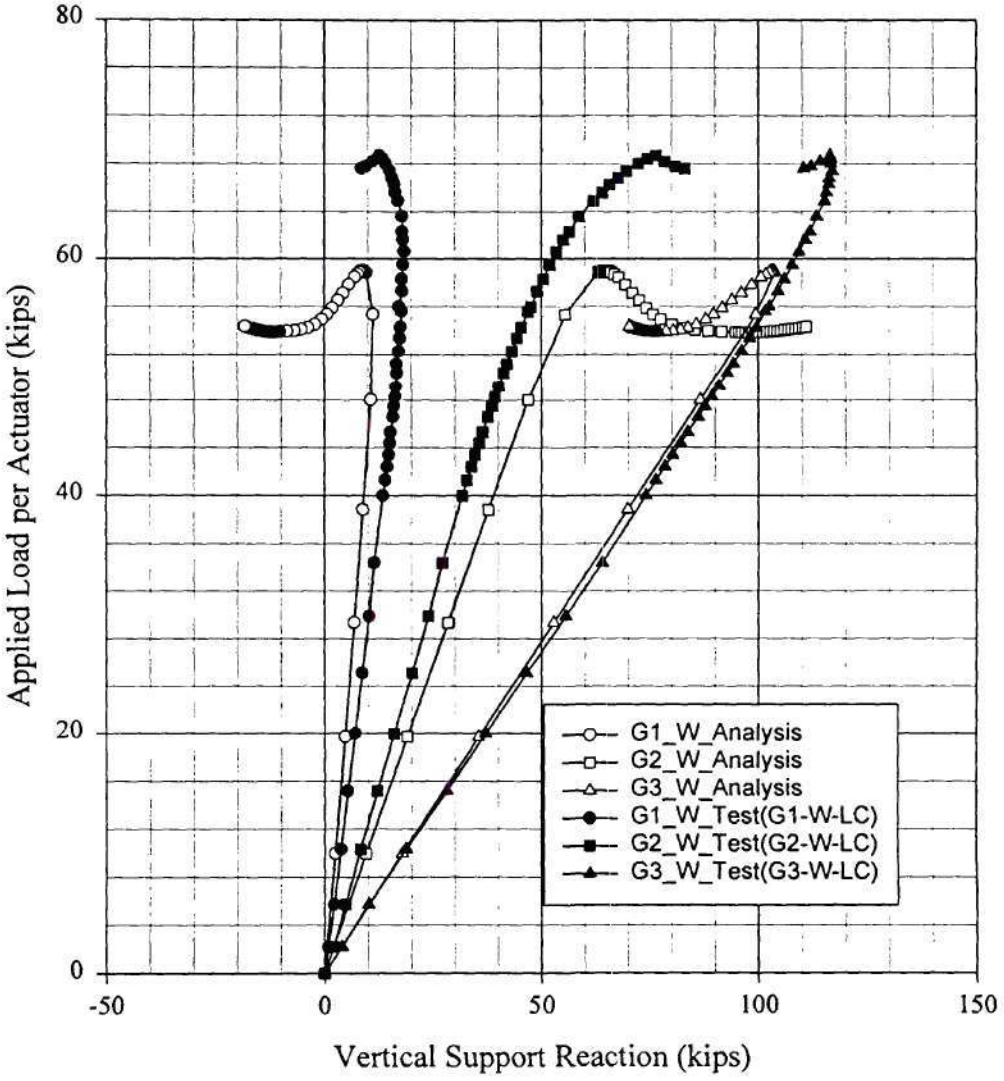

Comparison Between Analysis(B5h_3) and Test(9-30-99) for B5
Vertical Displacement of Bottom Flange (Outside) at Midspan

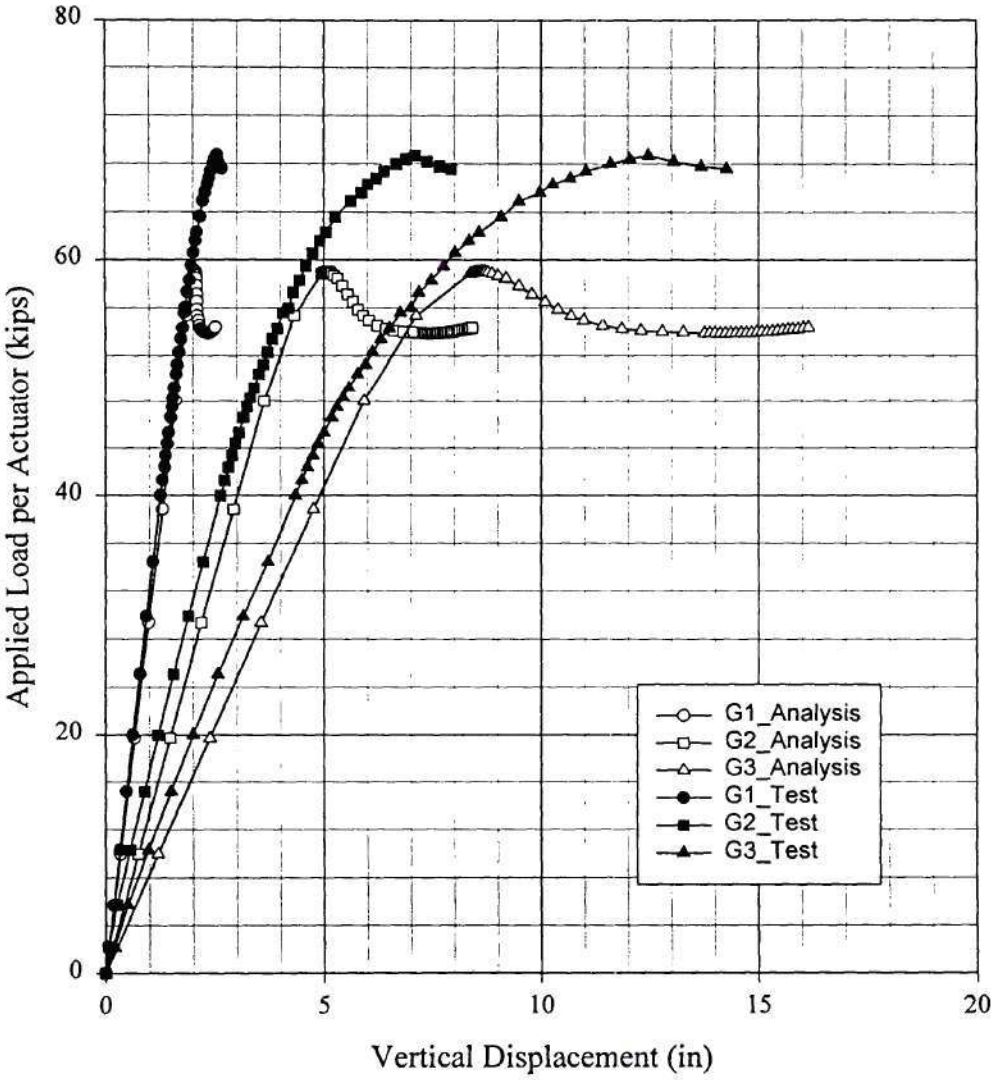

Comparison Between Analysis(B5h_3) and Test(9-30-99) for B5
Radial Displacement of Top Flange (Outside) at Midspan

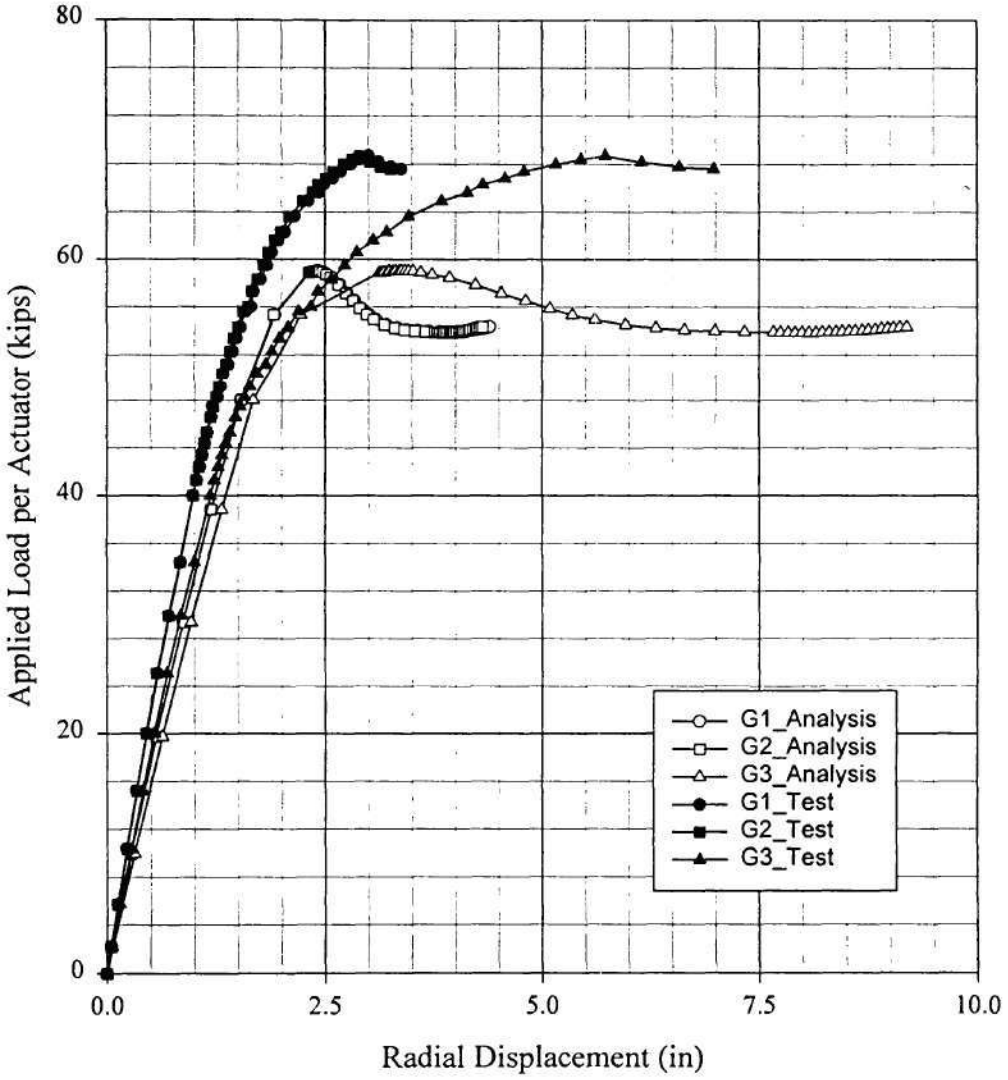

Comparison Between Analysis(B5h_3) and Test(9-30-99) for B5
Radial Displacement of Bottom Flange (Outside) at Midspan

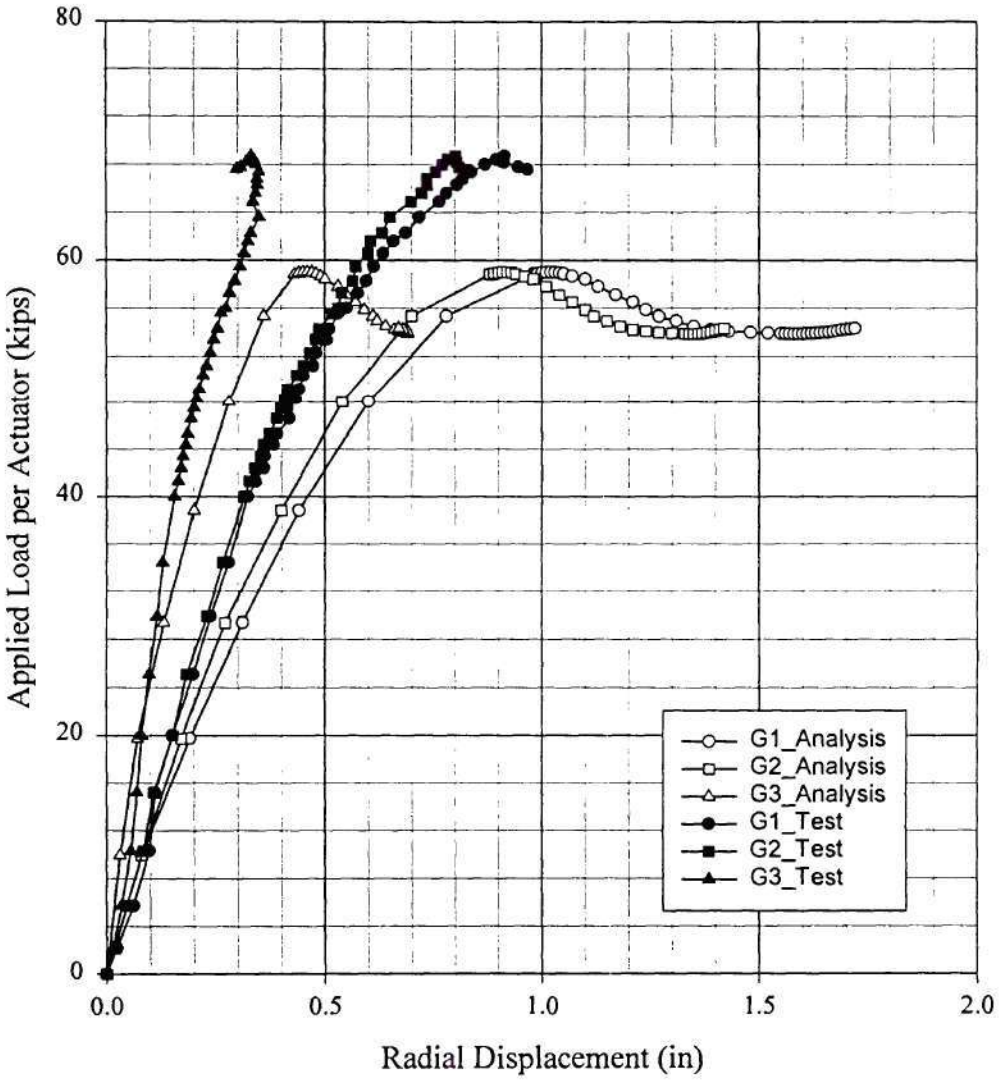

Comparison Between Analysis(B5h_3) and Test(9-30-99) for B5
Axial Force of Cross Frame at 6R Between G2 and G3

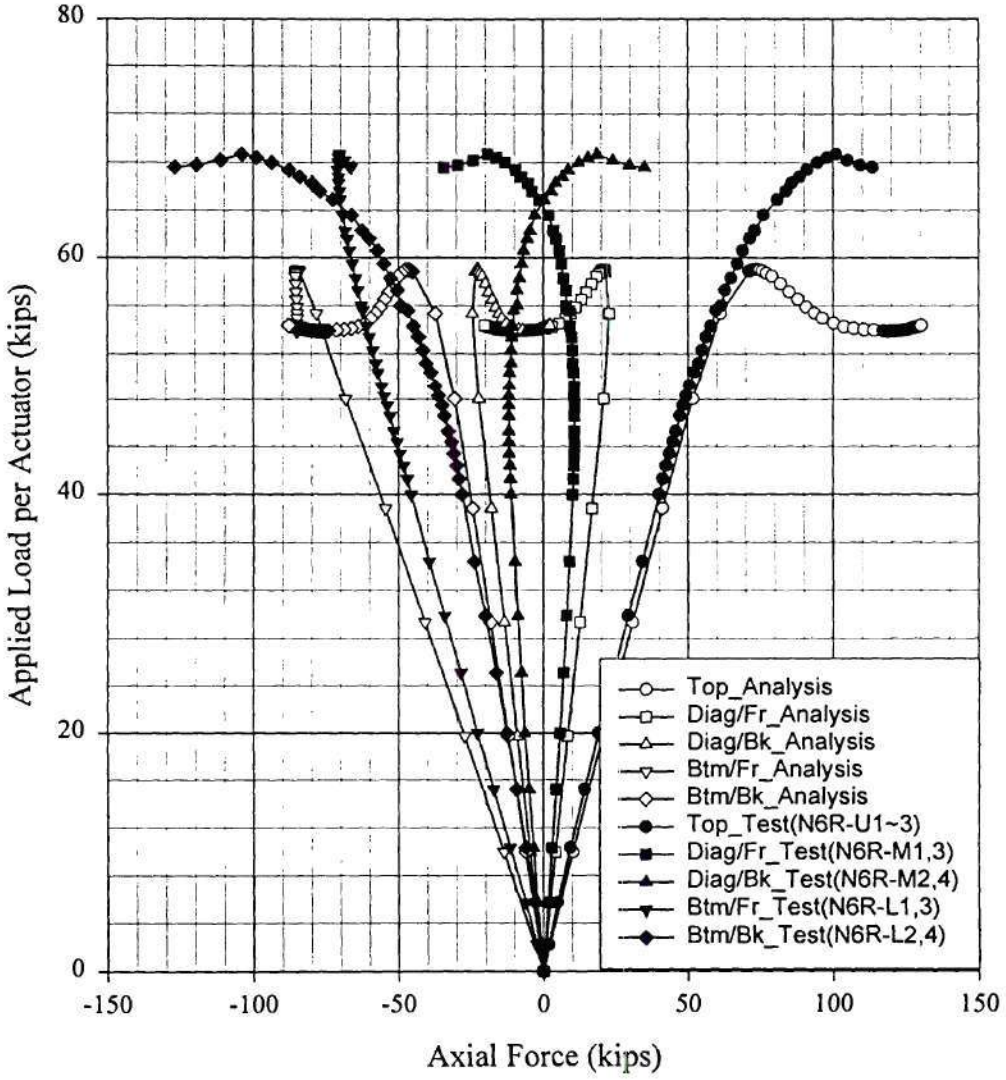

Comparison Between Analysis(B5h_3) and Test(9-30-99) for B5
Axial Force of Cross Frame at 6L Between G2 and G3

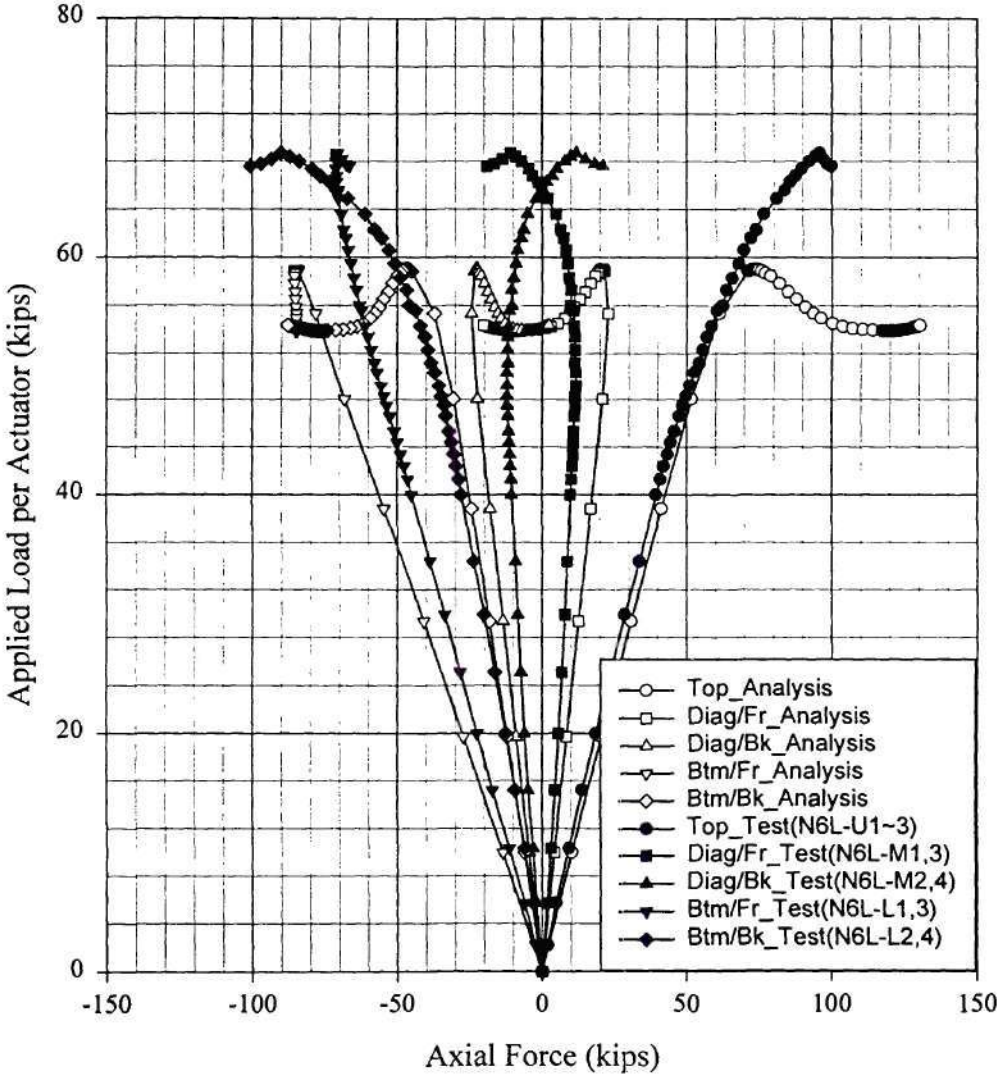

Comparison Between Analysis(B5h_3) and Test(9-30-99) for B5
Bending Moment at Midspan

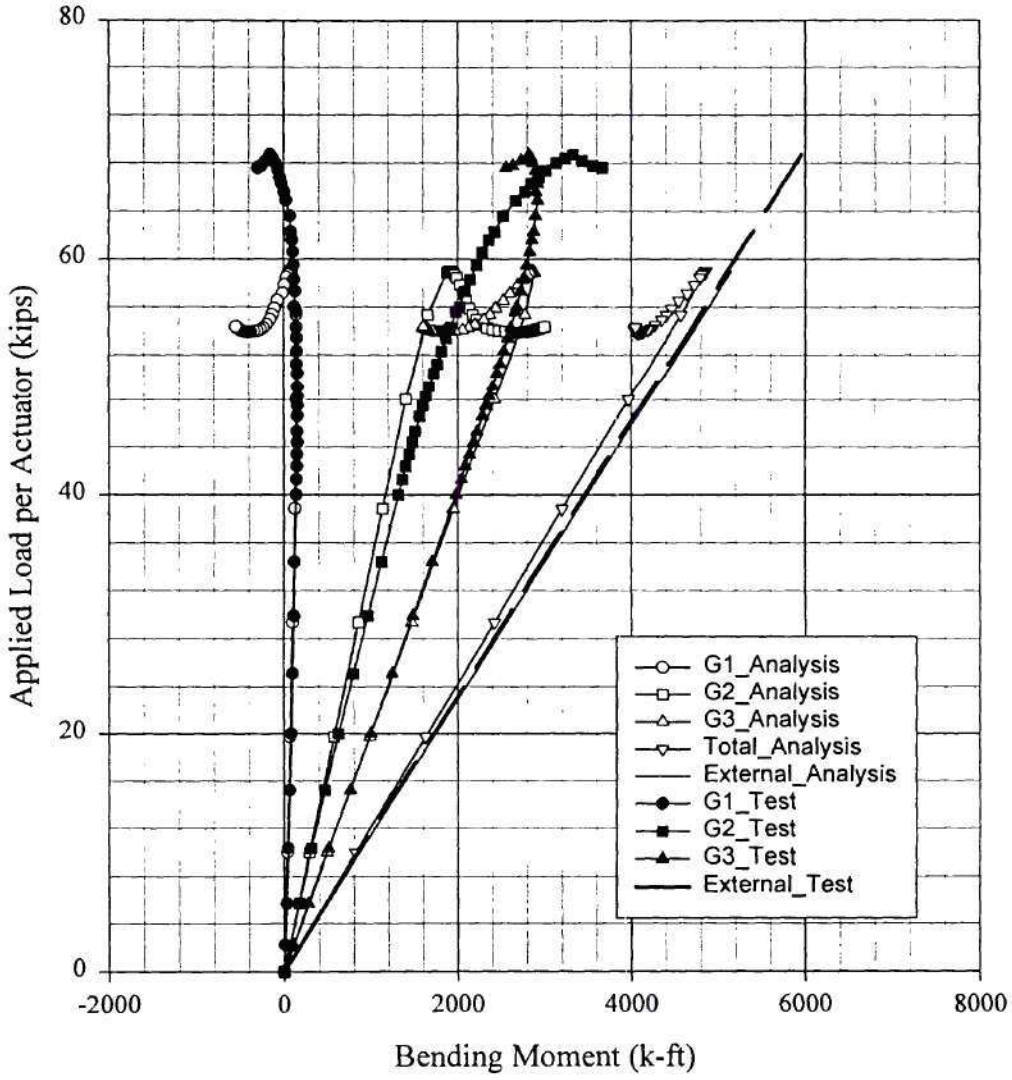

Comparison Between Analysis(B5h_3) and Test(9-30-99) for B5
Bending Moment at Midspan

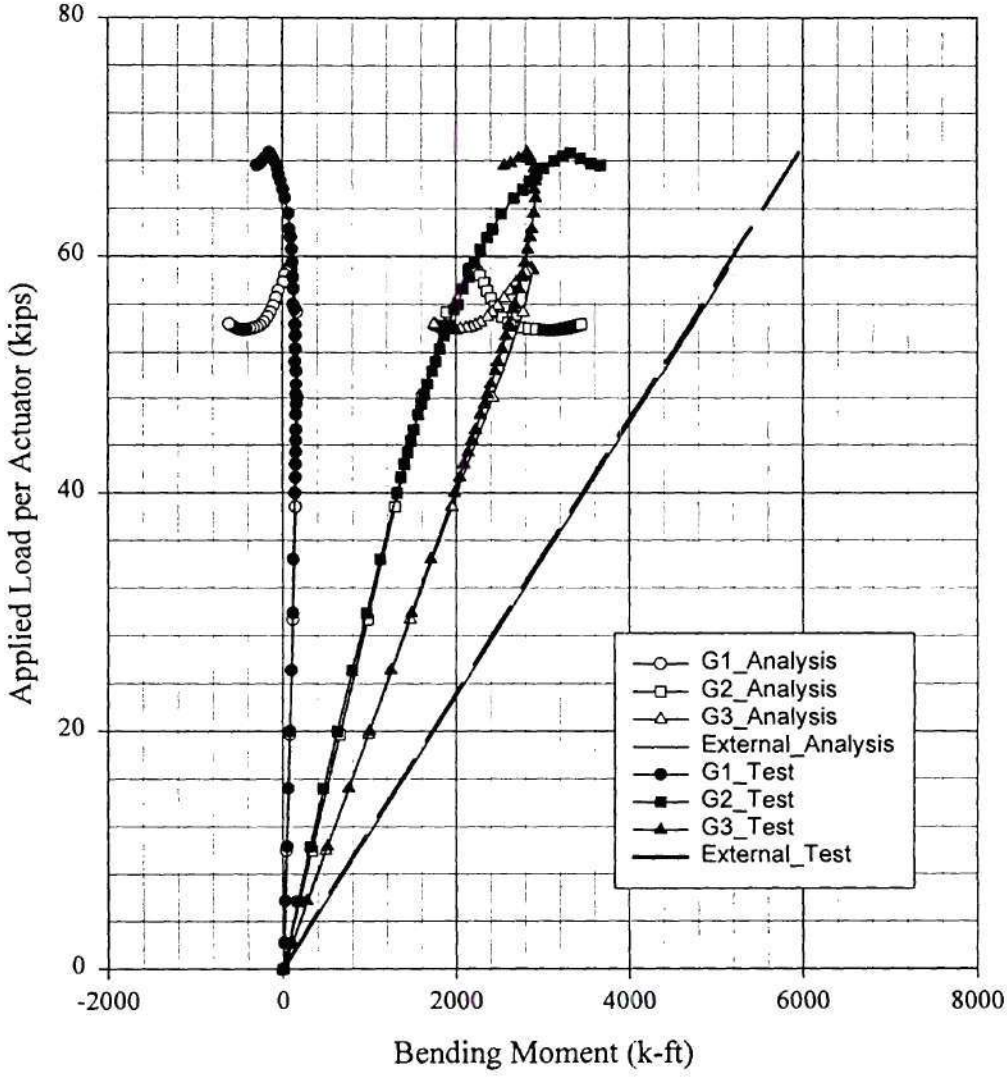

Comparison Between Analysis(B5h_3) and Test(9-30-99) for B5
Normal Strain of the Web Inside at the Location G1_B

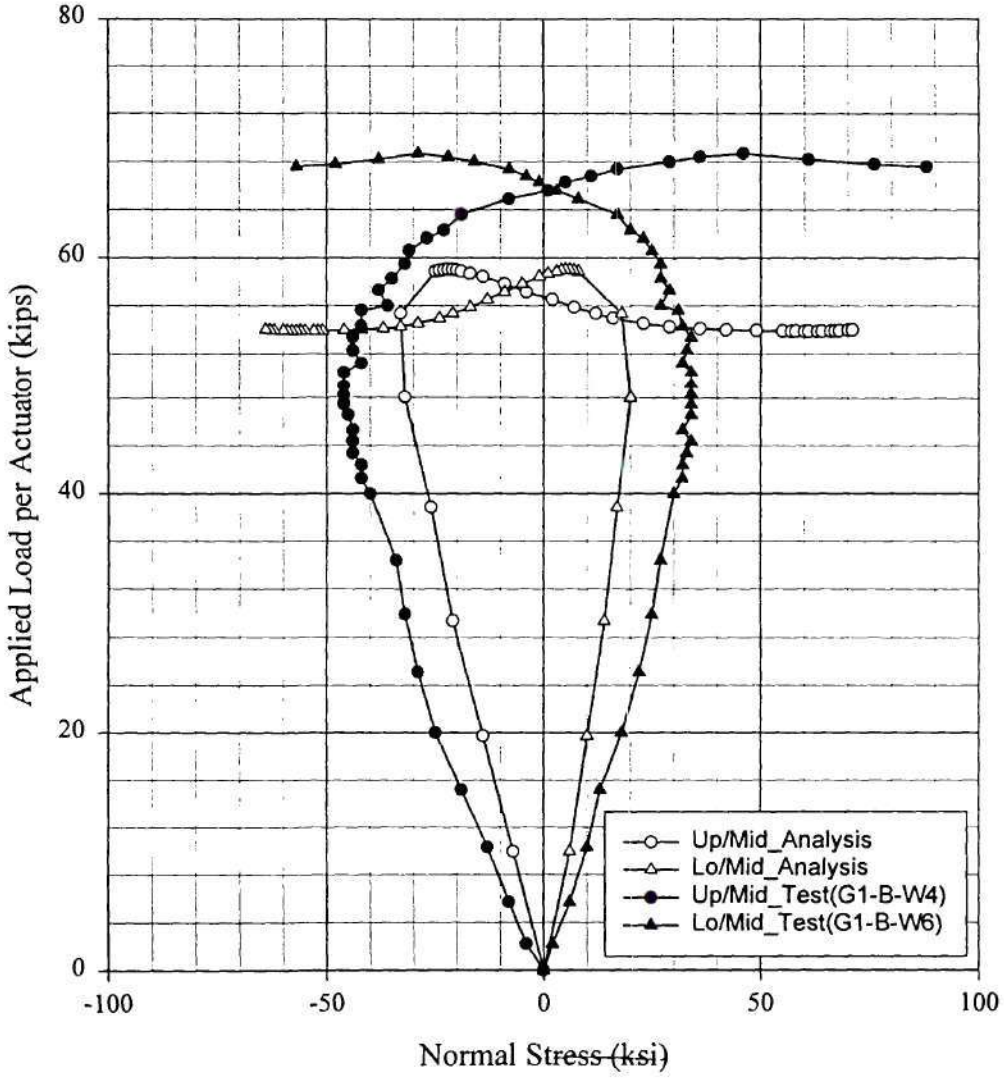

Comparison Between Analysis(B5h_3) and Test(9-30-99) for B5
Normal Strain of the Top Flange Topside at the Location G1_B

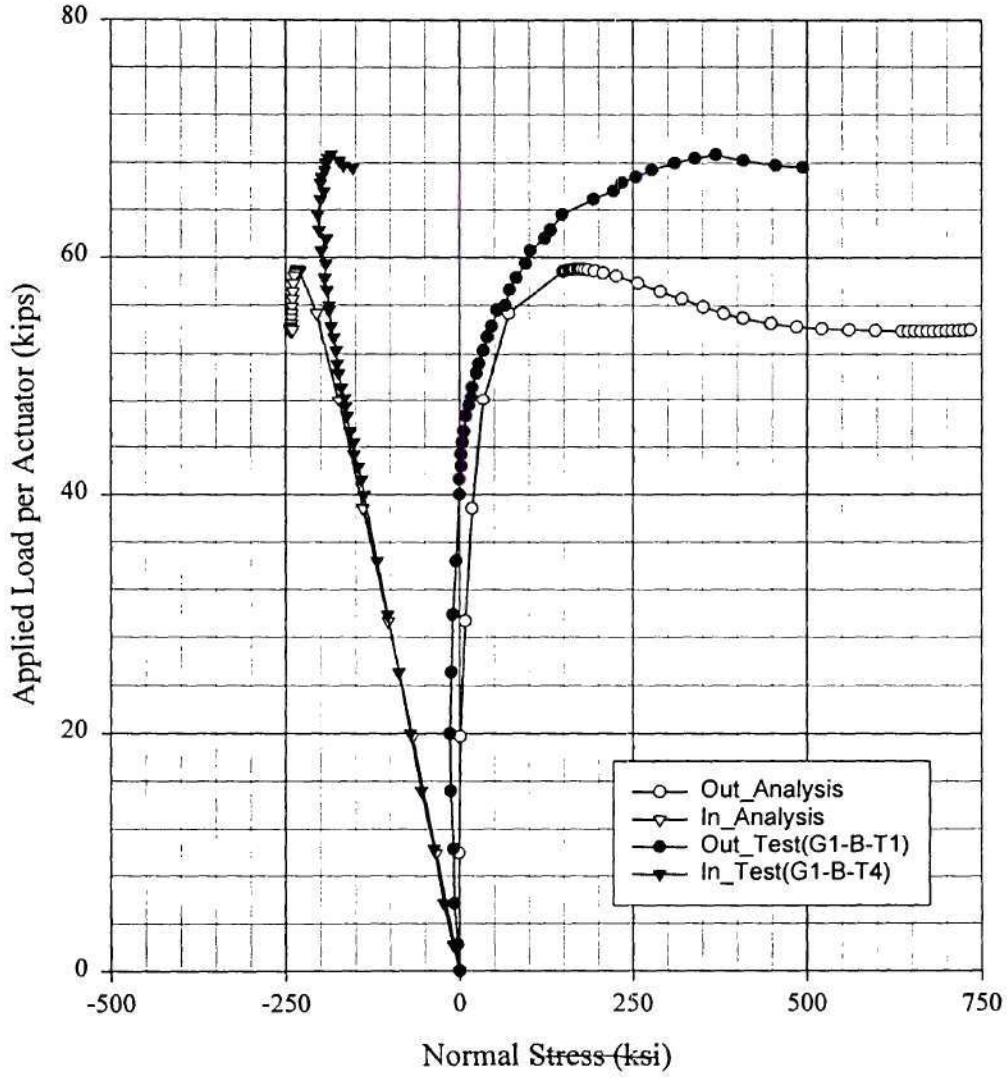

Comparison Between Analysis(B5h_3) and Test(9-30-99) for B5
Normal Strain of the Top Flange Btmside at the Location G1_B

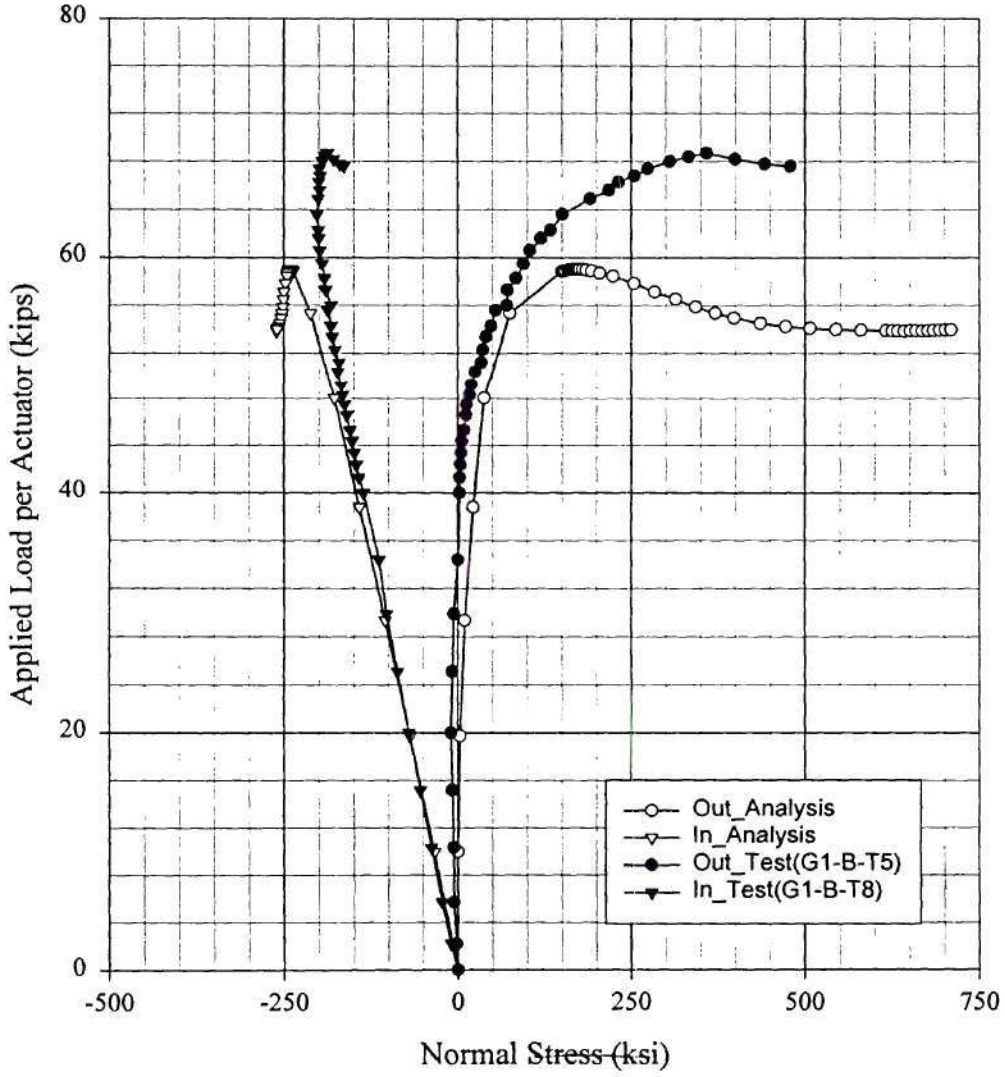

Comparison Between Analysis(B5h_3) and Test(9-30-99) for B5
Normal Strain of the Btm Flange Topside at the Location G1_B

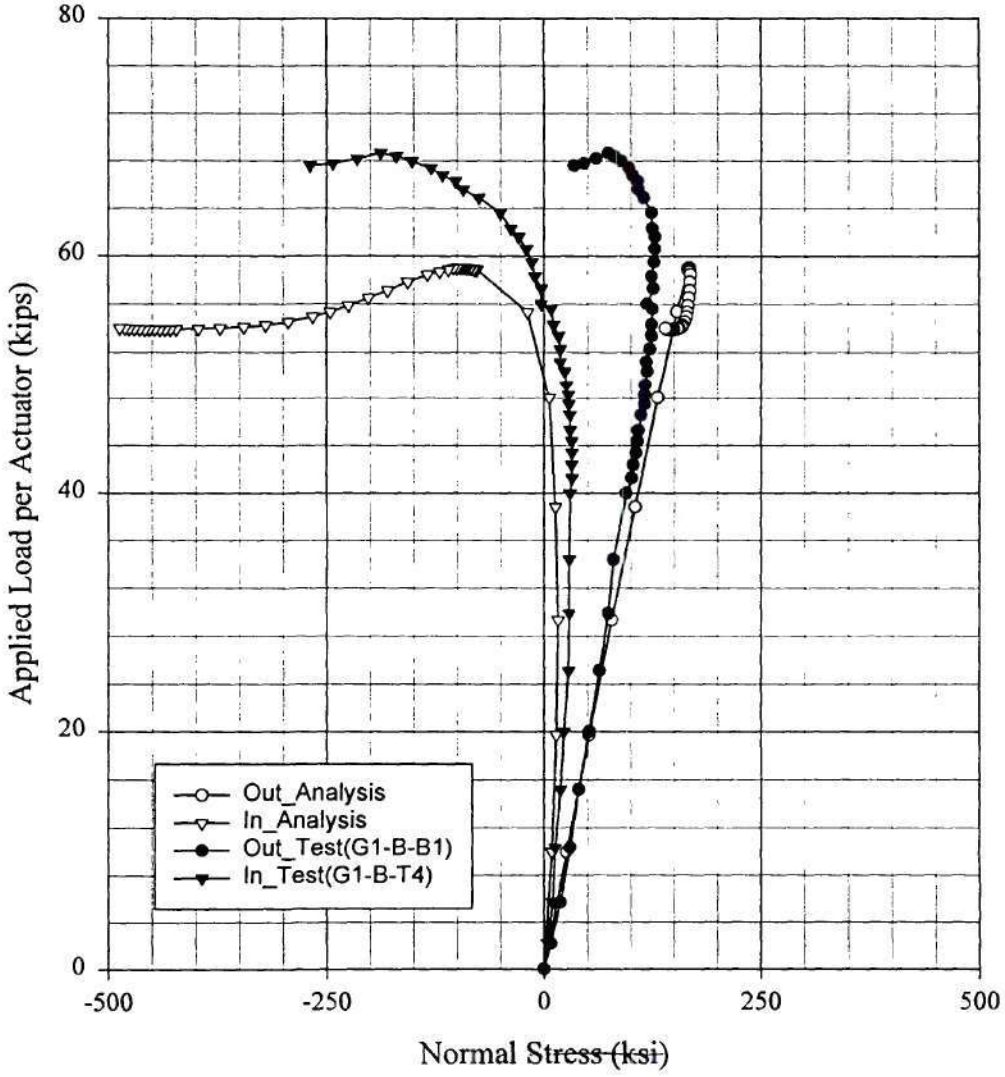

Comparison Between Analysis(B5h_3) and Test(9-30-99) for B5
Normal Strain of the Btm Flange Btmside at the Location G1_B

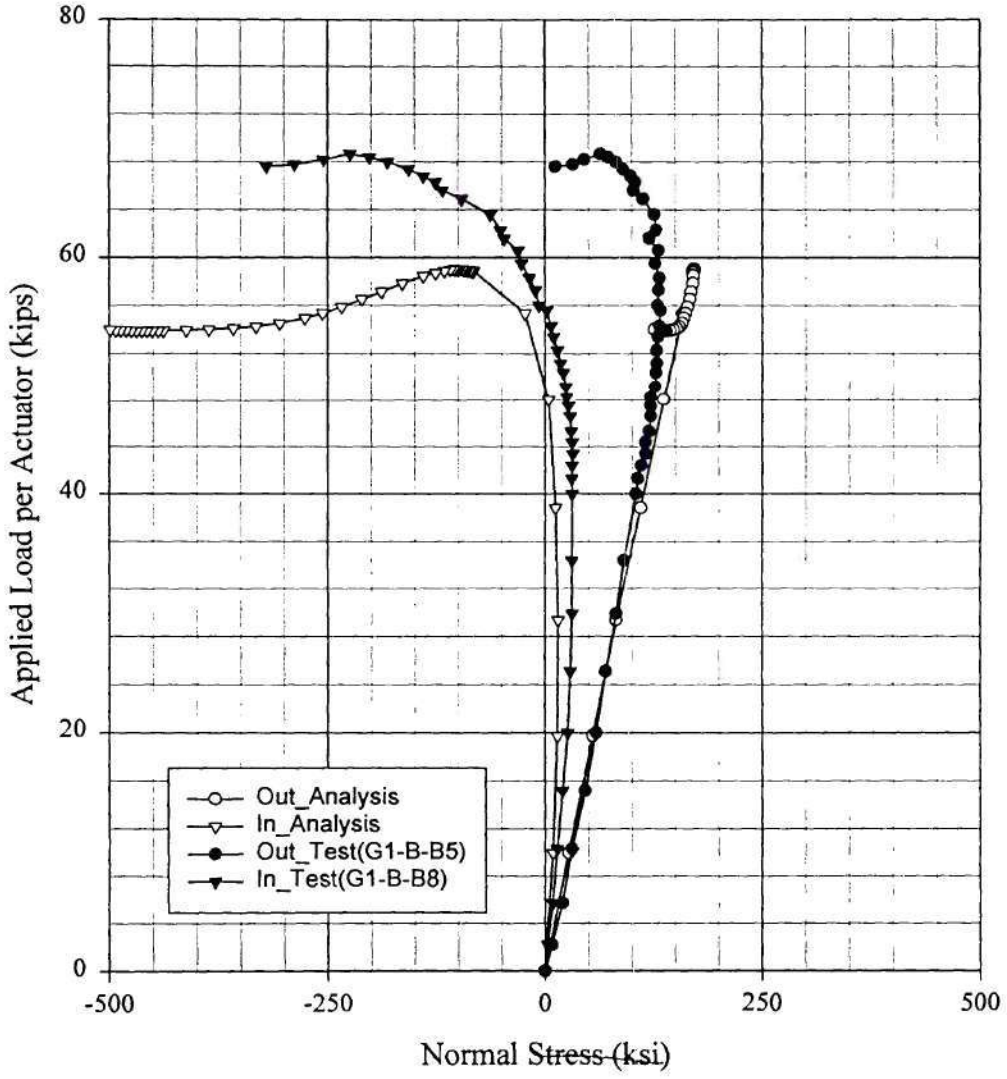

Comparison Between Analysis(B5h_3) and Test(9-30-99) for B5
Normal Strain of the Web Inside at the Location G2_B

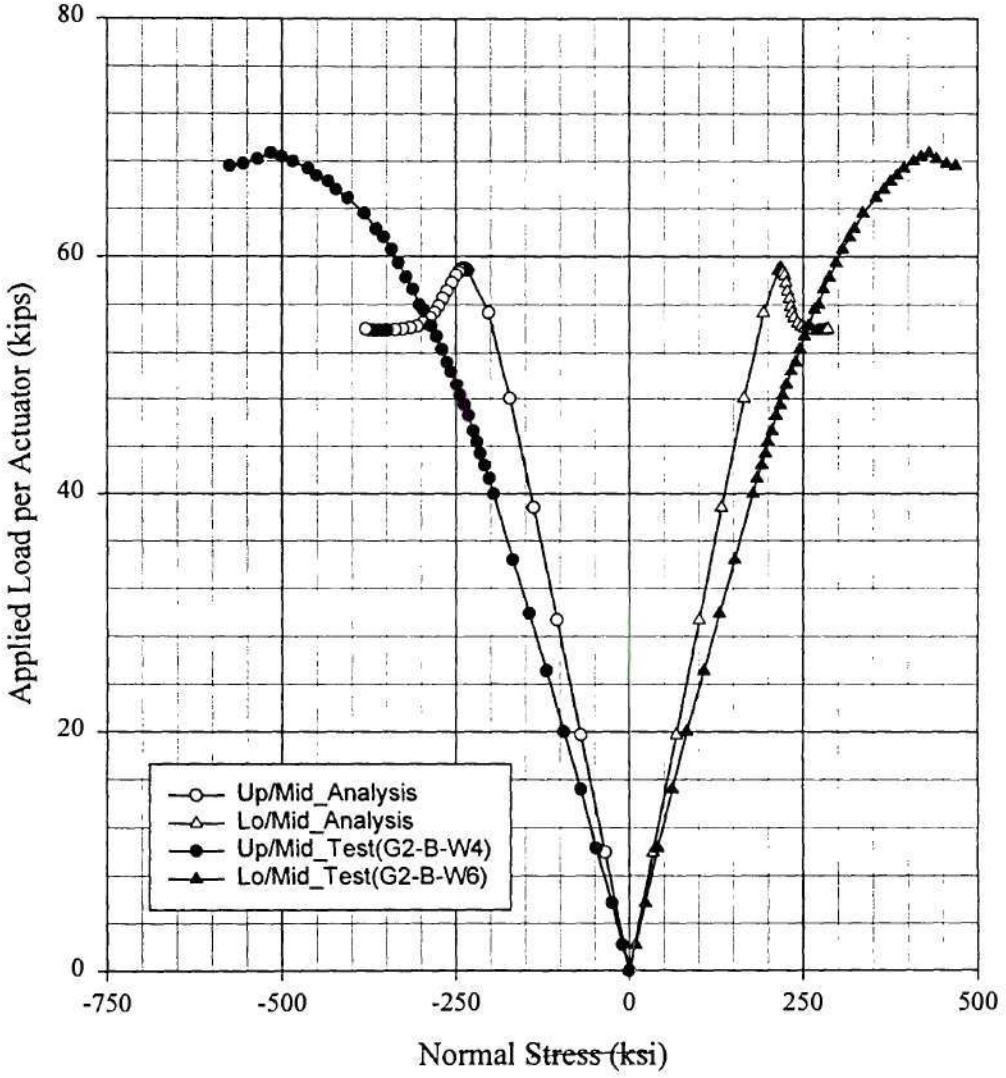

Comparison Between Analysis(B5h_3) and Test(9-30-99) for B5
Normal Strain of the Top Flange Topside at the Location G2_B

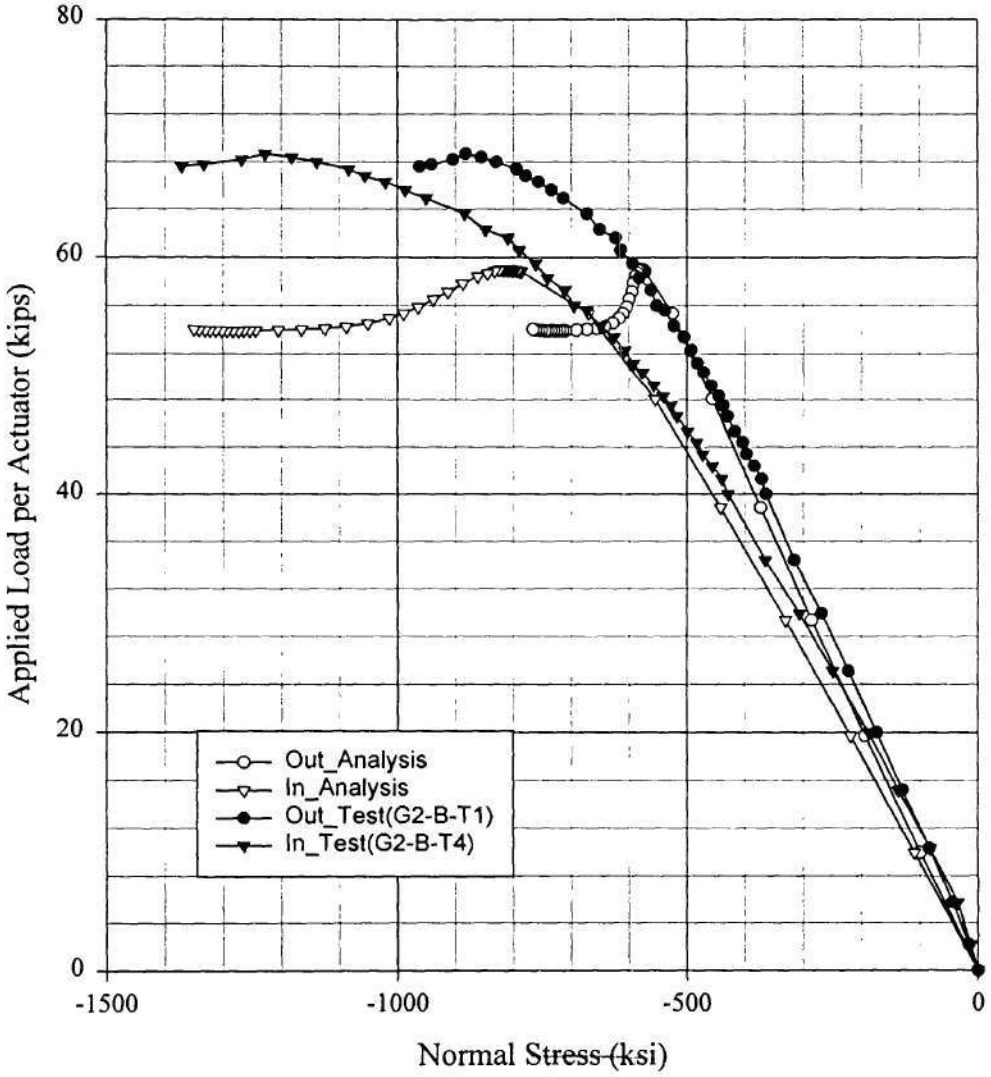

Comparison Between Analysis(B5h_3) and Test(9-30-99) for B5
Normal Strain of the Top Flange Btmside at the Location G2_B

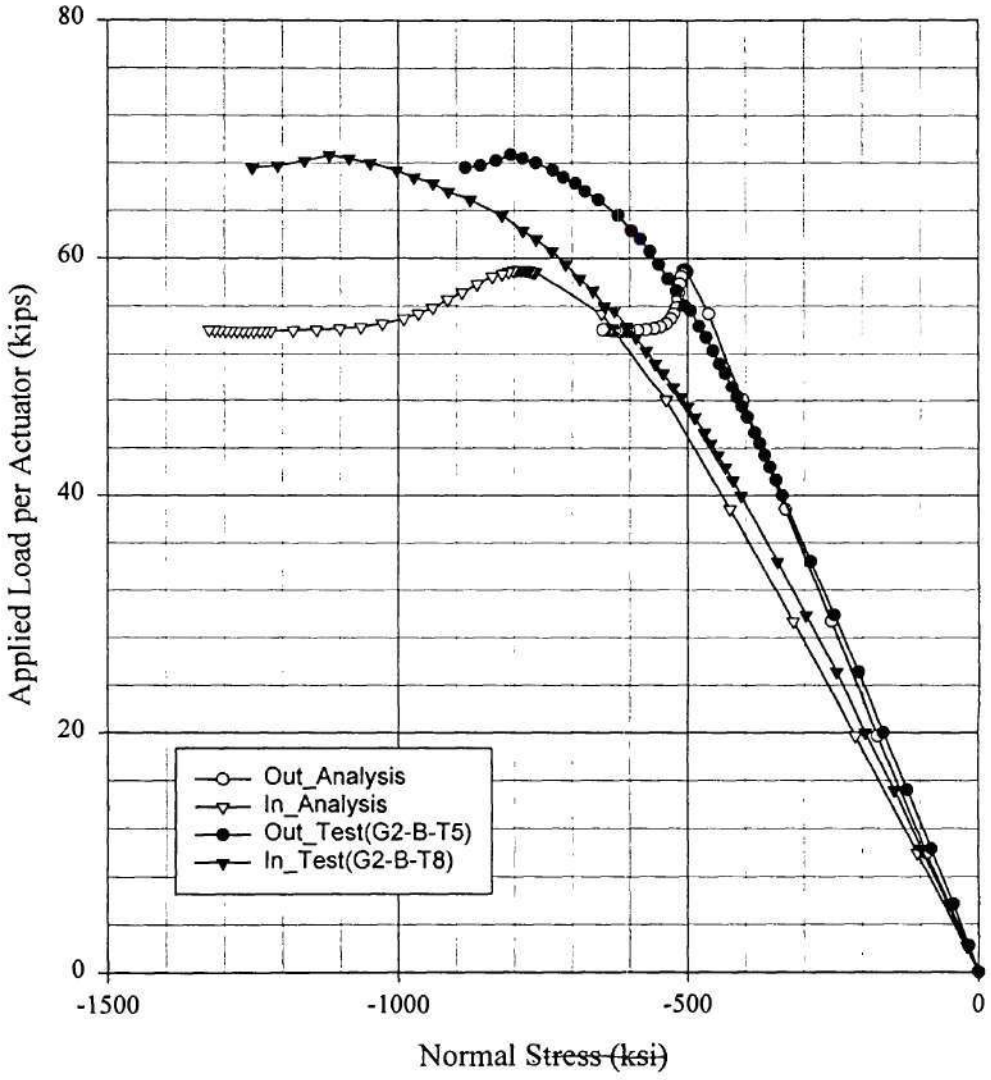

Comparison Between Analysis(B5h_3) and Test(9-30-99) for B5
Normal Strain of the Btm Flange Topside at the Location G2_B

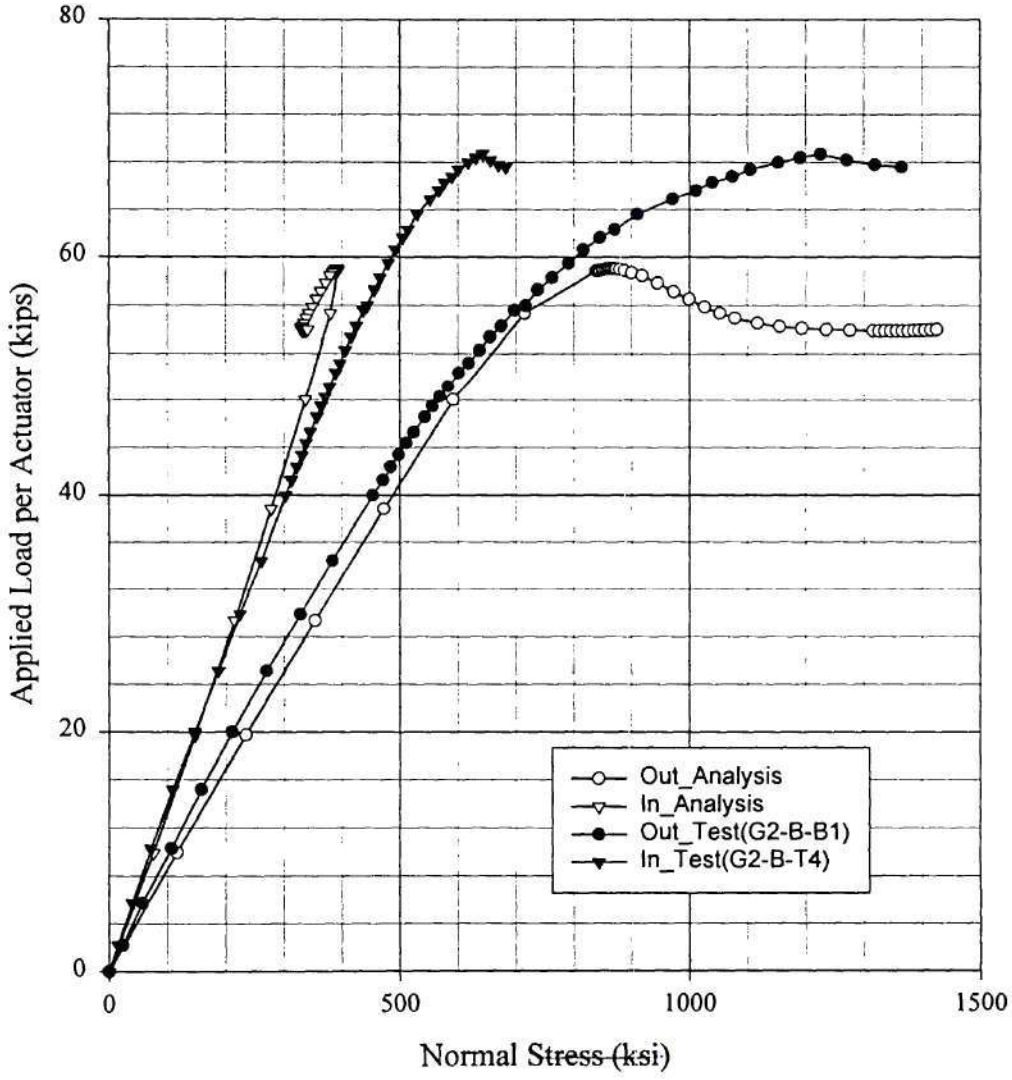

Comparison Between Analysis(B5h_3) and Test(9-30-99) for B5
Normal Strain of the Btm Flange Btmside at the Location G2_B

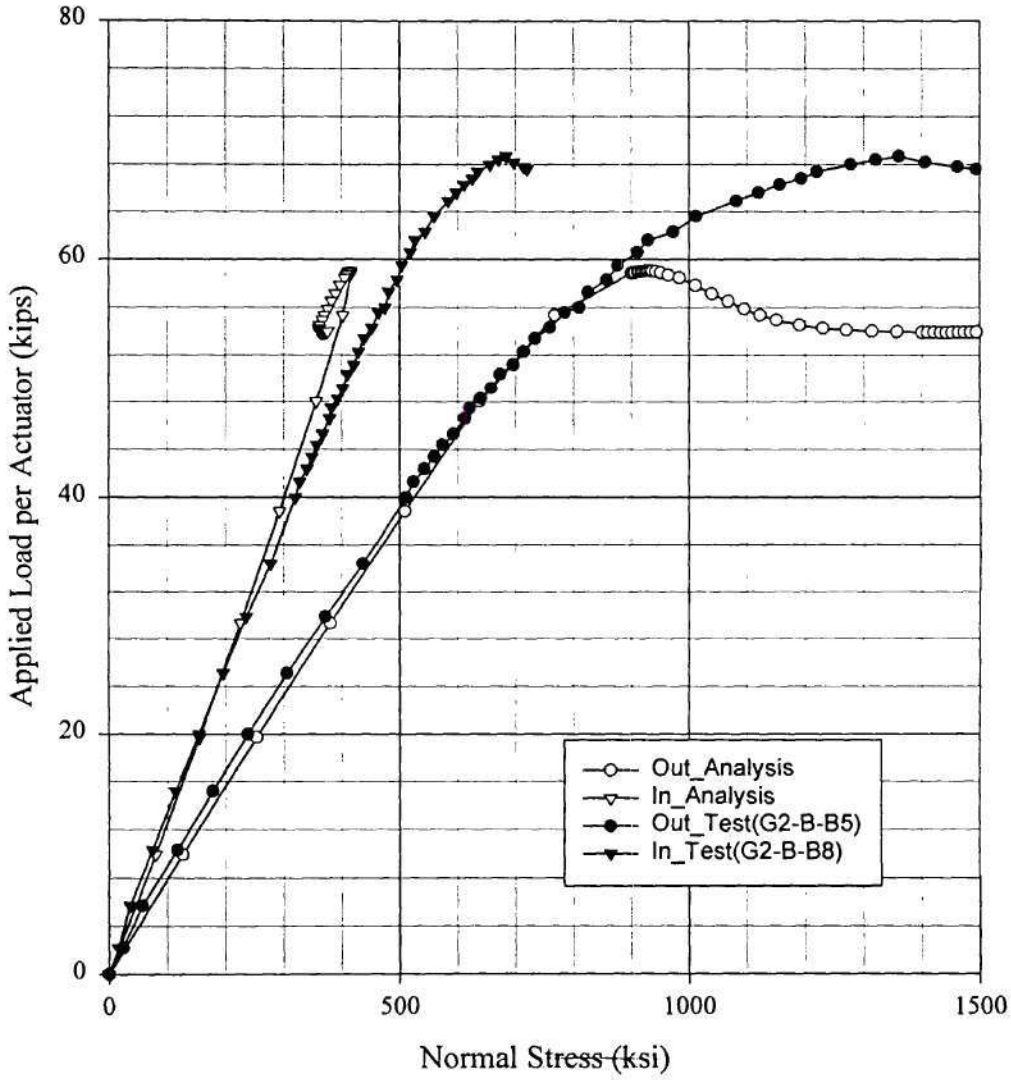

Comparison Between Analysis(B5h_3) and Test(9-30-99) for B5
Normal Strain of the Web Inside at the Location G3_E

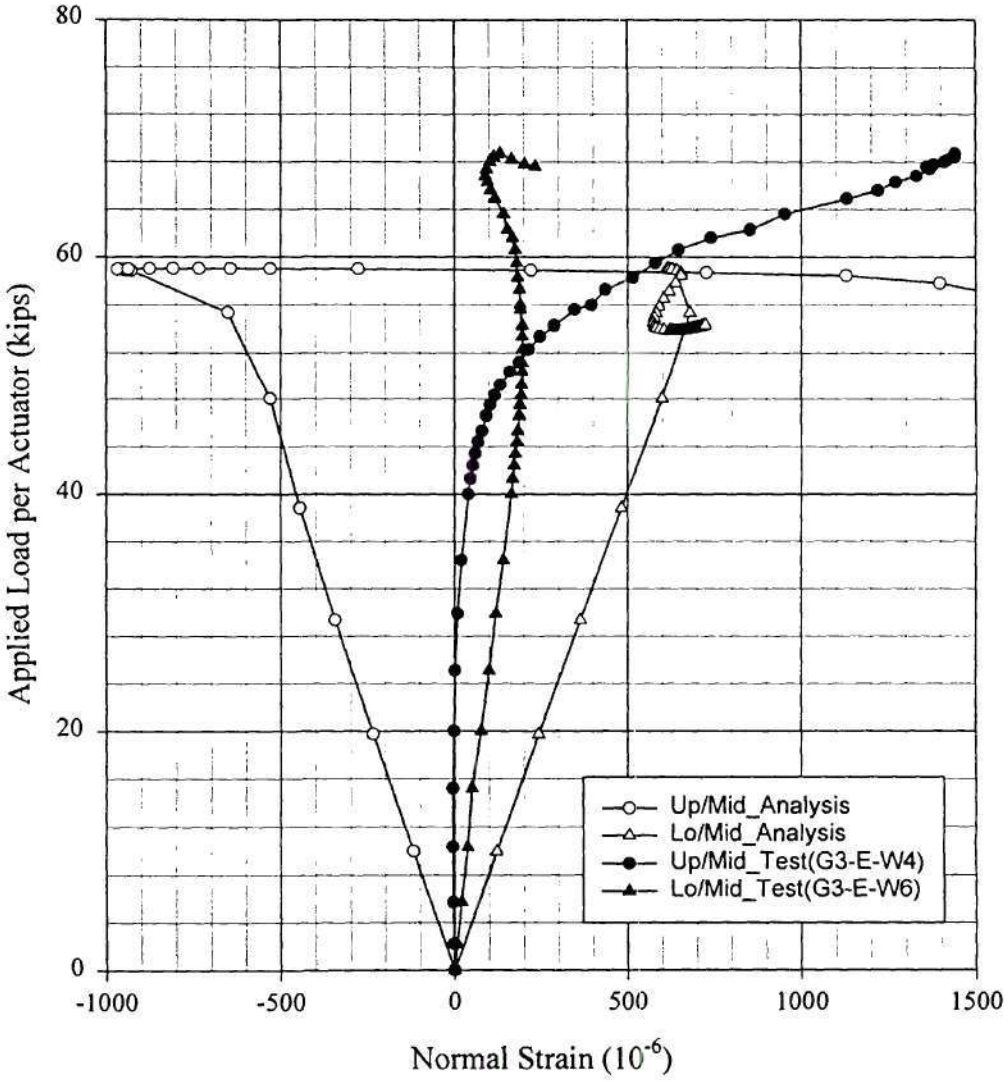

Comparison Between Analysis(B5h_3) and Test(9-30-99) for B5
Normal Strain of the Web Outside at the Location G3_E

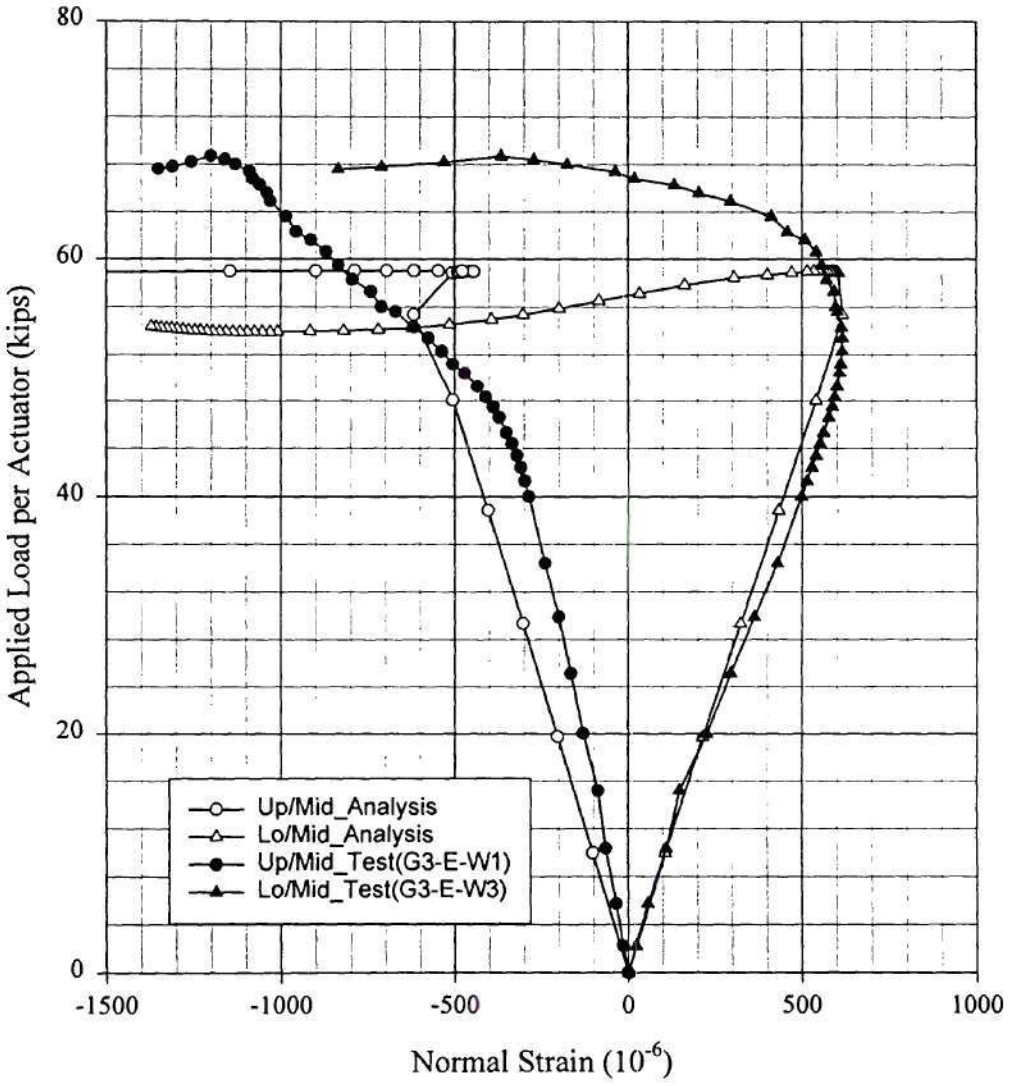

Comparison Between Analysis(B5h_3) and Test(9-30-99) for B5
Normal Strain of the Top Flange Topside at the Location G3_E

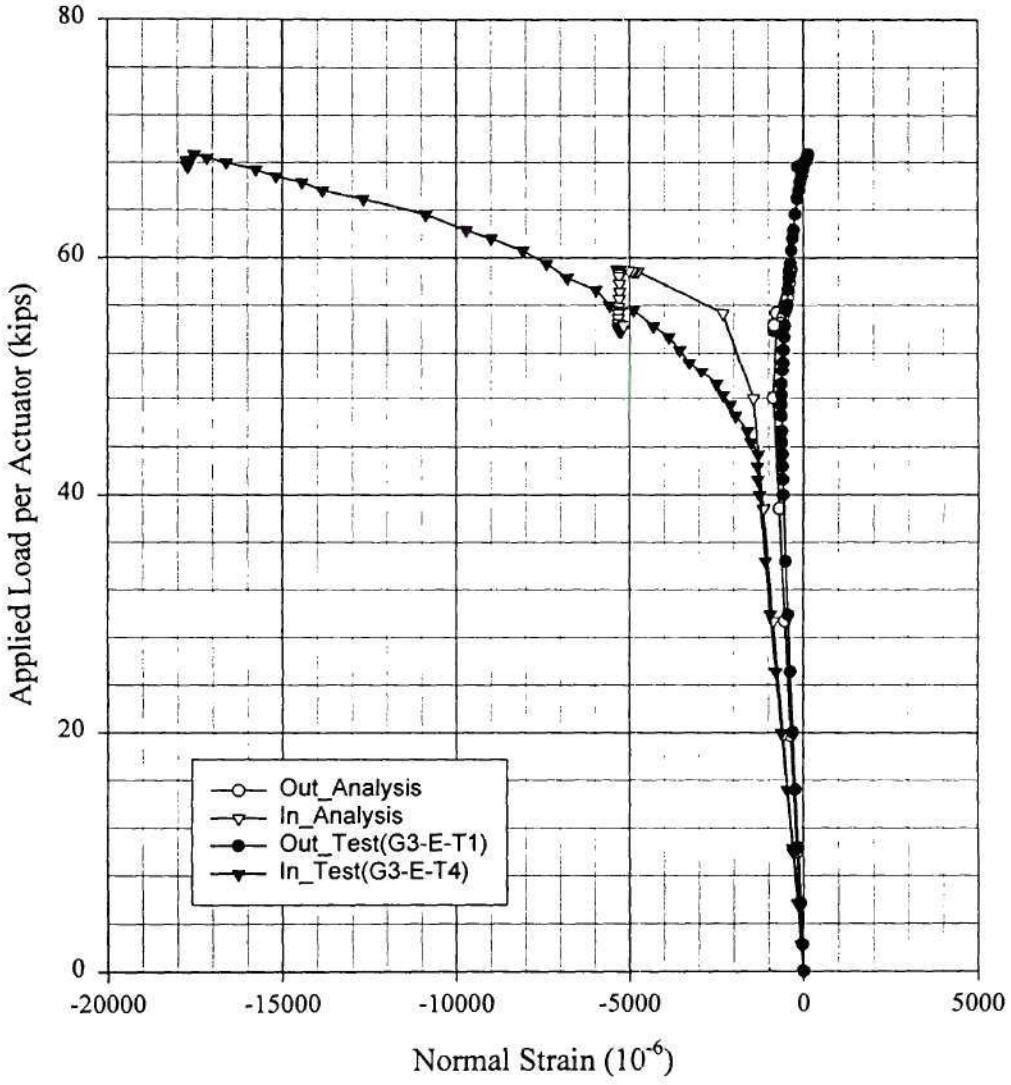

Comparison Between Analysis(B5h_3) and Test(9-30-99) for B5
Normal Strain of the Top Flange Btmside at the Location G3_E

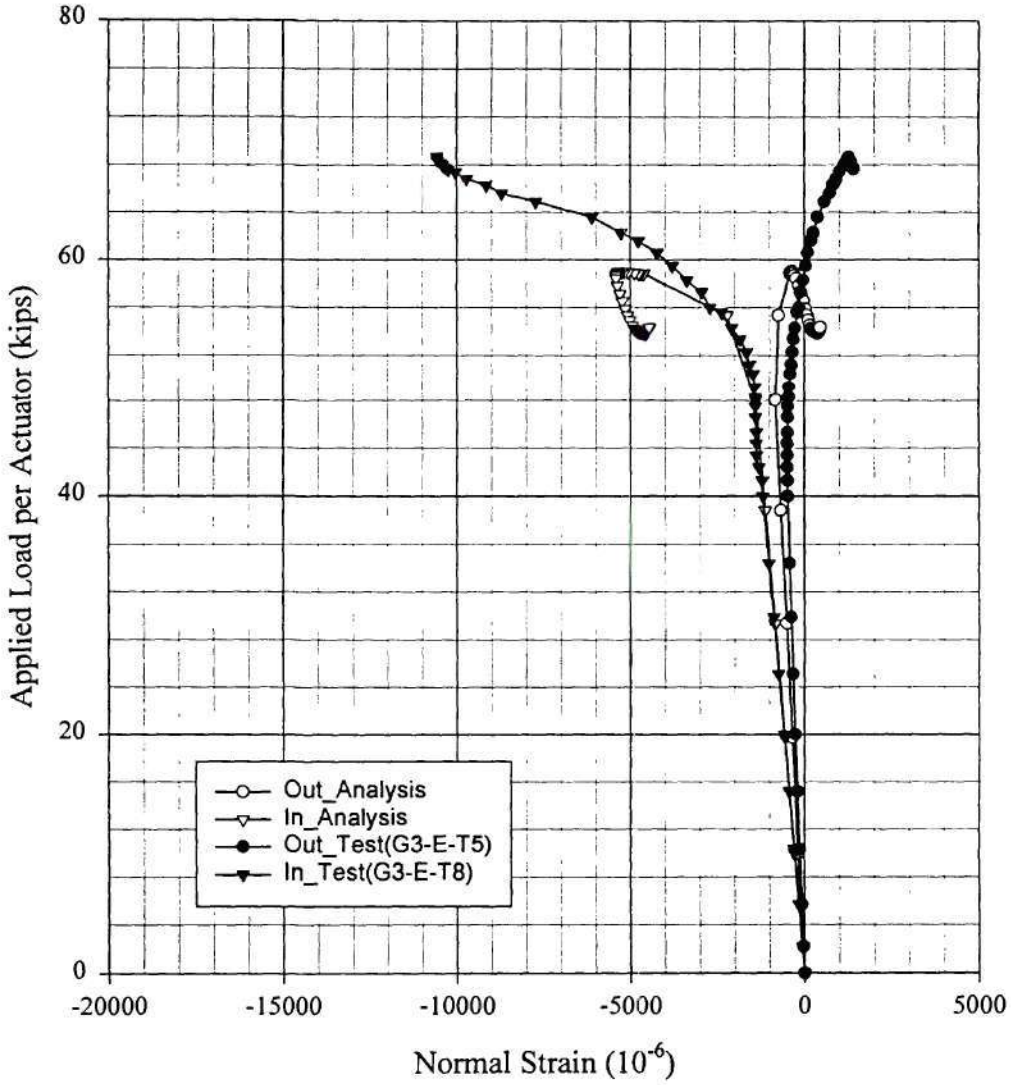

Comparison Between Analysis(B5h_3) and Test(9-30-99) for B5
Normal Strain of the Btm Flange Topside at the Location G3_E

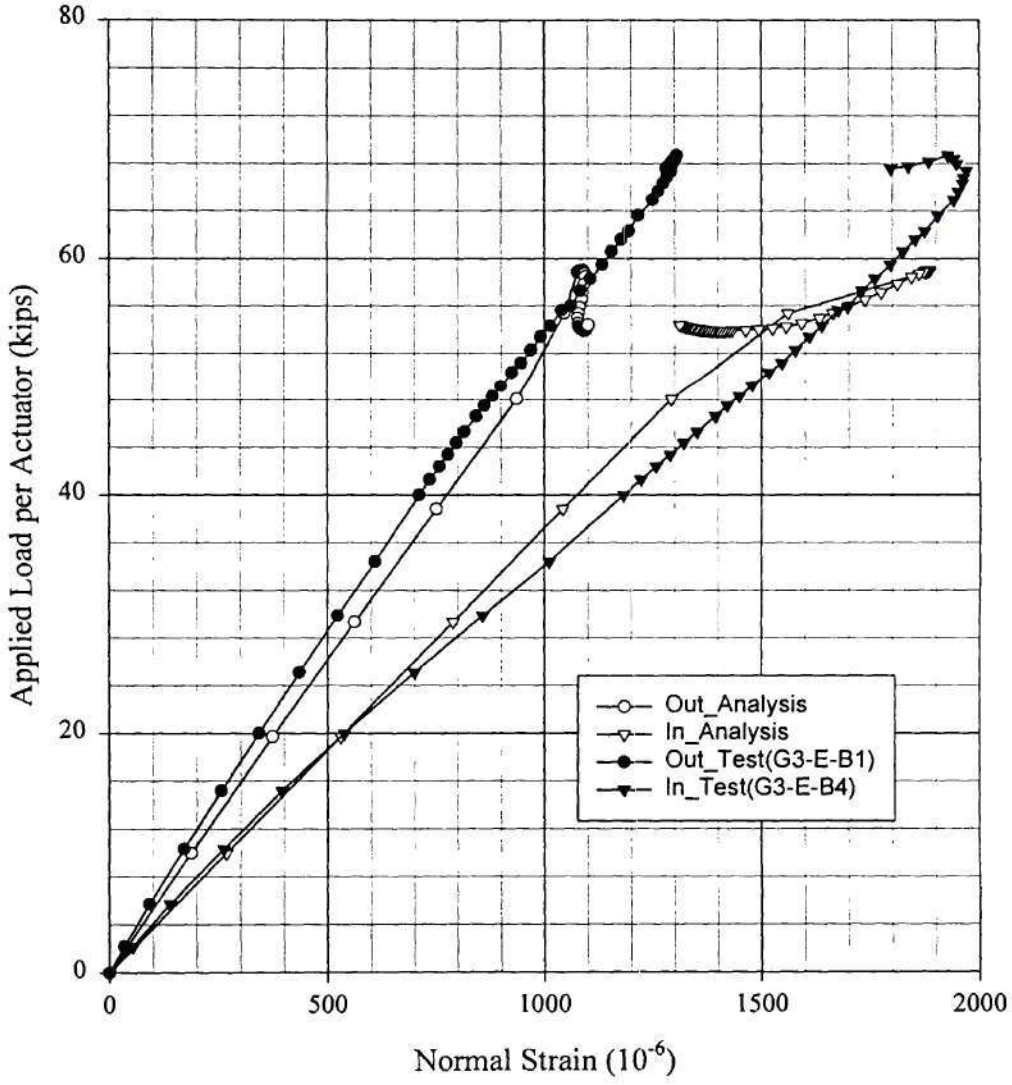

Comparison Between Analysis(B5h_3) and Test(9-30-99) for B5
Normal Strain of the Btm Flange Btmside at the Location G3_E

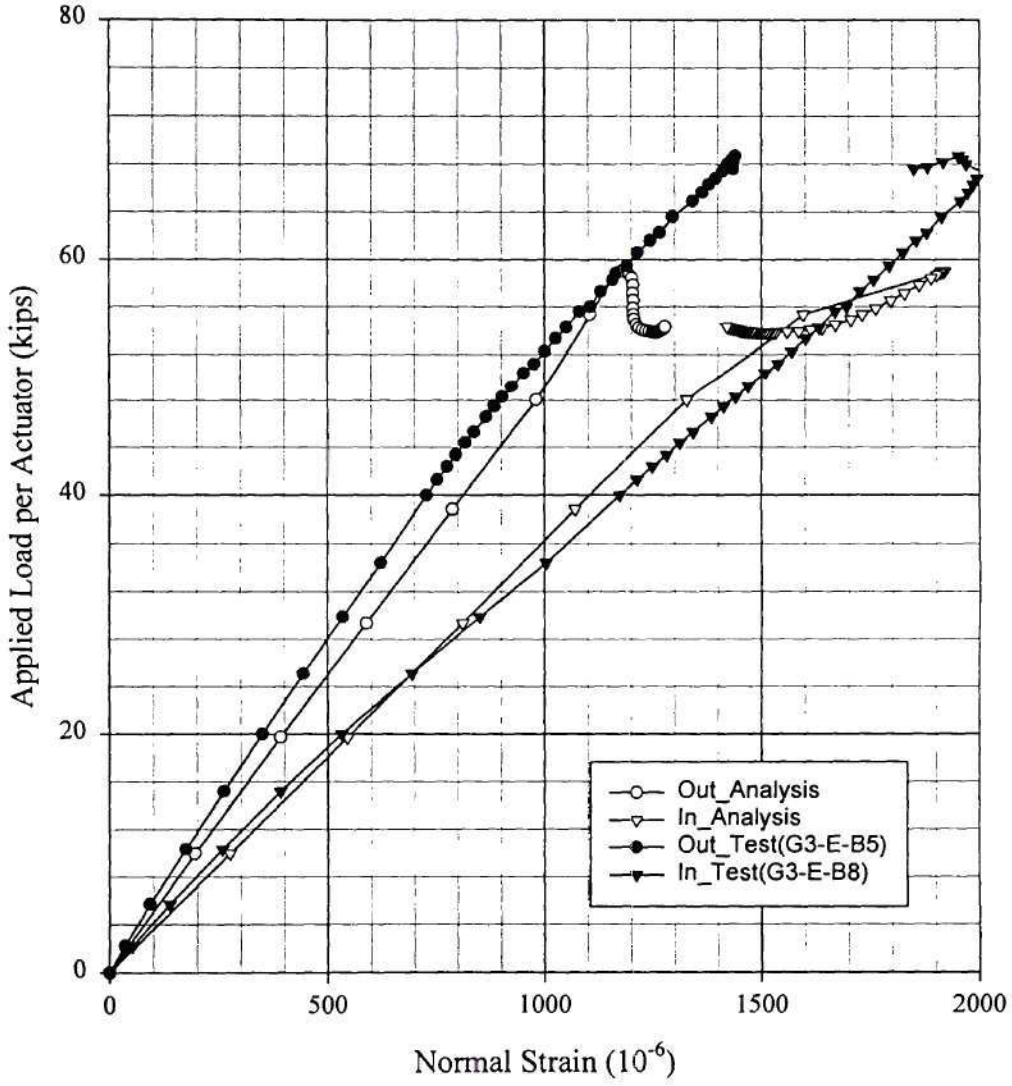

Test(9-30-99) for B5
Normal Strain of the Web at the Location G3_E

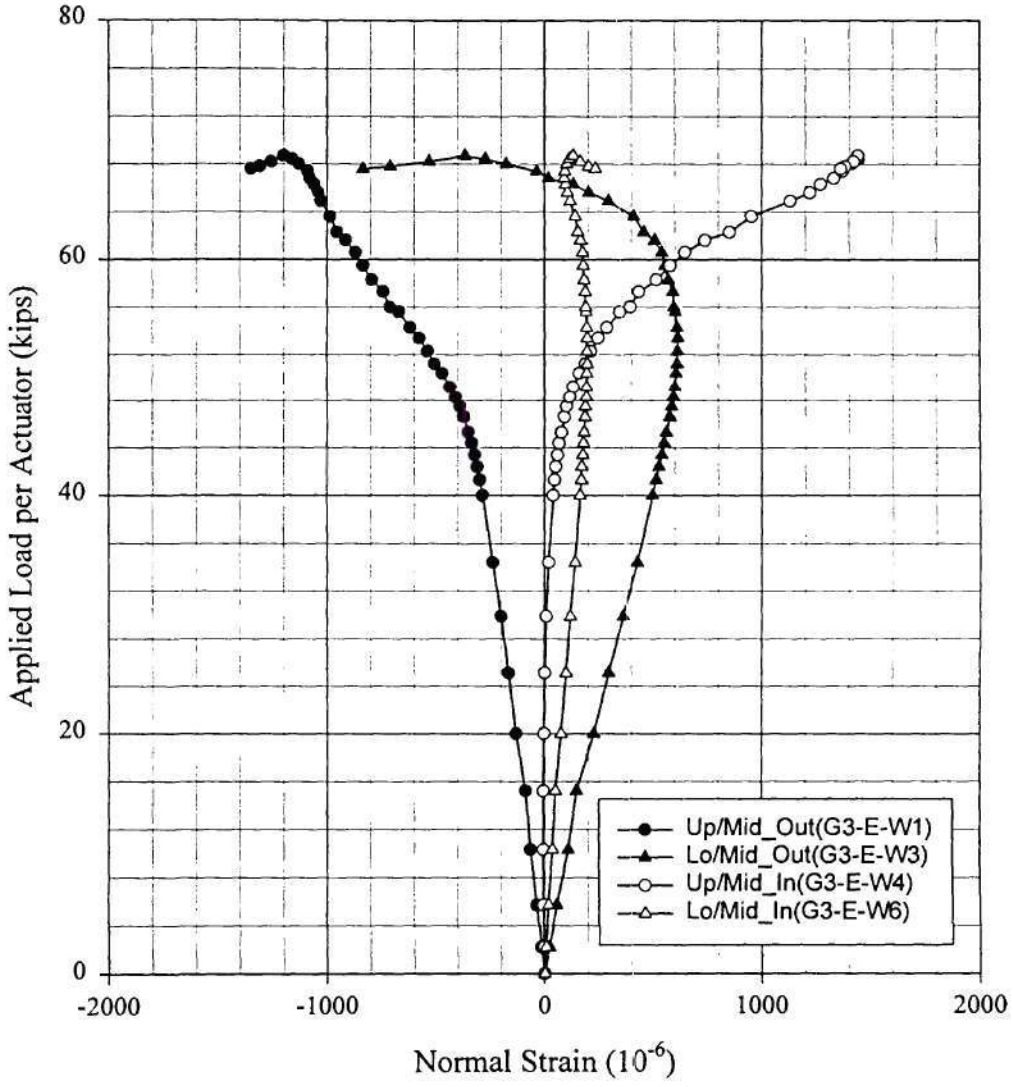

Test(9-30-99) for B5
Normal Strain of the Top Flange at the Location G3_E

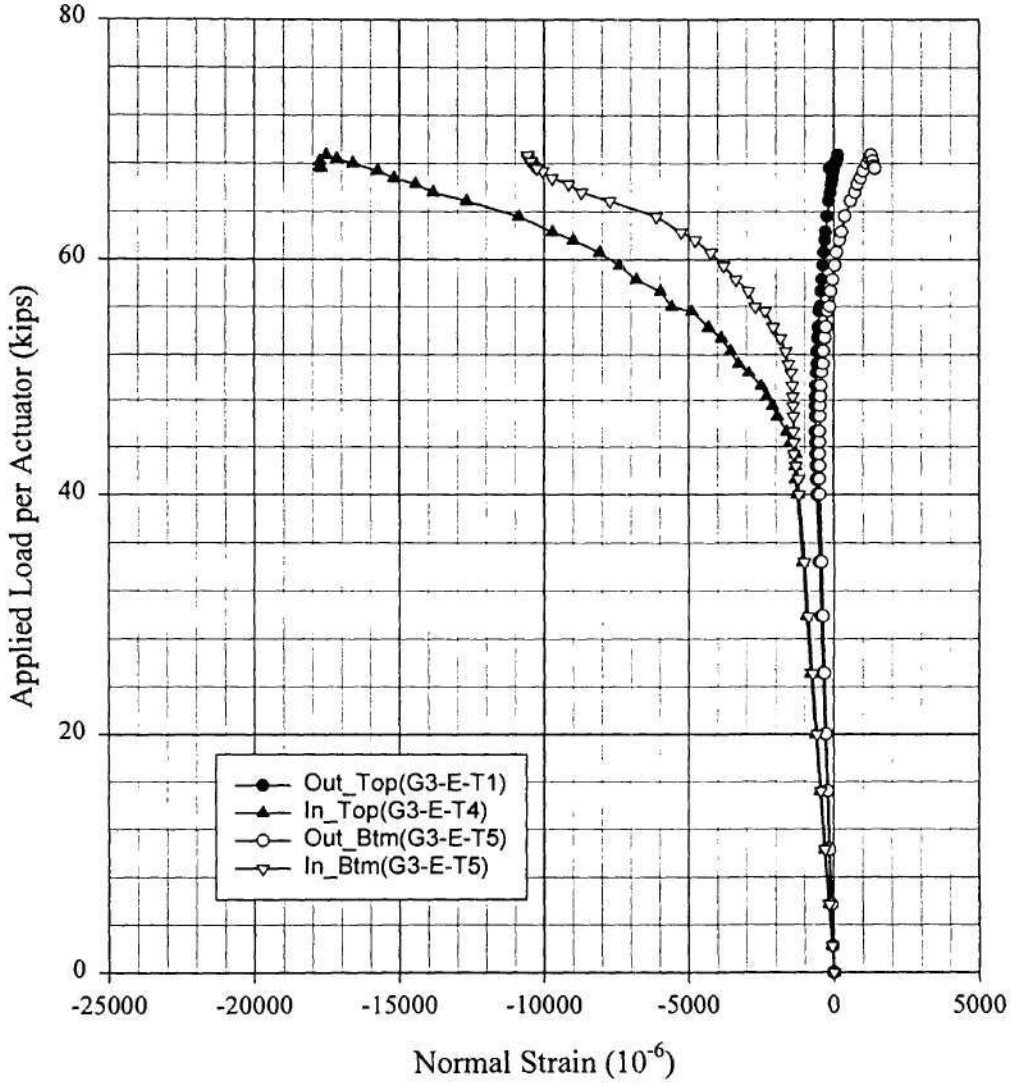

Test(9-30-99) for B5
Normal Strain of the Bottom Flange at the Location G3_E

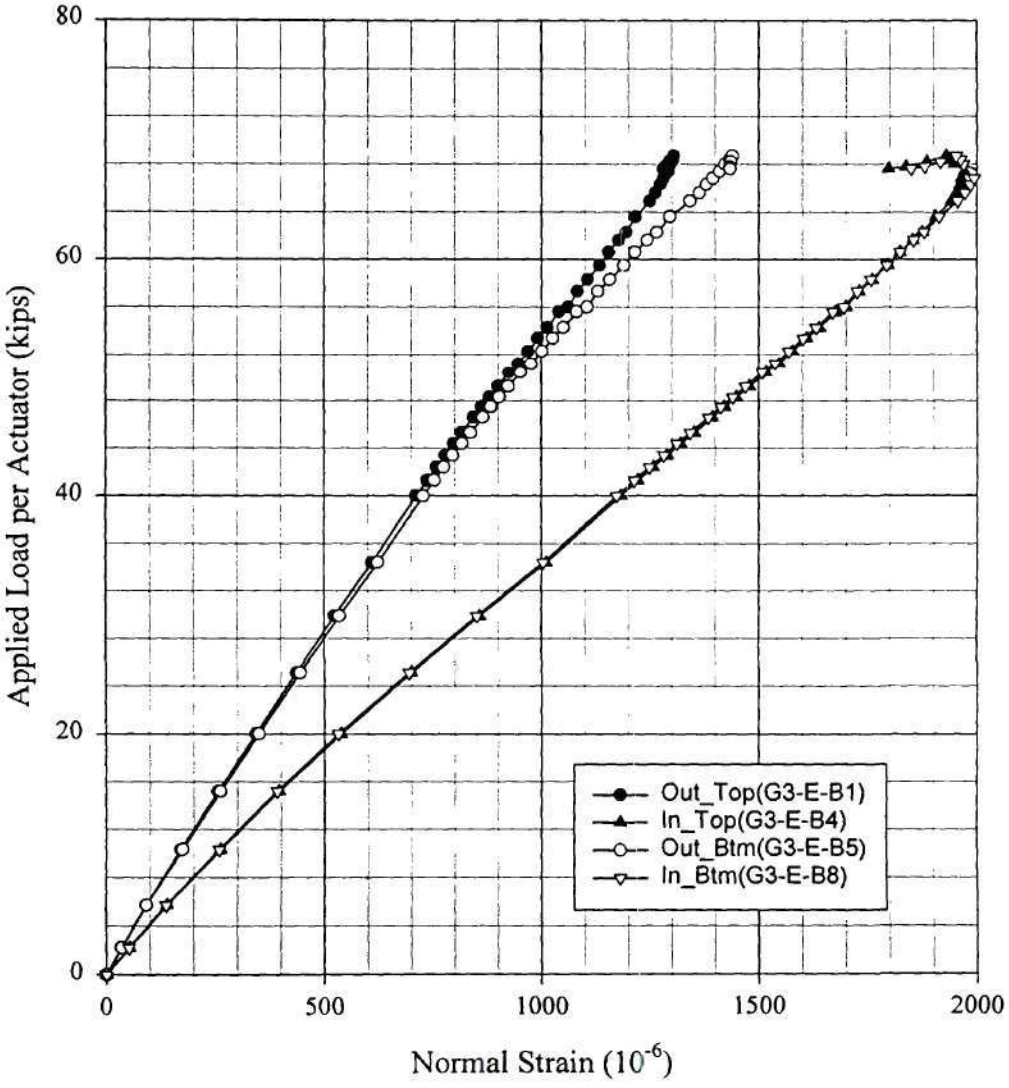

Comparison Between Analysis(B6h_3) and Test(8-26-99) for B6
Vertical Reactions at the East Supports

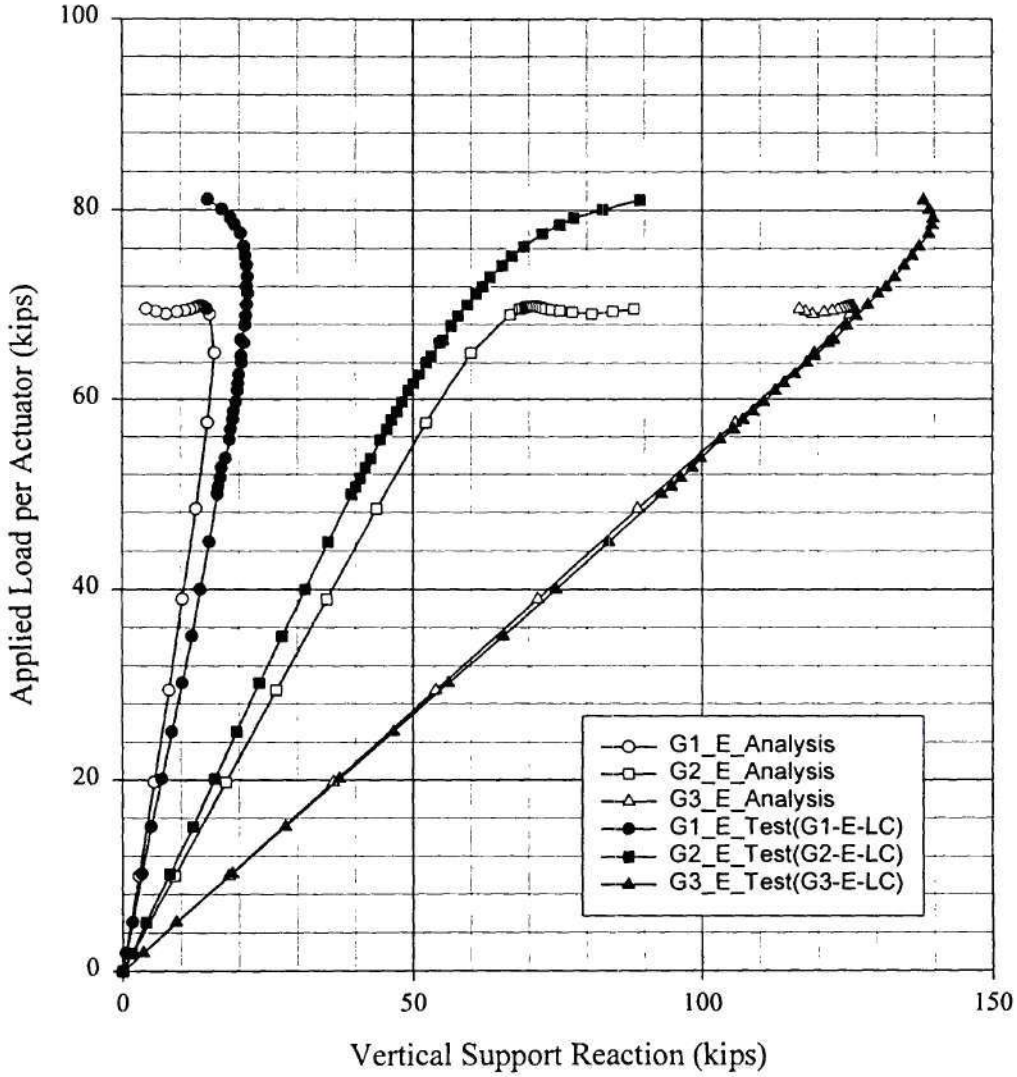

Comparison Between Analysis(B6h_3) and Test(8-26-99) for B6
Vertical Reactions at the West Supports

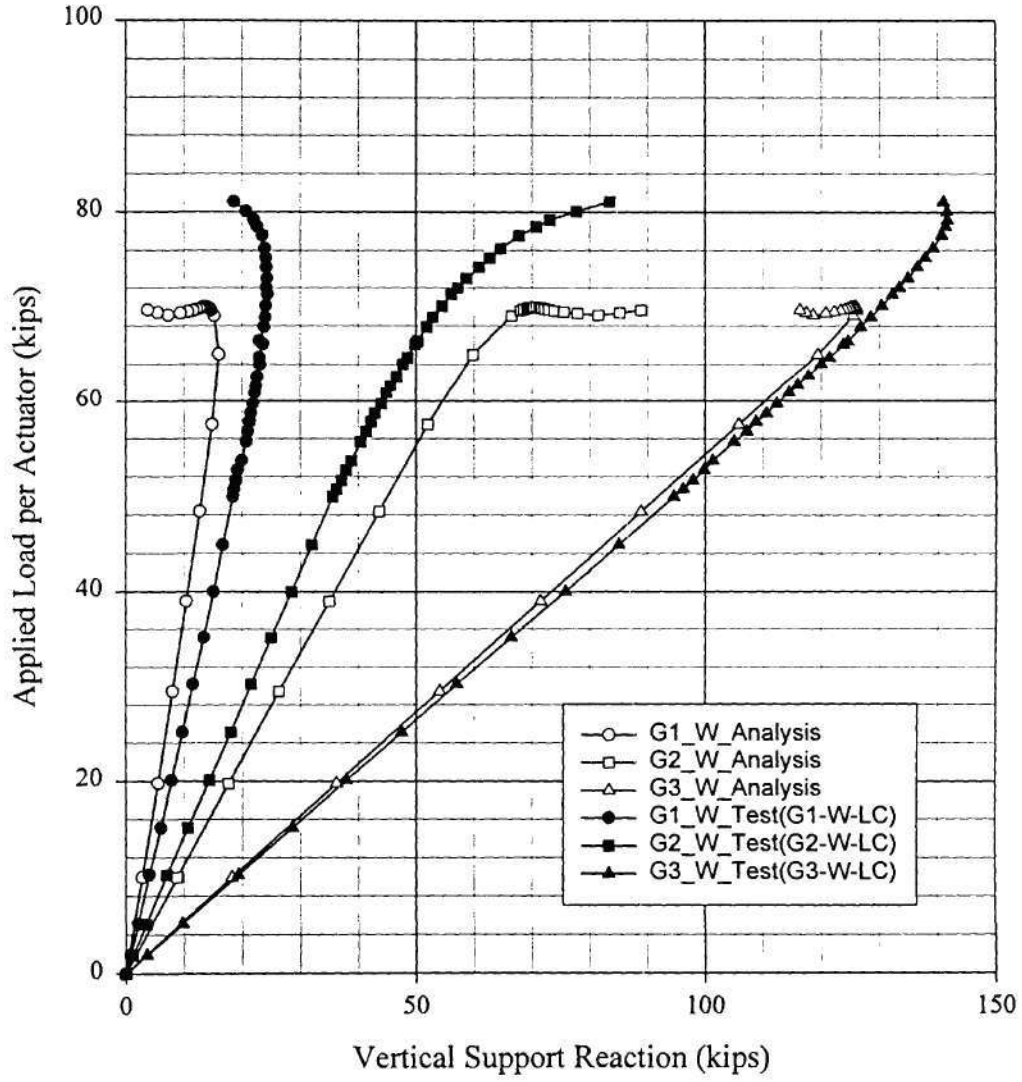

Comparison Between Analysis(B6h_3) and Test(8-26-99) for B6
Vertical Displacement of Bottom Flange (Outside) at Midspan

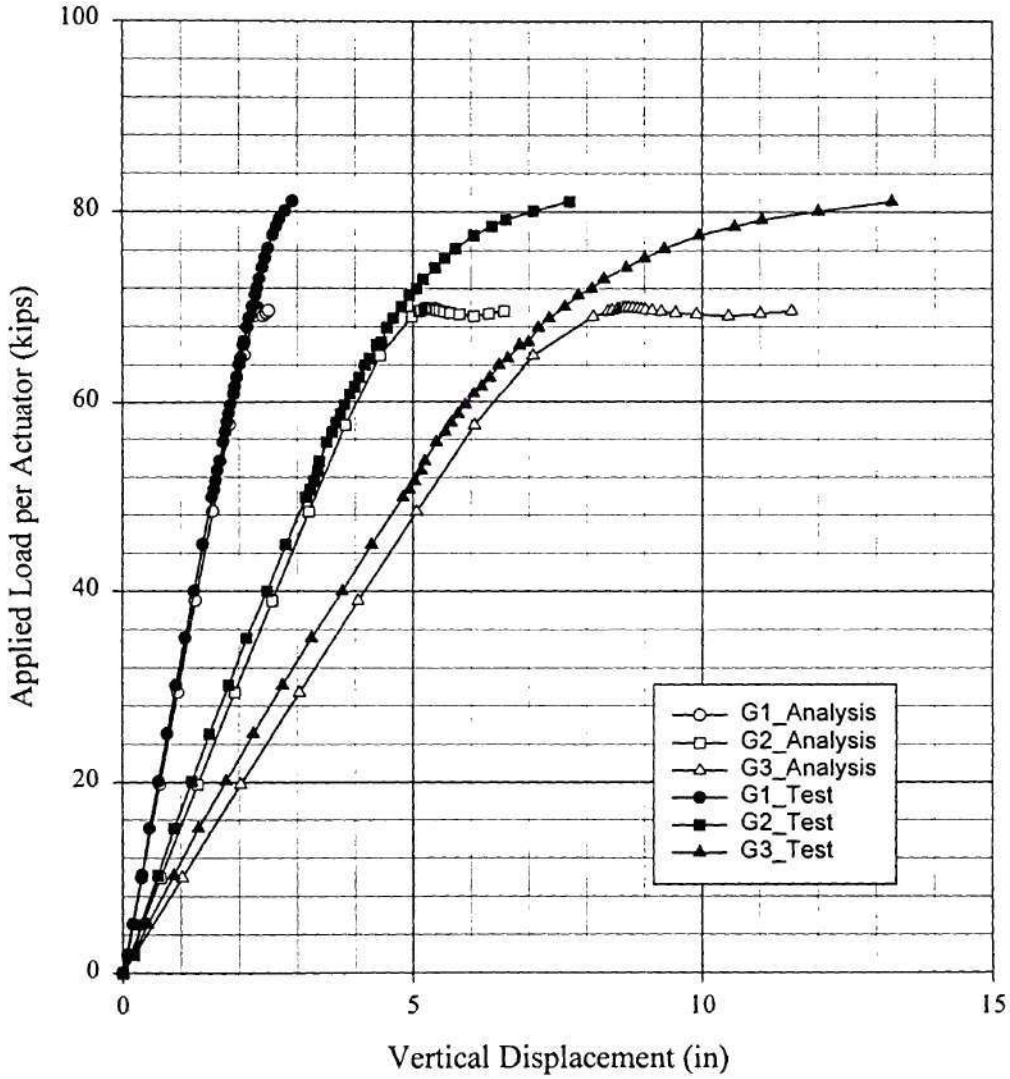

CComparison Between Analysis(B6h_3) and Test(8-26-99) for B6
Radial Displacement of Top Flange (Outside) at Midspan

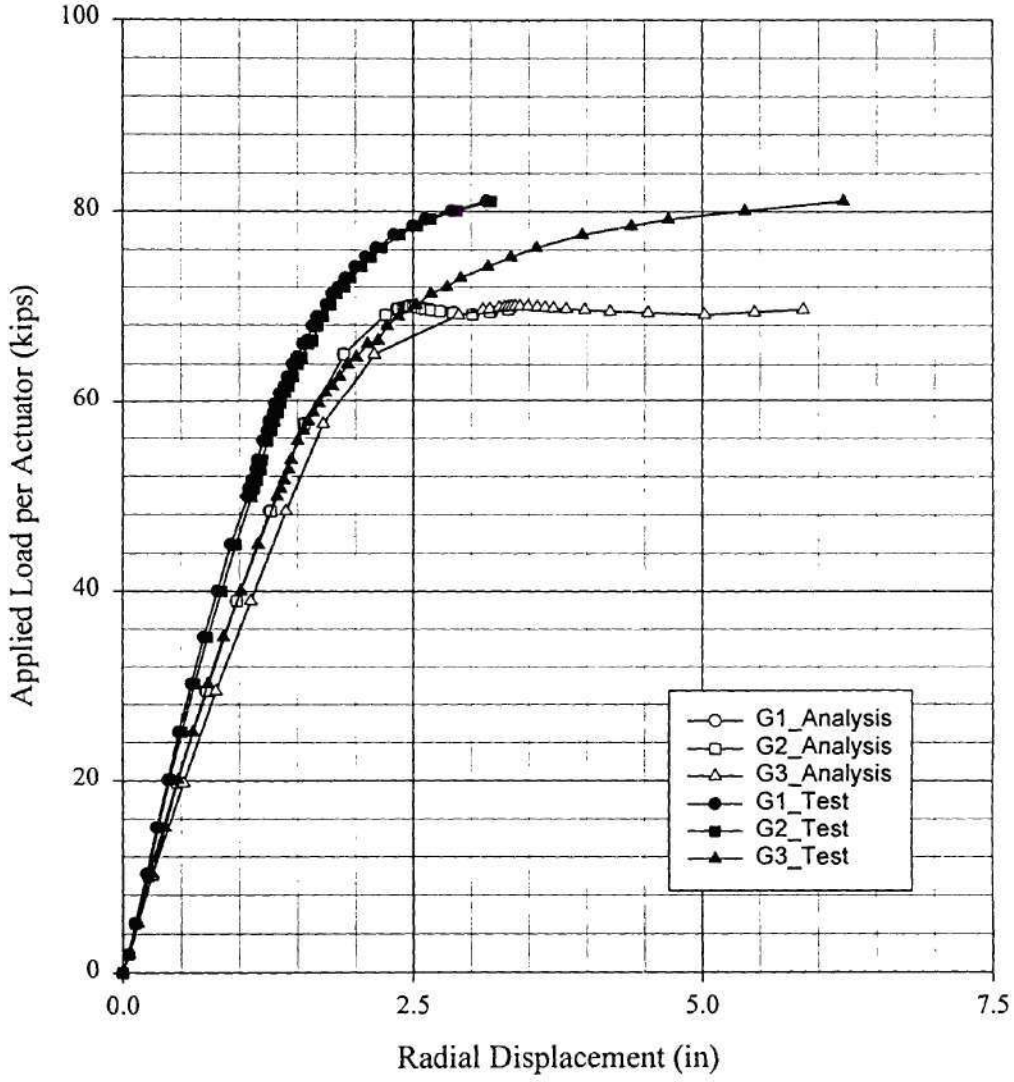

Comparison Between Analysis(B6h_3) and Test(8-26-99) for B6
Radial Displacement of Bottom Flange (Outside) at Midspan

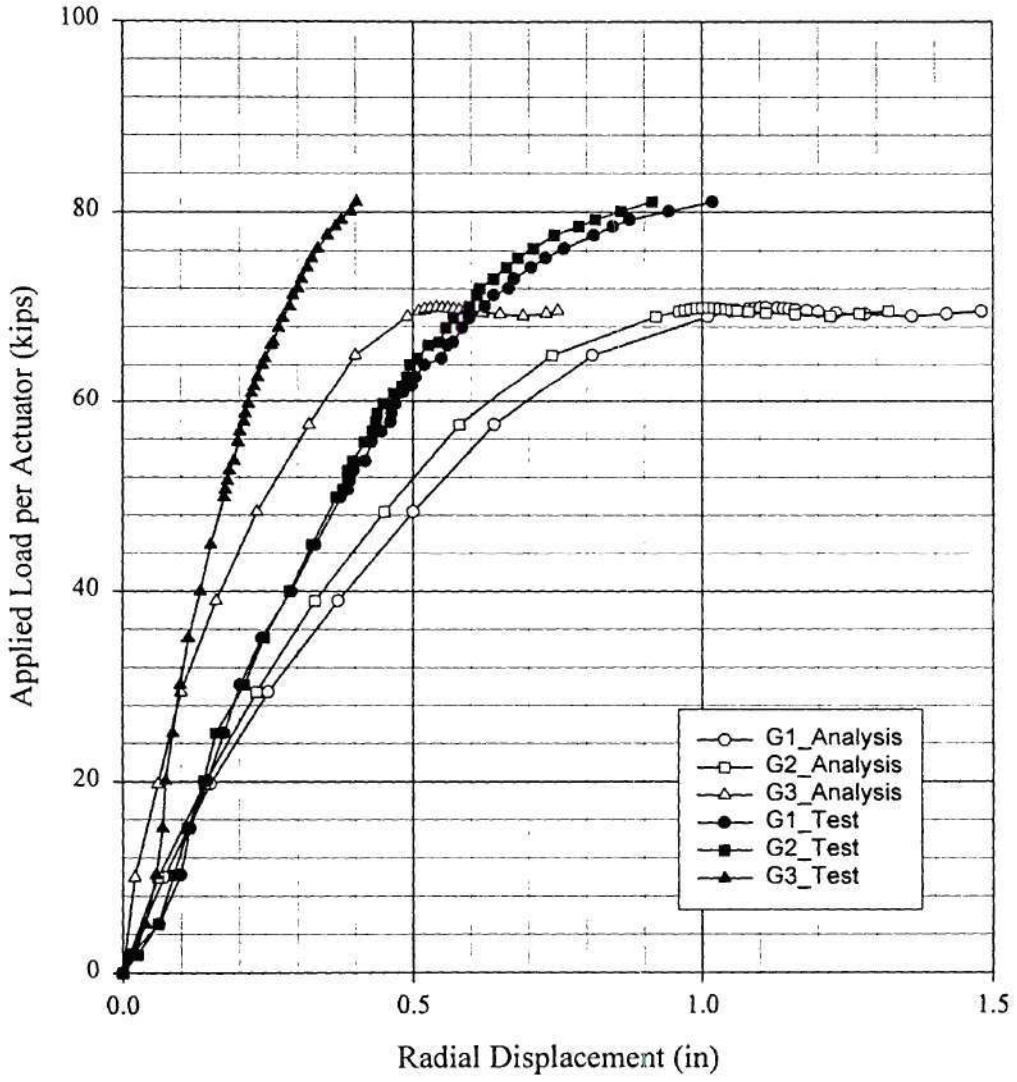

Comparison Between Analysis(B6h_3) and Test(8-26-99) for B6
Axial Force of Cross Frame at 6R Between G2 and G3

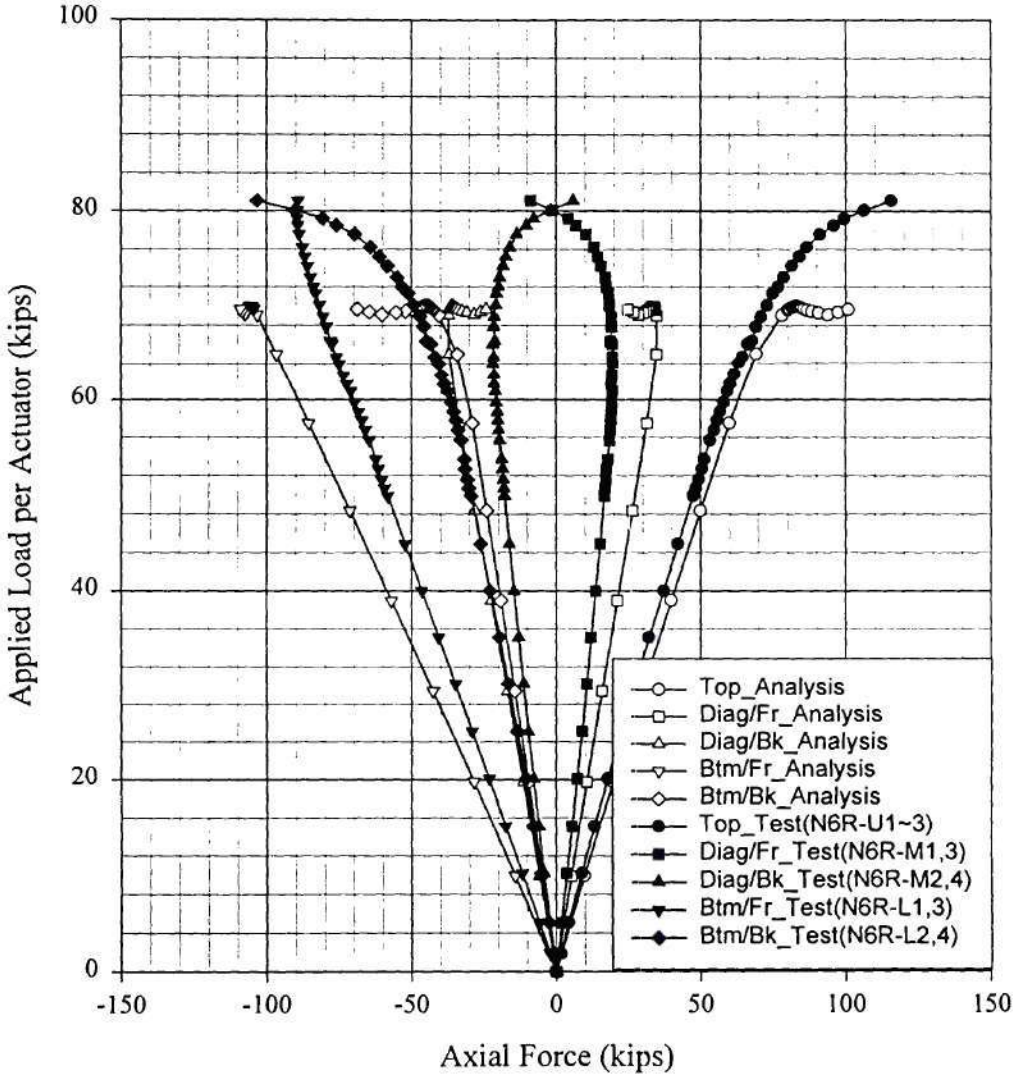

Comparison Between Analysis(B6h_3) and Test(8-26-99) for B6
Axial Force of Cross Frame at 6L Between G2 and G3

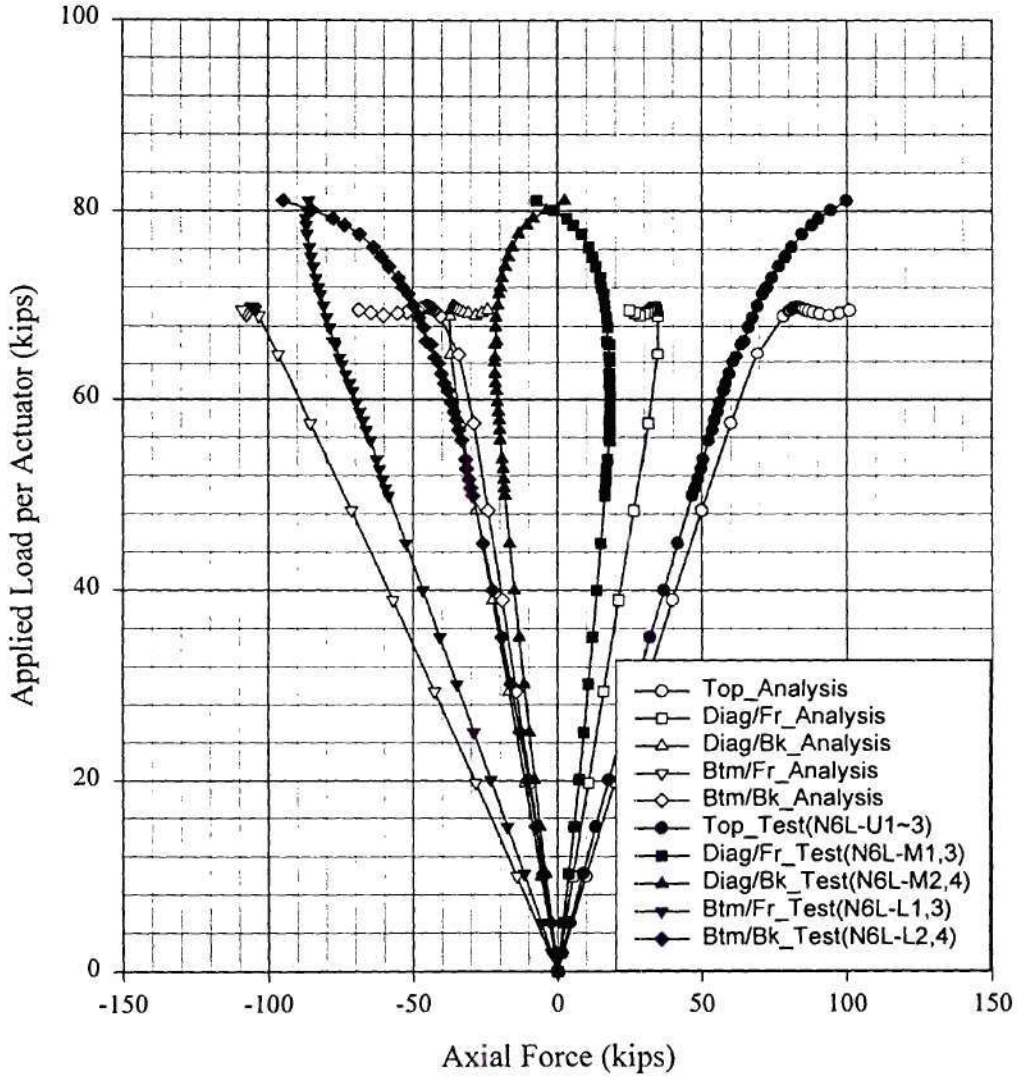

Comparison Between Analysis(B6h_3) and Test(8-26-99) for B6
Bending Moment at Midspan

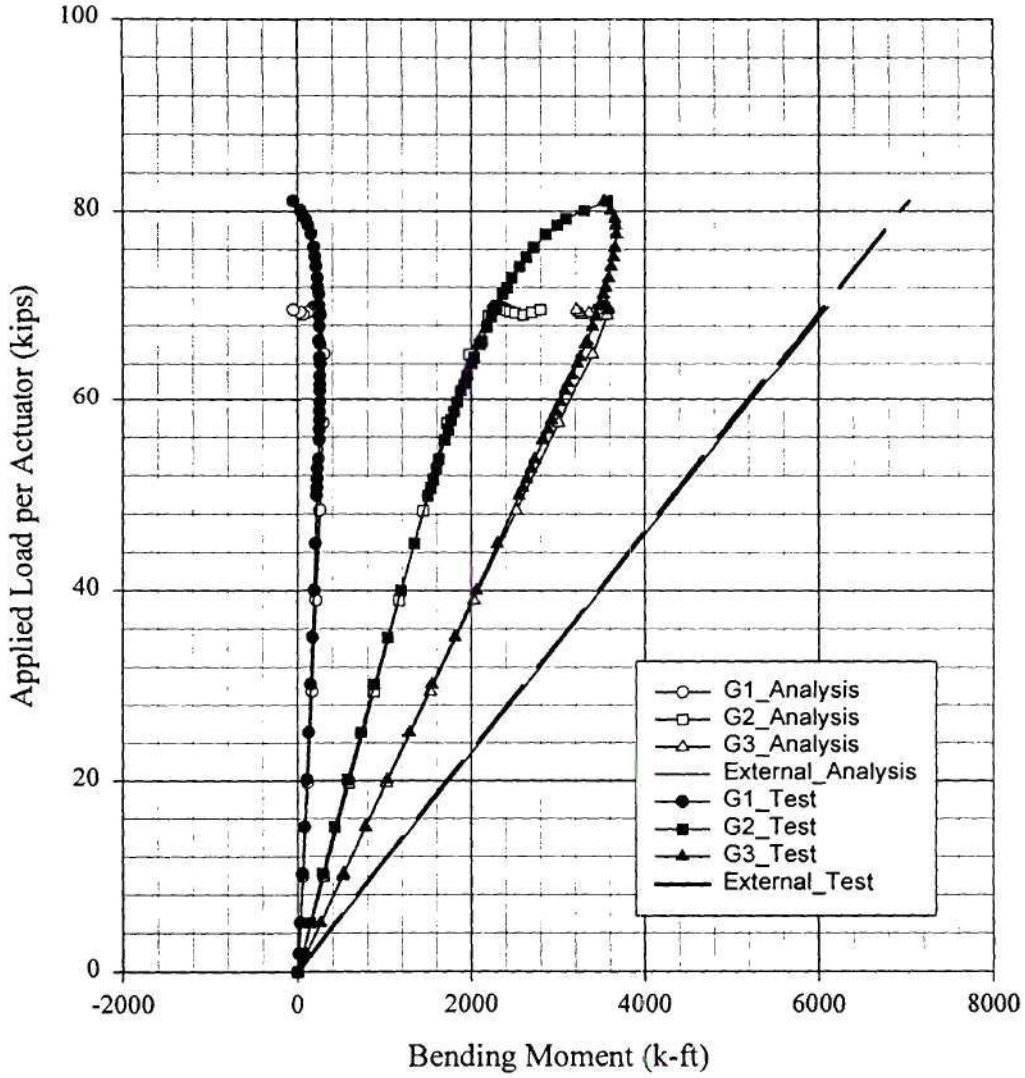

Comparison Between Analysis(B6h_3) and Test(8-26-99) for B6
Normal Strain of the Web Inside at the Location G1_B

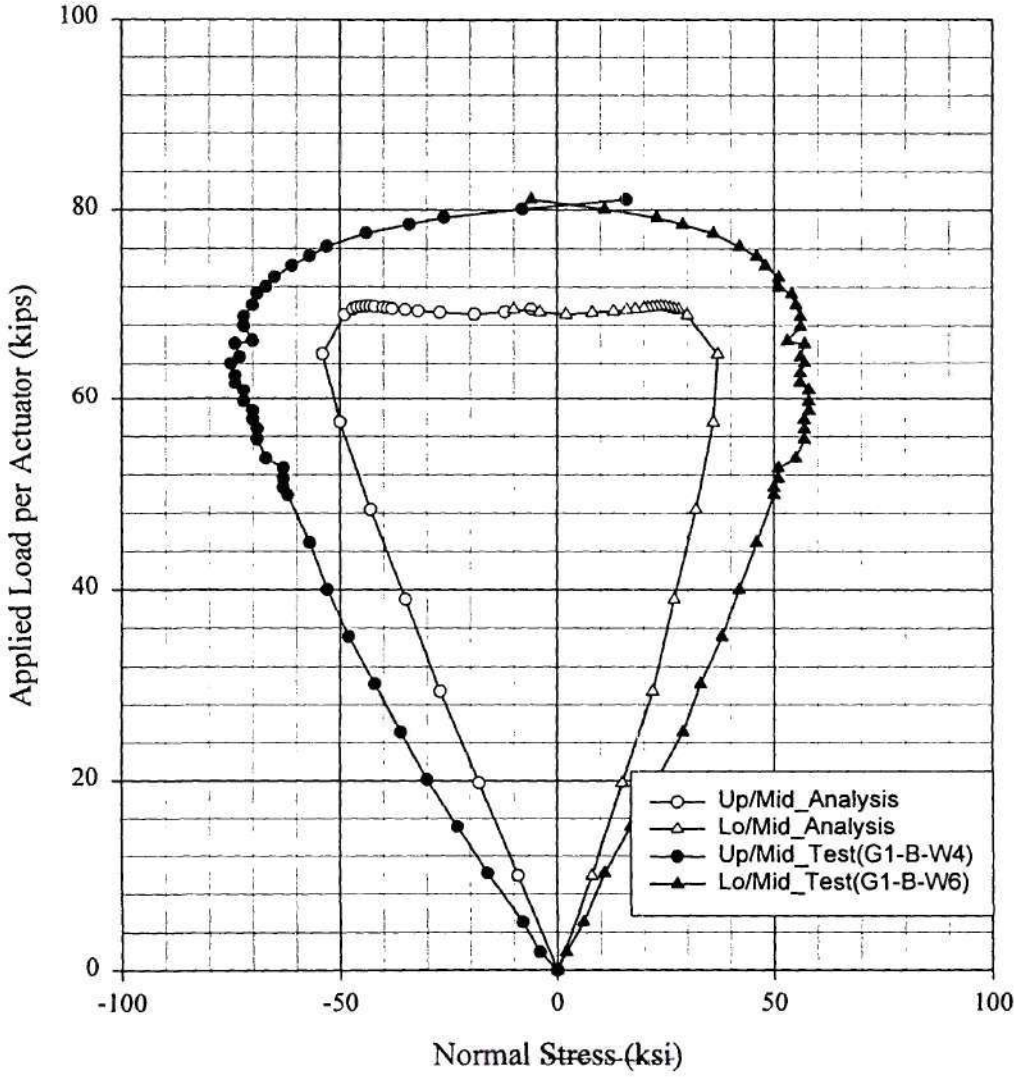

Comparison Between Analysis(B6h_3) and Test(8-26-99) for B6
Normal Strain of the Top Flange Topside at the Location G1_B

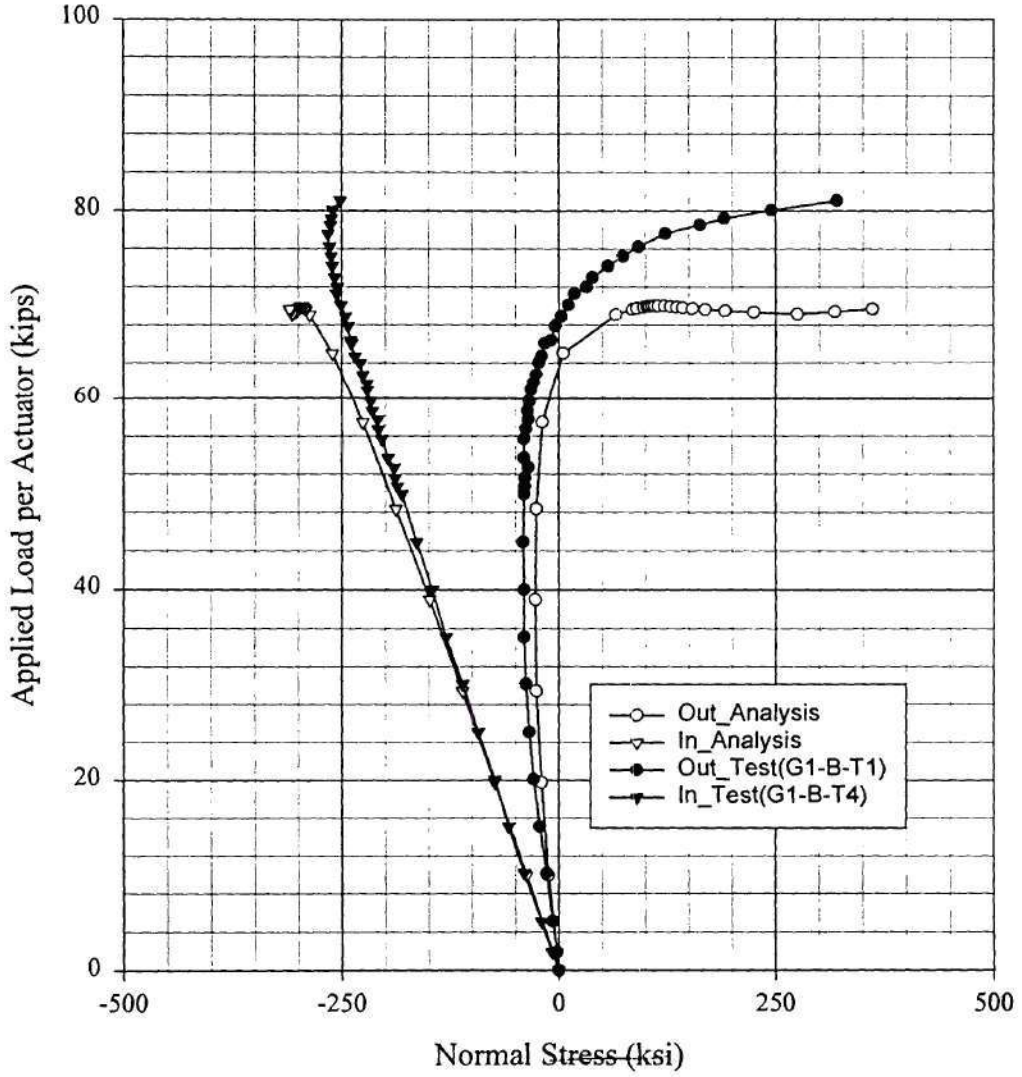

Comparison Between Analysis(B6h_3) and Test(8-26-99) for B6
Normal Strain of the Top Flange Btmside at the Location G1_B

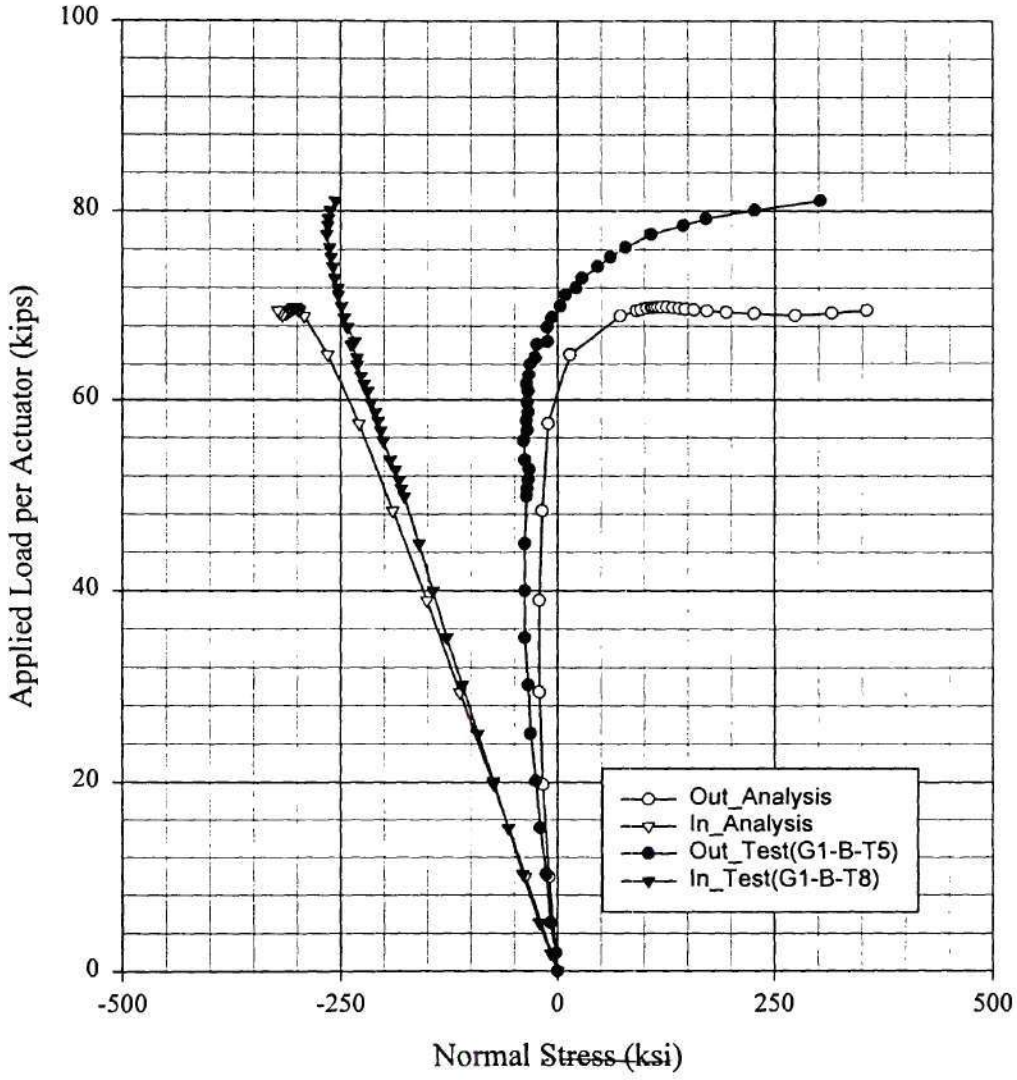

Comparison Between Analysis(B6h_3) and Test(8-26-99) for B6
Normal Strain of the Btm Flange Topside at the Location G1_B

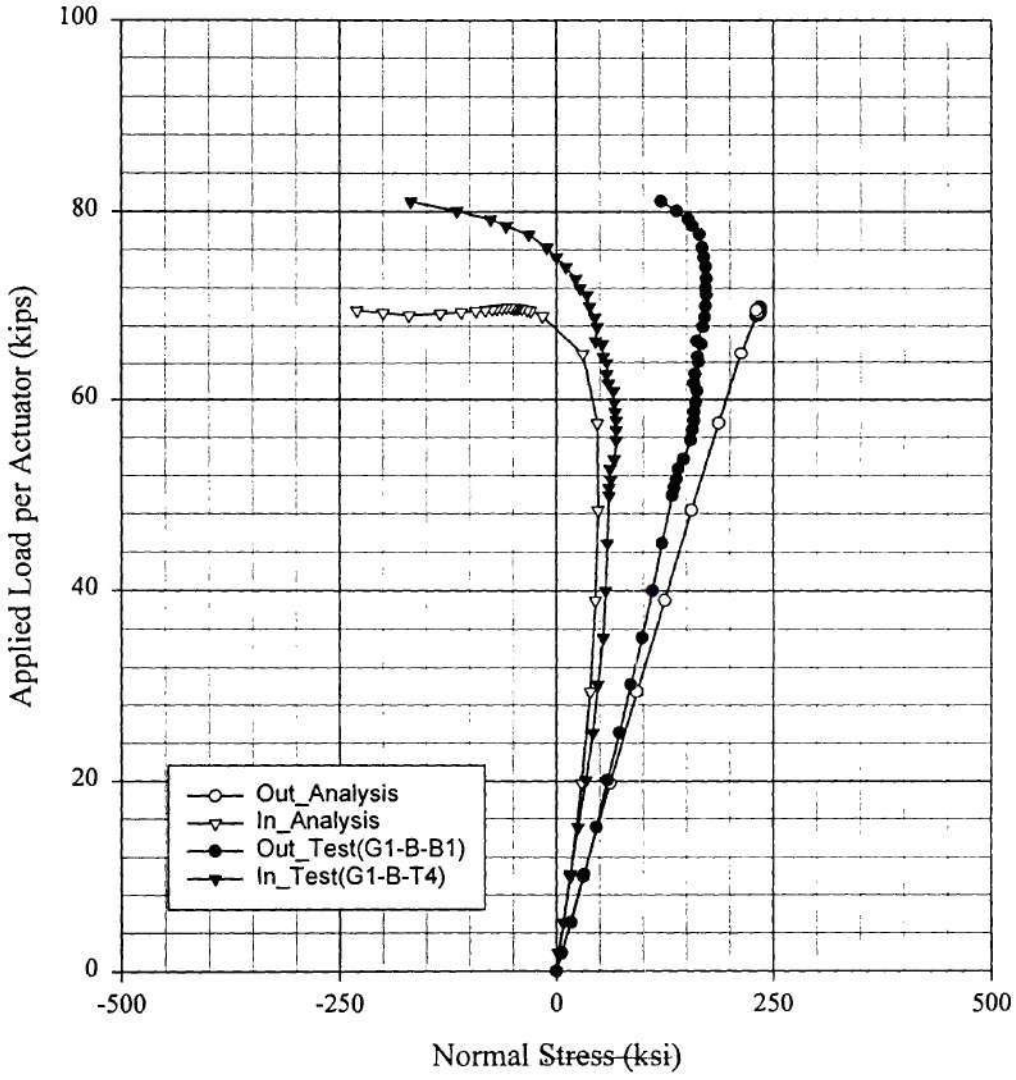

Comparison Between Analysis(B6h_3) and Test(8-26-99) for B6
Normal Strain of the Btm Flange Btmside at the Location G1_B

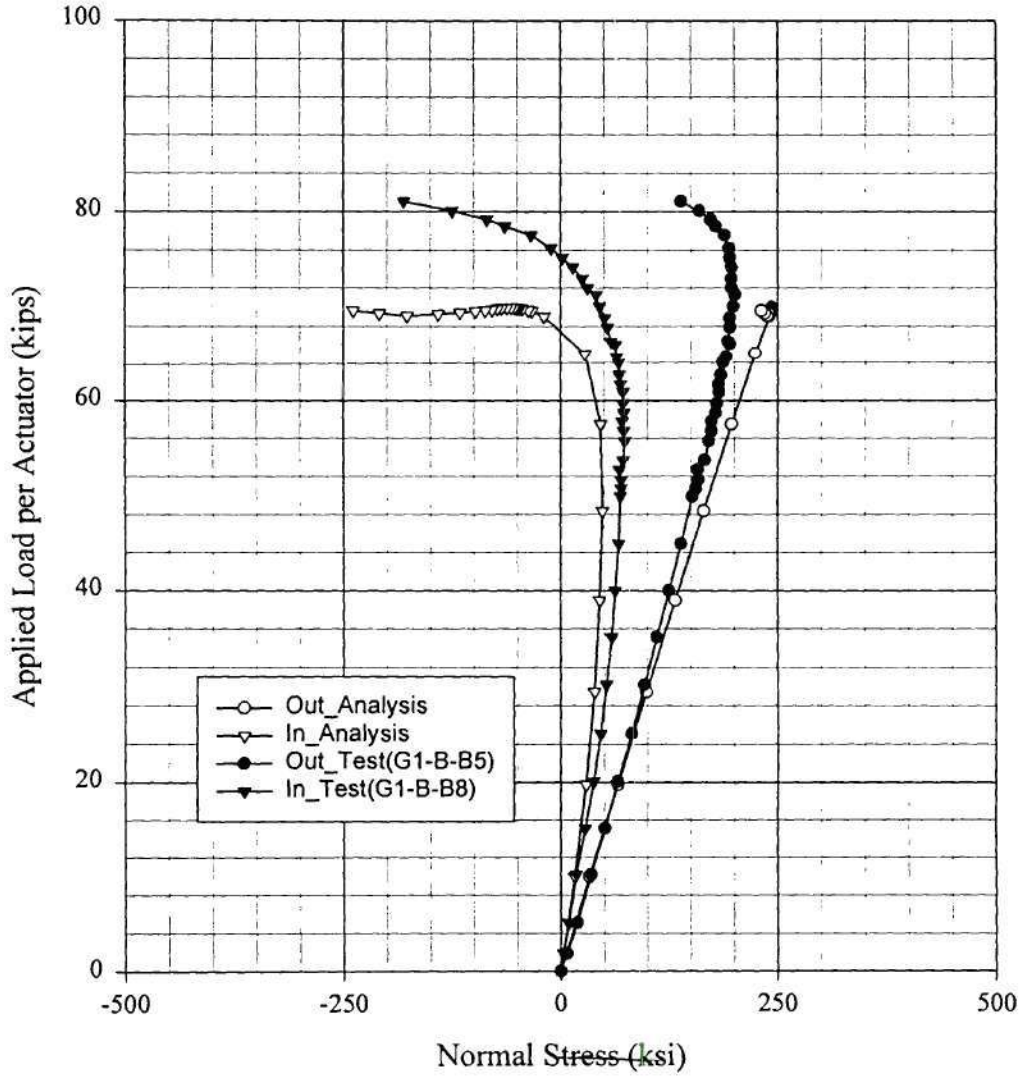

Comparison Between Analysis(B6h_3) and Test(8-26-99) for B6
Normal Strain of the Web Inside at the Location G2_B

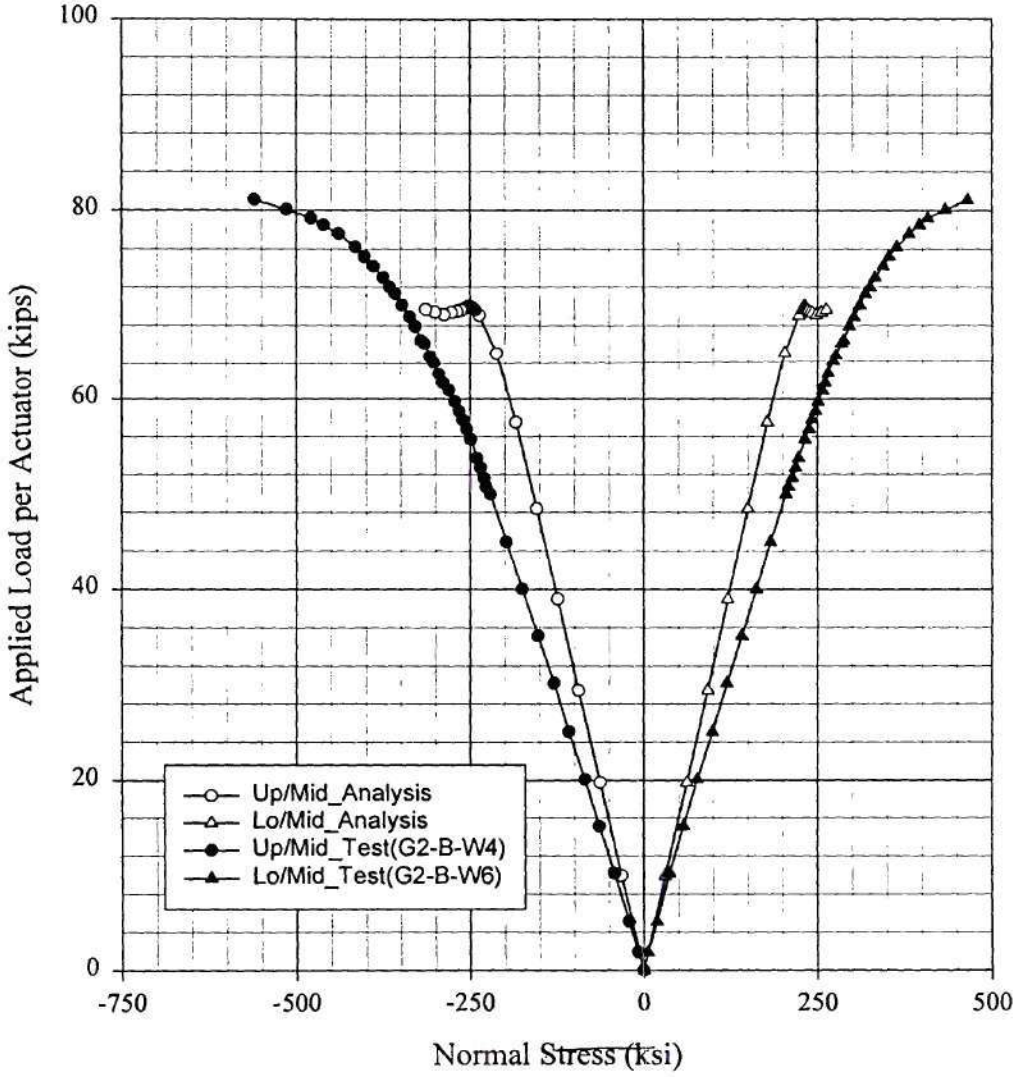

Comparison Between Analysis(B6h_3) and Test(8-26-99) for B6
Normal Strain of the Top Flange Topside at the Location G2_B

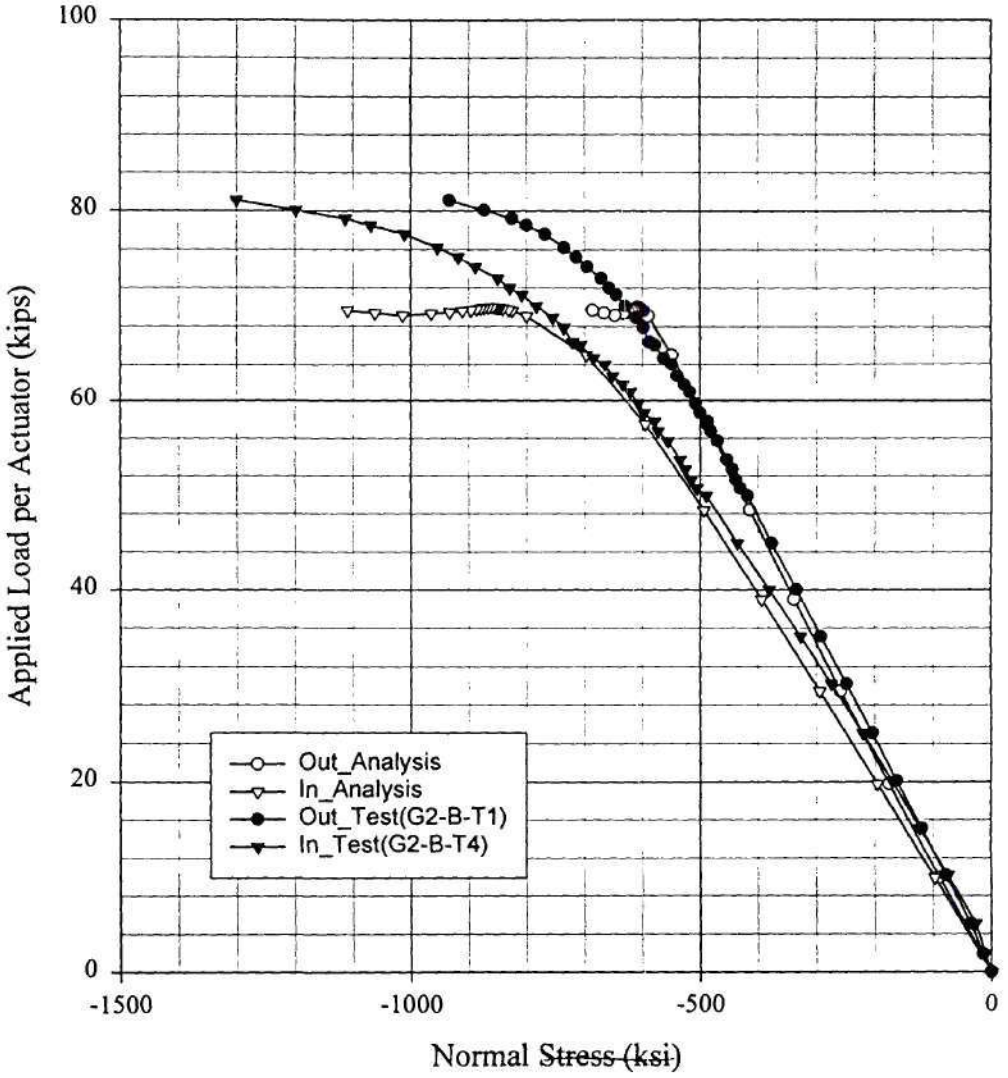

Comparison Between Analysis(B6h_3) and Test(8-26-99) for B6
Normal Strain of the Top Flange Btmside at the Location G2_B

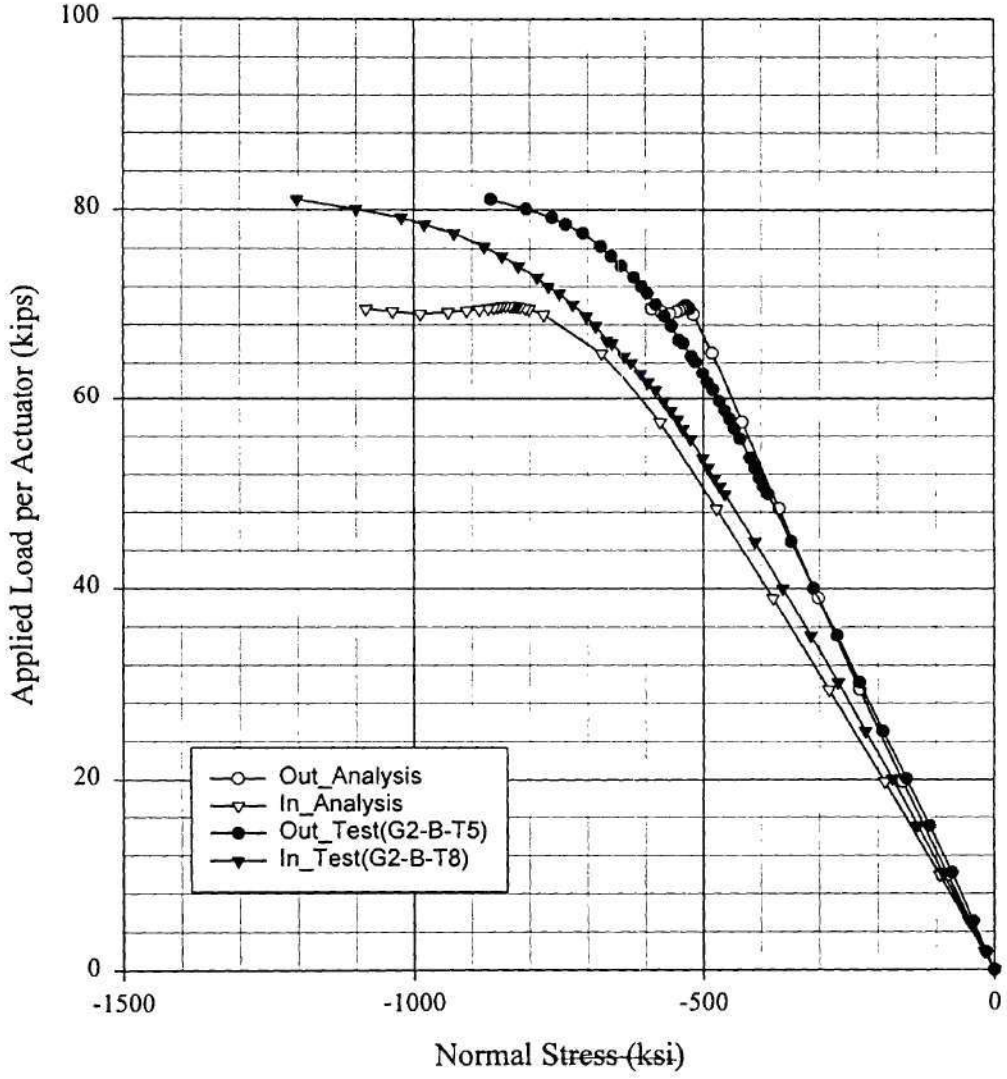

Comparison Between Analysis(B6h_3) and Test(8-26-99) for B6
Normal Strain of the Btm Flange Topside at the Location G2_B

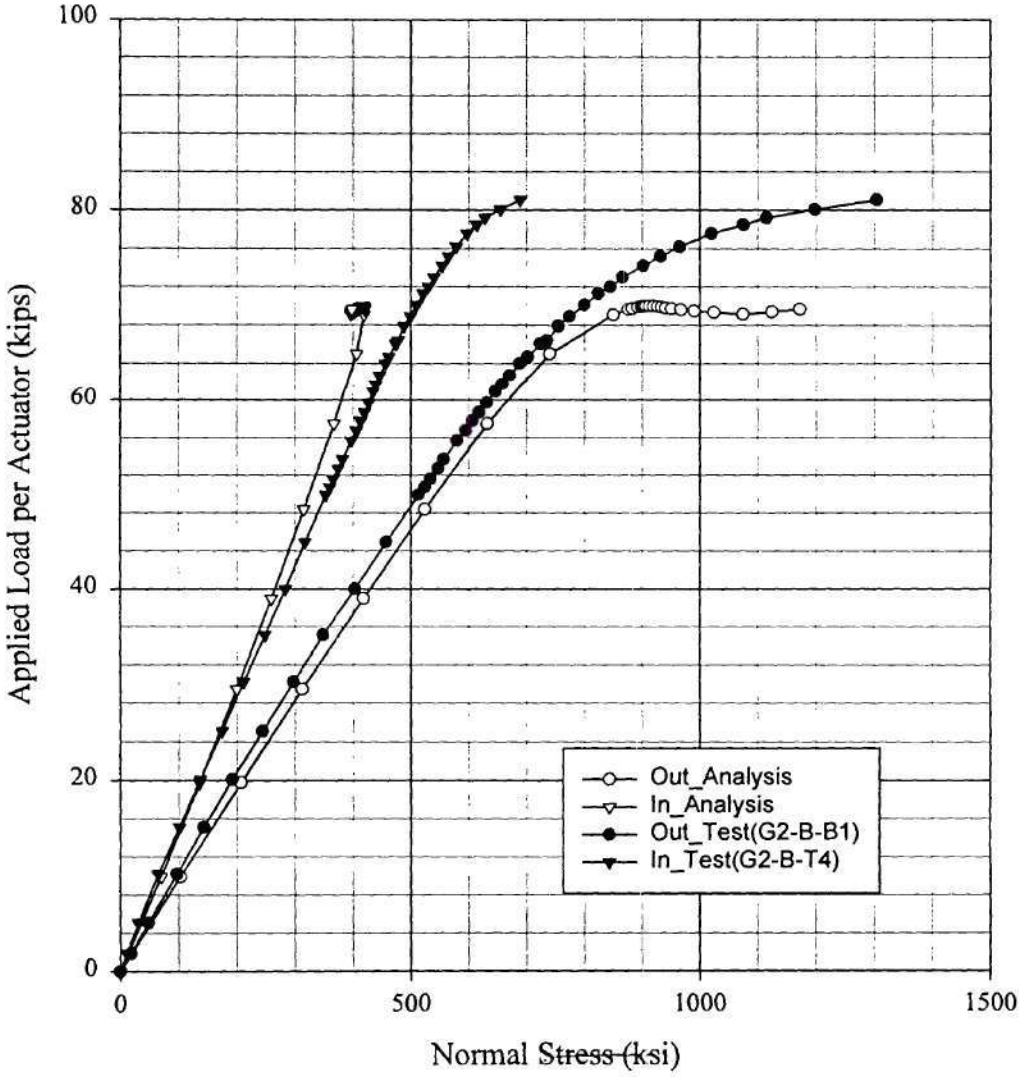

Comparison Between Analysis(B6h_3) and Test(8-26-99) for B6
Normal Strain of the Btm Flange Btmside at the Location G2_B

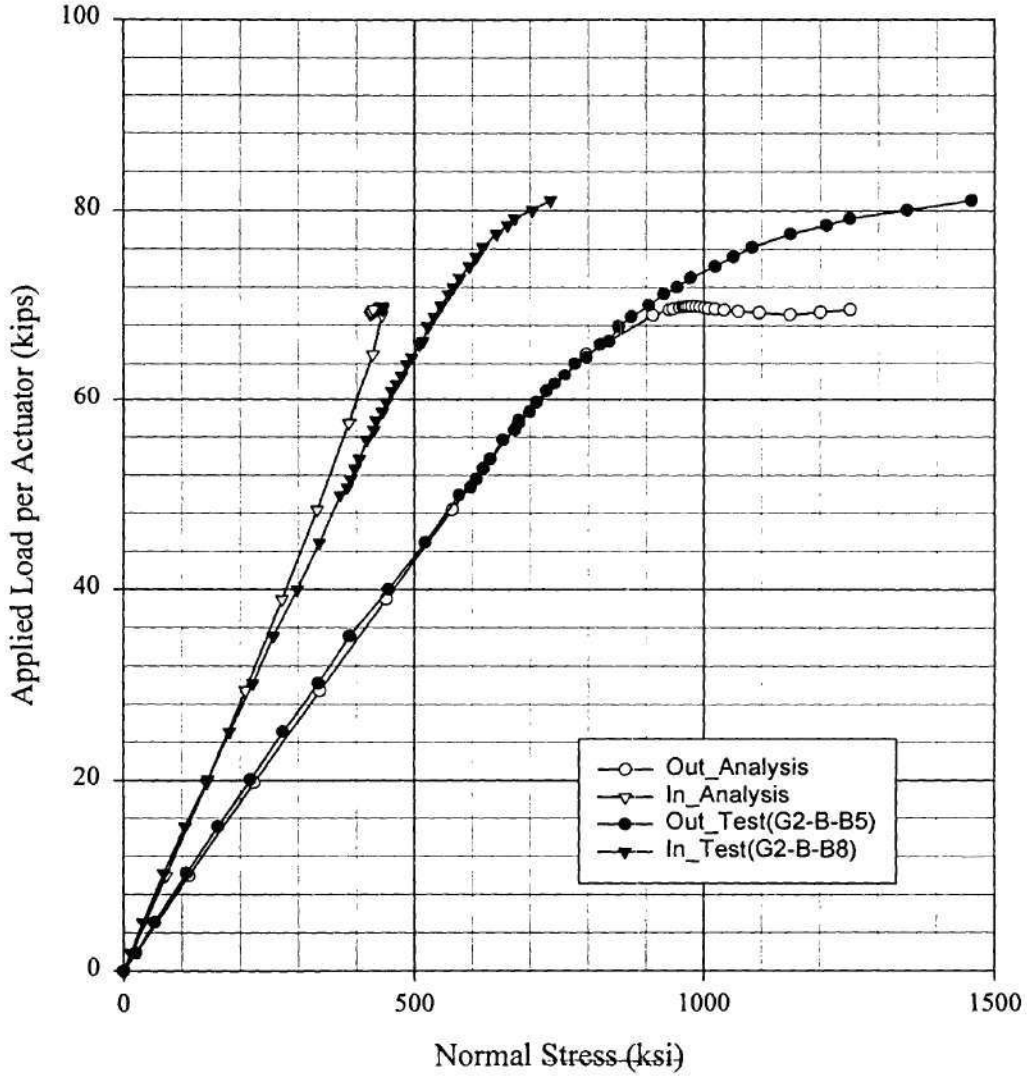

Comparison Between Analysis(B6h_3) and Test(8-26-99) for B6
Normal Strain of the Web Inside at the Location G3_E

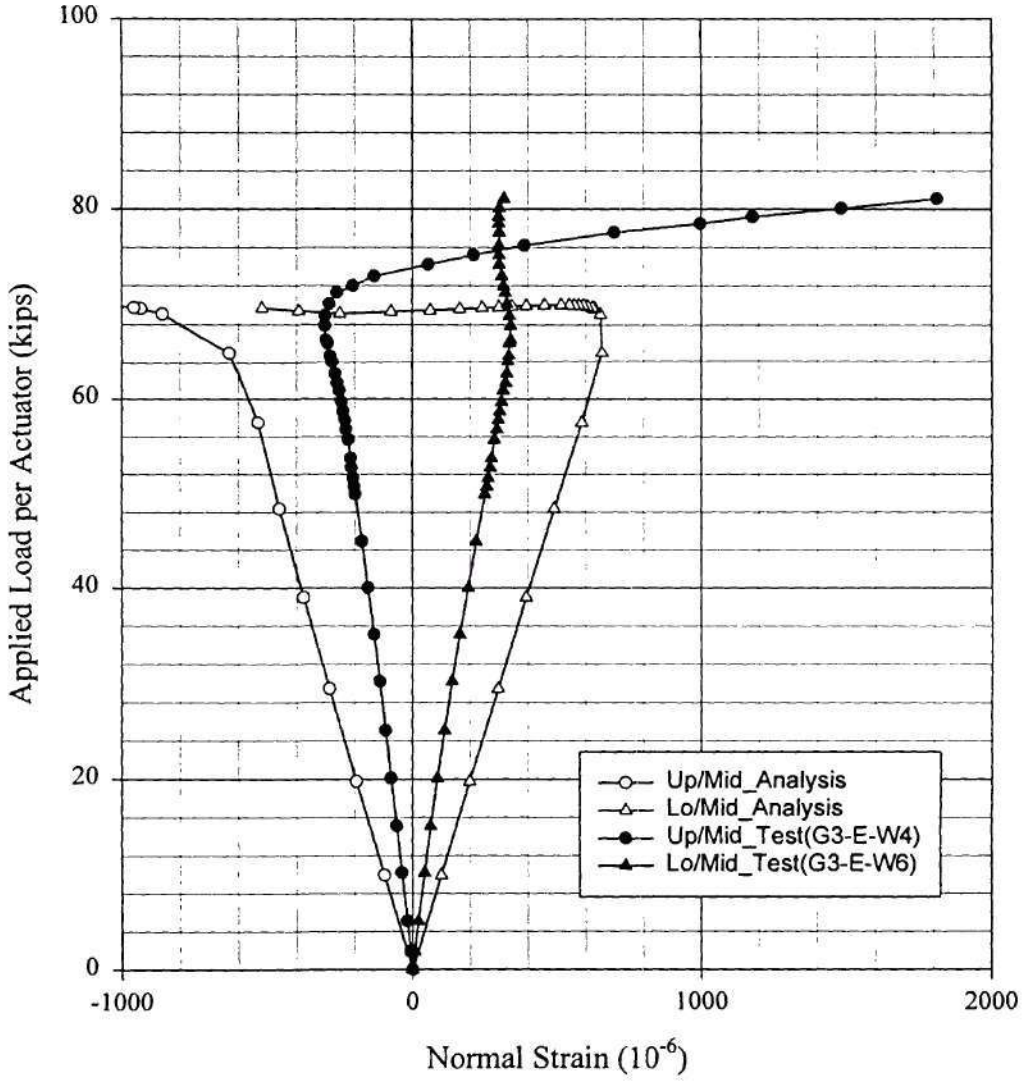

Comparison Between Analysis(B6h_3) and Test(8-26-99) for B6
Normal Strain of the Web Outside at the Location G3_E

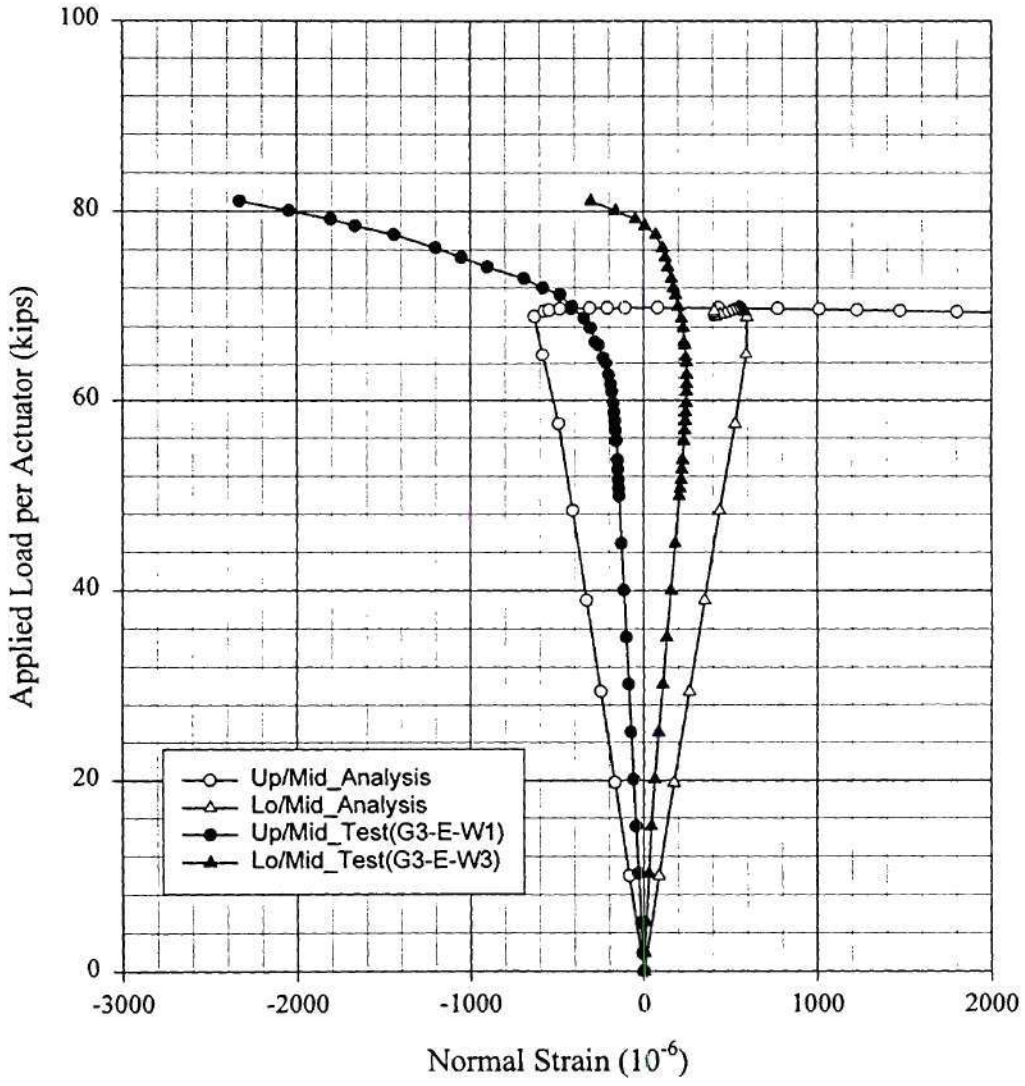

Comparison Between Analysis(B6h_3) and Test(8-26-99) for B6
Normal Strain of the Top Flange Topside at the Location G3_E

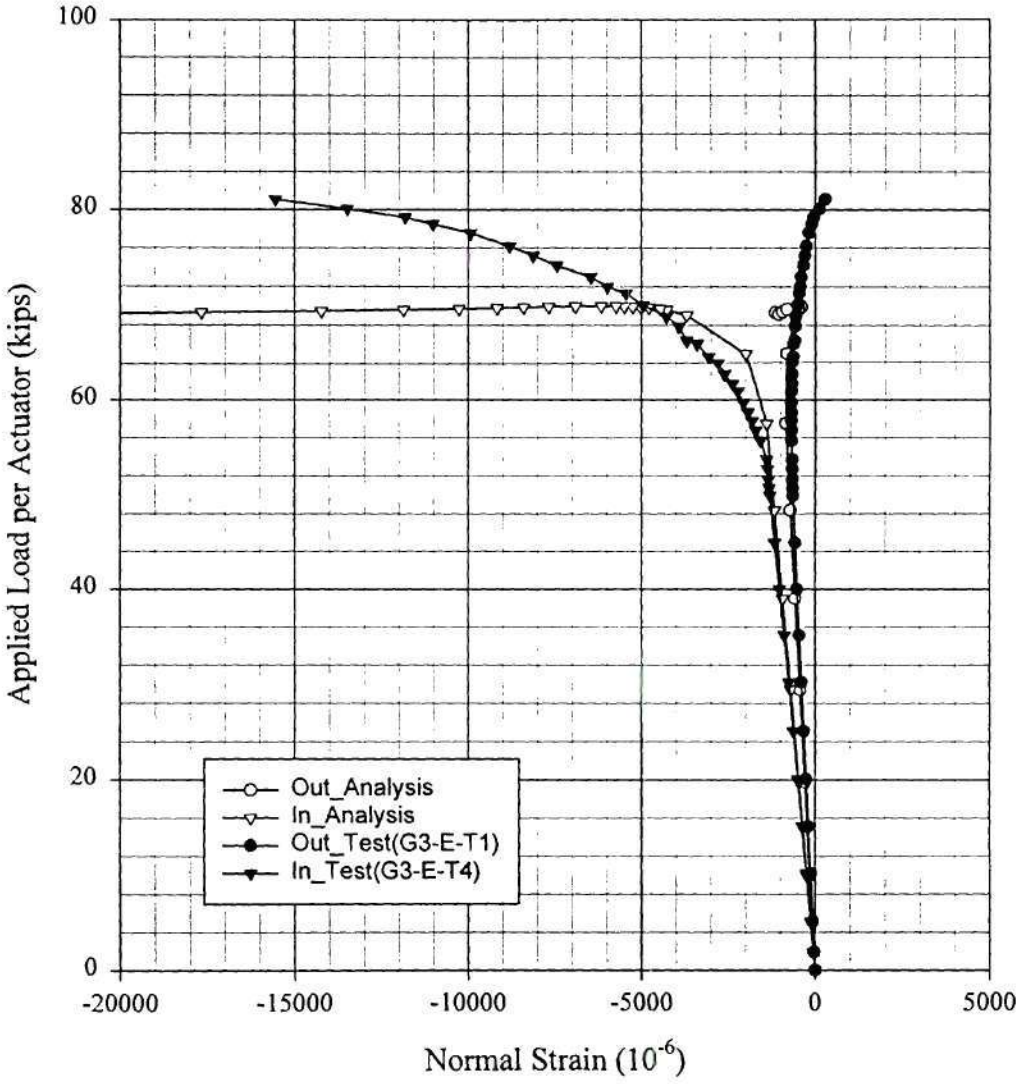

Comparison Between Analysis(B6h_3) and Test(8-26-99) for B6
Normal Strain of the Top Flange Btmside at the Location G3_E

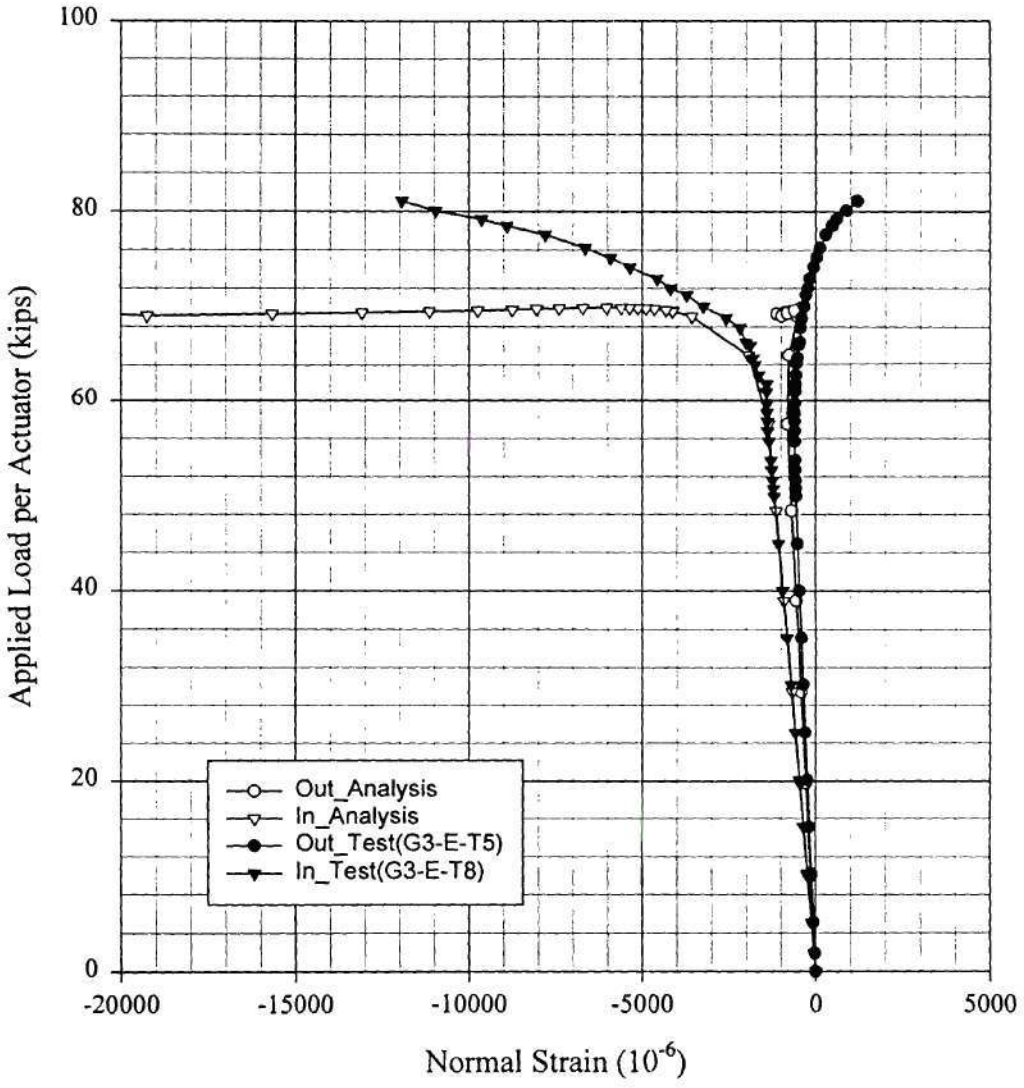

Comparison Between Analysis(B6h_3) and Test(8-26-99) for B6
Normal Strain of the Top Flange Btmside at the Location G3_E

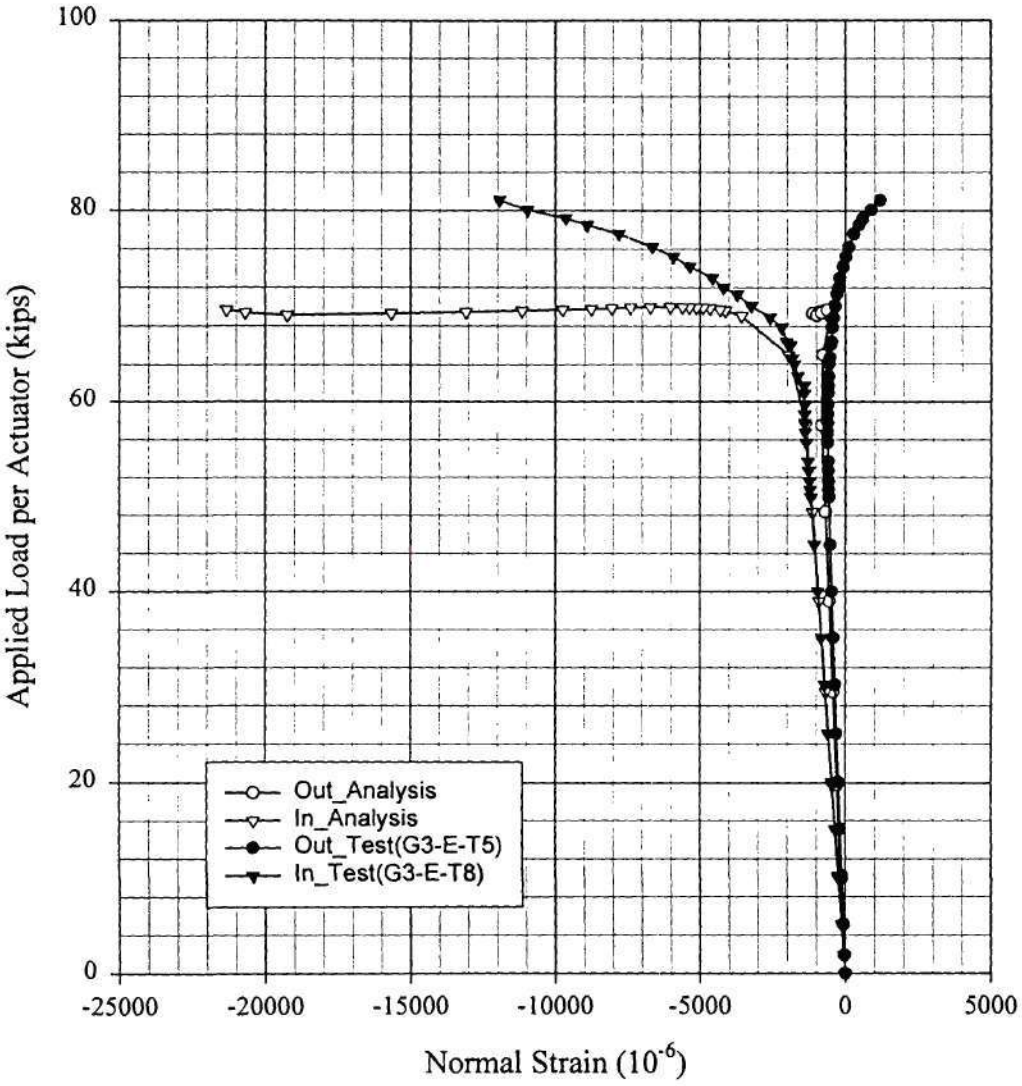

Comparison Between Analysis(B6h_3) and Test(8-26-99) for B6
Normal Strain of the Btm Flange Topside at the Location G3_E

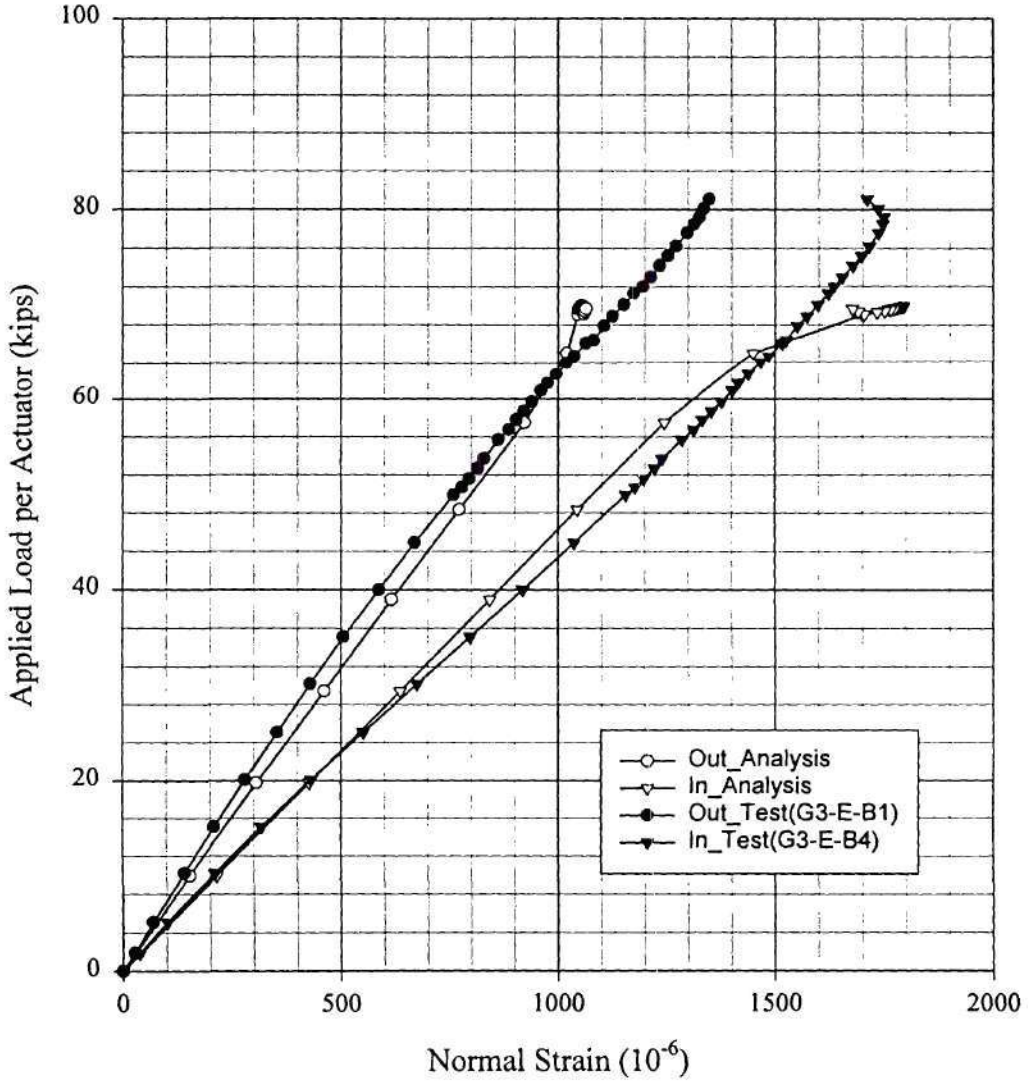

Comparison Between Analysis(B6h_3) and Test(8-26-99) for B6
Normal Strain of the Btm Flange Btmside at the Location G3_E

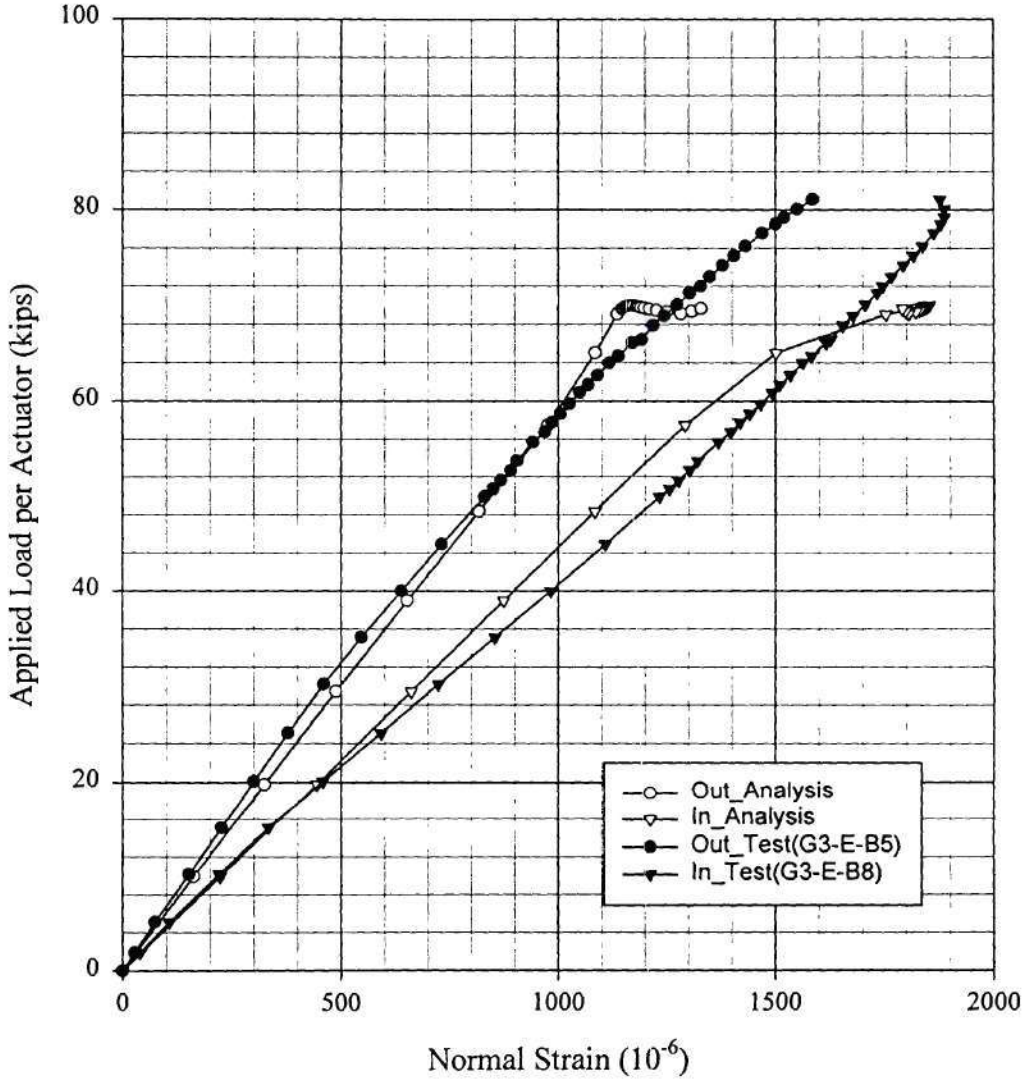

Test(8-26-99) for B6
Normal Strain of the Bottom Flange at the Location G3_E